Chemical and dynamical study towards the UC H$_{\rm II}$ region Monoceros R2

Ph.D. Thesis

Sandra Patricia Treviño Morales

Universidad de Granada

Academic advisors:
Carsten Kramer[1] & Asunción Fuente Juan[2]

[1]Institut de Radioastronomie Millimétrique
Granada, Spain

[2]Observatorio Astronómico Nacional
Madrid, Spain

Submitted: November 2015

Programa Oficial de Doctorado en Físicas y Matemáticas

2013–2015

Assessment committee:

Eduardo Battaner
Departamento de Física Teórica y del Cosmos, Universidad Granada, Spain.

Ute Lisenfeld
Departamento de Física Teórica y del Cosmos, Universidad Granada, Spain.

Javier R. Goicoechea
Instituto de Ciencia de Materiales de Madrid, Universidad Autónoma de Madrid, Spain.

Nicola Maria Schneider
I. Physik. Institut, University of Cologne, Germany.

Jerôme Pety
Institut de Radio Astronomie Millimetrique, France.

Mayra Carolina Osorio Gutiérrez
Instituto de Astrofísica de Andalucía, Spain.

Guillem Josep Anglada Pons
Instituto de Astrofísica de Andalucía, Spain.

Esta tesis está dedicada a Juan Morales Rodríguez...

Quien me enseñó los nombres de los planetas.

Diego no conocía la mar.
Su padre, Santiago Kovadloff, lo llevó a descubrirla.
Viajaron al sur.
Ella, la mar, estaba más allá de los altos médanos, esperando.
Cuando el niño y su padre alcanzaron por fin aquellas cumbres de arena,
después de mucho caminar, la mar estalló ante sus ojos.
Y fue tanta la inmensidad de la mar, y tanto su fulgor, que el niño quedó
mudo de hermosura.
Y cuando por fin consiguió hablar, temblando, tartamudeando, pidió a su
padre:
¡Ayúdame a Mirar!

El Libro de los Abrazos (Eduardo Galeano).

Agradecimientos

Antes de comenzar esta Tesis me gustaría agradecer a las personas que de manera directa o indirecta han contribuido a su realización.

Principalmente quiero agradecer a mis directores de tesis, Carsten y Asunción.

Thank you very much Carsten, for giving me the opportunity to work in IRAM. For the support, the confidence and the advices that you gave me during all this time.

Muchas gracias Asunción, por todo el apoyo que me has brindado desde el primer día, por tus enseñanzas, tu paciencia, tus consejos, por animarme a mejorar, por tu amistad y por mirar siempre por mi bienestar profesional y personal.

Agradezco a la Dra. Yolanda Gómez Castellanos por iniciarme en el mundo de la astronomía y en particular en el estudio de las regiones fotodisociadas. Muchas gracias Profe, por su alegría, su entusiasmo y su amor a la ciencia. Siempre será un ejemplo a seguir para todos los que tuvimos la oportunidad de trabajar con usted.

Agradezco a la Dra. Ute Lisenfeld, por toda su ayuda en la preparación de documentos, tramites y los cursos requeridos por el programa de doctorado.

I want to Thank to Pierre Didelon for giving me access to the to the Herschel maps used in the Chapter 5.

Agradezco a todo el personal de IRAM, por toda la ayuda y todo el tiempo compartido. A Esther, María, Gloria y Javier, por toda la ayuda en los tramites administrativos. Otra vez, a Esther y María, por estar siempre dispuestas a escuchar y ayudar, por todo su apoyo y su amistad. Gracias a Miguel, Pablo y Walter, por ayudarme siempre con los (múltiples) problemas computacionales. De nuevo, gracias Miguel, por los correctivos, los regaños y el intercambio cultural. Muchas gracias Nicolas, por toda tu ayuda con los horarios de las observaciones, por ser tan accesible y por estar siempre al pendiente de que todo salga bien. Quiero agradecer a todos los compañeros con los que he compartido tiempo en el 30m, Salvador, Santiago, Gabriel, Clemens, Albrecht, Gregorio, Dave, Pepe, Peri, Paco, Paulino y Juan.

Gracias especialmente a los operadores, por todos los buenos momentos. Muchas gracias Joaquín, Frédéric, Víctor, Kike, Juan Luís, Ignacio y Manolo, por los tuning, por las conversaciones, los chistes, los juegos de mesa, los cenayunos, los cotilleos, las navidades y las noches viejas... Ahí os quedáis :P.

Muchas gracias a todo el personal de cocina del 30m, María, Mari Carmen, Carmen, Rosa, Verónica, Isabel, y Mónica, por su compañía, por el cuidado que ponen siempre para que estemos más cómodos y contentos, por sus mimos maternales, y como no, por sus comidas.

A los que han sido mis amigos y compañeros AoDs (astronómos de soporte) durante estos años. Muchas gracias Denise, Jorge, Gabriele, Claudia, Israel, Christof y Manuel, por los buenos momentos y por todo lo que me han enseñado. Especialmente, muchas gracias Israel, por estar siempre dispuesto a ayudar y a hacerle la vida más fácil a los demás, por tu compañerismo y por todo el trabajo que me has ahorrado ayudándome con observaciones y los trámites. Muchas gracias Christof, por enseñarme a observar y entrenarme para ser AoD, pero sobre todo por tu amistad. Muchas gracias Manuel, por tenderme siempre la mano, por la gran ayuda que me has dado siempre, por todo lo que me has enseñado, por la música, el teatro y los libros, por tener siempre una sonrisa en la cara, pero sobre todo por llenar todo de arte y alegría.

Agradezco a Susana Pacheco y Paolo Pilleri por toda la ayuda que me dieron durante mis estancias en Alcalá. Muchas gracias por su tiempo, su paciencia y su amistad.

Agradezco a Luz García y Manuel González por brindarme su casa durante mis estancias en Madrid y Alcalá. Muchas gracias por toda su amabilidad, su cariño y su comprensión, por los desayunos, las cenas y los juegos de parchís.

A mis amigos granadinos, que la mayoría no son granadinos pero como si lo fueran. Los que se han ido y han venido a Granada durante estos años. Les agradezco por hacer la vida más divertida, por las fiestas, las cenas, las bromas, las películas, por animarme para salir de casa aunque estuviera cansada o estresada. Muchas gracias Vicente, Jesús, Kike, Mauro, Suso, Cata, Miguel Ángel, Trini, Ben, Ignacio, Robert, Manu, Christof, Clem, Katy y Caro. Especialmente a los roommates que han tenido que aguantarme. Muchas gracias Mauro (y Tilo) por darme un lugar en donde quedarme mis últimos meses en Granada, por escucharme y hacerme más llevadera la etapa más estresante de la tesis. Muchas gracias Chuy, por aguantarme más de dos años, por 'gritonearme' para que me moviera en lugar de quedarme en el sofá, por el inglishky, los vídeos y los proyectos literario-artísticos, en agradecimiento a todo eso no me queda más que decir que... Este trabajo no tiene nada que ver con Toalá et al. (2013, 2014, 2015).

Quiero agradecer a todos los investigadores del CRyA, ahora llamado IRyA (Instituto de Radioastronomía y Astrofísica), especialmente al Dr. Luis Felipe Rodríguez, por su interés, su apoyo, y por estar siempre dispuesto a ayudar. También a los compañeros de maestría, especialmente a Gerardo y Lola.

A la vaca esférica, mis compañeros y amigos de licenciatura. Muchas gracias Jorge, Diana, David, Daniel, Melina, Karina, Jesús, Flor, Abraham, Cesar, Jésica y Ángel, por los buenos momentos, por todo lo que me han enseñado y por seguir en contacto a pesar de la distancia.

Agradezco a mi profesor de toda la vida. Muchas gracias profesor Genaro Vidal, por enseñarme a usar mi primer telescopio, por animarme a avanzar y por estar siempre pendiente de mi carrera.

También quiero agradecerle a mi familia Española. Muchísimas gracias Bea y Rafa por todo su trabajo y empeño en la elavoración de los esquemas y las portadas de esta tesis, por toda la paciencia que han tenido durante el proceso, por el ánimo y la disposición que siempre muestran. Muchas gracias a Gabriel, por enseñarnos la solución al problema de los filamentos (con solo 6 meses de vida). Muchas gracias Concha y Gonzalo por estar siempre al pendiente de lo que necesito, por la llamadas, por los consejos, por estar siempre dispuestos a ayudar. A todos ustedes, muchas gracias por acogerme en su familia y darme su cariño y su apoyo. ¡Los quiero!

Muchas gracias Álvaro, por todo, son tantas cosas que no me cabrían aquí. Muchas gracias por apoyarme, por ayudarme, por desvelarte escuchándome sin importar que tan cansado estés, por sacar tiempo de donde sea para leer y re-leer y darme esos comentarios que siempre lo mejoran todo. Gracias por ser siempre tan positivo y levantarme el ánimo, por tu tiempo, tu paciencia y tu cariño, por el pasado y el futuro. Gracias por la persona que eres, sin tu ayuda nada seria posible. ¡Te amo!

Finalmente, agradezco a mi familia Mexicana. A mis tíos Onofre y Amparo, que siempre me han brindado su cariño, su casa y su Internet. A mi tía Ofelia, por ser ejemplo de fuerza y superación. A mis abuelos, porque en mis mejores recuerdos siempre estará el compartir una taza de café con ellos. A mi abuela Ofelia, por su cariño, por sus veladoras, por ser una luz en la obscuridad. A mi abuelo Juan, por ser un ejemplo a seguir, por apoyarme siempre e inspirarme para buscar saber más de lo que sé, por tratar de ver que hay más allá, por su ánimo y sus ganas de aprender. A mis hermanos, Jorge y Alejandro, por todas las risas, por los juegos, los golpes, los retos, por ser mis hermanos. A Anahí, por su alegría y por su energía, pero sobre todo por David. A mis padres, Lupita y Jaime, por su apoyo, por sus enseñanzas, por su trabajo, por aguantar tanta distancia y, sin embargo, siempre estar ahí. A todos ustedes les agradezco, por hacerme la persona que soy, por enseñarme el valor de la honestidad, de la puntualidad y del trabajo duro. ¡Los quiero!

Sandra Patricia
Colonia, Noviembre 2015.

Chemical and dynamical study
towards the UC HII region Monoceros R2

One of the first signposts of high-mass star formation is the presence of compact regions of ionized gas (called HII regions), surrounded by layers of atomic and molecular gas (photon-dominated regions or PDRs). The study of the properties (e. g., dynamics, chemistry, structure) of these objects is of special interest because they provide information on the dynamical and chemical evolution in the formation of high-mass stars. The main objective of this Thesis is to characterize the chemistry and dynamics of the ultracompact HII region and PDR system in Monoceros R2: the closest object of this type that stands out as an ideal case to study the transition from ionized to molecular gas. We have carried out large-scale (163.5 arcmin^2) mapping of the Monoceros R2 cloud in the ^{13}CO (1–0), C^{18}O (1–0), HCN (1–0), and N$_2$H$^+$ (1–0) lines. These maps show that the cloud has a filamentary structure with the gas infalling along the filaments towards the central hub with accretion rates of 10^{-4}–10^{-3} $M_\odot$ yr^{-1}. In order to explore the influence of the UV radiation on the chemistry, we carried out an unbiased spectral line survey towards the Mon R2 region covering a frequency range from 84 to 350 GHz. Our data show that a high UV PDR has been formed around the HII region with intense emission of HCN, DCN, CN, CO$^+$, CF$^+$ and C$_2$H species. A pseudo-time-dependent gas-phase chemical model has been used to interpret the emission of the deuterated compounds. The deuteration fraction measured in the dense clumps around the HII region is consistent with a chemical age of a few 10^5 yr.

Keywords: Star formation — Interstellar medium — Filamentary structure — Dynamics — Chemistry — Photon-dominated regions — Monoceros R2.

LIST OF ABBREVIATIONS

2MASS	Two Micron All-Sky Survey
ALMA	Atacama Large Millimeter Array
CARMA	Combined Array for Research in Millimeter Astronomy
DSS	Digital Sky Survey
EVLA	Expanded Very Large Array
FUV	Far Ultraviolet
FIR	Far Infrared
FWHM	Full Width at Half Maximum
IMYSO	Intermediate-Mass Young Stellar Object
ISM	Interstellar Medium
IR	Infrared
IRAC	Infrared Array Camera (on the Spitzer satellite)
IRAS	Infrared Astronomical Satellite
IRDC	Infrared Dark Cloud
HH object	Herbig-Haro object
NUV	Near Ultraviolet
NIR	Near Infrared
HI	Neutral hydrogen
HII	Ionized hydrogen
HCHII region	Hypercompact HII region
HMC	Hot Molecular Core
MIPS	Multiband Imaging Photometer (on the Spitzer satellite)
MSX	Midcourse Space eXperiment
NOEMA	NOrthern Extended Millimeter Array
PdBI	Plateau de Bure Interferometer
PDR	Photon Dominated (PhotoDissociated) region
RRL	Radio Recombination Line
SED	Spectral Energy Distribution
SMA	Submillimeter Array
UCHII region	Ultracompact HII region
UV	Ultraviolet
YSO	Young Stellar Object
ZAMS	Zero-age Main Sequence

Resumen

Tradicionalmente las estrellas se han clasificado en dos categorías, estrellas de baja masa ($M_* \leq 8\ M_\odot$) y estrellas masivas ($M_* \geq 8\ M_\odot$). Esta clasificación se hace en base a dos diferencias principales entre las estrellas de baja y alta masa. La primera diferencia está relacionada con sus últimos estados evolutivos, mientras que una estrella de baja masa termina su vida como una nebulosa planetaria (y luego como una enana blanca), una estrella masiva termina su vida como una supernova que, dependiendo de la masa inicial, puede evolucionar a una estrella de neutrones o un agujero negro. La segunda diferencia está relacionada a las etapas evolutivas anteriores a la secuencia principal, que marcarán los distintos tiempos de acreción y el tiempo que tardará la estrella en generar reacciones nucleares.

En general, la formación estelar se produce en el interior de las nubes moleculares suficientemente densas y frías como para colapsar gravitacionalmente. En particular, las estrellas de baja masa se forman en pequeños glóbulos (de 1–$100 M_\odot$) de forma individual, siguiendo el modelo estándar de formación estelar (e. g., Larson 1969; Stahler et al. 1980a,b, 1981; Shu et al. 1987, 1993). En el caso de las estrellas masivas, las nubes moleculares pueden presentar estructuras filamentarias que convergen a una zona común llamada "hub". El gas fluye a lo largo de estas estructuras y es en el interior del "hub" donde se forman las estrellas más masivas.

A pesar de que las estrellas masivas (del tipo O y B) son de suma importancia en la determinación de la estructura química, dinámica y morfológica de las galaxias, su proceso de formación es aún poco conocido. Los modelos teóricos (e. g., Larson 1969; Shu et al. 1987, 1993) que permiten explicar de forma acertada la formación de estrellas de baja masa, presentan problemas cuando se aplican a las estrellas masivas. Esto se debe, a que las estrellas masivas comienzan a producir reacciones de fusión nuclear cuando aún están acretando material de su entorno (Keto & Wood 2006). Esto plantea el primer problema importante, la presión de radiación que generan las estrellas recién

formadas arratraría el material que se está acretando, y por lo tanto, evitaría que la estrella alcanzase masas más elevadas.

Actualmente hay dos modelos teóricos que tratan de solucionar estos problemas en la formación de estrellas masivas: El primer método, llamado colapso monolítico (Yorke & Sonnhalter 2002), adapta el mecanismo de formación de estrellas de baja masa para resolver el problema de la presión de radiación. El segundo método, llamado acreción competitiva (Bonnell et al. 2011), propone que las estrellas masivas se forman en cúmulos. Estos cúmulos forman un pozo de potencial común que acreta el gas de la nube circundante. Dentro del pozo de potencial, la proto-estrella central tendería a acretar más material y a formar la estrella más masiva. Para poder discernir qué escenario explica la formación de estrellas masivas, es completamente necesario llevar a cabo observaciones detalladas de regiones de formación estelar de alta masa. A pesar de las dificultades observacionales (i. e., las estrellas masivas se encuentran generalmente muy lejos, embebidas en nubes moleculares con una elevada extinción y en cúmulos con varias estrellas en formación), se ha conseguido caracterizar las propiedades observacionales más relevantes en la formación estelar masiva (e. g., núcleos moleculares calientes, regiones de gas ionizado, flujos moleculares o jets, y máseres moleculares). A partir de las perspectivas observacionales se ha propuesto un escenario evolutivo para las estrellas masivas: comenzando con una nube colapsando y fragmentándose, continuando con el desarrollo de núcleos moleculares calientes, hasta el desarrollo de una región de gas ionizado (o regiones HII).

Las estrellas masivas tienen un efecto dramático sobre el medio que las rodea. Una estrella joven, de tipo espectral O o B, emitirá fotones ultravioleta (UV) capaces de ionizar el medio que la circunda. Estos fotones, con energías $h\nu > 13.6$ eV, pueden ionizar el hidrógeno, formando así una región HII. Esta estrella támbien emitirá fotones, con 6 eV$< h\nu < 13.6$ eV, capaces de disociar las moléculas de hidrógeno (H_2) y de monóxido de carbono (CO), además, pueden ionizar carbono y otros átomos de potenciales de ionización más bajos (e. g., S, Fe, Si, Mg). Esto fomentará la formación de una región fotodominada (o PDR) alrededor de la región HII. La composición química y física de las PDRs están dominadas por el campo de radiación de ultravioleta lejano (FUV, de sus siglas en inglés) generado por la estrella central. El estudio de las PDRs evidencia la importancia de la radiación de fotones del lejano ultravioleta (6 eV$< h\nu < 13.6$ eV) en la estructura física, química, termodinámica y en la evolución del medio interestelar neutro asociado a estrellas masivas.

La región Mon R2, localizada a una distancia de 830 pc, es el sitio de formación estelar más activo en la nube molecular de Monoceros. Mon R2 presenta una estructura filamentaria que converge hacia el área central o "hub". En el centro de la región se encuentra un grupo de estrellas masivas (IRS 1 a IRS 7) recién

formadas, asociadas a una región UCHII que, a su vez, está rodeada por una serie de PDRs con diferentes condiciones físicas y químicas. La PDR principal está siendo irradiada por un campo de radiación UV con una intensidad de $G_0 > 10^5$ (en unidades de campo de Habing) y corresponde espacialmente con la fuente infrarroja principal IRS 1 (esta posición coincide con el frente de ionización y es etiquetada como IF, por sus siglas en inglés). Las grandes densidades y temperaturas presentes en la región generan una química rica y diferente de la que se encuentra en las PDRs irradiadas con campos UV de baja (o mediana) intensidad. Además de la PDR principal, existe una segunda localizada a $40''$ al norte de IRS 1. Esta PDR corresponde con un pico molecular (posición MP2) y presenta una química similar a la encontrada en PDRs irradiadas con campos UV de baja (o mediana) intensidad, por ejemplo la PDR localizada en la Cabeza de Caballo ($G_0 \sim 100$–1000). Por lo tanto, debido a sus características, Mon R2 se convierte en una fuente ideal para estudiar la dinámica de una región de formación estelar masiva, así como para estudiar la química de dos PDRs con condiciones físicas diferentes.

Objetivos, estrategia y organización

El objetivo principal de esta Tesis es estudiar la dinámica-cinemática y la química de las PDRs asociadas a la región de formación estelar en Mon R2. Para realizar este estudio, se han utilizando el radio-telescopio 30m de IRAM, localizado en Sierra Nevada (Granada, España). Para el estudio de la dinámica-cinemática de la región, se ha cartografíado en ^{13}CO (1–0), C^{18}O (1–0), HNC (1–0) y N$_2$H$^+$ (1–0) una región de 163.5 arcmin^2 alrededor de IRS 1.

Para el estudio químico, se ha llevado a cabo un survey espectral (84.0–350.0 GHz) con alta resolución espectral y gran sensibilidad en dos posiciones claves de la región, IF y MP2. También se han observado mapas cubriendo una área de $2' \times 2'$ alrededor del la posición IF en algunas frecuencias seleccionadas. La reducción-análisis de los datos y la identificación de las líneas ha sido llevada acabo con el paquete CLASS/GILDAS.

En base a las observaciones a gran escala hemos realizado: *i)* mapas de intensidad integrada de las moléculas observadas y se han comparado con mapas de $N(H_2)$ obtenidos con Herschel y mapas de infrarrojo obtenidos con *Spitzer* y *WISE*. *ii)* Se han identificado una serie de filamentos que forman la nube molecular y se han calculado los gradientes de velocidad a lo largo de estos. *iii)* Se ha realizado un estudio de la estabilidad de dichos filamentos utilizando principalmente la emision de ^{13}CO (1–0) y C^{18}O (1–0). *v)* Se ha estudiado la cinemática de los filamentos a partir de las mismas líneas.

En base al survey espectral hemos realizado: *i)* un inventario químico de la región. *ii)* Un estudio estadístico de los anchos presentados por diversas familias de moléculas. *iii)* En base a los mapas observados se realizó un estudio morfológico de la región y se han comparado los resultados con los obtenidos por el estudio estadístico. *iv)* Se han hecho cálculos de columnas de densidad, temperaturas de rotación y abundancias de las especies químicas detectadas, y se han comparado estos resultados con los observados en otras fuentes. *v)* Se ha realizado un estudio detallado de las moléculas deuteradas y se han comparado los resultados observacionales con las predicciones de un modelo de evolución química pseudo dependiente del tiempo (Roueff et al. 2007).

Esta Tesis está estructurada en cuatro partes. La **Parte I**, titulada "Introducción", describe los constituyentes de la Vía Láctea, los principios básicos de formación estelar y los efectos de las estrellas masivas en su entorno (e. g., formación de regiones HII y PDR). En la **Parte II**, titulada "Monoceros R2", se presenta una descripción global de la región estudiada (Capítulo 4), el análisis de las observaciones a gran escala (Capítulo 5), el análisis del survey espectral (Capítulo 6) y un estudio más detallado, incluyendo modelización de la química de los compuestos deuterados (Capítulo 7). La **Parte III** resume los resultados principales, encontrados en la Parte II, y propone las bases del trabajo futuro. Finalmente, la **Parte IV** consta de tres Apéndices que presentan las Tablas y las Figuras correspondientes a los capítulos presentados en la Parte II.

Resultados principales

Nuestros mapas de intensidad integrada de ^{13}CO y C^{18}O muestran que la mayor parte de la masa se concentra en una región de unos $9' \times 9'$ que llamaremos "hub" en la que convergen varios filamentos. Nuestros datos revelan que la cinemática de la región es compleja, con una estructura filamentaria que converge en el centro de la región. Analizando los mapas de velocidad de diferentes trazadores moleculares, hemos identificado 13 filamentos (F1, F2, F3, F4, F5, F6, F7, F8, F9, F10-10A, F11, F12 y F13) que coinciden con los observados anteriormente con Herschel. Los gradientes de velocidad encontrados a lo largo de los filamentos corresponden con flujos de acreción de masa de $\sim 10^{-4}$–10^{-3} $M_\odot$ yr^{-1}. Todos los filamentos presentan evidencia de fragmentación, en particular, los mapas de canales de ^{13}CO y C^{18}O confirman la fragmentación de al menos cinco de estos filamentos (F1, F5, F9, F10 y F13). La estructura filamentaria de la región parece extenderse hasta el centro, donde se detectan tres filamentos principales con propiedades químicas diferentes: un filamento a 10 km s^{-1} que rodea la región UCHII y tiene un máximo cercano a IRS 1, un filamento a 8 km s^{-1} asociado a una PDR de menor campo UV que tiene

su máximo en la posición $(0'',40'')$ (MP2) y un filamento a 12 km s^{-1} que no presenta ninguna evidencia de interacción con los fotones UV. Estos filamentos convergen hacia la región HII formando una espiral alrededor de esta. Esto sugiere la idea de una región UC HII en expansión que comienza a romper la estructura filamentaria donde fue formada, mientras que el material sigue cayendo hacia el centro de la región a lo largo de los filamentos.

En base al survey espectral hemos realizado un inventario químico de Mon R2, enfocándonos en el estudio de las posiciones IF y MP2. Hemos encontrado mas de 65 especies, la lista incluye trazadores típicos de PDRs, moléculas complejas, moléculas deuteradas, iones y líneas de recombinación. Las líneas detectadas presentan diferentes perfiles de velocidad en ambas posiciones. La mayoría de las líneas presentan dos componentes de velocidad. La componente a 10 km s^{-1} está presente en las dos posiciones y parece estar asociada con la capa más expuesta a la radiación UV generada por IRS 1. La componente de velocidad a 12 km s^{-1} solo se detecta en la posición IF que está asociada la nube molecular. Finalmente, la componente a 8.5 km s^{-1} solo se detecta en la posición MP2 y está relacionada con una segunda PDR iluminada por un campo UV menor.

Hemos hecho una separación de las líneas detectadas en base a los elementos que conforman cada especie (moléculas deuteradas, iones, moléculas azufradas, moléculas nitrogenadas, moléculas complejas, hidrocarburos y especies con CO) y hemos realizado un estudio estadístico comparando los anchos de líneas y la energía del nivel superior de cada transición (E_{up}). En base a este estudio encontramos que la turbulencia (o los movimientos globales) controlan los anchos y los perfiles de las líneas en la región. Las transiciones con energías más bajas parecen estar trazando las capas más externas, en una envolvente más turbulenta, mientras que las transiciones con energía más alta están trazando los núcleos de gas densos.

Con la finalidad de investigar el efecto de la radiación UV, se han calculado las columnas de densidad, temperaturas de rotación y abundancias de las especies químicas detectadas, y se han comparado estos resultados con los observados en otras PDRs (la barra de Orion, NGC 7023 y la Cabeza de Caballo). En esta comparación encontramos que $C^{18}O$, HCO^+, N_2H^+, SO, SO^+, HCS^+, CS, CH_3OH y CH_3CCH presentan abundancias similares para ambientes con diferentes campos de radiación. Moléculas como DCO^+, l-C_3H^+, CH_3CN, CF^+, $HN^{13}C$ y los hidrocarburos tienden a incrementar sus abundancias en las PDRs irradiadas por campos UV de baja intensidad, mientra que CO^+ y CN tienden a incrementar sus abundancias en las PDRs irradiadas por campos UV de alta intensidad. También se realizó una comparación de las abundancia en las PDRs con los encontrados en diferentes tipos de fuentes (nubes oscuras, un núcleo caliente y un choque). La mayoría de las moléculas son más abun-

dantes en las otras fuentes que en las PDRs, sin embargo hay moléculas que presentan abundancias similares en PDRs y las nubes obscuras (e.g., CS y algunos hidrocarburos).

Se ha realizado un estudio detallado de las moléculas deuteradas y se han comparado los resultados observacionales de estas moléculas con las predicciones de un modelo de evolución química pseudo dependiente del tiempo. Se han calculado la fracciones de deuteración (D_{frac}) en las PDRs asociadas a las posiciones IF y MP2 y encontramos que no hay diferencias significativas entre estas dos posiciones. De lo cual puede concluirse que la emisión de las moléculas deuteradas proviene de núcleos densos dentro de la PDR, donde el gas está protegido de la radiación UV. Para HNC, HCN, C_2H y H_2CO se han encontrado valores de $D_{\mathrm{frac}} \sim 0.01$, mientras que para HCO^+, N_2H^+ y NH_3 hemos encontrado $D_{\mathrm{frac}} < 0.001$. Estos valores son consistentes con las predicciones del modelo en fase gaseosa para $T \sim 0.1$ Myr, que es el tiempo de vida estimado para una región UC HII. Finalmente, en base a nuestros resultados observacionales y su comparasión con los modelos químicos, hemos encontrado que la química de las moléculas deuteradas es un buen reloj químico para regiones de baja y alta masa.

SUMMARY

Traditionally, stars have been classified into two categories, low-mass stars (< 8 $M_\odot$) and high-mass (or massive) stars (> 8 $M_\odot$). This classification is done on basis of two main differences between low and high-mass stars. The first one is related to their last evolutionary stages. While a low-mass star ends its life as a planetary nebulae (and then as a white dwarf), a high-mass star ends its life as supernovae that, depending on the initial mass, can evolve to a neutron star or a black hole. The second difference is related to their pre-main sequence evolution. This difference is related to the Kelvin-Helmholtz (this time determines how quickly a star contracts before nuclear fusion starts) and free-fall timescales.

In general the star formation processes take place in the molecular clouds. In particular, the low-mass stars formation process occurs in condensations of gas that become gravitationally unstable, following the standard model of formation described by Shu et al. (1987, 1993). In the case of the massive stars, the molecular clouds are formed in a complex pattern of filamentary entities that can intersect in high-density regions called *hubs*. Star formation within molecular clouds has been found to occur preferentially along the filaments, with high-mass stars forming at the hubs and ridges junctions.

Massive stars (type O and B) play a major role in shaping the morphological, dynamical, and chemical structure of their host galaxies. However, their first stages of formation are still poorly understood. Observationally, it is not easy to study the formation of a massive star since they tend to form in clustered mode, deeply embedded in molecular dense cores highly obscured by circumstellar dust (with extinctions $A_V >100$), and at far distances (> 1 kpc). Moreover, from the theoretical point of view, there are some questions that remain unsolved. The theoretical model (e. g., Larson 1969, 1985; Stahler et al. 1980a,b, 1981; Shu et al. 1987, 1993) that explains the low-mass star formation are questioned for stars much more massive. The main differences that call into question this model is related to the timescales. The main problem is that, according with this model, the star would ignite before accreting its total mass.

Then, the radiation pressure exerted by the young star would push the material outwards avoiding the in-falling of new material and restricting the star final mass.

Different models have been proposed to explain the formation process of high-mass stars. The two most accepted models are the monolithic collapse (Yorke & Sonnhalter 2002) and the competitive accretion (Bonnell & Smith 2011). The monolithic collapse star formation model, adapts the mechanism of low-mass star formation to solve the problem of the radiation pressure. While the competitive accretion star formation model is based on the picture of massive stars forming in clustered environments. The gravitational potential of the cluster (in combination with the higher gas density) ensures that gas is funneled down to the center to be accreted by the central star, that becomes the most massive one. In order to discern which mechanism or scenario better explains and dominates the formation of massive stars, it is necessary to conduct detailed observations of high-mass star forming regions. Despite the observational difficulties mentioned before, a huge observational effort during the last years have revealed several observational features (hot molecular cores, HII regions, outflows and jets, disks, masers) associated with massive young stellar objects that can help to improve the theoretical models. From this observational perspective an evolutionary scenario for high-mass stars has been proposed starting from a contracting and fragmenting cloud, continuing with the development of a hot molecular core to the development of a region of ionized gas (or HII region).

High-mass stars (O and B-type stars, with masses > 8 $M_\odot$) have a dramatic impact on the interstellar medium. They emit extreme ultraviolet photons ($h\nu > 13.6$ eV) that ionize the surrounding molecular gas forming HII regions. Furthermore, their far-ultraviolet (FUV) photons (6 eV$< h\nu <$13.6 eV) penetrate beyond the HII region and into the molecular cloud where they dominate the physics and chemistry, giving rise to the so called photon-dominated (or photodissociated) regions (PDRs). Under these considerations, a PDR is the boundary between the ionized HII region, produced by a hot massive star, and its surrounding molecular cloud (e. g., Hollenbach & Tielens 1997, 1999). In the PDRs, FUV radiation plays a major role in their structure, heating, cooling and physical/chemical properties. This kind of regions are excellent targets to study the interaction between the UV radiation of young newly formed stars and the surrounding environment, as well as to unveil the details of the massive star formation process.

The high-mass star forming region Mon R2, located at a distance of 830 pc, is the most active site of star formation in the Monoceros molecular cloud. Mon R2 presents a complex filamentary structure converging into the central area or hub. A cluster of recently formed high-mass stars is located at the

junction of this filamentary structure and are associated to an UC HII region, surrounded by a series of PDRs with different physical conditions. The main PDR, is irradiated by a UV field with an intensity of $G_0 > 10^5$ (in units of Habing field) by the main infrared star IRS 1 (IF position). The high densities (10^6–10^7 cm^{-3}) and kinetic temperatures (Tk> 500 K) of the region drive a rich chemistry different of that found in low-UV irradiated PDRs. In addition to the main PDR, a second PDR is detected at $40''$ north from IRS 1, which corresponds to a second molecular peak (MP2 position). The chemical properties of this PDR are similar to those of low- to mild-UV irradiated PDRs such as the Horsehead. Therefore, due to its characteristics, Mon R2 turns out to be an ideal target to study the dynamic in a high-mass star forming region, as well as to study the physical and chemical conditions in an extreme and a low- to mild-UV irradiated PDRs.

Objectives, strategy and organization

The main objective of this Thesis is to characterize the chemistry and dynamics of the Mon R2 region. To study the dynamical properties, we performed observational maps covering a field of view of 163.5 arcmin^2 around IRS 1, using the IRAM-30m telescope. In these maps, the main observed species are ^{13}CO (1–0), C^{18}O (1–0), HCN (1–0), N$_2$H$^+$ (1–0) and HC$_3$N (1–0).

To study the chemical characteristics of the region, we did an unbiased spectral line survey (covering 84.0–330.0 GHz), towards the PDRs found around the UC HII region in Mon R2. The high spectral resolution of the IRAM-30m telescope (~ 0.25–0.65 km s^{-1}) allows us to resolve the line profiles of the detected species. We also observed OTF maps covering the central ($2' \times 2'$ around the IF position) area of the region at 3 and 1 mm band. The reduction and the analysis of the data were performed using the CLASS/GILDAS package.

Using the large-scale maps: We performed a comparison of the 30m emission with $N(H_2)$ maps. We also performed a comparison with infrared maps of *Spitzer* and *WISE*. *ii)* We have identified a series of filaments, and calculated velocity gradients along of them. *iii)* We performed a stability study of the filaments using the ^{13}CO and C^{18}O emission. *iv)* We did a kinematical study of the filaments using the same lines.

On basis of the spectral survey we did: *i)* a chemical inventory of the region. *ii)* A statistical study of the linewidths of the detected species. *iii)* Using the $2' \times 2'$ OTF maps we did a morphological study of the region and the results have been compared with those obtained in the statistical study. *iv)* We calculated the column density, the rotational temperature and the molecular abundances of the detected species. *v)* We did a detailed study of the deuterated molecules

and their corresponding hydrogenated species, including a comparison with sources with different properties and chemical models (Roueff et al. 2007).

This Thesis is structured in four parts. The **Part I**, entitled "Introduction", contains a description of the constituents of the Milky Way, the low and high-mass star formation processes and their effects in the surrounding gas (e.g., HII regions and PDRs). The **Part II**, is entitled "Monoceros R2", presents an overview of the region in **Chapter 4**, the analysis of the large-scale maps of Mon R2 (in **Chapter 5**), the spectral survey (in **Chapter 6**), and the study of the deuterated molecules (in **Chapter 7**). The **Part III** presents a summary of the main conclusions and an outline of the future work in **Chapter 8**. Finally, the **Part IV** concludes the work with three Appendices that present the maps and spectra corresponding to the Chapters presented in the **Part II**.

Main results

The ^{13}CO and C^{18}O integrated intensity maps show that most of the mass is concentrated in a region of about $9' \times 9'$ (the "hub") where several filaments converge. Our maps reveal a complex kinematics, with large-scale filaments and spiraling arms approaching the UC HII region. We analyze different integrated intensity maps for small velocity ranges (spanning 0.5 and 1.0 km s^{-1}) in different tracers. We have carefully inspected the distribution of the molecular emission, both spatially and kinematically. With this analysis we have identified 13 elongated or filamentary structures (named F1, F2, F3, F4, F5, F6, F7, F8, F9, F10-10A, F11, F12 and F13) as velocity-coherent elongated structures that spatially coincide with the continuum filaments detected with Herschel (Didelon et al. 2015). Position-velocity cuts along the filaments show velocity gradients that correspond to mass accretion rates of about 10^{-4}–10^{-3} $M_\odot$ yr^{-1}. All the filaments present evidence of fragmentation, in particular, ^{13}CO and C^{18}O channels maps confirm the fragmentation of five filaments (F1, F5, F9, F10 and F13). The filamentary structure seems to be also present within the hub, where we detected three filaments, with different chemical properties: a filament at 10 km s^{-1} is surrounding the UC HII region and presenting an intensity peak very close to the IRS 1, a filament at 8 km s^{-1} associated to the PDR in MP2 at offset $(0'', 40'')$, and finally, a filament at 12 km s^{-1} that does not present evidence of interaction with UV photons. These filaments seem to fall down following a spiral pattern towards the UC HII region. Overall, this suggests the idea of a young UC HII region just beginning to expand and break out of the dense filamentary hub where it was formed, with material still collapsing inward along the filaments.

On the basis of the spectral line survey, we conducted a chemical inventory focused in the study of the IF and MP2 positions. We found more than 65 different species, including typical PDR tracers, complex molecules, deuterated species, ionic species and radio recombination lines. Our observations show that Mon R2 presents a complex morphological and kinematical structure. We found that the detected lines present different velocity profile towards the IF and MP2 positions. Most of the lines present two velocity components. A component at 10 km s^{-1} is detected at both positions and seems associated with the layer most exposed to the UV radiation from IRS 1. The component at 12 km s^{-1} is only detected toward the IF position and is related to the bulk of the molecular cloud with its maximum in the SW. The component at 8.5 km s^{-1} is only detected toward the MP2 position and is related to the second low-UV PDR .

We did a separation of the detected lines based on their elements (deuterated molecules, ionic species, sulfurated species, nitrogenated species, complex molecules, hydrocardons and CO species) and we conducted a statistical study comparing the width of lines and the upper energy level of the transition (E_{up}). We found that a transition with higher E_{up} is likely to be excited in a different region than a transition of the same species with lower excitation energy. Lines with higher E_{up} are associated with narrower lines. This indicates that the turbulence or global motions are controlling the linewidths in Mon R2 and suggests that turbulence plays an important role in shaping the lines of some molecules (e. g., ions, S molecules and COM lines). Low energy transitions would be tracing outer layers from a colder and more turbulent envelope, while the emission of lines with higher energy seems to be associated with dense clumps.

In order to investigate the effects of the chemistry with the UV incident flux in PDRs, we calculated the column density, the rotational temperature and the molecular abundances of the detected species. We compared the abundances found in the Mon R2 with those found in other PDRs (Orion Bar, NGC 7023 and Horsehead). In this comparison we found that the $C^{18}O$, HCO^+, N_2H^+, SO, SO^+, HCS^+, CS, CH_3OH and CH_3CCH molecules present similar abundances for different G_0 environments. DCO^+, l-C_3H^+, CH_3CN, CF^+, $HN^{13}C$ and hydrocarbons tend to increase their abundances in the low-UV irradiated PDRs. While the CO^+ and CN molecular abundances seems to decrease in the low-UV PDRs. We also compare the molecular abundances in PDRs with those found in different sources (dark clouds, hot cores and a shock). We found that most of the species present lower abundances in PDRs that in other sources. However there are some molecules (CS, C_2H and C_4H) that present similar abundances in PDRs than in dark clouds.

We performed a detailed study of the deuterated molecules and a comparison

of our results with those presented in other works for different sources, as well as with the pseudo time-dependent model. We found that the deuteration in Mon R2 proceeds from the gas-phase via CH_2D^+ and C_2HD^+ reactions. We have determined the deuterium fraction (D_{frac}) toward the PDRs IF and MP2 position. We found that there are no important differences between the values of D_{frac} toward these PDRs. This is interpreted in the scenario of the deuterated compounds coming from dense and warm clumps, instead from the most exposed PDR layers. Values of D_{frac} of $\sim$0.01 are found for HNC, HCN, C_2H and H_2CO, and <0.001 for HCO^+, N_2H^+, and NH_3. These values are consistent with the predictions of the gas-phase model at an early time, $\sim$0.1 Myr. This time is consistent with the ages estimated for UC HII regions on the basis of statistical studies. On the basis of the gas-phase model, we found that the deuterium chemistry is a good chemical clock in both the low-mass and high-mass regime.

CONTENTS

Part I

INTRODUCTION

1

STAR FORMATION

This chapter introduces the different constituents of the interstellar medium in our Galaxy, and describes process of formation of low and high-mass stars.

Contents

1.1   The interstellar medium in the Milky Way

Our Galaxy, the Milky Way (see Figure 1.1), is a disk-shaped galaxy with an spiral arm structure. The length of the disk is about 30 kpc, with 250 pc of scale height. It has an elliptical bulge in the center (that extends to a radius of 3 kpc) with a bar-shaped distribution of gas, dust and stars. Finally, a spherical halo of old stars and globular clusters extends for several tens of kpc. The Solar System is located at a distance of 8.5 kpc from the Galactic center in a spiral arm within the local fluff of the local bubble. The Milky Way contains about 10^{11} stars, which are the fundamental units of luminous matter and the main mass component. However, with an average density of only 1 star per pc^3, they represent only a small percentage of its total volume.

The **interstellar medium (ISM)** is the component that exists in the region between the stars. The ISM, with a mass of $\sim 10^9$ $M_\odot$, constitutes only 1% of the mass of the Galaxy and is formed fundamentally by interstellar dust and interstellar gas with a ratio of approximately 1 particle of dust for each 100 particles of gas.

The **interstellar dust** is formed by small particles of irregular shapes (silicate, carbon and iron nuclei) with ice mantles. These dust grains are extremely small, with typical sizes about 0.01 μm. Despite their small size and reduced number (compared to gas particles), the interstellar dust has a major effect in the extinction of stellar light and interstellar polarization. *Extinction* is produced when a dust grain absorbs radiation with wavelengths shorter than its size, this radiation being then re-emitted at longer wavelengths (mainly infrared and radio wavelengths). A typical value of extinction in the Galaxy is about one magnitude per kpc. If the dust cloud is thick, the light can be totally blocked by the dust particles resulting in dark regions in the sky (see Figure 1.2). The amount of attenuation depends on the thickness and density of the dust cloud, as well as the wavelength of the light (with ultraviolet and blue wavelengths being more easily scattered off). Thus, the light that we see is redder than it would be without the interstellar medium. This effect is the interstellar reddening.

To explain the *interstellar polarization* produced by the interstellar dust we must realize that dust grains are not spherically symmetrical, but typically have very complex shapes. We can simplify our considerations by assuming the dust grains to be elongated. In this scenario, the long axis of a grain extinguishes the background light more efficiently than the short axis. Therefore, if a large ensemble of non-spherical dust grains is aligned preferentially in one direction, the background light is extinguished along one axis, causing the

Figure 1.1: View of the Milky Way (from Babak Tafreshi, Astronomy Picture of the Day).

transmitted light to be partially plane polarized. The Davis-Greenstein effect predicts that the grains spin around the direction of the magnetic field, with the long axis perpendicular to the field, this causing the grains to be aligned. Finally, there is a correlation between the presence of dust and interstellar gas (molecular gas). This is because the dust grains play an important role in the formation of some molecules, for example, the most abundant interstellar molecule (H_2) can only be efficiently formed in presence of dust grains, which operate as catalysts, absorbing the excess energy of the molecule formed from the union of two hydrogen atoms.

The composition of the *interstellar gas* ia typically 70% hydrogen, 28% helium and 2% heavier elements, such as oxygen, carbon and nitrogen. The gas (hydrogen) can be in neutral (atomic or molecular state, i. e., HI and H_2 respectively) or ionized (HII) forms. Table 1.1 lists the main physical parameters of the different phases of interstellar gas.

Atomic Hydrogen (HI regions): this kind of regions are composed by HI and some low-excitation ions (e. g., CII). They have typical temperatures of 80 K (in range between 50 K and 150 K), constitute clouds with typical sizes of 1–100 pc, densities between 10–100 cm^{-3} and masses 50–500 $M_\odot$. HI regions represent a small fraction of the total volume (2-3%) and are located within the Galactic disk with a scale height of $\sim$ 100 pc. A second component of atomic gas, not confined to individual clouds, is the **warm neutral inter-cloud gas**, with a heigth scale twice that of the cold component, and occupying 50% of the total volume. Its density is about 0.5 cm^{-3} and its temperature is estimated to be $\sim 8 \times 10^3$ K.

Ionized Hydrogen (HII regions): this kind of regions are composed by HII, whose ionization is due to photoionization or collisions with other particles. The HII regions are found inside the molecular clouds and are associated with young massive stars. They have typical sizes of $\sim$ 1 pc, densities of 10^2–10^4 cm^{-3}, and temperatures in the range from 5×10^3 to 1×10^4 K. Since the HII regions are associated with young stars, they are found near or within the spiral arms of the Galaxy. The **coronal gas** is formed by hydrogen collisionally
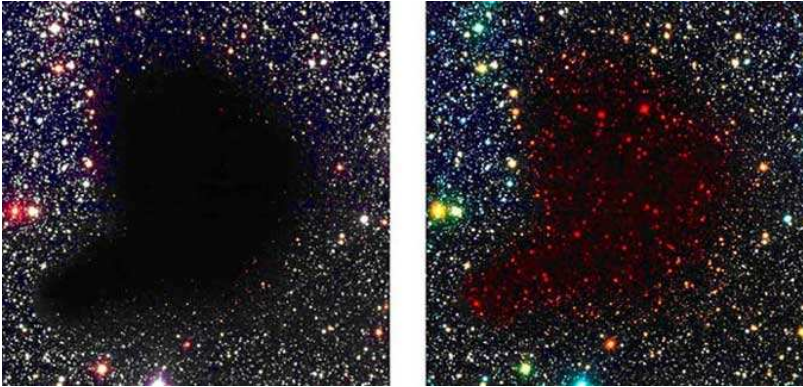
Figure 1.2: Barnard 68 dense cloud in the constellation Ophiuchus. *Left:* The dust absorbs the light of the stars behind it, creating an apparent void. *Right:* Infrared light penetrates the cloud, and reveals stars obscured by the dust. Image credit: FORS Team, VLT Antu/ESO, ESO.

ionized by the passage of supernovae wave shocks. This gas has densities of $\sim 3 \times 10^{-3}$ cm^{-3} and temperatures of 5×10^5 K. The coronal gas represents about 50% of the total volume, and is located in the Galactic plane with peaks of maximum density at a radius of 5 kpc.

Molecular Hydrogen (H$_2$): The molecular clouds (see Section 1.1.1) are mainly formed by molecular hydrogen, and other molecules (e. g., CO, CO$_2$, NH$_3$, H$_2$O, etc) in less proportion. They have typical densities of 10^3–10^5 cm^{-3}, masses of ~ 1000 $M_\odot$, and temperatures ranging from 10 to 50 K. The molecular gas represents about 2% of the total volume, and is located close to the galactic plane. It is important to note that even when the H$_2$ molecule is the most abundant component of the ISM, the CO molecule is used as the best tracer of molecular gas in the Galaxy. This is because in the interstellar molecular gas (with temperature of only 10–50 K), only rotational transitions can be excited (since vibrational and electronic transitions need higher energies), and the H$_2$ molecule does not have dipole rotational transitions (due to its symmetry, its dipole moment is zero).

1.1.1 Molecular clouds

The study of the molecular clouds in the Galaxy is of great importance, as they are the birth place of new stars. The study of these clouds helps us to understand the initial conditions of the star formation, build a picture of the earliest stages of the stellar evolution, and unveil the star formation process

Table 1.1: Different phases of the interestellar gas (Estalella & Anglada 1999).

	Density (cm^{-3})	Temperature (K)	Pressure $(dyn\ cm^{-2})$	Fractional volume
H_I gas	50–150	10–100	3.3×10^{-13}	2–3%
Warm neutral gas	0.01–10	8×10^3	2.5×10^{-13}	$\sim 50\%$
H_{II} region	$>10^2$	10^3–10^4	$>1.1 \times 10^{-10}$	$\sim 10\%$
Coronal gas	10^{-4}–10^{-3}	5×10^5	$<6.9 \times 10^{-13}$	$\sim 50\%$
Molecular clouds	10^3–10^5	10–50	1.4×10^{-13}	$< 1\%$

(see Section 1.2). Table 1.2 lists the main physical properties of different types of molecular clouds is ordered by visual extinction (A_V), from less to more opaque clouds. On basis of their physical parameters, the molecular clouds can be clasified as

i) **Diffuse Molecular Clouds:** they have low visual extinctions, similar amounts of atomic and molecular gas, represent a minor fraction of the molecular gas, and their evolution is driven by thermal pressure and gravity. These clouds are never found to form stars.

ii) **Giant Molecular Clouds (GMCs):** they have low visual extinctions, sizes from 5 to 200 pc and masses from $\sim 10^5$ to 5×10^6 $M_\odot$. They are known as the most important sites of star formation.

iii) **Dark Clouds:** they combine a large cloud structure with small sub-units or condensations. There are two types of dark clouds, *individual clouds* (with A_V $\sim$10 mag and M$\sim$ 30 $M_\odot$) and *complexes* (with A_V $\sim$5 mag and M$\sim$ 10^4 $M_\odot$). These clouds are the responsible for a significant fraction of the low mass star formation in the Galaxy.

iv) **Dense Cores:** they are the smallest and densest cloud entities. They are found in the inner and more dense regions of giant and dark molecular clouds. Dense cores have densities of 10^4 cm^{-3} and temperatures of $\sim$ 10 K. Infrared sources are associated with these dense cores, being the most direct evidence that these structures form stars.

As mentioned before, the vast ensembles of molecular gas called giant molecular clouds (GMCs) are responsible for most of the star formation in the Galaxy. The substructure of a GMC is a complex pattern of filamentary entities (Schneider & Elmegreen 1979; Loren 1989a,b; Nagai et al. 1998; Molinari et al. 2010; Peretto et al. 2014). The filamentary structure inside the molecular clouds is unstable toward both radial collapse and fragmentation (Larson 1985; Inutsuka & Miyama 1997; Miyama et al. 1987). The densest filaments may fragment into prestellar cores, the seeds of future stars (see

Table 1.2: Physical parameters of molecular clouds.

	A_V (mag)	n_{tot} (cm^{-3})	L (pc)	T (K)	M ($M_\odot$)
Diffuse Clouds	1	500	3	50	50
Giant Molecular Clouds	2	100	50	15	10^5
Dark Cloud: Complexes	5	500	10	10	10^4
Dark Cloud: Individual	10	10^3	2	10	30
Dense Cores	10	10^4	0.1	10	10

Figure 1.3). The origin or formation of these filamentary structures is still unclear, with different mechanisms such as turbulence or gravity plus the presence of magnetic fields playing a role (see theoretical simulations in Kirk et al. 2015). A possible scenario is that large-scale supersonic flows compress the gas, giving rise to the filamentary structure seen in the ISM. Then, gravity takes over and drives fragmentation of filaments into (prestellar) cores which will eventually form protostars and stars. The classical Jeans (1929) analysis of the gravitational stability of an infinite uniform medium predicts a critical mass (the classical Jeans mass) given by

$$M_J = \left[\frac{375}{4\pi\rho} \left(\frac{k_b T}{G\mu m_H} \right)^3 \right]^{1/2} \propto T^{3/2} \rho^{-1/2}, \tag{1.1}$$

for a critical length (the classical Jeans length[i]) given by

$$\lambda_J = \left(\frac{15 k_b T}{4\pi G \mu m_H \rho} \right)^{1/2} \propto T^{1/2} \rho^{-1/2}, \tag{1.2}$$

in a spherical gas distribution. In the previous equations k_b is the Boltzmann constant, T is the temperature of the cloud, μ is the mass per particle in the cloud, G is the gravitational constant and ρ is the cloud mass density ($n = \rho/\mu$). When a spherical gas distribution present a mass larger than the Jeans mass, in a radius equivalent to the Jeans length, the cloud gravitationally collapses allowing the formation of a new star.

In the case of an elongated structure, as is the case of a filament supported by turbulence pressure against its self-gravity, the Jeans mass per unit length is equal to

$$(M/l)_{crit} = \frac{2\sigma^2}{G} = 465 \left(\frac{\sigma}{1 \text{ km s}^{-1}} \right)^2 M_\odot \text{ pc}^{-1} \tag{1.3}$$

---

[i]Critical radius of a cloud where the thermal energy, which causes the cloud to expand, is counteracted by gravity
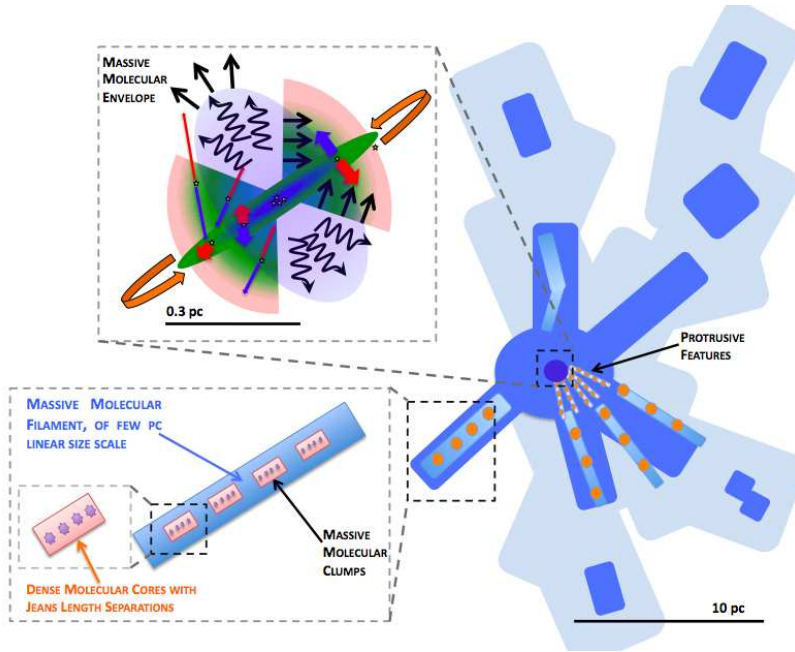
Figure 1.3: A simplified scheme of a filamentary, giant molecular cloud. The molecular gas has a filamentary and clumpy structure. The entire molecular cloud is gravitationally accelerated toward the densest central region, while the denser regions in the molecular filaments fragment into smaller structures locally. Subsequent fragmentation may occur if the volume density is high enough. Figure taken from Baobab Liu et al. (2010).

(Nagasawa 1987; Wang et al. 2014). When the mass of a filament exceeds this "modified" Jeans mass, it starts to fragment. The separation of the fragments, determined by the density of their parent molecular structures, is comparable to the local Jeans length that is given by the expression

$$\lambda = \frac{\Delta V}{\sqrt{4\pi G \rho}} \tag{1.4}$$

where ΔV is the line width, which corresponds to the initial turbulent and thermal broadening (before the fragmentation), and relates to the velocity dispersion by $\Delta V = \sigma(8\ln 2)^{1/2}$. In the last years, increasing observational evidence have confirmed the existence of **filamentary structures** or ridges (Peretto et al. 2014) that pervade large molecular clouds (e.g., André et al. 2010; Molinari et al. 2010; Busquet et al. 2013), and often intersect in high-density regions of low aspect ratio named **hubs**. Star formation within molecular clouds has been found to occur preferentially along the filaments, with high-mass stars forming at the hubs and ridges junctions (e.g., Liu et al. 2012;

Schneider et al. 2012; Louvet et al. 2014). The high densities observed in these regions ($N_H = 10^{23}$ cm^{-2} and $n_{H_2} \sim 10^6$ cm^{-3}) are likely achieved by infall of material along the filaments into the hub (e.g., Schneider et al. 2010; Peretto et al. 2013). A number of recent studies have started to characterize the properties of filaments in nearby star forming regions forming *only* low-mass stars (e.g., in the Taurus molecular cloud, Hacar et al. 2013, Tafalla & Hacar 2015). These works reveal that filaments are not solid entities but are constituted by small velocity-coherent elongated structures named *fibers*, that are also predicted in numerical simulations (e.g., Smith et al. 2014). Similar structures have also found (although still need to be confirmed by observing more regions) in ridges (e.g., Hennemann et al. 2012; Henshaw et al. 2014; Tackenberg et al. 2014) and should be investigated in hubs. High-mass stars inject, in the surrounding medium, large amounts of radiation and turbulence that may affect the structural properties of filaments (e.g., leading to a different level of fragmentation, Csengeri et al. 2011; Seifried & Walch 2015a,b) and the transport of mass along the filament until the hub, where stars form.

1.2   Star formation

Stars, the fundamental building blocks of galaxies, can be classified on basis of their physical parameters, for example, temperature (by spectral type; O, B, A, F, G, K, M, Jacoby et al. 1984; Dallier et al. 1996), luminosities, or masses. The classification by masses is traditionally divided into two parts, low-mass stars (< 8 $M_\odot$) and high-mass (or massive) stars (> 8 $M_\odot$). This classification is done on basis of two main differences between low and high-mass stars. The first one is related to the last evolutionary stages of stars (see Figure 1.4). While a low-mass star ends its life as a planetary nebulae (and then as a white dwarf), a high-mass star ends its life as supernovae that, depending on the initial mass, can evolve to a neutron star or a black hole. The second difference is related to their pre-main sequence evolution. While low-mass stars assemble their mass, end the accretion activity and then start nuclear reactions in their interior; for high-mass stars, the nuclear reactions initiate when the star is still accreting more material to reach the final mass. This difference is related to the Kelvin-Helmholtz and free-fall timescales that will be introduced in more detail in Section 1.2.2.

As described in Section 1.1, star formation occurs inside molecular clouds. The densest parts inside of the cold molecular can collapse gravitationally, leading to the high densities and temperatures required in the process of formation of
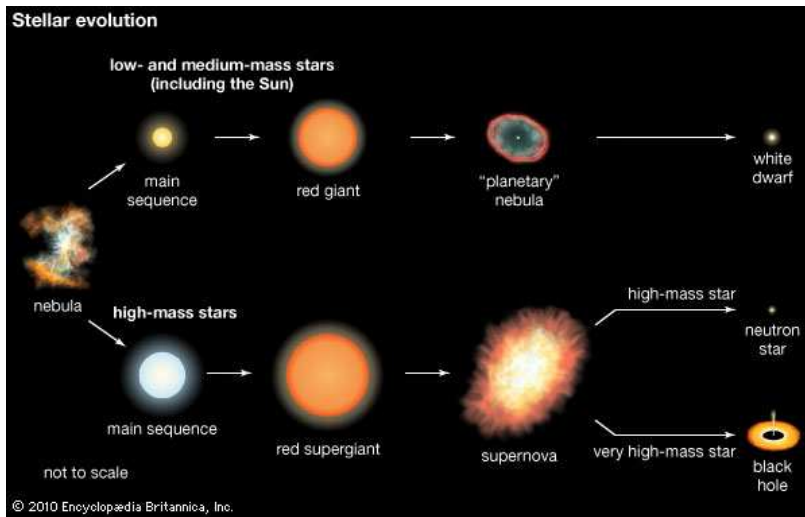
Figure 1.4: Stellar evolution on basis of the initial mass of the star.

a star. In this Section, I will briefly describe the formation process of both low and high-mass stars.

1.2.1 Low-mass star formation

The standard model of low-mass star formation is described in several works (e. g., Shu et al. 1987, 1993, Larson 2003b, McKee & Ostriker 2007 and references therein). Figure 1.5 shows a sketch of the low-mass star formation process from a prestellar cloud core to a protostar, in five stages. The first stage is the contraction and fragmentation of the molecular cloud forming slowly rotating cloud cores. In a second stage, the condensing cloud core begins to collapse, the material that is accumulated in the center gives rise to a protostellar object deeply embedded within an envelope of dust and gas. The distribution of mass, initially spherical, becomes flattened due to the centrifugal force generating an accretion disk. In the next stage, a strong stellar wind along the rotational axis stops the infalling of material through the poles, and breaks out as a collimated outflow of gas and dust. The outflow will affect the future evolution of the cloud, by transferring energy, momentum and turbulence to the surrounding material. The outflows create cavities in the molecular cloud, influence in the chemical evolution of the cloud and help to remove the surrounding of gas and dust. The opening angle of the outflow is expected to increase with time until the infall process is stopped. At this
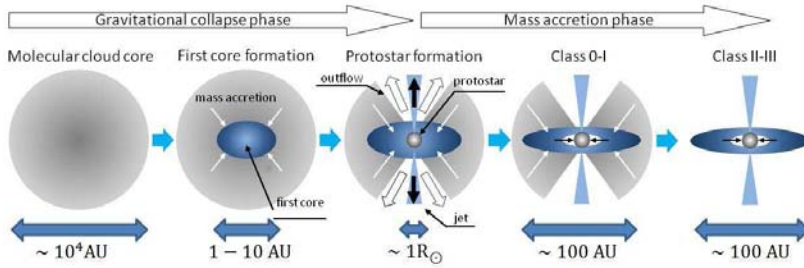
Figure 1.5: Sketch of the low-mass star formation process from a prestellar cloud core to a protostar and finally to a star. Image from Yusuke Tsukamoto's web-page.

stage, the newly-formed star (initially obscured by the dust) becomes visible at other wavelengths (e. g., visible and infrared).

During the first stages of formation, young stellar objects (YSOs) are deeply embedded inside molecular clouds, which absorb their radiation and re-emit them at longer wavelengths in the infrared. The spectral energy distribution (SED) at these wavelengths (between 1 and 100 μm) depends on the nature and distribution of the material surrounding the YSO. Protostellar SEDs are conventionally divided into four classes (e. g., Andre et al. 1993), and are thought to represent an evolutionary progression.

Class 0 objects are characterized by a central protostar that is extremely faint in the optical and near-IR, and with a large submillimeter luminosity. They present a typical SED of a black body at low temperatures ($<$ 30 K), coming from a cold dust envelope. Protostars are believed to acquire a significant fraction of their mass in this embedded phase. Most of the known Class 0 objects are associated with intense and collimated molecular outflows and Herbig–Haro objects, and a major fraction show centimeter emission coming from a thermal radio jet.

Class I objects have typical ages of $\sim 10^5$ years and are still deeply embedded in the molecular cloud (therefore not observable in visible wavelengths). Three main structures can be found in a Class I object: a large-scale dust envelope ($\sim 10^4$ AU) in free fall, a cavity surrounding the YSO with a size of ~ 200 AU, and a flattened disk at scales < 200 AU. Class I objects are more luminous than Class II and III sources, with the main contribution to their luminosity coming from the accretion of material.

Class II objects can be observed at optical and infrared wavelengths. The optical contribution corresponds to the black body emission of the photosphere of a pre-main sequence cold star, with an age of $\sim 10^6$ yr, while the excess at infrared wavelengths is due to an optically thick circumstellar disk of dust

with a mass of $\sim 0.01\ M_\odot$. Classical T Tauri stars or stars with FU Orionis episodes are typical of this evolutionary class.

Class III objects are observable at visible wavelengths, with low luminosities at mid- and far-infrared and are known as naked T Tauri stars. They have typical ages of $\sim 10^7$ years and their SED corresponds to a black body with a temperature of a typical reddened photosphere of a young star, attenuated due to the presence of some dust particles.

The presented evolutionary sequence and classification is only valid for low-mass stars. For more massive stars, the fast evolution to the main sequence makes it more difficult to establish a similar classification.

1.2.2 High-mass star formation

High-mass stars are very important for the morphological, dynamical, chemical and physical evolution of the galaxies. Therefore, the study of these stars are key to understanding many physical phenomena in our own Galaxy, and in other galaxies. However, their first stages of formation are still poorly understood. This is because it is not easy to perform observational studies of massive stars since they tend to form in clustered mode, deeply embedded in molecular dense cores highly obscured by circumstellar dust (with high extinction $A_V \sim 100$), and at distances > 1 kpc. However, there are some high-mass star forming regions at shorter distances (e. g., Orion at ~ 415 pc and Mon R2 at ~ 830 pc) that become excellent targets to study this process of formation of stars compared to the low-mass ones.

The star formation scenario described in the previous section is accepted for low-mass stars, however, it is questioned for stars much more massive. The main differences that call into question the previous model are related to the timescales. The Kelvin-Helmholtz timescale, that determines how quickly a star contracts before nuclear fusion starts (i. e., sets roughly the pre-main sequence lifetime), is given by

$$t_{\mathrm{KH}} = \frac{GM^2}{RL} \tag{1.5}$$

(Huang & Yu 1998), where G is the gravitational constant, M the protostellar mass, R the protostellar radius, and L the luminosity. The free-fall timescale indicated the period of accretion for the envelope and can be calculated as

$$t_{\mathrm{ff}} \simeq \left(\frac{3\pi}{32G\rho}\right)^{1/2}, \tag{1.6}$$
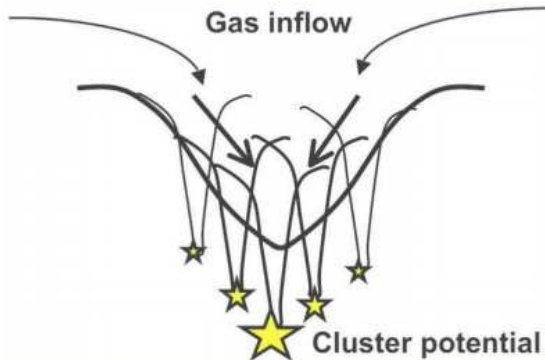
Figure 1.6: Schematic view of the competitive accretion process. In this model, the gas goes down to the cluster core. The stars located there are therefore able to accrete more gas and become higher-mass stars. The gas reservoir can be replenished by infall into the large-scale cluster potential. This figure is from Bonnell et al. (2001).

with ρ the density. For low-mass stars (with masses up to 8 $M_\odot$) $t_{\mathrm{KH}} >> t_{\mathrm{ff}}$, which indicates that the star acquires all the mass before starting the nuclear reactions. However, for high-mass (masses above 8 $M_\odot$, or spectral types O and B) stars $t_{\mathrm{KH}} << t_{\mathrm{ff}}$, which indicates that the star begins nuclear fusion while it is still accreting material (Palla & Stahler 1993; Keto & Wood 2006). In this situation, the main problem arises from the radiation pressure that a new formed massive stars exert on the surrounding ambient cloud as soon as they ignite, pushing against infalling material. It is the interaction between the accretion flow and the radiation field of the massive protostar what makes massive star formation different from low-mass star formation. In the past decades, early spherically symmetric calculations based on the low-mass star-formation scenario, demonstrated that the strong radiation pressure acting on dust grains might be enough to halt the accretion onto the massive protostar (Kahn 1974, Wolfire & Cassinelli 1987, Stahler et al. 2000), and therefore, the theory had to be adapted to account for the formation of massive stars.

Different models (or theories) have been proposed to explain the formation process of high-mass stars. The two most accepted models are the monolithic collapse (Tan & McKee 2002, Yorke & Sonnhalter 2002, Breen et al. 2014) and the competitive accretion (Bonnell & Bate 2006, Krumholz & Bonnell 2007, Bonnell et al. 2011). Some detailed reviews describe the pros and contras of both models (see for example Tan et al. 2006, Zinnecker & Yorke 2007, Krumholz 2014a, Krumholz 2014b, Krumholz et al. 2014, Tan et al. 2014, and references therein).

The **monolithic collapse** star formation model, also called the *gravotur-*
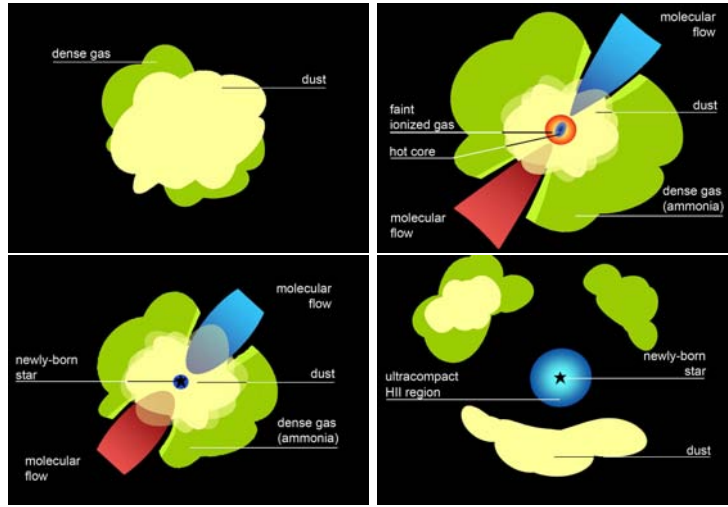
Figure 1.7: Schematic view of a possible evolutionary scenario for high-mass star formation. *Top-left:* rotating and collapsing dust and dense gas core. *Top-right:* a hot molecular core is detectable in the center, sometimes associated with faint ionized gas and powering molecular outflows. *Bottom-left:* development of an hypercompact HII region still associated with outflowing emission and deeply embedded in dust and gas. *Bottom-right:* strong ionized gas associated with ultracompact or compact HII regions that have already dispersed most of the dust and dense gas. Figure from Sanchez-Monge (2011), image credit: B. Sánchez-Monge and R. Delgado.

bulent high-mass star formation model, adapts the mechanism of low-mass star formation to solve the problem of the radiation pressure. Some theoretical works have revealed that the cavity created by a jet and outflow can be used by the radiation from the massive protostar to escape without hindering accretion through the disk and onto the protostar (Tan & McKee 2002, Yorke & Sonnhalter 2002, Kuiper et al. 2010). The radiation pressure in the disk is about 30 times lower than in other directions, this allows infall in the equatorial plane with rates of about 10^{-5} $M_\odot$ yr^{-1} (Zinnecker & Yorke 2007). Several observational works have found highly collimated jets, outflows and rotating structures around massive protostars (e. g., Martí et al. 1993, Martí et al. 1993, Beuther & Shepherd 2005, Beltrán et al. 2006, Sánchez-Monge et al. 2013, Sánchez-Monge et al. 2014), that would the monolithic collapse scenario. However, Zinnecker & Yorke (2007) suggest that the monolithic collapse could be possible only for stars with mass ≤ 18.0 $M_\odot$(B type stars) but not for the more massive stars (e. g., O type). In summary, the monolithic collapse model is a scaled-up version of low-mass star formation, where the fragments are produced by turbulence, then decouple from the rest of the cloud and collapse gravitationally. As a result, this model predicts that the core mass function already contains all information

about density, disks and the initial mass function describing the masses of the stars. This model predicts that high-mass stars can form in isolation.

The **competitive accretion** star formation model, is based on the physics of gravity and the picture of massive stars forming in clustered environments (e. g., Bonnell et al. 2011 and reference in there). The initial fragmentation of a stellar cluster in a turbulent cloud involves the rapid generation of structures, followed by the collapse of individual fragments at Jeans length separations (Larson 1984). The fragmentation is unaffected by heating from other stars, as they are far enough from each other. Numerical simulations show that the gravitational fragmentation of a turbulent medium drives structures into the molecular cloud (Bonnell & Bate 2006; Federrath et al. 2010) while the thermal physics determines the fragmentation scale and thus the characteristic mass of the stars (Larson 2005a,b; Bonnell & Bate 2006). Once individual fragments are formed, they constitute small N systems (or clusters) which grow through accretion of gas and other fragments. The gravitational potential of the cluster (in combination of the higher gas density) ensures that gas is funneled down to the center to be accreted by what will become the most massive star (see Figure 1.6). The gravitational potential is necessary to gather the mass required for the high accretion rate and thus the formation of the high-mass stars. Compared to the previous scenario, the stars have access to a larger mass reservoir (the whole cloud). The most massive fragments in the cluster will have a larger gravitational potential and therefore will become even more massive. Since all the fragments acquire mass from a common reservoir, the core mass function does not contain information on the initial mass function. This model predicts that high-mass stars form in clusters.

In order to discern which mechanism or scenario better explains and dominates the formation of massive stars, it is completely necessary to conduct detailed observations of high-mass star forming regions. Despite the observational difficulties mentioned before (namely the large distances, crowded environments and large extinctions), a huge observational effort during the last years have revealed several observational features (hot molecular cores, HII regions, outflows and jets, disks, masers) associated with massive young stellar objects that can help to improve the theoretical models. From this observational perspective an evolutionary scenario for high-mass stars has been proposed (see Figure 1.7) starting from a contracting and fragmenting cloud, continuing with the development of a hot molecular core (i. e., a chemically rich, dense object with temperatures $\sim$200 K) until the development of an HII region.

Among all the observational features, the presence of **HII regions** Kurtz (2005) is the one that better differentiates the bimodality of low-mass and high-mass star formation, since only massive stars can produce enough UV photons to ionize the surrounding gas. Furthermore, the development of an HII region
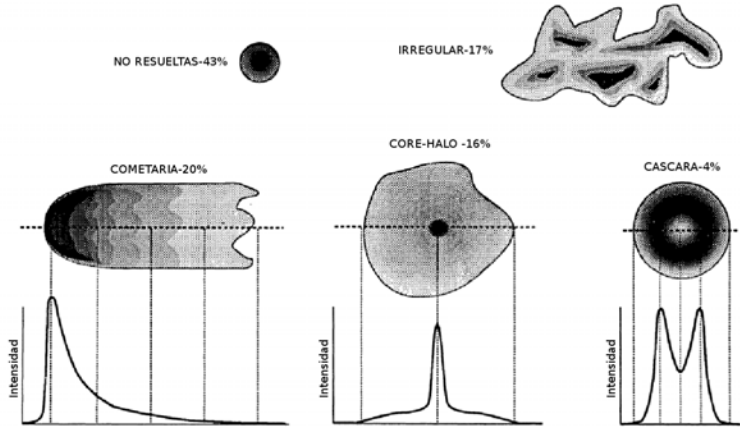
Figure 1.8: Classification of HII regions by morphology. Figure from Wood & Churchwell (1989).

Table 1.3: Physical parameters of the HII regions.

	Size (pc)	Density (cm^{-3})	Ionized mass ($M_\odot$)
Hypercompact	<0.03	>10^6	10^{-3}
Ultracompact	<0.1	>10^4	10^{-2}
Compact	<0.5	>5 × 10^3	1
Classic	10	100	10^5
Giant	100	30	10^3–10^6
Supergiant	>100	10	10^6–10^8

is one of the major effects that complicates the understanding of massive star formation with respect to the models for low-mass stars. HII regions consists of ionized gas (mainly hydrogen) that can emit in both spectral lines (known as recombination lines) and continuum emission (known as Bremsstrahlung radiation).

Massive young stars with temperatures 10^4 K and luminosities above 1000 $L_\odot$, radiate large amounts of UV photons beyond the Lyman limit (912Å or $h\nu > 13.6$ eV) that can ionize any hydrogen atom with which they interact. In this case, the electron is removed from the atom, creating an HII ion (i.e., a proton) and a free electron. The HII region extends as far as the luminosity of the star permits, to a radius known as the Strömgren radius. Within this radius protons and free electrons continually interact and recombine to form neutral hydrogen atoms, and photons continually ionize the atoms to create

protons and free electrons. The morphology and physical characteristics of the HII region depend on the initial distribution of the surrounding medium, and the total energy radiated by the central star. Table 1.3 summarize the different types of HII regions on basis to their physical parameters. In this classification the hypercompact and ultracompact HII region are associated with the most embedded and therefore youngest evolutionary stages; while the giants and supergiants are associated with more evolved stars, and are likely to be the overlap of multiple ionized gas bubbles produced by many high-mass young stars. Figure 1.8 shows the different morphologies found for HII regions (Wood & Churchwell 1989), which can be divided into unresolved ($\sim 43\%$), irregular ($\sim 17\%$), cometary ($\sim 20\%$), core-halo ($\sim 16\%$) and shell-like $\sim 4\%$ shape.

Not all the UV photons produced by a young massive star have enough energy to ionize hydrogen. Some UV photons will have lower energies (typically $6 > h\nu > 13.6$ eV) preventing them to be absorbed by hydrogen atoms but allowing them to go through the HII region and photodissociate the gas around it, generating the so called photodissociated or photon-dominated region (PDR). The study of the PDRs is the study of the effects of stellar far-ultraviolet ($6 > h\nu > 13.6$ eV) photons on the structure, chemistry, thermal balance, and evolution of the neutral ISM of galaxies. A detailed description is presented in Chapter 2.

2

PHOTON-DOMINATED REGIONS

This chapter describes the physical and chemical properties of the photon-dominated regions, also called photodissociated regions.

Contents

2.1   What is a Photon-Dominated Region?

High-mass stars (O and B-type stars, with masses > 8 $M_\odot$) have a dramatic impact on the ISM. They emit extreme ultraviolet photons ($h\nu > 13.6$ eV) that ionize the surrounding molecular gas forming HII regions. Furthermore, their far-ultraviolet[i] (FUV) photons (6 eV$< h\nu <$13.6 eV) penetrate beyond the HII region and into the molecular cloud where they dominate the physics and chemistry, giving rise to the so called photon-dominated (or photodissociated) regions (PDRs). Under these considerations, a PDR is the boundary between the ionized HII region, produced by a hot massive star, and its surrounding molecular cloud (e. g., Hollenbach & Tielens 1997, Hollenbach & Tielens 1999). This kind of regions are excellent targets to study the interaction between the UV radiation of young newly formed stars and the surrounding environment, as well as to unveil the details of the massive star formation process.

PDRs around massive stars are not the only kind of PDRs found in our Galaxy (and other galaxies), diffuse warm (WNM; with $T \sim 8000$ K) and cold (CNM; with $n \sim 30$ cm^{-3} $T \sim 100$ K) neutral hydrogen clouds, translucent clouds (with $A_V < 5$, $n_H < 1000$ cm^{-3} and weak interstellar FUV fields), and neutral interstellar medium in starburst galaxies (Kaufman et al. 1999) and galaxies with active galactic nuclei (AGNs; Meijerink et al. 2007) are also associated with PDRs. PDRs contain most of the atomic gas in a galaxy (both in diffuse clouds and in the surface of the more opaque molecular cloud), and about 90% of the Galactic molecular ISM may be "photon-dominated". Not only do PDRs include most of the mass of the ISM, but they also are the origin of most of the IR radiation from the ISM (the other significant sources are HII regions and dust heated by late-type stars).

In the PDRs, FUV radiation plays a major role in their structure, heating, cooling and physical/chemical properties (Tielens & Hollenbach 1985a, Tielens & Hollenbach 1985b). The properties of a PDR are strongly determined by the values of G_0 and n (see Section 2.2), where G_0 is the incident flux of the local FUV radiation field in units of Habing flux (1.6×10^{-3} erg cm^{-2} s^{-1}, Habing 1968) and n is the local hydrogen density (Hollenbach & Tielens 1997). The same physics that apply in PDRs associated with molecular cloud surfaces (Kaufman et al. 2006; Abel et al. 2005; Le Petit et al. 2006) are also applicable in the diffuse atomic interstellar medium (Wolfire et al. 2003, Shaw et al. 2006) but with weaker FUV fields (G$_0$ = 1–10) and lower column densities ($N = 10 \times 10^{19}$–10^{21} cm^{-2}; Wolfire 2010).

---

[i]6 eV is the ionization potential of dust/PAHs; 11.1 eV is the dissociation energy of CO; 11.3 eV is the ionization potential of C; 13.6 eV is the ionization potential of H and O; 14.5 eV then ionization potential of N.

The mid-infrared spectrum of a typical PDR is dominated by the stretching and bending modes of polycyclic aromatic hydrocarbons (PAHs) excited by the absorption of individual UV photons and by the lowest pure rotational lines of H_2 (Leger & Puget 1984). The H_2 molecule is formed on the surface of dust grains and is destroyed by photodissociation within PDRs. Its formation rate has been found to be related to PAH abundance (Habart et al. 2004), suggesting that there may be an observational relationship between these two species. Both PAHs and H_2 have been shown to be valuable probes of the physical conditions within PDRs (Bakes & Tielens 1994; Draine & Bertoldi 1996; Hollenbach & Tielens 1997; Berné et al. 2009; Fleming et al. 2010).

PDRs associated with star-forming regions, were not considered important until the end of 1970s, when they began to be considered as a link between the HII regions and the molecular gas. The study of dense PDRs on the surfaces of opaque ($A_V >> 2$) molecular clouds was stimulated by the observations of the massive star-forming regions Orion A and M17 in the fine-structure lines [CII] 158 μm and [OI] 63 μm by Melnick et al. (1979b), Storey+1979, Russell et al. (1980) and Russell et al. (1981). The early [CI] 609 μm observations of extensive columns of atomic carbon in molecular clouds also stimulated the modeling and understanding of dense PDRs (Phillips & Huggins 1981; Keene et al. 1985). These observations pointed to predominantly neutral, infrared-luminous regions lying outside the HII regions. In the recent years, PDRs have been the subject of many theoretical (e. g., Tielens & Hollenbach 1985a, 1985b, 1990, 1995, Sternberg & Dalgarno 1995, Roueff & Petit 2005, Roueff et al. 2007, Viti 2013a, 2013b) and observational studies (e. g., Herrmann et al. 1997, Brooks et al. 2003, Fleming et al. 2010, Fuente et al. 2005a, 2005b, 2008, 2010, Pilleri et al. 2012, 2013, 2014, 2015, Nagy et al. 2013, Cuadrado et al. 2015).

2.2 Physical structure

A PDR can be divided into chemical regimes (or layers) as a function of visual extinction (A_V) from the cloud surface[ii] (Sternberg & Dalgarno 1995). The layers of the PDR start in the HII region limit (or ionization front), where the gas is predominantly in neutral state (HI), and extend until the oxygen is found in its molecular state (O_2; Hollenbach & Tielens 1997, 1999, Lebrón et al.

[ii]Note that the usage of A_V to delineate the different layers of a PDR, permits to define a layer structure that will be applicable to any PDR (low or high-density, low or high-ionization). However, it is important to mention that the physical extension of the different layers will strongly depend on the density and incident flux.

2003). The incident FUV flux, G_0, that can be produced by the interstellar radiation field (ISRF) or by nearby hot stars, penetrates a neutral cloud of hydrogen with density n. The values of the incident flux (with 6 eV$< h\nu < 13.6$ eV) can range from the local average ISRF ($G_0 \sim 1.7$; Draine 1978) to $G_0 \geq 10^6$, for gas at a distance of 0.1 pc from an O star (Hollenbach & Tielens 1997). The value of density n can range from ~ 0.25 cm^{-3} in the warm neutral medium to ~ 10–100 cm^{-3} in diffuse clouds, to $\sim 10^3$–10^7 cm^{-3} in the PDRs associated with molecular gas. The values G_0 and n will determinate the physical extent of the PDR layers. Assuming that the HII region is described by a Strömgren sphere, the radius of a Strömgren sphere is given by

$$\left[\frac{R_\mathrm{S}}{\mathrm{pc}}\right] = 0.145 \left[\frac{\dot{N}_\mathrm{i}}{10^{49}\mathrm{photons\ s^{-1}}}\right]^{1/3} \left[\frac{n_\mathrm{e}}{10^4\mathrm{cm^{-3}}}\right]^{-2/3} \left[\frac{T_\mathrm{e}}{10^4\mathrm{K}}\right]^{1/4}, \quad (2.1)$$

where $\dot{N}_\mathrm{i}$ is the number of ionizing photons, n_e is the electron density and T_e is the electronic temperature. And considering that the PDR and the HII region are in hydrostatic equilibrium, it is possible to establish a relation between the density and the incident flux to calculate the radiation field in a PDR surrounding a HII region. The relation reads as (Tielens 2005)

$$G_0 \sim \left(\frac{n}{10^3\mathrm{cm^3}}\right)^{3/4}. \quad (2.2)$$

Figure 2.1 shows the parameter space for G_0 and n in the ISM. The parameter space breaks into three regions separated by the long dashed lines: radiation pressure on grains drives them supersonically through the gas in the upper left region with $G_0/n \geq 10$ cm^{-3}, the middle region includes those PDRs where grain attenuation of the FUV dominates over self-shielding, and the lower left region (with $G_0/n \leq 10^{-2}$ cm^{-3}) is where self-shielding by H_2 brings the HI/H_2 and CII/CO transitions to $A_\mathrm{V} < 1$. The neutral PDR gas associated with various astrophysical phenomena are labeled in Figure 2.1. The upper right hand region of high density and G_0 (short dashed line) is the range of parameter space where strong heating, self-shielding, and collisional de-excitation of H_2 combine to give intense emission from relatively high CO transitions (e. g., J=14–13) and low (2–1) over (1–0) H_2 ratios.

Figure 2.2, illustrates the structure of an opaque PDR. From left to right, it starts with an incident FUV flux, the HII region and the HII/HI interface that absorbs the Lyman continuum photons. As discussed above, the spatial position of this interface depends of G_0 and n, and it is established that the visual extinction at the beginning of the interface is about 0.1 mag, increasing up to 10 at the end of the PDR. The PDR itself is characterized by (**i**) a layer of atomic hydrogen which extends to a depth $A_\mathrm{V} \sim 1$–2 (or $N = 2$–4×10^{21} cm^{-2})
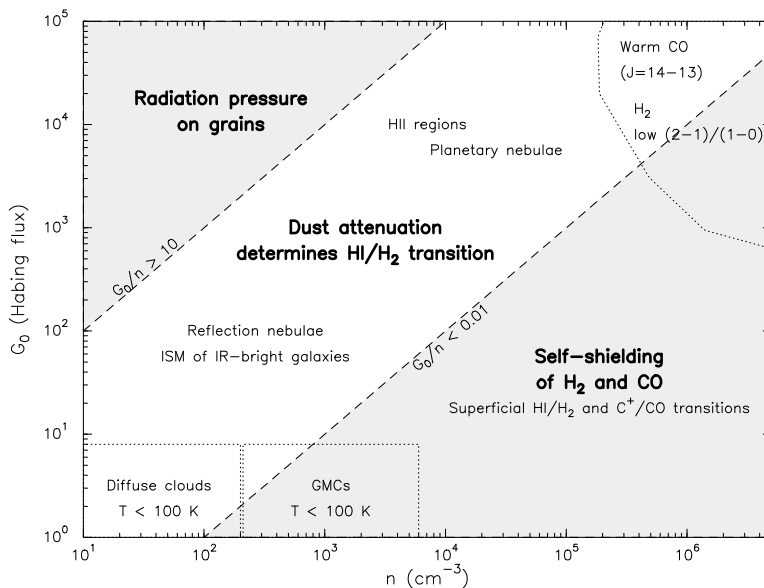
Figure 2.1: Parameter space G_0 and n in the ISM. The parameter space breaks into three regions separated by the long dashed lines, with radiation-dominated PDRs populating the top-left corner, and dense PDRs with H_2 and CO self-shielding populating the bottom-right corner. Figure adapted from Hollenbach (1990).

from the ionization front, (**ii**) FUV-pumped H_2 emission peaking at the HI/H_2 interface, (**iii**) a layer of CII (ionized carbon) which extends to a depth $A_V \sim 2$–4, (**iv**) a layer of atomic carbon that coexists near the CII/CO interface, and (**v**) a last layer mainly formed by H_2, CO and OI, that extends until all the species are in their molecular state (to a depth $A_V \sim 5$–10).

Traditionally, PDRs have been associated with atomic gas. However, PDRs include material in which the hydrogen is molecular and the carbon is mostly in CO, but where FUV photons still strongly affect the chemistry of oxygen and carbon not locked in CO (photodissociating OH, O_2, and H_2O) as well as the ionization fraction. Other elements such as sulfur are completely ionized inside the PDR due to its low ionization potential (of about 10.36 eV). In the following we describe in more detail the different transition zones within the PDR.

HI/H_2 transition, surface area: Although it depends on the value of the ratio G_0/n, the PDR is characterized by a layer of atomic hydrogen that extends to a visual extinction of $A_V \sim 1$–2 mag (or $N(HI) = 2$–4×10^{21} cm^{-2}) form the ionization front. This layer of the PDR, is called surface area (as it is the first part of the PDR). Despite the gas being predominantly neutral,
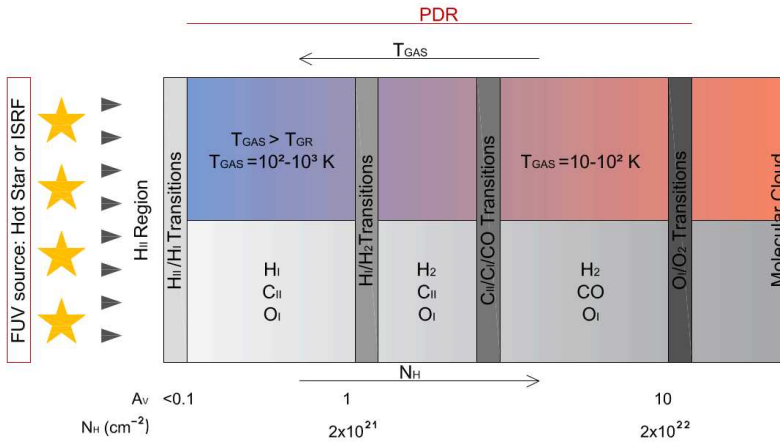
Figure 2.2: A schematic diagram of a photon-dominated region. The PDR is illuminated from the left and extends from the predominantly atomic surface region to the point where oxigen is in molecular state ($A_V \sim 10$). Large columns of warm OI, CI, CII, and CO, and vibrationally excited H_2 are produced in the PDR. Figure adapted from Hollenbach & Tielens (1997). Image credit: B. Sánchez-Monge and R. Delgado.

elements with lower ionization potential than hydrogen (e. g., C, Si), can still be ionized. This layer is mainly formed by HI, OI and ionized C (see Figure 2.2).

The incident FUV radiation is absorbed by dust and large carbon molecules (such as the PAHs), and is mostly used to excite the PAHs and heat the grains. The gas generally reaches higher temperatures (T$\sim$ 100–5000 K) than the grains (T$\sim$ 10–50 K) because the gas cooling is less effective (via [CII] 158 μ m and [O_I] 63 μm line emission) than the dust continuum cooling (see Section 2.3). In this area the warm gas leads to intense emission of [CII] 158 μm, and [OII] 63 μm, 145 μm, as well as IR dust continuum and near-infrared emission features from PAHs. At $1 \leq A_V \leq 3$, hydrogen presents self-shielding that allows the formation of molecular hydrogen on grain surfaces. As mentioned before, the photodissociation of H_2 proceeds through absorption of FUV photons. When the H_2 column density exceeds 10^{14} cm^{-2}, the FUV absorption lines become optically thick and self-shielding becomes important. Therefore, the photodissociation rate depends on the H_2 abundance as a function of depth in the cloud. For PDRs with $G_0/n \sim$ 0.01–0.1 cm^3 (e. g., diffuse clouds exposed to the ISRF or dense clumps expose to higher

FUV fluxes) self-shielding alone controls the dissociation of H_2 and hence the location of the HI/H_2 transition. Because of the self-shielding, the H_2 column density increases rapidly and the HI/H_2 transition zone is quite sharp. For PDRs associated with brighter FUV sources (with $G_0/n \sim 1$ cm^3), the location of the HI/H_2 transition is dominated by dust absorption. At $A_V \sim 2$, the dust reduces the H_2 photodissociation rate sufficiently that an appreciable column density of H_2 can build up, H_2 self-shielding takes over, the abundance of H_2 increases rapidly, and the HI/H_2 transition is again quite sharp. Several authors have discussed the H_2 self-shielding and photodissociation (e. g., Field et al. 1966, Draine & Bertoldi 1996, Hollenbach & Tielens 1997, 1999, and reference in there).

CII/CI/CO transition: Just after the first transition zone, we find the second layer of the PDR, which is dominated by the dust radiation and formed by H_2, CII and OI. The transition of CII to CI to CO occurs at a visual extinction of $A_V \sim 2$–4 mag. For low G_0/n PDRs, the effects of CO self-shielding can lead to isotopic fractionation effects at the borders of clouds, where the rarer CO isotopes are preferentially photodissociated. Since the abundance of CO with respect to H_2 is about 10^{-4}, the CII/CI/CO transition is much less sharp than the HI/H_2 transition. Like H_2, CO abundances can be appreciable near the surfaces of dense clumps. When the gas density is sufficiently high relative to the FUV flux ($G_0/n \leq 0.01$ cm^2), self-shielding of molecules can move the CII/CO and H/H_2 transitions close to the surface of the molecular cloud ($A_V < 1$), where they can feel the full effect of heating by the FUV radiation field. Comparison with observations suggests that a small volume filling factor of high density ($n \sim 10^6$–10^7 cm^{-3}) clumps embedded within a moderated density ($n \sim 10^3$–10^5 cm^{-3}) inerclump medium are a common phenomena in PDRs (Hollenbach & Tielens 1999). Several authors present a detailed study about the photodissociation and self-shielding of CO (e. g., Glassgold et al. 1985, Eidelsberg et al. 1992, van Dishoeck & Black 1988, Lee et al. 1996).

OI/O$_2$ transition: The oxygen present in a PDR is in atomic state until a visual extinction of $A_V \sim 8$–10 mag, where the OI/O$_2$ transition occurs. This is the deeper layer of the PDR (as it is the end limit of the PDR) and is mainly formed by H_2, CO and OI. The OI/O$_2$ transition occurs when $N(\text{HI}) \geq 2 \times 10^{22}$ cm^{-2} and the gas temperature is about 20 K. Except of oxygen that is contained in the CO molecule, all the oxygen within the first areas of the PDR remains neutral, while the oxygen after the transition zone remains in its molecular state.

2.3   Cooling and heating processes

Two important aspects of PDRs are the mechanisms of cooling and heating that describe the energy balance, and in the end the physical and chemical structure of these objects. In the following we summarize the main aspects of both processes.

The **cooling in a PDR** occurs via far infrared (FIR) fine structure lines (e. g., [CII] 158 μm, [OI] 63 and 146 μm, [SiII] 35 μm, [CI] 609 and 370 μm; Spaans et al. 1994; Natta et al. 1994; Hollenbach & Tielens 1997), by H_2 rovibrational transitions (Martin & Mandy 1995, Martí et al. 1996), and by molecular rotational lines (particularly of CO; Hollenbach & McKee 1979; McKee et al. 1982; Hollenbach & Tielens 1997). The left panel of Figure 2.3 shows the gas cooling contribution of every line as a function of A_V. At low visual extinctions (in the layers close to the ionization front) the cooling is dominated by the CII and OI fine structure lines. As we move in the PDR towards the molecular cloud, the main cooling lines are those of CI and CO. For high values of n and G_0, the gas at the surface of the PDR reaches temperatures ≥ 5000 K, and can cool down via [FeII] (1.26 and 1.64 μm), [OI] 6300 Å and [SII] 6730Å lines (Burton et al. 1990). At high densities, cooling by collisions with the cooler dust grains may also be significant (Burke & Hollenbach 1983). The local radiative-cooling rate of a species is also affected by radiative transfer and depends on the global distribution of the level populations throughout the PDR. In general, the escape-probability formalism is used to calculate the local cooling rate. As a result, in semi-infinite slabs, the PDR temperature structure can be calculated from the outside to the inside without the need for global iterations.

The **heating in a PDR** occurs mainly via photoelectric effect on PAHs and small dust grains, and via FUV pumping of H_2 molecules. Other heating mechanisms are *i)* gas collisions with warm grains, *ii)* cosmic ray ionization and excitation, *iii)* ionization of C, and *iv)* pumping of gas particles to excited states by the FIR radiation field of the warm dust followed by collisional de-excitation. These heating processes only become important at great depth in the PDR (Tielens & Hollenbach 1985a, 1985b, 1997). The right panel of Figure 2.3 shows the gas heating contribution of each process as function of A_V. The Figure reveals that the photoelectric heating is the most important heating mechanism in the inner part of the PDR, but at $A_V \geq 8$ the cosmic rays become the the most important heating mechanism.

Photoelectric heating is dominated by the smallest grains (Watson 1972a, 1972b, Jura 1976a, 1976b) and large PAHs (D'Hendecourt & Leger 1987;
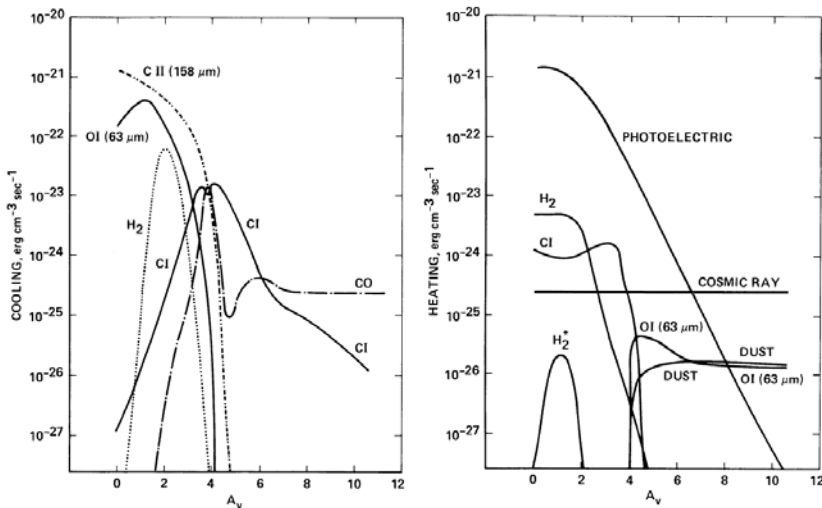
Figure 2.3: Gas cooling (left panel) and heating (right panel) terms in the energy balance of a PDR as a function of the visual extinction A_V. Figure from Hollenbach et al. (1991).

Lepp & Dalgarno 1988a; Verstraete et al. 1990; Bakes & Tielens 1994), and is the most important heating process. The left panel of Figure 2.4 shows a schematic view of the physics associated with the photoelectric effect on grains and PAHs. Photoelectric heating in a PDR starts when FUV photons are absorbed by a dust grain a PAH and transfer they energy to the grain (or PAH) electrons. This effect can then create energetic electrons that may diffuse in the grain, reach the surface, overcome the work function of the grain and any Coulomb potential if the grain is positively charged, and be injected into the gas phase with an excess of kinetic energy. The efficiency of the photoelectric effect on a grain is given by

$$\varepsilon_{\text{GRAIN}} \sim Y \left(\frac{h\nu - W - \phi_c}{h\nu} \right), \tag{2.3}$$

where Y is the yield that measures the probability that the electron escapes, $h\nu$ is the photon energy carried away as kinetic energy by the electron, W is the work function and ϕ_c is Coulomb potential. For large grains and photon energies, the photons are absorbed deep inside the grain (~ 100Å) and the photoelectrons rarely escape ($Y \sim 0.1$; Bakes & Tielens 1994). In the case of photoelectric heating by PAHs, the limiting factor is that the ionization potential of a charged PAH can be larger than 13.6 eV, and absorbed FUV photons do not lead to the creation of a photoelectron. The photoelectric
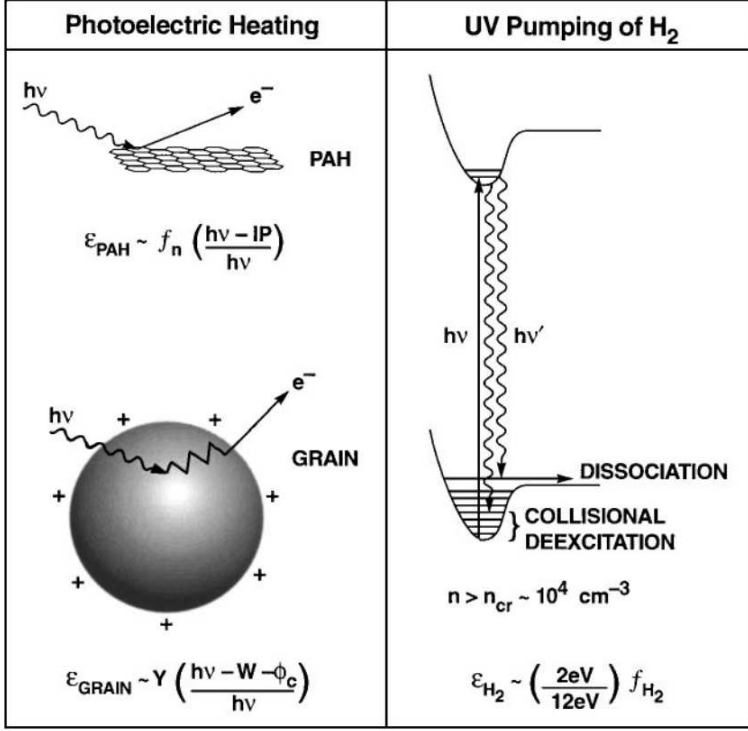
Figure 2.4: *Left:* Schematic view of the physics associated with the photoelectric heating effect on grains and PAHs. An FUV photon absorbed by a dust grain creates a photoelectron that diffuses through the grain until it loses all its excess energy in collisions with the matrix or finds the surface and escapes. *Right:* Schematic view of the H$_2$ heating mechanism for PDRs. FUV fluorescence can leave a H$_2$ molecule vibrationally excited in the ground electronic state. Collisional de-excitation of this excited molecule can then heat the gas. Figure from Hollenbach & Tielens (1997).

heating efficiency for small PAH is given by

$$\varepsilon_{\text{PAH}} \sim f_{\text{n}} \left(\frac{h\nu - IP}{h\nu} \right),\tag{2.4}$$

where f_{n} is the fraction of PAHs that can be ionized by FUV photons and IP is the ionization potential. Theoretical calculations show that PAHs and small grains are more efficient heating agents of the gas than large grains (Jura 1976a, 1976b, Bakes & Tielens 1994). About half of the gas heating is due is to grains with sizes less than 15Å (Bakes & Tielens 1994). The other half originates in grains with sizes between 15 and 100 Å. Larger grains contribute negligibly to the photoelectric heating of the interstellar gas.

The *H$_2$ heating process via UV pumping* is very important in the most external

layers of a PDR. The line absorption of an FUV photon will pump H_2 molecules to a bound excited electronic state, from which it will fluoresce back to the vibrational continuum of the ground electronic state and dissociate (10–15% of the time) or it will fluoresce back to an excited vibrational state in the electronic ground state (85–90% of the time). At low densities, the excited (bound) vibrational states can cascade down to the ground vibrational state through the emission of IR photons, giving rise to a characteristic far-red and near-IR ro-vibrational spectrum. At high densities (10^4 cm^{-3}) collisions with atomic hydrogen can also be an important de-excitation mechanism, leading to heating of the gas and thermalization of the ro-vibrational states. The heating efficiency of this process is given by

$$\varepsilon_{H_2} \sim f_{H_2} \left(\frac{2 \text{ eV}}{12 \text{ eV}} \right), \tag{2.5}$$

where the fraction of the FUV photon flux pumping H_2, f_{H_2}, depends on the location of the HI/H_2 transition zone. Thus, when $G_0/n < 10^{-2}$ cm^3, H_2 self-shielding is important, the H_2 transition is near the surface, and most of the photons that can pump H_2 are absorbed by H_2 rather than dust. Under these conditions, $n > 10^4$ cm^{-3}, $G_0/n < 10^{-2}$ cm^{-3}, $f_{H_2} \sim 0.25$ and this heating process provides an efficient coupling to the FUV photon flux of the star.

2.4   Chemistry

Before entering in the details of the chemistry in PDRs it is worth to briefly describe how chemistry occurs in the ISM. There is a variety of processes that lead to the formation of molecules in the ISM. These can be separated into two broad classes: *i)* gas phase reactions, and *ii)* grain surface reactions. Both processes are important, even though not for the same molecules. Indeed, there is a strong interplay of these two mechanisms in the process of forming simple and complex molecules. In sections 2.4.1, 2.4.2 and 2.4.3 we describe the gas phase and grain surface processes, as well as the different types of reactions. Finally, in section 2.4.4, we describe the chemistry in PDRs. These sections are based on Ward-Thompson, Withworth (2015) an introduction to star formation, Tielens (2005), and Hollenbach & Tielens (1999).

2.4.1 | Gas-phase chemistry

Different types of atoms can combine in the cold molecular clouds (with $T \sim 10$ K) to form molecules. Several molecules (molecular hydrogen, H_2, carbon monoxide, CO, water, H_2O, hydroxide, OH, ammonia, NH_3, silicon monoxide, SiO, carbon dioxide, CO_2, etc) are detected in molecular clouds. The most abundant molecules are the H_2 and CO. These molecules are spatially correlated, in fact, as the H_2 molecule does not emit in radio band CO molecule is used as H_2 tracer. For many years was a mystery how the molecules could form in the low-density environments of the ISM. The main problem present in the formation of molecules is that when two atoms collide in the gas phase it is most likely that they bounce off. Thus, a third body is normally required to carry away the extra energy. Most of the H_2 molecule forms on the dust grains. The grain acts as a sink for the energy excess, and then be released back into the gas. This molecule is formed on the grains surface by means of

$$H + H \rightarrow H_2. \tag{2.6}$$
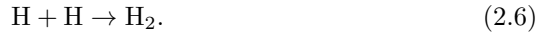
A way to increase the collisional cross-section in the gas phase is that one of the bodies in the reaction is ionized. The source of the ionization may occur by means of UV radiation or, in molecular clouds interiors, by cosmic rays

$$H_2 + cr \rightarrow H_2^+ + e^- + cr, \tag{2.7}$$
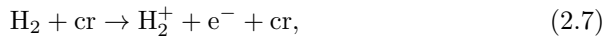
were "cr" is the cosmic ray. The ionization helps to drive the subsequent chemistry. For example

$$H_2^+ + H_2 \rightarrow H_3^+ + H. \tag{2.8}$$

This produces the highly reactive molecular ion H_3^+, and can drive the oxygen chemistry that forms H_2O molecule and OH radical by

$$H_3^+ + O \rightarrow OH^+ + H_2. \tag{2.9}$$
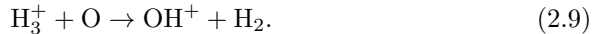
An alternative formation mechanism for OH^+ could be by means of ionized oxygen, via

$$H_2 + O^+ \rightarrow OH^+ + H, \tag{2.10}$$

then

$$HO^+ + H_2 \rightarrow H_2O^+ + H, \tag{2.11}$$

$$H_2O^+ + H_2 \rightarrow H_3O^+ + H, \tag{2.12}$$

and

$$H_3O^+ + e^- \rightarrow OH + 2H \quad \text{or} \quad H_3O^+ + e^- \rightarrow H_2O + H. \tag{2.13}$$
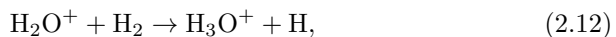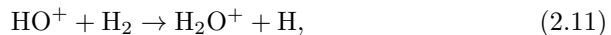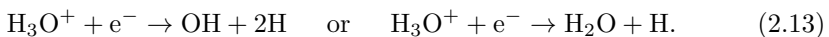
The carbon chemistry follows a similar rute. For example

$$C^+ + H_2 \rightarrow CH^+ + h\nu, \tag{2.14}$$

where $h\nu$ represent an emitted photon, and then

$$CH_2^+ + H_2 \rightarrow CH_3^+ + H, \tag{2.15}$$

and

$$CH_3^+ + e^- \rightarrow CH + 2H, \quad \text{or} \quad CH_3^+ + e^- \rightarrow CH_2 + H. \tag{2.16}$$
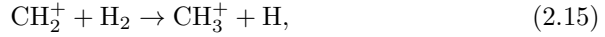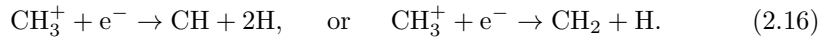
The major pathways to form CO is

$$C + OH \rightarrow CO + H, \tag{2.17}$$

or

$$C^+ + OH \rightarrow CO^+ + H, \tag{2.18}$$

These are known as exchange reactions. The latter proceeds to CO via

$$CO^+ + H_2 \rightarrow HCO^+ + H, \tag{2.19}$$

and

$$HCO^+ + e^- \rightarrow CO + H, \tag{2.20}$$
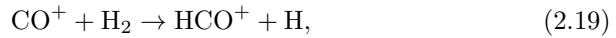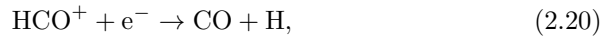
where HCO^+ can be the dominant ion in molecular clouds. Other neutral exchange reactions are important for sulfur chemistry, such as

$$OH + S \rightarrow SO + H. \tag{2.21}$$

Also for nitrogen chemistry

$$CH + N \rightarrow CN + H, \tag{2.22}$$

$$CN + N \rightarrow N_2 + C. \tag{2.23}$$

An alternative rute is

$$N + OH \rightarrow NO + H, \tag{2.24}$$

followed by

$$NO + N \rightarrow N_2 + O. \tag{2.25}$$

All of these different types of reaction are believed to take place in the gaseous ISM.
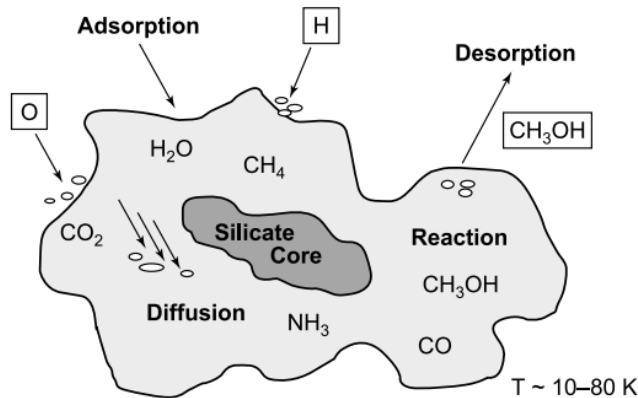
Figure 2.5: Schematic view of the principal physical processes involved in grain-surface chemistry, leading to the growth of interstellar ices (Ehrenfreund et al. 2005).

2.4.2   Grain surface chemistry

Some molecules have abundances much higher that can not be explained by gas-phase reactions alone, consequently, solid state chemical reactions on icy grain surfaces followed by sublimation and enriched gas-phase reactions are often invoked to form those molecules (see Figure 2.5). The grain surface chemistry require more complex reactions chains than the previous ones. In these kind of reactions, the grain acting as a heat sink for excess energy. Thus, grain surfaces reactions are fundamental for the physical and chemical evolution of the ISM. The main physical process involved in grain surface chemistry still being subject of research, but they can be divided in four steps: *i)* accretion of the atoms (or molecules) onto the dust grain surface, *ii)* their movement across the surface, *iii)* reaction between atoms (and/or molecules), and finally *iv)* the released of the new molecule into the gas-phase.

If an atom hits the grain and sticks it is said to be *absorbed* onto the grain surface. If it strikes a site where it can bind, the process is known as **chemisorption**. If it is held by Van der Waals forces the process is known as **physisorption**. The latter kind of binding allows an atom to move across the surface easily and interact with another atom either by *hopping* or quantum tunneling. This is known as *diffusion* and is dominated by hydrogen chemistry, hydrogen being the lightest and most mobile atom. This turns O into H_2O, C to CH_4, N to NH_3 and S to H_2S. CO is mainly formed in the gas phase, but it also can be adsorbed onto grains surface. In fact, the principal chemical components observed on grain surface are CO and H_2O. The chemical built up on grain surfaces are known as grain mantles, and the thickness of water and CO ice

mantles can be such as to more than double size of the original grain. While CO is more common in the gas phase, it appears that CO_2 is more common on the grain surfaces, where it is presumably formed. Atoms or molecules which are strongly bound, or chemisorbed, are not nearly so mobile as those which are physisorbed, and they can only interact with other atoms or molecules which happen to land very close by. These processes are therefore slower and less efficient.

Finally, the removal off molecules from grains surfaces and back into gaseous phase is known as *desorption*. At high densities UV induced desorption is inefficient due to the high extinction. However as soon as a star forms and heats its surroundings then the process known as *thermal desorption* becomes significant. Temperatures > 100 K are required to returns significant grain mantle material to the gaseous ISM. Other desorption processes include the action of cosmic rays or UV photons from the ISRF to remove molecules from grain surface. These provide a background, continuous desorption, and the latter is most significant in the edges of molecular clouds, or near newly formed high-mass stars. Heating caused by molecular formation on dust grains can also lead to desorption. The destruction of molecules by UV photons is the main mechanism responsible for returning molecular material to the atomic state. Two processes reduce the effects of this in the molecular could interiors. One is the process of self-shielding, whereby molecules at the edge of the cloud absorb the photons with high enough energy to dissociate molecules, thereby shielding the molecules in the cloud interiors. The other is absorption of high-energy photons by dust grains, the so-called *extinction* which renders the center of the molecular cloud *dark*.

Figure 2.5 presents a schematic view of the principal physical processes in a grain-surface. In the Figure, cold grain-surface kinetics occurs in two steps: First, atoms and molecules stick to the surface, then subsequently diffuse among surface binding sites either by quantum mechanical tunneling, as is the case for H and D atoms, or by thermal hopping.

2.4.3 | Chemical reactions

The ISM is cold and emptier than the best vacuums created on the Earth, thus, one can think that it is not possible to form molecules in such environment. However, more than 123 molecular species (see Table 2.1) have observed in the ISM, containing from 2 to 13 atoms, without consider the least abundant isotopes (D, ^{13}C, ^{18}O, ^{17}O, ^{15}N, etc). In the previous sections we have described the different chemical processes (gas-phase and grain surface) that take place

in the ISM. In the following we complement this by listing the different types of chemical reactions present in the gas-phase.

As the ISM present a low density, only binary reactions (e. g., A + B → C + D) are important in the gas-phase (although three-body reactions can be important in circumstellar disks).

The rate of a binary chemical reaction is determined by the rate coefficient k, and the abundance of each reactant is given by an equation of the form

$$\frac{dn(\mathrm{A})}{dt} = -kn(\mathrm{A})n(\mathrm{B}) \tag{2.26}$$

where k has unit of $\mathrm{cm}^3\ \mathrm{s}^{-1}$. Gas-phase reactions of the ISM are listed below. This reactions can be divided into three main different categories: *i)* bond formation reactions, that link atoms into simple or complex molecules; *ii)* bond destruction reactions, that breakdown molecules in smaller molecules; *iii)* and bond re-arrangement reactions, that transfer parts of one co-reactant to another one.

Radiative Association: is a bond formation reaction with a rate of $10^{-17}\ \mathrm{cm}^3\ \mathrm{s}^{-1}$ and the form

$$\mathrm{A} + \mathrm{B} \rightarrow \mathrm{AB} + h\nu. \tag{2.27}$$

In this reaction, two species (A and B) combine to generate an excited state AB and emit a photon or translate its excess energy to a third body through a collision to become stable and not dissociate again. However, a three-body encounter in the ISM is very unlikely due to the very low density. The CH^+ formation is an example of this type of reaction ($\mathrm{C}^+ + \mathrm{H} \rightarrow \mathrm{CH}^+ + h\nu$).

Associative detachment: also is a bond formation reaction with a rate of $10^{-9}\ \mathrm{cm}^3\ \mathrm{s}^{-1}$ and the form

$$\mathrm{A}^- + B \rightarrow \mathrm{AB} + \mathrm{e}^-. \tag{2.28}$$

This reactions take place between anions and atoms which collide and stabilize through emission of an electron. The only such reaction that plays a role in ISM chemistry is $\mathrm{H}^- + \mathrm{H} \rightarrow \mathrm{H}_2 + \mathrm{e}$.

Surface recombination: also is a bond formation reaction with the form

$$\mathrm{A} + \mathrm{B} + \mathrm{grain} \rightarrow \mathrm{AB} + \mathrm{grain}. \tag{2.29}$$

In this reaction, two species (A and B) combine in a grain surface to generate a new molecules that go back to the gas-phase. The H_2 formation is an example of this type of reaction.

Table 2.1: Molecules observed in the ISM. Information from CDMS catalog (http://www.astro.uni-koeln.de/cdms/molecules). * Indicates molecules that have been detected by their rotation-vibration spectrum; ** those detected by electronic spectroscopy only.

2 atoms	3 atoms	4 atoms	5 atoms	6 atoms	7 atoms	8 atoms	9 atoms	>10 atoms
H_2	C_3^*	c-C_3H	C_5^*	C_5H	C_6H	CH_3C_3N	CH_3C_4H	CH_3C_5N
AlF	C_2H	l-C_3H	C_4H	l-H_2C_4	CH_2CHCN	$HC(O)OCH_3$	CH_3CH_2CN	$(CH_3)_2CO$
AlCl	C_2O	C_3N	C_4Si	$C_2H_4^*$	CH_3C_2H	CH_3COOH	$(CH_3)_2O$	$(CH_2OH)_2$
C_2^{**}	C_2S	C_3O	l-C_3H_2	CH_3CN	HC_5N	C_7H	CH_3CH_2OH	CH_3CH_2CHO
CH	CH_2	C_3S	c-C_3H_2	CH_3NC	CH_3CHO	C_6H_2	HC_7N	HC_9N
CH^+	HCN	$C_2H_2^*$	H_2CCN	CH_3OH	CH_3NH_2	CH_2OHCHO	C_8H	CH_3C_6H
CN	HCO	NH_3	CH_4^*	CH_3SH	c-C_2H_4O	l-HC_6H^*	$CH_3C(O)NH_2$	C_2H_5OCHO
CO	HCO^+	HCCN	HC_3N	HC_3NH^+	H_2CCHOH	$CH_2CHCHO?$	C_8H6-	$CH_3OC(O)CH_3$
CO^+	HCS^+	$HCNH^+$	HC_2NC	HC_2CHO	C_6H^-	CH_2CCHCN	C_3H_6	c-$C_6H_6^*$
CP	HOC^+	HNCO	HCOOH	NH_2CHO	CH_3NCO	H_2NCH_2CN	$CH_3CH_2SH?$	n-C_3H_7CN
SiC	H_2O	HNCS	H_2CNH	C_5N		CH_3CHNH		i-C_3H_7CN
HCl	H_2S	$HOCO^+$	H_2C_2O	l-HC_4H^*				$C_2H_5OCH_3$
KCl	HNC	H_2CO	H_2CN	l-HC_4N				HC_11N
NH	HNO	H_2CN	HNC_3	c-H_2C_3O				C_60^*
NO	MgCN	H_2CS	$SiH4^*$	$H_2CCNH?$				C_70^*
NS	MgNC	H_3O^+	H_2COH^+	C_5N^-				C_60^{+*}
NaCl	N_2H^+	c-SiC_3	C_4H^-	HNCHCN				
OH	N_2O	CH_3^*	$HC(O)CN$					
PN	NaCN	C_3N^-	HNCNH					
SO	OCS	PH_3	CH_3O					

Continued on next page

Table 2.1 – *Continued from previous page*

2 atoms	3 atoms	4 atoms	5 atoms	6 atoms	7 atoms	8 atoms	9 atoms	>10 atoms
SO^+	SO_2	HCNO	$NH4^+$					
SiN	c-SiC_2	HOCN	H_2NCO^+?					
SiO	CO_2^*	HSCN	$NCCNH^+$					
SiS	NH_2	H_2O_2						
CS	H_3^{+*}	C_3H^+						
HF	SiCN	HMgNC						
HD	AlNC	HCCO						
FeO?	SiNC							
O_2	HCP							
CF^+	CCP							
SiH?	AlOH							
PO	H_2O^+							
AlO	H_2Cl^+							
OH^+	KCN							
CN^-	FeCN							
SH^+	HO_2							
SH	TiO_2							
HCl^+	C_2N							
TiO	Si_2C							
ArH^+								
NO^+?								

Photo-dissociation: is a bond destruction reaction with a rate of 10^{-9} cm^3 s^{-1} and the form

$$AB + h\nu \rightarrow A + B. \tag{2.30}$$

It is possibly the major means of molecules destruction in diffuse clouds. Molecules in these clouds, not protected by dust grains, can be destroyed by UV radiation in a timescale of few orders of few hundred years. The OH + $h\nu \rightarrow$ O + H is an example of photo-dissociation.

Dissociative electron recombination: is a bond destruction reaction with a rate of 10^{-6} cm^3 s^{-1} and the form

$$AB^+ + e^- \rightarrow A + B. \tag{2.31}$$

This reaction occurs when a molecular ion recombines with an electron and breaks down simpler species. Generally these are faster recombination than radiative recombination. The HCO$^+$ + e$^-$ $\rightarrow$ CO + H is an example of dissociative recombination.

Collision induced dissociation: also is a bond destruction reaction of the form

$$AB + C \rightarrow A + B + C. \tag{2.32}$$

In this reaction, two species combine to generate three species. The collision induced dissociation of molecules is an important mechanism in shock-heated gases and affects significantly their thermal and chemical evolution. The H$_2$ + H$_2$ $\rightarrow$ H$_2$ + H + H and H$_2$ + CO $\rightarrow$ H$_2$ + C + O are examples of these reactions.

Neutral-neutral: is a bond rearrangement reaction with a rate of 10^{-11} cm^3 s^{-1} and the form

$$A + BC \rightarrow AB + C. \tag{2.33}$$
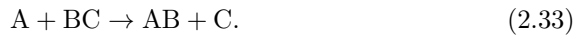
This kind of reactions have high activation barriers that can not be overcome by typical molecular gas with temperatures > 100 K and are therefore mainly of importance in warm gas. UV-pumping can help to overcome the activation barrier by which certain neutral-neutral reactions may be aided. The OH formation is an example of a neutral-neutral reaction (O + H$_2$ $\rightarrow$ OH + H).

Ion-molecule: also are a bond rearrangement reaction with a rate of 10^{-9} cm^3 s^{-1} and the form

$$A^+ + BC \rightarrow AB^+ + C. \tag{2.34}$$
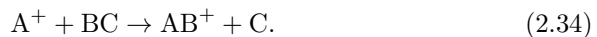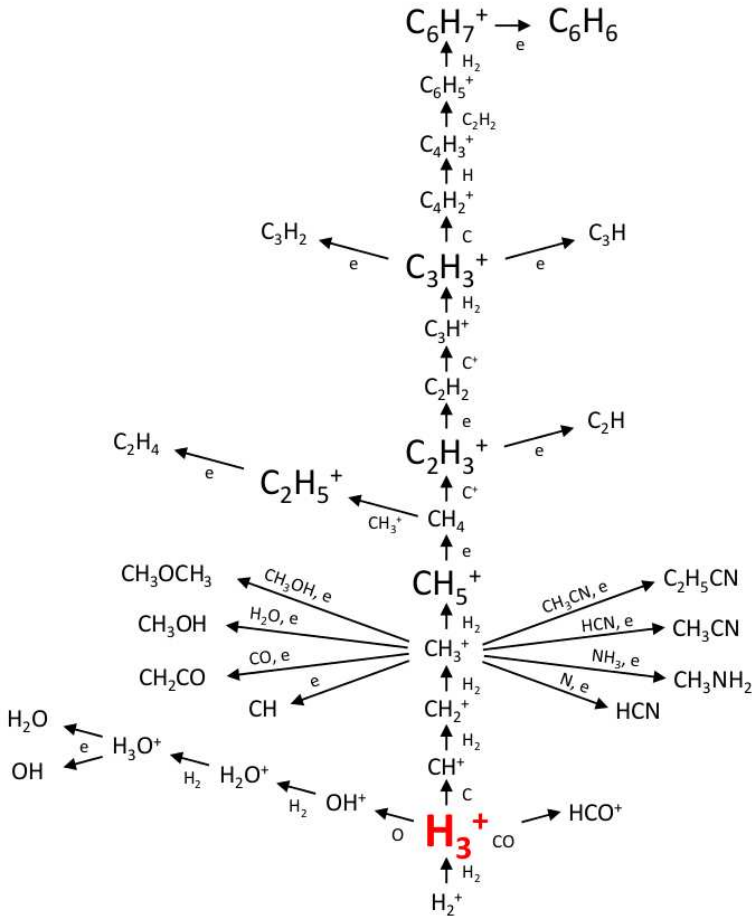
Figure 2.6: Summary of key ion-neutral reaction derived from H_3^+. Figure from McCall (2001).

This reaction is two orders of magnitude faster than neutral-neutral reactions and have lower activation barriers. They are the most important reactions of the cold gas-phase of the ISM. Electric charge of the reagents acts as an attraction force, helping the reaction. Ions are always present inside molecular clouds due to UV radiation or propagation of energetic like cosmic rays. Ion-molecules reactions frequently involve H_2 molecule. Figure 2.6 present a summary of key ion-neutral reaction derived from H_3^+.

Charge transfer reaction: also are a bond rearrangement processes with a rate of 10^{-9} cm^3 s^{-1} and with the form

$$A^+ + BC \rightarrow A + BC^+. \tag{2.35}$$

The $H^+ + O \longleftrightarrow H + O^+$ is an example of a charge transfer reaction. It is of importance as this reaction activates chemical pathways incorporating the oxygen ion O^+.

Cosmic ray ionization reaction: has a rate of 10^{-15}–10^{-17} s^{-1}, and a form

$$A + cr \rightarrow A^+ + e^-. \tag{2.36}$$

This reaction may enhance the HCO^+ abundance in lower density regions and decrease it at high densities (Baan et al. 2008).

Radiative recombination: has a rate of 10^{-12} cm^3 s^{-1}, and a form

$$A^+ + e^- \rightarrow A + h\nu. \tag{2.37}$$

In this kind of reaction interact an ionic specie with an electron to generate a neutral and emit a photon or translate its excess energy.

2.4.4 | Chemistry in the PDRs

Several authors have studied the PDRs chemistry (e.g., Tielens & Hollenbach 1985a; 1985b; Hollenbach et al. 1991, Le Bourlot et al. 1993, Fuente et al. 1993; 1995; Jansen et al. 1995; Sternberg & Dalgarno 1995; Turner 1996a; Turner 1996b; Ginard et al. 2012; Cuadrado et al. 2015). The chemical characteristics of any PDR are defined by the following key parameters. *i)* The strength of the radiation field or G_0, that determines the total available radiative flux at the edge of the PDR. *ii)* The ambient hydrogen density (n) and temperature, that set the pace of chemical reactions and the excitation rate of coolants. *iii)* The metallicity Z, that constrains the total abundances possible for carbon- and oxygen-bearing species and hence influences the chemical and thermal structure. *iv)* The spectral shape of the radiation, parameterized by the color temperature T_{eff}, that fixes the distribution of photon flux over energy.

As the FUV flux plays an important role in their chemistry, photo-dissociation and photo-ionization reactions driven by FUV photons are very important in the PDRs. However, other reactions such as the ion-molecule reactions are important in PDRs. Ion-molecule reactions are maintained by ionization of carbon (e.g., van Dishoeck & Black 1986). The ionization balance of atomic gas under the influence of photo-ionization reactions driven by FUV photons and counteracting recombination and charge transfer reactions with metals and particularly PAHs (e.g., Lepp & Dalgarno 1988a; Bakes & Tielens 1998).

As one moves into a PDR the radiation field is attenuated. Consequently, the chemical composition of the PDR changes in a fundamental way. One fundamental change occurs in the HI/H_2 transition and a second one occurs in the CII/CI/CO transition. Vibrationally excited H_2 can play a decisive role in PDR chemistry. If the gas gets very warm (≥ 500 K), the activation barrier of reactions of atoms and radicals with H_2 can be easily overcome and these types of reactions can dominate. Electron recombination and charge exchange reactions are important for the ionization balance. The FUV flux keeps OI very abundant throughout the PDR, and hence burning reactions are effective.

Photodissociation of CO has been studied by several authors (e.g., Bally & Langer 1982; Glassgold et al. 1985; van Dishoeck & Black 1988; Viala et al. 1988; Eidelsberg et al. 1992; Lee et al. 1996). High-resolution laboratory studies show that CO photodissociation occurs through discrete absorption into predissociating bound states, implying that CO is affected by self-shielding. For low ratios of G_0/n, the effects of self-shielding can lead to isotopic fractionation effects at the borders of clouds, where the rarer CO isotopes are preferentially photodissociated. The location of the CII/CI/CO transition in bright PDRs is largely governed by dust extinction.

The first few magnitudes of extinction of the PDR are referred as the radical region since many carbon hydrides and their ions (e.g., CH, CH^+, CN, HCN, HCO^+ and CO^+), reach their peak abundance there, caused by the presence of both CII and H_2 and the high ($\sim 10^2$–10^3 K) temperatures. Ion-molecule reactions take place that lead to the formation of a large number of different molecular species. Many of the atoms and molecules in the radical region of a PDR are collisionally excited at the ambient densities and temperatures.

Neutral-neutral reactions are often endothermic and/or possess appreciable activation barriers because bonds have to be broken or rearranged. In PDRs, reactions of molecular hydrogen with C^+ (CII), O, N, S^+, and Si^+ are particularly important in initiating the chemical reactions. However, state-to-state chemistry is very selective and vibrational excitation of OH does not enhance the reaction rate of OH + H_2. Translational energy can also be effective in promoting chemical reactions. In particular, the presence of turbulence can lead to non-Maxwellian velocity fields and, hence, non-Maxwellian reaction rates. This effect in PDRs has been shown to be important by Spaans & van Dishoeck (1997) for the reaction C^+ + H_2, which is endothermic. Because of their larger activation barriers, the reactions O + H_2 and N + H_2 are much less affected. Spaans 1995 evaluated in a simplified way, using estimated reaction rates, the effects of turbulence on sulfur chemistry. Finally, Falgarone et al. (1995) examined the enhancement of OH, H_2O, CH^+, and HCO^+ in turbulent PDRs.
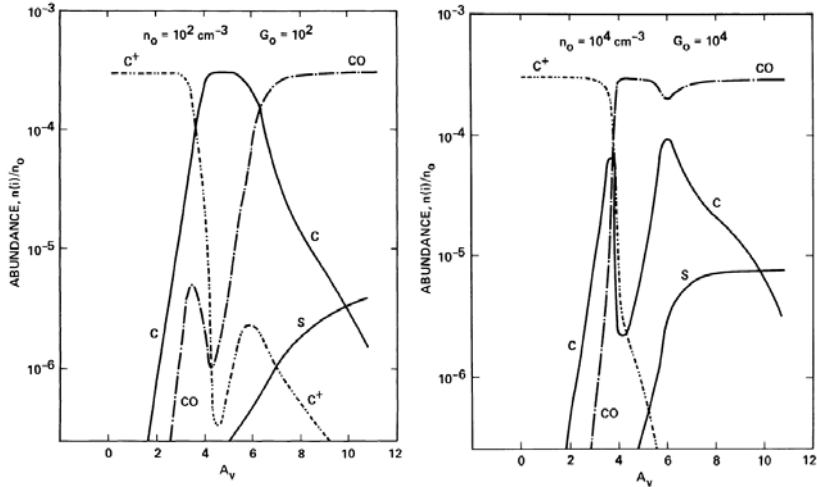
Figure 2.7: Relative molecular abundances (n_x/n_0) of the major carbon species and sulfur, shown as a function of the visual extinction into the cloud for $n_0 = 10^2$ cm^3 and $G_0 = 10^2$ (*left*) and for $n_0 = 10^4$ cm^3 and $G_0 = 10^4$ (*right*). Figure adapted from Hollenbach et al. (1991).

Hollenbach et al. (1991), performed models of PDRs to solve the chemical and thermal balance in the gas and predict the emission from these regions as a function of the FUV flux G_0 (ranging from 1 to 10^4 times of the Habing flux) and density n_0 (ranging from 10^2 to 10^4), considering that the flux is incident on one side ($A_V = 0$). Figure 2.7 shows relative molecular abundances derived for some models performed by Hollenbach et al. (1991). In the top part of the plots presented in this Figure, it is possible to distinguish the changes of the PDR phases along the A_V for different values of G_0 and n.

Sternberg & Dalgarno (1995) performed a detailed study of PDR chemistry. Figure 2.8 present a schematic view of the most important reactions in the chemistry of carbon, oxygen, sulfur and nitrogen compounds. The PDR surface layer consists largely of neutral or ionic atoms created by photodissociation and ionization reactions. Oxygen-bearing radicals are built up through reactions of O with H_2. Most of the OH produced is photodissociated again, but a small fraction reacts with C^+ to form CO^+, which charge exchanges with H to form CO. Some CO^+ is also formed through the reaction of CH^+ with O. The CI/C balance is dominated by photoionization and radiative recombination reactions. A small fraction of the CI reacts with H and H_2 to form CH^+. Likewise, a small fraction of the neutral C flows to CH through reaction with H_2. Through reactions with H, CH^+ and CH reform C^+ and C, respectively. Photoreactions are important for C, OH, and CO but not for the small hydrocarbon radicals and cations. With increasing depth in this
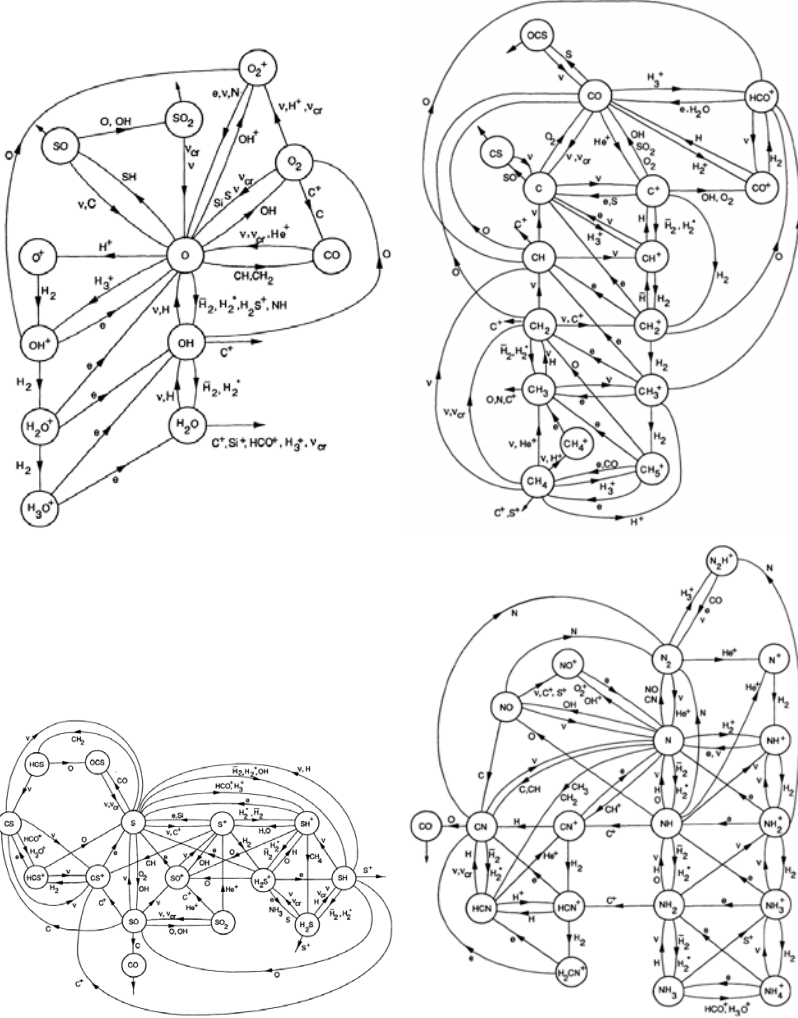
Figure 2.8: Most important reactions involved in the PDR chemistry of oxygen-bearing (top-left), carbon-bearing (top-right), sulfur-bearing (bottom-left) and nitrogen-bearing (bottom-right) compounds. Figure from Sternberg & Dalgarno (1995).

so-called radical zone (but recall it is largely atomic), the chemistry involving small radicals, such as the CH_n^+-family and OH, becomes more important. In cool low-density PDRs, reactions with FUV-pumped vibrationally excited H_2 are important, whereas in warm high-density PDRs, reactions with H_2 dominate. In this case, reactions of C^+ with H_2 followed by dissociative electron recombination of CH^+ to C can be an important recombination route for C^+. As the depth increases, CO formation by burning of small neutral

radicals (i. e., CH, CH$_2$) becomes more important than the OH-driven channel. The CO$^+$, produced through the reaction of CI with OH, reacts with H$_2$ to form HCO$^+$, which dissociatively recombines to CO. This is the start of the CI/C/CO transition zone. Neutralization of C$^+$ through charge transfer with atomic S becomes a dominant source of C. Eventually, PDR chemistry gives way to standard dark cloud, ion-molecule chemistry (Herbst & Leung 1989). Formation of OH and H$_2$O is now initiated through the reaction of H$_3^+$ with O. Reactions of atomic O with OH then forms O$_2$.

2.5 Chemical models

In order to study the chemical complexity of the PDRs, during the last years have been developed several models. This models have evolved into advanced computer codes that account for a growing number of chemical and physical parameters. Table 2.2 lists the most important codes to study the chemical and physical properties of the PDRs. Considering that there are several ways to implement physical effects in numerical codes, the codes listed in the Table differs between them in several aspects: *i)* geometry, *ii)* chemical reaction rates and network, *iii)* considerations of steady state or time-dependent, *iv)* radiative transfer, *v)* shielding, *vi)* atomic and molecular rate coefficients, *vii)* treatment of dust and PAHs, *viii)* treatment of heating-cooling, *ix)* input parameters, *x)* output parameters, *xi)* numerical treatment. The result of these differences is that it is difficult to perform a comparison between models outputs, as significant variations of the prediction in the PDR properties can occur.

As more computational power becomes available, the development of PDR models is in progress generating models more complex and detailed. Roueff et al. (2005, 2007, 2013) had developed a detailed gas-phase models including deuterated species and using large networks of gas-phase reactions with both, steady-state and pseudo-time-dependent. Through this thesis, we use this model to perform a comparison with observational results toward Mon R2. We chose this code to be consistent with previous conclusions by Pilleri et al. (2012) about early-time chemistry for small hydrocarbons. Chapter 7 present a detailed description of the physical parameters considered for this model.

Table 2.2: List of the most important PDR codes (Röllig et al. 2006, 2007).

Code name	Authors
Aikawa	Lee et al. (1996)
Cloudy	Ferland et al. (1998); Abel et al. (2005); Shaw et al. (2005)
COSTAR	Kamp & Bertoldi (2000); Kamp & van Zadelhoff (2001)
HTBKW	Tielens & Hollenbach (1985a,b); Kaufman et al. (1999); Wolfire et al. (2003)
Kosma-τ	Stoerzer et al. (1996); Bensch et al. (2003); Röllig et al. (2006)
Lee96mod	Lee et al. (1996)
Leiden	Black & van Dishoeck (1987); van Dishoeck & Black (1988); Jansen et al. (1995)
Meijerink	Meijerink & Spaans (2005)
Meudon	Le Petit et al. (2006); Le Bourlot et al. (1993)
Sternberg	Sternberg & Dalgarno (1995); Boger & Sternberg (2005)
UCL PDR	Taylor et al. (1993a,b); Papadopoulos et al. (2002); Bell et al. (2005)

3

ABOUT THIS WORK

This chapter describes the main goal of the thesis and its organization.

Contents

3.1   Goal of the thesis

One of the first signposts of high-mass star formation is the presence of UC HII regions, which appear surrounded by layers of partially ionized gas (PDRs). Determining the properties (e. g., dynamics, chemistry, structure, etc.) of these objects is of special interest as they provide important information to the process of formation of high-mass stars, and the surrounding environment in the first evolutionary stages. Among all the known high-mass star forming regions, Mon R2 (see Chapter 4) is the closest (830 pc) UC HII region associated with several PDRs with different physical conditions, and the only one that can be resolved with the current single-dish radio telescopes. Furthermore, Mon R2 seems to be surrounded by a complex filamentary structure. Therefore, this region is an excellent candidate to study the dynamical, chemical and physical properties in a region forming high-mass stars.

The main objective of this thesis is to characterize the chemistry and dynamics of the Mon R2 region. To do so, we have obtained large-scale maps around the central cluster in Mon R2 (see Chapter 5), and performed an unbiased spectral survey (see Chapter 6 and 7) using the IRAM-30m telescope.

3.2   Approach and strategy

As outlined in the previous section, we want to study the dynamics and chemical characteristics of the Mon R2 region.

To study the dynamical properties, we performed observational maps covering a field of view of 163.5 arcmin^2 at 3 mm, around the central cluster. The main observed species are ^{13}CO, $C^{18}O$, HCN, N_2H^+ and HC_3N. With these maps we were able to study the physical distribution of the molecules and compare it with previous observations at different wavelengths. These observations also permit us to look for velocity gradients and study the mass accretion rates along the filamentary structures observed in the region.

To study the chemical characteristics of the region, we did an unbiased spectral line survey covering a broad frequency range in the bands 3, 2, 1 and 0.8 mm, towards the PDRs found around the UC HII region in Mon R2. In total, we obtained more than 150 hours of observing time at the IRAM-30m telescope. The high spectral resolution of the IRAM-30m telescope (~ 0.25–0.65 km s^{-1}) allows us to resolve the line profiles of the detected species. The analysis of the

data is based on Gaussian fits of the detected lines. We perform a statistical study of properties of the lines and we calculate physical parameters (e. g., column density and temperature) for the observed species. We classify the different species in families and study how the properties change from one group to another. Special attention is paid for the deuterated molecules and their corresponding hydrogenated species for which we do a comparison of our results with those presented in other works for different sources, as well as with chemical models.

3.3   Outline and status of different works

This Thesis is the result of the work carried out between 2011 and 2015. During this time, I have observed and studied in detail the Mon R2 region. In the following I outline the different sections of the Thesis, and describe the status of the work. This Thesis is divided in four main parts.

The **Part I** is entitled "Introduction", it contains a description of the constituents of the Milky Way, the low and high-mass star formation processes and their effects in the surrounding gas (e. g., formation of HII regions and PDRs), in **Chapter 1**. **Chapter 2** contains a brief description of the physical and chemical properties of PDRs. This Chapter also describes the main chemical reactions that can take place in the interstellar medium and describes different models to study the PDRs.

The **Part II** of this Thesis is entitled "Monoceros R2", and it starts with an overview of the region in **Chapter 4**. In **Chapter 5** we present and analyze the large-scale maps of Mon R2. The observations reveals the presence of a filamentary hub. These filaments extend towards all directions and present complex kinematics, likely tracing the accretion of material from the outside to the central hub, where we find spiraling arms converging towards the expanding HII region. In **Chapter 6**, we present the spectral survey carried out toward two important positions in the Mon R2 region. More than 65 different species are identified. The list includes typical PDR tracers, complex molecules, deuterated species, ionic species and radio recombination lines (RRLs). The detected species can be related to several processes including shocks, UV-radiation, grain surface chemistry, gas-phase chemistry and hot core chemistry. **Chapter 7** present a detailed study of the deuterated molecules and their corresponding hydrogenated species, including a comparison with sources with different properties and chemical models. We found that the deuterated compounds come from dense and warm clumps with gas kinetic temperatures of ~ 50 K, and not from the most exposed PDR layers.

Furthermore, our results suggest that the deuterated molecules can be used as an evolutionary indicator in star-forming regions.

The **Part III** present a summary of the main conclusions and an outline of the future work in **Chapter 8**.

Finally, the **Part IV** concludes the work with three Appendices. **Appendix A** contains the maps and spectra use in the analysis described in **Chapter 5**. In **Appendix B**, we present the Gaussian fits for all the molecular lines detected in the spectral survey, as well as figures of the observed spectra and part of the maps. Finally, in **Appendix C**, we present the observational parameters, Gaussian fits and figures of the observed spectra for the deuterated molecules.

Additionally to the thesis work, I have been involved in other projects that have resulted in different publications. Here I list a complete list of publications in which I have been involved, including those of the thesis work (published and in preparation) and others projects:

Refereed publications

– **Treviño-Morales, S. P.**, Gómez, Y., Rodríguez-Rico, C. A., Garay, G., Rodríguez, L. F., Sánchez-Monge, Á. *H110α and C110α Emission toward the Photodissociated Region in the GGD 14 Complex*, 2011, Revista Mexicana de Astronomía y Astrofísica Conference Series, 40, 297.

– Pilleri, P., **Treviño-Morales, S. P.**, Fuente, A., Joblin, C., Cernicharo, J., Gerin, M., Viti, S., Berné, O., Goicoechea, J. R., Pety, J., Gonzalez-García, M., Montillaud, J., Ossenkopf, V., Kramer, C., García-Burillo, S., Le Petit, F., Le Bourlot, J. *Spatial distribution of small hydrocarbons in the neighborhood of the ultra compact HII region Monoceros R2*, 2013, Astronomy & Astrophysics, 554, A87.

– Spezzano, S., Brunken, S., Schilke, P., Caselli, P., Menten, K. M., McCarthy, M. C., Bizzocchi, L., **Treviño-Morales, S. P.**, Aikawa, Y., Schlemmer, S., *Interstellar Detection of c-C_3D_2*, 2013, The Astrophysical Journal, 769, L19.

– Pilleri, P., Fuente, A., Gerin, M., Cernicharo, J., Goicoechea, J. R., Ossenkopf, V., Joblin, C., González-García, M., **Treviño-Morales, S. P.**, Sánchez-Monge, Á., Pety, J.; Berné, O.; Kramer, C. *Kinematics of the ionized-to-neutral interfaces in Monoceros R2*, 2013, Astronomy & Astrophysic, 561, A69s.

– **Treviño-Morales, S. P.**, Pilleri, P., Fuente, A., Kramer, C., Roueff E., González-García M., Cernicharo, J., Gerin, M., Goicoechea, J. R., Pety, J., Berne, O., Ossenkopf, V., Ginard, D., García-Burillo, S., Rizzo, J. R.

and Viti, S., *Deuteration in the PDR around the ultracompact HII region Mon R2*, 2014, Astronomy & Astrophysics, 569, A19.

– Cernicharo, J., Bailleux, S., Alekseev, E., Fuente, A., Roueff, E., Gerin, M., Tercero, B., **Treviño-Morales, S. P.**, Marcelino, N., Bachiller, R., Lefloch, B. *Tentative Detection of the Nitrosylium Ion in Space*, 2014, The Astrophysical Journal, 795, 40.

– Ginard, D., Fuente, A., García-Burillo, S., Alonso-Albi, T., Krips, M., Gerin, M., Neri, R., Pilleri, P., Usero, A., **Treviño-Morales, S. P.**, *The chemical footprint of the star formation feedback in M 82 on scales of 100 pc*, 2015, arXiv:1502.05395.

In preparation

– González-García, M., Pilleri, P., Fuente, A., **Treviño-Morales, S. P.**, Le Bourlot, J., Cernicharo, J., Goicoechea, J., Roueff, E., and Le Petit, F., *Spatial distribution of HCl in the ultracompact HII region Monoceros R2*, 2015 in prep.

– **Treviño-Morales, S. P.**, Sanchez-Monge Á, Fuente, A., Tremblin P. Cernicharo J. , Didelon P., Kramer C, Motte F., Pilleri P., Rayner T., Schneider N., *A filamentary hub in Mon R2*, in prep.

– **Treviño-Morales, S. P.**, Pilleri, P., Fuente, A., Kramer, C., Roueff, E., González-García, M., Cernicharo, J., Gerin, M., Goicoechea, J. R., Pety, J., Berne, O., Ossenkopf, V., Ginard, D., García-Burillo, S., Rizzo, J. R. and Viti, S., *Spectral survey in Mon R2*, in prep.

– **Treviño-Morales, S. P.**, Sánchez-Monge, Á., Fuente A., Rodríguez L. F., Roueff, E., Rodriguez-Rico, C., Kramer, C., *Spectral survey in GGD 14 complex*, in prep.

Part II

Monoceros R2

4

MONOCEROS R2

This chapter presents an overview of the Monoceros R2 star forming complex. It starts describing the regions at large scales, to later zoom in the main star forming region: the Mon R2 cluster.

Contents

4.1 Monoceros Molecular Cloud

The Monoceros constellation, located in the sky close to the Orion constellation, contains several regions with sings of on-going star formation. The most studied of them is the Monoceros OB1 association, located at a Galactic latitude of $+2°$ and at a heliocentric distance of ~ 760 pc. Other important sites of active star formation are the molecular clouds Monoceros R1 and Monoceros R2. The Monoceros R1 cloud, at the same Galactic latitude $+2°$, is a reflection nebula that belongs to the Monoceros OB1 association and includes the cluster NGC 2264. Monoceros R2 is a GMC located at a Galactic latitude of $-12°$, close in the sky to the Orion A and Orion B molecular clouds (see Figure 4.1). This Thesis is focused in the study of the main star forming region in the Monoceros R2 cloud, and this Chapter presents an overview of the region, starting with a large-scale description and zooming in to the main star formation site.

The Mon R2 nomeclature is given by van den Bergh (1966) to indicate the second association of reflection nebulae in the constellation Monoceros (see Figure 4.2). Mon R2 has a mass of a few 10^4 $M_\odot$ (Kutner & Tucker 1975; Maddalena et al. 1986), covers an area in the sky of $3° \times 6°$, (Carpenter & Hodapp 2008) and it is located at a distance of about 830 pc[i] (Racine 1968). It is associated with several reflection nebulae that extend over $2°$ on the sky (Carpenter & Hodapp 2008), most of which are illuminated by A and B-type zero age main-sequence stars (ZAMS; Herbst & Racine 1976b). These nebulae were first studied by Seares & Hubble (1920) and Hubble (1922), who demonstrated that the extended emission can be attributed to the associated stars. Nebulae identification was done from inspection of the Palomar Observatory Sky Survey images and cataloged in different works (e. g., Dorschner & Gürtler 1963, 1966; van den Bergh 1966, and Herbst & Racine 1976b).

Figures 4.2 shows part of the of the Mon R2 molecular cloud in a color-composite image. Red, green and blue indicate the IR, red and blue bands from the Digitized Sky Survey (DSS), respectively. To the left edge of the image, we can distinguish a group of pink/blue nebulosities associated with the sources GGD12–15 (Gyulbudaghian et al. 1978), GGD 12-15 contains a small group of reflection nebulae, an HII region, a bipolar outflow and a H_2O maser (e. g., Harvey et al. 1985; Little et al. 1990). Roughly 45 ′ (11 pc) to the west, in the center of the image, there is the most extensively studied region. This is the active star forming site identified as "core", which is embedded in a dense

---

[i]We will use this distance throughout this thesis.
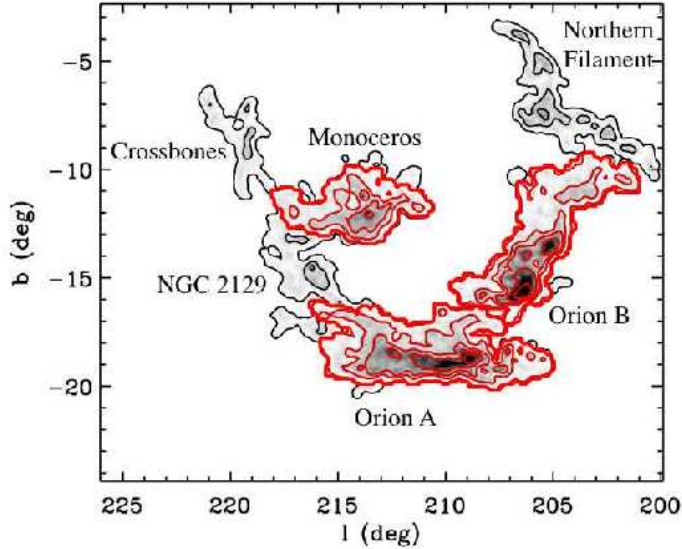
Figure 4.1: CO emission towards the Orion-Monoceros region. The three giant molecular clouds: Orion A, Orion B and Monoceros are depicted in red. Figure from Rosolowsky et al. (2008).

molecular core that lies between the reflection nebulae VdB 67[ii], VdB 68 [iii] and VdB 69[iv] (van den Bergh 1966). The "core" region (see Figure 4.3 for a close-up view) is an excellent target to study the massive star formation process, on a young embedded cluster. As it is the most representative star-forming site inside the molecular cloud, it also takes the name Mon R2. The image also shows the dusty NGC 2170 (VdB67; see Figure 4.2 and 4.3), that is a complex of blueish reflection nebula. Near-infrared images reveal signs of ongoing star formation and massive young stars hidden by the dust (Carpenter & Hodapp 2008).

In the last years, different groups of people used ground-based and space-based facilities to perform extensive multi-wavelength studies of the star formation activity in the Mon R2 molecular cloud. Some of these observational studies are

i) **Infrared observations** with 2MASS to study the low-mass stellar content, *Spitzer* to identify stellar clusters and H_2 jets, and IRAS to

---

[ii]VdB 67 has coordinates α(J2000)= 06h07m32.26s, δ(J2000)= $-06°23'57.58''$

[iii]VdB 68 has coordinates α(J2000)= 06h08m03.45s, δ(J2000)= $-06°13'36.85''$

[iv]VdB 69 has coordinates α(J2000)= 06h08m05.30s, δ(J2000)= $-06°21'40.99''$
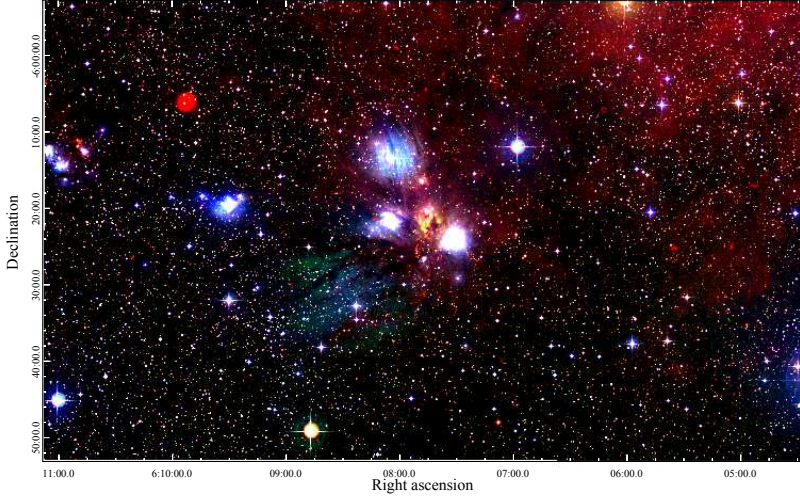
Figure 4.2: Color-composite image of the Monoceros molecular cloud. Red, green and blue represent the IR, red and blue bands from the Digitized Sky Survey (DSS), respectively.

    look for embedded star-forming regions (e. g., Carpenter & Hodapp 2008; Hodapp 2007; Casoli et al. 1986; Parker 1991).

ii) ***Herschel* observations** to study the kinematics of the Mon R2 core region (e. g., Rizzo et al. 2003; Pilleri et al. 2012, 2013a; Didelon et al. 2015).

iii) **Radio-continuum observations** to study the massive stars, the HII regions and maser emission (e. g., Hughes & Baines 1985; Downes et al. 1975; Massi et al. 1985; Wood & Churchwell 1989; Kurtz et al. 1994; Gómez et al. 1998, 2010).

iv) **Spectral surveys at radio wavelengths** to study the chemical properties of the Mon R2 core region (e. g., Ginard et al. 2012, see also Chapter 6 of this thesis).

v) **X-ray observations** using *ROSAT* and *CHANDRA* (e. g., Gregorio-Hetem et al. 1998; Kohno et al. 2002; Nakajima et al. 2003; Martí et al. 2013).

Among the different observational discoveries it is worth mentioning the first CO (1–0) observations performed towards Mon R2 by Loren et al. (1974). Following studies with improved sensitivity and resolution confirmed the existence of different molecular outflows (see Section 4.2.3) and out observations (see Chapter 5) revealed a filamentary molecular cloud in Mon R2.

Table 4.1: Stellar clusters in Monoceros molecular cloud (Carpenter & Hodapp 2008).

Region	α (J2000)	δ (J2000)	N_{star}
Mon R2	06:07:47.8	-06:22.20	371
GGD 12-15	06:10:49.1	-06:11:38	134
GGD 17	06:12:48.0	-06:13:56	23
IRAS 06046-0603	06:07:08.1	-06:03:53	15

Carpenter (2000) performed a low-mass stars content study, using the 2MASS point source catalog, and identified compact stellar clusters. Four clusters were found based on enhancements in the stellar surface density relative to the field star population. These clusters (see Table 4.1) are the Mon R2 core, GGD 12-15, GGD 17, and IRAS 06046-0603. Lynds (1962) identified 4 dark nebulae (L1643, 1644, 1645, and 1646) that form the main part of the molecular cloud that is associated with the reflection nebulae. Xie (1992) selected a sample of 36 IRAS sources having photometric properties consistent with star-forming regions (Beichman et al. 1986). The most luminous IRAS sources are associated with the Mon R2 core ($L_{\rm IR} \sim 26000\ L_\odot$) and GGD 12-15 (5700 $L_\odot$) regions. Most of the remaining IRAS sources have luminosities less than 1000 $L_\odot$.

Hughes & Baines (1985) found three radio continuum (at 3 GHz and 10 GHz) sources tracing HII regions. The first HII region located in the Mon R2 core, the second one in GGD 12-15, and the third one in a CO emission "gap" without correspondence of reflection nebula or IRAS source. Massi et al. (1985) found that the radio continuum emission on Mon R2 core is nearly circular with a diameter of 27″. They modeled the radio emission as a blister-type HII region where the ionizing star is on the surface of the molecular cloud (see Section 4.2.2). The HII region in the GGD 12–15 region exhibits a cometary structure with a maximum extent of $\sim 4''$–$5''$ (Kurtz et al. 1994) and seems that is undergoing a champagne flow (Gómez et al. 1998, 2010; Treviño-Morales et al. 2011).

4.2 Mon R2 core

The Mon R2 core is the most active star-forming site embedded in the Monoceros R2 molecular cloud, it lies between the reflection nebulae VdB 67, VdB 68 and VdB 69 (see Figure 4.3). The Mon R2 core contains a group of reflection nebulae, it is distinguished by a stellar cluster, a large (with a size of ~ 7 pc)

Figure 4.3: Close-up view of the Mon R2 core star forming region. This image was obtained with the wide-field view of the Mosaic II camera on the Blanco 4-meter telescope at Cerro Tololo Interamerican Observatory. The image was generated with observations in the Sulphur [SII] (blue) and Hydrogen-Alpha (red) filters. This Image is from the "National Optical Astronomy Observatory/Association of Universities for Research in Astronomy"

molecular outflow (Bally & Lada 1983; Wolf et al. 1990; Hodapp 2007), an UC HII region (Downes et al. 1975; Massi et al. 1985), H_2O and OH masers (Downes et al. 1975; Loren 1977; Knapp & Brown 1976; Bally & Lada 1983), and X-ray emission (Kohno et al. 2002; Nakajima et al. 2003).

Molecular line (Tafalla et al. 1997; Choi et al. 2000) and submillimeter continuum observations (Henning et al. 1992; Giannakopoulou et al. 1997) have shown that the cluster is embedded in a dense core which has a diameter of $\sim 3'$ (0.7 pc). The core displays a rich chemical structure that is driven by the
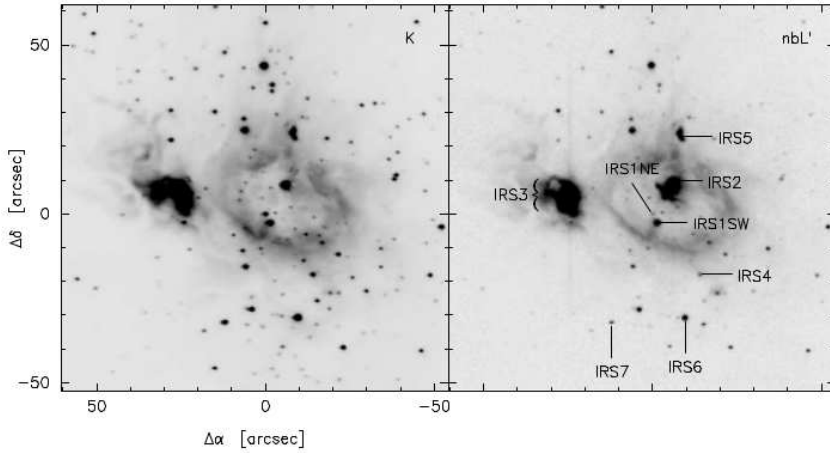
Figure 4.4: Location of the IRS sources, in K (1.6 μ)-band (left) and nbL (right) images. Figure from Carpenter et al. (1997).

high ultraviolet flux from the embedded B-type star that ionized the UC HII region (Rizzo et al. 2005). The core mass is estimated to be about 1000 $M_\odot$ (Tafalla et al. 1997), which is two orders of magnitude larger than those of the cores of forming low and intermediate-mass stars.

4.2.1   Mon R2 core: Infrared sources

Five bright IR sources (IRS 1–5) have been detected in the Mon R2 core at 10 μm and 20 μm, plus two additional sources (IRS 6 and IRS 7) identified in the H (1.6 μ) and K (2.1 μ) bands (Beckwith et al. 1976a). These bright stars are found to be surrounded by a cluster of a few hundred fainter stars detected in near-infrared images (Howard et al. 1994; Hodapp 1994b; Carpenter et al. 1997). Figure 4.4 shows the distribution of the IR sources in the Mon R2 core, and Table 4.2 lists their characteristics. IRS 1, IRS 2 and IRS 3 are the most luminous sources in the cluster (Thronson et al. 1978, 1980; Henning et al. 1992). The bolometric luminosities of these sources have been estimated to be 3000 $L_\odot$, 6500 $L_\odot$, and 14000 $L_\odot$ respectively (Henning et al. 1992).

IRS 3 was first observed by Beckwith et al. (1976a), and proposed to be a massive young stellar object (YSO). It is the brightest infrared source in the Mon R2 field and currently considered a likely candidate to drive the giant CO outflow in the region (see Section 5.2.3). In Figure 4.4 IRS 3 appears as an extended nebulosity, and Howell et al. (1981) identified IRS 3 as two point-

Table 4.2: Properties of the brightest IR sources identified in Mon R2 core.

Source	α (J2000)	δ (J2000)	$L_\odot$	$M_\odot$	Refs.
IRS 1	06:07:46.200	$-$06:23:08.30	3000	12.2	1,2
IRS 2	06:07:45.802	$-$06:22:53.50	6500	13.0	1,4
IRS 3	06:07:47.824	$-$06:22:56.11	14000	9.5	1,2
IRS 4	06:07:44.766	$-$06:23:24.49	$<$100	6.0	2,3
IRS 5	06:07:45.591	$-$06:22:39.46	300	7.0	2,5
IRS 6	06:07:45.677	$-$06:23:37.00			6
IRS 7	06:07:47.106	$-$06:23:37.90			6

References are 1: Thronson et al. (1980); 2: Giannakopoulou et al. (1996); 3: Beckwith & Evans (1975); 4: Jiménez-Serra et al. (2013); 5: Dierickx et al. (2015); and 6: Carpenter et al. (1997).

like sources (see also Dyck & Howell 1982; McCarthy 1982). Preibisch et al. (2002) resolved IRS 3 into several YSO components, three of them having estimated masses in the 5 to 15 $M_\odot$ range. Koresko et al. (1993) showed that the bright southern source in IRS 3 is surrounded by a bright conical nebula, probably produced by starlight scattered from a circumstellar disk. IRS 3 has also been found associated with highly variable maser emission. In particular, OH masers at 4.765 GHz can change its brightness by two orders of magnitude in time scales of a few weeks Smits et al. (1998).

IRS 2 is a compact YSO (Alvarez et al. 2004) with a luminosity of $\sim$ 5000–6500 $L_\odot$ (Henning et al. 1992; Howard et al. 1994; Preibisch et al. 2002) and coincident with the edges of the radio continuum emission associated with Mon R2 core (Massi et al. 1985). This source is thought to be embedded in the molecular cloud and seems to be in an early stage of formation. IRS 2 seems to be responsible for a ring-like IR nebula (Beckwith et al. 1976a; Aspin & Walther 1990), surrounding the infrared point source IRS 2 and also including the source IRS 1 (see Figure 4.4). Jiménez-Serra et al. (2013) reported detection of radio recombination line (RRL) maser emission towards this object. The authors find a double-peaked profile with a blue-shifted asymmetry in the H26α line, and suggest this emission arises from a dense and collimated jet embedded in an ionized wind, oriented nearly along the direction of the line of sight.

IRS 1 does not have the maximum luminosity of the cluster but it is spatially associated with the radio continuum source tracing the HII region. In Figure 4.4, IRS 1 is been resolved into two components (see also Aspin & Walther 1990; Howard et al. 1994), with the faintest one (IRS 1 NE) being foreground field star. From the radio continuum emission, IRS 1 is associated with a B0 ZAMS object, which is consistent with the infrared luminosity of about
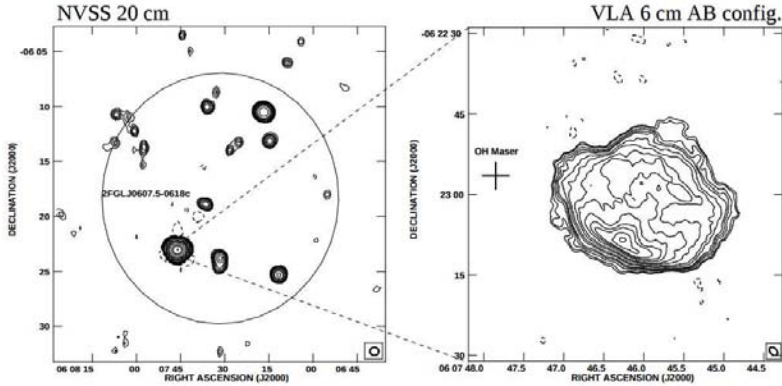
Figure 4.5: *Left:* Radio continuum map of the Mon R2 region from the NRAO-VLA Sky Survey at the 20 cm wavelength. *Right.* Zoom of the Mon R2 central region observed with the VLA at the 6 cm wavelength. The cross indicate the position of a OH maser in the field. In both panels, the contours correspond to -3, 3, 4, 6, 8, 10, 15, 20, 30, 40, 60, 80, 100, 140, and 180 times 0.7 mJy beam^{-1}, the rms noise. The restoring beam is $1.''80 \times 1.''25$ ellipse, with position angle $41°$. Figure from (Martí et al. 2013).

3000 $L_\odot$. This source is located at the center of a spherical cavity free of molecular gas which extends for about $20''$ (0.08 pc) in radius (Choi et al. 2000) and it is associated with several PDRs (see Section 4.2.2).

The physical properties of the less luminous IR sources (IRS 4–7) also detected in the Mon R2 core region, are less constrained. The IRS 4 luminosity is ~ 700–800 $L_\odot$ and the IRS 5 luminosity is ~ 300 $L_\odot$ (Henning et al. 1992; Dierickx et al. 2015). The IRS 5 emission is mainly because of the dust and seems to be in an earlier stage of evolution than IRS 2 (Dierickx et al. 2015).

4.2.2   Mon R2 core: The UCHII–PDR system

The NRAO VLA Sky Survey at 20 cm reported a number of continuum sources towards the Mon R2 region (see left panel of Figure 4.5). The brightest source is associated with Mon R2 core, has a cometary shape (see right panel of Figure 4.5), and its peak is spatially coincident with the source IRS 1. According to its size (≤ 0.1 pc), density ($n > 10^5$ cm^{-3}) and number of ionizing photons (N-Ly), it is classified as an UC HII region powered by a B0 ZAMS star. The position of IRS 1 is also known as IF or ionization front as depicted in Figure 4.6. Previous millimeter and far-infrared spectroscopic and continuum
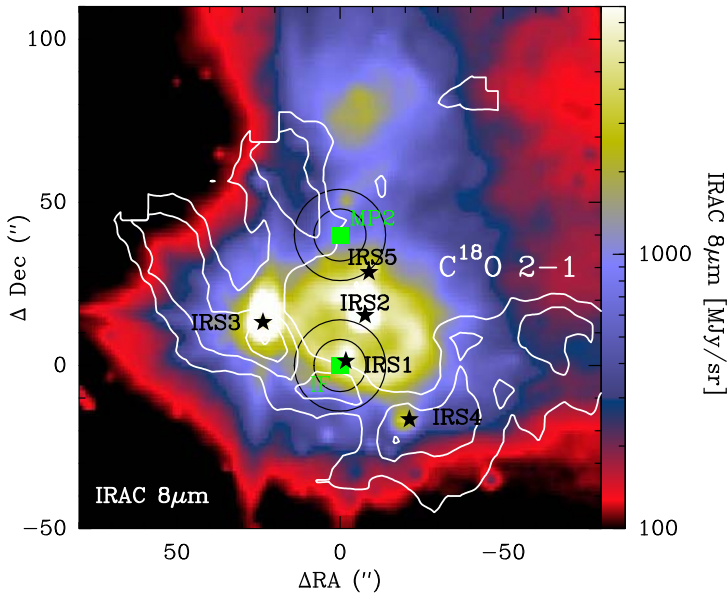
Figure 4.6: In colors, the *Spitzer*-IRAC 8μm emission from small dust (Ginard et al. 2012). In contours, the integrated emission between 5 and 15 km s^{-1} of the C^{18}O (2-1) line (Pilleri et al. 2012). Black stars show the positions of the brightest infrared sources, following the nomenclature of Henning et al. (1992).

studies have revealed that the molecular gas is distributed in an arc-like structure surrounding the HII region (Henning et al. 1992; Giannakopoulou et al. 1997; Tafalla et al. 1997; Choi et al. 2000; Rizzo et al. 2003, 2005; Pilleri et al. 2012, 2013a). UC HII region is surrounded by several PDRs with different physical/chemical conditions. A dense PDR (n= 4×10^5 cm^{-3}, $N(H_2)$= 1×10^{21} cm^{-2} and T_k = 574($\pm$20) K; Berné et al. 2009) delineates the interface between the ionization front and the dense molecular gas, and is well detected in pure rotational H$_2$ lines, mid-infrared PAHs bands and in rotational lines of reactive molecular ions such as CO$^+$ and HOC$^+$. A second PDR is detected 40" north from IRS 1, corresponding with a peak of molecular emission (hereafter, MP2; see Figure 4.6). The position MP2 is well detected in the PAH emission at 8 μm and its chemical properties are similar to those of low- to mild-UV irradiated PDRs such as the Horsehead (Ginard et al. 2012; Pilleri et al. 2013a).

The PDRs have a roughly circular spatial distribution, with a projected thickness between 4″ and 6″ ($\sim$0.02 pc, Berné et al. 2009). Rizzo et al. (2003) estimate the intensity of the UV radiation field to be G$_0 \sim 5 \times 10^5$ in units of the Habing field, by fitting the observed far-IR intensity with a blackbody curve, assuming an effective temperature of T$_{eff}$ = 25000 K and using the projected

radius of the HII region as the real distance from the star. The UC HII and the PDRs are surrounded by a moderate density ($n_{H2} = 5 \times 10^4$ cm^{-3}), cometary-shaped molecular cloud (Fuente et al. 2010; Pilleri et al. 2012, 2013a).

Observations of different molecular species (CO, OH$^+$, CH$^+$ and CH) combined with modeling of the gas kinematics (Fuente et al. 2010; Pilleri et al. 2012) show that the Mon R2 molecular cloud is relatively quiescent, with the systemic velocity of the main cloud being ~ 10 km s^{-1} and with expansion velocities of velocities ~ 1 km s^{-1}. High velocity wings, observed at red-shifted velocities relative to the cloud systemic velocity, can be attributed either to the expansion of the PDR surrounding the HII region or to the relic of a now inactive outflow (Giannakopoulou et al. 1997; Pilleri et al. 2012, 2013a). Jaffe et al. (2003) suggested that the HII region is expanding at a high velocity $v_{exp} = 10$ km s^{-1}. Zhu et al. (2005) suggested that the central HII region is not expanding, but the ionized gas runs along the walls of the surrounding cloud, this behavior is also found in others UC HII regions (Zhu et al. 2008).

4.2.3 | Mon R2 core: Outflows

The mass of molecular gas in the Mon R2 core has been determined by Ridge et al. (2003) using ^{13}CO and C^{18}O maps. The estimation of the mass based on the dense gas tracer (C^{18}O) is 1826 $M_\odot$, while the authors obtain about 2500 $M_\odot$ when using ^{13}CO, a tracer of more tenuous gas in the molecular core.

Mon R2 present signatures of a huge (likely inactive) molecular outflow. This bipolar CO outflow was first reported by Loren (1981). Wolf et al. (1990) (see also Hodapp 2007) found that this molecular outflow is one of the dynamically oldest, largest (7 pc) and massive (100–200 $M_\odot$) outflows. Tafalla et al. (1997) found that this outflow has created an hourglass-shaped cavity in the molecular cloud centered on the cluster of massive young stars. The cavity walls coincide with the limb-brightened shells of the blue-shifted component. The axis of the paraboloidal outflow shell and cavity are oriented roughly at a position angle of $-30°$.

Figure 4.7 shows the outline of the CO outflow, with the red-shifted emission depicted with dashed contours and the blue-shifted in solid contours (Wolf et al. 1990). The circles indicate the H$_2$ shocked gas (likely tracing jets) and the squares indicate small patches nebulosity as observed by Hodapp (2007). Since the outflowing material interacts turbulently with the molecular material of the ambient cloud, triggered star formation would be expected near the interface between the shell and the ambient cloud. The surface density of
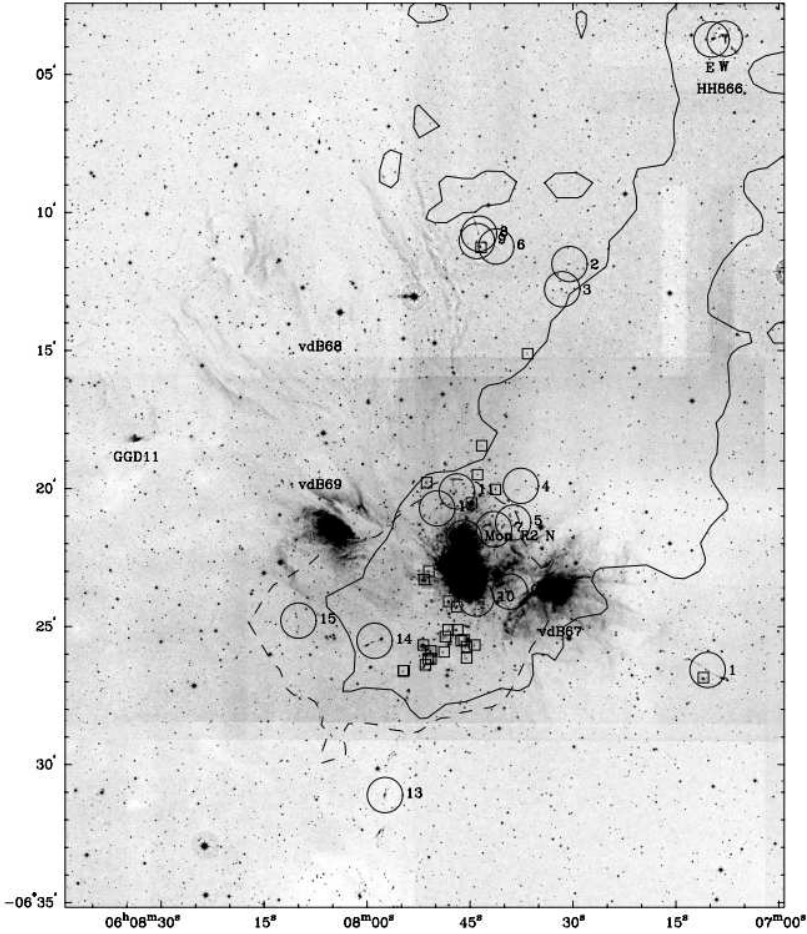
Figure 4.7: Image of the Mon R2 region in the 1–0 S(1) emission line of H_2 at 2.12 μm. The circles indicate the positions of H_2 jets. The Herbig-Haro object HH 866 is visible in the northwest corner of the image. The small reflection nebula near the eastern edge of the image is GGD 11 (Gyulbudaghian et al. 1978). Squares delineate small reflection nebulae. Superposed on this image are the lowest contours of the blue-shifted (−2–+6km s^{-1}, solid line) and red-shifted (14–22km s^{-1}, dashed line) CO emission from the map by Wolf et al. (1990). Figure from Hodapp (2007).

triggered star formation sites is expected to be higher in projection along the shell wall compared to the front and back sides of the outflow shell.

The outflow presents a high degree of collimation over a large angular extent. A velocity gradient of 1 km s^{-1} pc^{-1} is measured along the major axis of the core suggesting possible rotation about an axis parallel to the outflow. More recent observations with higher angular resolution (see also Chapter 5 of this thesis) do not reveal high-velocity emission close to the position of the young
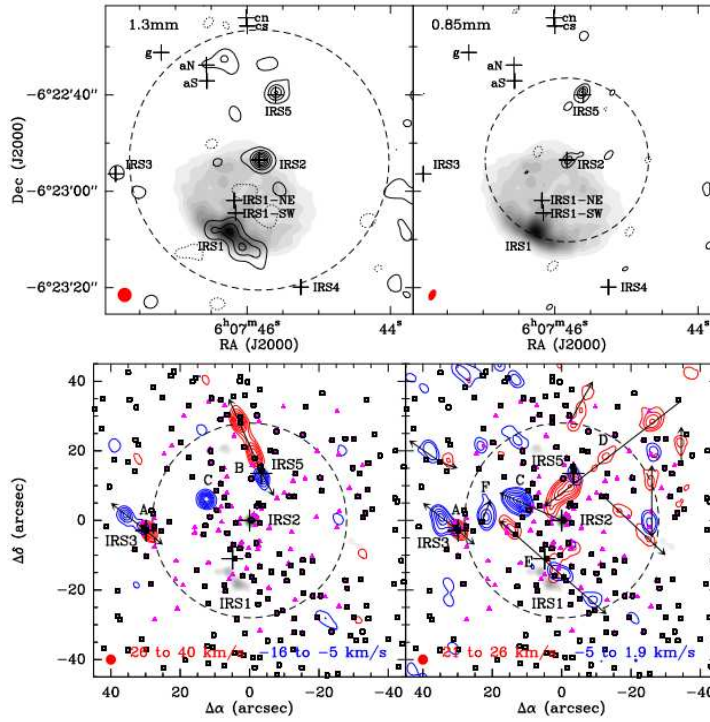
Figure 4.8: *Top:* Continuum emission detected at 1.3 mm toward the Mon R2 core region (contours) overlaid on the 1.3 cm continuum image (left). Continuum emission detected at 0.85 mm (right). The red ellipse indicate the beam size. The plus symbols indicate the position of IRS sources. *Bottom:* Zero-order moment maps of the CO (2–1) transition (colored contours) overlaid on the 1.3 mm continuum (gray scale). The redshifted emission has been integrated over the $+26$–$+40$ km s^{-1} velocity range and the blue-shifted emission over the velocity range -16–$+5$ km s^{-1} in the left panel. For the right panel, the redshifted emission is integrated between $+21$ and $+26$ km s^{-1}, while the blue-shifted emission is integrated in the range -5 to $+1.9$ km s^{-1}. Magenta triangles and black squares denote different IR sources. Black arrows indicate the conjectured orientation of the outflows. Figure from Dierickx et al. (2015).

stellar objects. This would suggest that the large-scale outflow structure traces only an old cavity or envelope of outflow material which has been swept up by the passage of a now inactive outflow.

Dierickx et al. (2015) detect 11 young outflows associated with the IRS sources in Mon R2. In Figure 4.8, we show the red-shifted and blue-shifted CO(2–1) emission overlaid with the dust continuum emission. The triangles and squares distributed all over the image pinpoint the position of IR sources. It is easy to distinguish, for example, bright collimated bipolar outflows associated with IRS 3 and IRS 5.
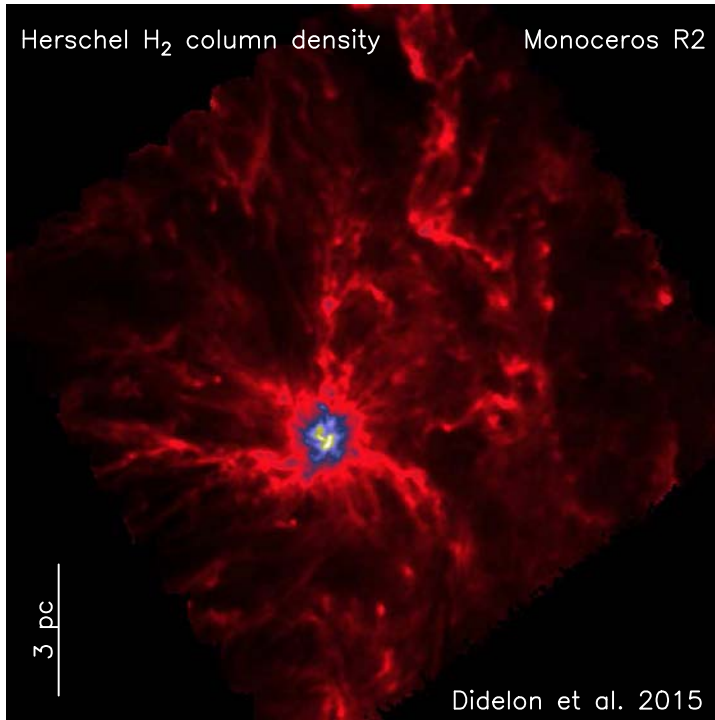
Figure 4.9: Filamentary structure in Mon R2. Herschel H_2 column density (on color scale), derived from SPIRE and PACS continuum observations.

| **4.2.4** | Mon R2 core: Filamentary structure |

It is worth remembering that the Mon R2 core is located within a larger molecular cloud, and one may wonder if this cloud has an internal filamentary structure (similar to other clouds in our Galaxy, see Chapter 1). If so, one may further ask if this filamentary structure exists until reaching the position of the Mon R2 core, and if so, what is the effect of the presence of an UC HII region.

Figures 4.3 and 4.7 reveal some filamentary structures in the dense gas. These elongated structures are seen in absorption against the background reflection nebulosities to the south-east of Mon R2 (e.g., Figure 4.3) and in emission towards the north (north-east) in both figures. Therefore, we can conclude that there are filamentary structures associated with Mon R2.

Several observational works studying the CO and ^{13}CO emission (Xie 1992; Xie & Goldsmith 1994; Bally et al. 1991; Miesch et al. 1999) have found a sharp filament of gas extending in nearly a north-south direction. Recently,

Didelon et al. (2015) have used the *Herschel* satellite to produce dust column density and temperature maps of the Mon R2 region (see Figure 4.9). The authors find that the hot bubbles associated with HII regions are surrounded by dense, cold and neutral gas envelopes, partly embedded into a filamentary structure with the UC HII region located at the junction of three main filaments. Therefore, Mon R2 appears as an excellent candidate to study the interaction of feedback from a massive young star and the surrounding filamentary environment. We will study this structure and the kinematics of the gas along filaments in Chapter 5 of this thesis.

5

A FILAMENTARY HUB IN MON R2

This chapter focuses on the study of the large-scale structure around the Mon R2 core by analyzing a set of large-scale maps observed towards the region, and discusses the main dynamical and kinematical results derived from the observations.

Contents

5.1   A filamentary hub

The processes that lead to high-mass star formation are still poorly constrained, in particular those related to the accretion of mass from cloud scales (10 pc) to core scales (0.1 pc) and how the HII region feedback may affect this process. In the last years, observations of star forming regions revealed intricate *filamentary structures* (Peretto et al. 2014) that pervade large molecular clouds (e.g., André et al. 2010; Molinari et al. 2010; Busquet et al. 2013), and often intersect in high-density regions so called *hubs*. Star formation within molecular clouds has been found to occur preferentially along the filaments, with high-mass stars forming at the hubs and ridges junctions (e.g., Liu et al. 2012; Schneider et al. 2012; Louvet et al. 2014). The observed column density in these regions ($N_H = 10^{23}$ cm^{-2} and $n_{H_2} \sim 10^6$ cm^{-3}) are likely achieved by in-fall of material along the filaments onto the hub (Schneider et al. 2010; Peretto et al. 2013).

A number of recent studies have started to characterize the properties of filaments in nearby star forming regions (e.g., Hacar et al. 2013; Tafalla & Hacar 2015; Smith et al. 2014; Hennemann et al. 2012; Henshaw et al. 2014; Tackenberg et al. 2014). These works reveal that filaments are not solid entities but are constituted by small velocity-coherent elongated structures named *fibers* (Hacar et al. 2013; Tafalla & Hacar 2015). Moreover, high-mass stars inject, in the surrounding medium, large amounts of radiation and turbulence that may affect the structural properties of filaments (e.g., leading to a different level of fragmentation, Csengeri et al. 2011; Seifried & Walch 2015a,b) and the transport of mass along the filament until the site where stars form.

Mon R2, located at a distance of only 830 pc, is the most active site of star formation in the Monoceros molecular cloud. As was mentioned in Section 4.2.4, *Herschel* observations have revealed an intriguing look of the cloud with several filaments converging into the central area or hub hosting Mon R2 (Didelon et al. 2015). The cluster of recently formed high-mass stars is located at the junction of this filamentary structure. The UC HII region, driven by the cluster, has created a cavity free of molecular gas that extends for about $30''$ (0.12 pc, e.g., Choi et al. 2000; Dierickx et al. 2015), and is surrounded by a PDR with a projected thickness of about $6''$ (0.025 pc, e.g., Pilleri et al. 2013a). The complexity in the line profiles of several molecular and ionic species was first interpreted in terms of different motions of the gas phases that co-exist in this region (expansion of the UC HII region, in-fall/rotation of the molecular gas; Pilleri et al. 2012, 2013a,b): a full modeling (radiative transfer, kinematics, chemistry) suggests the presence of a layer of warm (> 100 K) and dense ($> 10^5$ cm^{-3}) gas confining the UC HII region and expanding with a velocity
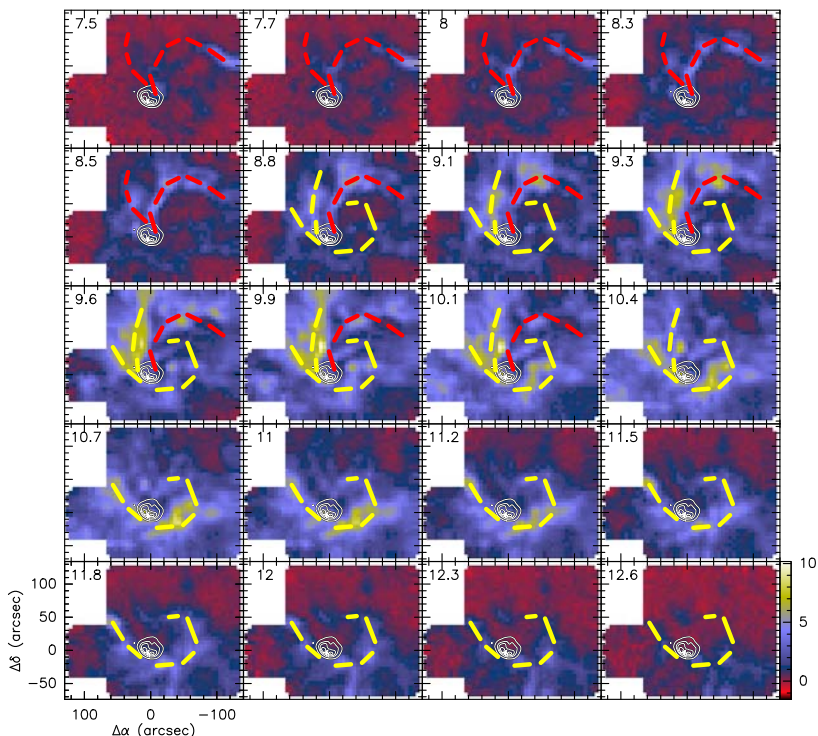
Figure 5.1: Mon R2 channel maps of the $C^{18}O$ (2–1) line observed with the IRAM-30m telescope toward the hub hosting the UC HII region. The spiraling filaments are depicted with dashed lines, while the UC HII region is depicted in black/white contours from the [NeII] emission line (Berné et al. 2009).

of $\sim 1\ \mathrm{km\,s^{-1}}$ (Fuente et al. 2010; Pilleri et al. 2012). Previous maps obtained with IRAM-30m reveal a complex kinematics, with spiraling arms approaching the UC HII region (see Figure 5.1). This in combination with the observational results found in large-scale maps (Didelon et al. 2015, see Figure 5.2) suggest the idea of a young UC HII region just beginning to expand and break out of the dense filamentary hub where it was formed, with material still collapsing inward along the filaments.

This Chapter is focused in the study of the filamentary structure seen towards Mon R2 and discusses the implications of the observations. Sections 5.2 and 5.3 describes the observational strategy, data reduction and results. Section 5.4, presents a comparison of our large-scale maps with observations at different wavelengths, describes the filamentary structure, analyzes the mass accretion rate and velocity gradients in the main filaments. Finally, Section 5.5 presents a summary of the main conclusions and future work.
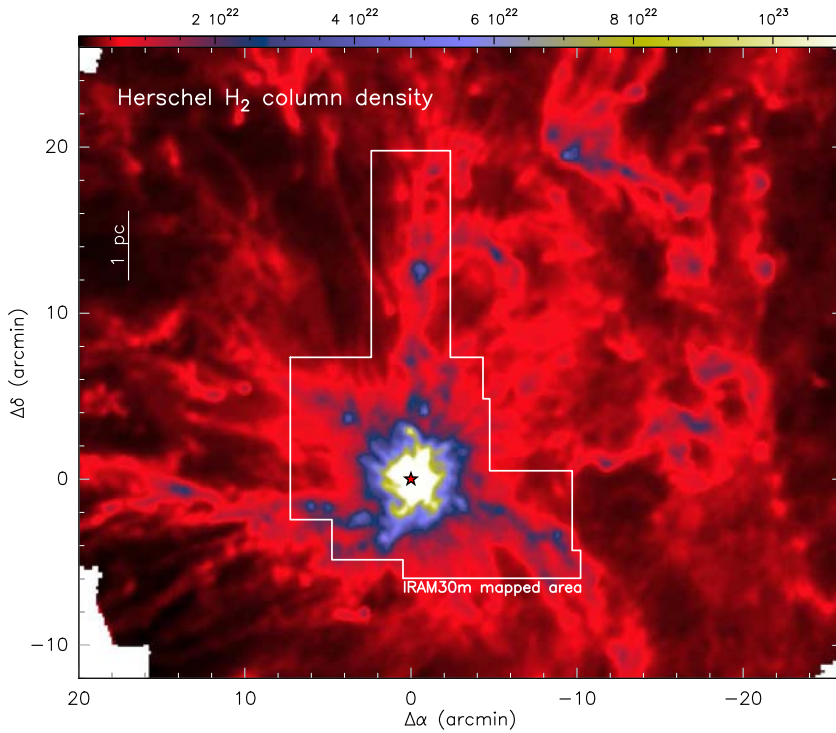
Figure 5.2: Herschel H_2 column density (on color scale), derived from SPIRE and PACS continuum observations. This image is courtesy of P. Didelon and T. Rayner (see Didelon et al. 2015). The red star indicates the position of the infrared star IRS 1. The white polygon shows the area mapped with the IRAM 30m telescope. This area covers a large square map of $9' \times 9'$ centered at IRS 1 and two additional maps covering the extended emission to the north ($4' \times 15'$) and to the west ($5' \times 4.5'$) of the central map.

5.2   Observations and data reduction

The data presented in this chapter were observed using the IRAM-30m telescope towards the Mon R2 region. We observed 43 hours during July and August 2014 under good weather conditions, within the project 027-14. On-the-fly (OTF) maps were performed to cover a field of view of 163.5 arcmin^2 in the 3 mm band. The observed area is shown in Figure 5.2, and consists of a large square map of $9' \times 9'$ centered at IRS 1 (with coordinates α(J2000)= 06h07m46.2s, δ(J2000)= $-06°23'08.3''$) and two additional maps covering the extended emission to the north ($4' \times 15'$) and to the west ($5' \times 4.5'$) of the central map. All observations were performed in dual polarization mode using the EMIR receivers (Carter et al. 2012), with the Fast Fourier Transform
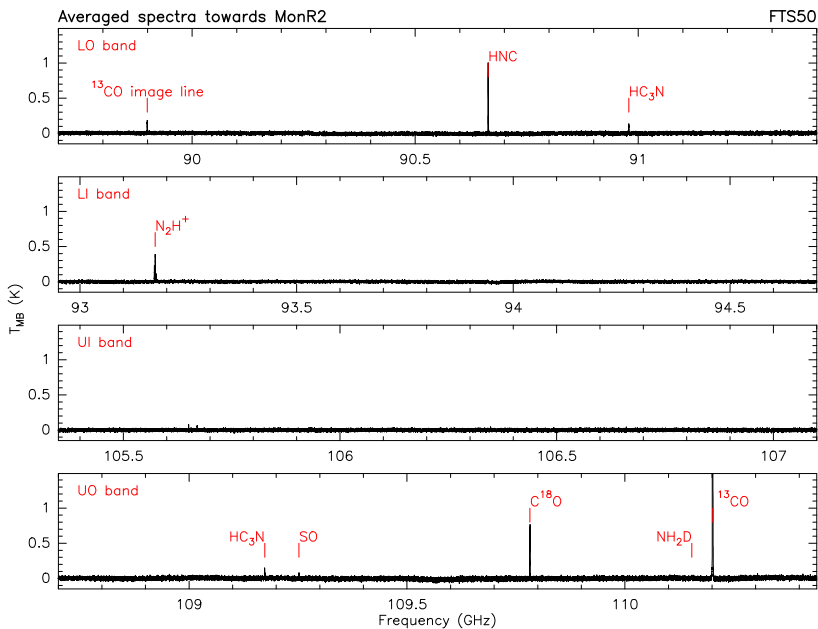
Figure 5.3: Spectra averaged over an area of 81 arcmin^2 towards Mon R2, centered at the position of IRS 1. The four panels show the frequency range observed within the observational project 027-14. The red labels mark the detected lines.

spectrometer (FTS) at 50 kHz of resolution (Klein et al. 2012b). Figure 5.3 shows the observed frequency range, while Table 5.1 lists the main detected transitions.

During the observations, the pointing was corrected by observing the strong nearby quasar 0605−058 every 1–2 hours, and the focus by observing a planet every 3–4 hours. Pointing and focus corrections were stable throughout the whole run. Line calibrators, Orion and W3OH, were observed for every tuning to confirm that the intensities of the lines in both polarizations were correct. The emission from the sky was subtracted using a reference position free of molecular emission (OFF position), with offsets $(+600'', -600'')$ for the central $9' \times 9'$ map, $(-770'', -135'')$ for the $5' \times 4.5'$ western map, and $(+360'', +870'')$ for the $4' \times 15'$ northern map. The offsets are given relative to the coordinates of the IRS 1 position. For the OTF maps, the OFF position was observed every 2 minutes during 20 seconds. Throughout this Thesis, we used the main beam brightness temperature (T_{MB}) as intensity scale, while the output of the telescope is usually calibrated in antenna temperature (T_{A}^*). The conversion between T_{A}^* and T_{MB} is done by applying the factor $F_{\mathrm{eff}}/B_{\mathrm{eff}}$, where F_{eff} and B_{eff} are the forward and beam efficiencies, respectively. The values of the F_{eff} and B_{eff}, and a summary of the observational parameters are shown

Table 5.1: Main observational parameters. *The values of HPBW, F_eff and B_eff were taken from http://www.iram.es/IRAMES/mainWiki/Iram30mEfficiencies.

Species	Transition	Frequency (GHz)	HPBW* (arcsec)	F_eff^* (%)	B_eff^* (%)	Spectral res. (km s^{-1})
HNC	$1_{0,0}$–$0_{0,0}$	90.663568	28.6	95	80	0.16
HC$_3$N	10–9	90.979023	28.5	95	80	0.16
N$_2$H$^+$	1–0	93.173397	27.8	95	80	0.16
CCS	7_8–6_7	93.870107	27.6	95	80	0.16
HC$_3$N	12–11	109.173634	23.8	95	80	0.14
SO	3_2–2_1	109.252220	23.7	95	80	0.14
C^{18}O	1–0	109.782173	23.6	95	80	0.14
NH$_2$D	$1_{1,1}$–$1_{0,1}$	110.153594	23.5	95	79	0.13
^{13}CO	1–0	110.201354	23.5	95	79	0.13

in Table 5.1. The data were reduced using the CLASS/GILDAS package[i] (Pety et al. 2005). An initial inspection of the data did not reveal platforming effects and/or spikes (bad channels) in the observed sub-bands. Moreover, the baselines do not show important problems (e. g., ripples) and are mainly flat throughout all the frequency band. A one-order polynomial baseline was applied for all the detected lines, and all of them have a velocity resolution between 0.13 and 0.16 km s^{-1}.

5.3 Large-scale emission

Figure 5.4 shows the spectra for the detected species (listed in Table 5.1). The ^{13}CO, C^{18}O, HNC, N$_2$H$^+$, HC$_3$N and SO spectra are averaged over the whole mapped area (163 arcmin^2). While the CCS and NH$_2$D spectra are averaged over an area of $3' \times 3'$ around IRS 1. The spectra show a different velocity profile for each species, with ^{13}CO, C^{18}O and HNC being the widest and most intense. For these species the emission spans a velocity range of $\sim$15 km s^{-1} for ^{13}CO, and $\sim$10 km s^{-1} for C^{18}O and HNC. The emission for the other species only spans a velocity range of 6–8 km s^{-1}. The blue dotted line in Figure 5.4 indicates the velocity (v_LSR) of the source, which is 10 km s^{-1}. The red dashed vertical lines in the same figure mark the velocity range where we have identified emission for the different species, and is the range that has been used to create the integrated intensity maps shown in Figure 5.5. These velocity ranges have been chosen where line intensity falls

---

[i]See http://www.iram.fr/IRAMFR/GILDAS for information on the GILDAS software.
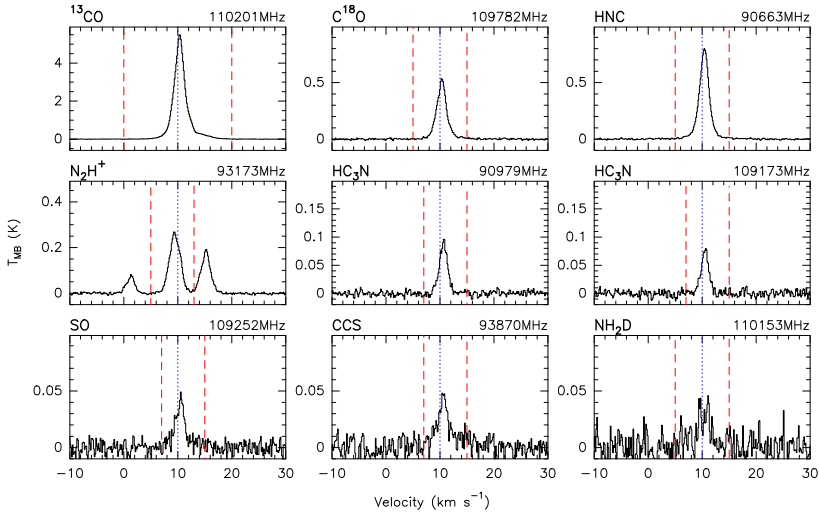
Figure 5.4: Spectra averaged over the observed area. The ^{13}CO, C^{18}O, HNC, N$_2$H$^+$, HC$_3$N and SO spectra are averaged over the whole mapped area. While the CCS and NH$_2$D spectra are averaged over an area of 9 arcmin^2 centered at the position of IRS 1. The red (dashed) vertical lines indicate the velocity range used to generate the integrated maps: 0–20km s^{-1} for ^{13}CO, 5–15km s^{-1} for C^{18}O, 5–15km s^{-1} for HNC, 5–13km s^{-1} for N$_2$H$^+$, 7–13km s^{-1} for HC$_3$N at 90.979 GHz, 7–13km s^{-1} for HC$_3$N at 109.173 GHz, 7–13km s^{-1} for SO, 7–13km s^{-1} for CCS, and 7–15km s^{-1} for NH$_2$D$^+$. The blue (doted) horizontal line indicate the source velocity.

below 5σ. After inspecting the channel maps, these limits were, in some cases, slightly modified, based on the detection of weak emission across the observed area.

Figure 5.5 shows the integrated intensity maps for the ^{13}CO, C^{18}O, N$_2$H$^+$, HNC and HC$_3$N (at 90.979 GHz[ii]). The top panels show the emission over the whole observed area, while the bottom panels show a close-up view of the same maps covering an area of $8.5' \times 8.5'$ around the position of IRS 1. All the maps have an angular resolution between 23$''$5 and 29$''$0, which permits a direct comparison between them. A first inspection shows that the spatial distribution of all the species is slightly different: ^{13}CO and C^{18}O have extended emission distributed across all the map, HNC and N$_2$H$^+$ emission is mainly concentrated in the central area around IRS 1, and HC$_3$N is the most compact, with emission slightly to the south of IRS 1. The emission of the ^{13}CO and C^{18}O species throughout the whole map reveals a filamentary structure that extends in all directions, probably beyond the surveyed area.

[ii]The map of the HC$_3$N transition at 109.173 GHz is essentially equal to the one shown in Figure 5.5. In the following, we will only show the maps for the transition at 90.979 GHz, but the same results are found for the other transition.
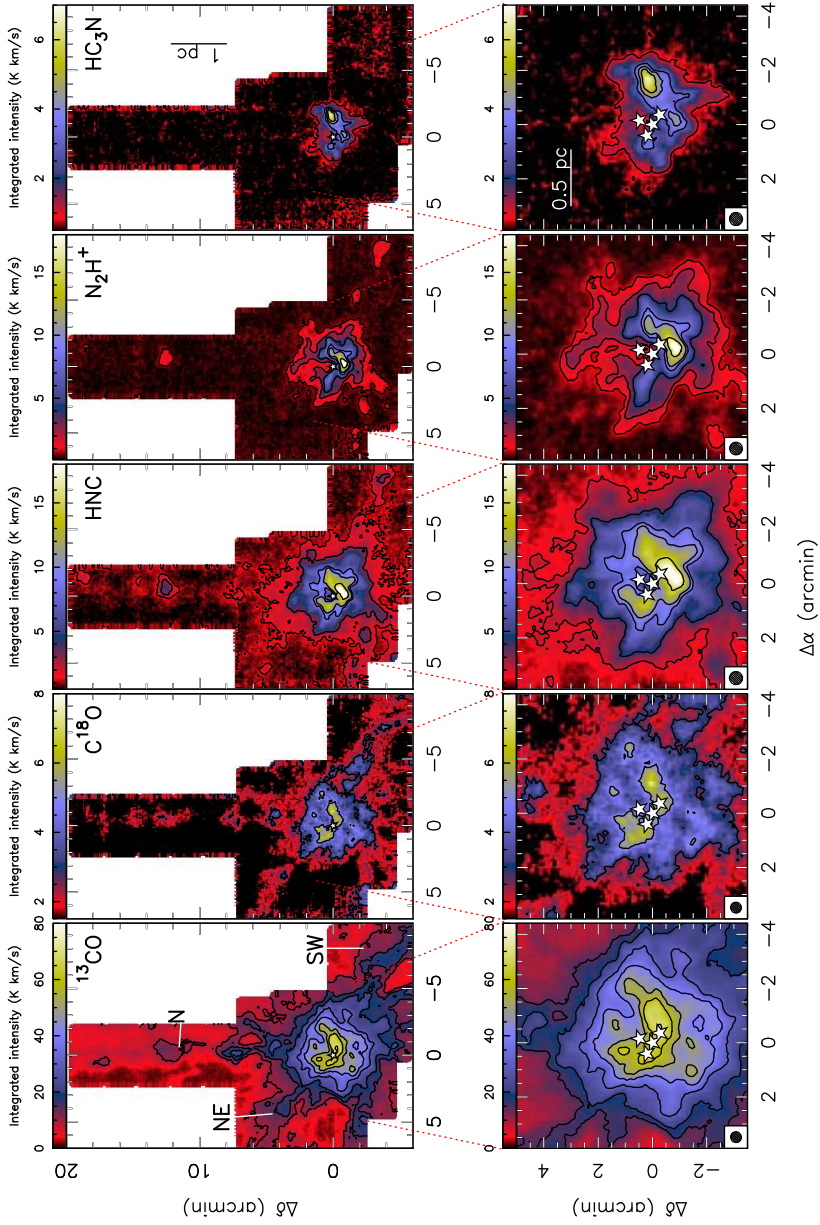
Figure 5.5: The integrated intensity maps for the ^{13}CO, C^{18}O, N$_2$H$^+$, HNC and HC$_3$N (at 90.979 GHz) molecules. The top panels show the emission over the whole observed area, while the bottom panels show a close-up view of the same maps covering an area of $8.3' \times 8.5'$ around the position of IRS 1. Three filamentary structure are labeled in the ^{13}CO map. The white stars indicate infrared sources positions (IRS 1 to IRS 4).
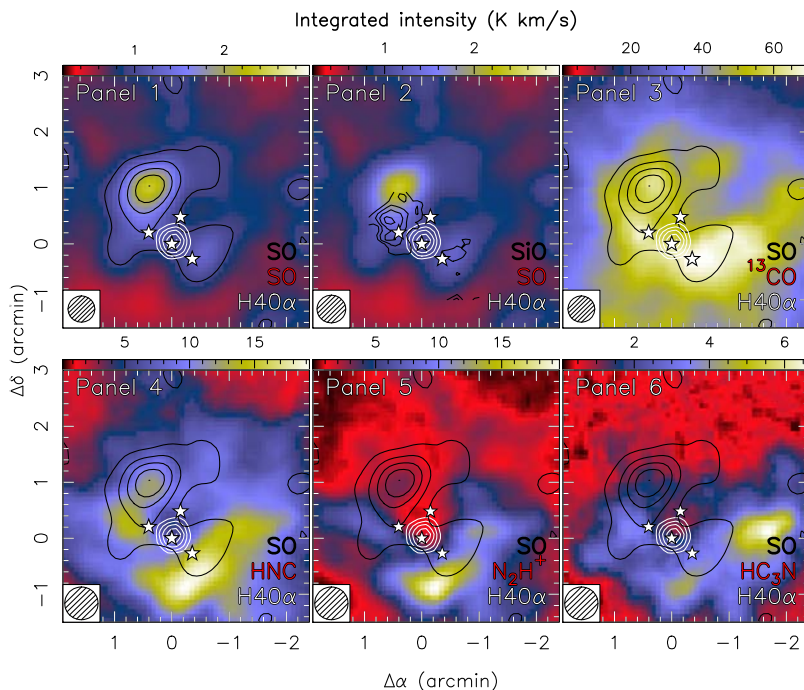
Figure 5.6: Comparison of the SO integrated emission convolved to $30''.0$, in color (Panel 1 and 2) and black contours (Panel 1, 3, 4, 5 and 6) with the SiO (black contours in the Panel 2), ^{13}CO (color scale in the Panel 3), HNC (color scale in the Panel 4), N_2H^+ (color scale in the Panel 5), HC_3N (color scale in the Panel 6) and $H40\alpha$ (white contours) emission. The contour levels are 40% to 100%, in steps of 15% of the peak intensity. The white stars indicate infrared sources positions (IRS 1 to IRS 4).

Three clear structures are identified and labeled in Figure 5.5: an elongated structure in the north-south direction (structure N), a second structure to the south-west of the central area (structure SW), and the last one extending to the north-east from the central zone (structure NE). A detailed inspection of the faint HNC and N_2H^+ emission reveals an extended structure that is in agreement with the filamentary emission seen in the CO species. This may indicate that these filaments are traced by all the molecules, but the low abundance of some of them result in a low signal-to-noise ratio, and difficult their clear detection. Section A.1 present the integrated (Figure A.1) and channels maps (Figure A.3 to A.6) of the CO, HNC and N_2H^+ emission in these three structures. In Section 5.4.2, we present a more detailed description and interpretation of these elongated structures, which seems to emanate from the central region: the brightest component covering an area of $5' \times 5'$ around IRS 1.
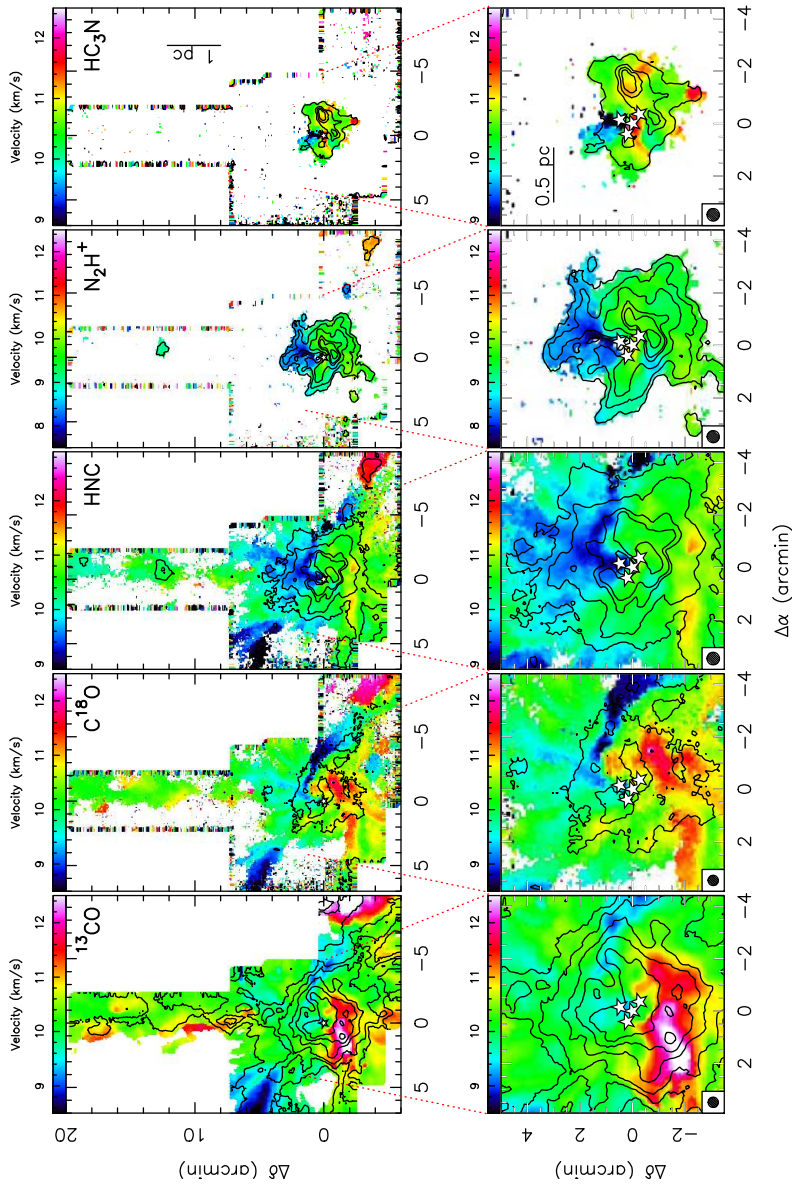
Figure 5.7: Velocity centroid for the molecules ^{13}CO, C^{18}O, N$_2$H$^+$, HNC and HC$_3$N at 90.979 GHz (on color scale). The black contours indicate the integrated intensity of the ^{13}CO, C^{18}O, N$_2$H$^+$, HNC and HC$_3$N molecules. The top panels show the velocity maps over the whole observed area, while the bottom panels show a close-up view of the same maps covering an area of $8.3' \times 8.5'$ around the position of IRS 1. The maps have been produced by computing the first order moment in the velocity range defined in Figure 5.4.
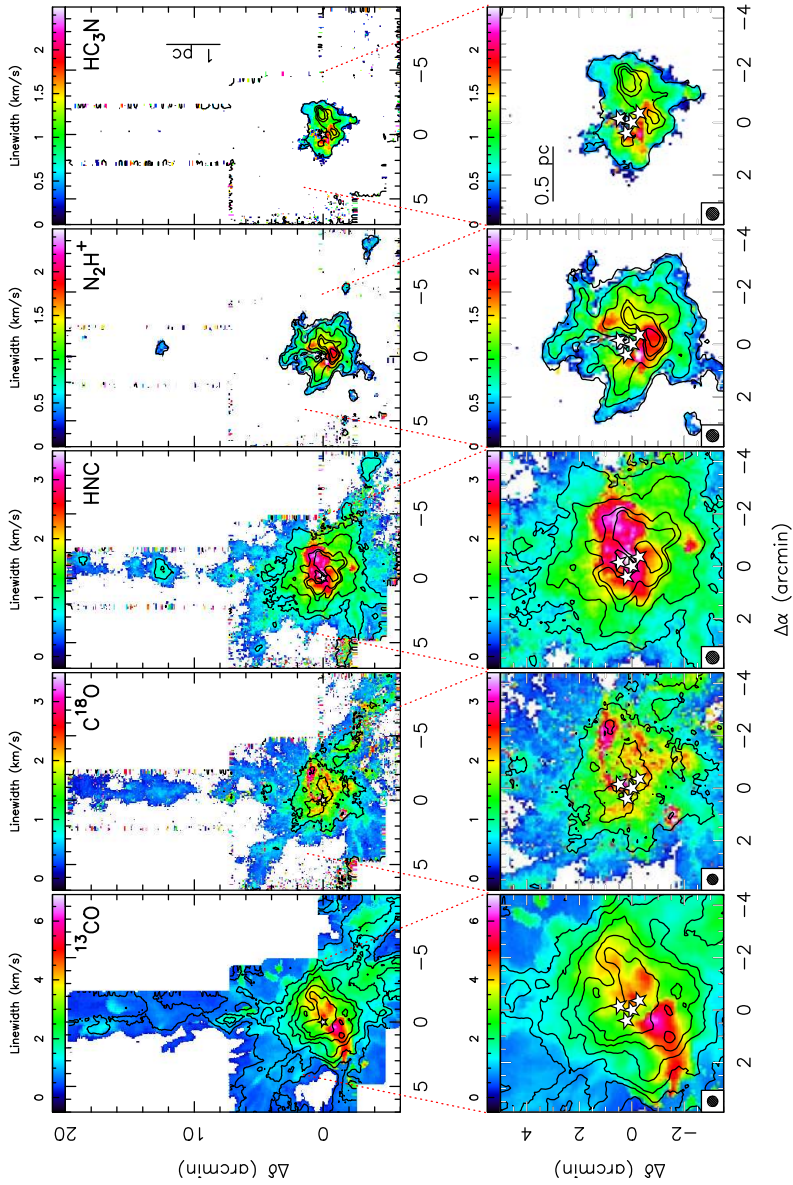
Figure 5.8: Linewidth maps for the molecules ^{13}CO, C^{18}O, N$_2$H$^+$, HNC and HC$_3$N at 90.979 GHz. The black contours indicate the integrated intensity of the ^{13}CO, C^{18}O, N$_2$H$^+$, HNC and HC$_3$N molecules. The top panels show the linewidth maps over the whole observed area, while the bottom panels show a close-up view of the same maps covering an area of $8.3' \times 8.5'$ around the position of IRS 1. The maps have been produced by computing the second order moment in the velocity range defined in Figure 5.4.

The central area, around IRS 1, is bright in the five species, but some different features can be distinguished in the close-up panels (Figure 5.5 bottom panels). The emission appears mainly in an arc/shell structure that surrounds the infrared stars (white stars in the Figure) that pinpoint newly-formed stars in Mon R2. The strongest emission within the arc points toward the south of the infrared cluster, in agreement with the cometary shape of the HII region as revealed in radio-continuum emission (see Figure 5.6). For both ^{13}CO and C^{18}O, the intensity peaks are located to the east and west, while for the other species (in particular for HNC and N_2H^+) there is a bright peak to the south of the cluster, where there is no evidence of CO emission. It is worth noting, that the molecules with this third peak contain a nitrogen atom, and therefore, this spatial differentiation seems to indicate different chemical/physical properties: the ^{13}CO and C^{18}O might be depleted onto dust grains. Alternatively, a high opacity that results in self-absorption of the CO lines could also explain the lack of emission at that position. However, the spectra at that position is close to a Gaussian profile, and does not reveal clear signatures of self-absorption.

Finally, Figures 5.6 presents the SO integrated emission (black contours) compared with the distribution of the ^{13}CO, HNC, N_2H^+, HC_3N and H40α (white contours) emission. The Panel 2 of the Figure 5.6 shows a comparison between SO (color scale) with the SiO (tracing shocked gas in black contours) and H40α (tracing the HII region in white contours) emission. The SiO and H40α maps are described in Chapter 6. The Figure shows that the SO, ^{13}CO, HNC, N_2H^+ and HC_3N emission is surrounding the HII region. The SO emission is much more compact that for the other molecules (centered in the inner $3' \times 3'$ area), and it has a clearly different spatial distribution. The brightest SO peak is located to the north-east of the infrared cluster, at the offset ($60''$, $65''$). A second component appears close to IRS 4, slightly shifted with respect to the molecular peak seen at this position for the other species. The bright SO peak is probably tracing shocked gas or an embedded dense core. The SO and SiO emission do not seem to be spatially correlated, but it is worth noting that the SiO map only covers an area of $2' \times 2'$, and this may result in a mis-interpretation of a lack of correlation between both species. To improve this interpretation, is necessary to observe deeper and larger SiO maps. We also detect the CCS and NH_2D lines in an spectrum averaged over a $3' \times 3'$ area (see Figure 5.4). The weak emission of these lines, combined with the relatively low maps sensitivity, prevents us from drawing firm conclusions on their spatial distribution.

Figure 5.7 shows the velocity maps for the molecules presented in Figure 5.5. The maps have been produced by computing the first-order moment in the velocity range defined in Figure 5.4. Different velocity components and gradients can be identified, in particular for the elongated structures identified in
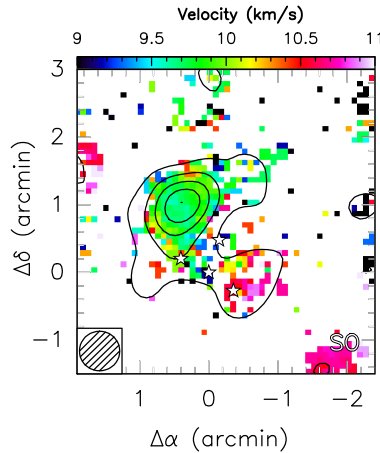
Figure 5.9: Velocity centroid for the SO molecule. The Figure shows the velocity maps over the central observed area (color scale), while black contours indicate SO integrated emission convolved to $30''.0$. The maps have been produced by computing the first order moment in the velocity range defined in Figure 5.4.

the integrated intensity maps: the NE structure is mainly blue-shifted, with a velocity around 9 km s^{-1}; the southern part of SW is red-shifted (11 km s^{-1}), but shows a velocity gradient when approaching to the central part, reaching velocities as low as 9.5 km s^{-1}; finally, the N elongated structure shows no clear velocity gradient, with most of the emission at systemic velocities ($\sim$10 km s^{-1}). It is also noticeable the high red-shifted emission seen in ^{13}CO towards the center of the map, with a velocity $\sim$12 km s^{-1}. Except for this high red-shifted component, the velocity structure of the core is similar in all the species (see close-up panels in Figure 5.7) with red-shifted emission to the south of IRS 1, and blue-shifted emission to the north. Interestingly, the blue-shifted gas is reminiscent of an elongated curved structure that starts to the west of IRS 1 and approaches the center through the north. The red-shifted emission, although not that clear as for the blue-shifted component, also seems to converge towards the position of IRS 1 from the east and then south, constituting a complementary curved structure to the blue-shifted one. In Figure 5.9, presents the velocity field of the SO line. The emission of the bright peak is mainly at the source velocity ($\sim$10 km s^{-1}). However, there is a slightly gradient that might be indicating the presence of two velocity components.

The linewidth for the different species is shown in Figure 5.8. The maps have been produced from the second-order moment map (velocity dispersion) taking into account the factor $2\sqrt{2\ln 2} \simeq 2.35$ to convert it to linewidths. The extended emission has a constant, relatively narrow linewidth of $\sim$1.5 km s^{-1},

which increases towards the central part, reaching a maximum value of
~ 6 km s^{-1} for ^{13}CO and ~ 3.5 km s^{-1} for the other species. The largest
linewidth in ^{13}CO is found at the position of the high red-shifted component
at 12 km s^{-1} (see Figure 5.7). The large values measured towards the cen-
tral core, but not in the extended filaments, suggest a complex kinematical
structure in the inner region (probably due to multiple velocity components),
and a more quiescent velocity distribution in the extended emission. The
linewidth towards the SO bright component is ~ 1.5 km s^{-1}, consistent with
the linewidths measured at that position for the other species.

5.4   Analysis

In this section we compare our IRAM-30m maps with maps at different wave-
lengths in the IR and sub-millimeter domains (see Section 5.4.1), present the
filaments identification (in Section 5.4.2) and analyze their stability (in Sec-
tion 5.4.3) and kinematics (in Section 5.4.4).

5.4.1   Large-scale structure: infrared emission

In order to better understand the large-scale structure of Mon R2 shown in
Figure 5.5, we have compared the IRAM-30m maps with different infrared
and sub-millimeter maps. We have searched for images of Mon R2 in the
near- and mid-infrared domains, covering a range from 1.2 μm to 24 μm,
in the databases of 2MASS (Cutri et al. 2003; Skrutskie et al. 2006), *WISE*
(Wright et al. 2010) and *Spitzer* (Werner et al. 2004). In addition, H$_2$ column
density and temperature maps have been obtained from *Herschel* observations
of the continuum dust emission at 70 μm, 160 μm, 250 μm, 350 μm and 500 μm
(Didelon et al. 2015).

In Figure 5.10, we show the H$_2$ column density map obtained with *Herschel*.
Several filamentary elongated structures are seen converging towards the cen-
tral position of Mon R2, similarly to the structure seen in our IRAM-30m maps
(see Figure 5.5). A direct comparison of the maps is shown in Figure 5.10,
where the H$_2$ column density is shown in a logarithmic scale to emphasize the
weak emission in the region. The ^{13}CO most extended emission is spatially
correlated with the *Herschel* filamentary structure, and confirms the presence
of other elongated structures in the IRAM-30m maps that were not identified
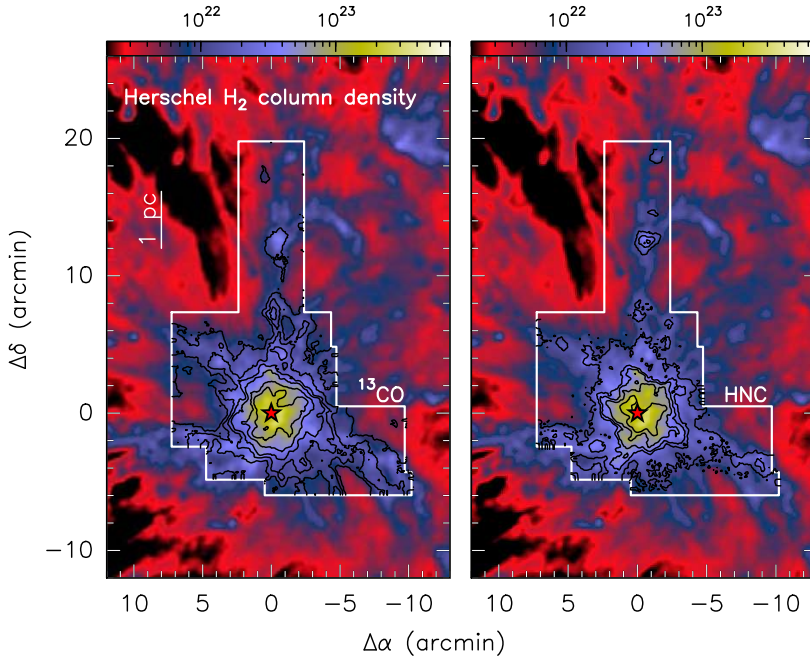
Figure 5.10: Herschel H_2 column density (on color scale). The red star indicate the position of the infrared star IRS 1. The white polygon shows the area mapped with the IRAM-30m telescope. The black contour indicate the ^{13}CO (left) and the HNC (right) integrated emission.

before due to their proximity to the edges of the mapped area (e.g., emission to the south-east of the central core). The spatial agreement is seen not only for ^{13}CO, but for all the other species. The major difference is that while ^{13}CO is spatially more extended, the $C^{18}O$ and HNC emission is more concentrated to the central part of the filaments seen in the *Herschel* map (e.g., the NE filamentary structure). This scenario can be interpreted as the ^{13}CO tracing the outer layers of the filamentary structure, and the $C^{18}O$ and HNC lines tracing the inner and denser parts, i.e., the "skeleton" or "bones" of the filaments. Although higher angular resolution observations are necessary to better spatially resolve them and confirm this different behavior of the dense gas tracers, this is consistent with the $C^{18}O$ and HNC tracing denser gas.

The distribution of the molecular emission in the central part also matches the spatial distribution of the *Herschel* H_2 column density (see Figure 5.11). The arc shape seen in the molecular emission is also seen in the H_2 column density map. Moreover, the different intensity molecular peaks coincide with some of the H_2 column density peaks, but (as mentioned in Section 5.3) with a slightly different spatial distribution for each molecule. The major differences are found in the H_2 column density peaks to the south and west of the infrared
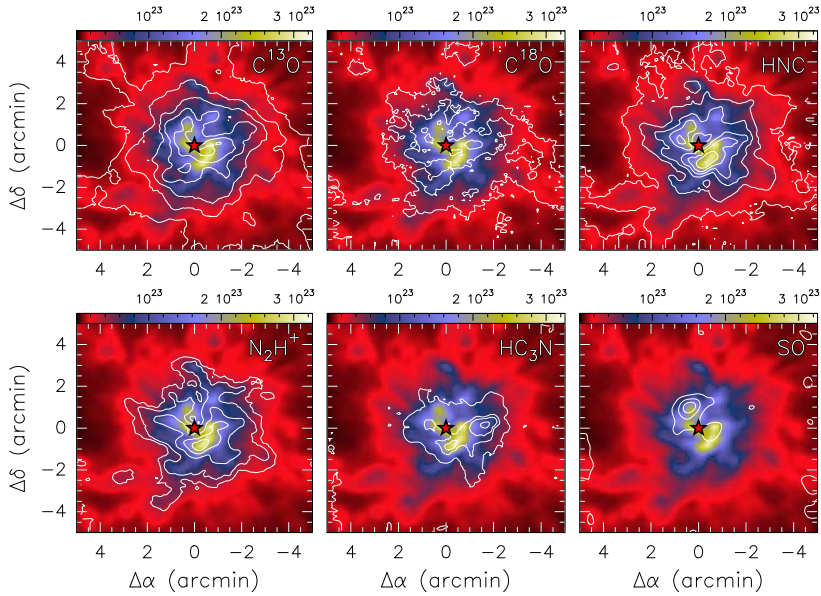
Figure 5.11: Zoom up in the central part of the Herschel H_2 column density (on color scale) map. The red star indicate the position of the infrared star IRS 1. The white contours indicate the ^{13}CO, $C^{18}O$, HNC, N_2H^+, HC_3N and SO integrated emission.

cluster. Molecules such as ^{13}CO and $C^{18}O$ do not show a clear peak on none of the two H_2 (dust continuum) peaks. On the contrary, N-bearing molecules (HNC, N_2H^+ and HC_3N) show a clear peak that coincides with the southern one. This can be interpreted as the ^{13}CO and $C^{18}O$ emission being optically thick and tracing only the outer layers. In addition to this, there is also some chemical differentiation between these two dust peaks: the southern one is bright in HNC, N_2H^+ and HC_3N molecules, while the western peak is bright in SO. Similarly, the brightest SO peak (to the northeast of the infrared cluster) is coincident with a dust condensation, that is associated with weak emission from the other molecular species. This indicates that we have three different condensations with a clear chemical differentiation regarding N-bearing and S-bearing molecules.

The temperature maps obtained with *Herschel* (Didelon et al. 2015) show four regions with a high temperature (above 50 K), one coincident with the central core, where the HII region lies, and three hot bubbles: two located to the east and west of the central core, and the largest one to the northeast, located in between of the NE and N filamentary structures seen in Figure 5.5. Note that the three hot bubbles are located in areas where the H_2 column density is low (typically below 5×10^{21} cm^{-2}), and therefore not coincident with the
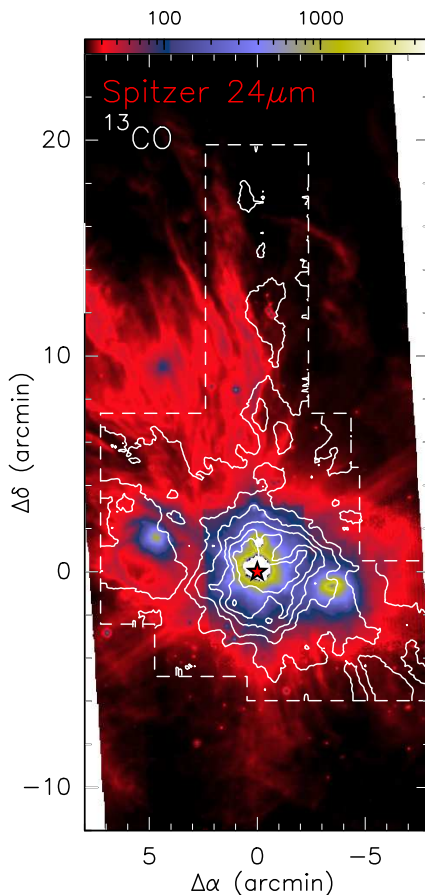
Figure 5.12: Comparison of the ^{13}CO (withe contour) emission and far-infrared emission at 24 μm (color scale) observed with *Spitzer* telescope. The red star indicates the position of the infrared star IRS 1. The white polygon shows the area mapped with the IRAM-30m telescope.

filamentary structures seen in the IRAM-30m maps. These hot bubbles are also visible in the mid-infrared images obtained with *Spitzer* (see Figure 5.12) and *WISE* (see Figure 5.13). The central, eastern and western hot regions are seen as bright nebulosities in the the mid-infrared images, while the hot bubble to the northeast consists of a group of filamentary structures when observed at mid-infrared wavelengths. The mid-infrared images, however, do not show the other filamentary structures seen, e. g., in the IRAM-30m maps. This may indicate that there are filaments, converging towards the central region, with different physical properties: Cold and dense filaments seen in the IRAM-30m molecular line maps and in dust continuum (or H_2 column density), and warm/hot filaments only visible in the mid-infrared. Observations of
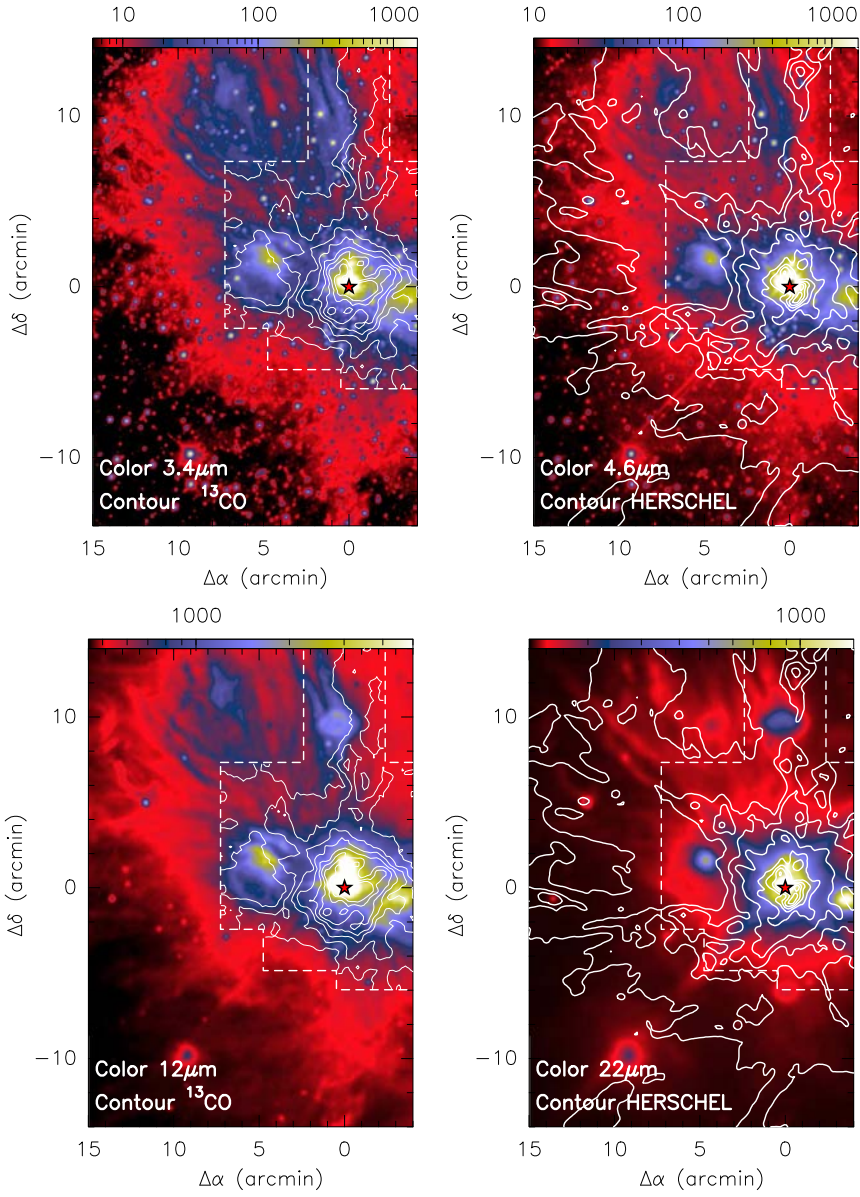
Figure 5.13: Comparison of the ^{13}CO (white contour in Panels 1 and 3) emission, H_2 column (white contour in Panels 2 and 4) density and the *WISE* maps (color scale) at 3.4 μm (Panel 1), 4.6 μm (Panel 2), 12 μm (Panel 3) and 22 μm (Panel 4). The red star indicates the position of the infrared star IRS 1 and the white polygon shows the area mapped with the IRAM-30m telescope.

higher excitation molecular transitions could reveal and confirm the presence of hot gas in this second type of filaments. Finally, one wonders if the hot gas

might be affecting the cold and dense gas. This can be analyzed by studying the northeastern hot bubble and the filamentary structure N. As seen in Figure 5.13, there is a bright mid-infrared source to the north of the central region, at the offset position $(0', 10')$, that is surrounded by molecular emission and dust emission peaks, i. e., there is a clear anti-correlation between the cold and hot gas. This indicates that the presence of the hot gas might be affecting the distribution of the cold gas, however, when inspecting the line-width maps (see Figure 5.8) there are no strong evidences of an enhancement in the line-width towards the edge that is close to the hot bubble.

5.4.2 Large-scale structure: filaments

As discussed in previous sections, the large-scale structure around Mon R2 is predominantly filamentary. In the inspection of the results obtained from our IRAM-30m maps, we have already identified three elongated structures that have been named N, NE and SW according to their position with respect to the central core. However, these three structures are not the only filamentary objects that can be identified in the maps. Therefore, and with the aim of conducting an extensive search of filamentary structures in the IRAM-30m maps, we have analyzed the ^{13}CO, C^{18}O, HNC and N$_2$H$^+$ maps, i. e., the ones that more clearly show extended emission. To do this, we have created different integrated intensity maps for small velocity ranges spanning 0.5 and 1.0 km s^{-1} (see Figures A.7–A.9). We have carefully inspected the distribution of the molecular emission, both spatially and kinematically, searching for structures that are elongated in the plane of the sky, and that are coherent in their velocity distribution. With this analysis we have identified 12 elongated or filamentary structures (named F1, F2, F3, F5, F6, F7, F8, F9, F10-10A, F11, F12 and F13) plus a tentative one (F4). It is worth noting that not all the filaments are clearly visible in all the different velocity intervals. Depending on the velocity range, they may be brighter or fainter, suggesting complex kinematics (see Section 5.4.4). Moreover, the structure of the filaments may differ from one species to the other, probably due to chemical or opacity effects. Therefore, the identification of the filaments has been performed by comparing carefully the different maps of each species. In Figures A.10 to A.13, we have marked each filament in those velocity intervals where its presence is more clear. All the identified filaments are marked in Figure 5.14 (Panel 2), where we overlay the "skeleton" of the filaments on the ^{13}CO integrated intensity emission. A direct comparison of the IRAM-30m filamentary objects with the *Herschel* maps (see Panel 1 of the Figure 5.14) shows that most of them fit well with the H$_2$ column density structure, and also suggest that they extend
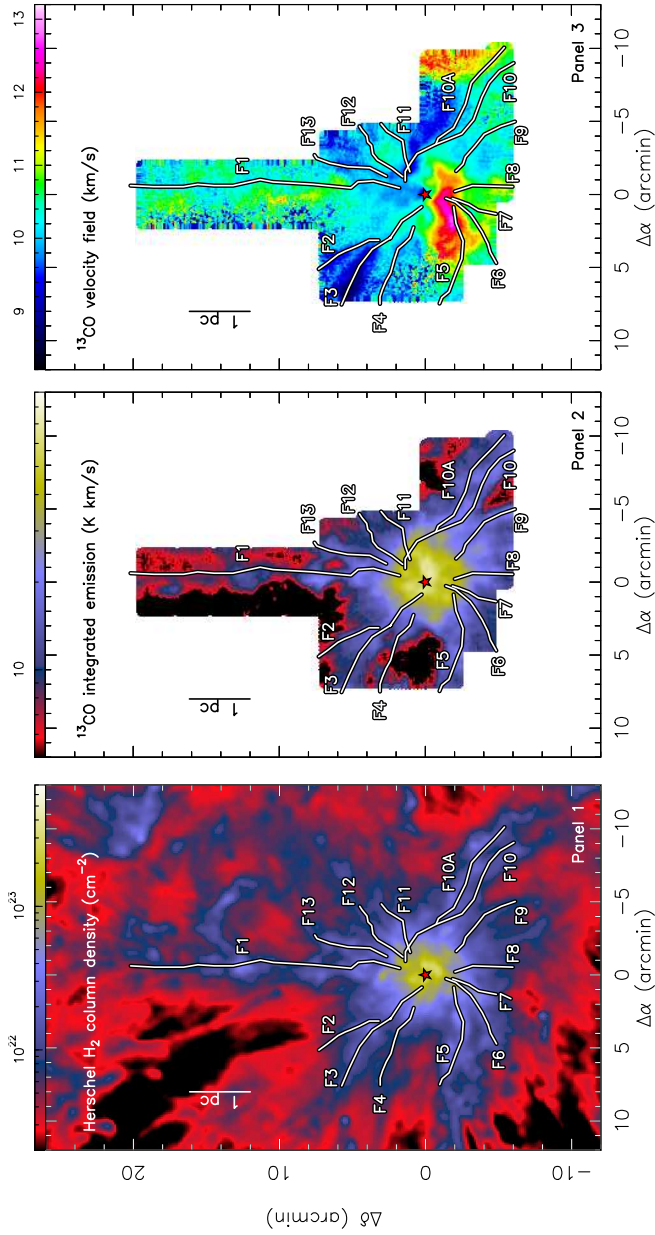
Figure 5.14: The *panel 1:* shows the H$_2$ column density map from Herschel (color image; Didelon et al. 2015). The *Panel 2:* presents Integrated intensity maps of the ^{13}CO molecule. The *Panel 3:* presents velocity centroid for the ^{13}CO molecule. The white/black contours indicate the "skeleton" of the identified filaments. The red star indicate the position of the infrared star IRS 1.

beyond the currently surveyed area of the IRAM-30m maps[iii]. The Panel 3 of Figure 5.14 compares the "skeleton" of the filaments with the velocity field of the dense gas, revealing that some of them (e. g., F3, F5, F6, F9 and F10) are likely associated with velocity gradients.

5.4.3   Filament stability

In Sections 5.4.3 and 5.4.4 we present calculations of physical parameters in the identified filaments (F1 to F13). In particular, in this section we calculate several stability parameters (see Table 5.2) with the aim of figure out if the filaments are fragmenting or if they remain stable. We start this analysis calculating the total mass (M) of each filament. This mass depends of the column density (N) and the relative abundance (X) of the observed molecule, and is given by the equation

$$M = \frac{N}{X} A(2.8 m_{\mathrm{H}}). \tag{5.1}$$

Where, A is the surface area of the filament and m_{H} is the hydrogen mass. Considering local thermodynamic equilibrium (LTE) conditions, the column density (N) of a linear molecule corresponding to the transition $J \to J - 1$ is given by,

$$N = \frac{3k}{4\pi^3} \frac{1}{\mu^2 \nu_{10} J} T_{\mathrm{ex}} \left[\frac{e^{\left(\frac{J(J+1)}{2} \frac{h\nu_{10}}{kT_{\mathrm{ex}}} \right)}}{e^{\left(J \frac{h\nu_{10}}{kT_{\mathrm{ex}}} \right)} - 1} \right] \tau_0 \Delta v. \tag{5.2}$$

Where k is the Boltzmann constant, μ is the electric dipolar momentum of the molecule, ν_{10} is the line frequency, T_{ex} is the excitation temperature, h is the Planck constant, τ_0 is the opacity and Δv is the velocity linewidth. In Equation 5.2, the opacity term can be written as

$$\tau_0 \Delta v = \int \tau(v) \, dv = \left(\frac{1}{J_v(T_{\mathrm{ex}}) - J_v(T_{\mathrm{bg}})} \right) \left(\frac{\tau_0}{1 - e^{-\tau_0}} \right) \int T_{\mathrm{L}}(v) \, dv \tag{5.3}$$

(Palau et al. 2006). Where $J_v(T_{\mathrm{ex}})$ is the intensity (in K) and T_{bg} is the background temperature. Considering that $J_v(T_{\mathrm{ex}}) \ll T_{\mathrm{bg}}$, the column density for the ^{13}CO molecule can be written as

$$\left[\frac{N(^{13}\mathrm{CO})}{\mathrm{cm}^{-2}} \right] = 4.7 \times 10^{13} \left[\frac{T_{\mathrm{ex}}}{J^2} \right] e^{\left(\frac{J(J+1)2.64}{T_{\mathrm{ex}}} \right)} \left[\frac{\tau_0}{(1 - e^{-\tau_0})} \right] \left[\frac{\int T(v) \, dv}{\mathrm{K \ km \ s}^{-1}} \right]. \tag{5.4}$$

[iii]We have been granted with a new observing proposal at the IRAM-30m telescope to cover a larger area, and better study the filaments in Mon R2.

For the ^{13}CO ($J = 1$–0) line[iv], assuming an optically thin emission ($\tau_0 \ll 1$), i.e., $\left[\frac{\tau_0}{(1 - e^{-\tau_0})} \right] \to 1$, and considering $T_{\mathrm{ex}} = 20$ K (see Chapter 6), the Equation 5.4 can be written as

$$\left[\frac{N(^{13}\mathrm{CO})}{\mathrm{cm}^{-2}} \right] = 1.22 \times 10^{15} \left[\frac{\int T(v) \, dv}{\mathrm{K \ km \ s}^{-1}} \right]. \tag{5.5}$$

Regarding the relative abundance of ^{13}CO, we have assumed a constant value of $X[^{13}\mathrm{CO}] = 6.8 \times 10^{-7}$. This value is consistent with the average abundances that can be derived for each filament using the H_2 column density map shown, for example, in Figure 5.10. The $N(H_2)$ towards the filaments is in the range 10^{22}–10^{23} cm^{-2}, while the average $N(^{13}\mathrm{CO})$ is 1.52×10^{16} cm^{-2} (see Table 5.2). With these considerations, the mass of the filament can be calculated from Equation (5.1) as

$$\left[\frac{M}{M_\odot} \right] = 3.29 \times 10^{-14} \left[\frac{A}{\mathrm{pc}^2} \right] \left[\frac{N(^{13}\mathrm{CO})}{\mathrm{cm}^{-2}} \right], \tag{5.6}$$

or

$$\left[\frac{M}{M_\odot} \right] = 39.92 \left[\frac{A}{\mathrm{pc}^2} \right] \left[\frac{\int T(v) \, dv}{\mathrm{K \ km \ s}^{-1}} \right], \tag{5.7}$$

The term $\int T(v) \, dv$ indicates the integrated flux of the molecule, in units of K km s^{-1}. To calculate this and other required observational parameters (e.g., A), we consider a polygon around each filament skeleton in the ^{13}CO maps using GILDAS software, then perform a Gaussian fit in the polygon integrated emission.

Other important parameters calculated for each filament are their "modified" Jeans masses (and lengths). As mentioned in the Chapter 1, in a spherical gas distribution the molecular cloud present a gravitationally collapse when gas distribution present a mass larger than the Jeans mass (see Eq. 1.1), in a radius equivalent to the Jeans length (see Eq. 1.2). In the case of filamentary structures, they could present the so-called "sausage instability" when the mass per length exceeds a critical value given by,

$$(M/l)_{\mathrm{crit}} = \frac{2\sigma^2}{G} = 465 \left(\frac{\sigma}{1 \ \mathrm{km \ s}^{-1}} \right)^2 \ M_\odot \ \mathrm{pc}^{-1} \tag{5.8}$$

(Nagasawa 1987; Wang et al. 2014; Sánchez-Monge et al. 2014). In the Equation 5.8, σ is the velocity dispersion given by $\sigma = \Delta v / \sqrt{8 ln 2}$, where Δv is the line linewidth. When the mass of a filament exceeds this "modified" Jeans mass, the support of the turbulent pressure is no longer able to inhibit the gravitational collapse of the filaments and they starts to fragment into clumps.

[iv]with $\mu = 0.11046$ Debye at $\nu_{10} = 110201354.1$ Hz; values form Cologne Database for Molecular Spectroscopy (http://www.astro.uni-koeln.de/cdms/entries).

The separation of the clumps, determined by the density of their parent molecular structures, is given by the expression

$$\lambda_{\text{cl}} = 1.24 \text{ pc} \left(\frac{\sigma}{1 \text{ km s}^{-1}} \right) \left(\frac{n_{\text{c}}}{10^5 \text{ cm}^{-3}} \right)^{-1/2}. \tag{5.9}$$

In this Equation, n_{c} is the particle number density of the gas in the center of the filament. Each fragment (or clump) would have a mass of,

$$M_{\text{cl}} = (M_{\text{crit}}/l) \times \lambda_{\text{cl}} = 575.3 \ M_{\odot} \left(\frac{\sigma}{1 \text{ km s}^{-1}} \right)^3 \left(\frac{n_{\text{c}}}{10^5 \text{ cm}^{-3}} \right)^{-1/2}. \tag{5.10}$$

In Equations 5.9 and 5.10, the particle number density of the gas can be estimated assuming that the filaments are homogeneous cylinders. In this case we have that $n_{\text{c}} = \frac{M_1}{V} = \frac{4LM_1}{\pi A^2}$, where the volume V of the cylinder is computed based on its length L and its surface area A as defined above (both parameters are listed in Table 5.2). Note that $M_1 = \frac{M}{2.8 m_{\text{H}}}$ in order to consider a particle number density. Then, the particle number density can be estimated as

$$\left[\frac{n_{\text{c}}}{\text{cm}^{-3}} \right] = 18.4 \left[\frac{L}{\text{pc}} \right] \left[\frac{M}{M_{\odot}} \right] \left[\frac{A}{\text{pc}^2} \right]^{-2}. \tag{5.11}$$

The derived central densities for the filaments in Mon R2 are in the range $1\text{--}4 \times 10^4$ cm^{-3}. We note that this is a lower limit for the central density, since we expect the filaments to have gradients with increasing densities towards their center. For this, we have also considered a central density one order of magnitude larger than the one derived with the expression given above.

Using Equations 5.1 to 5.11 we performed a study of the stability/fragmentation of the filaments. Table 5.2 lists the observational parameters (length, area and $\int T(v) \, dv$), as well as the calculated stability parameters for each filament. The mass of each filament was calculated using the Equation 5.7 and their lengths (L), presented in the Table 5.2, were calculated from the PV-diagrams (see Section 5.4.4 and Figures A.14 to A.17). In Mon R2 we found M/L values between 100 and 400 $M_{\odot}$/pc, this values are comparable with those found in DR21 filaments ($M/L =$ 100–700 $M_{\odot}$/pc; Hennemann et al. 2012). In the other hand, the M/L values found in Mon R2 are larger than those found in the Taurus dark cloud filaments. Based on C^{18}O emission, Hacar et al. (2013) found $M/L \sim 15 \ M_{\odot}$/pc in this region. While Palmeirim et al. (2013) found $M/L \sim 54 \ M_{\odot}$, on basis of Herschel continuum maps. In Mon R2, we find that all the filaments have $(M/L) > (M/L)_{\text{crit}}$ which is indicative of them undergoing fragmentation. The measured M/L are larger than the critical values by a factor of 3–6 in filaments F1–F12 and by a factor of 1.1 in F13 (see columns 8 and 9 in Table 5.2). It is important to note that among all the filaments F1, F3, F9 and F10 seem to be the most

unstable.

In the column 10 and 11 of the Table 5.2 we list the theoretical distances (λ_{cl}) between the possible fragments and their masses (M_{cl}). First of all, we note that the distance between fragments estimated using an homogeneous cylinder (frist number in the column 10) is in some cases larger than the filament length. This suggests that this value of n_{c} is a lower limit and the filaments have a radial density gradient. The distances between fragments measured with a n_{c} one order of magnitude larger are always smaller than the length of the filament (second number in the column 10). It is also worth noting that the length of the filament can be a lower limit, since for some filaments we are not covering its whole extent due to the limitations in the area covered with the telescope. Furthermore, we are observing a projection of the filament in the sky, then, we might be missing information about the real "shape" of the filaments. The filaments, might be bent in different direction and thus, we are underestimating their lengths. Finally, an important factor that may affect the distance between fragments is the velocity dispersion σ considered. As mentioned before, the velocity dispersion depends on the linewidth of the filament. To calculate the linewidth, we did Gaussian fits to the integrated ^{13}CO emission along each filament. However, due to the coarse angular resolution of our maps, we can be missing smaller substructures like for example the presence of two or more nearby filaments, which would appear as a single filaments in our maps. This would result in an overestimate of the linewidths of the filaments, and therefore on the velocity dispersion and the distance between fragments. For the masses of the fragments (M_{cl}) we find similar results. Under the assumption of an homogeneous filament, the masses of the fragments are larger than or similar to the total mass of some filaments (e. g., F2, F4, F8, F12 and F13, see first number in the column 11). If we assume that the filaments have a radial density gradient, then the masses derived for the fragments are always smaller than the total mass of the filament (see second number in the column 11). We note also, that the same effects that can affect the distance between clumps may be affecting the masses derived for the fragments.

It is worth noting that some filaments seem to present signposts of fragmentation in our maps. Figures A.10 to A.12 present channels maps of the ^{13}CO emission, covering a velocity range from 5 to 20 km s^{-1} in steps of 1 km s^{-1}. In these Figures we can see that filaments F1, F5 and F13 show clumps (or condensations) at different velocities. This seems confirmed in Figure A.13, where we show the channels maps of the C^{18}O emission in a velocity range from 8 to 19 km s^{-1} in steps of 1 km s^{-1}. In this Figure we can see, at different velocities, signposts of fragmentation in the filaments F1, F5, F9, F10 and F13. Whether these fragments will form or not stars is something that we can not confirm with the current data and analysis. If we consider that the

conditions of these condensations to form stars are fulfilled we can face two different scenarios. On one hand, the fragments can condense and form stars along the filamentary structures. On the other hand, the fragments can be dragged to the central part of the hub while they are condensing and forming stars. A recent work by Hennemann et al. (2012) suggests that this mechanism may occur in the filamentary-hub system of DR21. The physical properties of the filaments in Mon R2 resemble those found in DR21, with gravitationally unstable structures that will fragment and form cores and protostars. These kind of filaments differ to those found in other star forming regions like Taurus or Aquila (e. g., Goldsmith et al. 2008; André et al. 2010), where the striations and sub-filaments are less massive and more stable. We can evaluate the different timescales involved in this process to determine if the second scenario (cores being dragged to the central part) is possible. Assuming a typical distance of the fragments with respect to the hub of about 1 pc and a velocity gradient of about 1 km s^{-1}, the timescale for the fragments to move to the hub is about 10^6 yr. This timescale is comparable, although slightly larger, to the typical timescale of the formation of low-mass stars (10^5 yr for Class I and 10^7 yr for Class III objects; see Chapter 1), with indicates that some cores could be formed in the filaments but be dragged to the hub before they form stars.

5.4.4 | Filament kinematics

This Section presents calculations of kinematics parameters in the filaments (velocity gradients and mass accretion flows). Panel 3 of the figure 5.14 shows the overlaid of the filaments in the velocity field maps. This reveals that some filaments may show a change in velocity along its major axis, i. e., velocity gradients. One of the best approaches to study in detail these velocity gradients is the technique known as position-velocity diagram, in which we can directly see how the velocity changes at different positions along a given slice. Most of the available astronomical tools that permit to build position-velocity diagrams can only deal with straight lines, or become really inefficient when you need to analyze slices at different angles. The particular case of a filament is a clear example where multiple slices at different angles are necessary to properly track its curved structure. We have used a new Python radioastronomical tool named `pvextractor`[v] that produces position-velocity diagrams along any path or curved line, even if it has different angles.

---

[v]The Python tool `pvextractor` can be downloaded from the github repositories or from the webpage http://keflavich.github.io/pvextractor/

Table 5.2: Stability analysis of the filaments.

Filament	L^a (pc)	Area^b (pc^2)	$\int T_{\mathrm{MB}}\,dv^b$ (K km s^{-1})	σ^c (km s^{-1})	$N(^{13}\mathrm{CO})^d$ ($\times 10^{16}$cm^{-2})	M^e ($M_\odot$)	M/L ($M_\odot$/pc)	$(M/L)^f_{\mathrm{crit}}$ ($M_\odot$/pc)	λ^g_{cl} (pc)	M^h_{cl} ($M_\odot$)
F1	2.24	1.57	9.08	0.32	1.11	570	260	50	1.29–0.41	60–20
F2	0.55	0.38	8.69	0.39	1.06	130	240	70	1.59–0.50	110–35
F3	1.10	0.70	14.23	0.42	1.74	400	360	80	1.30–0.40	105–35
F4	0.70	0.39	9.11	0.40	1.11	140	200	70	1.43–0.45	105–35
F5	0.87	0.46	12.35	0.40	1.51	230	260	80	1.20–0.38	90–30
F6	0.70	0.29	12.20	0.36	1.49	140	200	60	0.95–0.30	60–20
F7	0.37	0.14	21.14	0.43	2.59	120	320	90	0.83–0.26	70–20
F8	0.47	0.26	17.98	0.55	2.20	190	400	140	1.40–0.44	195–60
F9	0.65	0.38	10.12	0.30	1.24	150	240	40	1.03–0.33	45–15
F10	1.40	0.70	20.19	0.38	2.47	570	400	70	0.86–0.27	60–20
F10A	1.00	0.65	12.31	0.47	1.51	320	320	100	1.56–0.49	160–50
F11	0.49	0.23	10.95	0.38	1.34	100	200	70	1.14–0.36	80–25
F12	0.58	0.31	9.33	0.42	1.14	120	200	80	1.46–0.46	120–40
F13	0.63	0.28	6.10	0.47	0.75	70	110	100	1.83–0.58	190–60

^{a}The lengths are calculated from the PV-diagrams (see Figures A.14 to A.17). ^{b}From a polygon defined from the ^{13}CO emission around each filament skeleton. ^{c}Velocity dispersion $\sigma = \Delta v/\sqrt{8ln2}$. ^{d}Calculated from $\left[\frac{N(^{13}\mathrm{CO})}{\mathrm{cm}^{-2}}\right] = 1.22 \times 10^{15}\left[\frac{\int T(v)\,dv}{\mathrm{K\ km\ s}^{-1}}\right]$. ^{e}Mass of the filament derived from $\left[\frac{M}{M_\odot}\right] = 39.92\left[\frac{A}{\mathrm{pc}^2}\right]\left[\frac{\int T(v)\,dv}{\mathrm{K\ km\ s}^{-1}}\right]$. ^{f}Calculated from $(M/l)_{\mathrm{crit}} = 465\left(\frac{\sigma}{1\ \mathrm{km\ s}^{-1}}\right)^2 M_\odot\ \mathrm{pc}^{-1}$. ^{g}Calculated from $\lambda_{\mathrm{cl}} = 1.24\ \mathrm{pc}\left(\frac{\sigma}{1\ \mathrm{km\ s}^{-1}}\right)\left(\frac{n_c}{10^5\ \mathrm{cm}^{-3}}\right)^{-1/2}$. ^{h}Calculated from $M_{\mathrm{cl}} = 575.3\ M_\odot\left(\frac{\sigma}{1\ \mathrm{km\ s}^{-1}}\right)^3\left(\frac{n_c}{10^5\ \mathrm{cm}^{-3}}\right)^{-1/2}$.

Table 5.3: Kinematical analysis of the filaments.

Filament	L (pc)	M ($M_\odot$)	V_Hub (km s^{-1})	V_Far (km s^{-1})	V_obs (km s^{-1})	$\nabla V_{\parallel\text{obs}}^a$ (km s^{-1}/pc)	M_accr^b (10^{-4} $M_\odot$ yr^{-1})	α^c (degrees)	$M_\text{accr}^{\text{corr},d}$ (10^{-4} $M_\odot$ yr^{-1})
F1	2.24	570	9.5	10.3	+0.8	+0.36	2.1	+18	6.5
F2	0.55	130	9.8	9.2	−0.6	−1.09	1.5	−45	1.4
F3	1.10	400	11.0	8.5	−2.5	−2.27	9.2	−65	4.3
F4	0.70	140	10.5	9.7	−0.8	−1.14	1.2	−47	1.5
F5	0.87	230	11.3	10.3	−1.0	−1.15	2.6	−47	2.5
F6	0.70	140	11.0	10.5	−0.5	−0.71	1.0	−34	1.5
F7	0.37	120	11.0	11.0	+0.0	+0.00	—	+0	—
F8	0.47	190	10.9	11.2	+0.3	+0.64	1.2	+31	2.0
F9	0.65	150	10.7	11.4	+0.7	+1.08	1.7	+45	1.7
F10	1.40	570	9.5	11.0	+1.5	+1.07	6.2	+45	6.2
F10A	1.00	320	9.0	10.0	+1.0	+1.00	3.3	+43	3.5
F11	0.49	100	9.5	10.5	+1.0	+2.04	2.1	+62	1.1
F12	0.58	120	9.5	10.4	+0.9	+1.55	1.8	+55	1.3
F13	0.63	70	9.6	10.2	+0.6	+0.95	0.7	+52	0.5

[a]Calculated with the equation $\nabla V_{\parallel\text{obs}} = \frac{V_\text{obs}}{L}$. [b]Calculated with the equation $M_\text{accr} = M\,\nabla V_{\parallel\text{obs}}$. [c]Calculated with the equation $\alpha = \tan^{-1}\left(\frac{\nabla V_{\parallel\text{obs}}}{\nabla V_{\parallel\text{real}}}\right)$. [d]Calculated with $M_\text{accr}^\text{corr} = \frac{M\,\nabla V_{\parallel\text{obs}}}{\tan\alpha}$.

In Figures A.14 to A.17, we present the position-velocity diagrams for the identified filaments (including F10A and F4). The paths used to generate the plots correspond to the "skeleton" of each filament as shown in Figure 5.14. We have considered the molecular species ^{13}CO, C^{18}O and HNC to analyze the velocity gradients because they are better tracing the extended elongated emission associated with the filaments. Note that we have excluded N$_2$H$^+$ to avoid possible misinterpretations on the velocity structure due to the hyperfine structure of the observed transition. In the position-velocity diagrams we can determine the velocity gradient for each filament. A first approach to determine the velocity gradient is just to compare the velocity at both extremes of the filament, and divide by its length as

$$\text{Vel. gradient} = \nabla V_{\|\text{obs}} = \frac{V_{\text{obs}}}{L}, \tag{5.12}$$

where

$$V_{\|\text{obs}} = V_{\text{hub}} - V_{\text{far}}. \tag{5.13}$$

This first simplified inspection reveals at least four different types of filamentary structures: (i) filaments with a strong velocity gradient (> 2 km s^{-1} pc^{-1}; e. g., F3 and F10A in Figure 5.15), (ii) filaments with weak velocity gradients (~ 1 km s^{-1} pc^{-1}; e. g., F1 and F9 in Figure 5.15), (iii) filaments with no velocity gradient detectable at our spectral and angular resolution limit (0.16 km s^{-1}, and 27 $''$; e. g., F7), and (iv) filaments with two velocity components (e. g., F9, F10). Figure 5.15 shows the position-velocity plots along the 'skeletons' of the filaments F1, F3, F9 and F10A. White arrows indicate the direction towards the hub. Other important parameter is the mass accretion flows implied by the velocity gradients. To calculate this flow in each filament we can use a simple cylindrical model (see Figure 5.16; Kirk et al. 2013). A cylinder with mass M, length L, radius r, an inclination to the plane of the sky of angle α, and true motions of velocities $V_\|$ along the filament long axis. The accretion rate, M_{accr}, along the filament onto the hub is therefore the velocity along the filament times the density and the area perpendicular to the flow, or

$$M_{\text{accr}} = \left(\frac{M}{\pi r^2 L}\right)(\pi r^2) \times V_\| = \left(\frac{M}{L}\right) \times V_\| \tag{5.14}$$

Due to projection effects, we have

$$L_{\text{obs}} = L \cos(\alpha), \tag{5.15}$$

and

$$V_{\|\text{obs}} = V_\| \sin(\alpha), \tag{5.16}$$

with $V_{\|\mathrm{obs}} = \nabla V_{\|\mathrm{obs}}\, L_{\mathrm{obs}}$. Therefore, the accretion rate is given by

$$M_{\mathrm{accr}} = \frac{\left(\frac{M}{L_{\mathrm{obs}}}\, V_{\|\mathrm{obs}}\right)}{\tan\alpha} = \frac{M\,\nabla V_{\|\mathrm{obs}}}{\tan\alpha} \tag{5.17}$$

For our calculation we assumed $\alpha = 45°$, then

$$M_{\mathrm{accr}} = M\,\nabla V_{\|\mathrm{obs}} \tag{5.18}$$

However, it is important to note that the filaments might be homogeneously distributed at all the projected angles in the plane of the sky. We can calculate the "real" angle presented for every filament using the following relation

$$\frac{V_{\|\mathrm{obs}}}{L_{\mathrm{obs}}} = \frac{V_{\|\mathrm{real}}}{L_{\mathrm{real}}}\left(\frac{\sin(\alpha)}{\cos(\alpha)}\right) = \frac{V_{\|\mathrm{real}}}{L_{\mathrm{real}}}\,\tan(\alpha), \tag{5.19}$$

then

$$\alpha = \tan^{-1}\left(\frac{\nabla V_{\|\mathrm{obs}}}{\nabla V_{\|\mathrm{real}}}\right). \tag{5.20}$$

Assuming that all the filaments are accreting material onto the Hub, an present the same velocity gradients at different angles, we calculate an average of all the observed velocity gradients ($\nabla V_{\|\mathrm{ave}}$=1.075) and considering that this is the gradient at $\alpha = 45°$. Then we can calculate α as

$$\alpha = \tan^{-1}\left(\frac{\nabla V_{\|\mathrm{obs}}}{1.075}\right). \tag{5.21}$$

With this "new" angle, we re-calculated the corrected mass accretion flows ($M_{\mathrm{accr}}^{\mathrm{corr}}$) and lengths ($L^{\mathrm{corr}}$). We found that the L^{corr} is larger than L by a factor of 1.4–2. This implies a decrease about 30% in the λ_{cl} and M_{cl} parameters. Table 5.3 summarizes the velocity gradients and the measured M_{accr}, α and $M_{\mathrm{accr}}^{\mathrm{corr}}$ for each filament. Using the velocity gradient and the "new" angles calculated in the filaments, we constructed a schematic view of the filamentary structure in Mon R2. Figure 5.17, present the schematic view of the filamentary structure. We found that the filaments F2 to F6 are placed behind the hub (blue shifted), being F6 the less blue shifted and F3 is the most blue shifted filament. The filaments F1 and F8 to F13 are placed in front of the hub (red shifted), being F1 the less red shifted and F11 the most red shifted filament. Finally, the filament F7 seems to be placed in the plane of the sky.

Regarding to the mass accretion flows, we found that almost all the filaments present signposts of accretion. We found that almost all the filaments present M_{accr} values about 10^{-4}–10^{-3} $M_\odot\ \mathrm{yr}^{-1}$, the exception is the filament F7. This
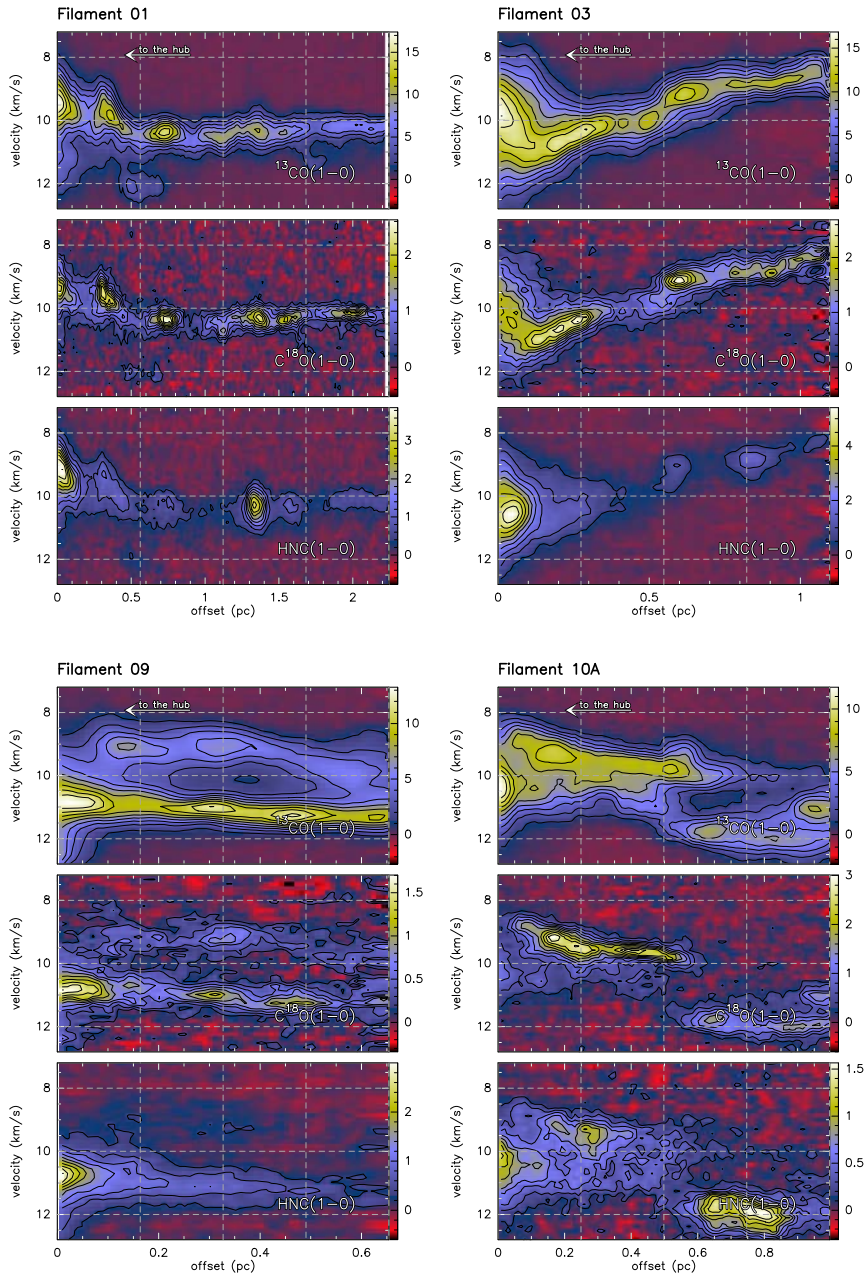
Figure 5.15: Position-velocity plots along the 'skeletons' of the filaments F1, F3, F9 and F10A. White arrows indicate the direction towards the hub. Multiple components, and velocity gradients are clearly visible.
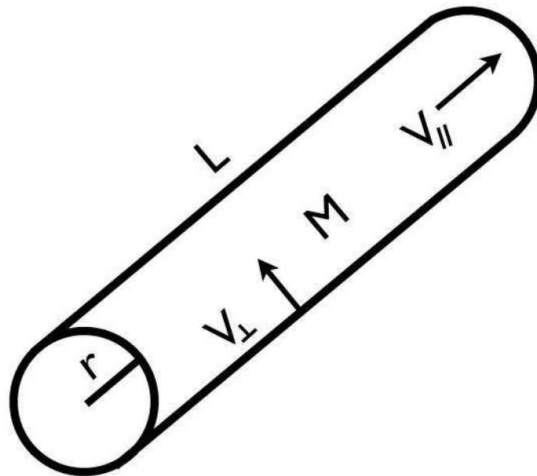
Figure 5.16: Cylinder model considered for the accretion rate analysis. A cylinder with length L, radius r, mass M, and velocities of $V_\parallel$ along the long axis and $V\perp$ in the radial direction. The cylinder is inclined an angle of α relative to the plane of the sky. Figure from Kirk et al. (2013).

filament seems to be in the plane of the sky, thus it does not present velocity gradients and we can not calculate its mass accretion flow. The filaments that present the largest mass accretion flow are F3 ($M_{\mathrm{accr}} \sim 1 \times 10^{-3} \ M_\odot \ \mathrm{yr}^{-1}$) and F10 ($M_{\mathrm{accr}} \sim 6.2 \times 10^{-4} \ M_\odot \ \mathrm{yr}^{-1}$). While the filaments F13 present the lowest $M_{\mathrm{accr}} \sim 0.7 \times 10^{-4} \ M_\odot \ \mathrm{yr}^{-1}$. The rest of the filaments (except for F7) present mass accretion flows between 1.0 and $3.3 \times 10^{-4} \ M_\odot \ \mathrm{yr}^{-1}$. These values are larger that the mass accretion flows found in Serpens by Kirk et al. (2013), $M_{\mathrm{accr}} \sim 0.03 \times 10^{-4}$. The corrected mass accretion flows confirm that the filaments are accreting material to the Hub. In the case of the corrected mass accretion flows, the F1 filament presents the largest value of $M_{\mathrm{accr}}^{\mathrm{corr}} \sim 6.5 \times 10^{-4} \ M_\odot \ \mathrm{yr}^{-1}$ followed by F10 that present $M_{\mathrm{accr}}^{\mathrm{corr}} \sim 6.2 \times 10^{-4} \ M_\odot \ \mathrm{yr}^{-1}$. The filaments F13 present the lowest $M_{\mathrm{accr}} \sim 0.5 \times 10^{-4} \ M_\odot \ \mathrm{yr}^{-1}$. The rest of the filaments (except for F7) present $M_{\mathrm{accr}}^{\mathrm{corr}}$ between 1.1 and $4.3 \times 10^{-4} \ M_\odot \ \mathrm{yr}^{-1}$.

Some filaments show complex kinematics, with more than one velocity component (see spectra in Figure 5.18), reminiscent of the velocity structure observed towards the fibers seen in other star forming regions (e. g., Hacar et al. 2013). However, due to the limitations of our data we can not determinate the presence of fibers in Mon R2. The filamentary structure also seems to be present within the hub (see Figure 5.19), where we detected three filaments, with different chemical properties. The first filament, at 10 km s^{-1}, is surrounding the UC HII region and presenting an intensity peak very close to the IRS 1.
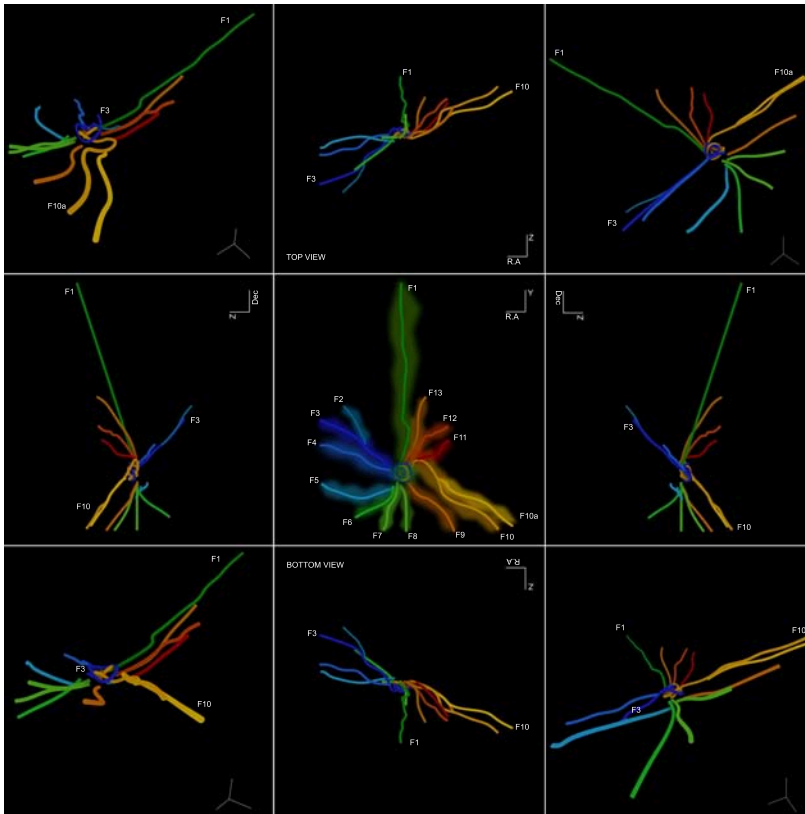
Figure 5.17: Schematic view of the filamentary structure in Mon R2. The central panel of the figure indicate the face on view of the filaments in Mon R2 and the rest of the panels show the filamentary structure at different angles. The filaments F2 to F6 are placed behind the hub (blue shifted), while the filaments F1 and F8 to F13 are placed in front of the hub (red shifted). Finally the filament F7 seems to be placed in the plane of the sky. Image credit: B. Sánchez-Monge and R. Delgado.

The second one, at 8 km s^{-1}, is associated to the PDR in MP2 at offset ($0''$, $40''$). Finally, the third one (at 12 km s^{-1}) does not present evidence of interaction with UV photons. These filaments seem to fall down following a spiral pattern towards the UC HII region. Overall, this suggests the idea of a young UC HII region just beginning to expand and break out of the dense filamentary hub where it was formed, with material still collapsing inward along the filaments.

Summarizing, our maps reveal a complex kinematics (see Figure 5.18), with large-scale filaments and spiraling arms approaching the UC HII region. Several filaments have been identified in different tracers (e. g., ^{13}CO, C^{18}O, HNC, N$_2$H$^+$) as velocity-coherent elongated structures that spatially coincide with

the continuum filaments detected with Herschel and the IRAM-30m telescope. Some filaments show complex kinematics, with more than one velocity component (see Figure 5.18). Furthermore, position-velocity cuts along the filaments show velocity gradients of up to 2 km s^{-1} pc^{-1} (see Figure 5.15), that correspond to mass accretion rates along the filaments of about 10^{-4}–10^{-3} $M_\odot$ yr^{-1}. The filamentary structure seems to be also present within the hub (see Figure 5.19), where we find filaments, with different chemical properties, that seem to fall down following a spiral pattern towards the UC HII region. This suggests the idea of a young UC HII region just beginning to expand and break out of the dense filamentary hub where it was formed, with material still collapsing inward along the filaments.

In order to improve our analysis, it is important to perform larger maps with higher angular resolution, as well as perform a comparison of the observations with numerical simulations. We have been granted with a new observing proposal at the IRAM-30m telescope to cover a larger area ($30' \times 30'$), to have an overview of the complete region providing new insights into the kinematics of this complex filaments-hub system. However, interferometric observations are required to resolve in detail the structure of the filaments (look for fibers) and to resolve the "spiral" structure of the hub. The best candidates to perform these observations are the **ALMA** and **NOEMA** interferometers as they provide the necessary resolution (angular and spectral) to resolve the velocity structure and the compact emission.Our plan is to ask for observing time to NOEMA to resolve the complex kinematics of the filaments and further study their fragmentation.
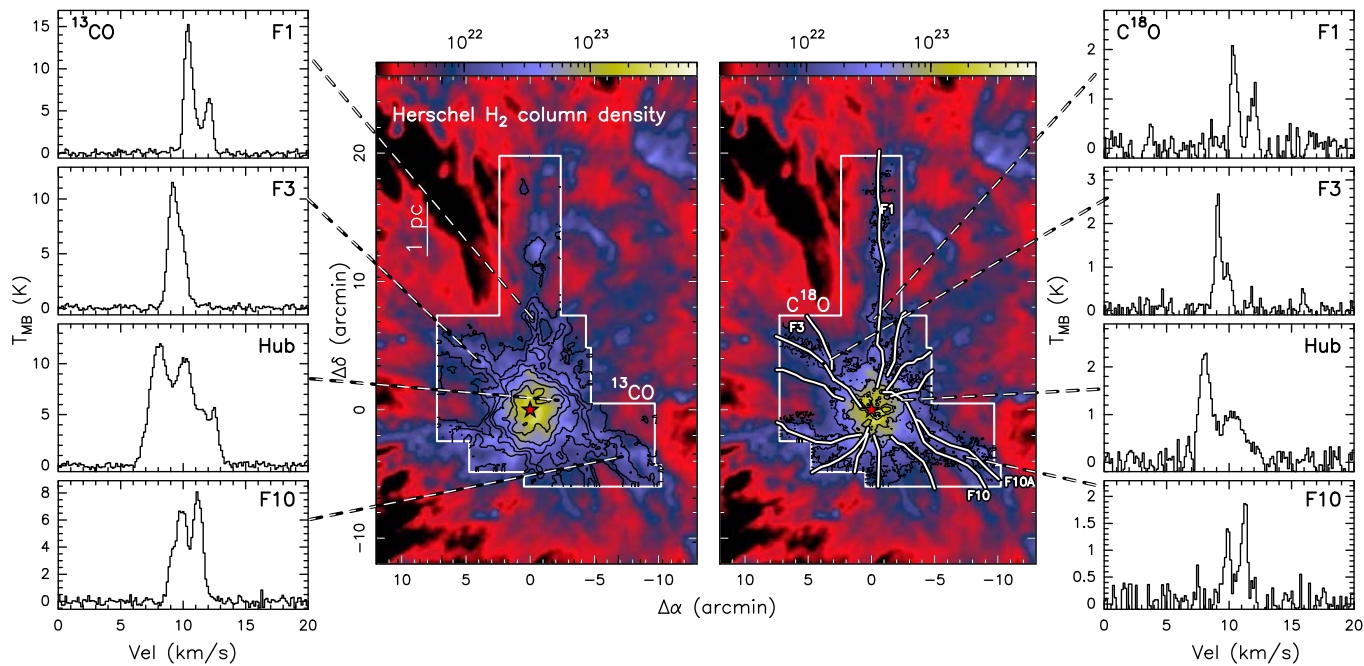
Figure 5.18: *Central panels:* H_2 column density map from Herschel (color image; Didelon et al. 2015), with the ^{13}CO and $C^{18}O$ integrated emission from IRAM-30m overlaid (black contours). The white polygon depicts the area surveyed with IRAM-30m. The red star marks the position of the UC HII region. All detected filaments are marked in the second panel. *Left/right panels:* Spectra extracted at different positions of filaments F1, F3, F10, and for the hub.
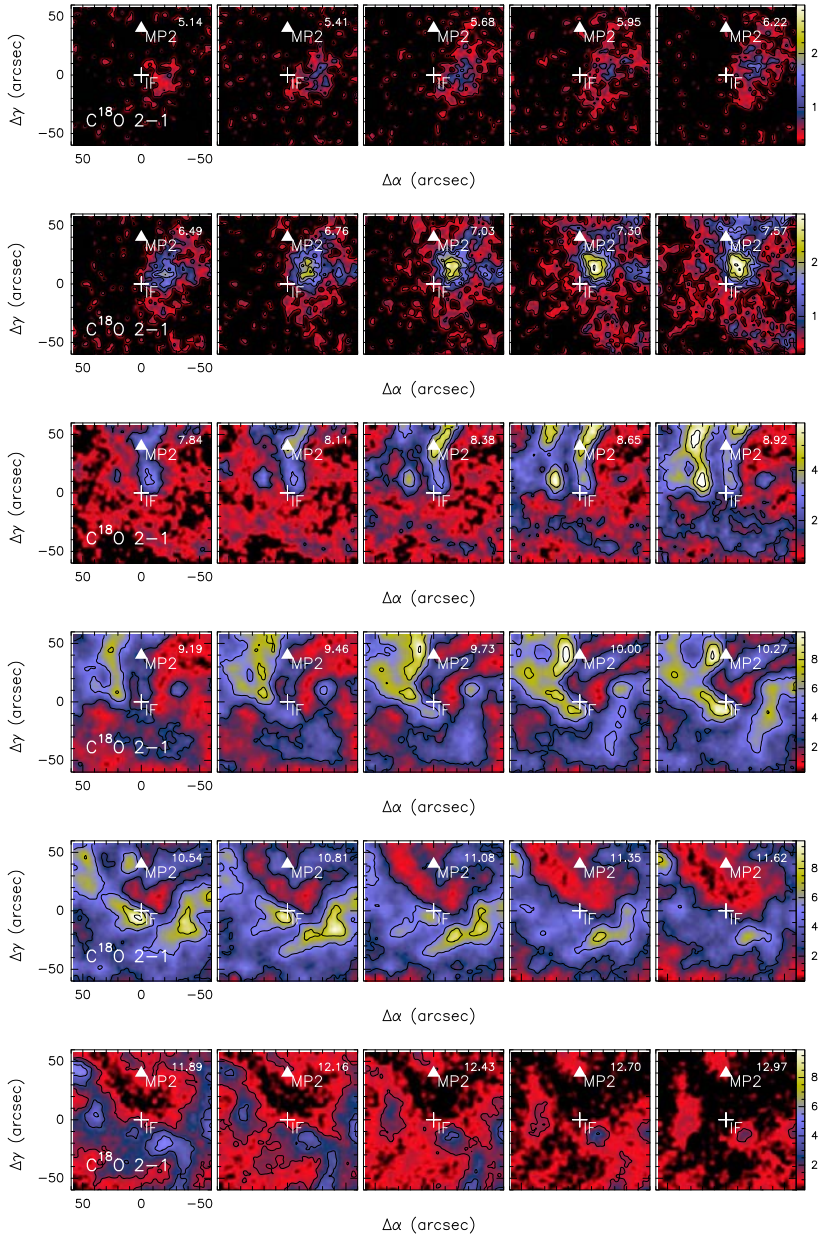
Figure 5.19: Zoom in the channel maps of the $C^{18}O$ molecule at 219.560 GHz. The velocities range for the map are from 6.49 to 12.97 km s^{-1} by steps of 0.27 km s^{-1}. Maps obtained with IRAM-30m, see Chapter 6.

5.5   Summary

On the basis of large-scale maps observed with the IRAM-30m telescope we performed a study of the filamentary structure seen towards Mon R2. Our results can be summarized as follows.

- The ^{13}CO, C^{18}O, HNC and N$_2$H$^+$ emission reveals a filamentary structure that extends in all directions, beyond the surveyed area. The detection of faint emission of nitrogenated molecules along the filaments shows that dense gas ($\sim 10^5$ cm^{-3}) is associated with the bones of the filaments.

- The area around IRS 1 ($4' \times 4'$), is bright in all the species and their emission appears in an arc structure surrounding the infrared stars. The ^{13}CO and C^{18}O intensity peaks are located to the East and West of the cluster, while the nitrogenated species present a bright peak at south of the cluster, where there is no evidence of CO emission. This indicates different chemical and physical properties in the region.

- Thirteen filaments (F1, F2, F3, F4, F5, F6, F7, F8, F9, F10-10A, F11, F12 and F13) have been identified in different tracers, as velocity-coherent elongated structures that spatially coincide with the continuum filaments detected with Herschel. We found velocity gradients along the filaments that correspond to mass accretion rates of about 10^{-4}–10^{-3} $M_\odot$ yr^{-1}.

- We found four different types of filamentary structures: *i)* filaments with a strong velocity gradient (> 2 km s^{-1} pc^{-1}; e. g., F3 and F10A), *ii)* filaments with weak velocity gradients (~ 1 km s^{-1} pc^{-1}; e. g., F1 and F9), *iii)* filaments with no velocity gradient detectable at our spectral and angular resolution limit (e. g., F7), and *iv)* filaments with two velocity components (e. g., F9, F10). Using the velocity gradient and the angles calculated in the filaments, we found that the filaments F2 to F6 are placed behind the hub (blue shifted), while the filaments F1 and F8 to F13 are placed in front of the hub (red shifted). Finally the filament F7 seems to be placed in the plane of the sky.

- Almost all the filaments (except for F7) present evidence of fragmentation as $M/L > (M/L)_{\mathrm{crit}}$ by a factor of 1.1–6. The fragmentation of the filaments F1, F5, F9, F10 and F13 seem to be confirmed by the channels maps. If the fragments will or not form stars, is something that we can not confirm with the current data and analysis. However, assuming a typical distance of the fragments with respect to the hub of about 1 pc

and a velocity gradient of about 1 km s^{-1}, the timescale for the fragments to move to the hub is about 10^6 yr. This timescale is comparable to the typical timescale of the formation of low-mass stars, this indicates that some cores could start to be formed in the filaments but be dragged to the hub before they form stars.

- Assuming that the filaments are homogeneous cylinders, we found that the n_c in the filaments are in the range 1–4×10^4 cm^{-3}. Using this values we derived a lower limit of M_{cl} and λ_{cl}. We found that the filaments F1, F3, F5, F6, F7, F9 and F10-10A present M_{cl} smaller than the filament mass by factors of $\sim$ 3–10. While the rest of them present similar (or higher) values of M_{cl} than M. In the case of the λ_{cl} values, we found similar (or higher) values of λ_{cl} than L in most of the filaments. Assuming that the filaments have a radial density gradient, then the masses and the distance between clumps derived for the fragments are always smaller than the total mass of the filament. However, also it is important to note that M_{cl} and λ_{cl} depend of several parameters (σ, L, etc.) that due to our limitations are we can not calculate they can not be calculated with accuracy, and thus we might be overestimating M_{cl} and λ_{cl}.

- We calculate the angle (α) of the filaments, with this angle we recalculated the corrected mass accretion flows (M_{accr}^{corr}) and lengths (L^{corr}). We found that the L^{corr} is larger than L by a factor of 1.4–2. This implies a decrease of about 30% in λ_{cl} and M_{cl} parameters. The M_{accr}^{corr} values confirm that the filaments are accreting material to the Hub. We found that the F1 filament presents the largest value of $M_{accr}^{corr} \sim 6.5 \times 10^{-4}$ $M_{\odot}$ yr^{-1} followed by F10 that presents $M_{accr}^{corr} \sim 6.2 \times 10^{-4}$ $M_{\odot}$ yr^{-1}. The filaments F13 present the lowest $M_{accr} \sim 0.5 \times 10^{-4}$ $M_{\odot}$ yr^{-1}. The rest of the filaments (except for F7) present M_{accr}^{corr} between 1.1 and 4.3×10^{-4} $M_{\odot}$ yr^{-1}.

- We constructed a schematic view of the filamentary structure in Mon R2. We found that the filaments F2 to F6 are placed behind the hub (blue shifted), being F6 the less blue shifted and F3 is the most blue shifted filament. The filaments F1 and F8 to F13 are placed in front of the hub (red shifted), being F1 the less red shifted and F11 the most red shifted filament. Finally, the filament F7 seems to be placed in the plane of the sky.

- The filaments seem to fall down following a spiral pattern towards the UC HII region. This supports the idea of a young UC HII region just beginning to expand and break out of the dense filamentary hub where it was formed, with material still collapsing inward along the filaments.

- Physical properties of the filaments in Mon R2 resemble those found in DR21 (Hennemann et al. 2012), with gravitationally unstable structures

that will fragment and form cores and protostars. These kind of filaments differ to those found in other star forming regions like Taurus or Aquila (Goldsmith et al. 2008; André et al. 2010), where the striations and sub-filaments are less massive and more stable.

6

UNBIASED SPECTRAL SURVEY (84.0–350.0 GHz)

This chapter presents an unbiased spectral line survey towards two carefully selected positions in the Mon R2 complex. We investigate the chemistry of gas around the ultracompact HII region and the possible variations due to different local physical conditions.

Contents

6.1   Introduction

Unbiased spectral line surveys are an excellent method to characterize the molecular content of different regions in the ISM. Spectral surveys are very important in the study of the physical and chemical properties of star forming regions. They provide multiple molecular lines, and allow us to develop a chemical study to figure out composition and structure of the gas in sites of active star formation.

In particular, the spectral surveys at sub-millimeter and millimeter wavelengths allow to detect a large number of molecules via the detection of rotational transitions. Observations with high spectral resolution of multiple lines from the same molecule, can be used to calculate physical parameters such as the column density and the temperature, thanks to the fact that different lines from transitions with different energies are excited at different temperatures and densities. A careful analysis can, therefore, distinguish between the various physical components. Moreover, the kinematic information provided by the line profiles can be used to identify sub-structures along the line of sight. Several unbiased spectral surveys have been obtained to study different regions going from low-mass to high-mass star forming regions, shocked gas sources, or hot molecular cores (e.g., Schilke et al. 1997; Hatchell et al. 1998; Schilke et al. 2001; Tercero et al. 2010; Caux et al. 2011; Pety et al. 2012 and Nagy et al. 2015). Herbst & van Dishoeck (2009) summarize the information of the most important surveys in star-forming regions and present their principal results.

Our aim is to study the influence the UV photons in the chemistry of massive star forming regions. For this, we carried out an unbiased spectral survey towards two important positions in the Mon R2 region. Then, we performed a comparison of our results with those found in different types of sources, such as PDRs (Orion Bar, NGC 7023 and Horsehead), dark clouds (TMC 1 and L134N) a hot core (Orion KL) and a shock (L1157). The UC HII region in Mon R2 is surrounded by a series of PDRs with different physical conditions. The main PDR ($n > 10^5$ cm^{-3}), is irradiated by a UV field with an intensity of $G_0 > 10^5$ (in units of Habing field) corresponding to IRS 1 (IF position; see Figure 6.1). The high densities (10^6–10^7 cm^{-3}) and kinetic temperatures (Tk> 500 K) of the Mon R2-IF region drive a rich chemistry different of that found in low-UV irradiated PDRs. Key reactions for PDR chemistry such as the production of OH (O+H$_2$ →OH+H), with an energy barrier of $\sim$ 3000 K, are very dependent on the temperature. In addition, an increase in the gas kinetic temperature in the HI/H$_2$ transition layer of the PDRs could have a dramatic effect on the production of OH and the derived molecular compounds (e.g., CO, HCO$^+$,
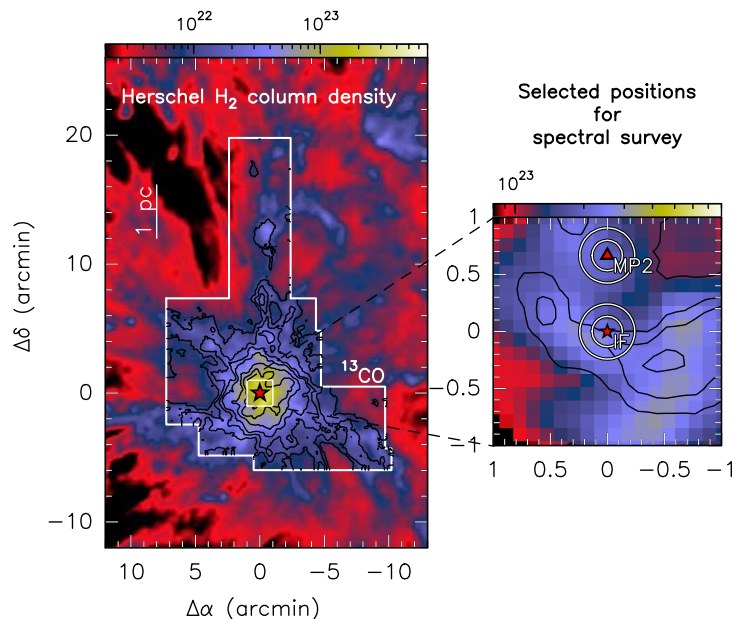
Figure 6.1: *Left:* Herschel H_2 column density (on color scale). The white polygon shows the large-scale area mapped with the IRAM-30m telescope. The black contours indicate the ^{13}CO integrated emission. *Right:* Zoom in the $2' \times 2'$ area mapped for the survey. The red star and triangle indicate the position of the selected positions for the spectral surveys. The circles indicate the beam size for the 3 and 2mm bands.

etc). Important reactions for the CN and HCN formation also proceed very rapidly at these temperatures and densities. Then, high abundances of PDR tracers as well as sulfurated molecules and complex molecules are expected in this region.

In addition to the main PDR, a second PDR is detected $40''$ north from IRS 1, which corresponds to a second molecular peak (MP2 position; see Figure 6.1). The chemical properties of this PDR are similar to those of low- to mild-UV irradiated PDRs ($G_0 \sim 100$–1000; in units of Habing field) such as the Horsehead (Ginard et al. 2012 and Pilleri et al. 2013a). Therefore, due to its characteristics (brightness, proximity, physical conditions), Mon R2 turns to be an ideal target to study the physical and chemical conditions in an extreme PDR (and a low- to mild-UV irradiated PDR) that can be used as a template for other (more distant) PDRs. Moreover, the comparison of the IF and MP2 positions allows us to study the difference of the chemical properties between a high and low-mild UV irradiated PDRs, without the drawbacks that involve to compare with other sources (e. g., different distances, different initial conditions of the gas and different observational strategies).

In this chapter we present our line survey covering a broad frequency range in the bands 3, 2, 1 and 0.8 mm, towards the Ionization Front (IF) and the MP2 positions (see Section 6.2). We also present on-the-fly (OTF) maps observation covering the central ($2' \times 2'$ around ISR 1) area of the region (see Figure 6.1) at 3 and 1 mm. Section 6.2, describes in detail the observational strategy and the data reduction. Section 6.3, contains the observational results, and shows the observed spectra in both positions, describes the line identification and presents the integrated (and channel) maps for some representative molecules. Section 6.4 contains a statistical analysis on the basis of Gaussian fits, calculation of column densities and abundances for selected molecules. A discussion on the different species is presented in Section 6.5. The discussion is based in the comparison of the properties in both, the IF and MP2 position, as well as with other PDRs and objects associated with star formation activity. Finally, Section 6.6 contains a summary with the main conclusions.

6.2   Observation and data reduction

The IRAM-30m telescope is one of the most sensitive millimeter telescopes, equipped with a series of heterodyne receivers at 3, 2, 1, and 0.8 mm. The telescope is located at Pico Veleta (Spain) in Sierra Nevada, at an altitude of 2850 m. We observe more than 150 h in different observational blocks from 2012 to 2014. All observations were performed in dual polarization using the EMIR receivers (Carter et al. 2012) with the fast Fourier Transform Spectrometer (FTS) at 200 kHz resolution (Klein et al. 2012b).

We performed single pointing (SP) observations in two important positions: the IF (Ionization Front corresponding to IRS 1; at α(J2000)= 06h07m46.2s, δ(J2000)= $-06°23'08.3''$) and MP2 position (at offset [$0''$,$40''$]). We also carried out OTF maps covering $120'' \times 120''$ area centered in the IF position at 3, 2 and 1 mm. During the observations we pointed on the strong nearby quasar (0605-058) every 2 hours, and we checked the focus on a planet every 4 hours. Pointing and focus corrections were stable throughout the whole run. Line calibrators (Orion and W3OH) were observed for every tuning to confirm that the intensities of the lines and their frequencies were correct. In every setup we performed a new tuning with a frequency shift of 50 MHz (in most of the cases) to identify the lines from the image band. The emission from the sky was subtracted using an OFF position free of molecular emission ($+400''$, $-400''$). The offsets are given relative to the coordinates of the IF position. For the OTF maps, the OFF position was observed every 2 minutes for 20 seconds. For the single pointing observations the OFF position was

Table 6.1: Telescope efficiencies. *The values of the efficiencies and beam are taken from http://www.iram.es/IRAMES/mainWiki/Iram30mEfficiencies.

Freq. (GHz)	$B_{\mathrm{eff}}{}^*$	$F_{\mathrm{eff}}{}^*$	HPBW* ($''$)
86.00	81	95	29.0
115.00	78	94	21.7
145.00	74	93	16.0
210.00	63	94	11.0
230.00	59	92	10.7
280.00	49	87	9.0
340.00	35	81	7.2
345.00	34	80	7.1

observed in position switching (Pws) mode every 30 seconds. We use the main beam brightness temperature (T_{MB}) as intensity scale, while the output of the telescope is usually calibrated in antenna temperature (T_{A}^*). The conversion between T_{A}^* and T_{MB} is done by applying the factor $F_{\mathrm{eff}}/B_{\mathrm{eff}}$, where F_{eff} and B_{eff} are the forward and beam efficiencies, respectively. The values of the F_{eff} and B_{eff} are listed in the Table 6.1. For intermediate frequencies we did a linear interpolation. Table 6.2 lists the frequency ranges observed in each project, which are summarized as follows

Project 159-11: Molecular study of the PDR around the ultracompact HII region Mon R2 (16 hours). In this project we observed the $120'' \times 120''$ OTF maps at 1 mm, covering a frequency range between 202 and 265 GHz. The project was observed in December 2011.

Project 005-12: Deuteration in the PDR around the ultracompact HII region Mon R2 (47 hours). In this project we did single pointing observations in the IF and MP2 positions covering several frequency ranges for the 3 mm, 2 mm and 1 mm bands (see Table 6.2). The project was observed from September to November 2012.

Project 130-12: Completing the molecular survey towards the ultracompact HII region Mon R2 (12 hours). In this project we did single pointing observations in the IF and MP2 positions covering the frequency ranges of 278–284.5 GHz and 293–350 GHz for the 1 mm band and 0.8 mm band, respectively. The project was observed in December 2012.

Project 011-14: Looking for CH_2D^+ in the PDR around the UC HII region Mon R2 (28.5 hours). In this project we did deep single pointing observations in the IF and MP2 positions covering the frequency ranges of 97.8–105.8 GHz for the 3 mm band and 200–208 GHz for the 1 mm band. The project was observed in August 2014.

Table 6.2: Observed frequencies ranges in every project.

Project	Obs. type	Frequency range	Position	Observed
159-11	OTF	202.0 – 265.0 GHz		Dec. 2011
005-12	SP	84.0 – 115.9 GHz	IF & MP2	Sep. to Nov. 2012
		132.8 – 136.9 GHz	IF & MP2	
		141.8 – 145.9 GHz	IF & MP2	
		150.6 – 154.7 GHz	IF & MP2	
		210.3 – 218.0 GHz	IF & MP2	
		225.9 – 233.7 GHz	IF & MP2	
		250.5 – 258.3 GHz	IF & MP2	
		266.2 – 274.0 GHz	IF & MP2	
130-12	SP	278.0 – 284.5 GHz	IF & MP2	Dec. 2012
		293.0 – 350.0 GHz	IF & MP2	
011-14	SP	97.8 – 105.8 GHz	IF & MP2	Aug. 2014
		200.0 – 208.0 GHz	IF & MP2	
010-14	OTF	84.1 – 91.9 GHz		Aug. to Nov. 2014
		96.2 – 104.1 GHz		
		109.3 – 116.3 GHz		
		155.5 – 162.5 GHz	IF & MP2	
		202.0 – 209.1 GHz		
		231.0 – 238.4 GHz		

Project 010-14: Reactive ions in the photon-dominated region Mon R2 (43 hours). In this project we performed $120'' \times 120''$ OTF maps covering different frequency ranges in the 3 mm, 2 mm and 1 mm bands. The project was observed from August to November 2014.

The data were reduced using the CLASS/GILDAS package[i] (Pety et al. 2005). Initial inspection of the data revealed the presence of a few single-channel spikes, platforming[ii], and complex baselines in some frequencies (mostly in the H polarization). The spikes were fixed by flagging individual channels and filling them with white noise corresponding to the rms measured by a baseline fit. To correct the platforming, a one-order baseline was subtracted from each FTS sub-band of each spectrum using a dedicated procedure provided by IRAM. In addition, a second-order baseline was needed for almost all the detected lines in the case of the OTF maps. In case of the single pointing observations, we fit second-order polynomial baselines for ranges of 50 to 200 MHz (depending in the tuning) to obtain a complete baseline corrected spectrum for the whole surveyed frequency range.

---

[i]See http://www.iram.fr/IRAMFR/GILDAS for more information about the GILDAS software.

[ii]Step effects of in the individual FTS units.

6.3 Results

In this section we present the observed spectra towards the IF and MP2 positions, and their corresponding Gaussian fits (Section 6.3.1). We also describe the method used for the line identification (Section 6.3.2) and families classification (Section 6.3.3). Finally, Sections 6.3.4 and 6.3.5 show the OTF maps.

6.3.1 Observed spectra

The observed frequency ranges are listed in Table 6.2. Figures 6.2 to 6.5 show part of the spectral survey towards the MP2 positions at 3 mm, 2 mm, 1 mm and 0.8 mm, respectively. In the figures, the red lines and labels indicate identified lines (see Section 6.3.2). Figures B.1 to B.14 present the whole spectra, in ranges of ~ 1 GHz, towards IF and MP2. While Figures B.15–B.38 show the spectra of representative species for each family (see Section 6.3.3) towards IF and MP2. Most of the species are detected in both positions, but there are some exceptions. For example, as expected, hydrogen radio recombination lines (HRRL) are clearly detected in the IF position, but not (or weakly) detected towards the MP2 position. The opposite situation occurs for the CCS molecule, that is only detected in the MP2 position. Also it is important to note that most of the detected lines show stronger intensities in the MP2, with some exceptions such as CO^+ or DCN. For some species such as CH_3OH, the lines at low frequencies are stronger in the MP2 position, but they become weaker (compared to the IF) when moving to higher frequencies.

The spectra show a different velocity profile towards the two positions. Most of the detected lines, present two velocity components. At the IF position we detect a velocity component at $\sim 10 \pm 0.5$ km s^{-1} and a second one at $\sim 12 \pm 0.5$ km s^{-1}; while at the MP2 position, the two velocity components correspond to $\sim 8.5 \pm 0.5$ km s^{-1} and $\sim 10 \pm 0.5$ km s^{-1}. The component at $\sim$10 km s^{-1} is detected at both positions and seems associated with the layer most exposed to the UV radiation from IRS 1. The component at $\sim$12 km s^{-1} is found towards the IF position but it is related to the SW part of the molecular cloud. Finally, the component at $\sim$8.5 km s^{-1} detected towards the MP2 position and is likely related to a low-UV irradiated PDR. There are also some lines (e. g., HCS^+, HOC^+ and CCS) that present a single component (at the corresponding PDR velocity, i. e., $\sim 8.5 \pm 0.5$ km s^{-1} for the MP2 and $\sim 10 \pm 0.5$ km s^{-1} for the IF position) and some optically thick lines that present more than two velocity components (e. g., H_2CO) or wings (e. g., HCN, HNC and CO).
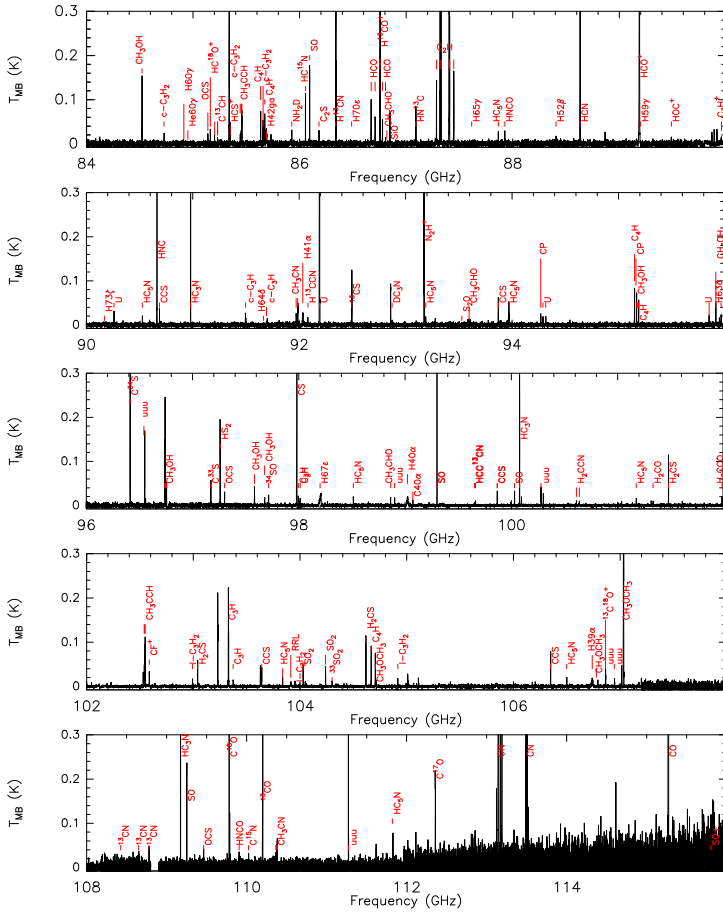
Figure 6.2: Spectral survey in the MP2 positions, the red labels mark the identified lines. *Continued in next page.*

In order to study the line differences in a quantitative way, we applied a Gaussian fit in each velocity component using the CLASS software of the GILDAS package. All the lines were convolved to the same spectral resolution of 0.70 km s^{-1}. Gaussian fits for both positions are shown in the Appendix B. The IF Gaussian fits are listed in Tables B.1, B.3, B.5 and B.7, while the MP2 Gaussian fits are listed in Tables B.2, B.4, B.6 and B.8. These Tables contain the following parameters: species, transition, frequency, beam width (HPBW), area (in K km s^{-1}), line velocity (in km s^{-1}), line width (in km s^{-1}), main beam temperature (in K) and rms (in mK). In the Tables, an empty space indicates that this line was not observed, while the "–" symbol indicates that it was not detected.

Figure 6.3: Spectral survey in the MP2 positions, the red labels mark the identified lines. *Continued in next page.*
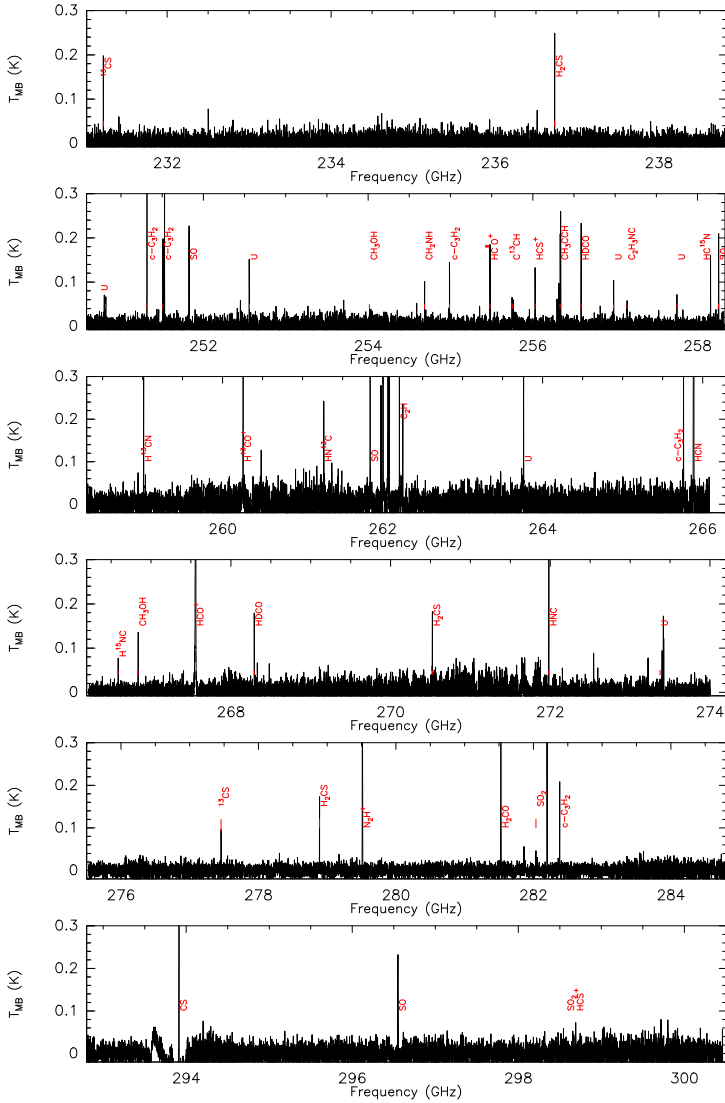
Figure 6.4: Spectral survey in the MP2 positions, the red labels mark the identified lines. *Continued in next page.*
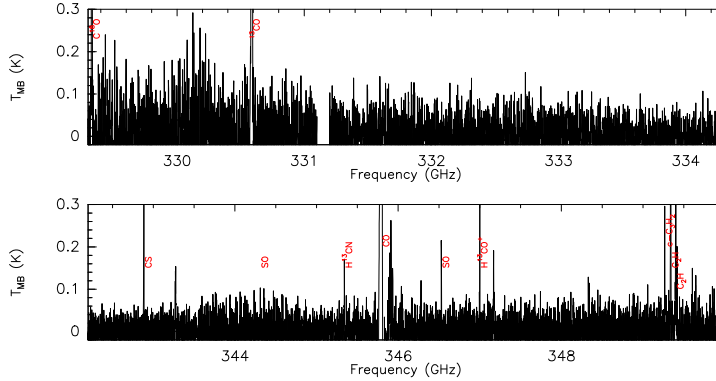
Figure 6.5: Spectral survey in the MP2 positions, the red labels mark the identified lines.

6.3.2 | Line identification

We have identified the lines detected towards Mon R2 at IF position and MP2 positions in a frequency range between 84 and 350 GHz. To perform the line identification we used the spectroscopic data contained in the Cologne Database for Molecular Spectroscopy (CDMS[iii], Müller et al. 2005) and the Jet Propulsion Laboratory (JPL[iv], Pickett et al. 1998) molecular databases. The identification is based on an initial search range of transitions with an upper level energy of 200 K, as the molecular gas does not reach temperatures above 200 K.

We consider a tentative detection when we have a signal-to-noise ratio (S/N) of 3–4σ and a well identified line when S/N> 4σ. In the case of tentative lines (3–4σ detections), we did an additional check to avoid possible artifacts such as baseline errors. For both, tentative and well detected lines, we performed a comparison between polarizations. To ensure a specie detection, we confirmed the detection of their most intense lines of the species. In addition, we confirmed that the detected lines did not come from the image band. To identify the image lines we did a shift (of 50 MHz in most of the cases) in all setups during the observation. Then, we did a comparison of both spectra to search for lines that present this shift (i. e., lines from the image band). We found more that 40 lines corresponding to the image band, these lines are not included in the tables presented in the Appendix.

For the identification we considered velocities in a range between ± 5 km s^{-1} around the expected source velocity of 10 km s^{-1}, and extended the range for

---

[iii]http://www.astro.uni-koeln.de/cdms/catalog
[iv]http://spec.jpl.nasa.gov

the most asymmetric and wide lines to ± 10 km s^{-1}. Towards the IF position we detected more that 440 lines in the 84–350 GHz frequency range, which belong to more than 55 different species. We also detected 16 unidentified lines (labeled as U in tables and figures). While in the MP2 position we detected 474 lines, in the same frequency range, related to 65 different species. In this case, we detected 25 U lines. For the $2' \times 2'$ OTF maps, with a lower sensitivity than the single-pointing spectral observations, we detected more than 260 lines related to 44 different species.

6.3.3 | Observed families

More than 65 different species (including isotopologues) were detected (see Tables 6.3 and 6.4). The list includes typical PDR tracers (such as CN, HCN, HCO, C$_2$H and c-C$_3$H$_2$), complex molecules common of warm molecular clouds (such as H$_2$CO, CH$_3$CN, HC$_3$N, CH$_3$OH or CH$_3$CH$_2$), deuterated species (CCD, DCN, DNC, DCO$^+$, D$_2$CO, HDCO, NH$_2$D and N$_2$D$^+$; see Chapter 7), ionic species (CF$^+$, CO$^+$, SO$^+$, l-C$_3$H$^+$, HCO$^+$ and HOC$^+$) and radio recombination lines (RRLs). The detected species can be related to several processes including shocks, UV-radiation, grain surface chemistry, gas-phase chemistry and hot core chemistry that includes complex organic molecules that are shielded from the dissociative UV-radiation. In summary, our results show that Mon R2 presents a rich chemistry that might be different from the one found in prototypical PDRs. We classify the detected species as

- *Deuterated molecules:* In the survey we detected several transitions of different deuterated molecules. In Chapter 7, we present a detailed analysis of these molecules (C$_2$D, DCN, DNC, DCO$^+$, D$_2$CO, HDCO, NH$_2$D, and N$_2$D$^+$) and their corresponding hydrogenated species (C$_2$H, H^{13}CN, HC^{15}N, HN^{13}C, H^{15}NC, H^{13}CO$^+$, HC^{18}O$^+$ H$_2$CO, H$_2^{13}$CO, N$_2$H$^+$). We compare our observational results with the deuteration levels measured towards other star forming regions, and use chemical models to explain the observed abundances.

- *Ionic species (Ions):* We have clear detections of several ionic species, including reactive ions that are thought to be one of the best tracers of PDRs and can be used to characterize their chemical and physical properties. For some of the detected ions, we calculate the column density and compare it with the abundances found in other PDRs (see Sections 6.5.2.2).

Table 6.3: Species detected towards the two positions in Mon R2, divided by the number of atoms.

2 atoms	3 atoms	4 atoms	5 atoms	6 atoms	7 atoms	9 atoms
CO	HCO	H_2CO	HC_3N	CH_3OH	C_2H_3CN	$C_2H_5CN^*$
^{13}CO	HCO^+	$H_2{}^{13}CO^*$	DC_3N^*	CH_3CN	HC_5N	$CH_3OCH_3^*$
$C^{18}O$	$H^{13}CO^+$	HDCO	C_4H		CH_3CCH	
$C^{17}O$	$HC^{18}O^+$	H_2CS	$l\text{-}C_3H_2$		$A\text{-}CH_3CHO$	
CO^+	DCO^+	H_2CN	$c\text{-}C_3H_2$		$E\text{-}CH_3CHO$	
SO	HOC^+	HNCO	t-HCOOH			
^{33}SO	HCN	t-HOCO	H_2CCO			
^{34}SO	$H^{13}CN$	$l\text{-}C_3H$	CH_2CO			
SO^+	$HC^{15}N$	$c\text{-}C_3H$	$HC^{13}CCN^*$			
CS	DCN	C_3H^+				
^{13}CS	HNC	C_3N^*				
$C^{33}S$	$HN^{13}C$	C_3S				
$C^{34}S$	$H^{15}NC$	NH_2D				
CN	DNC	SO_2				
^{13}CN	N_2H^+					
$C^{15}N^*$	$^{15}NNH^{+*}$					
NS	C_2H					
SiO	$^{13}C_2H$					
CF^+	$C^{13}CH^*$					
	C_2D					
	CCS					
	OCS					
	HCS^+					

* Tentative line.

Table 6.4: Species detected towards Mon R2, divided by families

Deuterated	Ions	Nitrogen	Sulfur	Complex	C-H	C-O	RRLs				Si
DCN	HCO^+	CN	SO	CH_3OH	C_2H	CO	$H42\alpha$	$H51\gamma$	$He42\alpha$	$C42\alpha$	SiO
DNC	$H^{13}CO^+$	C_3N^*	SO^+	CH_3CN	C_3H	^{13}CO	$H41\alpha$	$H50\gamma$	$He41\alpha$	$C41\alpha$	
DCO^+	$HC^{18}O^+$	^{13}CN	^{33}SO	CH_3CCH	C_4H	$C^{18}O$	$H40\alpha$	$H49\gamma$	$He40\alpha$	$C40\alpha$	
CCD	HOC^+	$C^{15}N^*$	^{34}SO	CH_2CO	$c\text{-}C_3H$	$C^{17}O$	$H39\alpha$	$H41\gamma$	$He39\alpha$	$C39\alpha$	
HDCO	HCS^+	HCN	SO_2	H_2CCO	$l\text{-}C_3H$		$H36\alpha$	$H65\delta$	$He36\alpha$	$C36\alpha$	
DC_3N^*	CO^+	$H^{13}CN$	$^{33}SO_2^*$	t-HCOOH	$c\text{-}C_3H_2$	———	$H34\alpha$	$H64\delta$	$He52\beta$	$C52\beta$	
NH_2D	C_3H^+	$HC^{15}N$	OCS	$E\text{-}CH_3CHO$	$l\text{-}C_3H_2$	HCO	$H31\alpha$	$H63\delta$	$He50\beta$	$C50\beta$	
	SO^+	HNC	CS	$A\text{-}CH_3CHO$	$^{13}C_2H$	H_2CO	$H30\alpha$	$H62\delta$	$He49\beta$	$C49\beta$	
	CF^+	$HN^{13}C$	CCS	C_2H_5CN	$C^{13}CH$	$H_2^{13}CO$	$H29\alpha$	$H61\delta$	$He57\gamma$	$C58\gamma$	
	N_2H^+	$H^{15}NC$	C_3S	$CH_3OCH_3^*$	$C^{13}CCH$		$H28\alpha$	$H60\delta$	$He58\gamma$	$C60\gamma$	
	$^{15}NNH^{+*}$	H_2CN	^{13}CS	$C_2H_3CN^*$			$H52\beta$	$H56\delta$	$He60\gamma$		
		HC_3N	$C^{33}S$	$HC^{13}CCN^*$			$H51\beta$	$H55\delta$			
		HC_5N	$C^{34}S$				$H50\beta$	$H70\varepsilon$			
		HNCO	H_2CS				$H49\beta$	$H68\varepsilon$			
		N_2H^+	HCS^+				$H48\beta$	$H67\varepsilon$			
		NS	NS				$H45\beta$	$H66\varepsilon$			
							$H44\beta$	$H65\varepsilon$			
							$H43\beta$	$H60\varepsilon$			
							$H39\beta$	$H52\varepsilon$			
							$H38\beta$	$H74\zeta$			
							$H36\beta$	$H73\zeta$			
							$H35\beta$	$H71\zeta$			
							$H60\gamma$	$H55\zeta$			
							$H59\gamma$	$H70\psi$			
							$H58\gamma$	$H69\psi$			
							$H57\gamma$	$H68\psi$			
							$H56\gamma$	$H67\psi$			
							$H55\gamma$	$H60\psi$			

* Tentative line.

- *Sulfurated molecules (S):* We detected several transitions of sulfurated species. We find that species such as HCS^+ present abundances larger than those observed in the Horsehead nebula (Goicoechea et al. 2006). We also detected the sulfurated species CS, SO, SO^+, CCS, H_2CS and SO_2 (see Section 6.5.2.3).

- *Complex molecules:* Within the spectral survey we have well detected CH_3OH, CH_3CN, HC_3N, CH_3CCH, H_2CCO and CH_2CO in both, IF and MP2 positions. We also have tentatively detected less abundant species such as CH_3CHO, HCOOH and H_2CCN towards the MP2 position (see Section 6.5.2.4).

- *Hydrocarbons (C-H):* In the survey we detected several transitions of different hydrocarbons, in both, single pointing and OTF maps. Some results on hydrocarbons combined with Herschel observations and chemical models have been presented in Pilleri et al. (2013a). See Section 6.5.2.5.

- *Nitrogenated molecules (N):* We detected several transitions of more than 15 nitrogenated species, in both, single pointing and OTF maps. In particular we find a larger HCN/HNC ratio compared to other PDRs. This, feature is explained in more detail in Section 6.5.2.6 and Chapter 7.

- *Other species (Si, C-O, H-C-O and RRL):* We also detected species such as SiO (shock tracer), CO and its isotopologues (^{13}CO, $C^{18}O$, $C^{17}O$), HCO and H_2CO (plus isotopologues), and more than 60 RRL, including Hydrogen, Carbon and Helium lines (see Section 6.5.2.7).

6.3.4 Integrated intensity maps

The maps carried out with the IRAM-30m telescope allow us to characterize the spatial distribution of different chemical species in Mon R2. Figures B.39 to B.45 show the integrated line intensity maps of some representative molecules at 3 mm (Figures B.39 –B.42) and at 1 mm (Figures B.43–B.45). The maps have an angular resolution between $9''$ and $29''$. The integrated intensity maps were done considering the velocity ranges where we have identified emission for the different species. These velocity ranges have been chosen where line intensity falls below 5σ. For example, the emission for radio recombination lines is wide and spans a velocity range over 30 km s^{-1} around the velocity source (10 km s^{-1}). For the most abundant species (e. g., C_2H, HCN, CO) the emission spans a velocity range of around 15–20 km s^{-1}. For species less abundant, we integrate a velocity range between 5 and 8 km s^{-1}(depending of the molecule). In general, the spatial distribution of the mapped molecules

consists of an arc structure of $\sim 30''$ in radius, pointing to the SE and opened to the NW, following the cometary shape of the nebula. The molecular emission is found surrounding the UC HII region that has created a cavity free of molecular gas (Choi et al. 2000; Dierickx et al. 2015; Figures 6.6 to 6.9). However, some species show important differences in their distribution. The most important differences are

i) CO lines ($C^{17}O$, $C^{18}O$ and ^{13}CO) present an extended arc structure surrounding the UC HII region. The fainter isotopologue, $C^{17}O$, seems to be tracing dense gas around the HII region (see panel A of the Figure 6.6 and panel I of the Figure 6.8).

ii) Hydrogen RRLs have their intensity peak clearly associated with the IF position (tracing ionized gas), while the carbon RRLs have a very close to the MP2 position and a second one that is at the south of the IF position in the labeled central clump (CC position) at offset [-10″, -10″] (see panel B of the Figure 6.6). This indicates that the carbon RRLs are tracing the PDRs around the UC HII region, however, the lines are weak and the maps are quite noisy.

iii) Hydrocarbons (c-C_3H_2, C_2H and C_4H) show a very extended and intense emission around a cavity centered at the IF position. The C_2H molecule, present four intensity peaks (see panel C of the Figure 6.6 and K of the Figure 6.8), the first one is spatially correlated with the MP2, while the second one with IRS 3. The other two intensity peaks are spatially correlated with the CC (very close to IRS 4) and the EC (east clump at offset [-40″,5″]) positions. The c-C_3H_2 intensity peaks also seems to be correlated with the MP2, IRS 3 and IRS 4 positions, but the spatial resolution of the map prevent us to distinguish their exactly positions (see panel C of the Figure 6.6) These molecules are known to be good PDR tracers (Gerin et al. 2005; Fuente et al. 2003). In particular the $N(c$-$C_3H_2)/N(C_2H)$ ratio is an excellent tracer of PDRs, reaching high values in low-UV PDRs. Thus, the emission of these tracers allowed us to determine that there is a low-UV PDR located in MP2 (Pilleri et al. 2013a).

iv) The $HC^{15}N$, $H^{13}CN$, and $H^{13}CO^+$ molecules show a compact distribution and their intensity peaks are spatially correlated with the IRS 3, IRS 4 and the EC position. They also present a peak at the $(5'', -10'')$ offset, very close to the IF position (see panel J of the Figure 6.8).

v) The emission of DCN and DNC species is compact and intense. DCN molecules present four peaks, the strongest one at the IRS 3 position, the second one at $(5'', -10'')$ offset, very close to the IF position. The other two peaks are at the EC and at the SW of the IRS 4 position. DNC also

shows the extended arc structure of $\sim 30''$ in radius, but it is less intense than other molecules. The DCO$^+$ emission is weaker and more extended than the DCN and DNC molecules (see panel K of the Figure 6.8).

vi) N$_2$H$^+$, HC$_3$N and HC$_5$N molecules present an arc structure pointing to the S and opened to the N of the map (see panel G of the Figure 6.7), roughly following the cometary shape of the nebula. These molecules present intensity peaks at the IRS 3 and SC (south clump at the offset[-40$''$,5$''$]) position. Another important nitrogenated molecule is CN. This molecule also present an extended arc structure around the IF position, but it is more closer to the central part of the map. It has four emission peak, the first one at the (10$''$,40$''$) offsets close to the MP2 position, the second one at the (5$''$,$-10''$) offset very close to the IF position, and the other two at the CC and EC position.

vii) The CH$_3$OH molecule presents extended emission with three intensity peaks (see panel H of the Figure 6.7 and panel L of the Figure 6.8). The first one is at the north of the map in the NC (north clump at [30$''$,55$''$] offset) position, the second one is associated with IRS 3, and the third one is at the south of the IRS 4 source and extends between the offsets ($-40''$,$-15''$) and ($-20''$,$-60''$). The emission of this species seems to arise from zone with high density and temperature (similar to those found in hot cores). The emission of other complex molecules (e. g., CH$_3$CCH, H$_2$CCO and CH$_3$CN) is weaker and more extended than CH$_3$OH. Due to the low signal to noise ratio (S/N) of our maps, it is not possible to distinguish their intensity peaks. Other abundant molecule is H$_2$CO. This molecule extends up to $\sim 1''$ from the IF position and consists of four peaks, of which three coincide with the CH$_3$OH peaks and the last one are located at the EC position, the H$_2$CO intensity peaks are surrounded by a faint emission (see panel L of the Figure 6.8).

viii) Sulfur-bearing molecules (SO, SO$_2$ and S^{34}O) are dense gas tracers. The most intense emission peaks of the SO, seem to be correlated with the CH$_3$OH emission at EC and IRS 3 positions. The SO molecule also presents other two emission peaks at the IRS 4 and EC positions. Other molecules with sulfur (e. g., CS, C^{34}S and H$_2$CS) that seem to be surrounding the SO emission, might be tracing a gas layer with a lower density.

ix) The SiO molecule present its intensity peak at (30$''$,30$''$) offset, in an extended area between the IRS 3 and NC positions (see panel H of the Figure 6.7). It also presents an extended emission around the IRS 4 source. The SiO molecule might be tracing a dense gas shock, and seems to be correlated with the sulfurated molecules (SO, SO$_2$ CS, C^{34}S and

OCS). Being the OCS molecule the one that present more morphologic similarity with it (see panel E of the Figure 6.7).

x) Finally, we also detected ionic species (e. g., CO^+, SO^+, CF^+, HOC^+, and HCS^+). The CF^+, SO^+ and HOC^+ molecules show a more extended emission than CO^+, and are likely tracing a shell around the CO^+ emission. However, the low intensity of these lines prevents us from clearly identifying their intensity peaks. The CO^+ line emission, is more compact and appears surrounding the HII region, likely the HII/PDR interphase. The CO^+ emission seems to be spatially correlated with the CH^+ and OH^+ lines (Pilleri et al. 2013a), which are originated in the layer of partially atomic gas. Finally, HCS^+ emission is more intense than the CO^+, SO^+ and CF^+ emission, and seems to come from an outer layer of the region.

6.3.5　Channel maps

Figures B.46 to B.55 show the channel maps for H_2CS (at 202.924 GHz), SO (at 206.176 GHz), $C^{17}O$ (at 224.714 GHz), H_2CO (at 225.697 GHz), CN (at 226.659 GHz), $C^{34}S$ (at 241.016 GHz), CH_3OH (at 241.791 GHz), CS (at 244.935 GHz), $H^{13}CN$ (at 259.011 GHz) and C_2H (at 262.004 GHz) molecules. All the species present more than one velocity component. The emission at $\sim$8–9 km s^{-1} is located to the north, the gas emitting at $\sim$10–11 km s^{-1} is surrounding the HII region, and the gas to the south-west is at a velocity of $\sim$12–13 km s^{-1} (e. g., Figure B.54). Moreover, two velocity components coexist at many positions, for example at the IF and MP2 positions. It is important to note that most of the molecules, (e. g., C_2H, CS and SO) present the same spiraling arms approaching the UC HII region that the CO lines presented in Chapter 5. This can be understood as a young UC HII region that starts to expand and break out the dense filamentary hub where it has been formed, with material still collapsing inwards along the filaments.
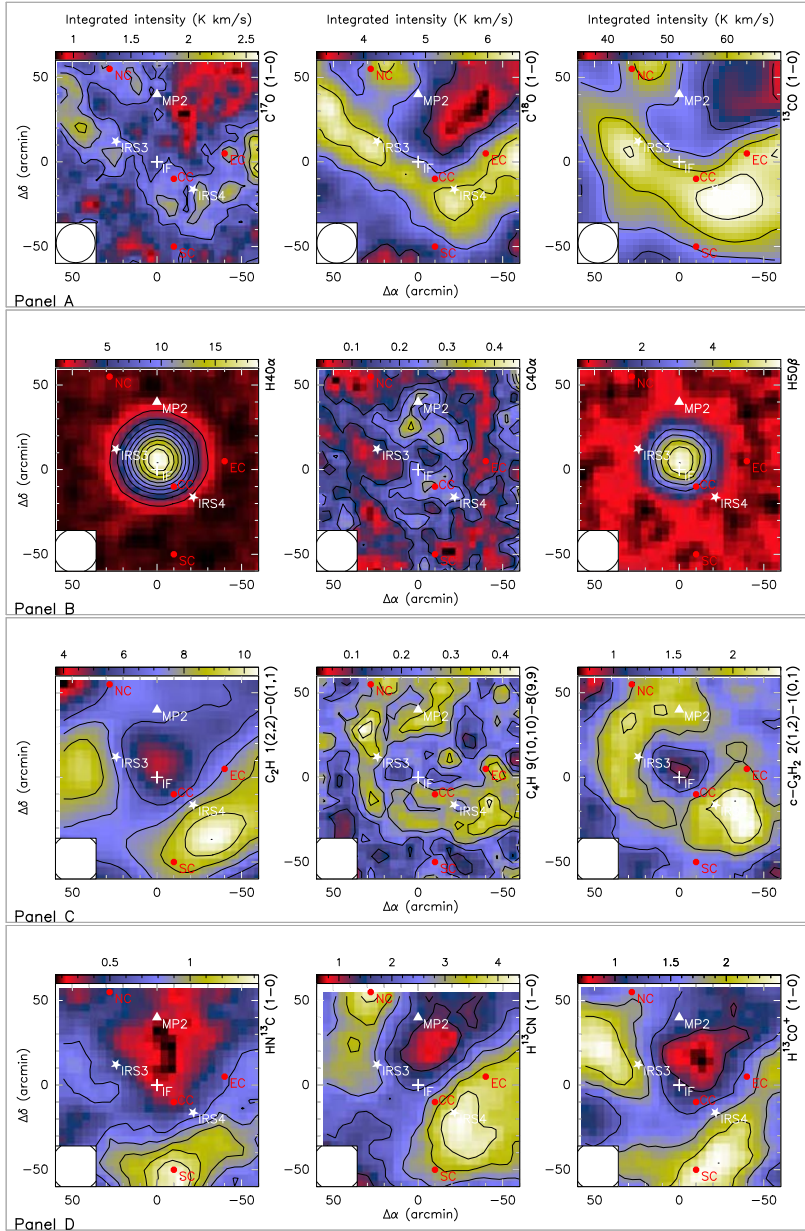
Figure 6.6: $2' \times 2'$ OTF maps of several lines at 3 mm (from Panel A to H) and 1 mm band (from Panel I to M). The cross marks the IF position, the triangle indicates the MP2 position, the white stars indicates the IRS 3 and IRS 4 positions, and the red circles shows the positions of four important clumps. The NC (north clump) is located at the $(30'', 55'')$ offset, the CC (central clump) is located at the $(-10'', -10'')$ offset, the EC (east clump) is located at the $(-40'', 5'')$ offset, finally, the SC (south clump) is located at the $(-10'', -50'')$ offset. The contour levels are 40% to 100%, in steps of 15% of the peak intensity. *Continued in next page.*
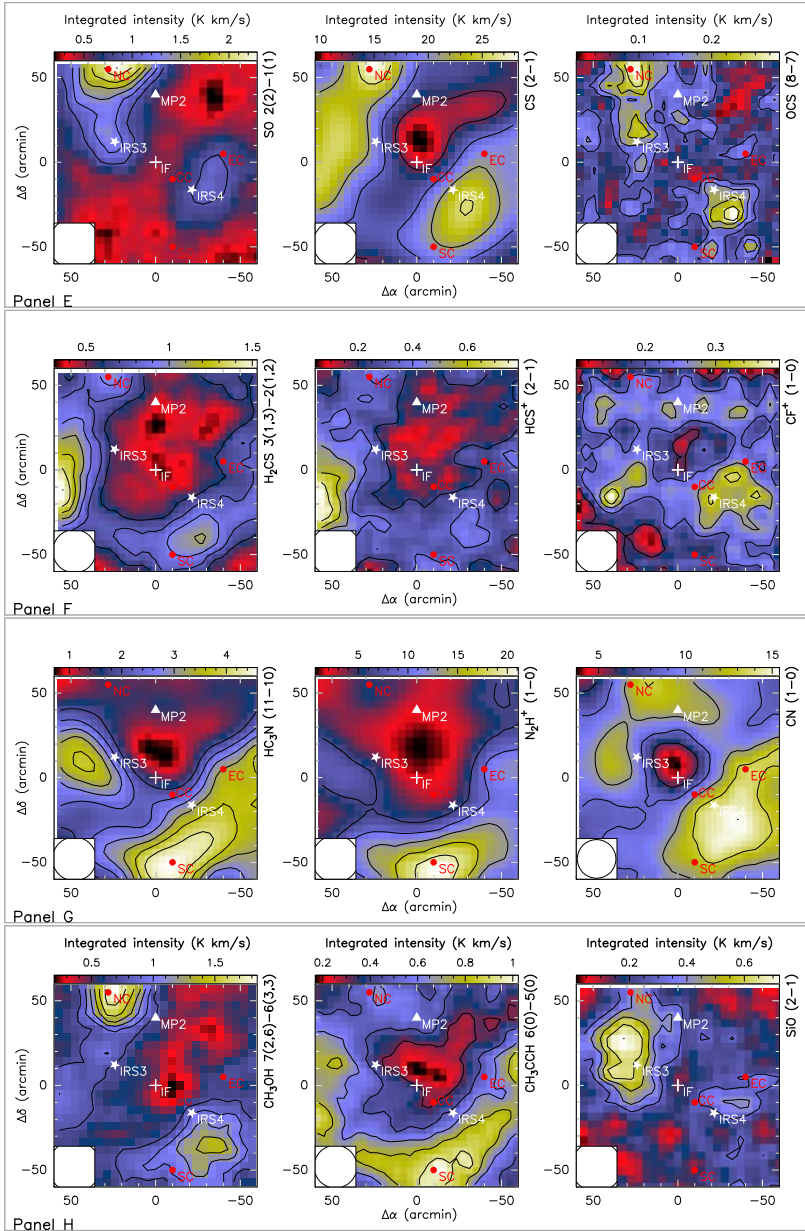
Figure 6.7: *Continued from previous page.*
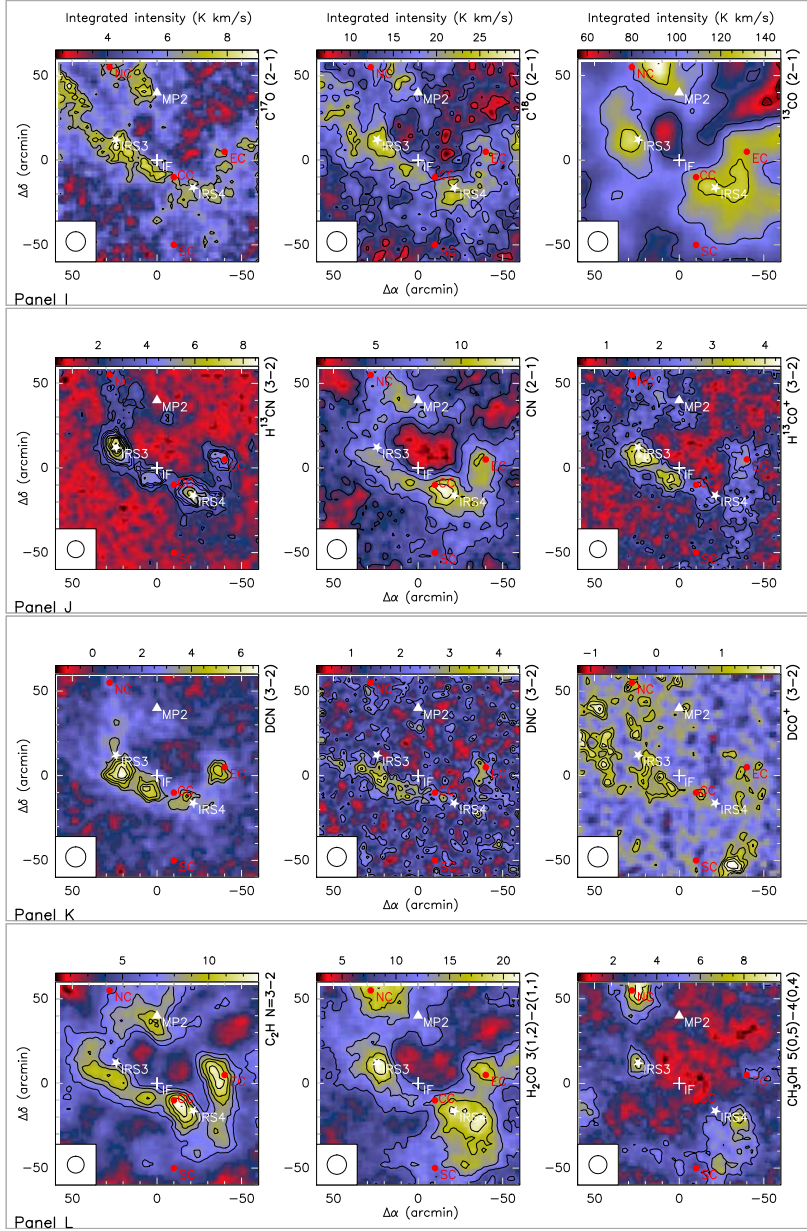
Figure 6.8: *Continued from previous page.*
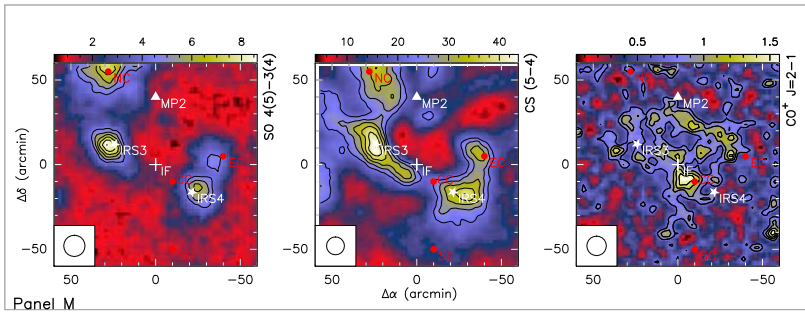
Figure 6.9: *Continued from previous page.*

6.4   Analysis

6.4.1   Statistic analysis

As described in Section 6.3.1, each identified line of the spectral survey has been fitted with a Gaussian profiles. The results can be found in the tables of Appendix B. In this section we compare quantitatively the properties (parameters from the fits) of all the lines. In the following we will describe the results of a comparison between the intensity of the line (main beam temperature, T_{mb}), the linewidth (D_v), the velocity (V) and the upper energy level of the transition (E_{up}).

In order to compare more than two parameters per plot, we have divided the lines in different groups depending on their velocity and intensity. On one side, we have divided the lines in four different regimes. This regimes are selected based on the velocities in which the detected lines present their intensity peaks: *(i)* lines with 7 km s^{-1}< V <9 km s^{-1}, *(ii)* lines with 9 km s^{-1}< V <11 km s^{-1}, *(iii)* lines with 11 km s^{-1}< V < 13 km s^{-1} and *(iv)* lines with V > 13 km s^{-1}. This permits to distinguish the two velocity components in the IF position (10 and 12 km s^{-1}), the two components in the MP2 position (8 and 10 km s^{-1}), and lines with larger velocities likely associated with red-shifted emission in outflows or spiraling arms. Regarding the intensity, we have considered three ranges depending on the signal-to-noise ratio: *(i)* lines moderately detected with 4 <S/N< 7, *(ii)* lines well detected with 7 <S/N< 15, and *(iii)* lines clearly detected with S/N> 15. This will allows us to avoid confusion of weak (low S/N) lines in possible trends between the parameters.
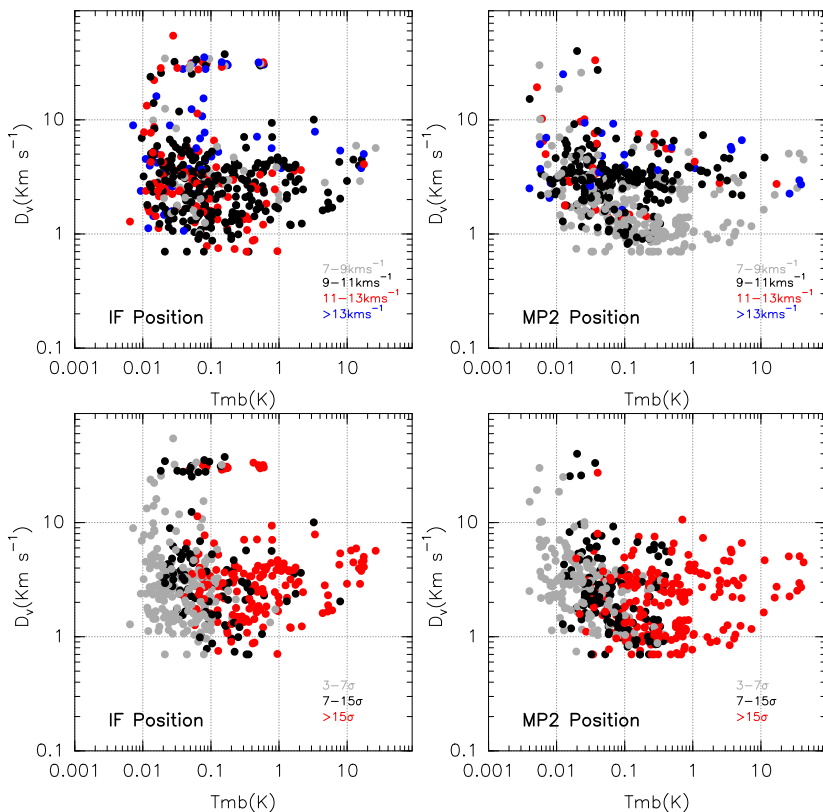
Figure 6.10: Comparison between the linewidth (D_v) and the main beam temperature (T_{mb}) of the detected lines (including RRLs) towards the IF (left) and MP2 (right) positions. *Top:* The colors of the symbols distinguish different velocity components: gray is [7–9] km s^{-1}, black is [9–11] km s^{-1}, red is [11–13] km s^{-1} and blue is >13 km s^{-1}. *Bottom:* The colors differentiate different ranges of S/N: gray corresponds to 3–7, black is 7–15, while red are well detected lines with S/N >15.

Figure 6.10 compares the linewidth (D_v) and main beam temperature (T_{mb}) in both positions. A quick look to the plots indicates that the distribution for both positions is similar, however, there are some differences. We can distinguish a clear cut (or lack of data) for $T_{mb} < 0.01$ K, and for $D_v <$ 0.7 km s^{-1}. These two limits are directly related to the sensitivity (about 10 mK) and to the spectral resolution (0.7 km s^{-1}). The distribution in the IF position is slightly more compact and skewed towards low values in terms of T_{mb} than for MP2. On the other hand, the distribution of linewidths seems to be very similar in both positions.

From this first inspection we can conclude that MP2 is associated with stronger and narrower lines than IF. Furthermore, the IF position does not show any significant trend regarding the separation in velocity components. However,
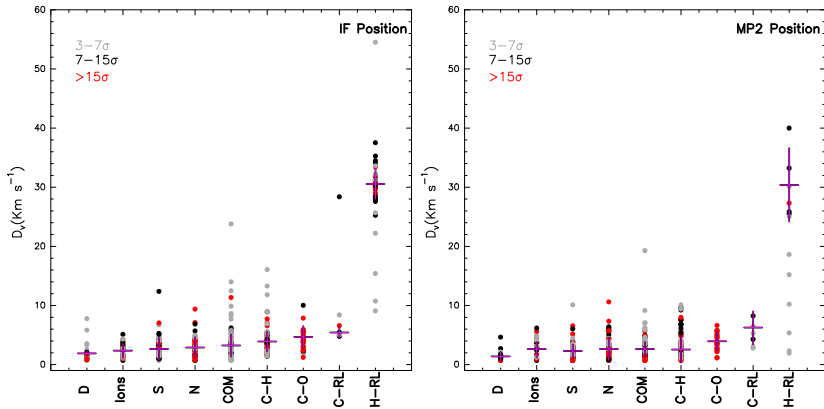
Figure 6.11: Linewidth (D_v) for each molecular family, for the IF (left) and MP2 (right) positions. The colors of the symbols differentiate the data according to their S/N (as in Figure 6.10 bottom panels). The different families are: deuterated molecules (D), ionic species (Ions), molecules containing sulfur (S), molecules containing nitrogen (N), complex molecules (COM), hydrocarbons (C-H), lines containing carbon and oxygen (C-O), carbon recombination lines (C-RL) and hydrogen recombination lines (H-RL).

for MP2, we can clearly distinguish that the velocity component [7–9] km s^{-1} is preferentially associated with low D_v values (covering the whole temperature range), while the other components are mainly associated with lower T_{mb} values and broader lines. The bottom panels in Figure 6.10 distinguish the data according to the different S/N ranges defined above. In both positions, the lines with low S/N data correspond to low temperatures, while high S/N values are associated with high temperatures.

The segregation of the S/N ranges in the figure is expected since the S/N ratio is directly related to T_{mb} and the sensitivity across the whole spectral survey is constraint to a reduced range (3–30 mK). Finally, it is worth mentioning that the IF position shows a horizontal branch at $D_v \sim 30$ km s^{-1} that is less evident in the MP2 position. This components is due to the presence of hydrogen RRLs tracing the ionized gas in the UC HII region. Therefore, one wonders if there could be a correlation between the linewidth and the molecular family that is not appreciable in Figure 6.10.

In Figure 6.11 we compare the linewidth for all the different family groups identified in Section 6.3.3. The labels indicate the family name as deuterated molecules (D), ionic species (Ions), molecules containing sulfur (S), molecules containing nitrogen (N), complex molecules (COM), hydrocarbons (C-H), lines containing carbon and oxygen (C-O), carbon recombination lines (C-RL) and hydrogen recombination lines (H-RL). The mean and median for the linewidth distribution have been calculated for each family and position and are listed

Table 6.5: Means (dispersion) and medians of the linewidth distribution (in km s^{-1}) for each molecular family and position.

	IF			
	S/N> 3		S/N> 7	
Family	mean	median	mean	median
D	2.04 (1.74)	1.34	1.90 (0.41)	1.23
Ions	2.40 (1.26)	2.07	2.37 (1.17)	2.24
S	2.47 (1.57)	2.09	2.64 (1.86)	2.19
N	2.77 (1.52)	2.61	2.90 (1.72)	2.78
COM	3.50 (3.16)	2.76	3.23 (1.87)	3.10
C-H	4.14 (2.63)	3.61	3.91 (1.64)	3.58
C-O	4.67 (1.79)	4.48	4.69 (1.83)	4.55
C-RL	9.48 (9.90)	7.23	5.43 (0.83)	5.17
H-RL	30.55 (5.13)	30.46	30.54 (2.50)	30.39
	MP2			
	S/N> 3		S/N> 7	
Family	mean	median	mean	median
D	1.40 (0.73)	1.28	1.39 (0.75)	1.26
Ions	2.86 (1.46)	2.84	2.62 (1.44)	2.75
S	2.43 (1.32)	2.37	2.30 (1.14)	2.24
N	2.70 (1.66)	2.44	2.65 (1.87)	2.22
COM	3.10 (2.17)	3.03	2.62 (1.25)	2.81
C-H	2.74 (2.28)	1.62	2.54 (2.17)	1.49
C-O	3.95 (1.53)	4.04	3.95 (1.53)	4.04
C-RL	4.41 (1.99)	4.27	6.27 (2.80)	6.27
H-RL	26.76 (7.35)	26.58	30.38 (6.21)	30.27

in Table 6.5 (see also big crosses in Figure 6.11). In general the linewidth seems to depend on the family. In the IF position, the narrowest lines correspond to deuterated species (mean of 2 km s^{-1}) followed by ions and sulfurated molecules. Nitrogenated, complex molecules, hydrocarbons and CO lines have linewidths of about 3–4 km s^{-1}, while carbon and hydrogen RRLs have linewidths of 10 and 30 km s^{-1}, respectively. A similar trend is found towards MP2. The fact that the deuterated molecules present the smallest width is a confirmation that the emission of these molecules are coming from the dense compact clumps and not from the PDR.

Transitions of a given family can be tracing gas at different locations within the IF and MP2 positions. For example, a transition with a higher excitation energy is likely to be excited in a different region than a transition of the same species but with a lower excitation energy. In Figure 6.12 we investigate this by comparing the linewidth (D_v) and the upper energy level of the transition (E_{up}). The top panels of the figure differentiate the data according to the
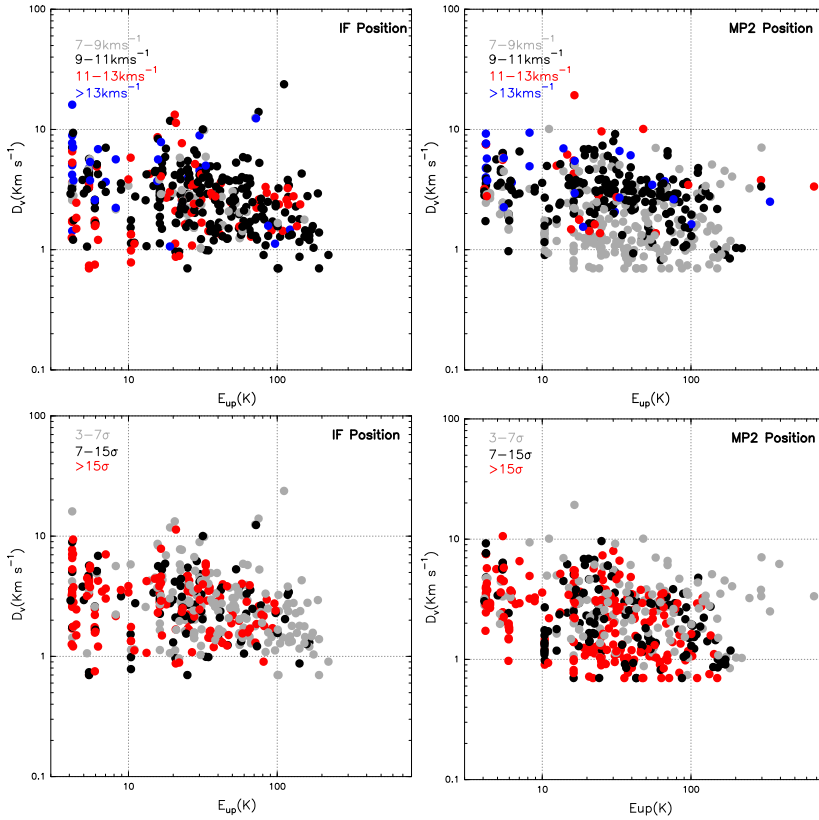
Figure 6.12: Comparison between the linewidth (D_v) and the upper energy level (E_u) of the detected lines (except RRLs) for the IF (left) and MP2 (right) positions. *Top:* The colors of the symbols distinguish different velocity components: gray is [7–9] km s^{-1}, black is [9–11] km s^{-1}, red is [11–13] km s^{-1} and blue is >13 km s^{-1}. *Bottom:* The colors differentiate different ranges of S/N: gray corresponds to 3–7, black is 7–15, while red are well detected lines with S/N >15.

velocity ranges defined above, while the bottom panels use the different S/N to color the data.

The transitions detected in our unbiased spectral survey span a range of excitation energies from a few K to a few hundred K. In general, it seems that lines with higher E_{up} are associated with narrower lines. A possible explanation to the observed trend is that turbulence or global motions are controlling the linewidths in Mon R2. In order to better inspect this scenario we will compare D_v against E_{up} considering different velocity components and molecular families.

Figures 6.13 to 6.16 compare D_v against E_{up} for each family (different rows) and for the four velocity ranges (different columns). For completeness, Fig-

ures B.56 to B.59 show similar plots comparing D_v and T_{mb}. For the IF position, in particular the $[9\text{–}11]$ km s^{-1} velocity component (i. e., the most populated), we identify different behaviors for different families: *(i)* N, C-H and C-O molecules do not present trends, as these molecules seem to present similar linewidths for all the E_{up} ranges. *(ii)* Deuterated species seem to have a slightly trend (higher D_v for higher E_{up}). Nevertheless, the sample of deuterated transitions is small and the S/N of most of the lines is lower than 7, thus it is difficult to set trends for this family. However, it is interesting to note that the emission of some deuterated lines comes from dense clumps as revealed in the OTF maps (see Figure 6.8). This is the case of the DCN and DNC molecules that present a compact and intense emission, with their intensity peaks close to the IRS 1 and IRS 3 sources. Finally, *(iii)* Ions, S and COM lines show lower D_v for higher E_{up}. This would suggest that turbulence plays an important role in shaping the lines of these molecules: low energy transitions would be tracing outer layers from a colder and more turbulent envelope. OTF maps (with high S/N) seem to confirm that the emission of lines with lower energy comes from external layers of the region, while the emission of lines with higher energy seems to be associated with dense clumps. For example CS, CH$_3$CCH and H^{13}CO$^+$ present this behavior (see Figure 6.6 to 6.9). It is important to note that some of the lines included in the sample do not follow this behavior. For example, in the case of the ionic species we are including the CO$^+$ line that originates in the layer of partially atomic gas. For the MP2 position, most of the species show the trend of lower D_v for higher E_{up}. This effect is better seen in the $[7\text{–}9]$ km s^{-1} velocity component, the most populated. As in the IF case, we can understand this trend if the low energy transitions are originated in the outer, colder and more turbulent layers, while the high energy transitions are originated in the dense quiescent clumps. However, it is worth to mention that we are plotting molecules that are tracers of high and low density regions, and this also may contribute to the observed trend in different families.
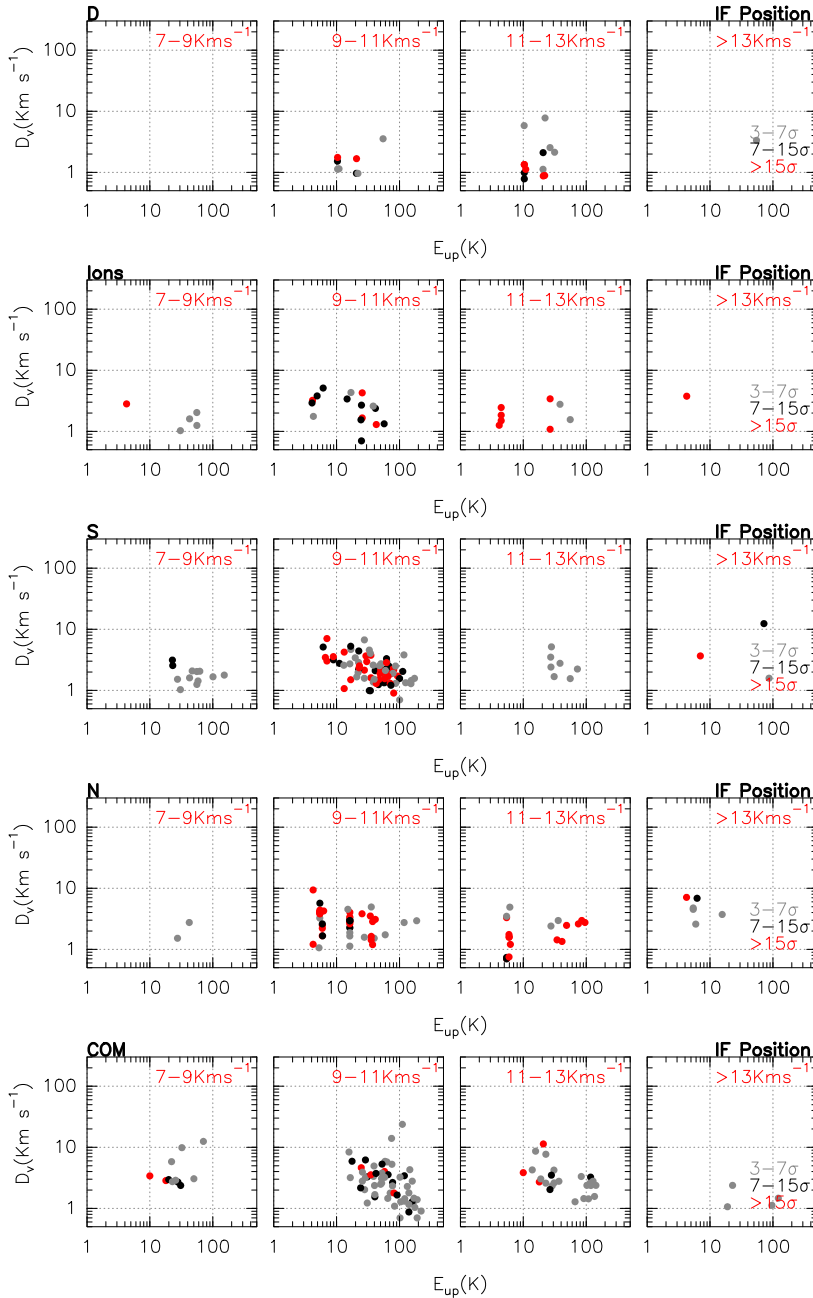
Figure 6.13: Comparison of the linewidth (D_v) against the energy of the upper level (E_{up}) for the IF position. Each row corresponds to a different molecular family, while each vertical column corresponds to a different velocity range (indicated in each panel). Colors differentiate different S/N as in Figure 6.10 (bottom panels). *Figure continues in the next page.*
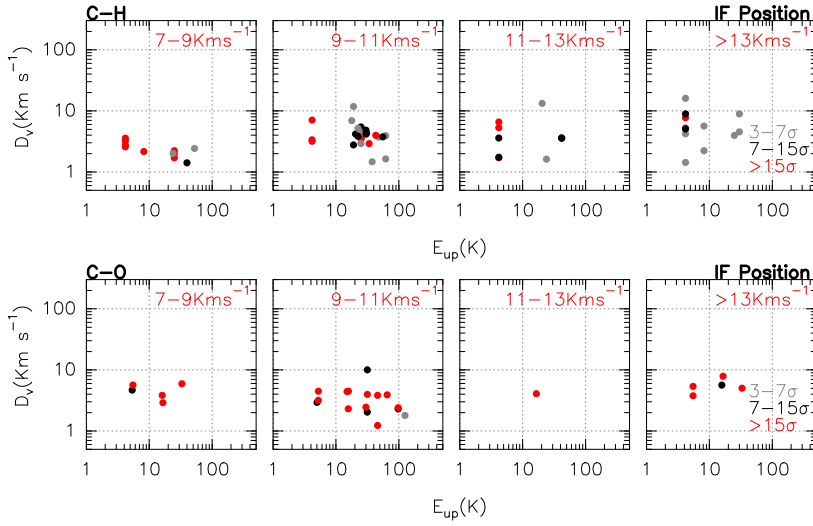
Figure 6.14: *Continued from previous page.*
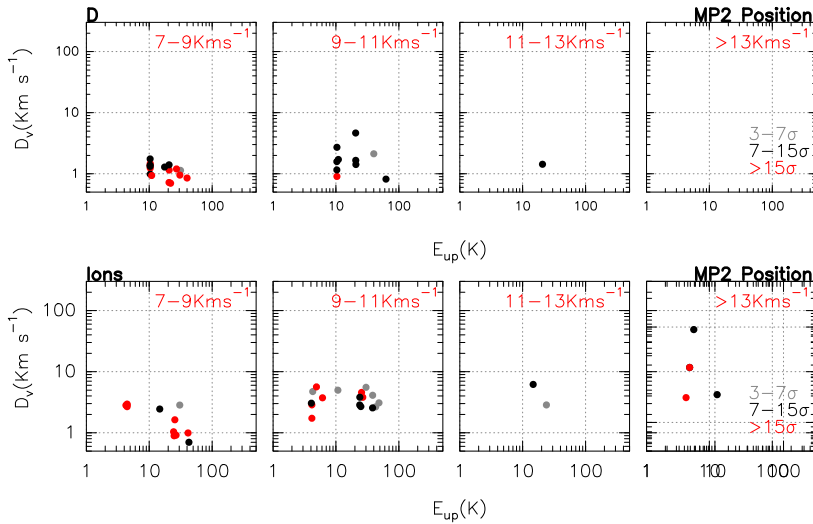
Figure 6.15: Comparison of the linewidth (D_v) against the energy of the upper level (E_{up}) for the MP2 position. Each row corresponds to a different molecular family, while each vertical column corresponds to a different velocity range (indicated in each panel). Colors differentiate different S/N as in Figure 6.10 (bottom panels). *Figure continues in the next page.*
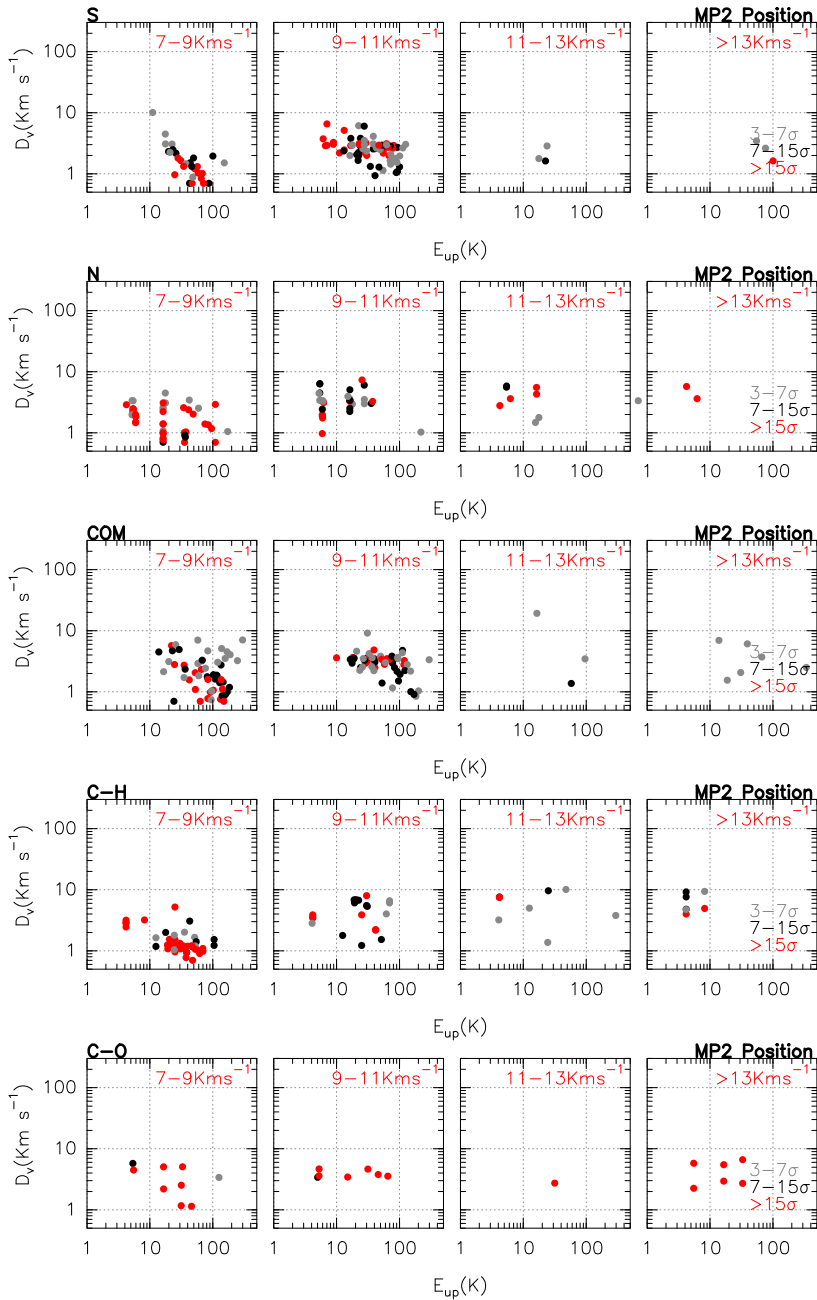
Figure 6.16: *Continued from previous page.*

6.4.2 Molecular column densities

Molecular line emission provides important information about physical conditions in dense interstellar clouds. Important physical properties (e. g., density, velocity structure, and the magnetic field distribution) can be obtained by observing multiple transitions, making maps, or employing specialized types of observations. The column density and the rotational temperatures of a specie can be derived from the observational parameters of multiples transitions. An optically thin transition produces an antenna temperature (T_A) that is proportional to the column density (N_{up}) in the upper level of the observed transition. In the case of multiple transitions, if they are thermalized and the kinetic temperature is known, it is possible to convert the single measured column density (N_{up}) into the column density of the species in question (N). One potentially important and frequently adopted technique to analyze cloud properties from molecular line emission is the *rotation diagram technique* (Goldsmith & Langer 1999). It consists in plotting of the column density per statistical weight of a number of molecular energy levels ($\ln N_{up}/g_{up}$), as a function of their energy above the ground state (E_{up}). In local thermodynamic equilibrium (LTE), this is a Boltzmann distribution, so a plot will yield a slope of $1/T$. The temperature inferred is the so-called rotational temperature (T_{rot}), and is expected to be equal to the kinetic temperatures if all levels are thermalized. Under certain conditions, the column density can be also obtained from observation of a single transition if the kinetic temperature is known.

In this Section, we use rotational diagram method to analyze the molecular emission in order to derive physical properties of the Mon R2 region. We derived column densities (N) and rotational temperatures (T_{rot}), for the main component in both, IF (at ~ 10 km s^{-1}) and MP2 (at ~ 8.5 km s^{-1}) positions. To do this, we use the multi frequency observed spectra. As was mentioned before, we fitted a Gaussian profile to each velocity component. All the lines were convolved to the same spectral resolution (0.70 km s^{-1}). Gaussian fits for both positions are presented in the Appendix B. The column densities were calculated assuming that the emission comes from a layer with uniform physical conditions. This rotational diagram method is valid for optically thin emission and assumes the same excitation temperature for all transitions. Within the approximation,

$$N_{up} = \frac{1.94 \times 10^3 \, \nu^2 \, W}{A_{ul}},$$

(6.1)

$$N_{Tot} = \frac{N_{up} \, Q \exp\frac{E_{up}}{T_{rot}}}{g_{up}},$$

(6.2)

where N_{up} is the column density, in cm^{-2}, of the upper level 'up' of the

corresponding transition, ν is the frequency of the transition in GHz, W is the area derived from the Gaussian fitting in K kms^{-1} (Table B.1–B.8), A_{ul} is the Einstein coefficient for spontaneous emission, N is the total column density of the molecule in cm^{-2}, E_{up} is the energy of the upper level in K, T_{rot} is the rotation temperature in K, and Q is the partition function, which depends on T_{rot}. The values of ν, A_{ul}, E_{up}, g_{up} and Q were taken from the Cologne Database for Molecular Spectroscopy (CDMS webpage[v]; Müller et al. 2001, 2005).

Rotational diagrams for most of the observed lines were performed using a FORTRAN program developed by Sanchez-Monge (2011). This program estimate column densities and make rotational diagrams. The program can be used to calculate column densities of almost all kind of molecules, for this it is necessary to generate a file including the information of the specific molecule (e. g., rotational molecular constants, a list of Q for different temperatures, E_{up}, g_{up}, if the molecule is linear, symmetric-top or asymmetric-top, etc)[vi] and a list of the the molecular transitions that you want to study. In the case of the rotational diagrams, it is necessary to create another input file, containing the observational information, i. e., the frequency of the transition, the main beam temperature, the linewidth, the integrated area, the optical depth (thin or thick), the source size, and the beam size. For Mon R2 we assume a optically thin emission and extended source size (about 30″), for lines observed in a beam size range between 7″ and 28″. Thus, we consider a beam filling factor of 1. This approximation is good only for the optically thin molecules, in the case of the optically thick molecules (e. g., HCN, HCO$^+$, CO, etc) we use the their corresponding isotopologues that are optically thin. For the ^{13}C and ^{18}O isotopologues we assumed $[^{12}$C$]/[^{13}$C$]=50$ (Savage et al. 2002; Ginard et al. 2012) and $[^{16}$O$]/[^{18}$O$]=500$[vii] (Wilson & Rood 1994; Ginard et al. 2012).

Rotational diagrams for most of the species are in Figures B.60 to B.65, and the Table 6.6 shows their results. The Table lists the calculated T_{rot} (in K), N (in $\times 10^{12}$ cm^2), number of the detected lines and their corresponding E$_{up}$ range. Rotation temperatures vary between ~ 7 K and ~ 55 K. As expected the T_{rot} derived for most of the molecules is higher in the IF position than in the MP2 position. The big range presented by the T_{rot} in the region could be explained due to the different dipole moments of the molecules (μ 1–5 Debye) and to the different spatial resolution of the lower energy transitions. Moreover, it also indicates that different molecules are tracing different layers in the region. The high rotation temperatures found in molecules such as H$_2$CO, DNC, DCN and CH$_3$OH towards IF position suggest that the emission of these molecules are

[v]http://www.astro.uni-koeln.de/cdms

[vi]These values are found in the CDMS and JPL webpage

[vii]The values of the $[^{12}$C$]/[^{13}$C$]$ and $[^{16}$O$]/[^{18}$O$]$ ratios correspond to the galactocentric distance of Mon R2, i. e., ~ 9 Kpc.

associated with dense clumps around the HII region at temperatures ~ 50 K instead of the cooler envelope. While most of the molecular emission in the MP2 position seems to come from the cooler envelope or for clumps illuminated from the outside.

However, there are some molecules that present higher temperatures in the MP2 than in the IF position (DCO$^+$ OCS, CCS and C$_4$H), and some molecules that present similar temperatures in both positions (^{13}CO, C^{18}O, ^{34}SO, SO$_2$, ^{13}CS, HC$_5$N, CH$_3$CCH, HNCO, SiO and CF$^+$). In the case of DCO$^+$, this molecule present an extended spatial distribution, where intense emission comes from the envelope. In this case, column density of all the molecules are averaged over a $\sim 16''$ beam (see Chapter 7), and this might be affecting the result. In the case of the OCS, CCS and C$_4$H molecules, we are considering more lines in a higher energy range for the MP2 position than for the IF position, thus it is possible that we are under-estimating the temperature in the IF position for those lines. It is important to mention that we observe the same number of CCS and OCS lines, but their emission in IF is much weaker than in MP2 (see Figure B.31 and B.33). This might indicate that the OCS and CCS emission in the MP2 position come from a near clump (in the north of the region) that seems to present a hot core chemistry (see Figures B.40 and B.44).

In the case of molecules with similar temperatures in both positions (^{34}SO, SO$_2$, ^{13}CS, HC$_5$N, CH$_3$CCH, SiO and CF$^+$), the emission of these molecules is surrounding the IF and MP2 position, but do not come from them (see Figures B.40 and B.42). In the case of the sulfurated molecules seems to come from the IRS 3 clump and the north clump (with hot core chemistry). In the case of the HC$_5$N and CH$_3$CCH molecules, the observed maps show that their emission come from an external layer (see Figures B.40), our beam can be contaminated from the external emission of this layer. Finally, the CF$^+$ molecule might come from a shell around the IF and MP2 position (inner to the HC$_5$N–CH$_3$CCH molecules layer), but the low quality of our maps prevent us to set firm conclusions about. Moreover, we only have information of two transitions for this species and we could be under-estimating the temperatures.

For some molecules (HDCO, D$_2$CO, NH$_2$D, N$_2$D$^+$, N$_2$H$^+$ and H$_2^{13}$CO), only one transition is detected. Thus, we calculated the column density assuming a fixed value of the rotation temperature. The selection of these temperatures is explained in the Chapter 7.

Table 6.6: Rotational temperatures and column densities of the main velocity components of the IF and MP2 positions. [a]Velocity component at 12 km s^{-1}. [b]Fixed temperature to calculate the column density. [*]Sum of the N_{tot} in both velocity components

Species	IF				MP2			
	T_{rot} [K]	N [$\times 10^{12}$ cm^{-2}]	lines	E_{up} range [K]	T_{rot} [K]	N [$\times 10^{12}$ cm^{-2}]	lines	E_{up} range [K]
^{13}CO	15±5	31204±2230	3	10–40	13±1	34971±130	2	10–40
C^{18}O	20±1	9271±100	3	10–40	17±1	8488±200	2	10–40
HCO	19^b	65.6±5.00	1	10–30	10^b	100±10.00	1	10–30
HCO$^+$	18±1	17.72±0.10	2	10–30	10±1	22.66±0.50	2	10–30
H^{13}CO$^+$	16±1	0.96±0.030	2	10–30	12±1	$1.49^{+0.382}_{-0.410}$	2	10–30
HC^{18}O$^+$	16±2	0.129±0.016	2	10–20	13±1	0.12±0.012	2	10–20
HDCO	38^b	0.430±0.126	1	10–50	49^{+16}_{-8}	$2.30^{+1.46}_{-0.99}$	4	10–50
D$_2$CO	38^b	< 23.70	1	10–20	38^b	2.50±3.76	1	10–20
DNC	45±5	$0.09^{+0.07}_{-0.06}$	2	10–20	12±2	$0.46^{+0.02}_{-0.09}$	2	10–20
C$_2$D	19^b	3.09±1.09	1	10–20	20^{+12}_{-8}	$9.60^{+3.9}_{-2.0}$	5	10–20
DCO$^+$	19±10	$0.111^{+0.09}_{-0.01}$	2	10–20	31±11	$0.27^{+0.04}_{-0.09}$	2	10–20
NH$_2$D	19^b	0.389±0.128	1	10–20	19^b	0.87±0.129	1	10–20
N$_2$D$^+$	19^{a,b}	0.065±0.012	1	10–20	19^b	< 0.16	1	10–20
DCN	44±10	2.09±0.7	2	10–20	12^{+10}_{-5}	$1.40^{+0.2}_{-0.4}$	2	10–20
HN^{13}C	19^b	0.176±0.017	2	10–20	12±1	$0.43^{+0.016}_{-0.020}$	2	10–20
H^{15}NC	19^b	0.057±0.041	2	10–20	13±2	$0.15^{+0.010}_{-0.040}$	2	10–20
H^{13}CN	14^{+5}_{-4}	$2.0^{+0.380}_{-0.380}$	2	10–20	7^{+3}_{-2}	$1.00^{+0.200}_{-0.350}$	2	10–20

Table 6.6 – *Continued from previous page*

Specie	IF				MP2			
	$T_{\rm rot}$ [K]	N [$\times 10^{12}$ cm^{-2}]	lines	$E_{\rm up}$ range [K]	$T_{\rm rot}$ [K]	N [$\times 10^{12}$ cm^{-2}]	lines	$E_{\rm up}$ range [K]
HC^{15}N	22±3	$0.38^{+0.060}_{-0.030}$	2	10–20	9±1	$0.45^{+0.050}_{-0.030}$	2	10–20
N$_2$H$^+$	19^{a,b}	4.28±0.046	1	10–20	19^b	3.29±0.054	1	10–20
SO	29±3	21.29±4.16	11	10–100	18±2	32.38±7.60	14	10–100
^{34}SO	23±1	1.39±0.10	3	10–50	20±5	2.03±0.65	5	10–50
SO$_2$	39±3	11.84±1.36	13	10–130	38±7	13.22±3.38	10	10–120
SO$^+$	18±9	4.66±4.00	3	10–40	13±2	5.59±2.10	6	10–40
HCS$^+$	18±3	2.03±0.70	4	10–60	13±2	1.93±0.40	3	10–50
H$_2$CS	40±13	8.64±3.0	11	10–150	19±4	9.07±3.00	10	10–100
CS	42±9	29.60±20.0	4	10–80	15±1	74.27±1.00	2	10–80
^{13}CS	14±1	2.10±0.30	3	10–50	11±2	2.87±0.90	3	10–50
C^{34}S	5±1	5.7±0.30	2	10–20	8±1	7.98±0.10	2	10–20
OCS	21±12	4.87±3.00	3	10–40	31±8	10.90±3.22	4	10–60
CCS	12±8	1.63±1.0	4	10–40	29±3	2.71±0.45	13	10–100
HC$_5$N	27±9	1.66±1.50	5	70–100	27±3	7.78±0.78	7	70–100
HC$_3$N	33±5	5.06±1.30	9	10–180	27±1	8.35±0.1	7	10–140
CH$_3$CN	31±6	1.38±0.50	9	10–150	25±5	1.71±0.80	7	10–100
CH$_3$OH	43±6.5	78.73±12	29	10–170	30±7	94±20	22	10–100
CH$_3$CCH	32±3	62.59±5.99	13	10–120	32±3	80±8	11	10–120
H$_2$CCO	34±11	5.65±1	3	10–50	17±2	6.24±1.20	5	10–80

Table 6.6 – *Continued from previous page*

Specie	IF				MP2			
	$T_{\rm rot}$ [K]	N [$\times 10^{12}$ cm^{-2}]	lines	$E_{\rm up}$ range [K]	$T_{\rm rot}$ [K]	N [$\times 10^{12}$ cm^{-2}]	lines	$E_{\rm up}$ range [K]
HNCO	21±3	1.98±0.22	3	10–30	23±5	2.18±0.41	3	10–30
H_2CO	55±19	$67.1^{+183}_{-13.72}$	6	10–40	$42^{+15.5}_{-8.5}$	$78.14^* \pm 9$	6	10–40
$H_2^{13}CO$	$38^{a,b}$	< 3.10	1	10–90	38^b	2.74±02.983	1	10–90
l-C_3H	23±10	2.42±1.7	3	10–60	13±5	5.01±1	5	10–60
c-C_3H_2	16±1	6±0.5	8	10–60	12±1	8.4±1	8	10–60
C_2H	30^{+34}_{-10}	158.00^{+50}_{-44}	4	10–20	12^{+3}_{-2}	120.00^{+38}_{-27}	4	10–20
C_4H	22±4	59.20±17	10	10–80	37±3	46.4±4.20	14	10–120
SiO	19±1	0.28±0.003	2	10–40	18±1	0.72±0.002	2	10–40
CF^+	8±0.5	2.13±0.02	2	10–20	9±0.5	1.22±0.01	2	10–20
CN	7±1	538±100	23	10–20	11±3	126±45	22	10–20

Most of the observed molecules present higher N in the MP2 than in the IF position, but some exceptions that seems to present higher N in the IF position (see Table 6.6). It is worth to perform a comparison between both positions. However, to do this in a proper way it is necessary to calculate molecular abundances. Section 6.5 present a comparison between IF and MP2 (Section 6.5.1), based on their molecular abundances and then with different kind of regions (Section 6.5.2).

6.5   Discussion

6.5.1   Comparison of the IF and MP2 positions

As was mentioned, the aim of this Chapter is to study the influence of the UV photons on the chemistry of massive star forming regions. For this aim, we are going to compare the chemical properties of the IF and MP2 position. The major advantage of perform a comparison between both positions (before than with other sources) is that they are PDRs, at the same star forming region, and are illuminated with UV fields of different intensities. This allows to perform a comparison of the chemical properties between a high and low-mild UV irradiated PDRs, using the same observational strategies. Moreover, as they are in the same star forming region (at ~ 830 pc), they can be studied neglecting the effect of the different distances and different initial conditions.

In order to obtain a normalization of the values in the Table 6.6, and thus perform a better comparison, we calculate the abundance of each species. Table 6.7 lists the column densities and abundances (X_1 and X_2) of the IF and MP2 positions for each specie, and the $X_1[\text{IF}]/X_1[\text{MP2}]$ ratio. Molecular abundances (X_1) were calculated assuming a canonical $C^{18}O$ abundance with respect to H abundance of 0.85×10^{-7}. The abundance of each species X_1 wrt H is then given by the expression $X_1 = N[X]/N[H] = (N[X]/N[C^{18}O])(0.85 \times 10^{-7})$. The $N[C^{18}O]$ value for each position is given in the one listed in the Table 6.6. These values are in good agreement with the ones found by Pilleri et al. (2013a). They found $N[C^{18}O] = 8.3 \times 10^{15}$ cm^{-2} for the IF position, while we found $N[C^{18}O] = 9.2 \times 10^{15}$ cm^{-2}. The slightly differences between these values, might be due to the different number of $C^{18}O$ transitions used to perform the rotational diagrams. Pilleri et al. (2013a), used the $C^{18}O$ (2-1) and $C^{18}O$ (5-4) lines, while we used $C^{18}O$ (1-0), $C^{18}O$ (2-1) and $C^{18}O$ (3-2). In our approximation, we assume the same $C^{18}O$ abundance with respect to H, in both

positions. However, this abundance is expected to be lower in the IF position, and thus the abundances of every specie in the IF position could be slightly higher than the calculated.

As comparison tool, we also calculate the molecular abundances called X_2. The X_2 molecular abundances of each species are calculated with respect to methanol column density. These abundances were calculated using the expression $X_2 = N[X]/N[CH_3OH]$. This method is used to calculate molecular abundances in hot cores and hot corinos, as methanol is very abundant in these sources. Also it is used to compare abundances of different type of regions with hot core-corinos. Table 6.7 list the molecular abundances X_1, X_2 and the $X_1[IF]/X_1[MP2]$ ratio. Figure 6.17 present the plot of the $X_1[IF]/X_1[MP2]$ ratio as comparison of the abundances. The most important findings in our comparison are

i) For most of the observed species, the abundances are higher in MP2 than in IF. However, in most of these cases they are different by a factor lower than 2.

ii) Molecules with H, C and O (e.g., HCO^+ and isotopologues) present higher abundances in MP2 than in IF. But $HC^{18}O^+$, that present similar abundances in both positions. This behavior could be due to opacity effect, being $HC^{18}O^+$ the most optically thin of these molecules and HCO^+ the most thick. Thus, within our uncertainties, we can conclude that HCO^+, and its isotopologues, present similar abundances in both positions.

iii) Most of the deuterated molecules present higher abundances in MP2 than IF, this is expected as the deuterated molecules are associated with cooler gas. The only exception could be the DCN molecule, that present higher abundances in IF position. This behavior is because of the higher HCN abundance towards this position (see Panel K of the Figure 6.8).

iv) Similar behavior is presented for the nitrogenated molecules, which most of them present higher abundances in MP2 than IF, but $H^{13}CN$. This molecule is a well known tracers of extreme PDRs, and its chemistry is linked with DCN chemistry (see Chapter 7). The CN molecule also is related with HCN, as CN is the product of the dissociation of HCN. This process is given by the reaction $HCN + \nu \rightarrow CN + H$ (Sternberg & Dalgarno 1995), throughout the HI zone and the H/H_2 transition layer. The HCN molecule are also removed by $HCN + H \rightarrow CN + H_2$ in the HI zone where the atomic hydrogen density in large. The CN/HCN ratio has been used as PDR tracer in our Galaxy (Fuente et al. 1993, 1996) and external galaxies (e.g., M82), as is predicted by Sternberg & Dalgarno (1995). Our result are in agreement

with this, we found that the CN molecule is more abundant in the IF than in the MP2 position.

v) Most of the sulfurated molecules present higher abundances in MP2 than IF. The exception are, SO_2, H_2CS, SO^+ and HCS^+ that are very similar in both positions. In the case of the ionic species, they are expected to be abundant in the HI/H_2 transition layer. However, as these are weak lines they present long errors and are difficult to interpret.

vi) Most of the complex molecules present higher abundances in MP2 than IF by a factor lower than 2. But HC_5N molecule that present much higher abundances in MP2 position. On basis of the T_{rot} value (see Table 6.6) and its spatial distribution (See Figure B.40) we can conclude that this molecule is associated with a cooler and external layer of the region.

vii) In the case of the hydrocarbons, l-C_3H and c-C_3H_2 molecules present higher abundances in the MP2 position, while C_2H and C_4H present similar abundances in the IF position. This is expected as the l-C_3H and c-C_3H_2 molecules are good low-mid PDRs tracers (Pilleri et al. 2012, 2013a).

viii) SiO molecule presents higher abundances in MP2 than IF, as was shown in the Panel H of the Figure 6.7, the emission of this molecule seems to be associated with the IRS 3 position, and present and extended emission close to MP2, but not to the IF position. This molecule seems to be tracing a shock, probably originated by the serie of jets in the region (Dierickx et al. 2015).

Summarizing, most of the observed species are higher in MP2 than in IF. However, in most of these cases they are different by a factor lower than 2. The DCN, $H^{13}CN$, CN, CF^+ and C_2H molecules, present higher abundances in IF than in MP2. These molecules seems to be good tracers of extreme PDRs, with high G_0, and their high abundances allow to distinguish extreme PDRs from low-mid UV irradiated PDRs and dark clouds.

In order to better confirm the IF and MP2 comparison, we calculate some column density ratios. Table 6.8 lists these results, $[HCS^+]/[CS]$, $[HCO^+]/[CS]$, $[CN]/[HCN]$ and $[SO^+]/[SO]$ ratios are higher in the IF position by a factor of 2-3. In the case of the $[CS + C_2S + H_2CS + HCS^+]/[SO + SO_2 + SO^+ + OCS]$ and $[C_2H + C_3H + C_3H_2 + C_4H + CH_3CCH]/[H_2CO + CH_3OH + HCO]$ ratios are quite similar in both positions, indicating similar properties of the sulfur and complex chemistry. The $[HCN + HNC + CN + CH_3CN]/[N_2H^+]$ ratio is used to know the relation between the atomic and molecular nitrogen $[N/N_2]$. In general, the N_2H^+ abundance is low in PDR as this molecules is easily

dissociated by the UV field and destroyed by CO molecule. This is a typical tracer of cold gas.

It is worth to perform a comparison of the PDRs associated to Mon R2 with other PDRs and other kind of regions. Section 6.5.2 present a comparison of the molecular abundances of IF and MP2 positions, with those found in other PDRs (Orion Bar, NGC 7023 and Horsehead), a hot core (Orion KL), dark clouds (TMC 1 and L134N) and a shock (L1157).

Table 6.7: Column densities (N) and abundances (X_1 and X_2) of the IF and MP2 positions. The molecular abundances X_1 were calculated assuming $X_1 =N[X]/N[H]=(N[X]/N[C^{18}O])(0.85\times10^{-7})$. The abundance X_2 of each species with respect to methanol is given by $X_2 =N[X]/N[CH_3OH]$.

Species	IF			MP2			$X_1[IF]/X_1[MP2]$
	N [$\times10^{12}$ cm^{-2}]	X_1 [$\times10^{-10}$]	X_2	N [$\times10^{12}$ cm^{-2}]	X_1 [$\times10^{-10}$]	X_2	
^{13}CO	31204.000±2230.000	2860.899±206.770	396.342±66.721	34971.000±130.000	3502.044±83.538	372.032±79.168	0.817±0.062
$C^{18}O$	9271.000±100.000	850.000±12.966	117.757±17.993	8488.000±200.000	850.000±28.324	90.298±19.330	1.000±0.037
HCO	65.600±5.000	6.014±0.463	0.833±0.142	100.000±10.000	10.000±1.029	1.064±0.250	0.601±0.077
HCO^+	17.720±0.100	1.625±0.020	0.225±0.034	22.660±0.500	2.269±0.074	0.241±0.052	0.716±0.025
$H^{13}CO^+$	0.960±0.030	0.088±0.003	0.012±0.002	$1.490^{+0.382}_{-0.410}$	0.149±0.039	0.016±0.005	0.590±0.153
$HC^{18}O^+$	0.129±0.016	0.012±0.002	0.002±0.001	0.120±0.012	0.012±0.001	0.001±0.000	0.984±0.159
HDCO	0.430±0.126	0.039±0.012	0.005±0.002	$2.300^{+1.46}_{-0.99}$	0.231±0.101	0.025±0.012	0.171±0.090
D_2CO	< 23.700	2.173±0.024	0.301±0.046	2.500±3.760	0.251±0.377	0.027±0.040	<8.679
DNC	$0.090^{+0.07}_{-0.06}$	0.009±0.007	0.001±0.001	$0.460^{+0.02}_{-0.09}$	0.046±0.005	0.005±0.001	0.179±0.141
C_2D	3.090±1.090	0.284±0.099	0.040±0.015	$9.600^{+3.9}_{-2.0}$	0.962±0.302	0.102±0.039	0.295±0.139
DCO^+	$0.111^{+0.09}_{-0.01}$	0.010±0.005	0.001±0.001	$0.270^{+0.04}_{-0.09}$	0.027±0.005	0.003±0.001	0.376±0.184
NH_2D	0.389±0.128	0.036±0.012	0.005±0.002	0.870±0.129	0.087±0.013	0.009±0.002	0.409±0.148
N_2D^+	0.065±0.012	0.006±0.001	0.002±0.001	< 0.16	0.016±0.001	0.002±0.001	>0.372
DCN	2.090±0.700	0.192±0.064	0.027±0.010	$1.400^{+0.2}_{-0.4}$	0.142±0.030	0.015±0.005	1.366±0.545
$HNs^{13}C$	0.176±0.017	0.016±0.002	0.002±0.001	$0.430^{+0.016}_{-0.020}$	0.043±0.002	0.005±0.001	0.375±0.041
$H^{15}NC$	0.057±0.041	0.005±0.004	0.002±0.001	$0.150^{+0.010}_{-0.040}$	0.015±0.003	0.002±0.001	0.346±0.260
$H^{13}CN$	$2.000^{+0.38}_{-0.38}$	0.183±0.035	0.025±0.006	$1.000^{+0.200}_{-0.350}$	0.100±0.025	0.011±0.004	1.831±0.577
$HC^{15}N$	$0.380^{+0.06}_{-0.03}$	0.035±0.004	0.005±0.001	$0.450^{+0.050}_{-0.030}$	0.045±0.004	0.005±0.001	0.773±0.116
N_2H^+	4.280±0.046	0.393±0.006	0.054±0.008	3.290±0.054	0.329±0.010	0.035±0.008	1.191±0.039
SO	21.290±4.160	1.952±0.382	0.270±0.067	32.380±7.600	3.243±0.765	0.345±0.109	0.602±0.185
^{34}SO	1.390±0.100	0.128±0.010	0.018±0.003	2.030±0.650	0.204±0.066	0.022±0.008	0.627±0.206
SO_2	11.840±1.360	1.086±0.125	0.150±0.029	13.220±3.380	1.323±0.340	0.141±0.047	0.820±0.231
SO^+	4.660±4.000	0.427±0.367	0.059±0.052	5.590±2.100	0.559±0.211	0.060±0.026	0.763±0.715
HCS^+	2.030±0.700	0.186±0.064	0.026±0.010	1.930±0.400	0.193±0.041	0.021±0.006	0.963±0.388
H_2CS	8.640±3.000	0.792±0.275	0.110±0.042	9.070±3.000	0.908±0.301	0.097±0.038	0.872±0.419
CS	29.600±20.000	2.714±1.000	0.376±0.260	74.270±1.000	7.438±0.202	0.790±0.168	0.365±0.247
^{13}CS	2.100±0.300	0.193±0.028	0.027±0.006	2.870±0.900	0.288±0.091	0.031±0.012	0.666±0.231

Continued on next page

Table 6.7 – *Continued from previous page*

Specie	IF			MP2			$X_1[\mathrm{IF}]/X_1[\mathrm{MP2}]$
	N [$\times 10^{12}$ cm^{-2}]	X_1 [$\times 10^{-10}$]	X_2	N [$\times 10^{12}$ cm^{-2}]	X_1 [$\times 10^{-10}$]	X_2	
C^{34}S	5.70±0.300	0.523±0.028	0.072±0.012	7.980±0.100	0.799±0.022	0.085±0.018	0.654±0.039
OCS	4.870±3.000	0.447±0.275	0.062±0.039	10.900±3.220	1.092±0.324	0.116±0.042	0.409±0.280
CCS	1.630±1.000	0.149±0.092	0.021±0.013	2.710±0.450	0.272±0.046	0.029±0.008	0.552±0.350
HC$_5$N	1.660±1.500	0.152±0.138	0.021±0.019	7.780±0.780	0.779±0.080	0.083±0.019	0.195±0.178
HC$_3$N	5.060±1.300	0.464±0.120	0.064±0.019	8.350±0.100	0.836±0.022	0.089±0.019	0.555±0.143
CH$_3$CN	1.380±0.500	0.127±0.046	0.018±0.007	1.710±0.800	0.173±0.080	0.018±0.009	0.739±0.438
CH$_3$OH	78.730±12.000	7.218±1.103	0.010±0.216	94.000±20.000	9.413±2.015	1.000±0.301	0.767±0.202
CH$_3$CCH	62.590±5.990	5.739±0.553	0.795±0.143	80.000±8.000	8.012±0.823	0.851±0.200	0.716±0.101
H$_2$CCO	5.650±1.000	0.518±0.092	0.072±0.017	6.240±1.200	0.625±0.121	0.066±0.019	0.829±0.218
HNCO	1.980±0.220	0.182±0.020	0.025±0.005	2.180±0.410	0.219±0.042	0.023±0.007	0.832±0.183
H$_2$CO	67.100$^{+183}_{-13.72}$	6.152±1.901	0.852±0.294	78.140±9.000	7.825±0.809	0.831±0.135	0.786±0.173
H$_2^{13}$CO	< 3.100	0.284±0.003	0.039±0.006	2.740±02.983	0.275±0.299	0.029±0.032	<1.036
l-C$_3$H	2.420±1.700	0.222±0.156	0.031±0.022	5.010±1.000	0.502±0.101	0.053±0.016	0.442±0.323
c-C$_3$H$_2$	6.000±0.500	0.550±0.046	0.076±0.013	8.400±1.000	0.841±0.102	0.089±0.022	0.654±0.097
C$_2$H	158.000$^{+50}_{-44}$	14.490±4.312	0.020±0.671	120.000$^{+38}_{-27}$	12.017±3.217	1.277±0.436	1.121±0.483
C$_4$H	59.200±17.000	5.428±1.560	0.752±0.245	46.400±4.200	4.647±0.435	0.494±0.114	1.168±0.353
SiO	0.280±0.003	0.026±0.001	0.004±0.001	0.720±0.002	0.072±0.002	0.008±0.002	0.356±0.010
CF$^+$	2.130±0.020	0.196±0.003	0.027±0.004	1.220±0.010	0.122±0.003	0.013±0.003	1.598±0.046
CN	538.000±100.00	49.326±9.184	0.068±0.016	126.000±45.000	12.618±4.516	1.340±0.557	3.909±1.577
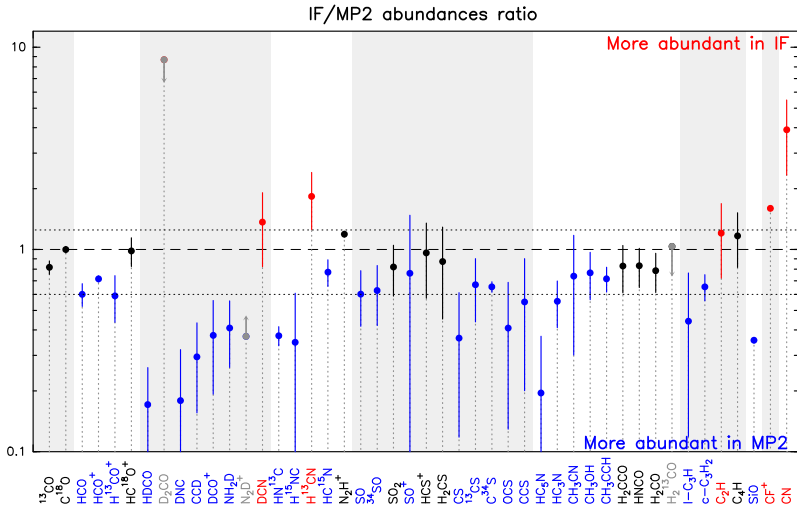
Figure 6.17: Comparison of the $X_1[\text{IF}]/X_1[\text{MP2}]$ ratio. The molecular abundances were calculated using the $C^{18}O$ as surrogate for H abundance, assuming $X_1 = N[x]/N[H] = (N[x]/N[C^{18}O])(0.85 \times 10^{-7})$. The blue dots indicate the species that are more abundant in the MP2 position. The red one the species that are more abundant in the IF position, the black one indicate the species that present similar abundances. Finally the gray dots indicate limits values.

Table 6.8: Column density ratios.

	IF	MP2
$[\text{HCS}^+]/[\text{CS}]$	0.068	0.025
$[\text{HCO}^+]/[\text{CS}]$	0.598	0.305
$[^{13}\text{CO}]/[\text{CS}]$	1054.189	470.863
$[\text{HCS}^+]/[\text{HCO}^+]$	0.115	0.085
$[\text{SO}^+]/[\text{SO}]$	0.219	0.172
$[\text{CN}]/[\text{HCN}]$	5.380	2.520
$[\text{CS} + \text{C}_2\text{S} + \text{H}_2\text{CS} + \text{HCS}^+]/[\text{SO} + \text{SO}_2 + \text{SO}^+ + \text{OCS}]$	0.982	1.417
$[\text{HCN} + \text{HNC} + \text{CN} + \text{CH}_3\text{CN}]/[\text{N}_2\text{H}^+]$	150.053	56.294
$[\text{C}_2\text{H} + \text{C}_3\text{H} + \text{C}_3\text{H}_2 + \text{C}_4\text{H} + \text{CH}_3\text{CCH}]/[\text{H}_2\text{CO} + \text{CH}_3\text{OH} + \text{HCO}]$	1.363	0.995

6.5.2 Comparison with other sources

In order to complete our study of the dependence of the chemistry with the UV incident flux in PDRs, we did a comparison of the molecular abundances presented in the last Section with those found in different kind of regions. First, we compared the abundances found in the PDRs associated with the Mon R2 region (at IF and MP2 positions) with molecular abundances in other PDRs (Orion Bar, NGC 7023 and Horsehead). After that, we compared the PDRs abundances with those found in a hot core (Orion KL), two dark clouds

(TMC 1 and L134N) and a shock (L1157). Tables 6.9, 6.10 and 6.11 present the column densities and abundances in the Orion Bar, NGC 7023 and the Horsehead PDRs, respectively. While the Table 6.12 presents the molecular abundances in Orion KL, TMC 1, L134N and L1157. It is important to note that there are different facts that affect the interpretation of the chemical conditions, such as: *i)* distance effects, *ii)* observational strategies, *iii)* geometry, and *iv)* evolution. In our case, we select sources at distances < 1 kpc. In fact, Mon R2 is the most distant source. Most of the results of the selected sources used in the comparison, were observed with the IRAM-30m telescope, but Orion KL that combine IRAM-30m and SMA data (Feng et al. 2015). Thus, the distance and the observational strategies effects are negligible in our comparison. The geometry effects also are minimized in the PDRs comparison, as all of them seems to present an edge-on geometry. Finally, the temporal evolution might be important for the chemistry in very young sources such as Mon R2 (Pilleri et al. 2013a). However, to determine the importance of the temporal evolution it is necessary the development of models that combine chemical and dynamical effects.

Table 6.9 lists the column densities and abundances in the most important positions of the Orion Bar; PDR-peak (Fuente et al. 1996; Cuadrado et al. 2015), clump 3 and clump 1 (Lis & Schilke 2003; Parise et al. 2009). For every position, the total column densities are calculated as the sum of the ortho- and para-species in the case of molecules such as H_2CO and C_3H_2. The data from this table are from detailed studies of the Orion Bar (Fuente et al. 1996, 2003; Leurini et al. 2006; Parise et al. 2009; Nagy et al. 2015; Cuadrado et al. 2015). Table 6.10 lists the total column densities and abundances in the NGC 7023 PDR. This table is based on the data from Fuente et al. (1993) and Fuente et al. (2003). The abundance of each specie are calculated in the offsets ([-30″, 50″] or [-25″, 40″]) corresponding to the PDR-peak. Table 6.11 presents the total column densities and abundances in the Horsehead PDR. This table is based on the data from several detailed studies of the source (Teyssier et al. 2004, 2005; Pety et al. 2005, 2007; Goicoechea et al. 2006, 2009a; Agúndez et al. 2008; Gerin et al. 2009, 2013; Gratier et al. 2013; Guzmán et al. 2013, 2014). In the table we indicate the offsets in which were calculated the molecular abundances, the offset (-5″,0″) corresponds to the PDR-peak. The molecular abundances of each specie in each source were calculated with respect to H nuclei (assuming $N(X)/N(H) = N(X)/N(H) + 2N(H_2)$). Left panels of the Figures 6.18 to 6.26, show the comparison of the abundances for some representative species in the PDRs. In the Figures, the PDRs are placed in order of their calculated UV flux (G_0), from higher to lower, i. e., Mon R2 (IF and MP2 position), Orion Bar (PDR-peak, clump 3 and clump 1), NGC 7023, and Horsehead. We chose this order on basis of the previous cited works.

To perform the comparison, we looked for reported observations of several molecules ($C^{18}O$, HCO^+, DCO^+, DCN, $HN^{13}C$, $H^{13}CN$, N_2H^+, SO, SO^+, HCS^+, H_2CS, OCS, CS, HC_3N, CH_3CH, CH_3OH, CH_3CCH, H_2CO, l-C_3H, c-C_3H_2, C_2H, C_4H, CF^+ and CN) in the previous mentioned PDRs. Due to the lack of information, we can not identify any behavior for H_2CS, OCS, HNCO and HC_3N molecules. However we can set some trends for the other molecules: *i)* The $C^{18}O$, HCO^+, DCN, $H^{13}CN$, N_2H^+, SO, SO^+, HCS^+, CS, CH_3OH and CH_3CCH molecules present similar abundances for different G_0 environments. *ii)* The DCO^+, CH_3CN and CF^+ molecule, seems to increase their abundance in the low-UV irradiated PDRs. However lack of information in some PDRs that prevent us from set clear trends in these molecules. It is important to note that in the DCO^+ case, the abundance in the Horsehead PDR do not correspond to the PDR-peak, but a molecular peak at offset $(20'',22'')$. *iii)* Hydrocarbons (l-C_3H, c-C_3H_2, C_2H and C_4H) tend to increase their abundances in the low-UV irradiated PDRs, i.e., at higher G_0 fields lower hydrocarbons abundances. Another important molecules that seems to increase its abundances in the low-UV irradiated PDRs is $HN^{13}C$ molecule. *iv)* The H_2CO, CN, $H^{13}CN$ and DCN molecular abundances seems to decrease in the low-UV PDRs. However the lack of information for NGC 7023 (in the case of H_2CO) and Horsehead (in the case of CN) that prevent to set firm conclusions.

Table 6.12 lists the molecular abundances in Orion KL, TMC 1, L134N and L1157. This table is based on the data from several detailed studies of Orion KL (Tercero et al. 2010; Esplugues et al. 2013; Feng et al. 2015; Turner 2001), TMC 1, L134N (Agúndez & Wakelam 2015) and L1157 (Mendoza et al. 2014; Podio et al. 2014). The molecular abundances of each specie in each source were calculated with respect to H nuclei (assuming $N(X)/N(H) = N(X)/N(H) + 2N(H_2)$). Right panels of the Figures 6.18 to 6.26, show the comparison of the abundances for some representative species in these sources, on basis of histograms plots.

As for the PDRs, we looked for reported observations of several molecules ($C^{18}O$, HCO^+, DCO^+, DCN, $HN^{13}C$, $H^{13}CN$, N_2H^+, SO, SO^+, HCS^+, H_2CS, OCS, CS, HC_3N, CH_3CH, CH_3OH, CH_3CCH, H_2CO, l-C_3H, c-C_3H_2, C_2H and C_4H, CF^+ and CN) in the previous mentioned sources. Due to the lack of information, we can not identify any behavior for DCO^+, DCN, $HN^{13}C$, $H^{13}CN$ and CF^+ molecules. However we can set some trends for the other molecules, that are explained from Section 6.5.2.1 to 6.5.2.7

Table 6.9: Total column densities and abundances in the Orion Bar from the literature. The abundances of each species is with respect to H nuclei. [a]Fuente et al. (1996); [b]Cuadrado et al. (2015); [c]Fuente et al. (2003); [d]Nagy et al. (2015) [e]Leurini et al. (2006); [f]Parise et al. (2009); [*]Neufeld et al. (2006).

| | Orion Bar | | | | | |
| | PDR-peak | | Clump 3 | | Clump 1 | |
Species	N [cm^{-2}]	X	N [cm^{-2}]	X	N [cm^{-2}]	X
H	3×10^{21b}	...	...	...	...	...
H$_2$	3×10^{22b}	...	1.3×10^{23f}	...	1.6×10^{23f}	...
C^{18}O	5×10^{15bd}	1.1×10^{-7bd}	...	...	...	...
HCO$^+$	4.5×10^{13a}	7.5×10^{-10ab}	...	...	...	...
DCO$^+$	...	...	$(6.2 \pm 1.0) \times 10^{11f}$	2.3×10^{-12f}	$< 2.2 \times 10^{11f}$	$< 5.8 \times 10^{-11f}$
DCN	...	...	$1.9 \pm 0.3 \times 10^{13f}$	7.3×10^{-11f}	$1.4 \pm 0.3 \times 10^{13f}$	4.4×10^{-11f}
HCN	4.7×10^{13a}	7.8×10^{-10ab}	...	...	...	...
HN^{13}C	$< 7 \times 10^{11a}$	$< 1.16 \times 10^{-11ab}$	...	...	...	...
HNC	2×10^{13a}	3.3×10^{-10ab}	1.1×10^{13f}	4.2×10^{-11f}	...	...
H^{13}CN	...	...	$2.5 \pm 0.3 \times 10^{13f}$	9.6×10^{-11f}	$3.1 \pm 0.4 \times 10^{13f}$	9.6×10^{-11f}
N$_2$H$^+$	$< 1.5 \times 10^{12a}$	$< 2.5 \times 10^{-11ab}$	...	...	...	...
SO	4.4×10^{12c}	7.3×10^{-11ab}	...	...	$(1.0 \pm 0.2) \times 10^{14e}$	3×10^{-10f}
SO$^+$	...	5×10^{-11c}	...	...	$(2.0 \pm 0.5) \times 10^{13e}$	6.3×10^{-11f}
HCS$^+$	...	...	...	...	$(2.5 \pm 0.7) \times 10^{12e}$	7.8×10^{-12f}
H$_2$CS	...	...	...	...	$(2.5 \pm 0.4) \times 10^{13e}$	7.8×10^{-11f}
CS	2×10^{13a}	3.3×10^{-10ab}	...	...	...	...
OCS	...	...	...	...	$< 4 \times 10^{13e}$	1.3×10^{-10f}
CH$_3$OH	...	...	$3 \pm 1 \times 10^{14f}$	1×10^{-9f}	$3 \pm 1 \times 10^{14f}$	9.4×10^{-10f}
H$_2$CO	3.6×10^{13a}	6×10^{-10ab}	...	...	$2.8–5.4 \times 10^{14e}$	1×10^{-9f}
l-C$_3$H	$7.0 \pm 1.1 \times 10^{11b}$	1.1×10^{-11b}	...	...	...	...
c-C$_3$H$_2$	$1.3 \pm 0.2 \times 10^{13b}$	2.1×10^{-10b}	...	...	...	...
C$_2$H	$4.2 \pm 0.2 \times 10^{14b}$	0.7×10^{-8b}	...	...	...	...
C$_4$H	$3.8 \pm 0.3 \times 10^{13b}$	0.6×10^{-9b}	...	...	...	...
CF$^+$	...	...	$1.9 \times 10^{12*}$	$7.3 \times 10^{-12f*}$	$1.1 \times 10^{12*}$	$4.2 \times 10^{-12f*}$
CN	9×10^{13a}	1.5×10^{-9}	...	...	...	...

Table 6.10: Total column densities and abundances in the NGC 7023 PDR peak. The abundances of each species is given with respect to H nuclei. [g]Fuente et al. (1993); [h]Fuente et al. (2003).

	NGC 7023		
Species	N [cm^{-2}]	X	offset
H	6.6×10^{22g}	...	(-30$''$,50$''$)
H$_2$	1.1×10^{22g}	...	(-30$''$,50$''$)
C^{18}O	5.0×10^{15g}	7.4×10^{-8g}	(-30$''$,50$''$)
HCO$^+$	3.0×10^{13g}	0.2×10^{-9g}	(-30$''$,50$''$)
HCN	9.1×10^{12g}	1.4×10^{-10g}	(-30$''$,50$''$)
HNC	4.9×10^{12g}	0.7×10^{-10g}	(-30$''$,50$''$)
HN^{13}C	$< 2.9 \times 10^{11g}$	$< 2.6 \times 10^{-11g}$	(-30$''$,50$''$)
N$_2$H$^+$	$< 4.8 \times 10^{12g}$	$< 0.7 \times 10^{-10g}$	(-30$''$,50$''$)
SO	6×10^{11h}	5.4×10^{-11hg}	(-25$''$,40$''$)
SO$^+$	5.5×10^{11h}	5×10^{-11h}	(-25$''$,40$''$)
CS	5.0×10^{12g}	0.8×10^{-10g}	(-30$''$,50$''$)
c-C$_3$H$_2$	1.2–2.1×10^{12h}	2×10^{-10h}	(-25$''$,40$''$)
C$_2$H	3.8×10^{13g}	0.6×10^{-9g}	(-30$''$,50$''$)
CN	4.1×10^{13g}	6.2×10^{-10g}	(-30$''$,50$''$)

Table 6.11: Total column densities and abundances in the Horsehead PDR. The abundances of each species is given with respect to H nuclei. [a]Gerin et al. (2009); [b]Gerin et al. (2013); [c] Gratier et al. (2013); [d]Guzmán et al. (2013); [e]Guzmán et al. (2014).

	Horsehead		
Species	N [cm^{-2}]	X	offset
H	$3.8 \times 10^{22*}$	...	(-5$''$,0$''$)
H$_2$	1.9×10^{22a}	...	(-5$''$,0$''$)
C^{18}O	$4.0 \pm 0.5 \times 10^{15a}$	1.9×10^{-7a}	(-6$''$,-4$''$)
HCO$^+$	3.5×10^{13b}	9.0×10^{-10d}	(-5$''$,0$''$)
DCO$^+$	$7.5 \pm 2.5 \times 10^{12a}$	8.0×10^{-11a}	(20$''$,22$''$)
HCS$^+$	$6.8 \pm 0.5 \times 10^{11a}$	1.7×10^{-11a}	(4$''$,0$''$)
CS	$8.1 \pm 1.0 \times 10^{13a}$	2.0×10^{-9a}	(4$''$,0$''$)
HC$_3$N	$(2.5$–$3.16) \times 10^{11c}$	6.3×10^{-12d}	(-5$''$,0$''$)
CH$_3$CN	$(1.0$–$1.58) \times 10^{13c}$	2.5×10^{-10d}	(-5$''$,0$''$)
CH$_3$OH	$((E)2.7$–$(A)2) \times 10^{12d}$	$((E)7$–$(A)5.3) \times 10^{-11d}$	(-5$''$,0$''$)
CH$_3$CCH	2×10^{13e}	4.4×10^{-10d}	(-5$''$,0$''$)
H$_2$CO	$((o)3.6$–$(p)7.2) \times 10^{12*}$	$((o)19$–$(p)9.5) \times 10^{-11d}$	(-5$''$,0$''$)
l-C$_3$H	$2.1 \pm 0.7 \times 10^{12a}$	1.4×10^{-10a}	(-10$''$,0$''$)
c-C$_3$H$_2$	$2.4 \pm 1.0 \times 10^{13a}$	1.1×10^{-9d}	(-6$''$,-4$''$)
C$_2$H	$3.0 \pm 0.5 \times 10^{14a}$	1.4×10^{-8a}	(-6$''$,-4$''$)
C$_4$H	$4.0 \pm 1.0 \times 10^{13a}$	1.0×10^{-9a}	(-6$''$,-4$''$)
CF$^+$	$(1.5$–$2.0) \times 10^{12j}$	5.7×10^{-10d}	(-5$''$,0$''$)

Table 6.12: Molecular abundances in the different kind of sources.[k]Tercero et al. (2010); [j]Esplugues et al. (2013); [*]Feng et al. (2015) using SMA and 30m; [l]Turner (2001); [m]Agúndez & Wakelam (2015), and reference there; [n]Daniel et al. (2013); [o]Bachiller & Pérez Gutiérrez (1997); [p]Mendoza et al. (2014); [q]Podio et al. (2014).

Species	Ori KL		TMC 1	L134N	L1157
	Plateau	Hot core			
$C^{18}O$	8.0×10^{-7j}	1.0×10^{-6j}	3.4×10^{-7m}	1.74×10^{-7m}	1.4×10^{-7o}
HCO^+	...	...	4.65×10^{-9m}	3.95×10^{-9m}	2.6×10^{-8o}
DCO^+	...	...	2.2×10^{-11lm}	...	...
DCN	...	...	1.9×10^{-10lm}	...	...
$HN^{13}C$	...	...	3.6×10^{-10lm}	...	...
$H^{13}CN$	...	...	3.15×10^{-10l}	...	...
N_2H^+	...	...	1.4×10^{-10m}	3.05×10^{-10m}	4×10^{-9q}
SO	1.19×10^{-8j}	1.07×10^{-8j}	0.75×10^{-9m}	2.85×10^{-9m}	1.5×10^{-7o}
SO^+	$< 5.95 \times 10^{-10j}$	$< 2.29 \times 10^{-10j}$	...	...	4×10^{-10q}
HCS^+	0.009×10^{-8k}	2.5×10^{-11k}	1.5×10^{-10m}	3×10^{-11m}	1.55×10^{-9o}
H_2CS	0.15×10^{-8k}	0.05×10^{-8k}	3.5×10^{-10m}	3×10^{-10m}	0.55×10^{-7o}
CS	0.35×10^{-8k}	1.0×10^{-8k}	1.45×10^{-9m}	4.95×10^{-10m}	0.95×10^{-7o}
OCS	1.95×10^{-8k}	2.6×10^{-8k}	1.1×10^{-9m}	1.75×10^{-9m}	1.5×10^{-8o}
HC_3N	...	$0.284 \times 10^{-8*}$	0.8×10^{-8m}	2.15×10^{-10m}	0.5×10^{-8o}
CH_3CN	...	$5.8 \times 10^{-8*}$	3×10^{-10m}	$< 0.5 \times 10^{-9m}$	...
CH_3OH	...	$1.06 \times 10^{-7*}$	1.6×10^{-9m}	2.55×10^{-9m}	1×10^{-5o}
CH_3CCH	...	...	3×10^{-9m}	3×10^{-9m}	...
$HNCO$	...	$4.45 \times 10^{-9*}$	2×10^{-10m}	1.25×10^{-10m}	2.05×10^{-8p}
H_2CO	...	...	2.5×10^{-8m}	1×10^{-8m}	3×10^{-7o}
$l-C_3H$	...	...	4.2×10^{-11m}	0.63×10^{-10m}	...
$c-C_3H_2$	...	...	2.9×10^{-9m}	1.04×10^{-9m}	...
C_2H	...	...	3.6×10^{-9m}	1.15×10^{-9m}	0.6×10^{-7o}
C_4H	...	...	3.05×10^{-8m}	0.89×10^{-9m}	3×10^{-8o}
CN	...	...	3.7×10^{-10m}	2.4×10^{-10m}	1.4×10^{-7o}
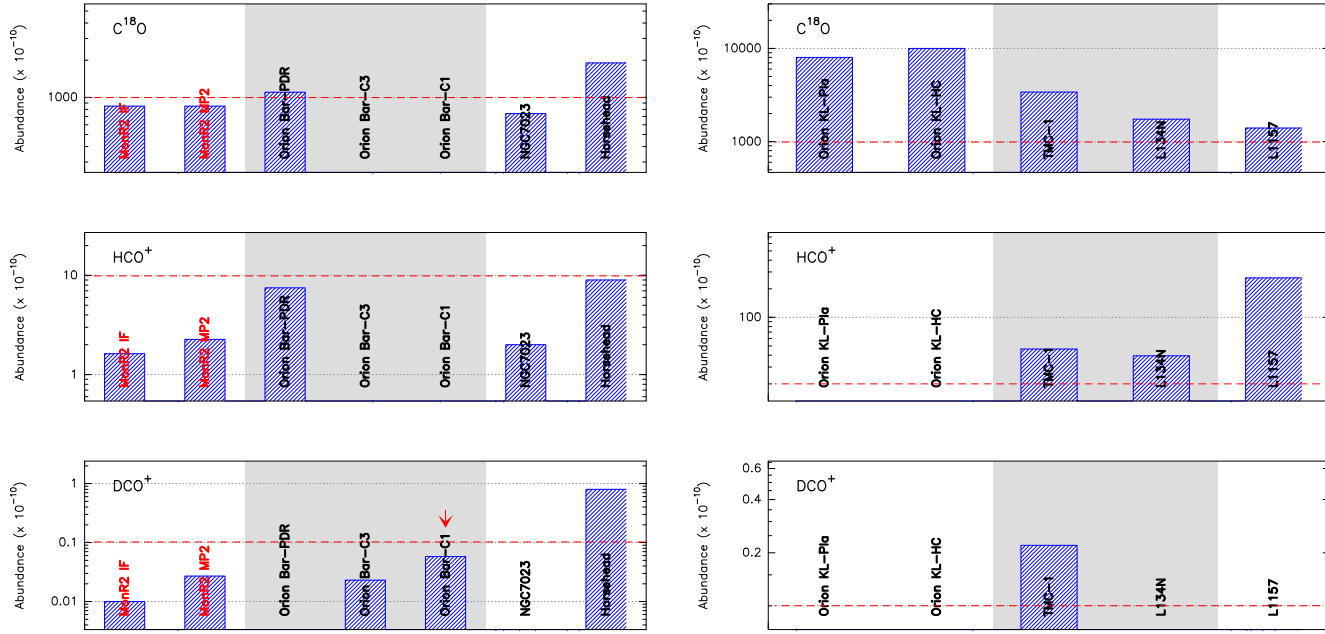
Figure 6.18: *Left:* Histogram comparing the molecular abundances, $N(\mathrm{X})/N(\mathrm{H})$, in different PDRs: the Mon R2 region (IF and MP2 position), Orion Bar (PDR-peak, clump 3 and clump 1), NGC 7023, and Horsehead. PDRs are placed in order of their calculated UV flux, i. e.,from higher to lower G_0. *Right:* Histogram comparing the molecular abundances, in different the Orion KL (Plateau and Hot core), TMC 1, L134N and L1157. Red arrows indicate when the abundance is a upper limit value. References for the plotted values are shown in Tables 6.9 to 6.12. *Figure continues in the next page.*
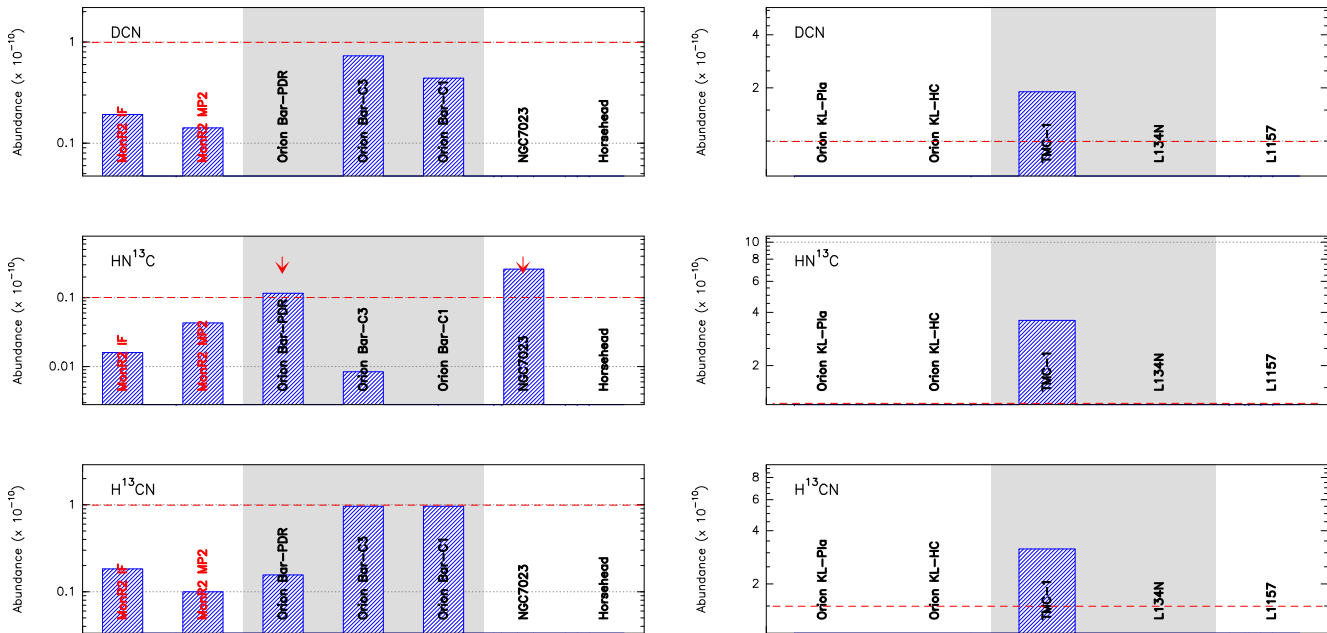
Figure 6.19: *Left:* Histogram comparing the molecular abundances, $N(\mathrm{X})/N(\mathrm{H})$, in different PDRs: the Mon R2 region (IF and MP2 position), Orion Bar (PDR-peak, clump 3 and clump 1), NGC 7023, and Horsehead. PDRs are placed in order of their calculated UV flux, i.e.,from higher to lower G_0. *Right:* Histogram comparing the molecular abundances, in different the Orion KL (Plateau and Hot core), TMC 1, L134N and L1157. Red arrows indicate when the abundance is a upper limit value. References for the plotted values are shown in Tables 6.9 to 6.12. *Figure continues in the next page.*
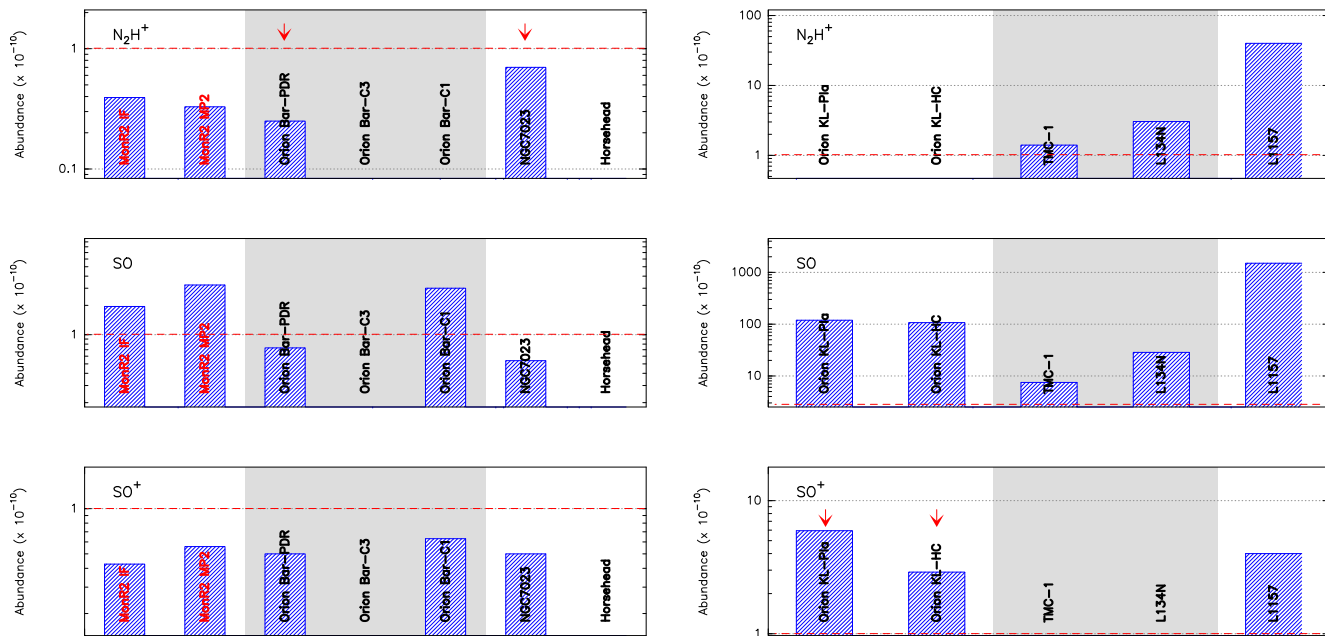
Figure 6.20: *Left:* Histogram comparing the molecular abundances, $N(\mathrm{X})/N(\mathrm{H})$, in different PDRs: the Mon R2 region (IF and MP2 position), Orion Bar (PDR-peak, clump 3 and clump 1), NGC 7023, and Horsehead. PDRs are placed in order of their calculated UV flux, i. e.,from higher to lower G_0. *Right:* Histogram comparing the molecular abundances, in different the Orion KL (Plateau and Hot core), TMC 1, L134N and L1157. Red arrows indicate when the abundance is a upper limit value. References for the plotted values are shown in Tables 6.9 to 6.12. *Figure continues in the next page.*
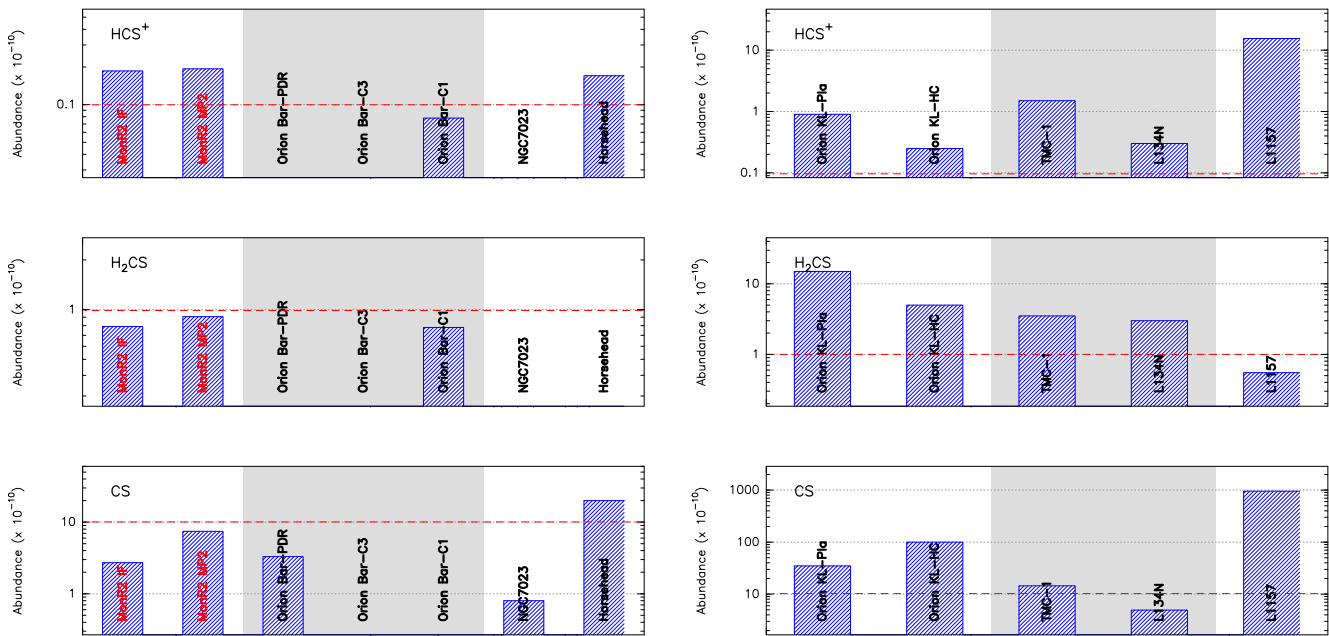
Figure 6.21: *Left:* Histogram comparing the molecular abundances, $N(X)/N(H)$, in different PDRs: the Mon R2 region (IF and MP2 position), Orion Bar (PDR-peak, clump 3 and clump 1), NGC 7023, and Horsehead. PDRs are placed in order of their calculated UV flux, i.e.,from higher to lower G_0. *Right:* Histogram comparing the molecular abundances, in different the Orion KL (Plateau and Hot core), TMC 1, L134N and L1157. References for the plotted values are shown in Tables 6.9 to 6.12. *Figure continues in the next page.*
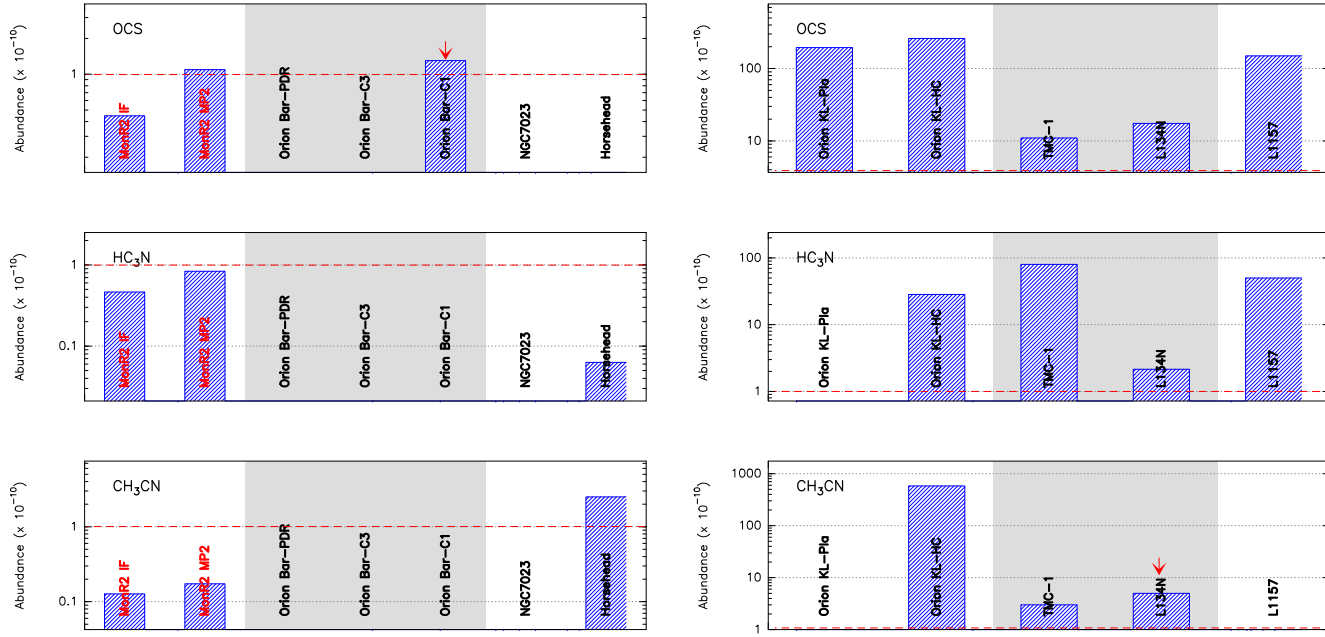
Figure 6.22: *Left:* Histogram comparing the molecular abundances, $N(X)/N(H)$, in different PDRs: the Mon R2 region (IF and MP2 position), Orion Bar (PDR-peak, clump 3 and clump 1), NGC 7023, and Horsehead. PDRs are placed in order of their calculated UV flux, i. e.,from higher to lower G_0. *Right:* Histogram comparing the molecular abundances, in different the Orion KL (Plateau and Hot core), TMC 1, L134N and L1157. Red arrows indicate when the abundance is a upper limit value. References for the plotted values are shown in Tables 6.9 to 6.12. *Figure continues in the next page.*
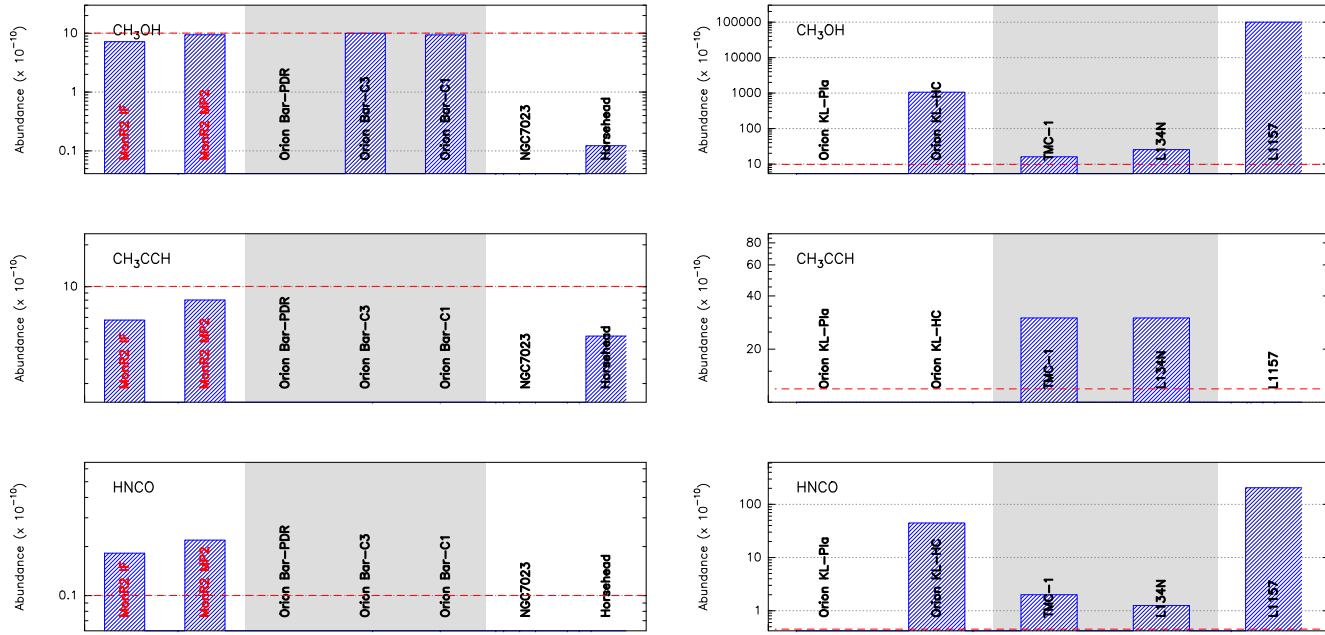
Figure 6.23: *Left:* Histogram comparing the molecular abundances, $N(X)/N(H)$, in different PDRs: the Mon R2 region (IF and MP2 position), Orion Bar (PDR-peak, clump 3 and clump 1), NGC 7023, and Horsehead. PDRs are placed in order of their calculated UV flux, i. e.,from higher to lower G_0. *Right:* Histogram comparing the molecular abundances, in different the Orion KL (Plateau and Hot core), TMC 1, L134N and L1157. References for the plotted values are shown in Tables 6.9 to 6.12. *Figure continues in the next page.*
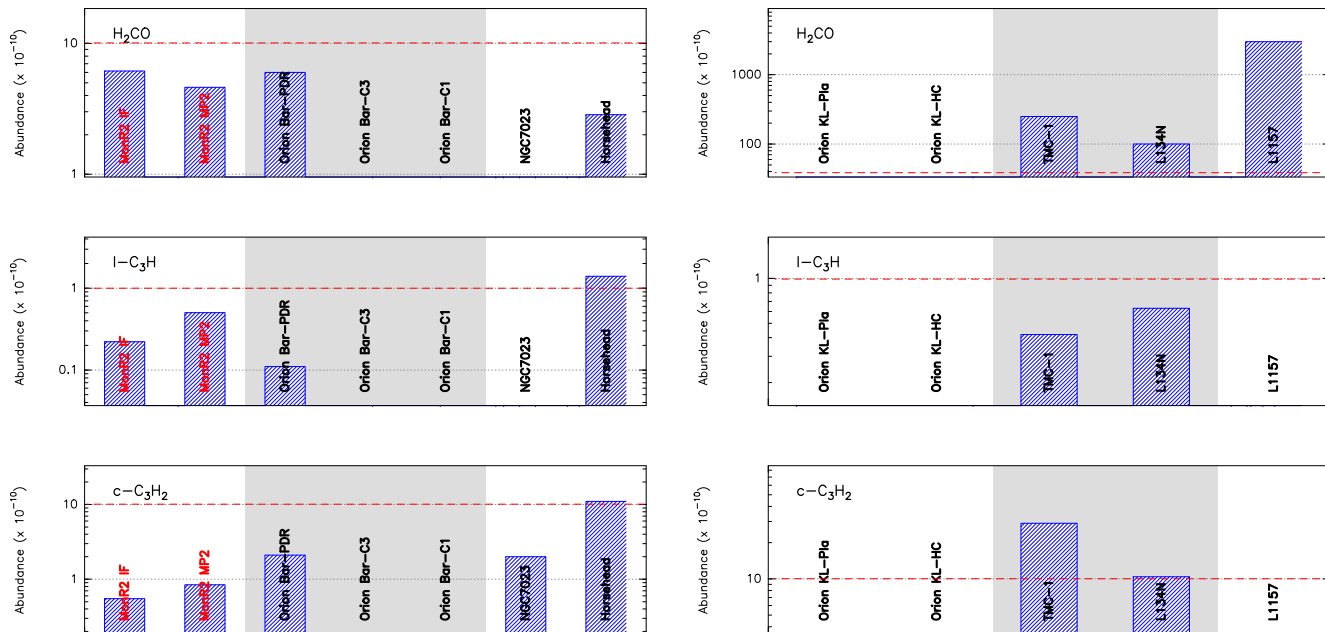
Figure 6.24: *Left:* Histogram comparing the molecular abundances, $N(\mathrm{X})/N(\mathrm{H})$, in different PDRs: the Mon R2 region (IF and MP2 position), Orion Bar (PDR-peak, clump 3 and clump 1), NGC 7023, and Horsehead. PDRs are placed in order of their calculated UV flux, i.e.,from higher to lower G_0. *Right:* Histogram comparing the molecular abundances, in different the Orion KL (Plateau and Hot core), TMC 1, L134N and L1157. References for the plotted values are shown in Tables 6.9 to 6.12. *Figure continues in the next page.*
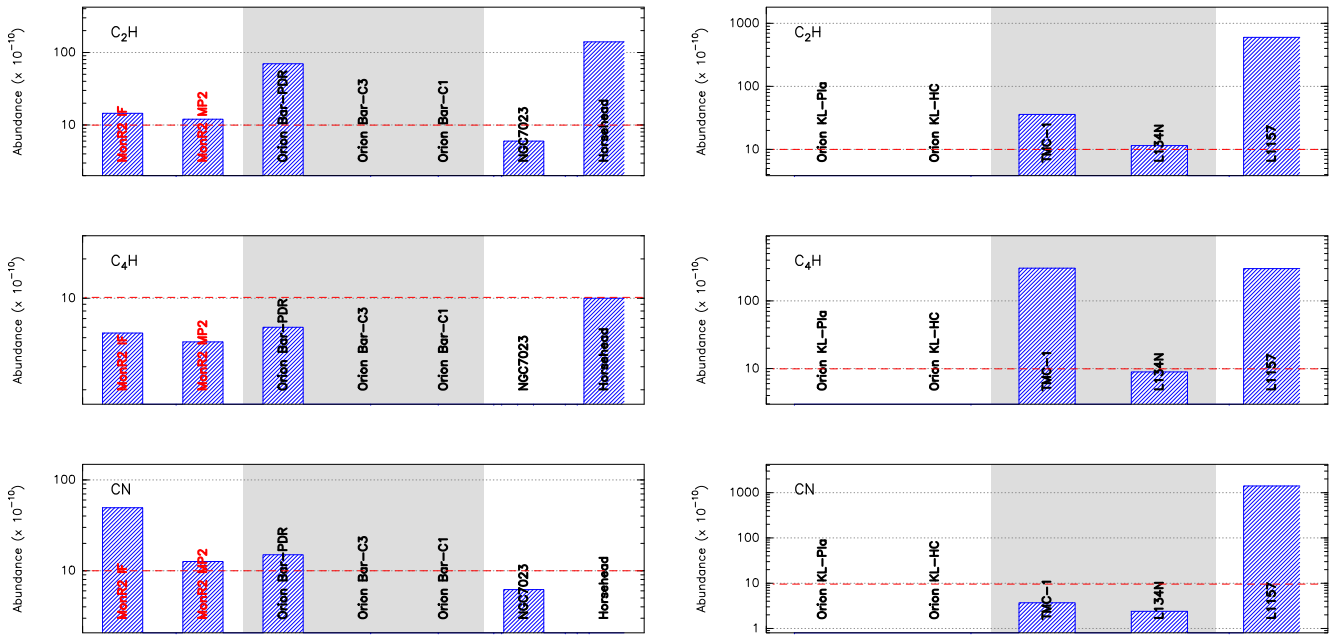
Figure 6.25: *Left:* Histogram comparing the molecular abundances, $N(X)/N(H)$, in different PDRs: the Mon R2 region (IF and MP2 position), Orion Bar (PDR-peak, clump 3 and clump 1), NGC 7023, and Horsehead. PDRs are placed in order of their calculated UV flux, i. e.,from higher to lower G_0. *Right:* Histogram comparing the molecular abundances, in different the Orion KL (Plateau and Hot core), TMC 1, L134N and L1157. References for the plotted values are shown in Tables 6.9 to 6.12. *Figure continues in the next page.*
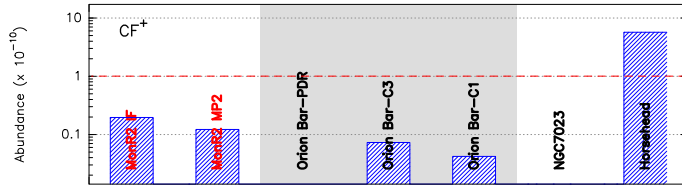
Figure 6.26: Histogram comparing the molecular abundances, $N(CF^+)/N(H)$, in different PDRs: the Mon R2 region (IF and MP2 position), Orion Bar (PDR-peak, clump 3 and clump 1), NGC 7023, and Horsehead. PDRs are placed in order of their calculated UV flux, i.e.,from higher to lower G_0. References for the plotted values are shown in Tables 6.9 to 6.11.

6.5.2.1 Deuterated molecules

High abundances of deuterated molecules have been observed in many astrophysical environments, including PDRs, hot cores and cold dense cores. To perform the comparison, we looked for DCN and DCO^+ molecules in the previous mentioned sources. In the PDRs comparison, we can not identify any trend for DCN molecule, while DCO^+ is more abundant in the low-UV irradiated PDRs. However, the information about these compounds in PDRs is very scarce. In the case DCN molecule, we miss information in the Orion Bar (PDR peak), NGC 7023 and Horsehead. In clumps 3 and 1 of the Orion Bar the abundances are higher than in Mon R2 by a factor of 4-5. The clump 3 is the closest clump to the PDR-peak in the Orion Bar. In the case of DCO^+ molecule, we miss information in the Orion Bar (PDR peak) and NGC 7023. The abundance of DCO^+ found in the clump 3 (Orion Bar) is quite similar to the abundance in MP2. The upper limit of this abundance in the clump 1 is higher than in Mon R2 by a factor of 2-4. While, the abundance of DCO^+ found in the Horsehead is higher than in Mon R2 by an order of magnitude. However, it is important to note that the DCO^+ abundance in the Horsehead do not correspond to the PDR-peak, but a molecular peak at offset (20″, 22″).

For the comparison with different kind of regions, we only found information for the dark cloud TMC 1. We found that TMC 1 present higher abundances of DCN than Mon R2 (by an order of magnitude) and Orion Bar (by a factor of 2). While DCO^+ abundances are higher in TMC 1 than in Mon R2 (by an order of magnitude) and Orion Bar (by a factor of 2), but is lower than in Horsehead (by a factor of 5).

The fact that DCN and DCO^+ molecules are more abundant in TMC 1 than in the PDRs was expected. Deuterated molecules are expected to be present

in cold environments (Gerlich et al. 2002; Pagani et al. 2011, 2013). Moreover, these molecules are easily destroyed by UV radiation and, thus, are not expected in PDRs. More difficult to understand is the high DCN abundances observed in high-UV PDRs like Mon R2 and the Orion Bar. The DCN abundances in Mon R2 can be explained considering that the DCN emission comes from dense warm clumps (see Figure 6.8). These clumps are being heated by outside and seem to be shielded from the UV radiation. In the statistical study we found that the deuterated molecules present typical linewidths of 1km s^{-1} (see Section 6.4.1), this is a confirmation that their emission comes from the dense clumps.

Chapter 7 presents several chemical pathways proposed to produce the deuterium enrichment in the ISM. It also explains in detail the chemistry of the deuterated molecules in Mon R2 based on the observational results and their comparison with a pseudo-time-dependent gas phase chemical model.

| 6.5.2.2 | Ionic species |

Molecular ions are believed to drive an important part of the chemistry in interstellar clouds. In particular, reactive molecular ions (HOC$^+$ and CO$^+$) are thought to be excellent tracers of PDRs, and they also reveal significant chemical differences between them. These compounds are destroyed in almost every collision with H and H$_2$ and recombines rapidly with e$^-$. Thus, their abundances are expected to be negligible in the shielded parts of molecular clouds, where atomic and molecular hydrogen are dominant species. The abundance of these ions become significant in the hot layers of PDRs (Sternberg & Dalgarno 1995), where the FUV field is only partially attenuated and maintains high densities of the parent species C$^+$ and S$^+$.

The CO$^+$ molecule has been detected in several PDRs (e. g., Orion Bar and Mon R2; Latter & Walker 1994 and Rizzo et al. 2003, respectively). The CO$^+$ rotational populations do not have time to become thermalized, so that its rotational line emission probably represents a kind of measure of its production rate. It has been argued (Black 1998) that CO$^+$ arises in the hot HI/H$_2$ transition layer of PDRs and constitutes a potential diagnostic probe of this very interesting boundary layer. Within the PDR, CO$^+$ is formed mainly by C$^+$+ OH $\rightarrow$ CO$^+$+ H reaction, and destroyed by reactions with H$_2$ to form HCO$^+$ and HOC$^+$, and by dissociative recombination. In regions of high ionization rate, CO$^+$ can also be produced by a charge transfer reaction between CO and CH$^+$, and/or even by direct ionization of CO. The CO$^+$ ion takes part in the chemical reactions to produce the HOC$^+$ or HCO$^+$ ions.

There are two pathways to form HOC^+; i) via the reaction $C^+ + H_2O \rightarrow HOC^+ + H$ and ii) via $CO^+ + H_2 \rightarrow HOC^+/HCO^+ + H$ and its destruction is mainly by reactions with H_2 (Smith et al. 2002a). The large abundances of C^+ and CO^+ in PDRs could result in an enhanced HOC^+ abundance. Within this scheme, one expects some correlation between low $[HCO^+]/[HOC^+]$ ratios and high CO^+ abundances (Savage et al. 2000).

Another chemically related ion that is expected to be abundant in the HI/H_2 transition layer is SO^+. SO^+ is primarily formed via $S^+ + OH \rightarrow SO^+ + H$ and removed by dissociative recombination in $S + O$. The neutral atoms S will then follow a series of reactions to give SO and SO_2. In regions exposed to high UV fields, the sulfur is mainly in the form of S^+ and SO^+, while in the well shielded cloud it is in the form of SO and SO_2. Thus, gradients in the $[SO^+]/[SO]$ and $[SO^+]/[SO_2]$ abundance ratios are expected across PDRs.

Less studied but very interesting related ions are CF^+ and $l\text{-}C_3H^+$. CF^+ is formed through the chemical path: $F + H_2 \rightarrow HF + H$; $HF + C^+ \rightarrow CF^+ + H$ and is destroyed by dissociative recombination with electrons (Neufeld et al. 2006) and by far-UV photons. This ion has been detected towards the Orion Bar (Neufeld et al. 2006; first astronomical detection), the Horsehead PDR (Pety et al. 2012; Guzmán et al. 2012a,b) and Mon R2 (Treviño-Morales et al. in preparation). There are uncertainties in some reaction rate coefficients (e. g., CF^+ photodissociation), the current models predict that CF^+ is present in regions where C^+ and HF are abundant. In that regions CF^+ is the second-most important fluorine reservoir after HF. To observe CF^+ in a region with strong radiation UV, as Mon R2, can help to understand the chemistry of this ion. Ion-molecule reactions with the C_2H^+ and C_3H^+ cations are thought to be the most important gas-phase channels to form small hydrocarbons (Turner 2000; Wakelam et al. 2010). Constraining the abundances of these intermediate hydrocarbon cations will shed light on the formation routes of hydrocarbons. Pety et al. (2012) reported the first detection in the inter-stellar medium of the $l\text{-}C_3H^+$ ion towards the Horsehead PDR. This detection was contested by Fortenberry et al. (2013) but finally confirmed by Brünken et al. (2014).

In summary, ionic species (e. g., CO^+, HCO^+, HOC^+ SO^+, CF^+ and $l\text{-}C_3H^+$) are good PDRs tracers and can reveal important chemical characteristics in these regions. They can be also very useful to determinate the variation of the UV field towards the region. In our spectral survey we detected these molecules towards both positions (see Figure 6.27 and 6.28). In the case of the $l\text{-}C_3H^+$ molecule we have a tentative detection at 89.957, 134.932 and 202.386 GHz, being MP2 the position in which this detection is clearer. As mentioned before, the $l\text{-}C_3H^+$ molecule was detected for the first time in the Horsehead PDR (Pety et al. 2012), but also was detected in the Orion Bar (Cuadrado et al. 2015). Guzmán et al. (2015) found a $l\text{-}C_3H^+$ abundance of
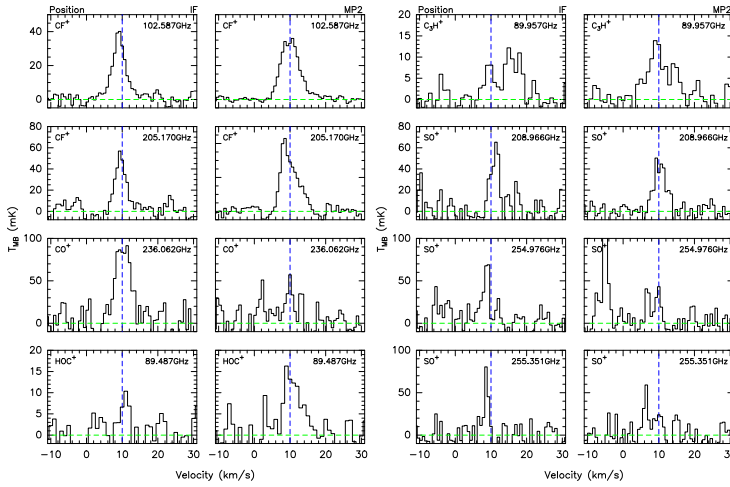
Figure 6.27: Observed spectra of the ionic species at the IF (column 1 and 3) and MP2 position (column 2 and 4).

$\sim 1.4 \times 10^{-11}$ in the PDR-peak of the Horsehead PDR. While Cuadrado et al. (2015) found an abundance of $\sim 0.8 \times 10^{-11}$ in the PDR-peak of Orion Bar. In Mon R2 at the MP2 position we found N(l-C$_3$H$^+$)=2.2×10^{12}[viii] and an abundance of $\sim 2.2 \times 10^{-11}$. These abundances might indicate that the l-C$_3$H$^+$ molecule is more abundant in the PDRs with lower UV fields. However, to set firm conclusions it is necessary to perform more observation of this molecule in Mon R2 (to improve the spectra quality and thus get a better estimation of its abundance), and in general in other PDRs. These abundances suggest that CO$^+$ is more abundant in the PDRs with high UV fields (with $G_0 > 10^3$). Figure 6.28 show OTF maps of different species in Mon R2, and a Herschel CII map.

In the case of CO$^+$, we have detected the 236.0626 GHz line in the IF position (see Figure 6.27). At this position we found N(CO$^+$)=6.5×10^{12} (assuming $T_{rot} = 19$ K) and an abundance of 5.95×10^{-11}. This molecule was also detected in the NGC 7023 and Orion Bar (Fuente et al. 2003), but not in the Horsehead. However, Goicoechea et al. (2009a) calculated a superior limit for this molecule in this region ($< 5 \times 10^{-11}$). The NGC 7023 and Orion Bar PDRs present abundances of 3×10^{-11} and 6×10^{-11}, respectively.

These abundances suggest that CO$^+$ is more abundant in the PDRs with high UV fields. Figure 6.28 show OTF maps of different species in Mon R2, and a Herschel CII map. The Figure show that the CO$^+$ emission is spatially correlated with the CII emission. The CO$^+$ emission seems to surround the HII region and present its intensity peak close to the IF position.

[viii]from the observational parameters of the 89.957 GHz line and considering a $T_{rot} = 19$ K.
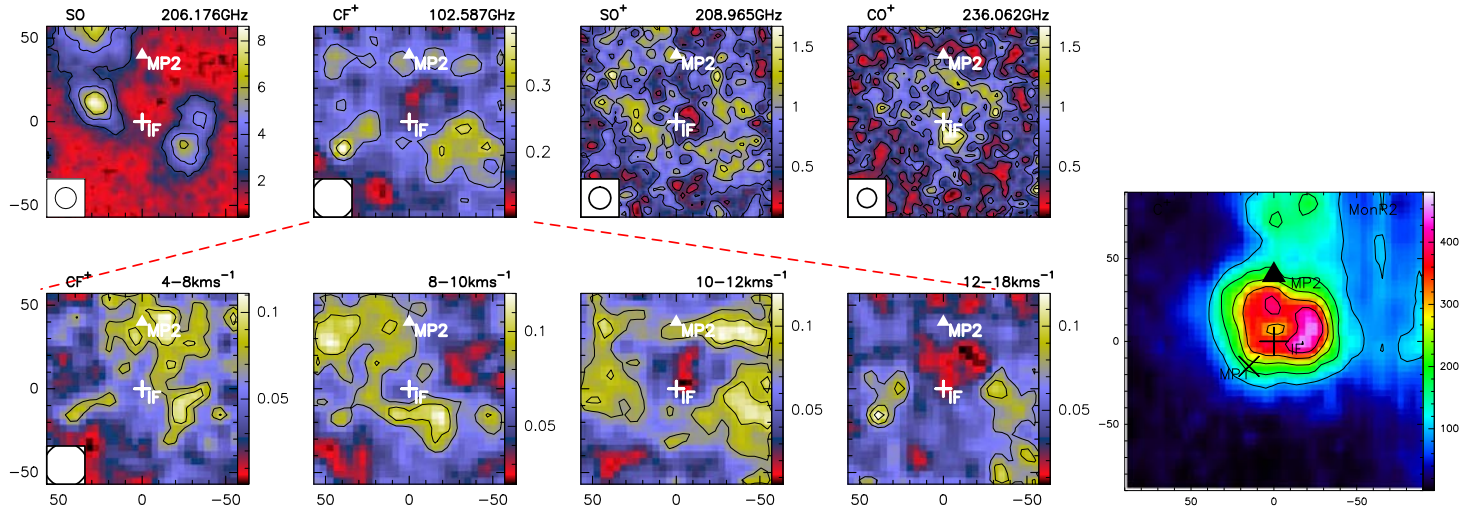
Figure 6.28: *Top:* SO, CF$^+$, SO$^+$ and CO$^+$ integrated maps. *Bottom:* CF$^+$ (102.587 GHz) integrated at different velocities ranges. *Right:* Herschel map of the C$^+$ line, (Pilleri et al. 2014).

The spatial distribution of the CO^+ molecule was expected, as this molecule is formed by $C^+ + OH \rightarrow CO^+ + H$ and $CO^+ + \nu \rightarrow CO^+ + H_2$ reactions. These reactions are part of the sequence of reactions that form CO molecules, this sequence maintain large densities of CO, CO^+ and HOC^+ near the H/H_2 transition region, near of the OH peak (Sternberg & Dalgarno 1995).

To complete the comparison, we examined for HCO^+, SO^+ and CF^+ molecules in the Orion Bar, NGC 7023 and Horsehead PDRs. In the PDRs comparison, we can not identify any trend. In the case of the HCO^+ molecule, we found the highest abundances in the Orion Bar (PDR-peak) and the Horsehead PDRs. The HCO^+ abundances in these sources are higher by a factor of 5 than in the NGC 7023 and Mon R2 PDRs, that present very similar abundances. The SO^+ molecule present similar abundances for different G_0 environments. The CF^+ molecule does not present any trend. However the lack of information in Orion Bar (PDR-peak) and NGC 7023 prevent us from set clear conclusions. For this molecule we found similar abundances in all the sources, but the Horsehead PDR that present abundances higher by a two order of magnitude.

For the comparison with different kind of regions, we only found information for the HCO^+ and SO^+ molecules. In the case of the HCO^+ molecule, we found that the dark clouds present abundances higher than the PDRs by a factor 2 (Orion Bar and Horsehead) and by a factor 10 (NGC 7023 and MP2), while the shock and the hot core present abundances higher than the PDRs (Orion Bar and Horsehead) by an order of magnitude. In the case of the SO^+ molecule, we found information for the hot core and the shock. In the case of the hot core we only found a upper limit of the abundance of $X < 2.29 \times 10^{-10}$. While for the shock, we fount that it presents abundances higher than the PDRs by a factor of two.

In order to have a deeper insight into the ions chemistry in IF and MP2, we calculate some column density ratios (see Table 6.8). In the case of the $[SO^+]/[SO]$ ratio, we found that the IF position present values slightly higher. This difference is because the SO molecule is more abundant in the MP2 position. However, the SO^+ emission seems to be stronger around the IF position (see Figure 6.27 and 6.28).

As was mentioned before, the formation of SO^+ is associated with OH molecule. Thus a large density of the SO^+ molecule is maintained in the H/H_2 transition layer, and the dissociative recombination of this molecule is the dominant source of atomic sulfur (S) in the hot gas (Sternberg & Dalgarno 1995). The neutral atoms S will then follow a series of reactions to give SO and SO_2. In regions exposed to high UV fields, the sulfur is mainly in the form of S^+ and SO^+, while in the well shielded cloud it is in the form of CS, SO and
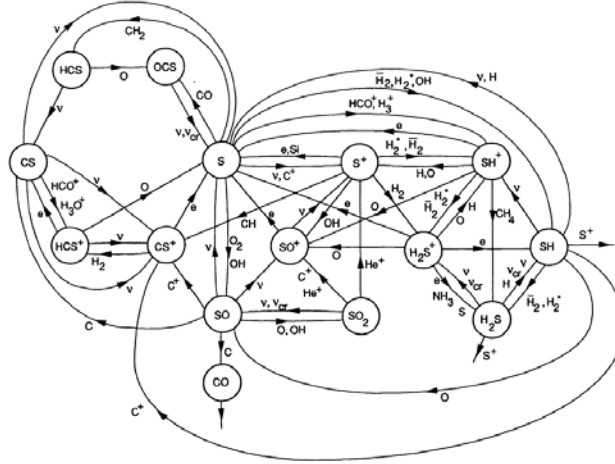
Figure 6.29: Sulfur network (Sternberg & Dalgarno 1995).

SO$^+$. Thus, gradients in the [SO$^+$]/[SO] and [SO$^+$]/[SO$_2$] abundance ratios are expected across PDRs.

6.5.2.3   Sulfurated species

Sulfur-bearing molecules are good tracers of early protostellar evolution. Chemical evolution of these molecules have been studied in low-mass star forming regions, (van der Tak et al. 2003a; Buckle & Fuller 2003; Li et al. 2015). These studies demonstrated that the sulfur molecules are a potential good clock on time scales relevant to the embedded phase of star formation. The H$_2$S molecule could be formed on interstellar grains (van Dishoeck & Black 1998), during the cold collapse phase, sulfur atoms freeze out onto grains and remain there in the form of H$_2$S until core heating begins. Then, H$_2$S is evaporated from the grains, and rapidly undergoes reactions which drive the production of SO and SO$_2$ (e. g., Wakelam et al. 2004, 2011).

In general sulfurated molecules are much less abundant in PDRs than in other kind of regions. This is because an important amount of their formation seems to be driven by the grain chemistry, that is not dominant in PDRs. Moreover, these molecules are easily destroyed by the strong UV-radiation present in these regions (e. g., SH, H$_2$S). Figure 6.29 shows a sulfur network presented by Sternberg & Dalgarno (1995). This network summarize the reactions involved to generate sulfur molecules in PDRs. The photodestruction of the sulfur bearing molecules and photoionization of atomic sulfur (S) maintains

most of the sulfur in singly ionized from throughout the HI zone and the H/H$_2$ transition layer, and the sulfur chemistry is initiated by the endothermic reaction S$^+$ + H$_2$ $\rightarrow$ SH$^+$ +H. The dissociative recombination of SH$^+$ is the dominant source of atomic sulfur in the warm part of the H/H$_2$ transition zone (Sternberg & Dalgarno 1995).

In our spectra survey, we detected several sulfur molecules. We calculated column densities and abundances of the well sampled lines (i. e., SO, HCS$^+$, H$_2$CS, CS, OCS and SO$^+$), and compare their abundances in Mon R2 with those found in different kind of regions. In the PDRs comparison, we can not identify any trend for these molecules. We found the highest SO abundance in Mon R2, while Orion Bar (PDR-peak) and NGC 7023 present abundances lower by a factor of 2-3. In the comparison with other sources, the PDRs present abundances much more lower than these sources, being the TMC-1 dark cloud the source that present abundances more similar to the abundances in PDRs (higher by an order of magnitude). The abundance of SO is three orders of magnitude larger in the L1157 shock than in PDRs. This molecule is associated with grain chemistry and use to be very abundant in environments associated with protostars, hot cores and shocks.

In the case of CS, we found the lower abundance in the NGC 7023 PDR and the highest in the Horsehead PDR. The MP2 position present higher CS abundance than IF position by a factor $\sim$ 2. The Orion Bar (PDR-peak) presents very similar CS abundance than IF, while the Horsehead PDR presents very similar CS abundance than MP2. Finally, the NGC 7023 PDR presents CS abundance lower than IF by a factor of 2-3. In the comparison with other sources we found that the PDRs present abundances very similar to the dark clouds. While the hot core presents abundances higher than PDRs by an order of magnitude, and the shock presents abundances higher than PDRs by two orders of magnitude. In the case of HCS$^+$, abundance measured are quite similar in the Mon R2 and the Horesehead PDRs. In the comparison with other sources we found that these PDRs present very similar abundances than Orion KL (hot core) and the dark cloud L134N, abundances lower by a order of magnitude than Orion KL (plateau) and TMC-1, and abundances lower by two orders of magnitude than the shock L1157. The HCS$^+$ abundance towards MP2 and IF, are very similar. In order to better confirm the IF and MP2 comparison, we calculate the [HCS$^+$]/[CS] ratio. We found that this ratio is higher in the IF than the MP2 position by a factor of 3. However, this ratio is uncertain because the CS lines are optically thick. Considering the ^{13}CS isotopologue observations and assuming ^{12}CS/^{13}CS= 50, we obtain that the [HCS$^+$]/[CS]$\sim$ 0.019 in the IF position and [HCS$^+$]/[CS]$\sim$ 0.013 in the MP2 position. Other important ratios are [SO$^+$]/[SO] and [CS]/[SO]. We found that these ratios are higher in the PDRs than in the other sources, this

is because these sources present higher abundances of SO than the PDRs.

The HCS^+ and CS are formed via reaction that involve CS^+. The CS^+ molecules is easily formed by $CH + S^+ \rightarrow CS^+ + H$, this reaction is followed by $CS^+ + H_2 \rightarrow HCS^+ + H$ and $HCS^+ + e \rightarrow CS + H$. This sequence is interrupted when the CS^+ is recombinated and when HCS^+ is photodissociated. The CS molecule is formed by reaction $HCS^+ + e \rightarrow CS + H$ and is removed by photodissociation and photoionization ($CS + \nu \rightarrow C + S$ and $CS + \nu \rightarrow CS^+ + e$). All these reactions produce CS, CS^+ and HCS^+ density peaks near the CH density peak.

In the case of the H_2CS and the OCS molecules, we did not find information for other PDRs. In the comparison of the H_2CS molecule with other sources we found that the PDRs present abundances very similar to L1157, while the hot core and the dark clouds present abundances higher than Mon R2 by a factor of 3-5. Finally, in the OCS molecule with other sources we found that the PDRs present abundances lower than the dark clouds by an order of magnitude and lower than the hot core and the shock by two orders of magnitude. This molecule is the main carrier of sulfur on grains and present high abundance in the protostars (van der Tak et al. 2003a).

In summary the most abundant molecule in PDRs is CS, this molecule present similar abundances in dark clouds and hot cores. However it is important to note that the sulfur molecules are much more abundant in the dark clouds, hot cores and the shock, this is because the main reservoir of sulfur in PDRs is in the form of S^+ and S. In particular, in Mon R2 the SO, CS and OCS molecules seems to be associated to the IRS 3, IRS 4 and to the CN clump (see Figure 6.9). While the H_2CS and HCS^+ emission seems to come from an outer layer.

6.5.2.4   Complex molecules

Complex organic molecules (COMs; e. g., CH_3OH, CH_3CN, CH_2CO, CH_3CHO, HCOOH, NH_2CHO, CH_3CCH, $HCOOCH_3$ and CH_3OCH_3), are widely observed in hot cores and hot corinos. The formation of these molecules is not fully understood. However, the most accepted scenario is that they form on the icy mantles when the grain temperature is >20 K. These complex molecules are released into the gas phase when dust grains are radiatively heated by the newly formed stars, increasing their temperature to ~100 K and producing the evaporation of their mantles. Ulterior warm gas-phase chemistry might also produce new molecules increasing the chemical complexity. However, the radiative heating mechanism is debated, as some observations suggest that

the COMs could be associated with shocks as well (see e. g., Mendoza et al. 2014; Codella et al. 2015). Several COMs (HCOOH, CH_2CO, CH_3CHO and CH_3CCH) have been observed in the Horsehead nebulae (Guzmán et al. 2014). These species present enhanced abundances in the PDR compared to the dense core, proving that photodesorption is also an efficient mechanism to release complex molecules into the gas-phase in far-UV illuminated regions. Moreover, Bacmann et al. (2012) detected COMs in a cold ($\sim$10 K) prestellar core. These observations challenged the current formation scenario of complex molecules on dust grains, because the diffusion reactions that lead to the formation of species are not efficient on dust grains with temperatures of $\sim$10 K, suggesting an alternative gas-phase formation path.

Within our blind spectral survey we have detected several COMs (CH_3OH, CH_3CN, CH_3CCH, H_2CCO, CH_2CO, HC_3N and HC_5N) in both, single pointing (see Figures B.15 to B.23) and OTF maps (see Figures B.39 to B.45). In addition to these molecules, we also detected H_2CO molecule. It is not a complex molecule, as it only has four atoms. However, it seems to be spatially correlated with COMs (e. g., CH_3OH and CH_3CN) and is thought that is formed in similar way that complex molecules. It is interesting to note that some sulfurated molecules, (e. g., SO, SO_2; see Section 6.3.4) present the same behavior. These molecules (COMs and sulfur-bearing molecules) are tracers of dense gas, and use to be associated with hot cores/corinos. Thus, their spatial distribution encourage us to think that might exist a compact hot cores/corinos associated with IRS 3 and IRS 4.

For our study of the dependence of the chemistry with the UV incident flux in PDRs, we looked for reported observations of some complex molecules (CH_3CN, CH_3OH, CH_3CCH, HNCO and H_2CO) in different regions. For these molecules (but HNCO), we only found information in the Horsehead PDR. The CH_3CN molecule seems to increase its abundance in the low-UV irradiated PDRs. The CH_3OH, CH_3CCH and H_2CO molecules decrease its abundance in the low-UV irradiated PDRs. The CH_3OH, CH_3CCH and H_2CO molecules present very similar abundances (between them) for the Mon R2 and the Horsehead PDRs. While the CH_3CN and the HNCO molecule present lower abundances than the other molecules (CH_3OH, CH_3CCH and H_2CO) by an order of magnitude. For the HNCO molecule, we did not found information in other sources, but present higher abundances in the MP2 than the IF position. Thus, HNCO seems to present higher abundances in the low-UV irradiated PDRs. However, it is important to note that this molecule use to be correlated with OCS and SiO (as shocks tracers), thus it is possible that our beam are recollecting emission from the clump at the north of the IRS 3 position. In the comparison with other sources we found that dark clouds present abundances of CH_3CN, CH_3OH and CH_3CCH molecules higher that

the PDRs by a factor of two, and that the other molecules (HNCO and H_2CO) present abundances higher than the PDRs by an order of magnitude. While, the hot core presents abundances higher that the PDRs by two (for CH_3OH and HNCO) and three (for CH_3CN) orders of magnitude. Finally the shock present COMs abundances much more higher than the PDRs, by two, three and four orders of magnitude for the H_2CO, HNCO and CH_3CN molecules, respectively. The HCNO and H_2CO abundances might indicate that there are mechanisms of formation in the gas phase that are not efficient in PDRs.

Complex molecules are rapidly destroyed by UV radiation. Assuming a typical photodissociation rate of 10^{-10} s^{-1}, their lifetime would be $>10^5$ yr (the dynamical time of this object assuming the expansion velocity of 1.0 km s^{-1} derived by Fuente et al. 2010 and Pilleri et al. 2012) only for $A_V > 10$ mag. Higher angular resolution observations are needed to determine whether these molecules comes from the center or the irradiated surface of dense clumps ($A_V > 10$ mag).

One problem to discern between different formation mechanisms is that a complete inventory of complex molecules in different environments is missing. Simple organic molecules such as H_2CO, CH_3OH and CH_3CN are quite ubiquitous in the ISM, but the detection of the most complex ones is restricted to only a few well known massive hot cores. High sensitivity surveys with deep integrations are required to detect this large compounds in different environments and to shed some light into their chemistry.

6.5.2.5 Hydrocardons

Small hydrocarbons, such as C_2H and $c-C_3H_2$, present a complex chemistry in which UV photons, grain-surface chemistry and time dependent effects contribute to determine their abundances. Pilleri et al. (2013a) studied the chemistry of the small hydrocarbons. We found that the emission of the small hydrocarbons show different spatial patterns. The ratio $N(c-C_3H_2)/N(C_2H)$ shows spatial variations up to a factor of a few, increasing from ~ 0.004 in the envelope to a maximum of ~ 0.015–0.029 towards the 8 μm emission peak.

In the comparison of hydrocarbons ($l-C_3H$, $c-C_3H_2$, C_2H and C_4H) within PDRs, we found that these molecules tend to increase their abundances in the low-UV irradiated PDRs, i.e., at higher G_0 fields, lower hydrocarbons abundances. This is in agreement with previous works (Pety et al. 2005; Ginard et al. 2012; Pilleri et al. 2012, 2013a). This trend seems to be followed by all hydrocarbons, but it is more evident for the $l-C_3H$ and $c-C_3H_2$ molecules. In Mon R2 (Pilleri et al. 2013a), Horsehead (Pety et al. 2005) and

in NGC 7023 (Pilleri et al. in prep.), these molecules present a clear spatial correlation. As was mentioned previously, C_2H and c-C_3H_2 are good low-UV illuminated PDR tracers, in particular the $N(c-C_3H_2)/N(C_2H)$ that becomes very important in these kind of regions. Gerin et al. (2011) developed a study of the correlation of these molecules in several line of sights in the diffuse medium. In low- to mild-UV irradiated PDRs (e. g., Horsehead and NGC 7023) the correlation between C_2H and c-C_3H_2, suggests a common origin. Several authors suggest that these molecules may form through non gas-phase processes such as the photo-destruction of larger PAHs (Pety et al. 2005; Ginard et al. 2012; Pilleri et al. 2012, 2013a). However new models (includes reactions with H_2 excited) presented by Cuadrado et al. (2015), suggest that the hydrocarbons could be formed primarily with reactions in the gas-phase in regions with high-UV fields.

In the comparison of the hydrocarbons with different kind of sources, we found that the shock (L1157) present higher abundances of hydrocarbons than PDRs by two (for C_4H) and three (for C_2H) orders of magnitude. While the dark clouds present similar abundances of hydrocarbons than PDRs. An exception is the C_4H abundance in TMC 1 that is higher than PDRs by an order of magnitude.

6.5.2.6 Nitrogenated species

Nitrogenated molecules are ubiquitous in the ISM. In particular the hydrogen cyanide (HCN) and hydrogen isocyanide (HNC), have been detected in diffuse clouds (Liszt & Lucas 2001a), dark clouds (Hirota et al. 1998), starless cores (Hily-Blant et al. 2010) and low- and high-mass star forming regions (Schilke et al. 1992; Godard et al. 2010). The typical abundance of HCN in molecular clouds is $\sim 10^{-9}$–10^{-8}, it can be as high as $\sim 10^{-5}$ in dense $(n(H_2) > 10^7$ cm$^{-3})$ and warm (> 400 K) PDRs and the planet-forming region of protoplanetary disks (Goicoechea et al. 2008; Fuente et al. 2010). In these regions, HCN becomes the most abundant molecule with CO, H_2O and C_2H_2. The full comprehension of the HCN and HNC chemistry is therefore of paramount importance in the study of the physics and chemistry of the interstellar gas. The HNC molecule is less stable than HCN. Steady state gas phase models predict an HNC abundance comparable to that of HCN at ~ 10 K. The HCN and HNC molecules form primarily via the dissociative recombination of HCNH$^+$ and the recombination branching ratio regulates their abundance ratio provided that they are protonated via reactions with ions, (H$^+$ and HCO$^+$; Churchwell et al. 1984). The Figure 6.30 present a scheme with the main synthetic routes for the formation of CN, HCN and HNC molecules.
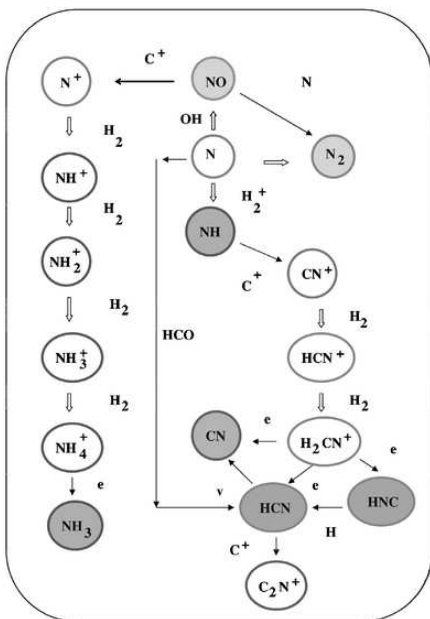
Figure 6.30: Scheme with the main synthetic routes for the formation of nitrogenated molecules (Maciá 2005).

At high temperatures, new paths to form HCN via neutral-neutral reactions produce [HCN]/[HNC] ratios larger than 1. Daniel et al. (2013) found [HCN]/[HNC]$\sim$ 1 in cold cores, [HCN]/[HNC]$\sim$ 1–3 in giant molecular clouds, and [HCN]/[HNC]$>>$ 1 in hot cores (Schilke et al. 1992), young Stellar Objects (YSOs; Jørgensen et al. 2004) and luminous galaxies (Baan et al. 2010). However, some exceptions show that the chemistry of the H-C-N system is not fully understood yet (Aalto et al. 2009; Hily-Blant et al. 2010).

Chemical models have been developed to progress in the comprehension of the N chemistry (Loison et al. 2014; Roueff et al. 2015). On basis of laboratory experiments, Wu et al. (2012) found that C_nN (n= 1–3), HNC, HCN (together with other molecules) are formed when a mix of solid N_2 and CH_4 are irradiated with UV photons. The release of these compounds to gas phase by thermal evaporation, photo-desorption or sputtering would produce an increase of the nitriles (CN, HCN and HNC) abundances. These improvements in the theoretical understanding of N chemistry make it worth to revisit the problem from the observational point of view.

In our spectral survey, we detected several nitrogenated molecules (i. e., HNC, HCN, HN^{13}C, H^{13}CN, N_2H^+, CN, etc.). In Mon R2, the HCN and HNC lines are optically thick. Moreover, the clear self-absorption features of these lines prevent from calculating reliable molecular abundances. Instead, we use

the rare isotopes HN^{13}C and H^{13}CN, considering ^{12}C/^{13}C ratio of 50. In the comparison with other sources, we look for HN^{13}C, H^{13}CN, N$_2$H$^+$, CN and HC$_3$N molecules. In the PDRs comparison these molecules present different trends. In the case of the HN^{13}C molecule, it seems to increase its abundance in the low-UV irradiated PDRs. However it is important to note that we only have an upper limit of the HN^{13}C abundances for the Orion PDR peak and NGC7026, thus it is not possible to set firm concutions. The H^{13}CN, N$_2$H$^+$ and HC$_3$N molecules present similar abundance in different UV irradiated PDRs. Finally, the CN molecule seems to decrease its abundance in the low-UV irradiated PDRs.

For the comparison with different kind of regions, we only found information for HN^{13}C and H^{13}CN molecules in the dark cloud TMC 1. We found that this source present higher abundances than PDRs by an order of magnitude. In the case of the N$_2$H$^+$ and CN molecules, we found information for the dark clouds (TMC 1 and L134N) and the shock (L1157). The dark clouds present similar CN abundances than the Orion Bar and MP2, but lower than IF by an order of magnitude. While the shock present abundances higher than IF by an order of magnitude. For the N$_2$H$^+$ molecule, dark clouds present similar abundances than the PDRs, while the L1157 shock present abundances higher than the PDRs by two orders of magnitude. In the case of the HC$_3$N molecule, the L134N dark cloud present abundances similar molecules than the PDRs, the hot core and the shock present higher abundances than PDRs by an order of magnitude, and the TMC 1 dark cloud present higher abundances than PDRs by two order of magnitude.

In Mon R2 we found a [HCN]/[HNC] ratio of ~ 11–20, it is higher than in the other PDRs, and in general is higher than in any observed PDR associated with galactic star forming regions. To try to explain the [HCN]/[HNC] value, we compare observational results with a state-of-art time-dependent chemical model (Roueff et al. 2013) considering different physical conditions (see Chapter 7). Even, taking into account similar physical conditions, it is difficult to explain the difference in the [HCN]/[HNC] ratio measured in the Orion Bar and Mon R2. This difference might be due to the large sensitivity of the [HCN]/[HNC] ratio to the time and molecular hydrogen density. Another possible interpretation is that the HCN and HNC emission (in Mon R2) is coming from the illuminated surface of the clumps (see Figure 6.31). Figure 6.31 shows comparison of the NeII, PAH (11.3μ m) and H$_2$ (9.7μ m) emission observed with Spitzer with integrated intensity maps (H^{13}CN, CN, C$_2$H and c-C$_3$H$_2$), H$_2$ emission is tracing the dense PDRs on the illuminated surfaces and the NeII emission is tracing the HII region.

Another important ratio is [CN]/[HCN]. The CN molecule is the product of photodissociation of HCN (see Figure 6.30). This ratio is higher in the Mon R2
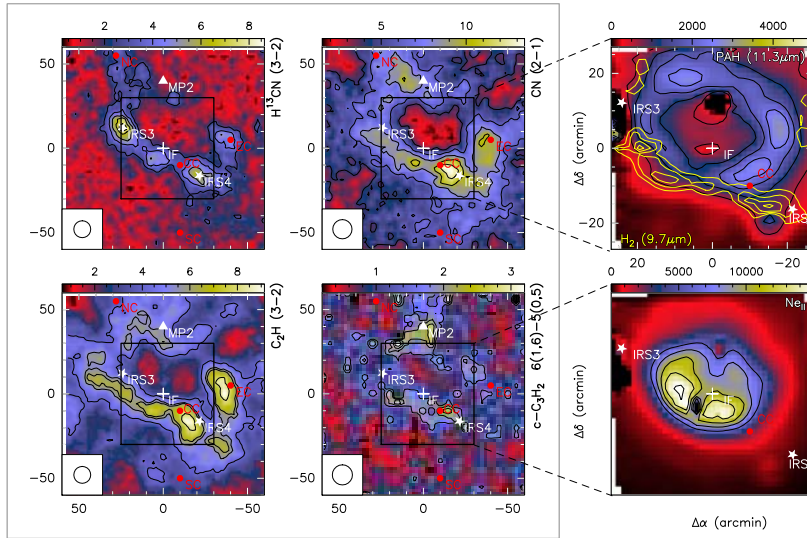
Figure 6.31: Comparison of the integrated intensity $H^{13}CN$, CN, C_2H and c-C_3H_2 maps with H_2 (9.7μ m), PAH (11.3μ m) and with NeII emission tracing the HII region (Berné et al. 2009).

than in the other PDRs. Fuente et al. (1993) detected a [CN]/[HCN] abundance ratio larger than unity in the north-west PDR of NGC 7023 and interpreted it as the consequence of the photodissociation of HCN into CN. Since then, the [CN]/[HCN] ratio has been successfully used as a PDR tracer in different environments (Ginard et al. 2012).

6.5.2.7   Other lines

In the previous sections were analyzed the characteristics presented by different species. However there are other species that was not mentioned yet, such as SiO, RRLs and CO (and its isotopologues). We perform the comparison of **$C^{18}O$** abundances in Mon R2 with PDRs and other sources. In the comparison with other sources we found that the $C^{18}O$ abundance tend to increase their abundances in the low-UV irradiated PDRs, i. e., at higher G_0 fields, lower $C^{18}O$ abundances. In the comparison with different kind of sources, we found that the PDRs present abundances similar to those found in the dark clouds and the shock, while the Hot core present higher abundances than the PDRs by a order of magnitude.

In the case of the **SiO** molecule (see Figure 6.32), we derived a column density of 2.8×10^{11}cm^{-2} towards the IF position. This is consistent with the up-
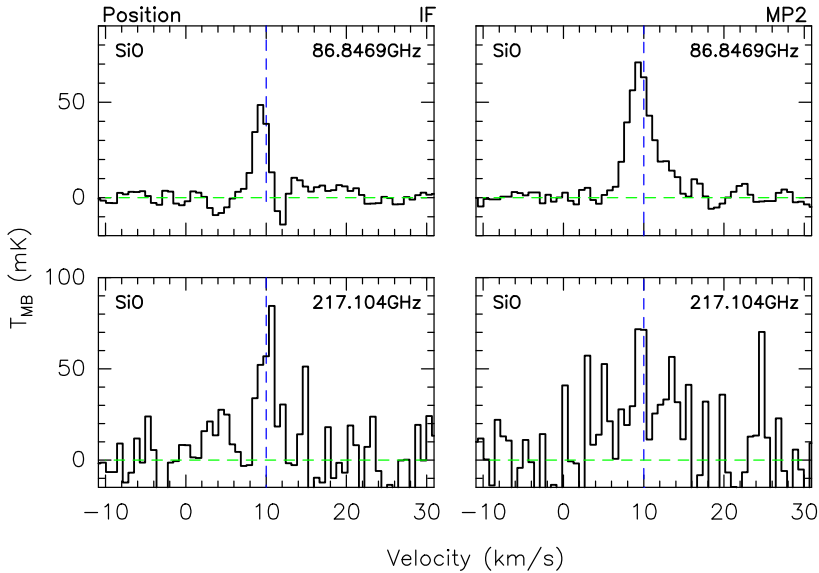
Figure 6.32: Spectra of the SiO molecule towards the IF (left) and MP2 (right) positions. The blue dashed line shows the velocity of 10 km s^{-1} relative to 86.846 and 217.104 GHz, respectively.

per limit of $< 3.0 \times 10^{11} \text{cm}^{-2}$ (an abundance of $2.6 \times 10^{-12} \text{cm}^{-2}$), derived by Ginard et al. (2012). We also detected SiO towards MP2 with an abundance of $7.2 \times 10^{-12} \text{cm}^{-2}$, which is lower than that determined by Schilke et al. (2001) towards the Orion Bar ($\sim 7 \times 10^{-11}$ in the IF) and consistent with that expected in PDRs. There is no hint of an enhanced SiO abundance produced by the shocks associated with the bipolar outflows or the expected shock front associated with the expansion of the UC HII. This is unsurprising since an expansion velocity of 1.0 km s^{-1}(Fuente et al. 2010; Pilleri et al. 2012) is not high enough to destroy the core of the silicates grains. This molecule presents its intensity peak in a clump at the north of the IRS 3 position, very close to MP2 (see Figure 6.33). The SiO molecule might be tracing a dense gas shock, and seems to be correlated with the sulfurated molecules (SO, SO$_2$ CS, C^{34}S and OCS). Being the OCS molecule the one that present more morphologic similarity with it (see panel E of the Figure 6.7).

Figure 6.33 shows the channel map at different velocities for SiO (2→1). In this Figure we can see emission at different velocities. The emission at ∼8 km s^{-1} seems to be the strongest one, and it is located between the IRS 3 and the CN position. A secondary peak emission is located at the offset (5$''$,-10$''$) offset, close to IF position. The emission of this molecule is surrounding the HII region. The transition from one component to another is smoothly, as velocity components coexist at different positions. Observations of larger maps with
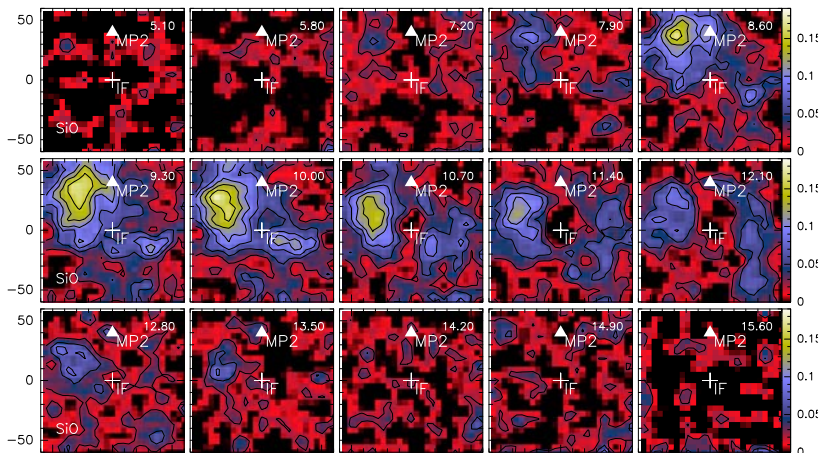
Figure 6.33: Channel maps of the SiO molecule at 86.846 GHz. The velocities for every channel are from 5.10 to 15.6 km s^{-1} by steps of 0.70 km s^{-1}. The peak intensity is ~ 50 mK.

higher angular resolution are needed to determine the origin of this molecule.

In the case of the **Radio Recombination Lines** (see Figure 6.34), we detected 56 hydrogen RRLs (of which ten are α lines, twelve are β lines, ten are γ lines, eight are δ lines, seven are ε lines, four are ζ lines and five are ψ lines) 11 helium lines (of which five are α lines, three are β lines and three are γ lines) and 10 carbon lines (of which five are α lines, three are β lines and two are γ lines). The HRRLs have their intensity peak clearly associated with the IF position, while the CRRLs have a very close to the MP2 position and a second one that is at the south of the IF position in the CC position (see panel B of the Figure 6.6). This indicates that the CRRLs are tracing the PDRs around the UC HII region.

In addition to the RRLs observed in the 30m telescope, we have observations in the JVLA of 15 hydrogen and carbon RRLs (between 98α to 117α), complemented with B-array, L-band observations of 22 more hydrogen and carbon RRLs (between 151α to 186α). The combination of these data with the 30m RRLs, will permit to constrain the physical properties of the UC HII region and the PDR, and lead to the solution of the unsolved issues in the kinematics of the HII region.

The observation of HRRLs together with the radio continuum emission of the ionized gas will permit to measure the line-to-continuum ratio that will be used to constrain the physical parameters (electron density and temperature) of the UC HII region (see e. g., Rodríguez et al. 2010). In addition, the observation of multiple HRRLs of different quantum numbers, at centimeter and
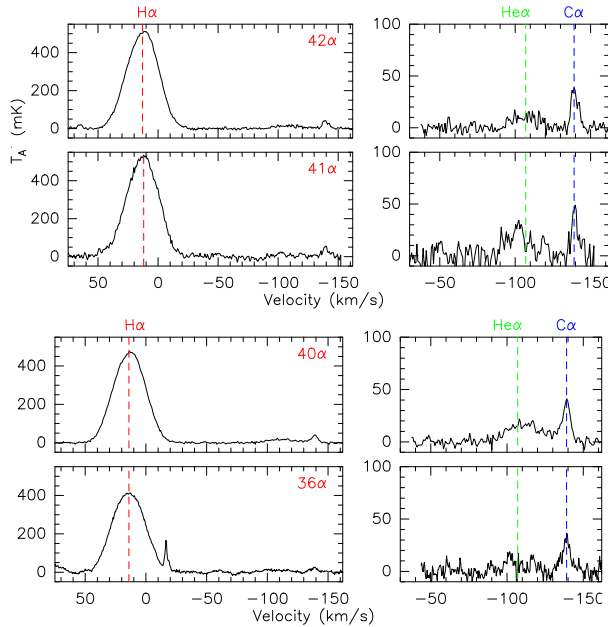
Figure 6.34: Millimeter radio recombination lines. The large panels show the clear detection of several hydrogen RRLs, while the small panels show a close-up view of the carbon (and helium) RRLs.

millimeter wavelengths, will be used to resolve the contributions from thermal, turbulent and pressure broadening in the observed linewidths, taking into account also the different beam sizes (see e.g., Keto et al. 2008). It is expected that RRLs with higher quantum numbers are more affected by pressure broadening than those RRLs observed in the millimeter domain. In the other hand, the observation of multiple CRRLs at different quantum numbers is necessary to determine the physical properties (electron density and temperature) of the PDR. This can be done by fitting the observed intensities of the CRRLs with a PDR model that solves the radiative transfer equation for non-LTE cases, assuming homogeneous 'slabs' of PDR material placed in front and back of the UC HII region.

These data will be used to evaluate the expansion of the UC HII region by comparing the gas pressure of the UC HII region and the PDR. A large pressure for the ionized gas will imply that the HII region is expanding, this scenarios have been proposed by Jaffe et al. (2003) to describe the kinematics observed in Mon R2. While the opposite will be a signature of confinement of the HII region, with the gas probably flowing along the walls, this scenarios have been proposed by Zhu et al. (2005). The total gas pressure will be measured from

the sum of the thermal and turbulent pressures, where the thermal pressure can be obtained via the density and temperature of the gas, and the turbulent pressure will be derived from the turbulent contribution to the measured linewidths (see e.g., Roshi et al. 2005a,b). This result of these data will be presented in Treviño-Morales et al. (in prep).

6.6 Summary

To study the chemical characteristics of Mon R2, we did an unbiased spectral line survey at 3, 2, 1 and 0.8 mm bands, towards the Ionization Front (IF) and a Molecular Peak (MP2) positions. We also did on-the-fly (OTF) maps observation covering the central ($2' \times 2'$ around IF) area of the region at 3 and 1 mm. We classify the different species in families and study how the properties change from one group to another. For all the families we did a comparison of our results with those presented in other works for other PDRs and objects associated with star formation activity. In the following we summarize the main results of this study.

- We found more than 65 different species (including isotopologues). The list includes typical PDR tracers, complex molecules, deuterated species, ionic species and radio recombination lines.

- Most of the species are detected in both positions, with some exceptions (e.g., HRRL and CCS associated with IF and MP2, respectively). Most of the detected lines present stronger intensities in MP2 with the exception of CO^+ and DCN. However, some species (e.g., CH_3OH, SO and CH_3CCH) are associated to the IRS 3 and IRS 4 position.

- Mon R2 presents a complex morphological and kinematical structure. We found that the detected lines present different velocity profiles towards the IF and MP2 positions. Most of the lines present two velocity components. A component at 10 km s^{-1} is detected at both positions and seems associated with the layer most exposed to the UV radiation from IRS 1. The component at 12 km s^{-1} is only detected toward the IF position and is related to the bulk of the molecular cloud with its maximum in the SW. The component at 8.5 km s^{-1} is only detected toward the MP2 position and is related to the second low-UV PDR (Ginard et al. 2012, and Pilleri et al. 2013a).

- Most of the mapped species present an arc structure emission, pointing to the SE and opened to the NW, surrounding the UC HII region. The size

of the arc structure depends on the species and the molecular transition. Lines at low frequencies present a structure more extended, while the lines at high frequencies, present a compact emission with dense clumps along the arc structure. This effect might be because of the different beam sizes of the maps and are excitation effects.

- The linewidth seems to depend on the family. The narrowest lines correspond to deuterated species followed by ions, S molecules, N molecules, COMs, hydrocarbons and CO. Transitions of a given family can be tracing gas at different locations within the IF and MP2 positions. A transition with higher E_{up} is likely to be excited in a different region than a transition of the same species with lower excitation energy. Lines with higher E_{up} are associated with narrower lines. This indicate that the turbulence or global motions are controlling the linewidths in Mon R2 and suggest that turbulence plays an important role in shaping the lines of some molecules (e.g., ions, S molecules and COM lines). Low energy transitions would be tracing outer layers from a colder and more turbulent envelope, while the emission of lines with higher energy seems to be associated with dense clumps.

- Abundances of most of the observed species are higher in MP2 than in IF. However, the DCN, $H^{13}CN$, CN, CF^+ and C_2H molecules present higher abundances in IF than in MP2. These molecules seems to be good tracers of extreme PDRs, with high G_0, and their high abundances allow to distinguish extreme PDRs from low-mid UV irradiated PDRs and dark clouds.

- We did a comparison of the molecular abundances in Mon R2 with those found in other PDRs (Orion Bar, NGC 7023 and Horsehead). We found that the $C^{18}O$, HCO^+, N_2H^+, SO, SO^+, HCS^+, CS, CH_3OH and CH_3CCH molecules present similar abundances for different G_0 environments. DCO^+, $l-C_3H^+$, CH_3CN, CF^+, $HN^{13}C$ and hydrocarbons tend to increase their abundances in the low-UV irradiated PDRs. While the CO^+ and CN molecular abundances seems to decrease in the low-UV PDRs.

- We did a comparison of the molecular abundances in Mon R2 with those found in objects associated with star formation activity (Orion KL, TMC 1, L134N and L1157). We found that most of the lines present lower abundances in PDRs that in other the sources. However there are some molecules (CS, C_2H and C_4H) that present similar abundances in PDRs than in dark clouds. While, CN presents higher abundances in PDRs than in dark clouds by an order of magnitude.

- In Mon R2 we found that the CO^+ emission is spatially correlated with the CII emission and seems to be surrounding the HII region. We found a molecular abundance of 5.95×10^{-11} in the IF position of Mon R2. This value is similar to the molecular abundance found in Orion Bar ($X = 6 \times 10^{-11}$; (Fuente et al. 2003)) and larger than those found in NGC 7023 ($X = 3 \times 10^{-11}$; Fuente et al. 2003) and in the Horsehead ($X < 5 \times 10^{-11}$; Goicoechea et al. 2009a). These abundances suggest that CO^+ is more abundant in the PDRs with high UV fields (with $G_0 > 10^3$).

- In Mon R2 we found a [HCN]/[HNC] ratio of $\sim$ 11–20, it is higher than in the other PDRs. Even, taking into account similar physical conditions, it is difficult to explain the difference in the [HCN]/[HNC] ratio measured in the Orion Bar and Mon R2. This difference might be due to the large sensitivity of the [HCN]/[HNC] ratio to the time and molecular hydrogen density. Another possible interpretation is that the HCN and HNC emission (in Mon R2) is coming from the illuminated surface of the clumps.

7

DEUTERIUM CHEMISTRY

This chapter presents a detailed study of the deuterated molecules and their corresponding hydrogenated species. The study is done on basis of observational results and their comparison with chemical models.

Contents

7.1 Deuteration and star formation

During the past decade, the chemistry of deuterium has become an important tool for understanding the formation of stars and planets. However, the deuteration processes are not fully understood yet, and important uncertainties remain in the interpretation of observational data. The cosmological ratio of the elemental abundances between deuterium and hydrogen (D/H) is $\sim$ 1–2$\times 10^{-5}$ (Roberts & Millar 2000; Linsky et al. 2006; Pety et al. 2007). However, higher abundances of deuterated molecules have been observed in many astrophysical environments, including cold dense cores (Guelin et al. 1982), mid-planes of circumstellar disks (van Dishoeck et al. 2003; Guilloteau et al. 2006) hot molecular cores (Hatchell et al. 1998), and even photon-dominated regions (PDRs; see Leurini et al. 2006). Several chemical pathways have been proposed to produce this deuterium enrichment.

Deuteration in the gas phase is driven by ion-molecule reactions in which deuterium and hydrogen atoms are exchanged. For a cold source with kinetic temperatures T_k=10−20 K, the dominant process is H_3^++HD$\rightleftharpoons$ H_2D^++H_2. This reaction proceeds left-to-right with an exothermicity of $\sim$232 K (Gerlich et al. 2002; Pagani et al. 2011, 2013) and is very rapid at low temperatures, raising the abundance ratio $[H_2D^+]/[H_3^+]$ to values much higher than 10^{-5} (see e. g., Caselli et al. 2003). The production of the deuterated ions of H_3^+ leads to high abundances of other deuterated species through secondary ion-molecule reactions. In addition to singly deuterated isotopologues, doubly and triply deuterated species such as NHD_2, ND_3, and D_2CO can be explained, at least partially, in terms of gas-phase synthesis (Gerin et al. 2006; Roueff et al. 2005). The deuteration via H_2D^+ becomes very inefficient when T_k is higher than 30 K. At temperatures T_k=30−50 K, CH_3^+ and $C_2H_2^+$ react rapidly with HD, leading to the ions CH_2D^+ and C_2HD^+ (Herbst et al. 1987; Millar et al. 1989) via the reactions CH_3+HD$\rightleftharpoons$ CH_2D^++H_2; $C_2H_2^+$+HD$\rightleftharpoons$ C_2HD^++H_2. The left-to-right exothermicities, $\sim$390 K (Asvany et al. 2004) and $\sim$550 K (Herbst et al. 1987), respectively, are considerably higher than for the reaction involving H_3^+. Detailed gas-phase models including deuterated species have been constructed using large networks of gas-phase reactions with both the steady-state and pseudo-time-dependent pictures showing that significant deuterium fraction enhancements can be detected at temperatures up to $T_k\sim$70 K (Roueff et al. 2005, 2007, 2013).

Deuterated isotopologues of methanol and formaldehyde have been detected in hot cores and corinos where T_k >100 K (see e. g., Parise et al. 2002, 2004; Fuente et al. 2005b). In these cases, the deuteration is thought to occur on grain surfaces. The deuterium and hydrogen atoms on the grain surface react

with complex molecules, leading to both deuterated and normal isotopologs (Tielens 1983; Stantcheva & Herbst 2003; Nagaoka et al. 2005). The deuterated compounds are released to the gas phase when the ice is evaporated, producing high abundances of the deuterated isotopologs of methanol and formaldehyde (Parise et al. 2002, 2004, 2006).

Observationally, deuteration has been widely studied in cold pre-stellar regions and hot corinos, and the results are interpreted on the basis of the deuteration pathways explained above. Much less studied is the deuteration in warm ($T_k = 30$–70 K) cores, in which the dust temperature is too high for the deuteration via H_2D^+ to proceed efficiently and it is not high enough for the icy mantles to evaporate. Parise et al. (2007) observed a sample of deuterated species toward a warm ($\sim$30 K) clump in the Orion Bar. They detected DCN, DCO$^+$ and HDCO and derived [XD]/[XH] fractions (hereafter D_{frac}) of 0.01, 0.0006 and 0.006 for HCN, HCO$^+$ and H_2CO, respectively. Because of the good agreement with chemical models (Roueff et al. 2005, 2007), they interpreted these high values of deuteration as the consequence of gas-phase chemistry driven by ion-molecule reactions with CH_2D^+ and C_2HD^+. Later, Guzmán et al. (2011) proved that photo-desorption from the grain mantles could also be an important formation mechanism in the PDRs for species like H_2CO, suggesting that the deuteration on grain surfaces could also contribute to the enhancement of the deuterium fraction in UV-irradiated regions. Species such as C_2D and DNC, which are not expected to form on grain surfaces, were not detected in the Orion Bar, and an extensive comparison with gas-phase models was not possible in this source. A complete observational study including more deuterated species is necessary to distinguish among the different deuteration mechanisms at work.

In this Chapter, we present an extensive study of deuterated compounds in the PDRs around the UC HII Mon R2. The list includes DCN, DNC, DCO$^+$, C_2D, HDCO, D_2CO, NH_2D, and N_2D^+. We focus our study on the chemistry toward the ionization front (hereafter IF) and the second PDR in MP2 position (see Figure 7.1) and discuss the implications of our observations. In Sections 7.2 and 7.3 the observational setup and results are described. In Section 7.4, we calculate column densities and abundances for each species, the comparison of the results between positions, and then, with different kind of regions. Sections 7.5 and 7.6 we discuss our main results, and finally, in Section 7.8 we summarize them.
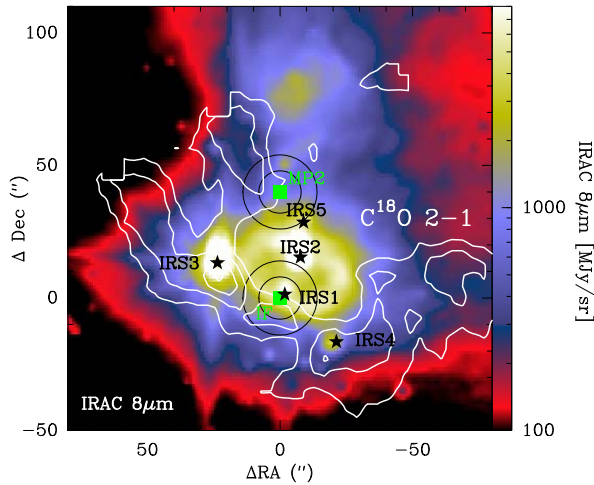
Figure 7.1: In colors, the *Spitzer*-IRAC 8 μm emission from small dust (Ginard et al. 2012). In contours, the integrated emission between 5 and 15 km s^{-1} of the C^{18}O (2-1) line (Pilleri et al. 2012). Green squares show the two positions analyzed in this Chapter. Black stars show the positions of the brightest infrared sources, following the nomenclature of Henning et al. (1992). The beams at 3 mm ($\sim$29$''$) and 2 mm ($\sim$16$''$) toward the IF and MP2 positions are drawn.

7.2   Observations and data reduction

The data presented in this Chapter are part of the data presented in the Chapter 6, focusing on the study of the deuterated molecules and their corresponding hydrogenated molecules. As was mentioned before, we use the main-beam brightness temperature ($T_{\rm MB}$) as intensity scale. Table C.1 summarize the observational parameters for the deuterated molecules and their corresponding hydrogenated species.

The data were reduced using the CLASS/GILDAS package[i] (Pety et al. 2005). Initial inspection of the data revealed a few single-channel spikes, platforming of individual FTS units, but otherwise clean baselines. To fix the spikes problem we flagged individual channels and filled them with white noise corresponding to the rms measured by a baseline fit. To correct for the platforming, a zero-order baseline was subtracted from each FTS sub-bands of each spectrum using a dedicated procedure provided by IRAM. In addition, a second-order baseline was needed for almost all the detected lines. All resulting spectra were smoothed to a velocity resolution of 0.65 km s^{-1}.

---

[i]See http://www.iram.fr/IRAMFR/GILDAS for more information about the GILDAS software.

7.3   Results

7.3.1   Observed spectra

Figures C.1–C.12 show the spectra of hydrogenated (Figs. C.1–C.8) and deuterated (Figs. C.9–C.12) species toward the IF and MP2 positions. The spectra show a different velocity profile toward the two positions. Two velocity components were found at each position for almost all the molecules. At the IF position we detect a velocity component at $\sim$10 km s^{-1} and a second one at $\sim$12 km s^{-1}; while at the MP2 position, the two velocity components correspond to $\sim$8 km s^{-1} and $\sim$10 km s^{-1}. The component at 10 km s^{-1} is detected at both positions and seems associated with the layer most exposed to the UV radiation from IRS 1 (see Section 7.3.3). The component at 12 km s^{-1} is found toward the IF position but it is related to the SW part of the molecular cloud. Finally, the component at 8.5 km s^{-1} is only detected toward the MP2 position and related to a low-UV irradiated PDR.

All the hydrogenated species are detected toward the two positions, and with a few exceptions, e. g., H^{13}CN at 259.011 GHz and HC^{15}N at 258.156 GHz, the lines are more intense at the MP2 than at the IF position (see Figure 7.2). The deuterated species DCN, DNC, DCO$^+$, C$_2$D, HDCO, and NH$_2$D are detected at both positions. We have detected N$_2$D$^+$ only toward the IF position, but the lack of detection toward the MP2 position is very likely due to the poor quality of our spectrum at this frequency. D$_2$CO is only detected toward the MP2 position.

Initial inspection of the spectra reveals some differences in the intensity line ratios between the two velocity components at each position. For instance, toward the IF position the H^{13}CN (3$\rightarrow$2) line is more intense at 10 km s^{-1}. However, the intensity of the HNC (1$\rightarrow$0) line is similar for the two components (see Figure 7.2). To study these differences quantitatively, we fitted a Gaussian to each velocity component using the CLASS software of the GILDAS package. Table C.2 and C.3 list the results of the Gaussian fits for the deuterated species, and Tables C.4 and C.5 list the Gaussian fits for the hydrogenated species.
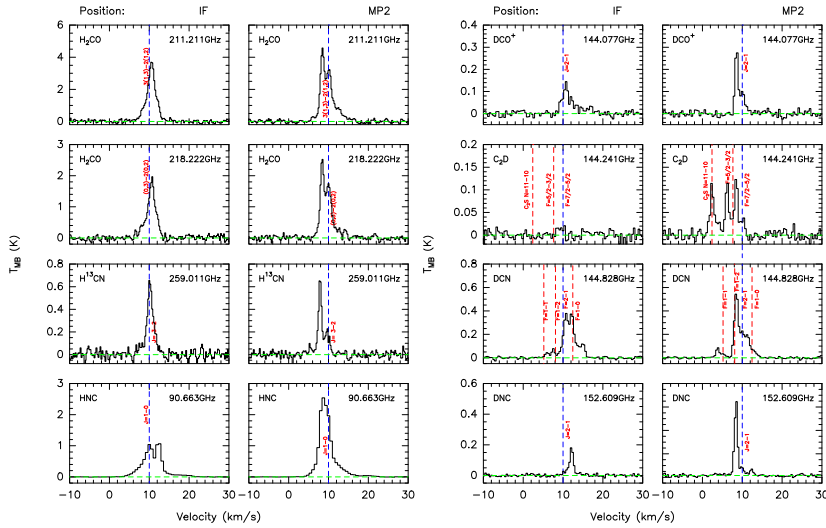
Figure 7.2: Observed spectra toward the IF and MP2 position. The blue dashed line shows the velocity of 10 km s^{-1} relative to the rest frequency of the transition. Two different velocity components can be distinguished at each position. *Left:* transitions of H_2CO (211.211 and 218.222 GHz), $H^{13}CN$ at 259.011 GHz and HNC at 90.663 GHz (from top to bottom) at the IF and MP2 positions. *Right:* observed spectra for the deuterated species DCO^+, C_2D, DCN and DNC transitions toward the IF and MP2 positions. The velocities are relative to the frequencies 144.077, 144.241, 144.828, and 152.609 GHz (from top to bottom).

7.3.2   Integrated intensity maps

The maps carried out with the IRAM-30m telescope allow us to characterize the spatial distribution of different deuterated and hydrogenated species in Mon R2. In Figure 7.3 we show the integrated line intensity maps of different transitions of DCO^+, DCN, DNC, H_2CO, C_2H, $HC^{15}N$, $H^{13}CN$, and $H^{13}CO^+$. All the maps have an angular resolution between 9″ and 11″, allowing a direct comparison. The spatial distribution of all these molecules is quite similar, consisting of an arc structure of $\sim$30″ in radius, pointing to the SE and opened to the NW, following the cometary shape of the nebula. H_2CO is a very abundant species in PDRs and therefore presents a very intense and extended structure. This molecule extends up to $\sim$ 1″ from the IF position and consists of three peaks at the positions $(-25″,+55″)$, $(+10″,-25″)$, and $(+20″,+35″)$ surrounded by faint emission. The C_2H molecule is also very abundant and presents an extended structure, with an intense peak toward the MP2 position. The emission of both, the H_2CO and C_2H molecules, come from the inner clumps and the envelope of the region, but seems to be dominated by a lower density envelope. The $HC^{15}N$, $H^{13}CN$, and $H^{13}CO^+$ molecules are less

abundant and their distributions are more compact, they present peaks at the offsets $(+10'',+25'')$, $(-10'',-10'')$, and $(-20'',+20'')$. The emission of DCN and DNC species are compact and intense, while the DCO^+ emission is weaker and more extended.

7.3.3 Spectral maps

Figure 7.4 shows the intensity maps at different velocities for DCN (3→2), DNC (3→2), $H^{13}CN$ (3→2), $HN^{13}C$ (3→2) and $H^{13}CO^+$ (3→2). In all the species we find the three velocity components described above. The emission at ~ 8 km s^{-1} is located in the NW, the gas emitting at ~ 10 km s^{-1} is surrounding the HII region, and the gas in the SW is at a velocity of ~ 12 km s^{-1} (see Figure 7.4). The transition from one component to another is abrupt and does not occur smoothly, as expected in the case of a global and coherent rotation. Moreover, two velocity components coexist at many positions, for example at the IF and MP2 positions. This suggests that the observed velocity behavior is the result of the superposition of three filaments around the expanding UC HII region or, alternatively, the existence of a twisted filament, with the gas at ~ 12 km s^{-1} and at ~ 8 km s^{-1} located at the front and the back of the UC HII region as observed from the Sun.

7.4 Analysis

7.4.1 Molecular column densities

To derive reliable column densities, we combined our 1mm maps with single-pointing observations obtained at 3 mm and 2 mm toward both the IF and MP2 positions. To do that, we convolved the 1mm maps to the angular resolution of the lower excitation transitions at 3 mm or 2 mm. The beam averaged column densities were calculated assuming that the emission comes from a layer with uniform physical conditions and using the rotational diagram technique as explained in Chapter 6. The areas derived from the Gaussian fitting (W) are listed in the Tables C.2–C.5. This approximation requires optically thin emission, we used the ^{13}C and ^{18}O isotopologs to calculate the column density of the hydrogenated species, assuming $[^{12}C]/[^{13}C]=50$ (Savage et al. 2002;
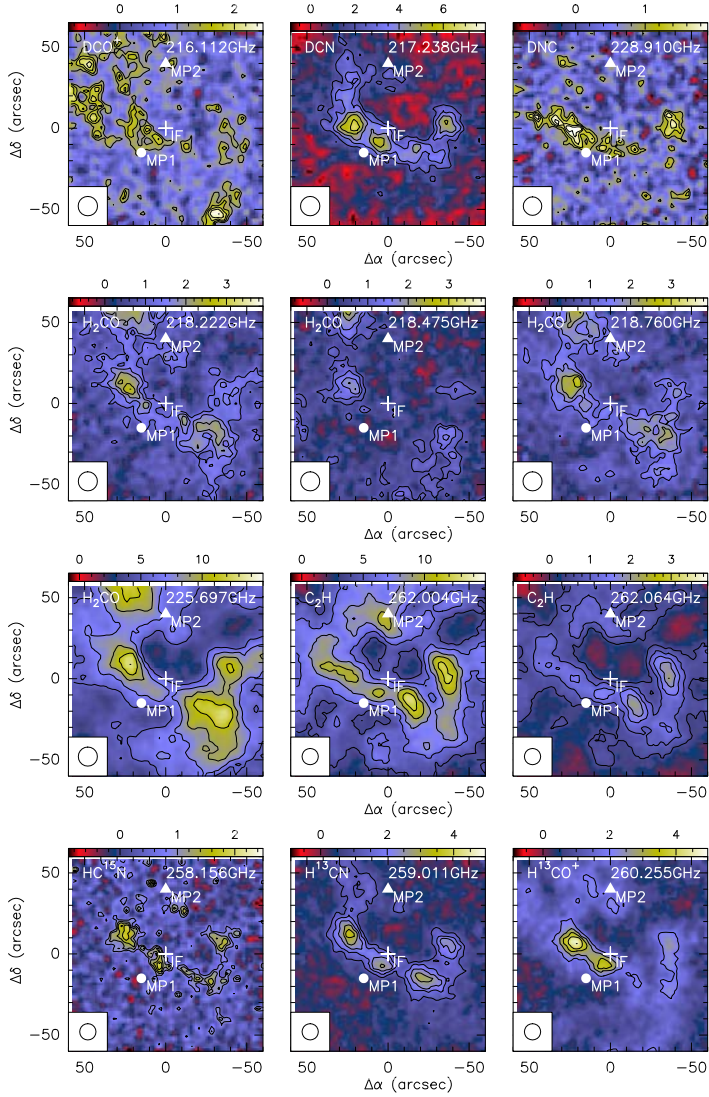
Figure 7.3: $2' \times 2'$ OTF maps of DCO$^+$ (at 216.112 GHz), DCN (at 217.238 GHz), DNC (at 228.910 GHz), H$_2$CO (218.222, 218.475, 218.760 and 225.697 GHz), C$_2$H (at 262.004 and 262.064 GHz), HC^{15}N (at 258.156 GHz), H^{13}CN (at 259.011 GHz) and H^{13}CO$^+$ (at 260.255 GHz). The cross marks the IF position, the triangle marks the MP2 position, and the circle shows the MP1 position at the offset (-15",15"). The contour levels are 40% to 100%, in steps of 15% of the peak intensity; ~ 2 km s^{-1} for DNC; ~ 3 km s^{-1} for DCO$^+$ and HC^{15}N; ~ 4 km s^{-1} for H$_2$CO at ~ 218.00 GHz; ~ 5 km s^{-1} for H^{13}CN and H^{13}CO$^+$; ~ 7 km s^{-1} for DCN; ~ 15 km s^{-1} for H$_2$CO and C$_2$H at ~ 262.00 GHz.
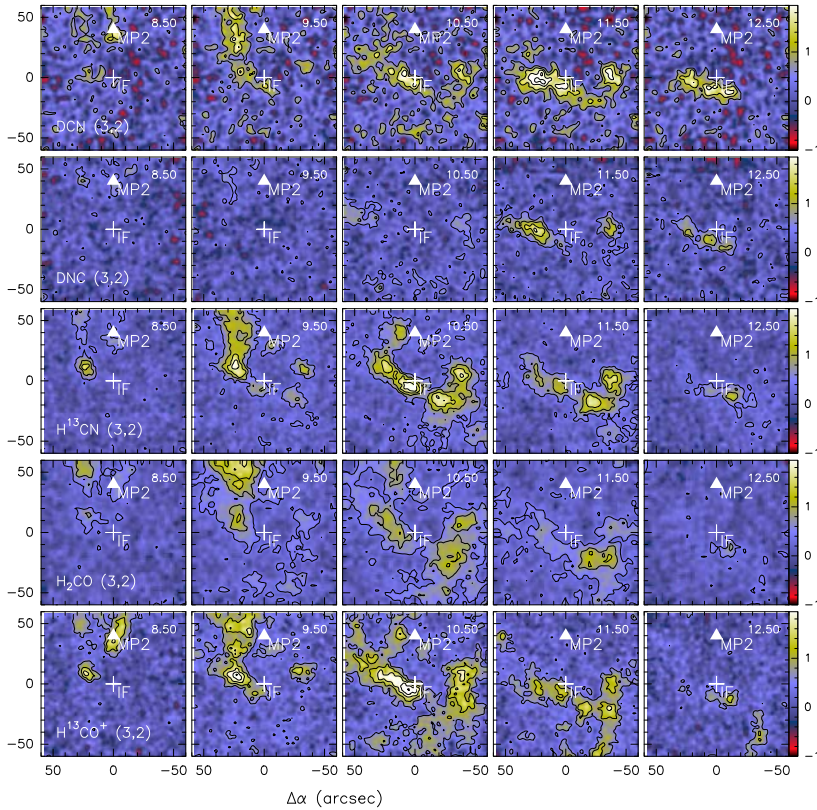
Figure 7.4: Channel maps for the molecules DCN at 216.112 GHz, DNC at 217.238 GHz, $H^{13}CN$ at 259.011 GHz, H_2CO at 218.960 GHz and $H^{13}CO^+$ at 260.255 GHz, from top to bottom. The velocities for every channel are 8.5, 9.5, 10.5, 11.5, and 12.5 km s^{-1} from left to right. The peak intensity is ~ 2 K km s^{-1} for each line.

Ginard et al. 2012) and $[^{16}O]/[^{18}O]=500$[ii] (Wilson & Rood 1994; Ginard et al. 2012). We assumed a beam filling factor of 1 for all the transitions, and the obtained values were averaged values within the beam of the lower energy transitions (at 3 mm or 2 mm, depending on the species).

Tables 7.1 and 7.2 show the results of the rotational diagrams. Rotation temperatures vary between ~ 10 K and ~ 40 K. These differences are due to the different dipole moments of the molecules ($\mu \sim 1-5$ Debye) and to the different spatial resolution of the lower energy transitions. For instance, the rotation temperature obtained from $H^{13}CN$ lines corresponds to a 29″ beam, while the rotational temperature of DCN corresponds to a 16″ beam. The 29″ beam encompasses a larger fraction of cold gas than the 16″ one, and the average

---

[ii]The values of the $[^{12}C]/[^{13}C]$ and $[^{16}O]/[^{18}O]$ ratios correspond to the galactocentric distance of Mon R2, i.e., ~ 9 Kpc.

rotation temperature is therefore lower (see Figure 7.3). This different spatial resolution is also the cause of the higher rotation temperature measured for the deuterated species of HNC compared with that of the ^{13}C isotopolog. Moreover, the high rotation temperatures found in DCN and DNC towards IF position confirm that the high deuterium fractions are associated with dense clumps around the HII region at temperatures $\sim$50 K instead of the cooler envelope. In the case of HCO$^+$, the rotation temperature is similar for the ^{13}C isotopolog and the deuterated species. This is consistent with the spatial distribution of DCO$^+$ (see Figure 7.3), where intense emission comes from the envelope. The rotation temperatures are similar for H$_2$CO and their related species. In this case, all the column densities of all the molecules are averaged over a $\sim$16$''$ beam. Similarly to DCN and DNC, the emission of this family of molecules comes mainly from the warm clumps around the HII region.

For some compounds, only one transition is detected. In these cases, we calculated the column density assuming a fixed value of the rotation temperature. For these cases we considered three rotational temperatures ($T_{\rm rot}$=10 K, $T_{\rm rot}$=19 K and T$_{\rm rot}$=38 K) and calculated the column density for every case. We found that the variation of a factor 2 in the rotation temperature affects the column density by less than a factor 2. For H$_2$^{13}CO and its deuterated compounds, HDCO and D$_2$CO, we used $T_{\rm rot}$=38 K (because this temperature is more similar to that derived from H$_2$CO) and for the remaining species we assumed $T_{\rm rot}$=19 K.

Table 7.3 shows the deuterium fractions ($D_{\rm frac}$(XH)=[XD]/[XH]) for each velocity component toward the IF and MP2 positions. When possible, we derived them by comparing the ^{13}C isotopolog with the deuterated species and assuming ^{12}C/^{13}C=50. Since the abundances and excitation conditions of both molecules are similar, the derived $D_{\rm frac}$ are not strongly affected by possible line opacity effects. As commented above, we have assumed a beam filling factor of 1 for the emission of all the studied transitions. To check the validity of our assumption and the possible impact on the estimated values of $D_{\rm frac}$, we produced maps of the [DCN (3$\rightarrow$2)]/[H^{13}CN (3$\rightarrow$2)] and [DCO$^+$ (3$\rightarrow$2)]/[H^{13}CO$^+$ (3$\rightarrow$2)] line-integrated intensity ratios (see Figures 7.5). These maps have an angular resolution of $\sim$ 10$''$ and provide information about the spatial variations of the values of $D_{\rm frac}$ in the region. For the two family of species, HCO$^+$ and HCN, the values of the line-integrated intensity ratio varies by less than a factor of 2 within the 29$''$ beam, suggesting that the beam-filling assumption is good enough and our values of $D_{\rm frac}$ are correct within the same factor. Toward the MP2 position, the deuterium fractions are highest toward the center, suggesting that the center is cooler and this PDR represents a clump illuminated from the outside, rather than one harboring a young star.

Table 7.1: Column densities and excitation temperatures for the deuterated molecules.

| Species | IF position | | | | MP2 position | | | |
| | 10.5 km s^{-1} | | 12 km s^{-1} | | 8.5 km s^{-1} | | 10 km s^{-1} | |
	$T_{\rm rot}$ (K)	N (10^{12} cm^{-2})	$T_{\rm rot}$ (K)	N (10^{12} cm^{-2})	$T_{\rm rot}$ (K)	N (10^{12} cm s^{-1})	$T_{\rm rot}$ (K)	N (10^{12} cm s^{-1})
C$_2$D	19^a	3.09 ± 1.09	. . .	. . .	20^{+12}_{-8}	$9.60^{+3.9}_{-2.00}$	19^a	3.0 ± 0.490
DCN	44^{+10}_{-10}	$2.09^{+0.75}_{-0.60}$	8^{+6}_{-2}	$0.67^{+0.10}_{-0.14}$	12^{+10}_{-5}	$1.40^{+0.20}_{-0.40}$	31^{+10}_{-10}	$0.40^{+0.020}_{-0.15}$
DNC	45^{+5}_{-5}	$0.091^{+0.070}_{-0.060}$	45^{+10}_{-5}	$0.434^{+0.050}_{-0.010}$	12^{+2}_{-2}	$0.46^{+0.020}_{-0.090}$	. . .	. . .
DCO$^+$	19^{+10}_{-10}	$0.111^{+0.087}_{-0.011}$	19^a	0.201 ± 0.90	31^{+10}_{-12}	$0.27^{+0.040}_{-0.095}$	12^{+10}_{-4}	$0.10^{+0.034}_{-0.013}$
D$_2$CO	38^a	< 23.70	38^a	< 15.00	38^a	2.50 ± 3.760	38^a	1.97 ± 3.113
HDCO	38^a	0.430 ± 0.126	38^a	0.745 ± 0.126	49^{+16}_{-8}	$2.30^{+1.46}_{-0.99}$	38	0.32 ± 0.055
NH$_2$D	19^a	0.389 ± 0.128	. . .	. . .	19^a	0.87 ± 0.129	19^a	0.36 ± 0.129
N$_2$D$^+$	. . .	. . .	19^a	0.065 ± 0.012	19^a	< 0.16	19	< 0.16

[a] Fixed temperature to calculate the column density.

Table 7.2: Column densities and excitation temperatures for the hydrogenated molecules.

| | IF position | | | | MP2 position | | | |
| | 10.5 km s^{-1} | | 12 km s^{-1} | | 8.5 km s^{-1} | | 10 km s^{-1} | |
Species	$T_{\rm rot}$ (K)	N (10^{12} cm^{-2})	$T_{\rm rot}$ (K)	N (10^{12} cm^{-2})	$T_{\rm rot}$ (K)	N (10^{12} cm s^{-1})	$T_{\rm rot}$ (K)	N (10^{12} cm s^{-1})
C$_2$H	30^{+34}_{-10}	158.00^{+50}_{-44}	8^{+1}_{-1}	455.00^{+145}_{-98}	12^{+3}_{-2}	120.00^{+38}_{-27}	19^{+9}_{-5}	213.00^{+69}_{-46}
H^{13}CN	14^{+5}_{-4}	$2.0^{+0.380}_{-0.380}$	6^{+5}_{-3}	$0.4015^{+0.180}_{-0.180}$	7^{+3}_{-2}	$1.00^{+0.200}_{-0.350}$	8^{+4}_{-2}	$2.50^{+0.300}_{-0.460}$
HC^{15}N	22^{+3}_{-3}	$0.38^{+0.060}_{-0.030}$	19^a	0.330 ± 0.042	9^{+1}_{-1}	$0.45^{+0.050}_{-0.030}$	12^{+3}_{-2}	$0.17^{+0.040}_{-0.030}$
HN^{13}C	19^a	0.176 ± 0.017	19^a	0.396 ± 0.057	12^{+1}_{-1}	$0.43^{+0.016}_{-0.020}$	6^{+2}_{-1}	$0.12^{+0.026}_{-0.030}$
H^{15}NC	19^a	0.057 ± 0.041	19^a	0.177 ± 0.058	13^{+2}_{-1}	$0.15^{+0.010}_{-0.040}$	$\ldots$	$\ldots$
H^{13}CO$^+$	16^{+1}_{-1}	$0.96^{+0.032}_{-0.030}$	25^{+11}_{-7}	$0.14^{+0.010}_{-0.036}$	12^{+1}_{-1}	$1.49^{+0.382}_{-0.410}$	9^{+1}_{-1}	$0.31^{+0.002}_{-0.002}$
HC^{18}O$^+$	16^{+2}_{-2}	$0.129^{+0.016}_{-0.015}$	$\ldots$	$\ldots$	13^{+1}_{-1}	$0.12^{+0.010}_{-0.014}$	$\ldots$	$\ldots$
H$_2$CO	55^{+20}_{-18}	$67.1^{+182.9}_{-13.72}$	$\ldots$	$\ldots$	44^{+17}_{-9}	$46.15^{+9.5}_{-7.20}$	39^{+14}_{-8}	$31.99^{+11.15}_{-8.40}$
H$_2$^{13}CO	38^a	< 3.10	38^a	< 2.84	38^a	2.74 ± 02.983	$\ldots$	$\ldots$
N$_2$H$^+$	$\ldots$	$\ldots$	19^a	4.28 ± 0.046	19^a	3.29 ± 0.054	$\ldots$	$\ldots$

^{a} Fixed temperature to calculate the column density.

Table 7.3: Fractional abundances ratios.

Species	IF		MP2	
	10.5 km s^{-1}	12 km s^{-1}	8.5 km s^{-1}	10 km s^{-1}
$\frac{H^{13}CN}{HN^{13}C}$	11.36	1.013	2.33	20.83
$\frac{HC^{15}N}{H^{15}NC}$	6.66	1.86	3.00	. . .
$\frac{H^{13}CN}{HC^{15}N}$	5.26	1.22	2.22	14.70
$\frac{DCN}{H^{13}CN\times 50}$	2.0×10^{-2}	3.3×10^{-2}	2.8×10^{-2}	0.32×10^{-2}
$\frac{DNC}{HN^{13}C\times 50}$	1.0×10^{-2}	2.2×10^{-2}	2.1×10^{-2}	. . .
$\frac{C_2D}{C_2H}$	1.9×10^{-2}	. . .	8×10^{-2}	1.4×10^{-2}
$\frac{HDCO}{H_2CO}$	0.63×10^{-2}	. . .	4.9×10^{-2}	1.0×10^{-2}
$\frac{HDCO}{H_2^{13}CO\times 50}$	$> 0.3 \times 10^{-2}$	$> 0.5 \times 10^{-2}$	1.7×10^{-2}	. . .
$\frac{DCO^+}{H^{13}CO^+\times 50}$	0.23×10^{-2}	2.8×10^{-2}	0.4×10^{-2}	0.6×10^{-2}
$\frac{DCO^+}{HC^{18}O^+\times 500}$	0.17×10^{-2}	. . .	0.45×10^{-2}	. . .
$\frac{D_2CO}{HDCO}$	< 55.89	< 20.13	1.08	6.15
$\frac{D_2CO}{H_2^{13}CO\times 50}$	< 0.152	< 0.010	0.018	. . .
$\frac{N_2D^+}{N_2H^+}$	. . .	0.015	< 0.05	. . .
$\frac{NH_2D}{NH_3}$*	0.39×10^{-2}	. . .	0.62×10^{-2}	. . .

*NH$_3$ column densities were taken from Montalban et al. 1990

The only exception is the [NH$_2$D]/[NH$_3$] ratio. To calculate the [NH$_2$D]/[NH$_3$] ratio, we took the NH$_3$ column density derived by Montalban et al. (1990) from the integrated intensity maps of the (1,1) and (2,2) lines observed with the Effelsberg-100m telescope. The beam of the NH$_3$ observations was $\sim$42″. Taking into account possible calibration differences between the two telescopes and that the pointing are not exactly the same, we consider that the uncertainty could be as large as a factor of $\sim$5.

7.4.2 Comparison of the IF and MP2 positions

In this Section we compare the chemistry of the different velocity components. The 10 km s^{-1} component presents similar abundance ratios toward the two positions, and these ratios are different from those in the 12 km s^{-1}
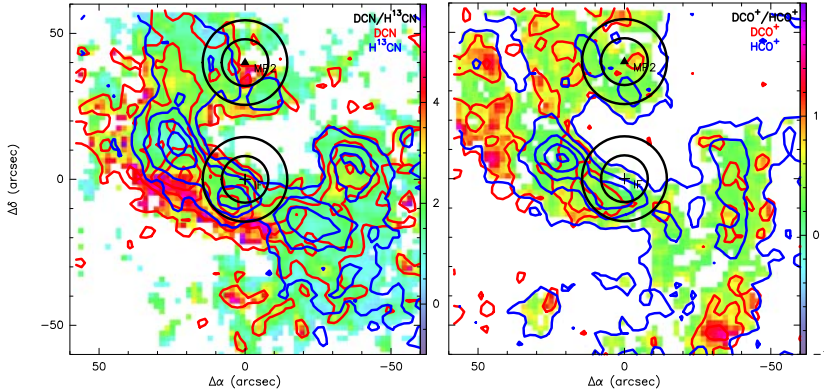
Figure 7.5: *Left:* The color scale shows the [DCN]/[HCN] ratio, the red contours mark the DCN emission at 216.112 GHz, the blue contours the H^{13}CN emission at 259.011 GHz. *Right:* The color scale shows the [DCO$^+$]/[HCO$^+$] ratio, the red contours mark the DCO$^+$ emission at 144.07728 GHz, the blue contours the H^{13}CO$^+$ emission at 260.255 GHz. The contour levels are 5 σ, 10 σ, 15 σ, 20 σ, and 25 σ. The black circles represent the 2 and 3mm beams.

and 8 km s^{-1} components. This component is characterized by a very high [HCN]/[HNC] abundance ratio, [HCN]/[HNC]$\sim$10. Regarding the spatial distribution, this component is surrounding the HII region and is the closest (in projected distance) from IRS 1. The 8 km s^{-1} and 12 km s^{-1} components present [HCN]/[HNC] ratios of about $\sim$1–3, characteristic of cold or moderately warm clouds. There are no important chemical differences between the 8 km s^{-1} and 12 km s^{-1} components, suggesting that they correspond to gas at a similar kinetic temperature, probably because they are equidistant from IRS 1.

The values of the deuterium fractions are quite similar for the three velocity components. Values around 0.01 are found for all of the observed species except for DCO$^+$ and N$_2$D$^+$ which present a deuterium fraction 10 times lower. The largest differences are found for C$_2$D, D_{frac}(C$_2$H) being $\sim$4 times higher in the 8 km s^{-1} component toward the MP2 position than in the others. The hydrogenated compound of this species is also very abundant in this component, suggesting that opacity effects could contribute to this higher value of the deuterium fraction. We would need to observe the ^{13}C isotopologue to obtain a more accurate value of D_{frac}(C$_2$H). The deuterated species N$_2$D$^+$ and D$_2$CO have only been detected in the more shielded components at 12.0 km s^{-1} (N$_2$D$^+$) and 8 km s^{-1} (D$_2$CO), again consistent with these velocity components being associated with colder gas, farther from IRS 1.

7.4.3   Comparison with other sources

Table 7.4 presents a comparison of the deuterium fractions measured in
Mon R2 with those in some prototypical objects. In particular, we com-
pare with a dark cloud (TMC 1; Turner 2001), a young protostellar ob-
ject (Barnard 1; Daniel et al. 2013; Gerin et al. 2001; Marcelino et al. 2005),
a hot corino (IRAS 16293-2422; Lis et al. 2001; Loinard et al. 2000, 2001;
Tiné et al. 2000), and a hot core (Orion KL; Turner 1990). While the
deuterium fractions of HCN and HNC are quite similar for all the sources
([DCN]/[HCN] $\sim$ [DNC]/[HNC] $\sim$ 0.01), the deuterium fractions of H_2CO,
HCO^+, N_2H^+ and NH_3 do change. Values of the [HDCO]/[H_2CO] ratio mea-
sured toward hot cores and hot corinos are found to be higher ($\sim$ 0.15) than
those in dark clouds ($\sim$ 0.05) and PDRs ($\sim$ 0.01). This indicates that the
deuteration of formaldehyde proceeds more efficiently on the grain surfaces
and the deuterated compounds are released into the gas phase when the dust
is heated to high temperatures (>100 K). The low values of D_{frac} found in
Mon R2 suggest that surface chemistry and subsequent ice evaporation is not
the main deuteration pathway, as in the case of hot corinos (see Figure 7.6).

In contrast, the [DCO^+]/[HCO^+] ratio is higher in dark clouds ($\sim$0.01) than in
hot cores ($\sim$0.007) and the PDRs associated with Mon R2 and the Orion Bar
($\sim$0.002). This result is also supported by the study carried out by Pety et al.
(2007) toward the Horsehead nebula. They found that the HCO^+ deuterium
fraction is larger than 2% in the cold dense core and lower than 0.1% in the
PDR. The deuteration of HCO^+ proceeds via ion molecule reactions in the gas
phase that are quite sensitive to the gas temperature. The behavior observed
in Figure 7.6 can be explained as the consequence of the increasing kinetic
temperature. Note that for IRAS 16293−2422, the observed DCO^+ more
likely comes from the envelope in which the hot corino is embedded.

For the other N-bearing molecules the [N_2D^+]/[N_2H^+] ratio is higher in the
very first evolutionary stages of the stellar formation, represented the by the
dark cloud TMC 1 ($\sim$0.08) and the young protostellar object Barnard 1 ($\sim$0.3),
than in more evolved objects such as Mon R2 ($\sim$0.03). This result agrees with
the recent study of Fontani et al. (2011), in which the authors derived the
N_2H^+ deuterium fraction for a large sample of massive young stellar objects.
They showed that the N_2H^+ deuteration is lower ($\sim$0.02) in objects associated
with UC HII regions (i. e., similar to our PDRs).

The situation is less clear for the NH_3. From the ratios listed in Table 7.4,
the [NH_2D]/[NH_3] ratio is similar in hot cores ($\sim$0.06), dark clouds ($\sim$0.02)
and PDRs ($\sim$0.06), but it reaches a value of $\sim$0.33 toward Barnard 1 (see
Table 7.4).

Table 7.4: DX/HX ratio comparison.

	Mon R2[a]		Ori Bar[b] (Clump 3)	TMC1[c]	Barnard 1[d]	IRAS 16293[e]	Ori KL[f]
	IF	MP2					
$H^{13}CN/HN^{13}C$	10	2.33	2.5	0.9–1.5	1.04	...	...
DCN/HCN	0.02	0.03	0.01	0.008	0.03	0.01	...
DNC/HNC	0.01	0.02	< 0.01	0.01	0.11	...	...
DCO^+/HCO^+	0.2×10^{-2}	0.5×10^{-2}	0.6×10^{-3}	0.01	...	0.7×10^{-2}	0.14
C_2D/C_2H	0.02	0.08	< 0.11	0.03–0.06	...	...	...
$HDCO/H_2CO$	0.01	0.01	0.6×10^{-2}	0.05	0.14	0.15	0.14
$D_2CO/HDCO$	< 38.47	1.00	...	...	0.40	0.3	0.021
N_2D^+/N_2H^+	0.015*	$< 5.0 \times 10^{-2}$	...	0.08	0.35	...	< 0.30
NH_2D/NH_3	0.39×10^{-2}	0.6×10^{-2}	...	0.02	0.63	...	0.062

*From the component at 12 km s^{-1}. [a]This work. [b]Parise et al. (2009). [c]Turner (2001). [d]Daniel et al. (2013); Gerin et al. (2001), Marcelino et al. (2005). [e]Lis et al. (2001); Loinard et al. (2000); Loinard et al. (2001); Tiné et al. (2000). [f]Turner (1990).
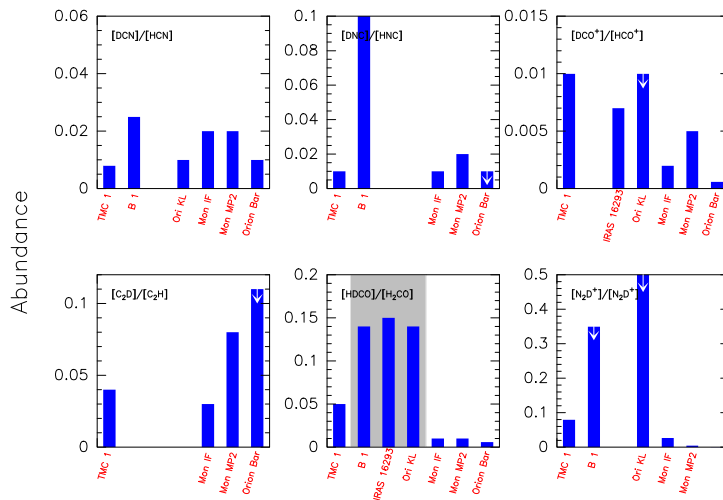
Figure 7.6: Histogram comparing the deuterium fractions in different regions: the dark cloud TMC 1, the young protostellar object Barnard 1, the hot corino IRAS $16293 - 2422$, the hot core Orion KL, and the PDRs in the Orion Bar and Mon R2. References for the plotted values are shown in Table 7.4.

The young protostellar object (YSO) Barnard 1 is a special object where the deuterium fractions are known to be higher than in other cold cores. Daniel et al. (2013) interpreted the high $[NH_2D]/[NH_3]$ ratio as a time evolution effect, the consequence of its peculiar evolutionary stage, with less than 500 yr after the formation of the early hydrostatic core. This interpretation was based on calculations by Aikawa et al. (2012).

Finally, because of their similarities, it is natural to compare our results in more detail with those in the Orion Bar (Parise et al. 2009). Both clouds are massive star-forming regions, and in the two cases the PDRs are located at the interface of the HII region and the molecular cloud. The only difference is that the Orion Bar is a more evolved HII region, and the densities and the radiation field in the PDR associated with it are a factor of ~10 lower than in Mon R2. Both regions have been observed using the IRAM-30m telescope, which avoids possible calibration problems when comparing lines observed with different telescopes, but the spatial scales are different because the distance to Mon R2 is twice than to Orion. The [DNC]/[HNC] ratio is ~0.01 in Mon R2, similar to the [DCN]/[HCN] ratio. Parise et al. (2009) did not detect DNC toward the so-called "clump 3" in the Orion Bar and derived an upper limit to the deuterium fraction of 0.01, which is still consistent with our results. The same can be said for C_2D which was not detected toward clump 3, with an upper limit of <0.11 for $D_{frac}(C_2H)$. For HDCO, we have the opposite behavior, the $D_{frac}(H_2CO)$ in the 10 km s^{-1} component is a factor of 2 lower than in the Orion Bar. Taking into account the uncertainties because of the beam-filling

factor and the different distance of Mon R2 and the Orion Bar from the Sun, we do not consider that this difference is significant. Summarizing, although the number of deuterated compounds detected in Mon R2 is higher than in the Orion Bar, the values of D_{frac} agree, within the uncertainties, in both PDRs.

The main difference between Mon R2 and Orion Bar is the different [HCN]/[HNC] ratio, which is a factor of $\sim$3 higher in the 10 km s^{-1} Mon R2 component. It is well known that the [HCN]/[HNC] ratio depends on the gas temperature with values $\sim$1 in cold clouds and higher in warm regions. This is consistent with the values shown in Table 7.4. The [H^{13}CN]/[HN^{13}C] ratio in the 10 km s^{-1} component in Mon R2 is significantly higher than in the Orion Bar, in line with the different gas kinetic temperatures ($\sim$30 K in the Orion Bar and $\sim$50 K in Mon R2). As discussed in Section 7.5, this difference can also be due to the different timescales and densities, because the Orion Bar is a more evolved object than Mon R2. Within Mon R2, the [H^{13}CN]/[HN^{13}C] ratio is higher in the 10 km s^{-1} component than in the PDR toward MP2 position. The lower rotation temperature of the HCN and the HNC isotopologs toward the MP2 position suggests that the gas kinetic temperature and/or density are lower at the latter.

7.5   Pseudo time dependent model

We compare our observational results with a pseudo-time-dependent gas phase chemical model. We chose this code to be consistent with previous conclusions by Pilleri et al. (2012) about early-time chemistry for small hydrocarbons.

One concern could be the influence of the UV radiation on the deuteration (not accounted by our pseudo-time-dependent model). The detection of the reactive ions CO$^+$ and HOC$^+$ (Rizzo et al. 2003) and the pure H$_2$ rotational lines (Berné et al. 2009) toward the IF position showed that the UV radiation is impinging into molecular gas at this region. We used the steady-state PDR Meudon code to investigate the influence of UV photons on the deuterium fractions. The UV photons do not influence the deuterium fractions directly, but through the increased gas temperature because of the UV heating. With high UV fields, $\sim 10^5$ Habing field, the gas temperatures are very high in the first layers of the PDR, and consequently, the deuterium fractions are very low. Since the deuteration via ion-molecule reactions is not efficient for temperatures >70 K, the emission of the deuterated species is more likely arising from shielded ($A_V \sim$8-10 mag) dense clumps where the gas kinetic temperature is $\sim$50 K.

Table 7.5: Model parameters.

Parameter		Model A	Model B	Model C	Model D
T_k	Temperature	50 K	50 K	50 K	50 K
n_H	H density	2×10^6 cm^{-3}	3×10^5 cm^{-3}	2×10^6 cm^{-3}	3×10^5 cm^{-3}
He/H	Helium abundance	0.1	0.1	0.1	0.1
O/H	Oxygen abundance	1.8×10^{-4}	1.8×10^{-4}	3.3×10^{-4}	3.3×10^{-4}
C/H	Carbon abundance	7.3×10^{-5}	7.3×10^{-5}	1.3×10^{-4}	1.3×10^{-4}
N/H	Nitrogen abundance	2.1×10^{-5}	2.1×10^{-5}	7.5×10^{-5}	7.5×10^{-5}
S/H	Sulfur abundance	8×10^{-8}	8×10^{-8}	1.8×10^{-5}	1.8×10^{-5}
Fe/H	Iron abundance	2×10^{-8}	2×10^{-8}	2×10^{-8}	2×10^{-8}
D/H	Deuterium fraction	1.5×10^{-5}	1.5×10^{-5}	1.5×10^{-5}	1.5×10^{-5}
ortho/para ratio	OPR	1×10^{-2}	1×10^{-2}	1×10^{-2}	1×10^{-2}
ζ	Cosmic ray ionization rate	5×10^{-17} s^{-1}	5×10^{-17} s^{-1}	5×10^{-17} s^{-1}	5×10^{-17} s^{-1}

Parameter		Model E		Model F	
		Phase 1	Phase 2[a]	Phase 1	Phase 2[b]
T_k	Temperature	15 K	50 K	15 K	50 K
n_H	H density	2×10^6 cm^{-3}	2×10^6 cm^{-3}	2×10^6 cm^{-3}	2×10^6 cm^{-3}
He/H	Helium abundance	0.1	...	0.1	...
O/H	Oxygen abundance	1.8×10^{-4}	...	1.8×10^{-4}	...
C/H	Carbon abundance	7.3×10^{-5}	...	7.3×10^{-5}	...
N/H	Nitrogen abundance	7.5×10^{-5}	...	7.5×10^{-5}	...
S/H	Sulfur abundance	2.1×10^{-5}	...	2.1×10^{-5}	...
Fe/H	Iron abundance	8×10^{-8}	...	8×10^{-8}	...
D/H	Deuterium fraction	2×10^{-8}	...	2×10^{-8}	...
ortho/para ratio	OPR	1×10^{-4}	1×10^{-2}	1×10^{-4}	1×10^{-2}
ζ	Cosmic ray ionization rate	5×10^{-17} s^{-1}	5×10^{-17} s^{-1}	5×10^{-17} s^{-1}	5×10^{-17} s^{-1}

[a] Initial abundances of phase 2 were taken from phase 1 at a time of 10^5 yr.
[b] Initial abundances of phase 2 were taken from phase 1 at a time of 10^6 yr.

At these moderate temperatures, 50 K, the high deuterium fractions measured toward Mon R2 cannot be explained with steady-state chemistry, and we needed to use a time-dependent code to account for them.

The chemical network used in our pseudo-time-dependent code includes recent modifications of the reaction rate coefficients involving nitrogen, as reported in Wakelam et al. (2013) following recent experiments on neutral-neutral reactions at low temperatures by Daranlot et al. (2011, 2013) and is based on previous studies by Roueff et al. (2005, 2013) and Pagani et al. (2011). The ortho/para ratio of H_2 (hereafter OPR) is considered as an input parameter that does not evolve with time, and influences the reverse reaction of the H_3^+ fractionation reaction with HD, where the presence of ortho H_2 reduces the endothermicity of the reaction by a significant amount of energy (170.5 K), and then the deuteration efficiency as first pointed out by Pagani et al. (1992). The contribution of para- and ortho-H_2 is also explicitly introduced in the initial step of nitrogen hydride chemistry, the $N^+ + H_2$ reaction, following the prescription by Dislaire et al. (2012). Within this approximation, the chemical network includes 214 species and 3307 chemical reactions.

To fit the observed abundance ratios we considered a grid of chemical models with the temperature fixed to 50 K and varied the density, initial conditions, and OPR. We considered two densities: $n_H = 3 \times 10^5$ cm^{-3} and $n_H = 2 \times 10^6$ cm^{-3}, which are representative of the range of densities measured in this region (Pilleri et al. 2012, 2013a). Table 7.5 shows the elemental abundances of the low (A and B) and high (C and D) metallicity models. In the model, the adsorption and evaporation of molecules on/from the grains are not included. When molecules such as H_2CO or CH_3OH evaporate, the elemental abundances of O and C in the gas phase increase. Given the limitation of our model, we mimicked this situation with the high metallicity case.

We also used a constant OPR because it is difficult to deal with the full ortho-para chemistry in the time-dependent code, but we considered different values of OPR: 0.3, that is the equilibrium value at $T_K = 50$ K, 1×10^{-2}, 1×10^{-3} and 1×10^{-4} for every model. The results of these models were quite similar for t<1 Myr. The OPR mainly affects the [NH$_2$D]/[NH$_3$] ratio. We can fit the observed values with both OPR= 1×10^{-2} and 0.3.

In Figure 7.7, we show the results of our pseudo-time-dependent model. The first important conclusion is that all the models give values of D$_{frac}$ and the [HCN]/[HNC] ratio very far from the observed ones in the steady state, i.e., for ages >1 Myr. We find, however, values closer to our observations for ages between 10^4 to a few 10^5 yr. Similarly, Pilleri et al. (2013a) showed that the abundances of small hydrocarbons are better explained with an early time
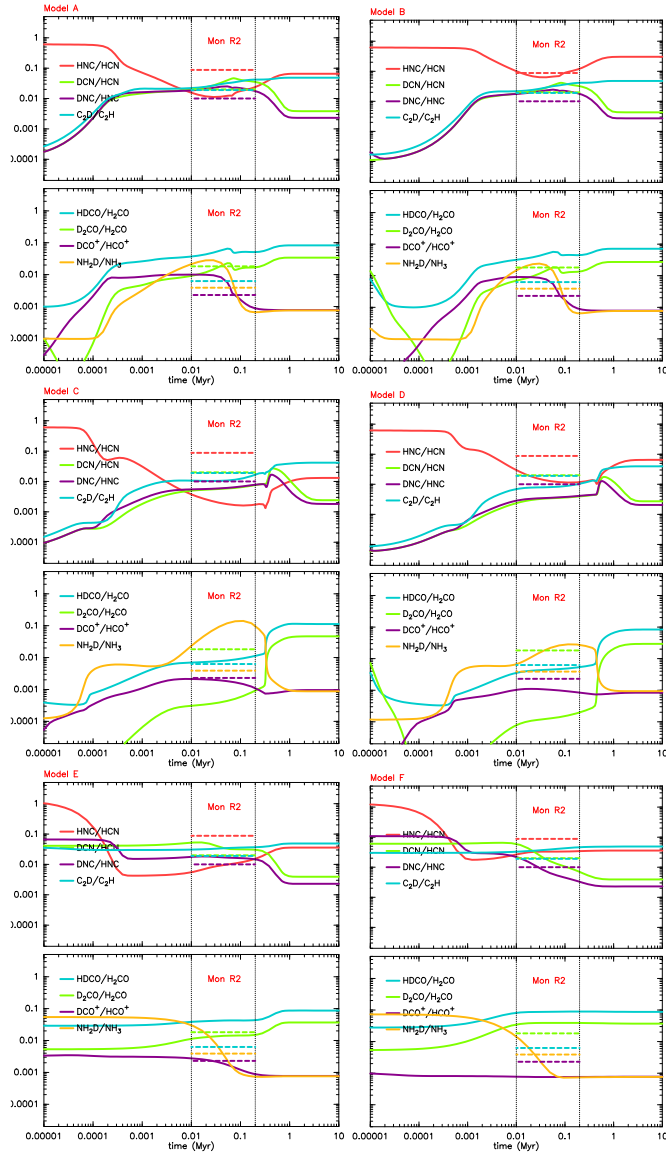
Figure 7.7: Chemical models considering a gas kinetic temperature of $T_k = 50$ K and OPR=1×10^{-2} (from model A to model D). Models E and F consider a temperature $T_k = 50$ K, but their initial abundances are obtained using another model (with $T_k = 15$ K and OPR=1×10^{-4}) at a time of 10^5 yr (for model E) and 10^6 yr (for model F). At the top part of the figures of every model, the red line represents the [HNC]/[HCN] ratio, the green represents the [DCN]/[HCN] ratio, the purple line shows the [DNC]/[HNC] ratio, and the blue line shows the [C_2D]/[C_2H] ratio. In the bottom part of the figures of every model, the blue line represents the [HDCO]/[H_2CO] ratio, the green line shows the [D_2CO]/[H_2CO] ratio, the purple line shows the [DCO^+]/[HCO^+] ratio, and the yellow one shows the [NH_2D]/[NH_3] ratio. The dashed lines shows the ratios of observational results toward Mon R2 for the 10.5 km s^{-1} component at the IF position.

chemistry. This age, from 10^4 to a few 10^5 yr, also agrees with the typical ages of UC HII regions.

The data suggest that the collapse and the chemical evolution of the region occur quickly. Nevertheless, it is important to stress the fact that our models (from A to D) consider that the temperature and the density of the region are constant when in fact these parameters are variable. As a consequence, our age estimate is illustrative and mainly proves that the deuterium chemistry is out of equilibrium. The second conclusion is that the observations cannot be fitted with the high metallicity case, i. e., the models C and D. This is also consistent with the emission from the deuterated molecules coming from shielded clumps where the temperature is not high enough to fully evaporate the ice mantles.

The deuterium fractions are not very dependent on the assumed density within the range considered in our grid of models (see Figure 7.7), but it is the [HCN]/[HNC] ratio. The variation of the [HCN]/[HNC] ratio comes from the differences in the atomic oxygen abundance. HCN does not react with O, whereas we allow the reaction; HNC+ O $\rightarrow$ NH + CO. This reaction was introduced by Pineau et al. (1990), but has never been measured in the laboratory, however. When O increases, the [HNC]/[HCN] ratio decreases drastically. The [HCN]/[HNC] ratio measured in the 10.5 km s^{-1} component is higher than the values predicted by high-metallicity models.

The [HCN]/[HNC] ratio is very dependent on the time and density (e. g., models A and B in Figure 7.7). Taking into account that we expect a density gradient in the region, we consider that there is a reasonable agreement with the low-metallicity case. This also suggests that the different [HCN]/[HNC] ratios measured among the three velocity components in Mon R2 could be the consequence of small differences in density and gas kinetic temperature.

The best fit is obtained model A (see Figure 7.7). As commented above, this model assumes constant density and temperature. To obtain a more realistic view, we ran two more models (E and F) consisting of two sequential phases at a different temperature and OPR: (i) in phase 1, we ran a model with $T =15$ K and OPR= 1×10^{-4} to simulate the cold collapse phase, (ii) then in phase 2, we ran a second model with $T =50$ K and OPR= 1×10^{-2}, using as input the abundances of the previous models for the ages 10^5 yr (model E) and 10^6 yr (model F). Table 7.5 summarizes the parameters of all the models. Model E is quite similar to model A, while model F is very different from the others. This model provides a good fit for the [C$_2$D]/[C$_2$H], [DNC]/[HNC], [DCN]/[HCN], and [NH$_2$D]/[NH$_3$] ratios, but it fails for the other observed ratios. The main disagreement of model F are the low absolute abundances of the molecular species, in particular, the C$_2$H abundance is two orders of
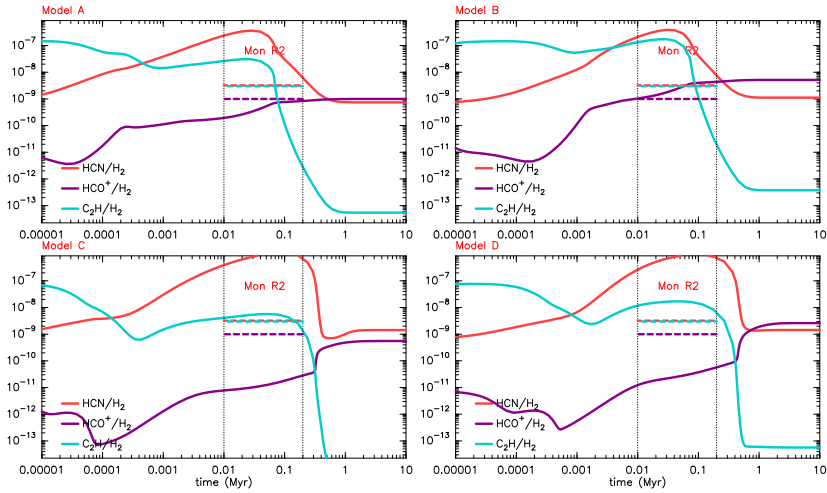
Figure 7.8: Molecular abundances relative to H_2 predicted by models A to D. The input parameters of these models are shown in Table 7.5. The red line represents the $[HCN]/[H_2]$ ratio, the purple line shows the $[HCO^+]/[H_2]$ ratio, and the blue line shows the $[C_2H]/[H_2]$ ratio. The dashed lines shows the ratios of observational results toward Mon R2 for the 10.5 km s^{-1} component at the IF position.

magnitude lower than those obtained for the other models. This indicates that the collapse phase prior to the formation of the UC H$_{II}$ region should be fast enough to avoid the gas to achieve the steady state (see also Pilleri et al. 2012). In model E, we assumed a constant density of 2×10^6 cm^{-3} during phase I. The chemical equilibrium is reached faster at higher densities. In a real time-dependent model in which the density is low at the beginning and increases with time, the collapse time could be longer than 0.1 Myr.

Figure 7.8 shows the abundances fits of HCN, HCO$^+$, and C$_2$H relative to H$_2$ considering a gas kinetic temperature of $T_k = 50$ K and OPR=1×10^{-2} (from model A to model D). The red line represents the $[HCN]/[H_2]$ ratio, the purple line shows the $[HCO^+]/[H_2]$ ratio, and the blue line shows the $[C_2H]/[H_2]$ ratio. The dashed lines shows the ratios of observational results toward Mon R2 for the 10.5 km s^{-1} component at the IF position. As commented above, the best fit is obtained for the model A and the worst one is the model D (see Figure 7.8). The observational abundances relative to H$_2$ were calculated considering $N(C^{18}O) = 7.3 \times 10^{15}$ cm^{-2} and X(C^{18}O)= 1.7×10^{-7} for the IF position (Ginard et al. 2012).

7.6 Is $D_{frac}(N_2H^+)$ as evolutionary indicator?

Deuteration has been used extensively as an evolutionary indicator in low-mass star-forming cores. $D_{frac}(N_2H^+)$ is found to be >0.1 in starless cores close to the onset of gravitational collapse (Crapsi et al. 2005). After the formation of the star, $D_{frac}(N_2H^+)$ decreases as the core evolves (Emprechtinger et al. 2009; Caselli et al. 2008). The reason is that D_{frac} and $N(H_2D^+)$ are very dependent on the gas temperature in the range 10 K−30 K in which the CO frozen out on the grain surfaces is released to the gas phase.

It is not clear, however, that $D_{frac}(N_2H^+)$ can be used as evolutionary indicator in the high-mass regime. Fontani et al. (2011) showed that the $D_{frac}(N_2H^+)$ in massive starless cores is ∼0.2, i.e., as high as in low-mass pre-stellar cores, but it drops to values of ∼0.04 for high-mass protostars and HII regions. Less clear results were obtained by Miettinen et al. (2011) toward a sample of IRDCs. They found that CO was not depleted in the observed sources and that $D_{frac}(N_2H^+)$ was lower than in low-mass starless cores (see Tan et al. 2013, for a recent review).

Our results for Mon R2 suggest that the deuterium fractions of molecules in massive protostars are dominated by ion-molecule reactions and are strongly time dependent. When the gas temperature increases over 20 K and the CO on the icy mantles is released to the gas phase, $D_{frac}(N_2H^+)$ decreases rapidly and reaches the steady-state value in less than 0.1 Myr. Even in the starless phase, if the core is turbulent and the temperature is higher than 20 K, $D_{frac}(N_2H^+)$ can reach values lower than those typical in the low-mass starless cores. The same is true for $D_{frac}(HCO^+)$. Other molecules such as HCN and HNC need about 1 Myr to reach the steady the state and could be useful to age massive protostellar cores and UC HII regions. $D_{frac}(H_2CO)$ in only useful to prove the hot core phase. Once all the icy mantles are evaporated, $D_{frac}(H_2CO)$ reaches the steady-state value in a short time.

7.7 CH_2D^+ molecule

The good agreement with chemical models suggest that high values of deuteration are consequence of gas-phase chemistry driven by ion-molecule reactions with CH_2D^+ and C_2HD^+ (Roueff et al. 2005, 2007). The CH_2D^+ molecule
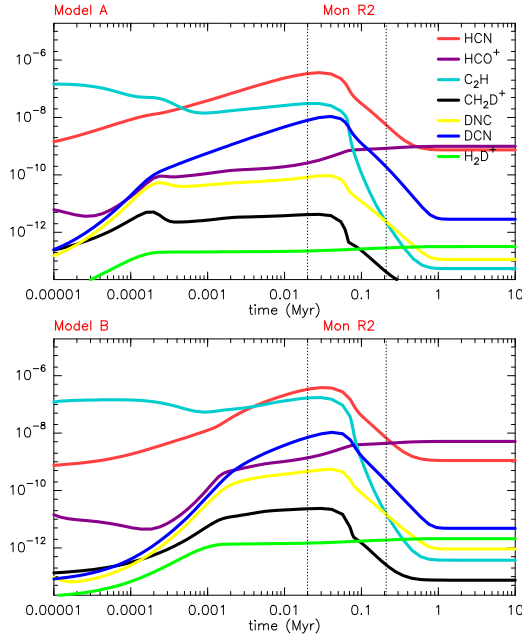
Figure 7.9: Molecular abundances fits of HCN (red line), HCO$^+$ (purple line), C$_2$H (cyan line), CH$_2$D$^+$ (black line), DNC (yellow line), DCN (blue line) and H$_2$D$^+$ (green line) predicted by models A (top) and B (bottom). The input parameters of these models are shown in Table 7.5.

plays an important role in the deuteration processes driven by the gas chemistry in regions with T>30 K, and is a benchmark of current gas phase models on deuteration. The detection of this molecule in the millimeter domain is quite difficult because it is weak and requires high temperatures to be excited. However, several attempts have been done in order to identify this interesting ion in the ISM. Recently, a possible first detection of CH$_2$D$^+$ was presented by Roueff et al. (2013). They observed CH$_2$D$^+$ at 201.753 GHz and 278.691 GHz toward Orion IRC2 using IRAM-30m telescope and the Caltech Submillimeter Observatory (CSO).

In our spectral survey we have a tentative detection of CH$_2$D$^+$ (at 278.691 GHz) toward the MP2 position (with 3–4σ). In order to confirm the molecule detection we carried deep single pointing observations in the IF and MP2 positions to observe the CH$_2$D$^+$ lines at 101.483 GHz and 201.753 GHz (see Section 6.2). We performed more than 30 h of observation at these frequencies, the lowest rms ($\sim$ 2 mK) was reached in the position MP2 for the 101.483 GHz line, with a spectral resolution of 1 km s^{-1}. However, we did not detect the CH$_2$D$^+$ molecule in any position. Figure 7.9 shows the abundances fits of HCN (red line), HCO$^+$ (purple line), C$_2$H (cyan line), CH$_2$D$^+$

Table 7.6: LTE estimation of the CH_2D^+ intensity.

Frequency (GHz)	Transition	$T_k = 10$ K T_b (mK)	$T_k = 25$ K T_b (mK)	$T_k = 50$ K T_b (mK)	rms (mK) IF	MP2
101.483	$11_{(6,5)} \rightarrow 11_{(6,6)}$	1.1×10^{-5}	3.6×10^{-3}	1.3×10^{-2}	3	2
201.753	$2_{(1,1)} \rightarrow 2_{(1,2)}$	2.5×10^{-2}	1.1×10^{-1}	1.1×10^{-1}	5	3
278.691	$1_{(0,1)} \rightarrow 0_{(0,0)}$	3.2×10^{-1}	2.7×10^{-1}	1.3×10^{-1}	–	5

(black line), DNC (yellow line), DCN (blue line) and H_2D^+ (green line), for the Model A (top) and Model B (bottom). Our chemical models predicts that CH_2D^+ abundance is an order of magnitude lower than the DNC abundance (see Figure 7.9). For example, at $t \sim 1$ Myr the DNC abundance is 0.114×10^{-12} (Model A) and 0.926×10^{-12} (Model B), while the CH_2D^+ abundances is 0.107×10^{-13} (Model A) and 0.757×10^{-13} (Model B). Considering the DNC column densities and a OPR=3 for CH_2D^+ (Roueff et al. 2013), we derived a column density of $N = 3.9 \times 10^{-10}$ (for the ortho lines) and $N = 1.3 \times 10^{10}$ (for the para lines). On base of these column densities, and assuming a linewidth of 1 km s^{-1}, we estimated the line intensities (T_b) of CH_2D^+ using the MADEX code (Cernicharo 2012) in a LTE regimen. Table 7.6 lists the derived line intensities for $T_k = 10$ K, $T_k = 25$ K and $T_k = 50$ K.

The no detection of the CH_2D^+ molecule in the Mon R2 region, is consistent with the predictions of our model. However, we decided to try to detect it as the model could be wrong by a factor of few that might affect our results. Moreover, we had a previous tentative line that encouraged us to observe it. It is important to note that the calculation of the lines intensity was done on basis of the DNC column density for a beam sizes of 16″. In the case that the emission come from a very dense compact clump, we could be degrading the emission, and thus, underestimating the column density. Observations with better spatial and spectral resolution might help to the detection of this ion. Until now the best tentative detection was observed in Orion IRC2 by Roueff et al. (2013).

7.8 Summary

We have determined the values of D_{frac} for a large sample of molecules (C_2H, HCN, HNC, HCO$^+$, H_2CO, N_2H^+, and NH$_3$) toward the PDRs IF and MP2 position, around the UC Hɪɪ region Mon R2. Our results can be summarized as follows:

- On the basis of the comparison of our observational results with those found in other sources, and with a gas phase model, we found that the deuteration in Mon R2 proceeds from the gas-phase via CH_2D^+ and C_2HD^+ reactions.

- Our observations show that Mon R2 presents a complex morphological and kinematical structure. We detected two velocity components toward the IF and MP2 positions. The component at 10 km s^{-1} is detected at both positions and seems associated with the layer most exposed to the UV radiation from IRS 1. The component at 12 km s^{-1} is only detected toward the IF position and is related to the bulk of the molecular cloud with its maximum in the SW. The component at 8.5 km s^{-1} is only detected toward the MP2 position and is related to the second low-UV PDR described by Ginard et al. (2012) and Pilleri et al. (2013a).

- We have determined the deuterium fraction (D_{frac}) for a large sample of molecules (C_2H, HCN, HNC, HCO^+, H_2CO, N_2H^+, and NH_3) toward the PDRs IF and MP2 position. There are no important differences between the values of D_{frac} toward the two PDRs. This is interpreted in the scenario of the deuterated compounds coming from dense and warm clumps with gas kinetic temperatures of 50 K, instead from the most exposed PDR layers. Values of D_{frac} of $\sim$0.01 are found for HNC, HCN, C_2H and H_2CO, and $<$0.001 for HCO^+, N_2H^+, and NH_3. These values are consistent with the predictions of the gas-phase model at an early time, $\sim$0.1 Myr. This time is consistent with the ages estimated for UC HII regions on the basis of statistical studies.

- The deuterium chemistry is a good chemical clock in both the low-mass and high-mass regime. However, the values of $D_{\mathrm{frac}}(N_2H^+)$ and $D_{\mathrm{frac}}(HCO^+)$ cannot provide a good estimate of the evolutionary stage of massive protostar regions because this abundance ratio reaches the steady-state value on a short scale time after all the CO is released from the grains into the gas phase. We need to use the values of D_{frac} for different molecules (e. g., HCN, HNC and C_2H) with longer chemical scales time to provide accurate age estimates.

- Using MADEX code (Cernicharo 2012), we derived CH_2D^+ lines intensity from abundances predicted in the chemical models. Being CH_2D^+ abundances lower that the DNC abundances by an order of magnitude. We found that the no detection of the CH_2D^+ molecule in the Mon R2 region, is consistent with the predictions of the model. However, observations with better spatial and spectral resolution might help to the detection of this ion.

Part III

GENERAL CONCLUSIONS

8

GENERAL CONCLUSIONS AND FUTURE WORK

In this chapter we summarize the main conclusions of this work. It also contains its perspectives and the future work.

Contents

8.1   General conclusions

The high-mass star forming region Mon R2, located at a distance of 830 pc, is the most active site of star formation in the Monoceros molecular cloud. Mon R2 presents a complex filamentary structure converging into the central area or hub. A cluster of recently formed high-mass stars is located at the junction of this filamentary structure and they had driven an UC HII region, surrounded by a series of PDRs with different physical conditions. Due to its characteristics, Mon R2 is an ideal target to study the dynamics/kinematics in a high-mass star forming region, as well as to study the physical and chemical conditions of PDRs that are irradiated with UV fields of different strengths.

The main objective of this Thesis is to characterize the chemistry and dynamics of the Mon R2 region. **To study the dynamics/kinematics in the region**, we performed large-scale maps covering a field of view of 163.5 arcmin^2 at 3 mm, around the central cluster. The main observed species are ^{13}CO, C^{18}O, HCN, N$_2$H$^+$ and HC$_3$N. In the following we summarize the main results of this study.

   i) The ^{13}CO, C^{18}O, HNC and N$_2$H$^+$ emission reveals a filamentary structure that extends in all directions, beyond the surveyed area. The detection of faint emission of nitrogenated molecules along the filaments shows that dense gas ($\sim 10^5$ cm^{-3}) is associated with the bones of the filaments.

   ii) The area around IRS 1 ($4' \times 4'$), is bright in all the species and their emission appears in an arc structure surrounding the infrared stars. The ^{13}CO and C^{18}O intensity peaks are located to the East and west of the cluster, while the nitrogenated species present a bright peak at south of the cluster, where there is no evidence of CO emission. This indicates different chemical and physical properties in the region.

   iii) Thirteen filaments (F1, F2, F3, F4, F5, F6, F7, F8, F9, F10-10A, F11, F12 and F13) have been identified in different tracers, as velocity-coherent elongated structures that spatially coincide with the continuum filaments detected with Herschel. We found velocity gradients along the filaments that correspond to mass accretion rates of about 10^{-4}–10^{-3} $M_\odot$ yr^{-1}.

   iv) All the filaments (except for F7) present evidence of fragmentation as the $M/L > (M/L)_{\mathrm{crit}}$ by a factor of 1.1–6. The fragmentation is confirmed by the channels maps in some of the filaments (F1, F5, F9, F10 and

F13). If the fragments will or not form stars, is something that we can not confirm with the current data and analysis. However, assuming a typical distance of the fragments with respect to the hub of about 1 pc and a velocity gradient of about $1 \, \mathrm{km \, s^{-1}}$, the timescale for the fragments to move to the hub is about 10^6 yr. This timescale is comparable to the typical timescale of the formation of low-mass stars, this indicates that some cores could start to be formed in the filaments but be dragged to the hub before they form stars.

v) We constructed a schematic view of the filamentary structure in Mon R2. We found that the filaments F2 to F6 are placed behind the hub (blue shifted), being F6 the less blue shifted and F3 is the most blue shifted filament. The filaments F1 and F8 to F13 are placed in front of the hub (red shifted), being F1 the less red shifted and F11 the most red shifted filament. Finally, the filament F7 seems to be placed in the plane of the sky.

vi) The filaments seem to fall down following a spiral pattern towards the UC HII region. This supports the idea of a young UC HII region just beginning to expand and break out of the dense filamentary hub where it was formed, with material still collapsing inward along the filaments.

vii) Physical properties of the filaments in Mon R2 resemble those found in DR21 (Hennemann et al. 2012), with gravitationally unstable structures that will fragment and form cores and protostars. These kind of filaments differ to those found in other star forming regions like Taurus or Aquila (Goldsmith et al. 2008; André et al. 2010), where the striations and sub-filaments are less massive and more stable.

To study the chemical characteristics of the region, we did an unbiased spectral line survey covering a broad frequency range in the bands 3, 2, 1 and 0.8 mm, towards the PDRs found around the UC HII region in Mon R2. We classify the different species in families and study how the properties change from one group to another. For all the families we did a comparison of our results with those presented in other works for different sources. In the following we summarize the main results of this study.

i) We found more than 65 different species, including typical PDR tracers, complex molecules, deuterated species, ionic species and radio recombination lines.

ii) Our observations show that Mon R2 presents a complex morphological and kinematical structure. We found that the detected lines present different velocity profiles towards the IF and MP2 positions. Most of the lines present two velocity components. A component at $10 \, \mathrm{km \, s^{-1}}$

is detected at both positions and seems associated with the layer most exposed to the UV radiation from IRS 1. The component at 12 km s^{-1} is only detected toward the IF position and is related to the bulk of the molecular cloud with its maximum in the SW. The component at 8.5 km s^{-1} is only detected toward the MP2 position and is related to the second low-UV PDR (Ginard et al. 2012, and Pilleri et al. 2013a).

iii) Most of the mapped species present an arc structure emission, pointing to the SE and opened to the NW, surrounding the UC HII region. The size of the arc structure depends on the species and the molecular transition. Lines at low frequencies present a structure more extended, while the lines at high frequencies, present a compact emission with dense clumps along the arc structure. This effect might be because of the different beam sizes of the maps. However, there are excitation effects that are affecting the morphology of the emission too.

iv) The linewidths of the detected species seem to depend on their family. The narrowest lines correspond to deuterated species followed by ions, S molecules, N molecules, COMs, hydrocarbons and CO species. Transitions of a given family can be tracing gas at different locations towards the IF and MP2 positions. A transition with higher E_{up} is likely to be excited in a different region than a transition of the same species with lower excitation energy. Lines with higher E_{up} are associated with narrower lines. This indicates that the turbulence or global motions are controlling the linewidths in Mon R2 and suggest that turbulence plays an important role in shaping the lines of some molecules (e.g., ions, S molecules and COM lines). Low energy transitions would be tracing outer layers from a colder and more turbulent envelope, while the emission of lines with higher energy seems to be associated with dense clumps.

v) Abundances of most of the observed species are higher in MP2 than in IF. However, DCN, H^{13}CN, CN, CF$^+$, CO$^+$ and C$_2$H present higher abundances in IF than in MP2. These molecules seem to be good tracers of extreme PDRs, with high G_0, and their high abundances allow to distinguish extreme PDRs from low-mid UV irradiated PDRs and dark clouds.

vi) Comparing the Mon R2 molecular abundances with those found in other PDRs (Orion Bar, NGC 7023 and Horsehead), we found that the C^{18}O, HCO$^+$, N$_2$H$^+$, SO, SO$^+$, HCS$^+$, CS, CH$_3$OH and CH$_3$CCH molecules present similar abundances for different G_0 environments. DCO$^+$, CH$_3$CN, CF$^+$, l-C$_3$H$^+$, HN^{13}C and hydrocarbons tend to increase their abundances in the low-UV irradiated PDRs. While the CO$^+$ and CN molecular abundances seems to decrease in the low-UV PDRs.

vii) Comparing molecular abundances in PDRs with those found in different sources (dark clouds, hot cores and a shock), we found that most of the lines present lower abundances in PDRs that in other sources. However there are some molecules (CS, C_2H and C_4H) that present similar abundances in PDRs than in dark clouds. CN presents higher abundances in PDRs than in dark clouds by an order of magnitude.

viii) In Mon R2 we found a [HCN]/[HNC] ratio of $\sim$ 11–20, it is higher than in the other PDRs. Even, taking into account similar physical conditions, it is difficult to explain the difference in the [HCN]/[HNC] ratio measured in the Orion Bar and Mon R2. This difference might be due to the large sensitivity of the [HCN]/[HNC] ratio to the time and molecular hydrogen density. Another possible interpretation is that the HCN and HNC emission (in Mon R2) is coming from the illuminated surface of the clumps.

The **deuterated chemistry** has been widely studied in cold pre-stellar regions and hot corinos. However, it is much less studied in environments with $T_k = 30$–70 K. In our chemical study in Mon R2, we paid special attention for the deuterated molecules and their corresponding hydrogenated species. In order to distinguish what kind of processes are dominating the chemistry of the deuterated molecules in Mon R2, we did a comparison of our results with those presented in other works for different sources an with chemical models. In the following we summarize the main results of this study

i) On the basis of the comparison of our observational results with those found in other sources, and with a gas phase model, we found that the deuteration in Mon R2 proceeds from the gas-phase via CH_2D^+ and C_2HD^+ reactions.

ii) We have determined the deuterium fraction (D_{frac}) for a large sample of molecules (C_2H, HCN, HNC, HCO^+, H_2CO, N_2H^+, and NH_3) toward the PDRs IF and MP2 position. We found that there are no important differences between the values of D_{frac} toward these PDRs. This is interpreted in the scenario of the deuterated compounds coming from dense and warm clumps with gas kinetic temperatures of 50 K, instead from the most exposed PDR layers. Values of D_{frac} of $\sim$0.01 are found for HNC, HCN, C_2H and H_2CO, and <0.001 for HCO^+, N_2H^+, and NH_3. These values are consistent with the predictions of the gas-phase model at an early time, $\sim$0.1 Myr. This time is consistent with the ages estimated for UC HII regions on the basis of statistical studies.

iii) On the basis of the gas-phase model, we found that the deuterium chemistry is a good chemical clock in both the low-mass and high-mass regime. However, the values of $D_{frac}(N_2H^+)$ and $D_{frac}(HCO^+)$ cannot provide

a good estimate of the evolutionary stage of massive protostar regions because this abundance ratio reaches the steady-state value on a short time scale after all the CO is released from the grains into the gas phase. We need to use the values of D_{frac} for different molecules (e. g., HCN, HNC and C_2H) with longer chemical time scale to provide accurate age estimates.

As we mentioned before, in our chemical study we only performed a detailed study of the deuterated molecules. However, the complete set of molecular lines available from our unbiased spectral survey will allow to make a complete chemical study of this interesting region. Future works will be centered on the different families of molecules (ions, S-bearing compounds, COMs, etc).

8.2   Future work

In this section, we present four main projects and their perspective for further work aimed at better establishing the properties of Mon R2 and different evolutionary stages in the formation of massive stars.

8.2.1   Filamentary structure

In our IRAM-30m maps we found that the filamentary structure present in Mon R2 goes beyond the mapped area and that the filaments show complex kinematics. To perform a detailed study of the kinematical and dynamical characteristics of the filaments it is necessary to obtain larger and more sensitive maps, as well as perform a comparison of the observations with numerical simulations. To complete our IRAM-30m data we requested extra observational time in this telescope to map a larger area, in order to study and improve our knowledge of the kinematics in the region. For the **new IRAM-30m data**, we proposed to complete our CO (1–0) maps to cover a region of $30' \times 30'$ to have an overview of the complete region providing new insights into the kinematics of this complex filaments-hub system. Furthermore, we proposed to map the central densest part of the filaments F1 and F2 in the SiO (2–1) line to determine the extension of the SiO emission and discern the possible turbulent origin of these molecular filaments. This proposal has been accepted, and the observations are being (will be) observed during this semester.

Interferometric observations are required to resolve in detail the structure of the filaments and the hub. The best candidates to perform these observations are the **ALMA**[i] and **NOEMA**[ii] interferometers as they provide the necessary resolution (angular and spectral) to resolve the velocity structure and the compact emission. Observations with these telescopes could help us to distinguish if the filaments are formed by fibers, and to confirm (and resolve) the existence of spiral arms in the central part of the region. Our plan is to ask for observing time to NOEMA to resolve the complex kinematics of the filaments and further study their fragmentation.

On the other hand, it is necessary to perform a comparison of the observations with **numerical simulations**. We plan to use the model developed by Geen et al. (2016,in prep) to predict the evolution of an UC H II region using magnetohydrodynamical simulations which includes self-gravitation. In a preparatory work, we simulate a 10^4 $M_\odot$ cloud (radius 1 pc) with imposed magnetic and turbulent velocity fields (setup similar to Iffrig & Hennebelle 2015). We allow the cloud to evolve under self-gravity, and after 1 free-fall time we turn on a source of UV photons. As a general result, we find that gas fragments quickly evolve into clumps, which fall into the center of the cloud and may cause the H II region to flicker. By comparing this simulation setup directly to Mon R2 we will be able to provide a direct link between observations, simulations and analytic theory.

8.2.2 | Dynamical study of the UC H II region

We have asked for observations at the JVLA of 37 hydrogen and carbon RRLs. The proposal has been approved and these observations have recently been completed. The combination of these data with our 30m maps will permit to constrain the physical properties of the UC H II region and the PDR, and lead to the solution of the unsolved issues in the kinematics of the H II region. The observation of HRRLs together with the radio continuum emission of the ionized gas will permit to measure the line-to-continuum ratio that will be used to constrain the physical parameters (electron density and temperature) of the UC H II region (see e. g., Rodríguez et al. 2010). The observation of multiple HRRLs of different quantum numbers, at centimeter and millimeter wavelengths, will be used to resolve the contributions from thermal, turbulent and pressure broadening to the observed linewidths (see e. g., Keto et al. 2008). On the other hand, the observation of multiple CRRLs at different quantum

---

[i] Atacama Large Millimeter/submillimeter Array, located in the Llano de Chajnantor, Chile.
[ii] NOrthern Extended Millimeter Array, located in Grenoble, France.

numbers is necessary to determine the physical properties (electron density and temperature) of the PDR. These data will be used to evaluate if the UC HII region is in expansion or not, by comparing the gas pressure of the UC HII region and the PDR.

8.2.3 | Chemical study

In order to improve our chemical analysis in Mon R2, it is necessary to carry out a detailed study of each family (ions, S molecules, N molecules, COMs, etc.) and to perform a comparison of the observations with both gas-phase and grain surface chemical models. On the basis of our spectral survey we are planing to develop the following studies

Sulphurated molecules (SO, SO^+, CS, H_2CS, C_2S, HCS^+, etc): The chemistry of sulphurated molecules in PDRs is not fully understood yet, as they are easily destroyed by the strong UV-radiation. We plan to develop a morphological and chemical study of this family in Mon R2. With the aim of discerning between different formation paths, we plan to study their emission along the mapped area, compare the abundances with those measured towards different environments and perform a full chemical modeling.

Ionic species (CF^+, l-C_3H^+, SO^+, HCO^+, HCS^+, CO^+ and HOC^+): We aim to observationally and theoretically investigate the chemistry of ions in Mon R2. Moreover, previous Herschel maps (e. g., CII, CH^+ and OH^+; Pilleri et al. 2014) will permit to compare to the spatial distributions of these ions and their precursors, providing new insights into their chemistry.

Complex molecules (CH_3CN, HC_3N, CH_3OH, CH_3CCH, etc): We plan to develop a chemical study using a large number of transitions from these species in four selected positions in the Mon R2 region. The aim is to compare the emission of these molecules towards the PDRs (MP2 and IF), and in the dense hot cores (corresponding to the positions of IRS 3 and IRS 4) where we expect to detect stronger emission. We plan to compare their abundances with those measured toward different environments as well as to perform a comparison with different theoretical models, including both stationary and non-stationary chemical modeling. The comparison of the observational data with models will help us to discern between different formation paths (surface chemistry, gas phase) for complex molecules.

Nitrogenated molecules as PDR tracers (CN, HCN, HNC, etc): The high abundances found in the Mon R2-PDRs encourages us to keep studying this molecules towards the region. We plan to study the chemistry of nitriles (CN,

HCN, HNC) and small hydrocarbons (C_2H, c-C_3H_2, C_4H) across the clumps surrounding the UC HII region using the NOEMA (or ALMA) interferometer. These observations will be compared with state-of-the-art PDR models including grain surface chemistry and time dependence.

8.2.4 Expanding to other sources: GGD 14

Spectral line surveys in different environments are necessary to constrain the chemical properties of the ISM. We are planning to perform a detailed chemical study in other PDRs (sources) with different physical conditions and at different evolutionary stages. Observations and modeling of these objects could help to construct the chemical evolution, and thus, determine the chemistry that domains at different evolutionary stages. With this aim, we have decided to expand our study on deuteration to other regions with similar warm temperatures. In this sense, the PDR associated with the GGD 14 star forming region (located at the same distance of Mon R2, but in an earlier evolutionary stage) is an excellent target to be studied. In September 2014 (and March 2015), we proposed to conduct a spectral survey at 3, 2 and 1 mm towards the GGD 14 region using the 30m telescope. This project has been already observed and we are working on these new data.

Part IV

APPENDICES

A

A FILAMENTARY HUB IN MON R2: FIGURES

This appendix includes the large-scale channels maps indicating the filaments and the position-velocity plots.

Contents

A.1   Structures maps

This section present the integrated intensity (Figure A.1) and channel maps (Figure A.3 to A.6) of the CO, HNC and N_2H^+ emission in the three structures structures identified and labeled in Figure 5.5. Figure A.3 to A.4 present the channel maps of the elongated structure in the north-south direction (structure N). Figure A.5 presents the channel maps of the structure extending to the north-east from the central zone (structure NE). Finally, Figure A.6 presents the channel maps of the structure extending to the south-west of the central area (structure SW).
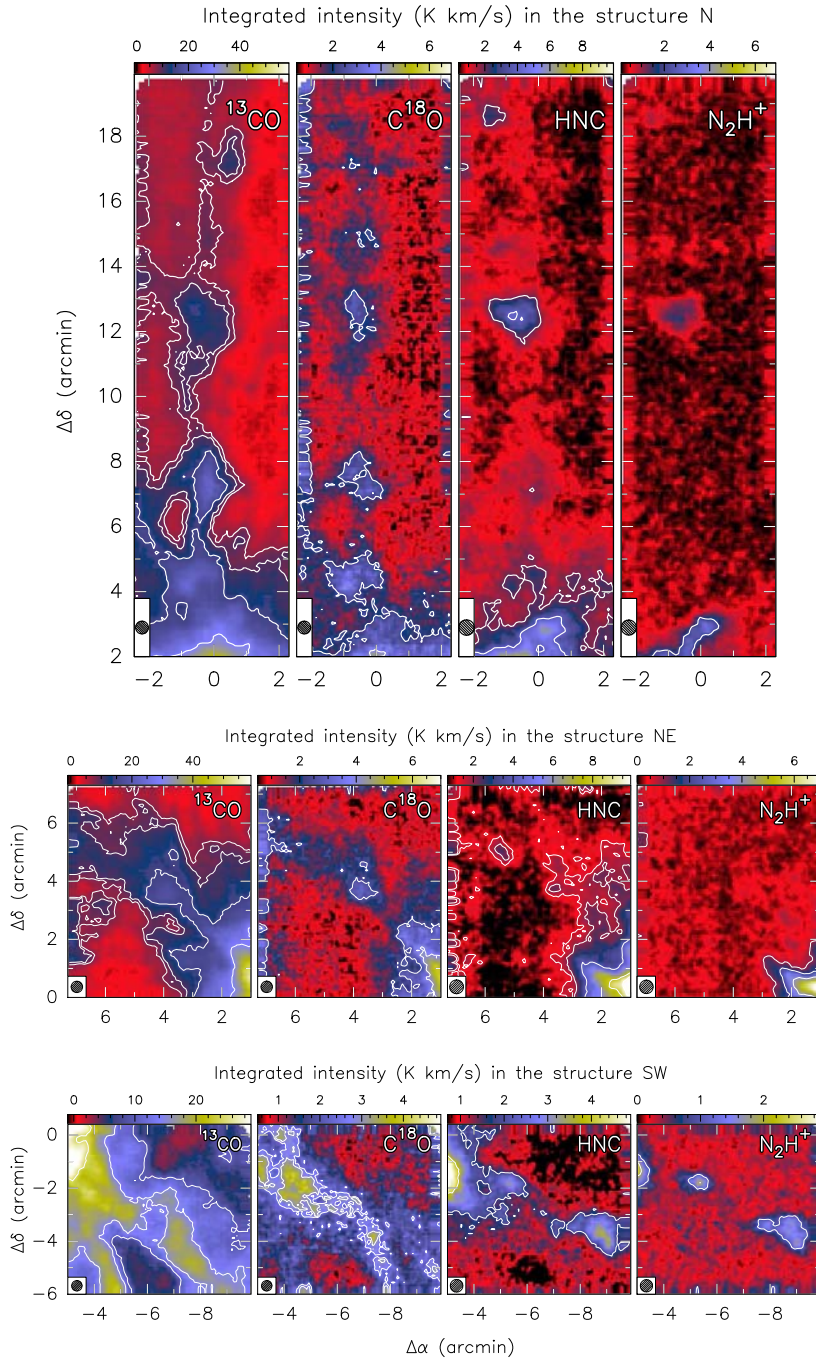
Figure A.1: Integrated intensity maps of the ^{13}CO, C^{18}O, HNC and N$_2$H$^+$ emission in the three structures N, NE and SW.
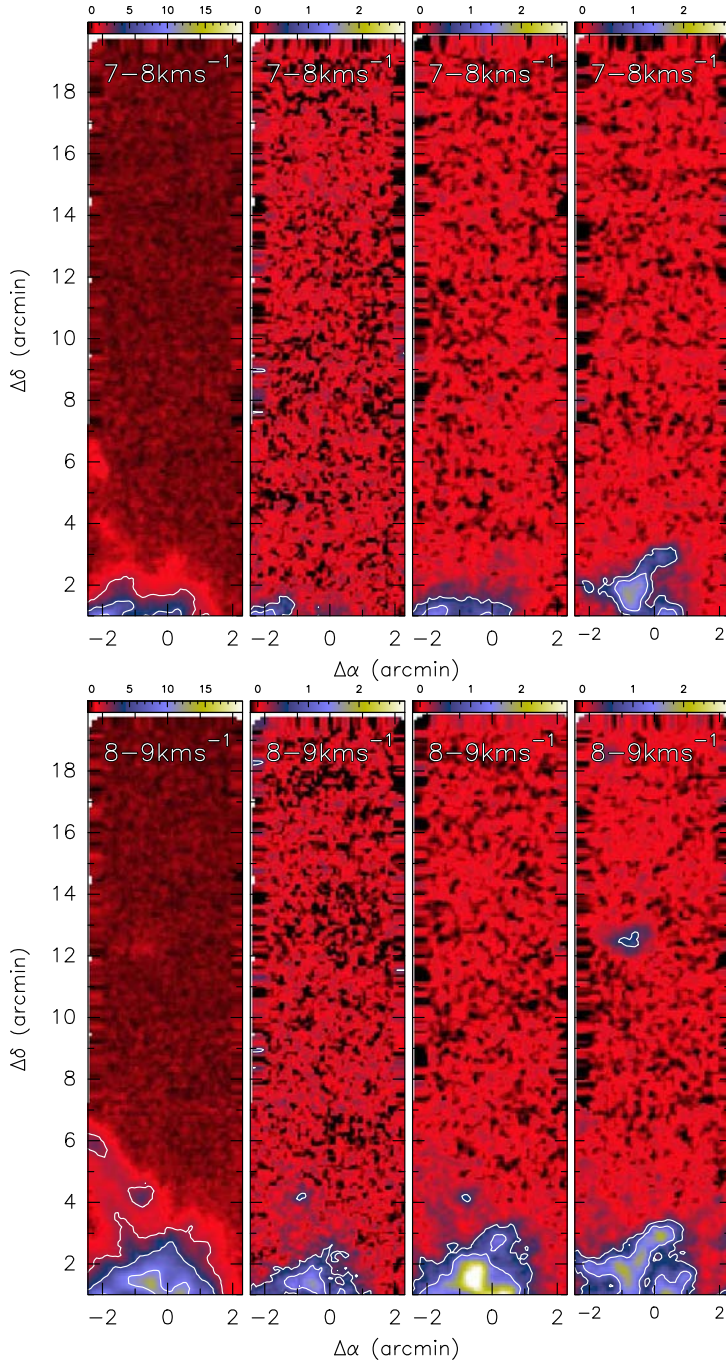
Figure A.2: Channel maps of the ^{13}CO, $C^{18}O$, HNC and N_2H^+ emission in the structure N. *Continued in next page.*
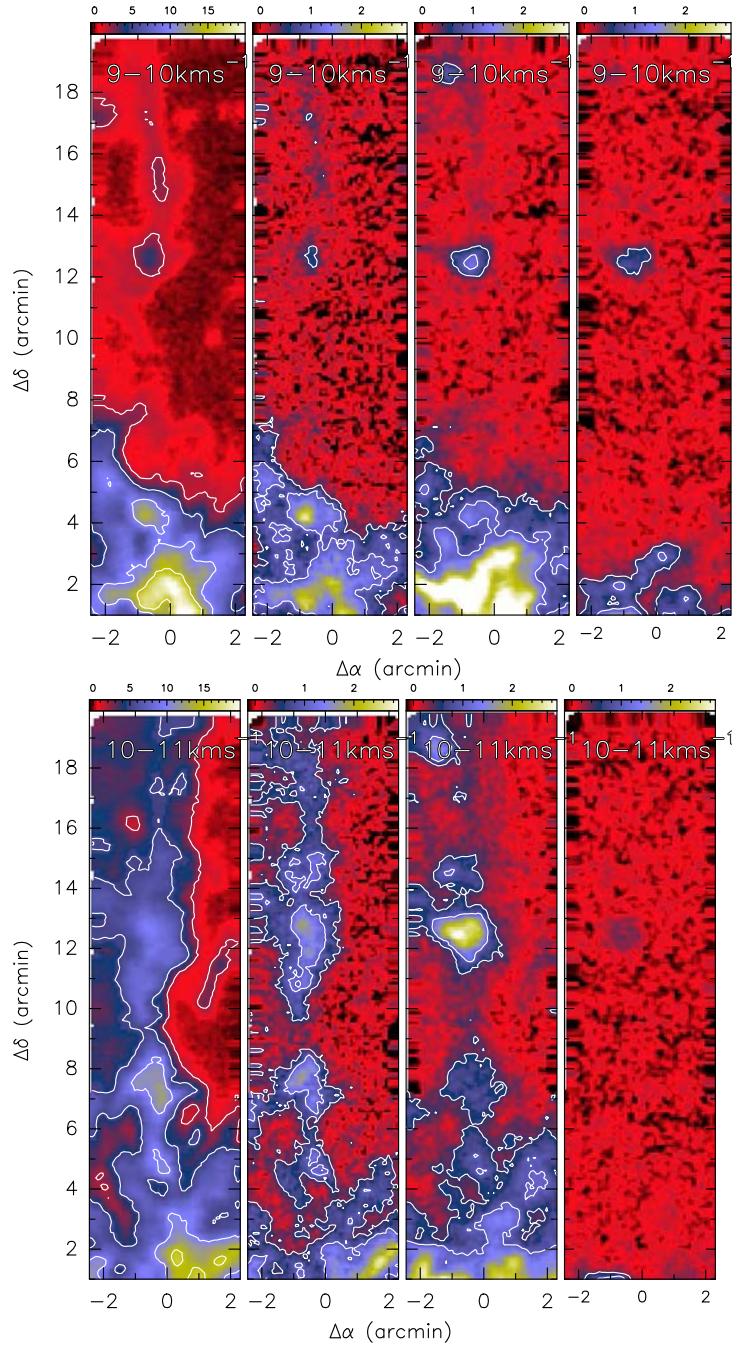
Figure A.3: *Continued from previous page.*
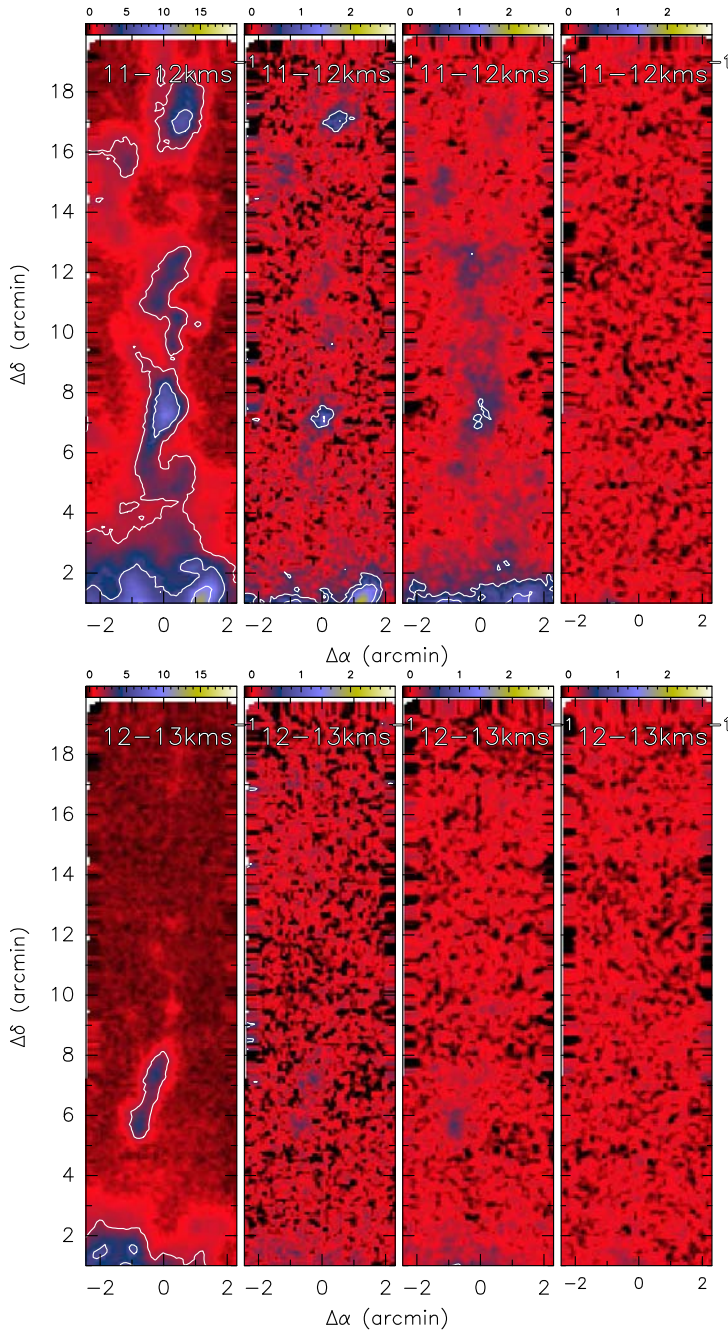
Figure A.4: *Continued from previous page.*
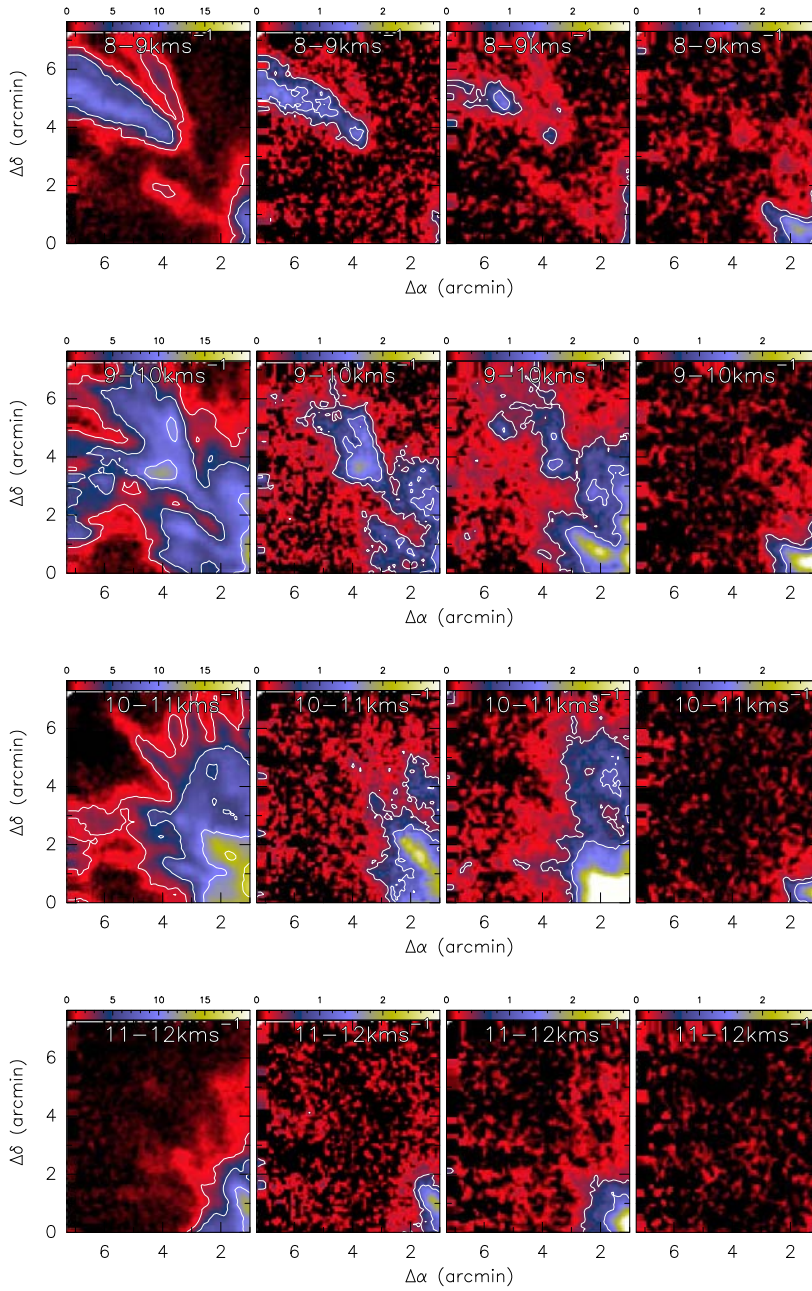
Figure A.5: Channel maps of the ^{13}CO, C^{18}O, HNC and N$_2$H$^+$ emission in the structure NE.
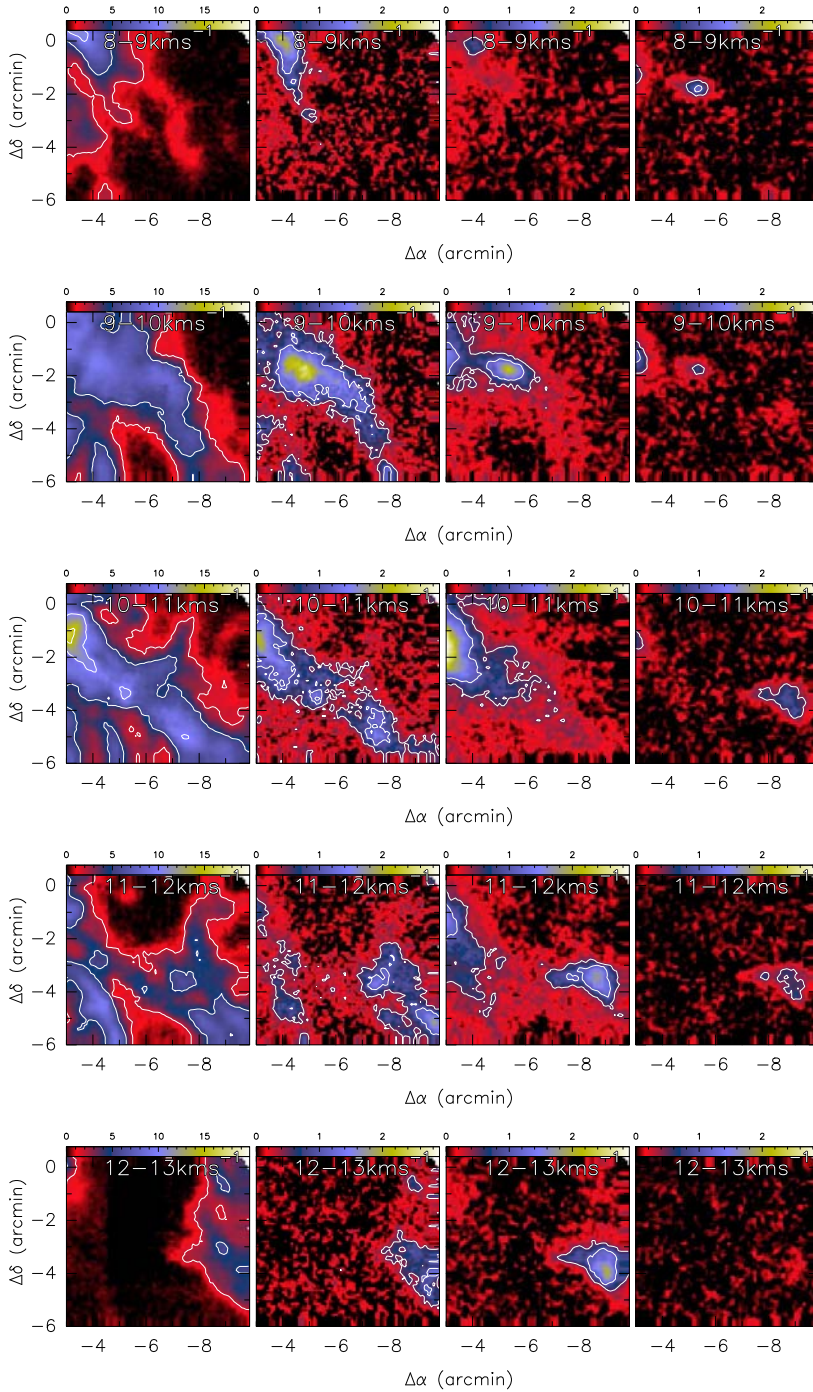
Figure A.6: Channel maps of the ^{13}CO, $C^{18}O$, HNC and N_2H^+ emission in the structure SW.

A.2 Channel maps

This section present the channel maps (Figure A.7 to A.7) of the ^{13}CO, C^{18}O, HNC, N$_2$H$^+$ and HC$_3$N emission in the whole integrated area. Also present the overlay of the filaments skeleton in the ^{13}CO (Figure A.10 to A.10) and C^{18}O (Figure A.13) channel maps.
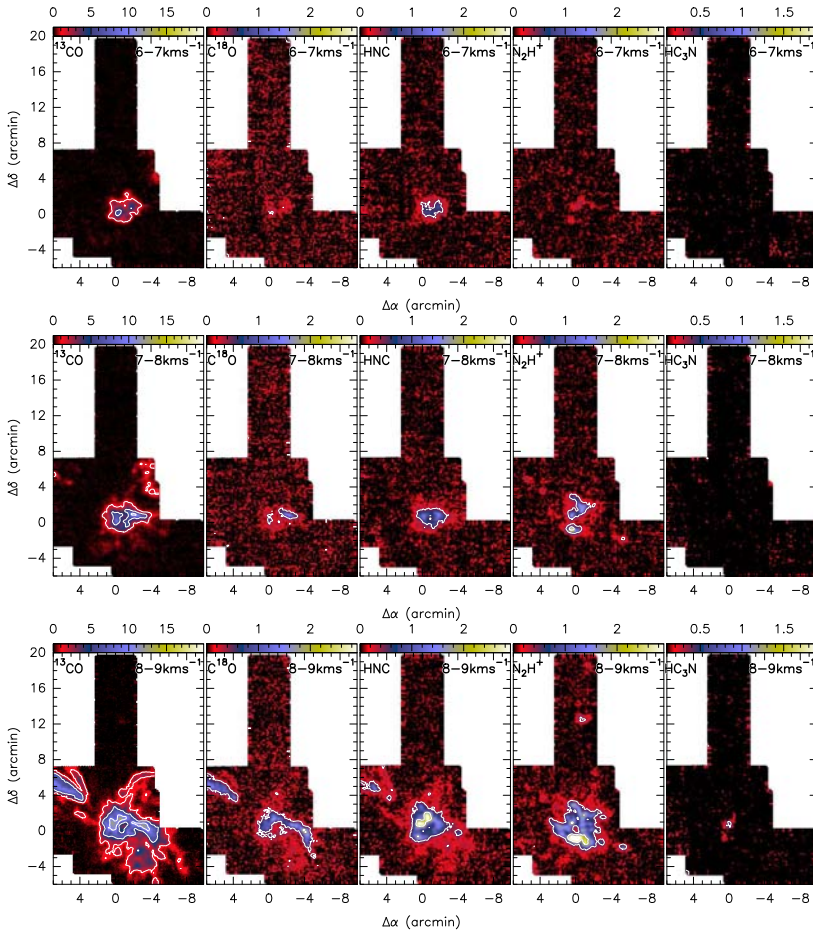
Figure A.7: Channel maps (Figure A.7 to A.7) of the ^{13}CO, C^{18}O, HNC, N$_2$H$^+$ and HC$_3$N emission in the whole integrated area. The velocities range for the map are from 6.0 to 17.0 km s^{-1} by steps of 1.00 km s^{-1}. *Continued in next page.*
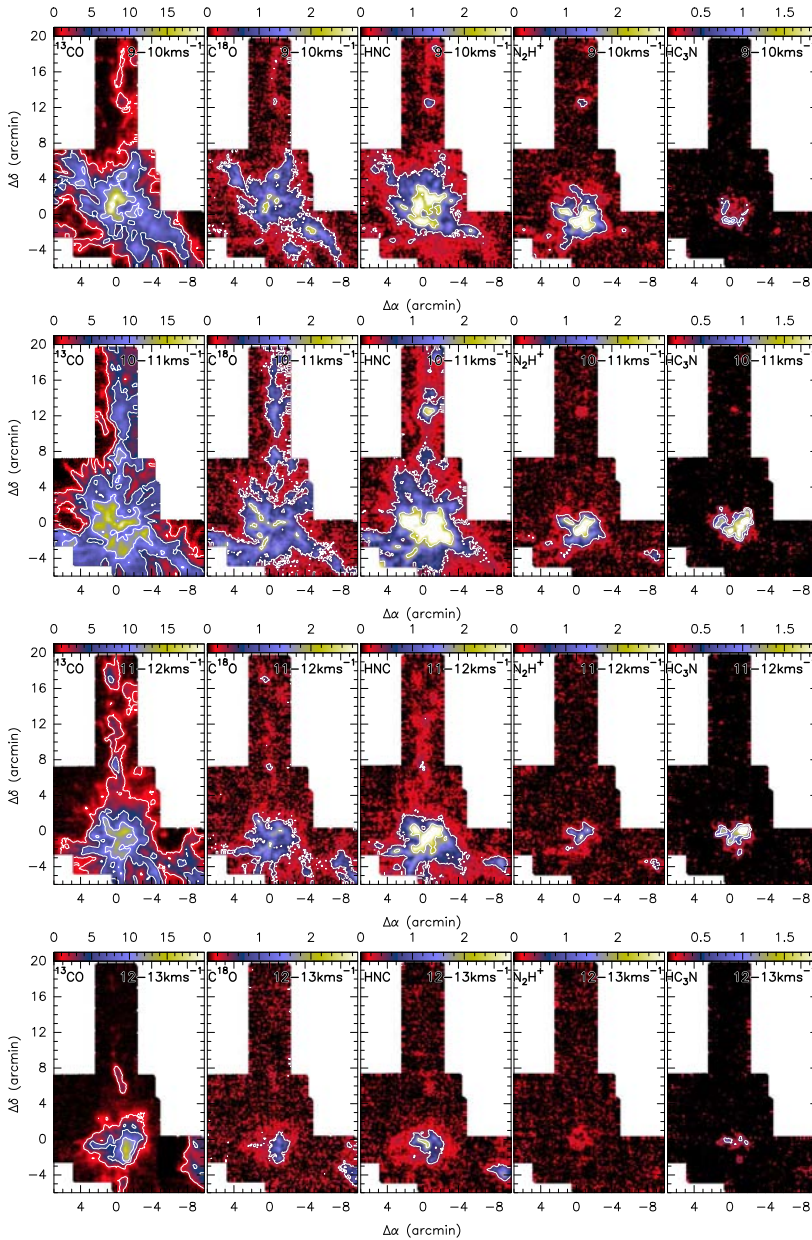
Figure A.8: *Continued from previous page.*
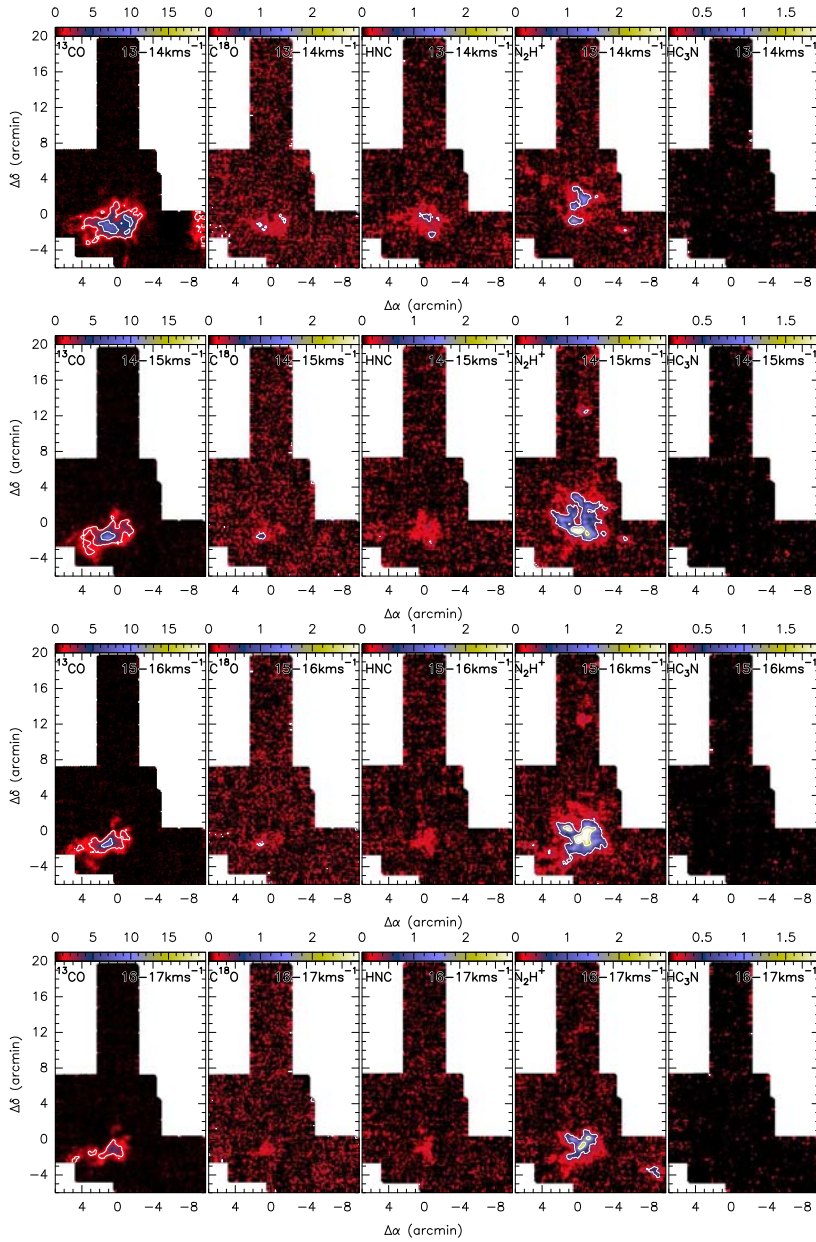
Figure A.9: *Continued from previous page.*
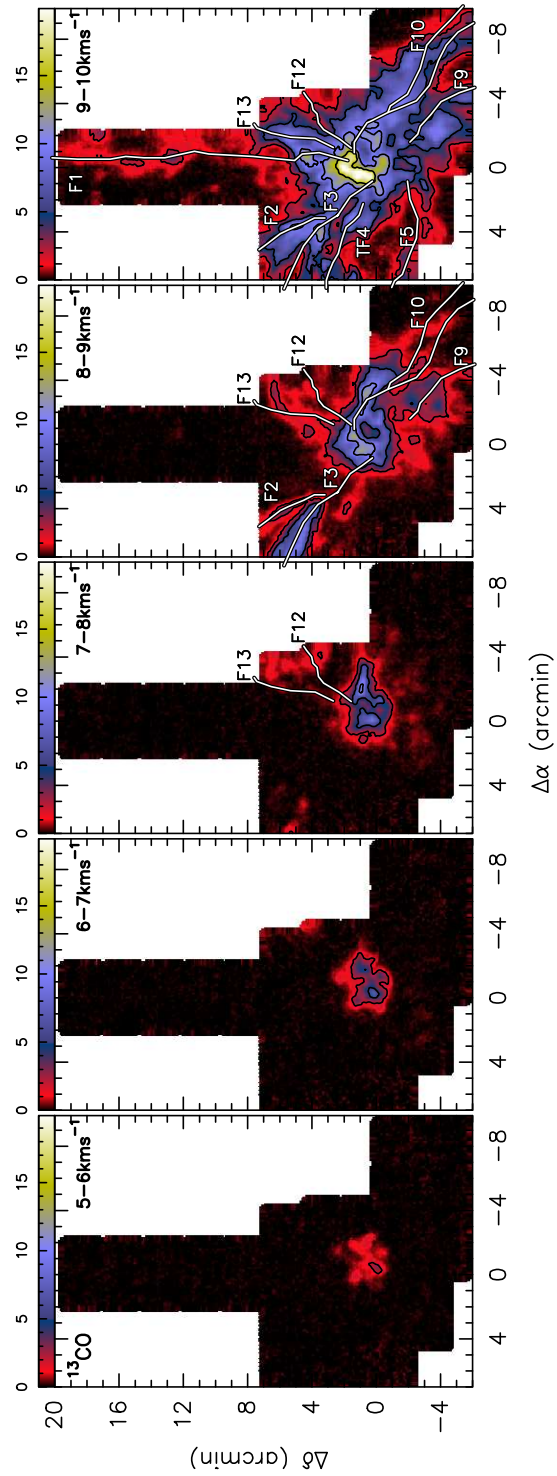
Figure A.10: Overlay of the filaments skeleton in the ^{13}CO channel maps. *Continued in next page.*
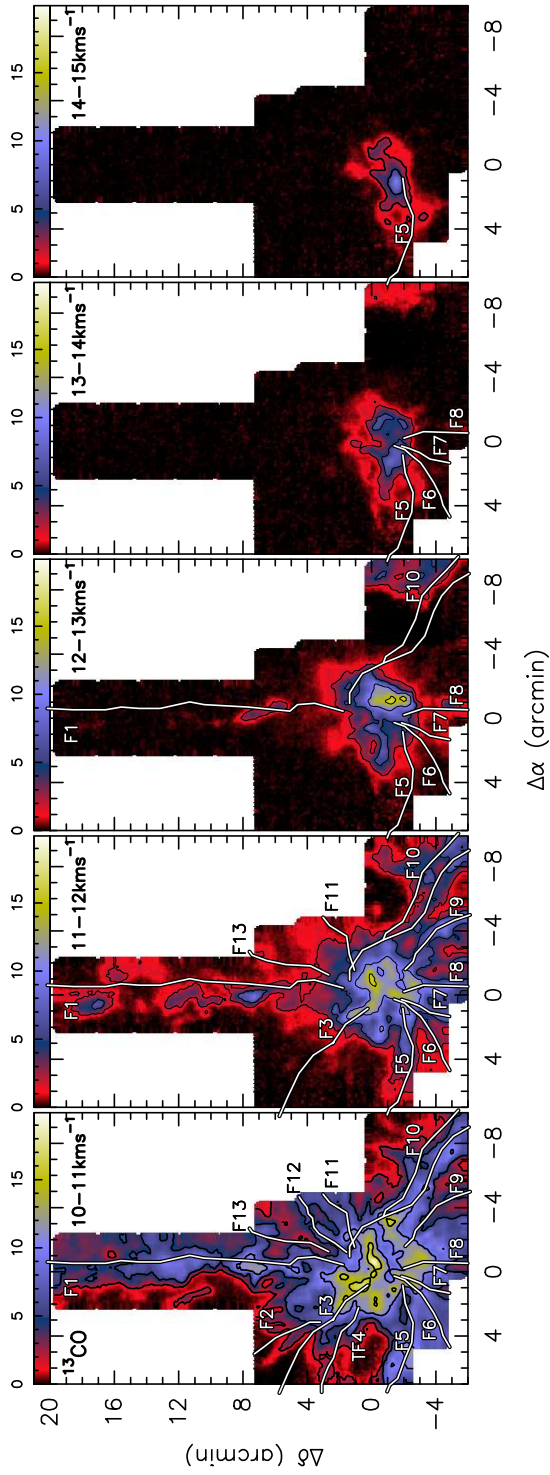
Figure A.11: *Continued from previous page.*
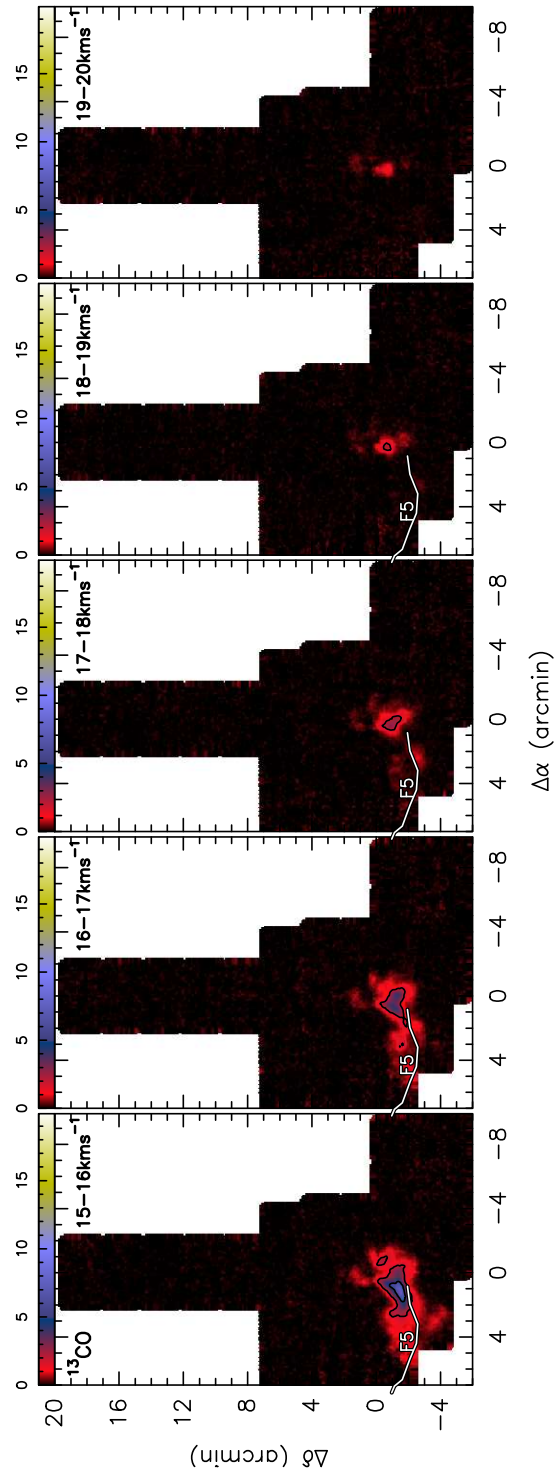
Figure A.12: *Continued from previous page.*
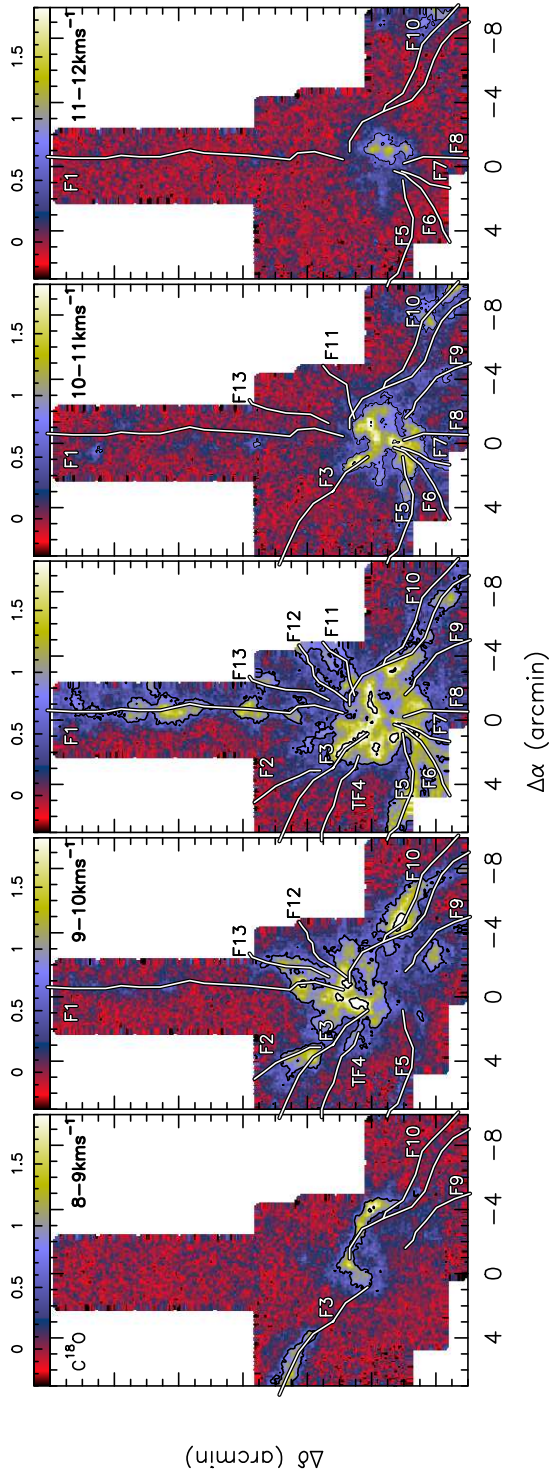
Figure A.13: Overlay of the filaments skeleton in the $C^{18}O$ channel maps.

A.3   Position-Velocity maps

THis section presents the position-velocity plots along the "skeletons" of the filaments (F1 to F13) for the ^{13}CO, C^{18}O and HNC molecules. In these plots, multiple components, and velocity gradients are clearly visible. The white arrows indicate the direction towards the hub.
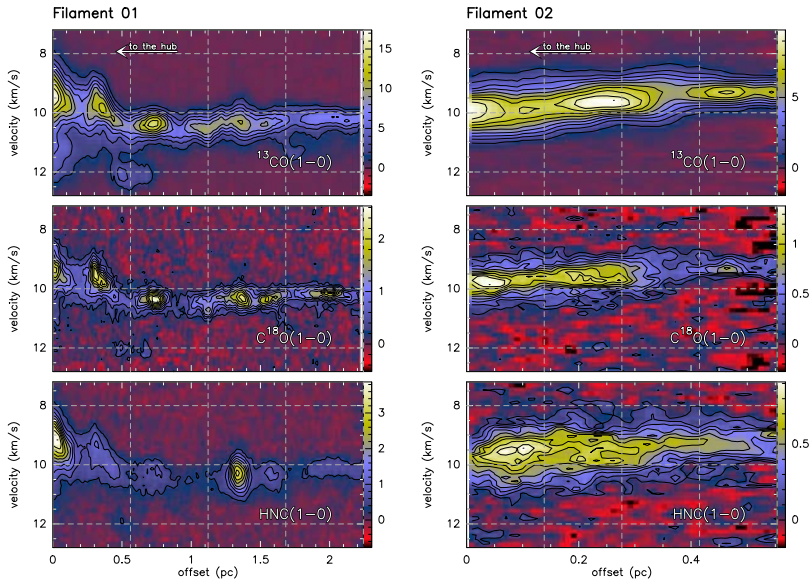
Figure A.14: Position-velocity plots along the "skeletons" of the filaments F1 and F2 for the ^{13}CO, C^{18}O and HNC molecules. The white arrows indicate the direction towards the hub.
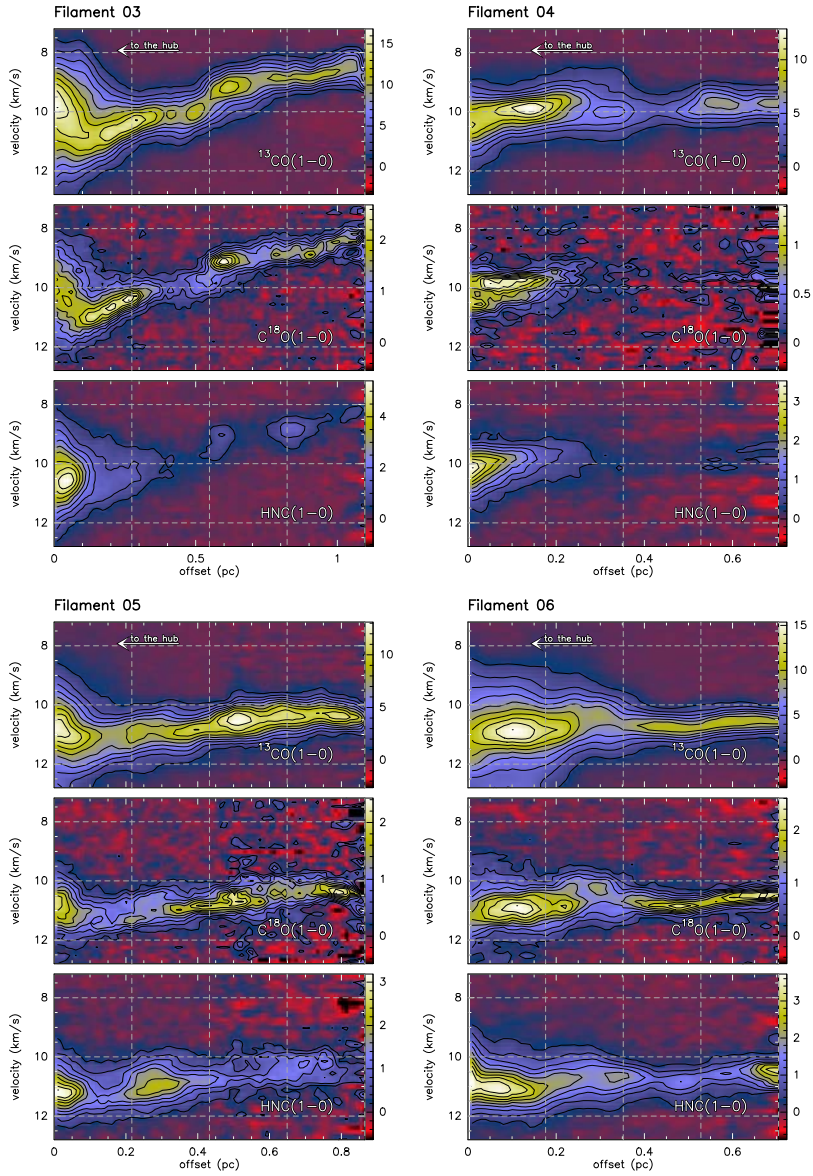
Figure A.15: Position-velocity plots along the "skeletons" of the filaments F3, F4, F5 and F6 for the ^{13}CO, C^{18}O and HNC molecules. The white arrows indicate the direction towards the hub.
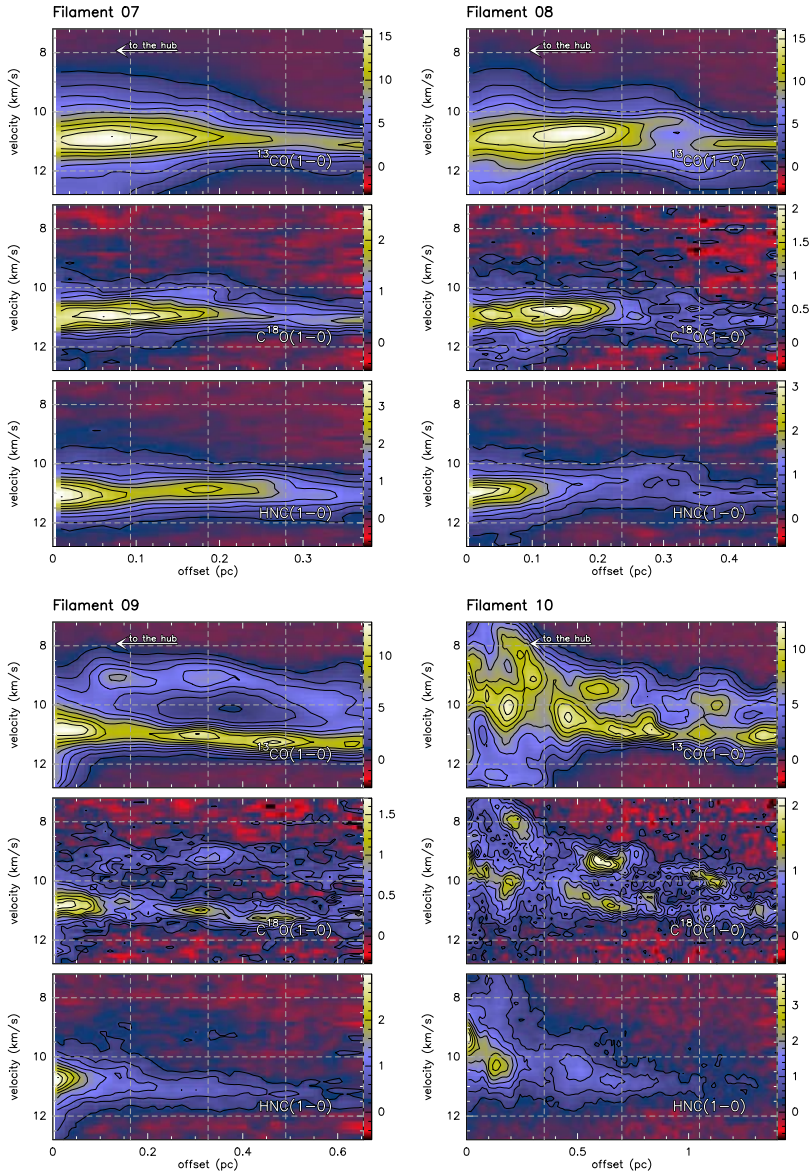
Figure A.16: Position-velocity plots along the "skeletons" of the filaments F7, F8, F9 and F10 for the ^{13}CO, C^{18}O and HNC molecules. The white arrows indicate the direction towards the hub.
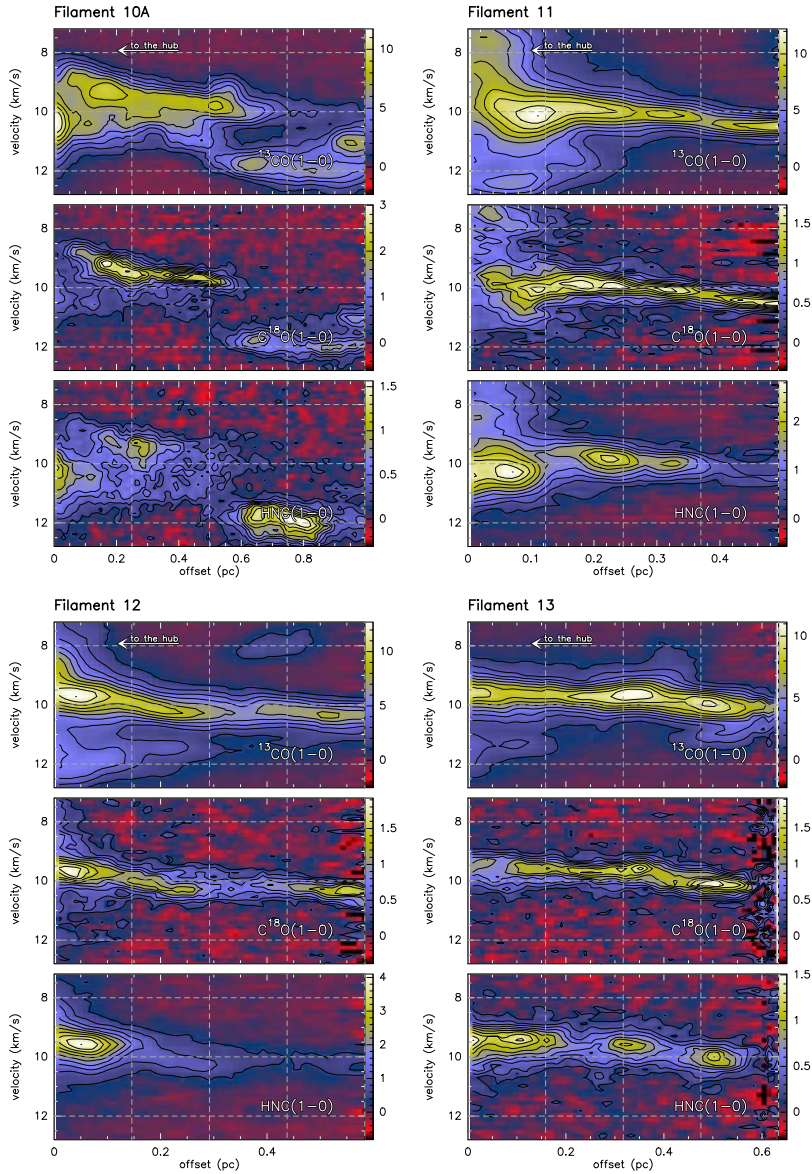
Figure A.17: Position-velocity plots along the "skeletons" of the filaments F10A, F11, F12 and F13 for the ^{13}CO, C^{18}O and HNC molecules. The white arrows indicate the direction towards the hub.

B

SURVEY: TABLES & FIGURES

This appendix includes the images for the whole survey and the observed spectra for some family in the IF and MP2 position. It also includes the results of the Gaussian fits, integrated and channels maps covering and area of $(2'' \times 2'')$ around IRS 1, and finally rotational diagrams.

Contents

B.1   Spectral survey

In this section we show the whole observed spectra at 3 mm (see Figures B.1–
B.4), 2 mm (see Figures B.5–B.6), 1 mm (see Figures B.8–B.12), and 0.8 mm
(see Figures B.13–B.14), towards the IF (left) and MP2 (right) position.
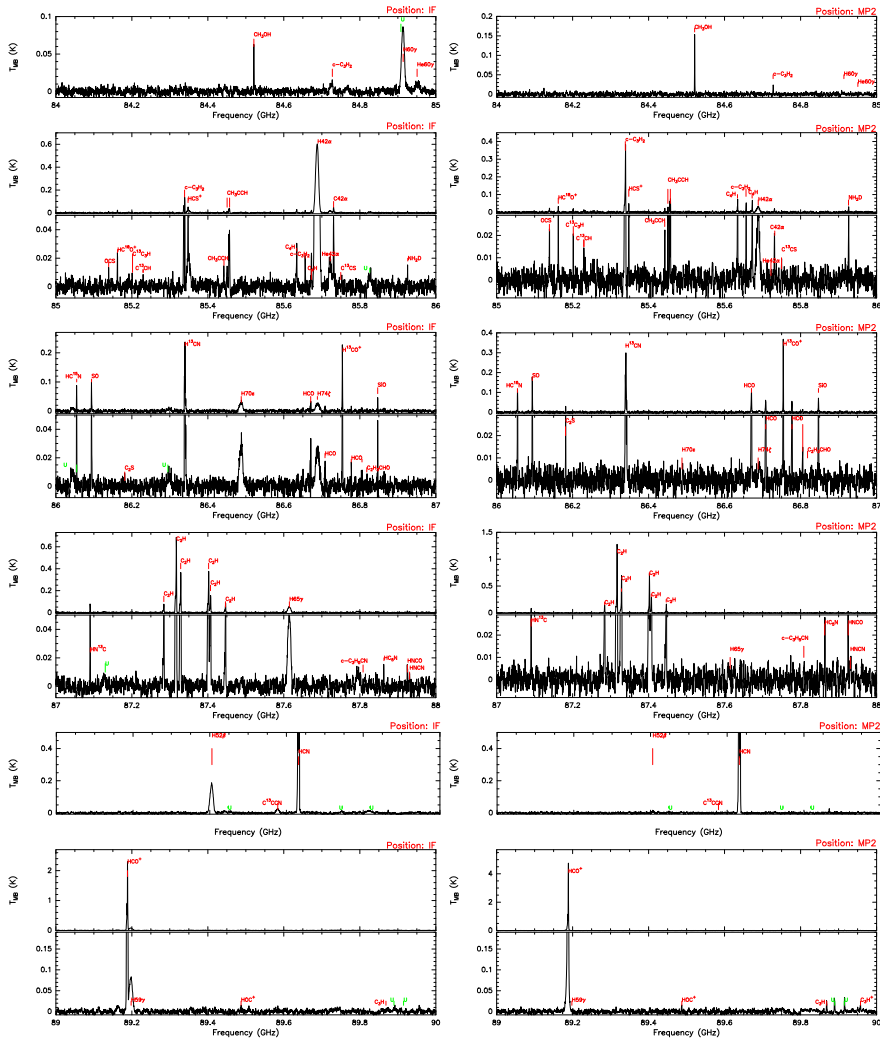
Figure B.1: Spectral survey at 3 mm towards the IF (left) and MP2 (right) position.
Continued in next page.
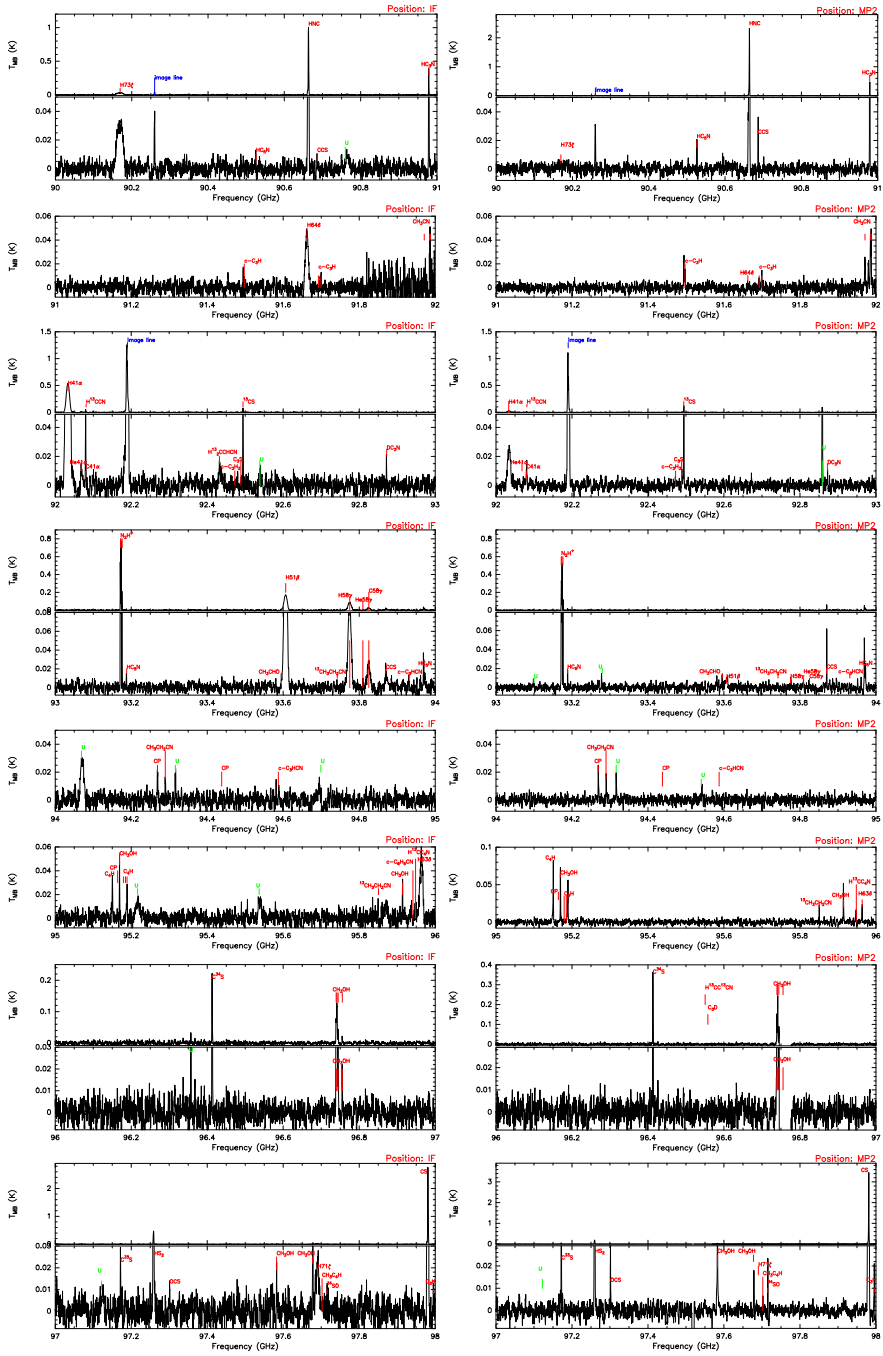
Figure B.2: Spectral survey at 3 mm towards the IF (left) and MP2 (right) position. *Continued in next page.*

Figure B.3: Spectral survey at 3 mm towards the IF (left) and MP2 (right) position. *Continued in next page.*
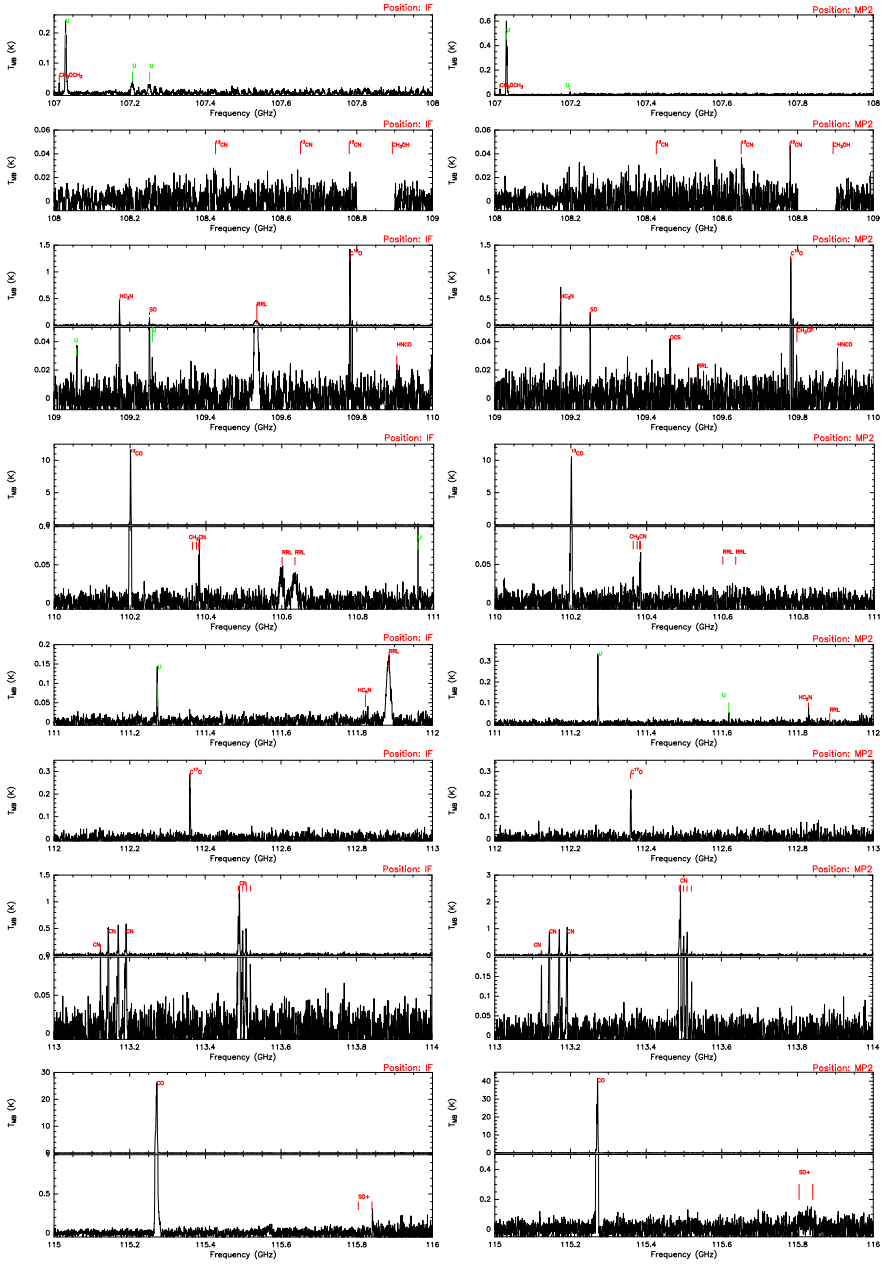
Figure B.4: Spectral survey at 3 mm towards the IF (left) and MP2 (right) position.
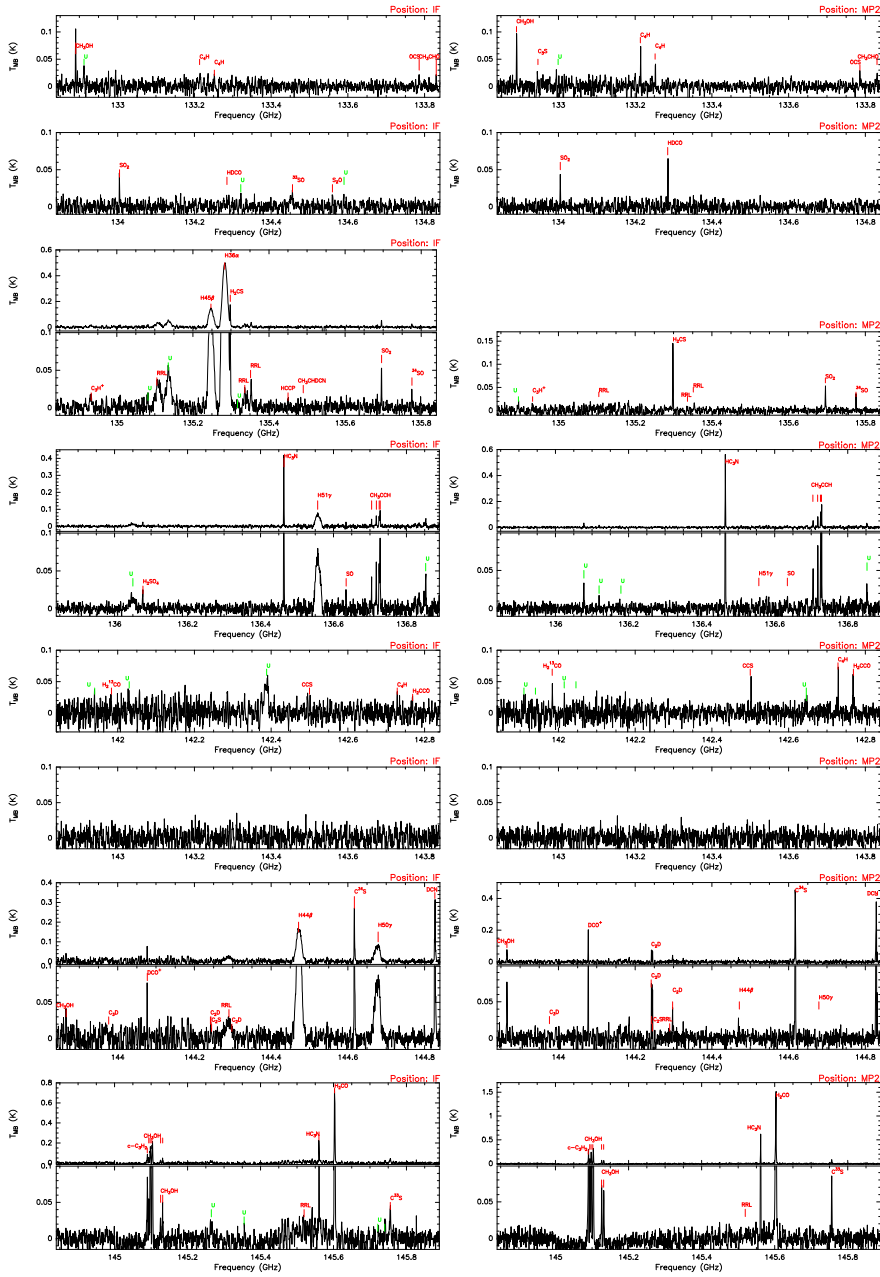
Figure B.5: Spectral survey at 2 mm towards the IF and MP2 position. *Continued in next page.*
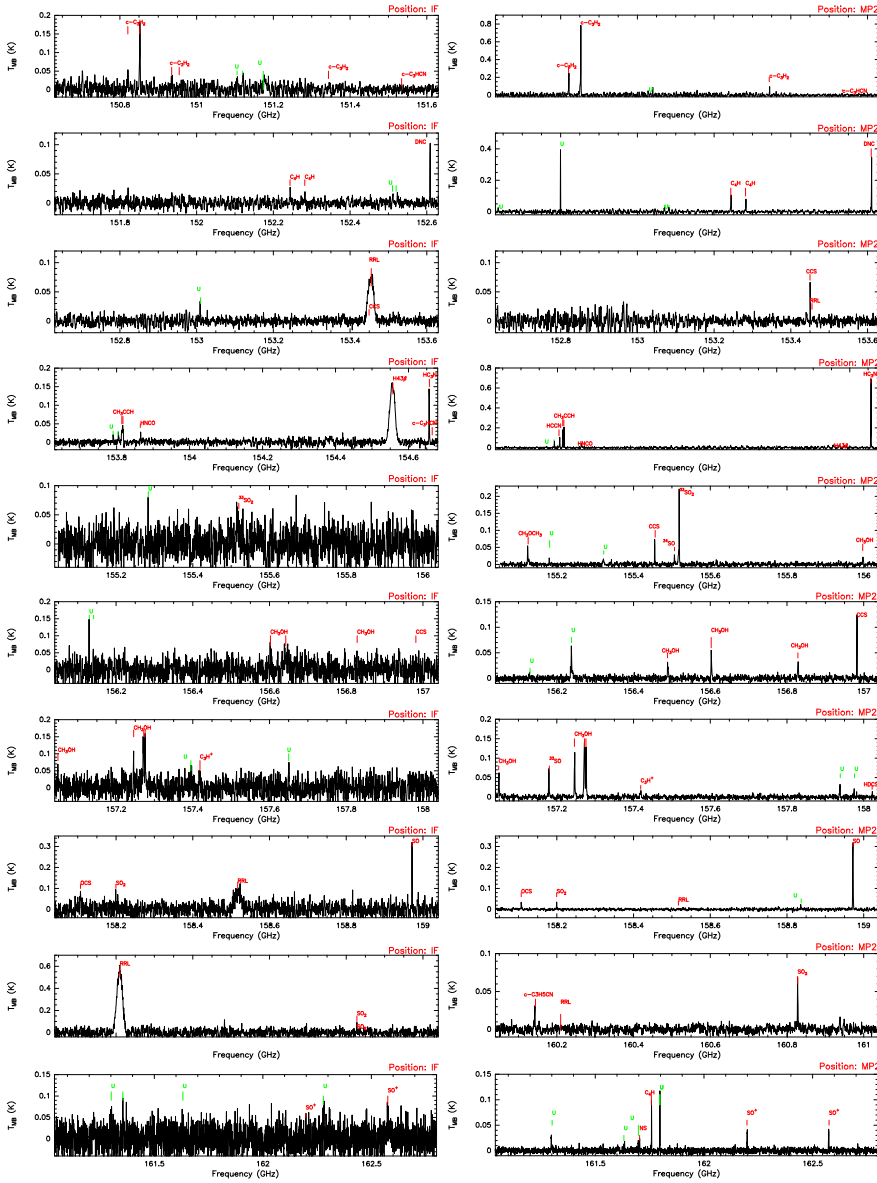
Figure B.6: Spectral survey at 2 mm towards the IF and MP2 position. *Continued in next page.*
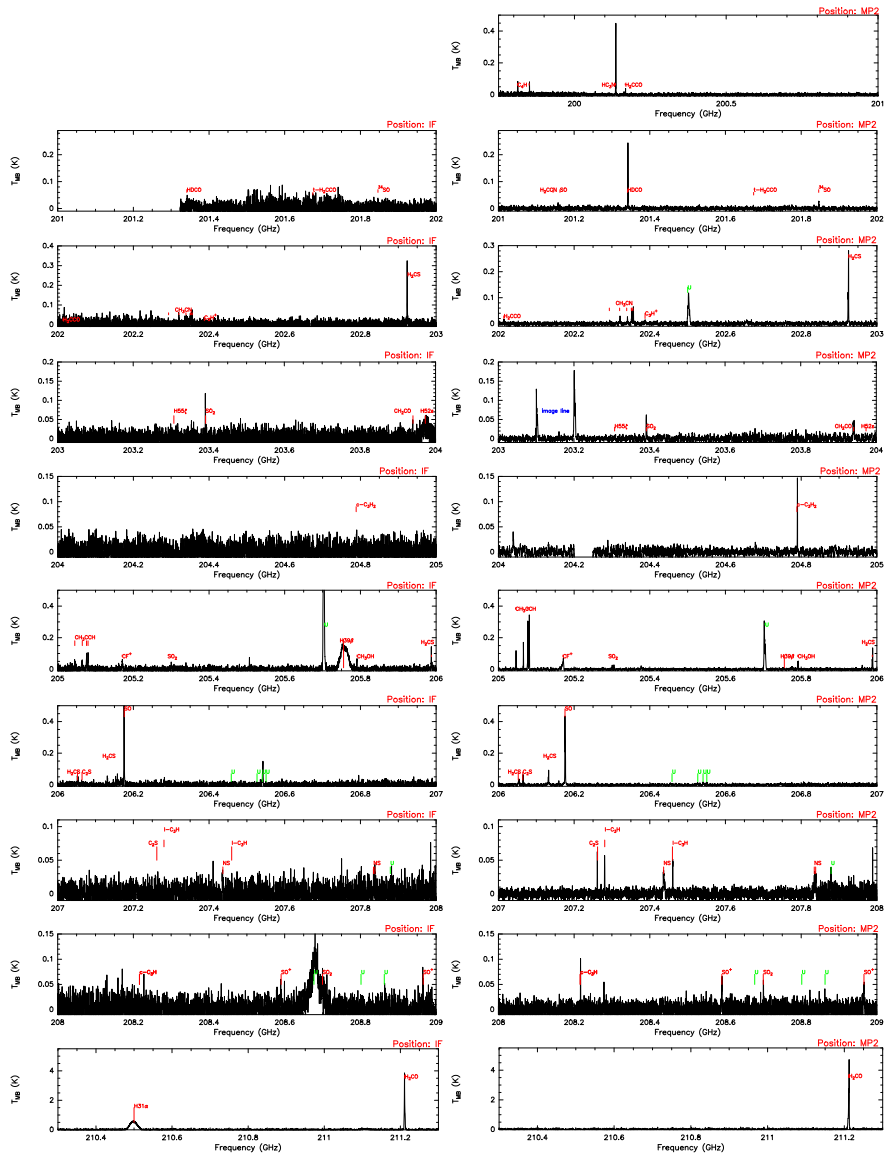
Figure B.7: Spectral survey at 1 mm towards the IF and MP2 position. *Continued in next page.*
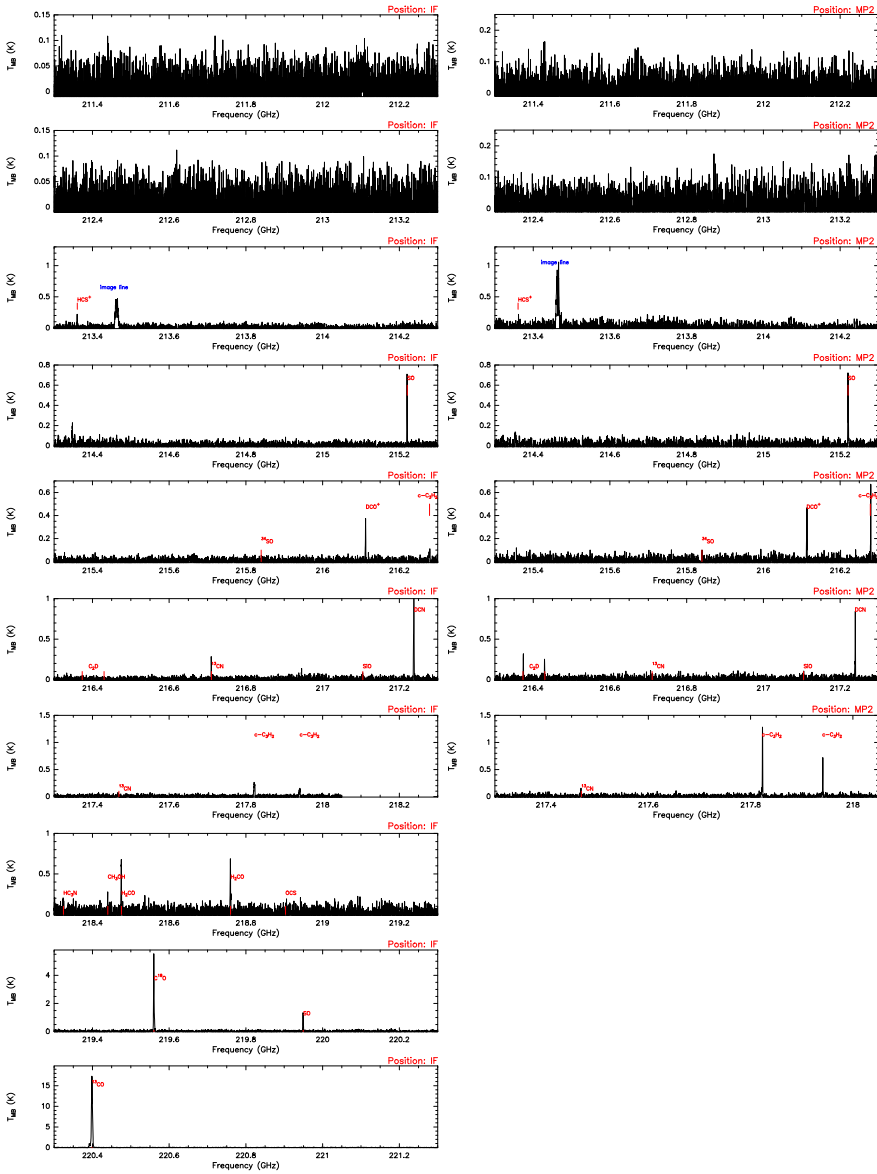
Figure B.8: Spectral survey at 1 mm towards the IF and MP2 position. *Continued from previous page.*
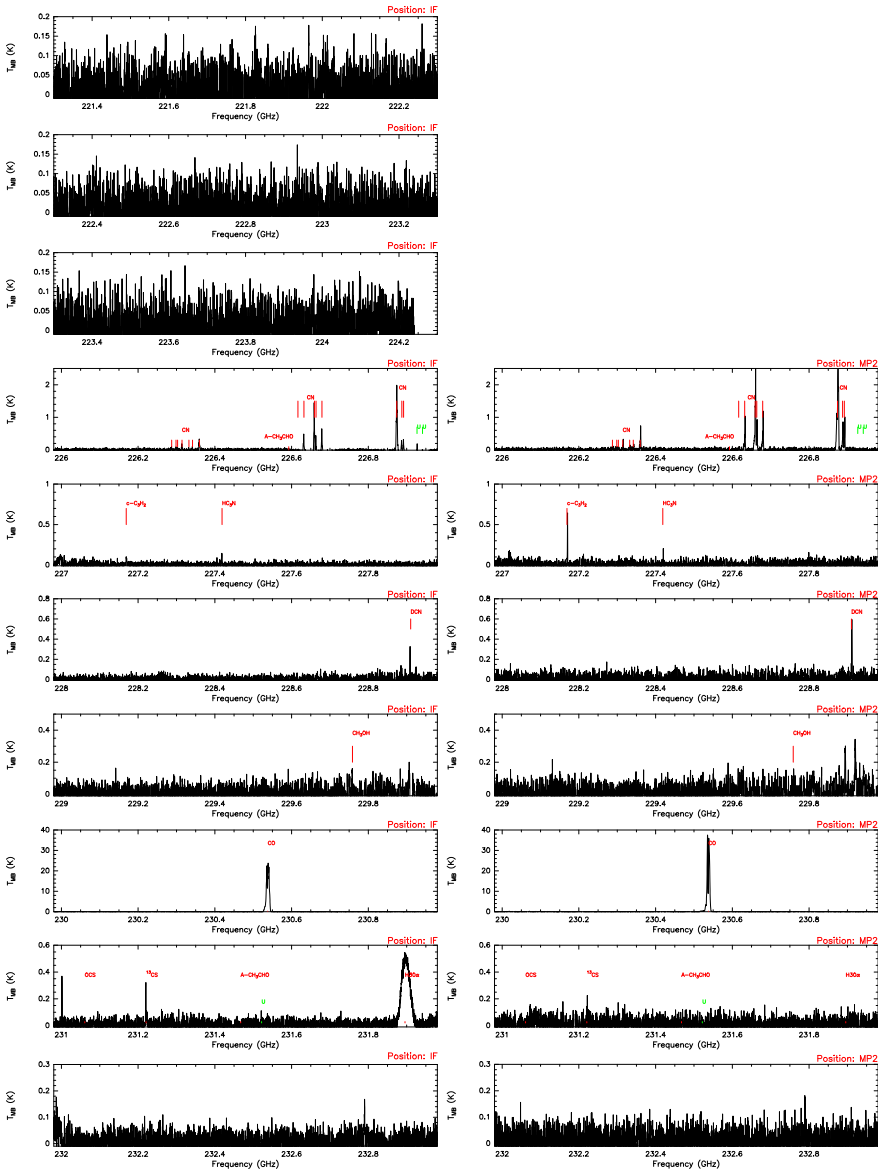
Figure B.9: Spectral survey at 1 mm towards the IF and MP2 position. *Continued from previous page.*
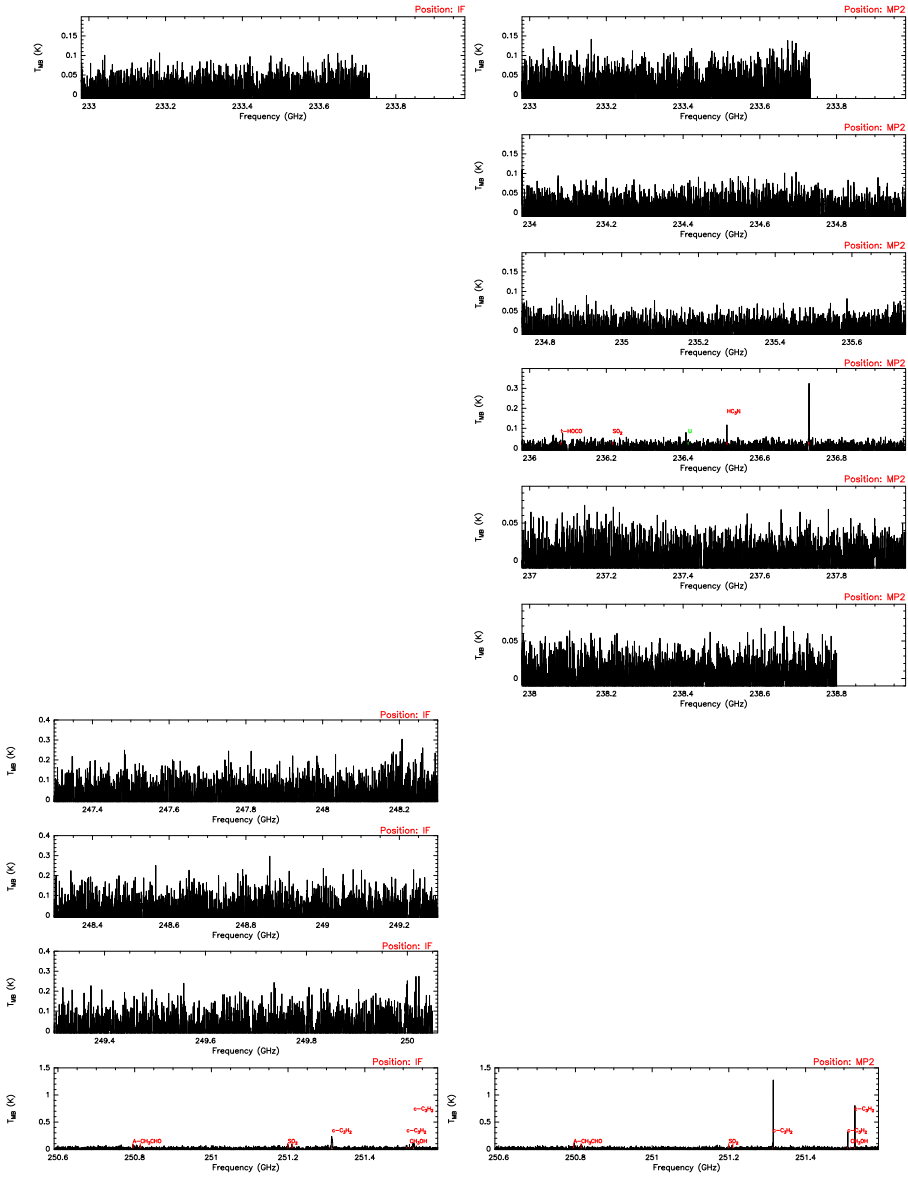
Figure B.10: Spectral survey at 1 mm towards the IF and MP2 position. *Continued from previous page.*
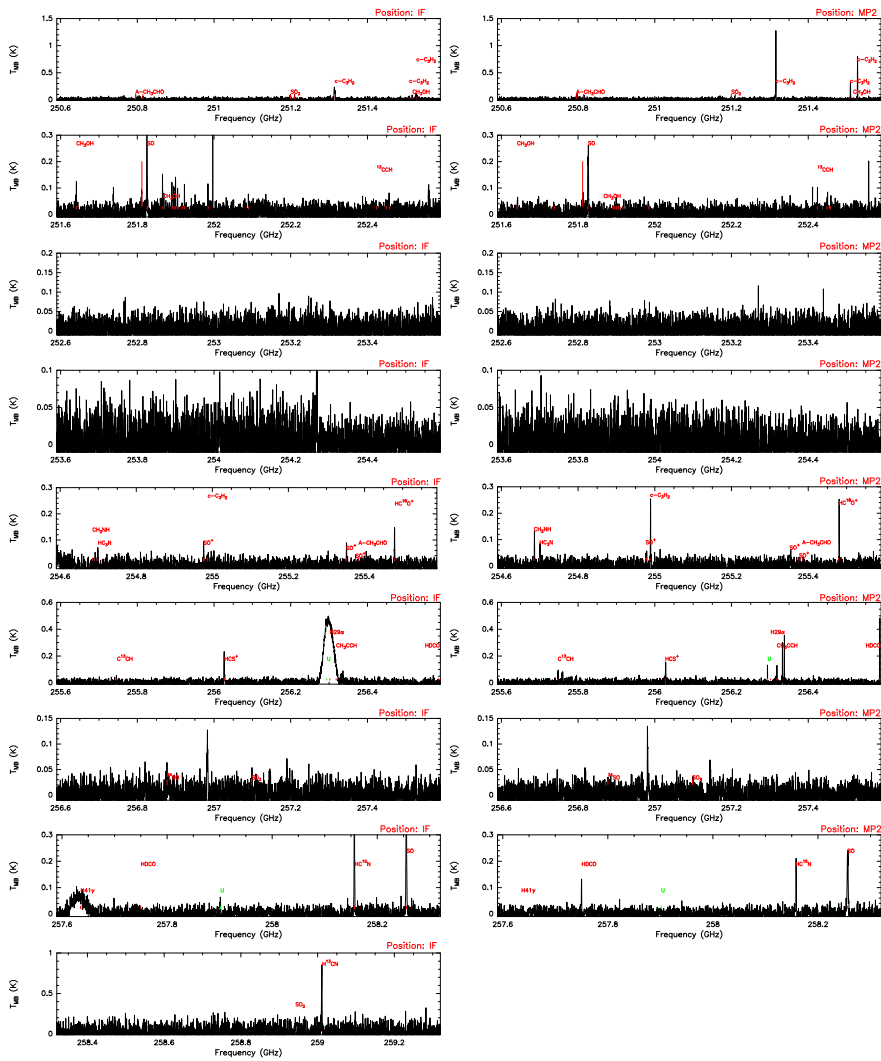
Figure B.11: Spectral survey at 1 mm towards the IF and MP2 position. *Continued from previous page.*
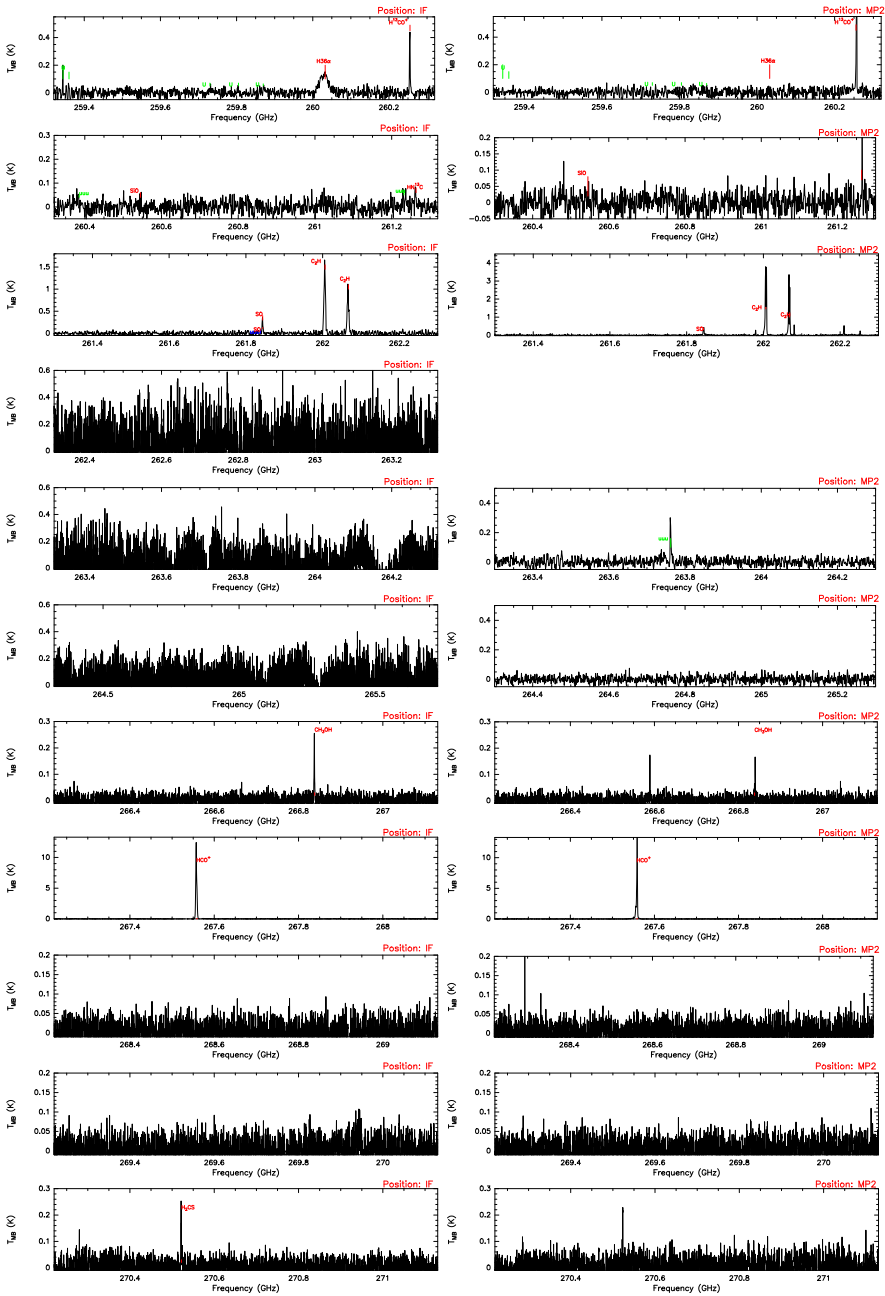
Figure B.12: Spectral survey at 1 mm towards the IF and MP2 position. *Continued from previous page.*
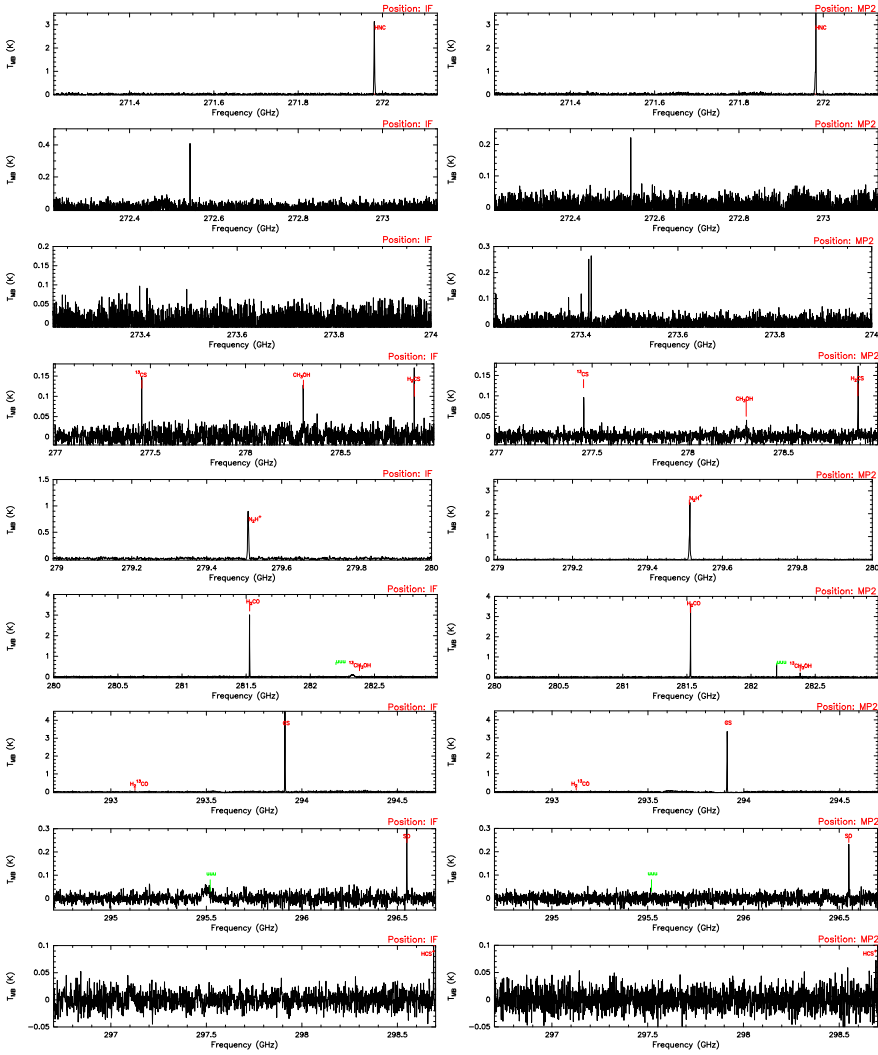
Figure B.13: Spectral survey at 0.8 mm towards the IF and MP2 position. *Continued from previous page.*
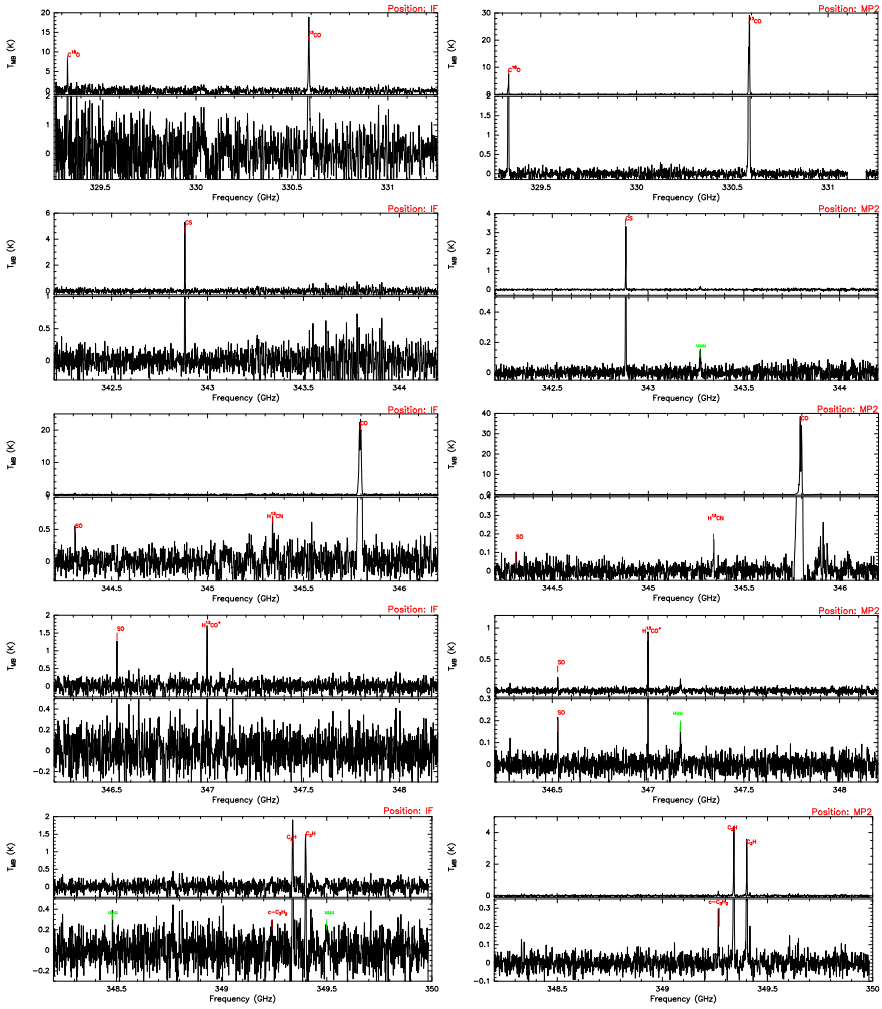
Figure B.14: Spectral survey at 0.8 mm towards the IF and MP2 position. *Continued from previous page.*

B.2   Spectra

In this section we show the observed spectra of different families toward the IF and MP2 position. The Figures B.15–B.21 show the spectra of some of the detected complex molecules, Figures B.22–B.26 show the spectra of molecules with nitrogen, Figures B.27–B.35 show the spectra of molecules with Sulfur, Figure B.36 present the desuterated molecules and de Figures B.37 and B.38 their corresponding hydrogenated molecules.
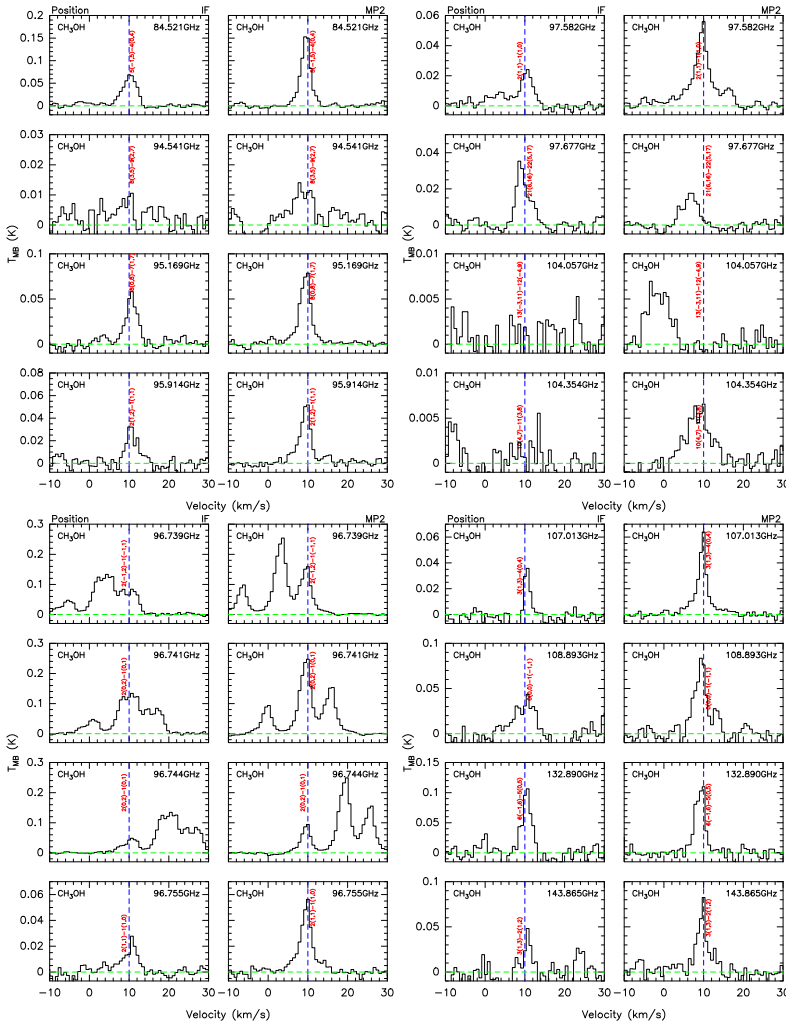
Figure B.15: Observed spectra of the CH_3OH molecule at the IF (column 1 and 3) and MP2 position (column 2 and 4).
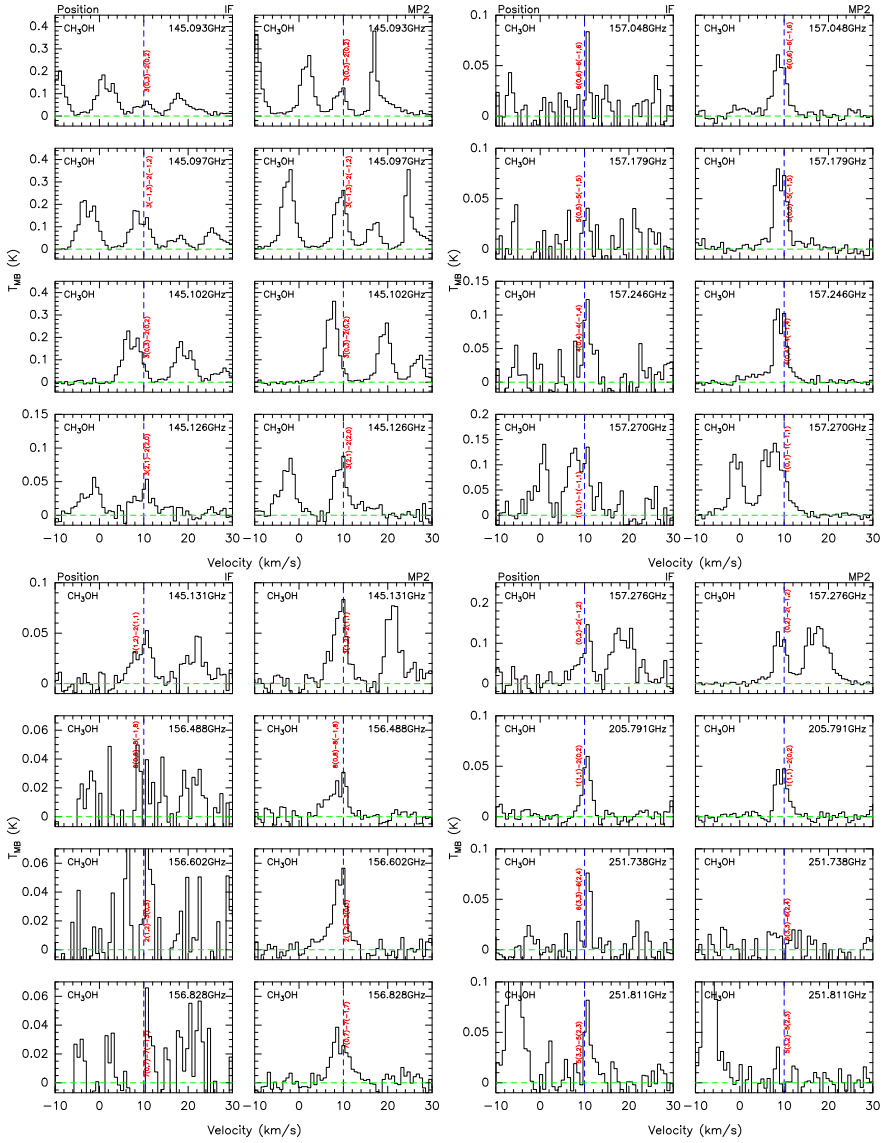
Figure B.16: Observed spectra of the CH₃OH molecule at the IF (column 1 and 3) and MP2 position (column 2 and 4).
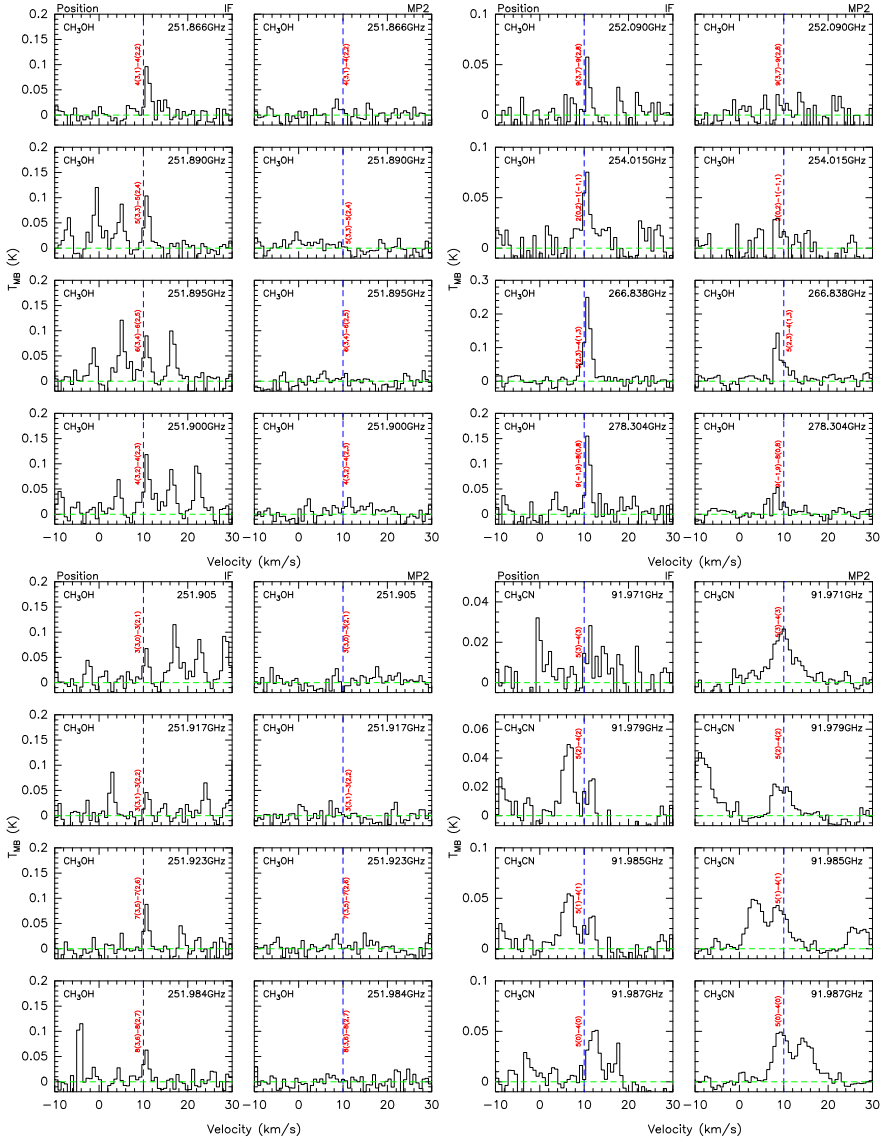
Figure B.17: Observed spectra of the CH$_3$OH and CH$_3$CN molecules at the IF (column 1 and 3) and MP2 position (column 2 and 4).
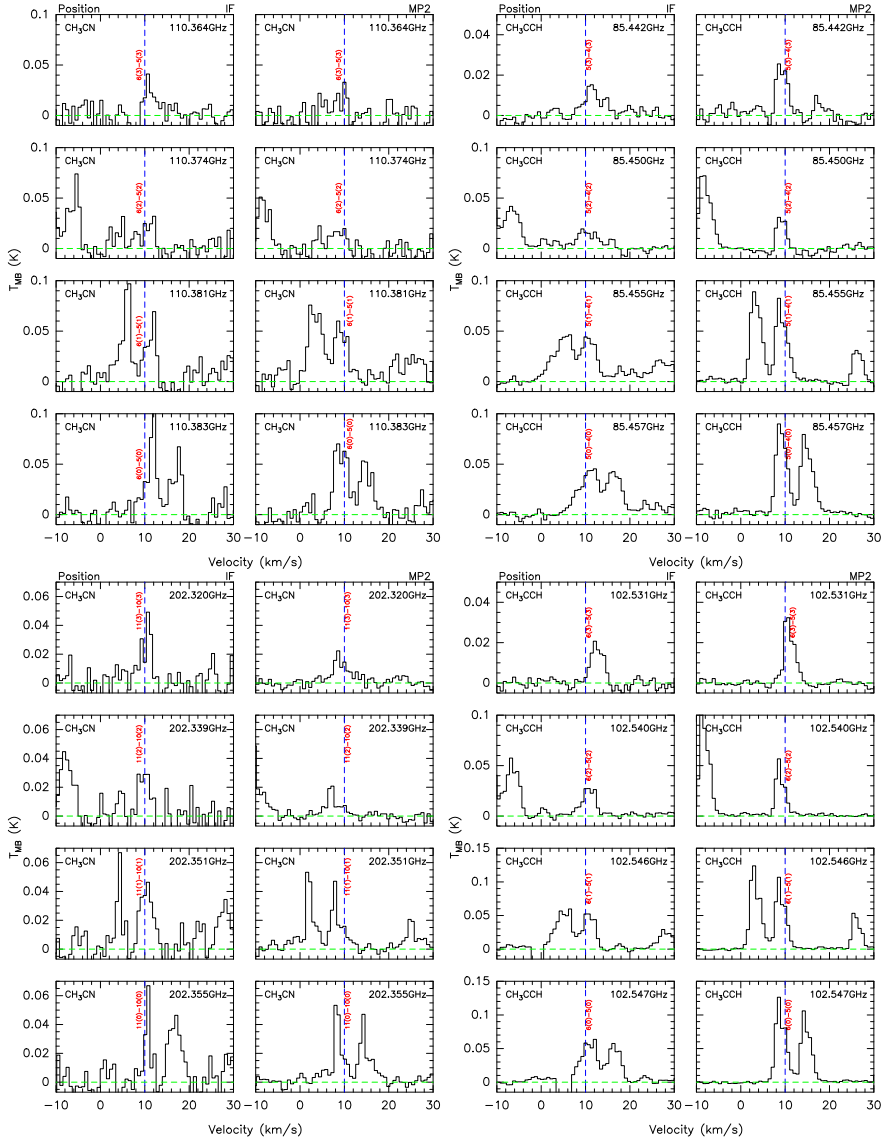
Figure B.18: Observed spectra of the CH₃CN molecule at the IF (column 1) and MP2 position (column 2). Observed spectra of the CH₃CCH molecule at the IF (column 3) and MP2 position (column 4).
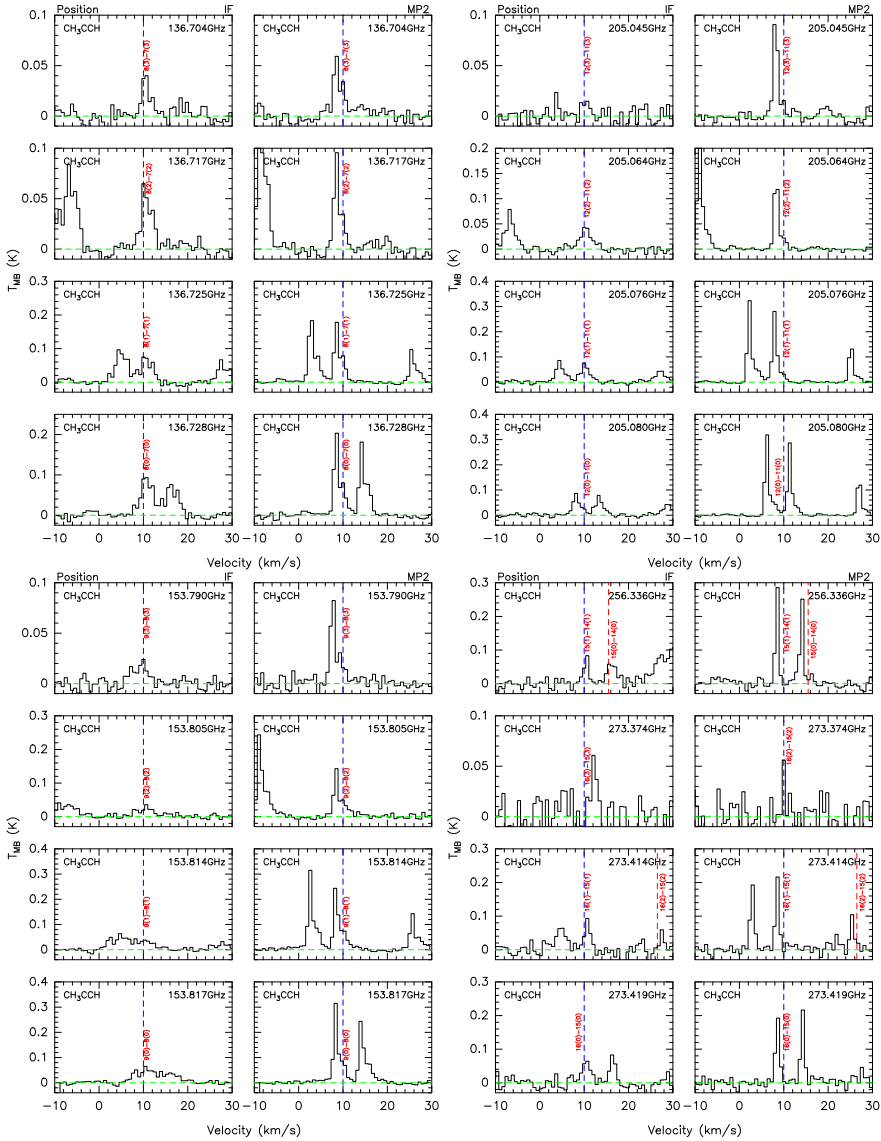
Figure B.19: Observed spectra of the CH₃CCH molecule at the IF (column 1 and 3) and MP2 position (column 2 and 4).
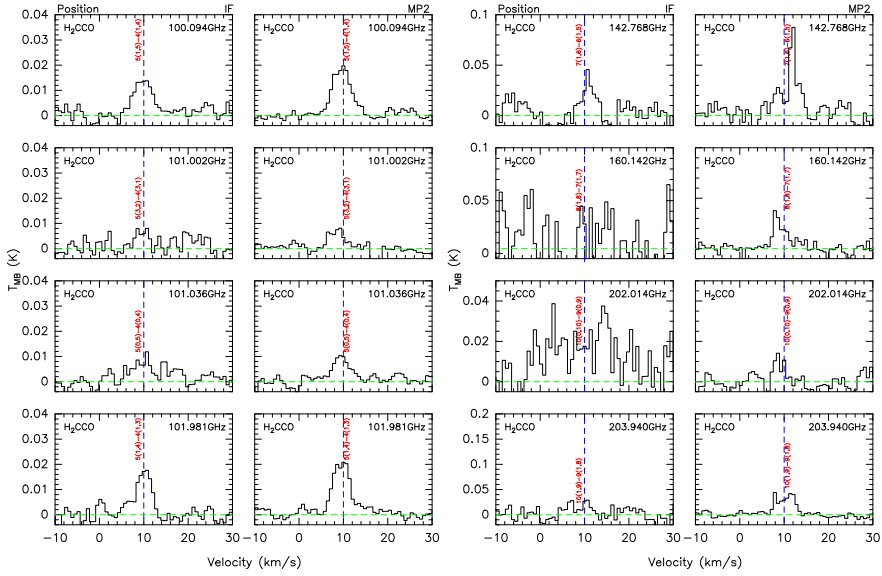
Figure B.20: Observed spectra of the H$_2$CCO molecule at the IF (column 1 and 3) and MP2 position (column 2 and 4).
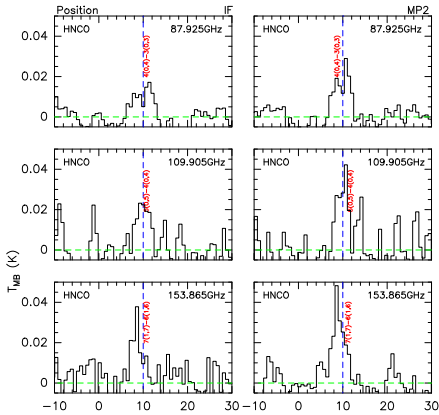
Figure B.21: Observed spectra of the HNCO molecule at the IF (column 1) and MP2 position (column 2).
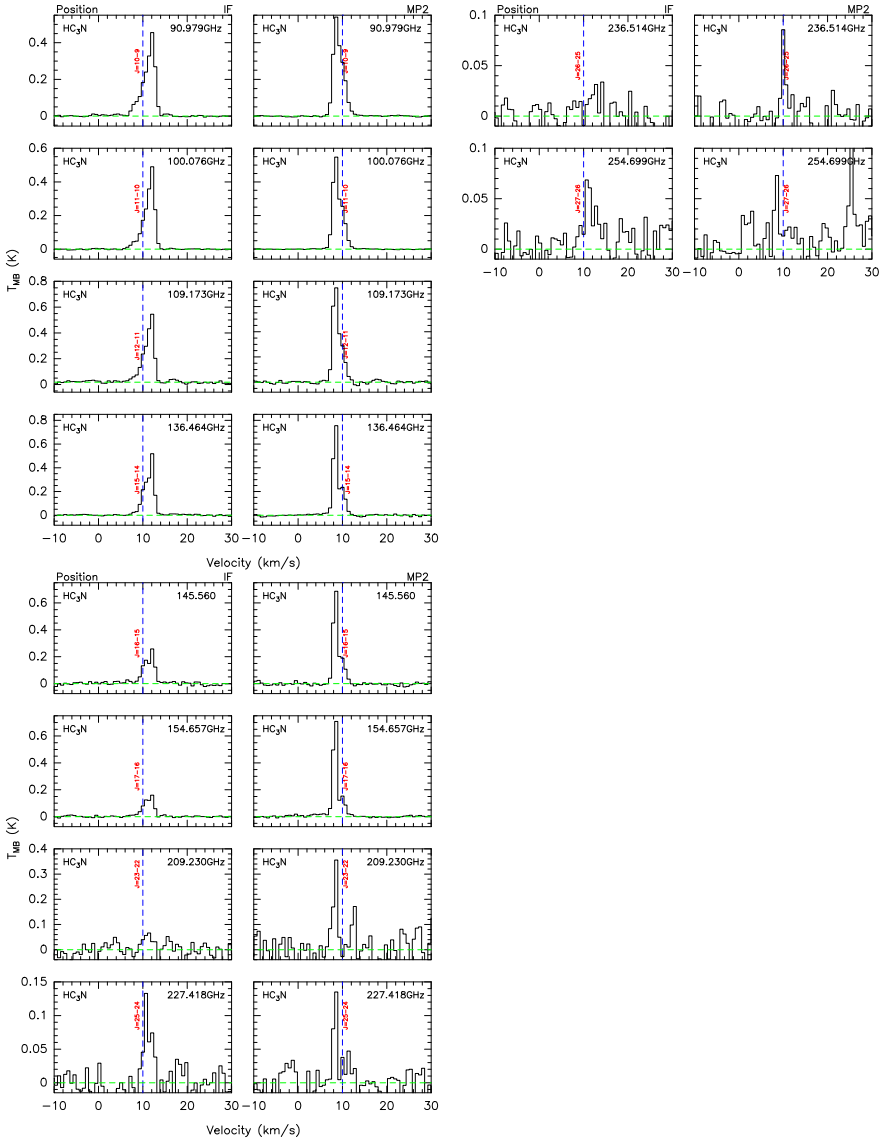
Figure B.22: Observed spectra of the HC₃N molecule at the IF (column 1 and 3) and MP2 position (column 2 and 4).
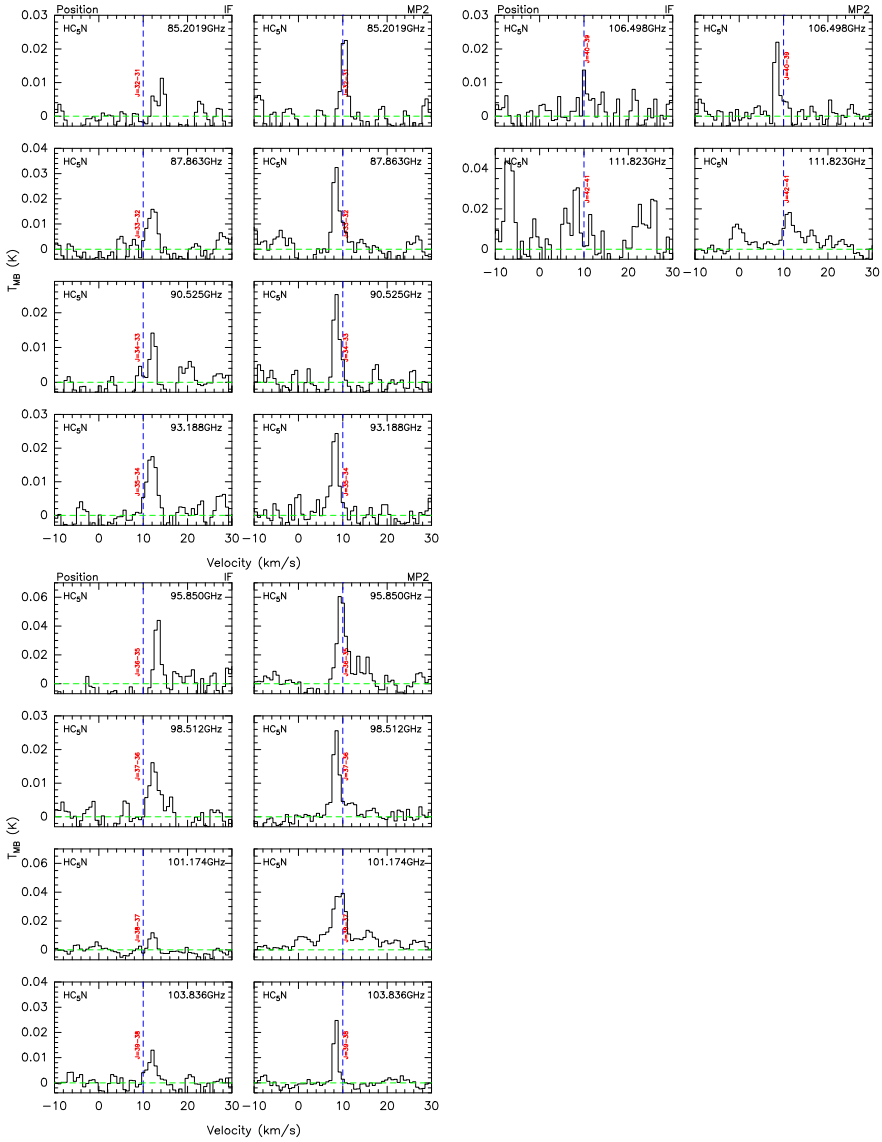
Figure B.23: Observed spectra of the HC$_5$N molecule at the IF (column 1 and 3) and MP2 position (column 2 and 4).
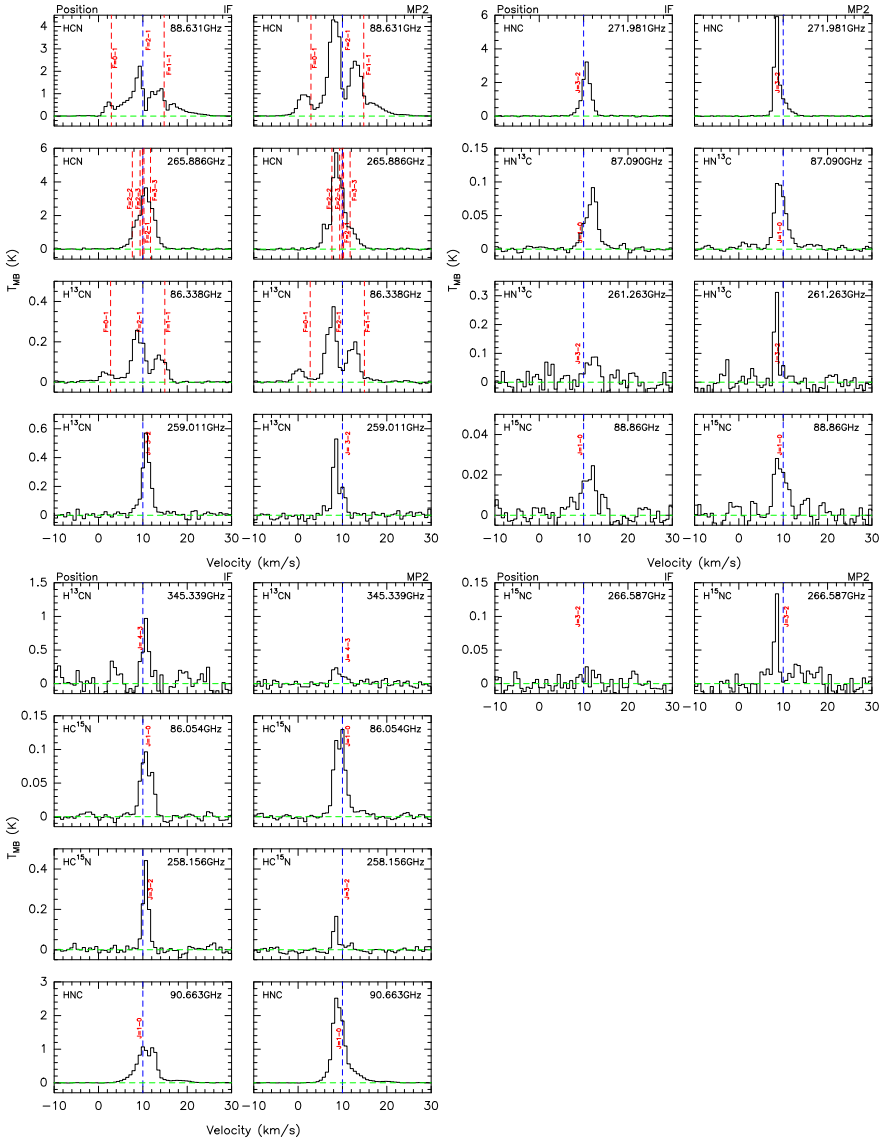
Figure B.24: Observed spectra of the HCN, HNC and their corresponding isotopologues at the IF (column 1 and 3) and MP2 position (column 2 and 4).
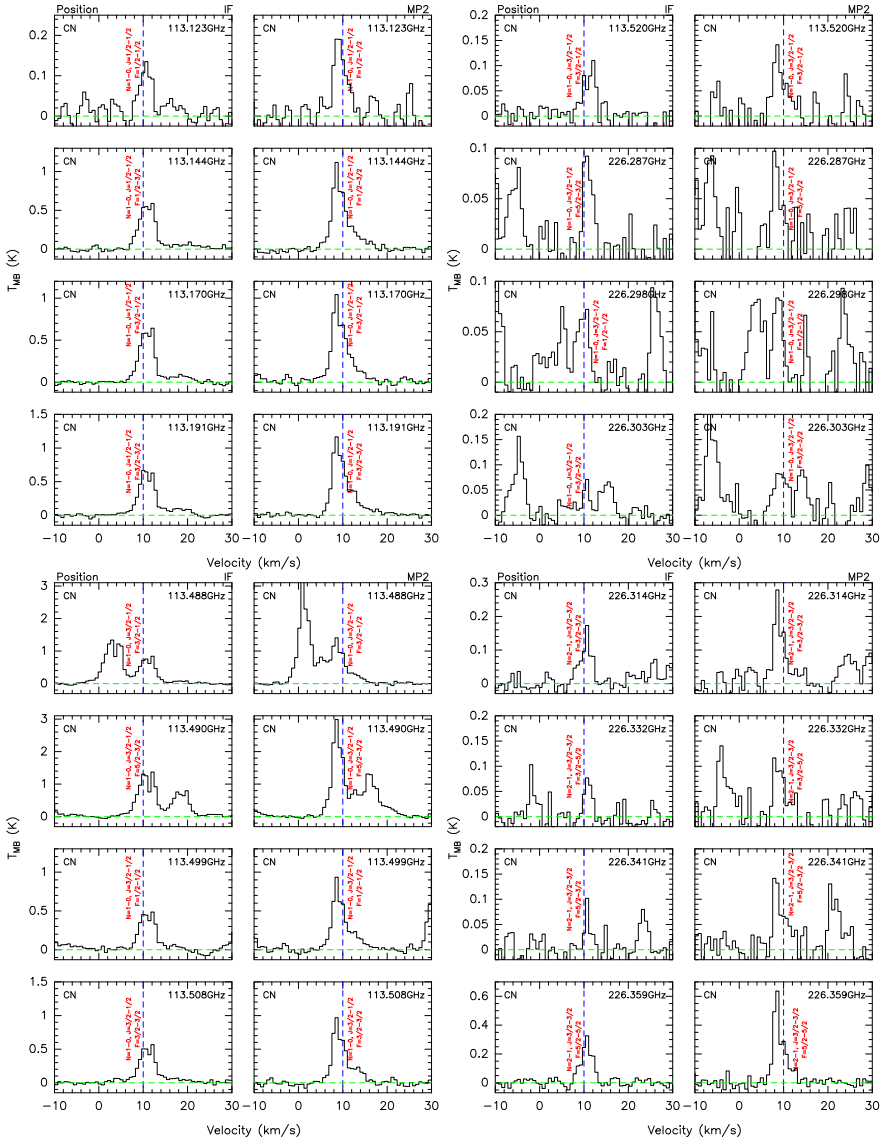
Figure B.25: Observed spectra of the CN molecule at the IF (column 1 and 3) and MP2 position (column 2 and 4).
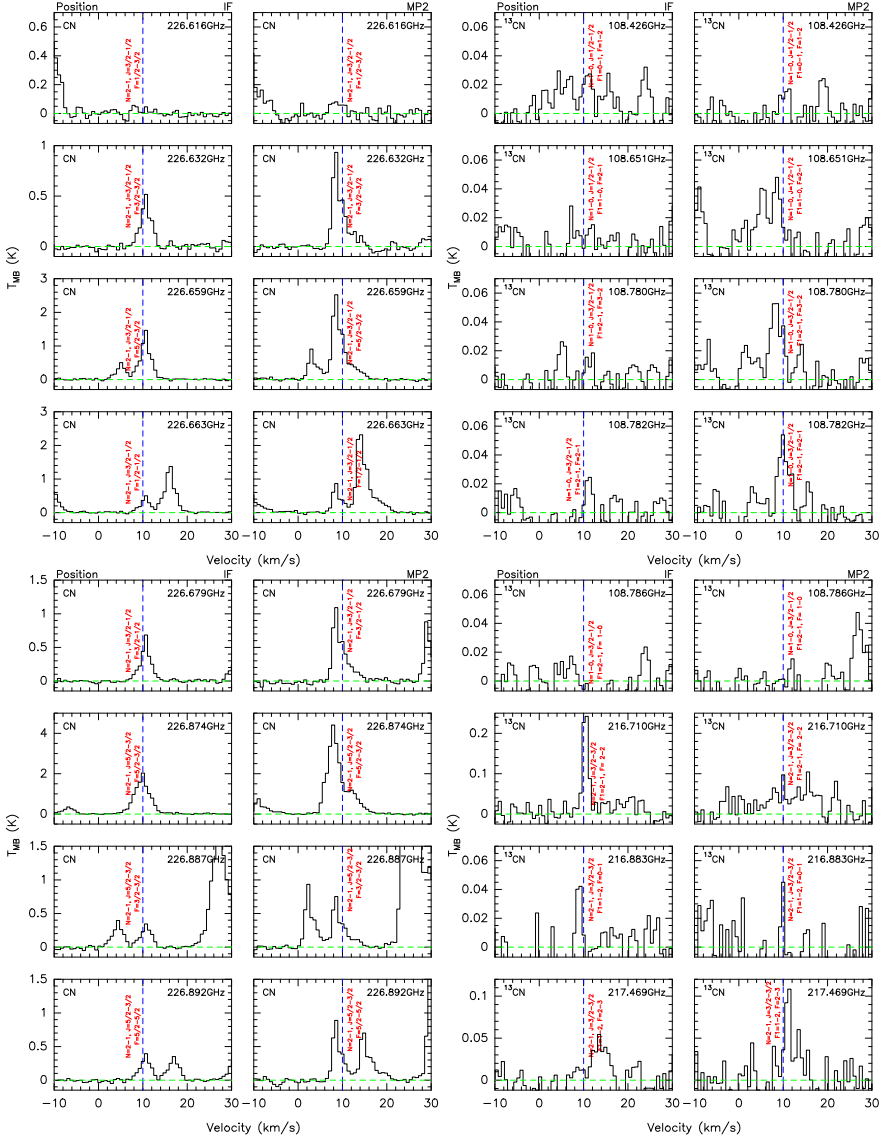
Figure B.26: Observed spectra of the CN molecule at the IF (column 1) and MP2 position (column 2). Observed spectra of the [13]CN molecule at the IF (column 3) and MP2 position (column 4).
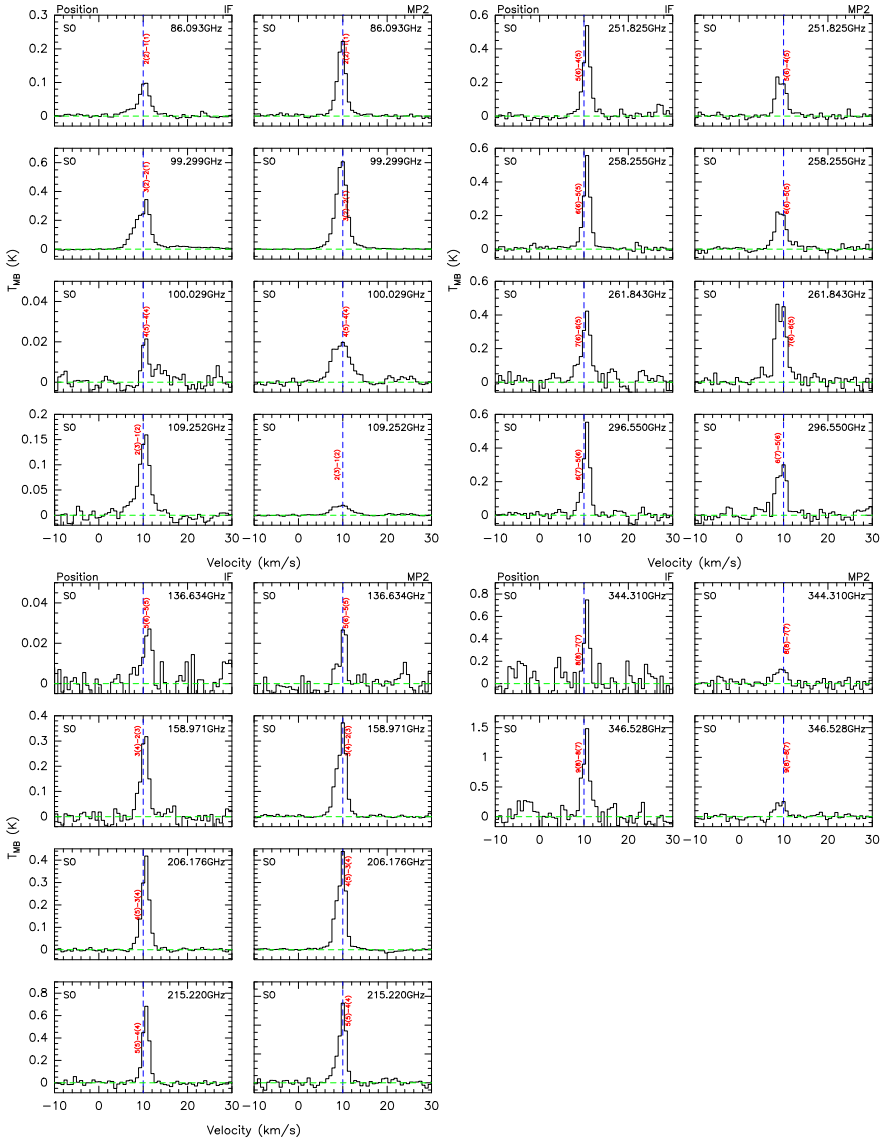
Figure B.27: Observed spectra of the SO molecule at the IF (column 1 and 3) and MP2 position (column 2 and 4).
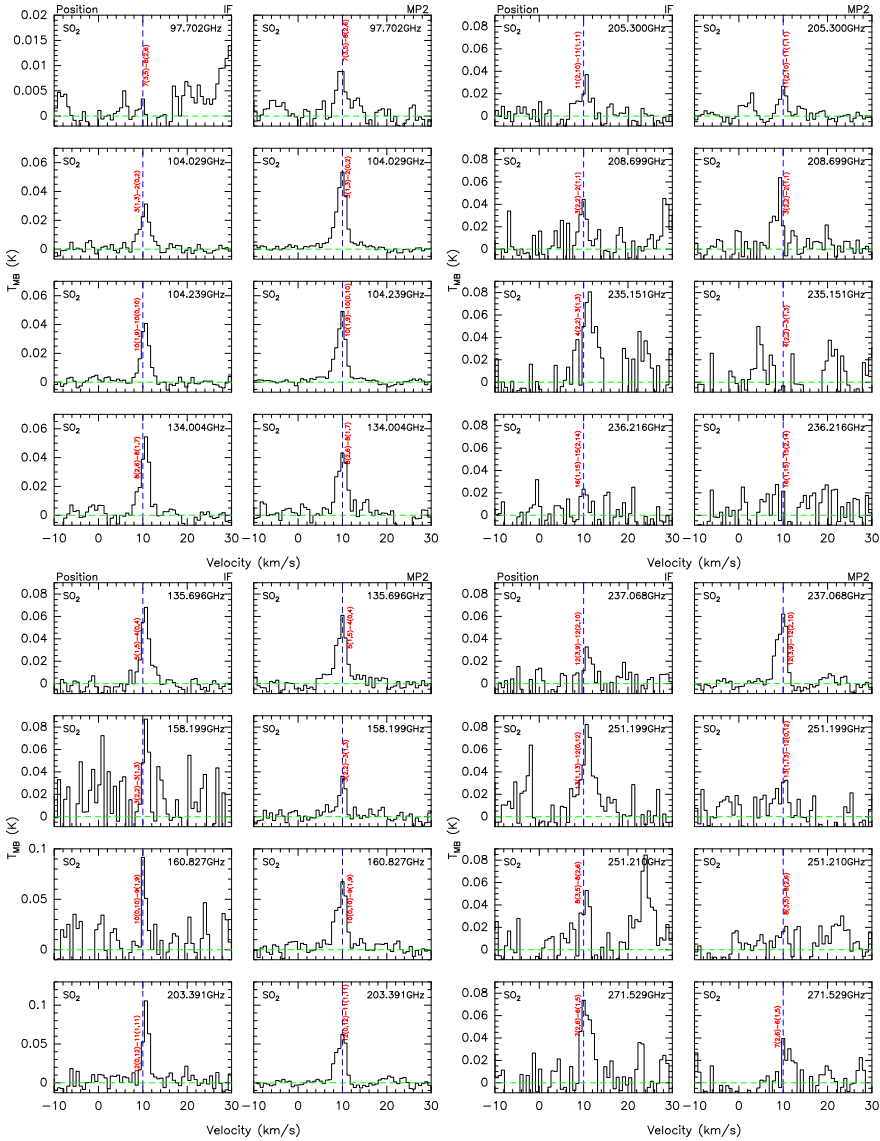
Figure B.28: Observed spectra of the SO_2 molecule at the IF (column 1 and 3) and MP2 position (column 2 and 4).
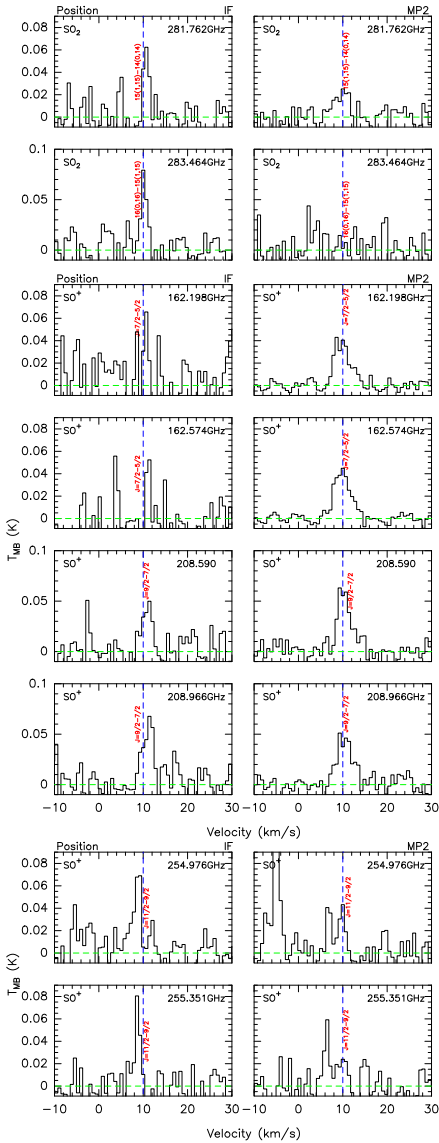
Figure B.29: Observed spectra of the SO_2 and SO^+ molecule at the IF (column 1) and MP2 position (column 2).
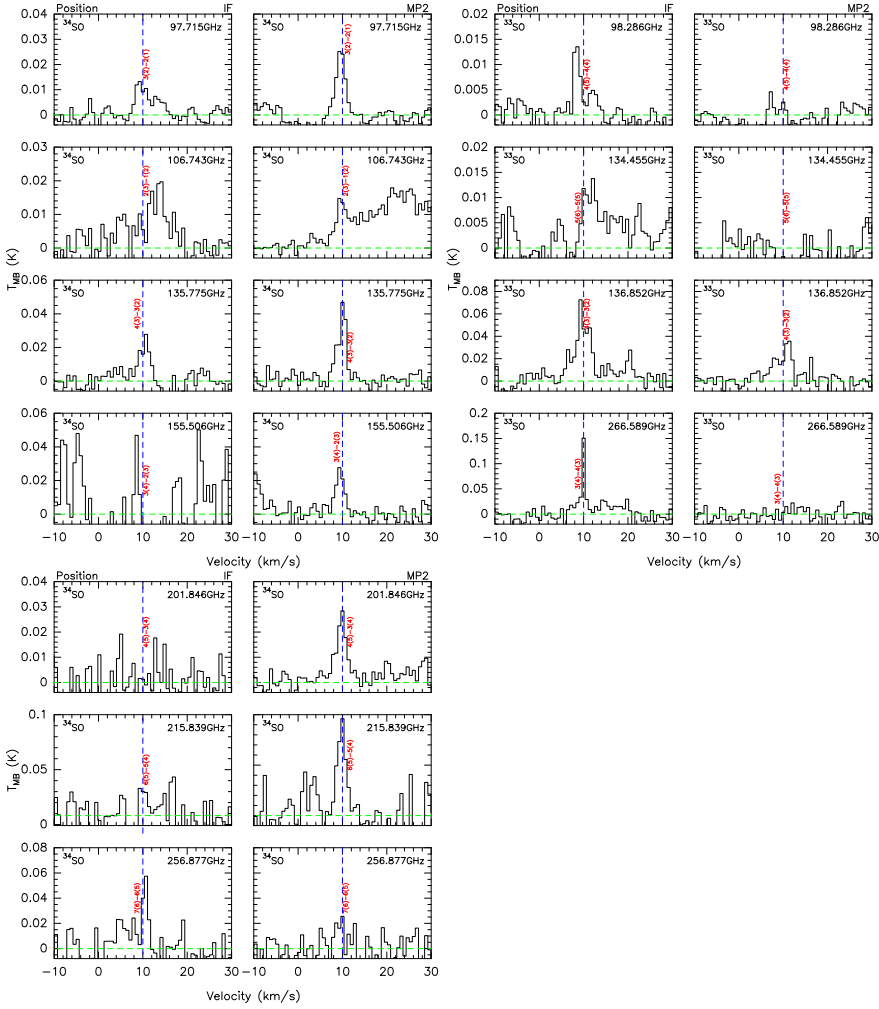
Figure B.30: Observed spectra of the ^{34}SO molecule at the IF (column 1) and MP2 position (column 2). Observed spectra of the ^{33}SO molecule at the IF (column 3) and MP2 position (column 4).
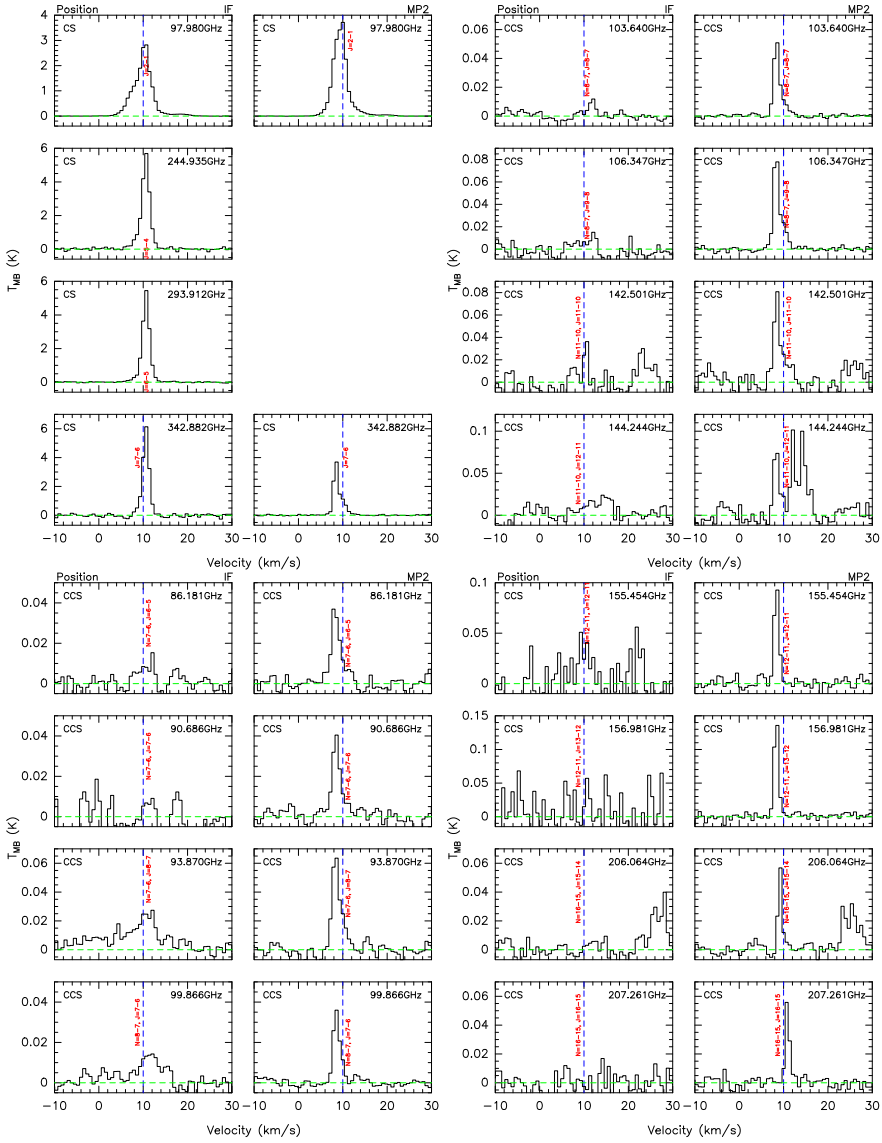
Figure B.31: Observed spectra of the CS and CCS molecules at the IF (column 1 and 3) and MP2 position (column 2 and 4).
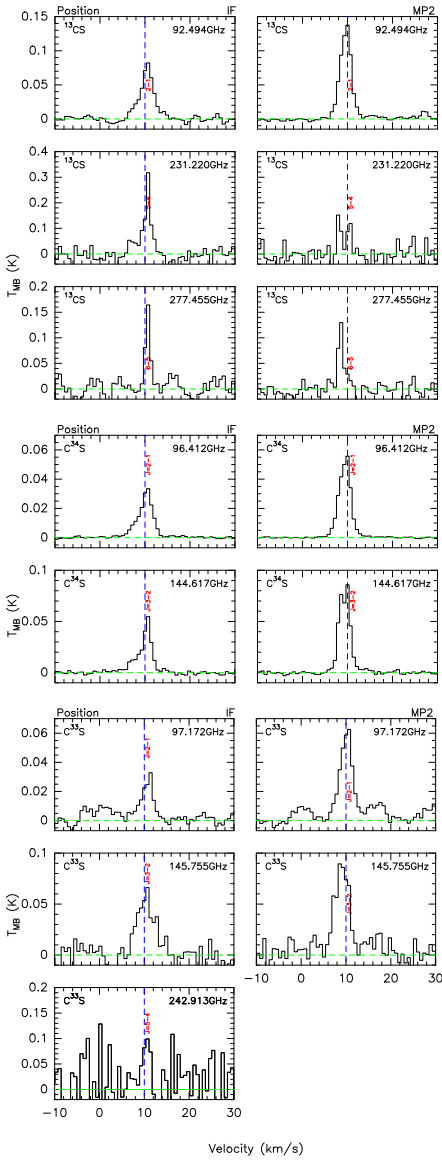
Figure B.32: Observed spectra of the ^{13}CS, C^{33}S and C^{34}S molecules at the IF (column 1) and MP2 position (column 2).
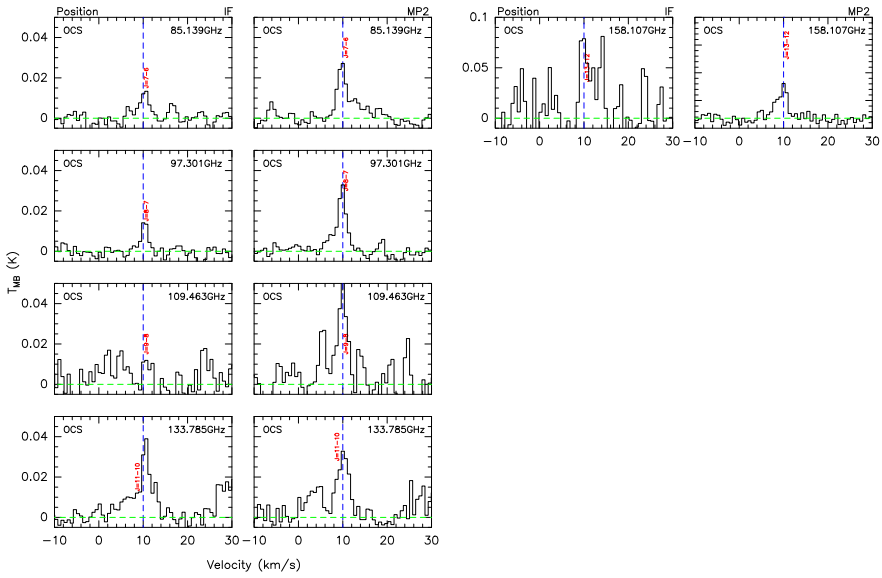
Figure B.33: Observed spectra of the OCS molecules at the IF (column 1 and 3) and MP2 position (column 2 and 4).
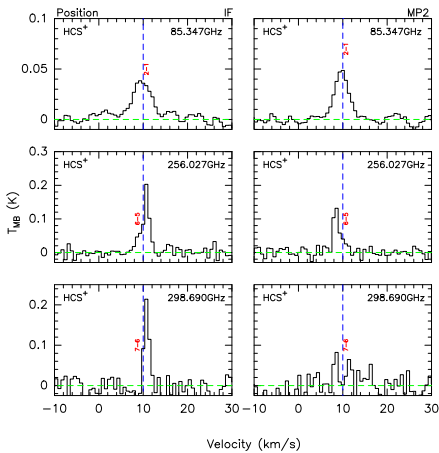
Figure B.34: Observed spectra of the HCS^+ molecules at the IF (column 1 and 3) and MP2 position (column 2 and 4).
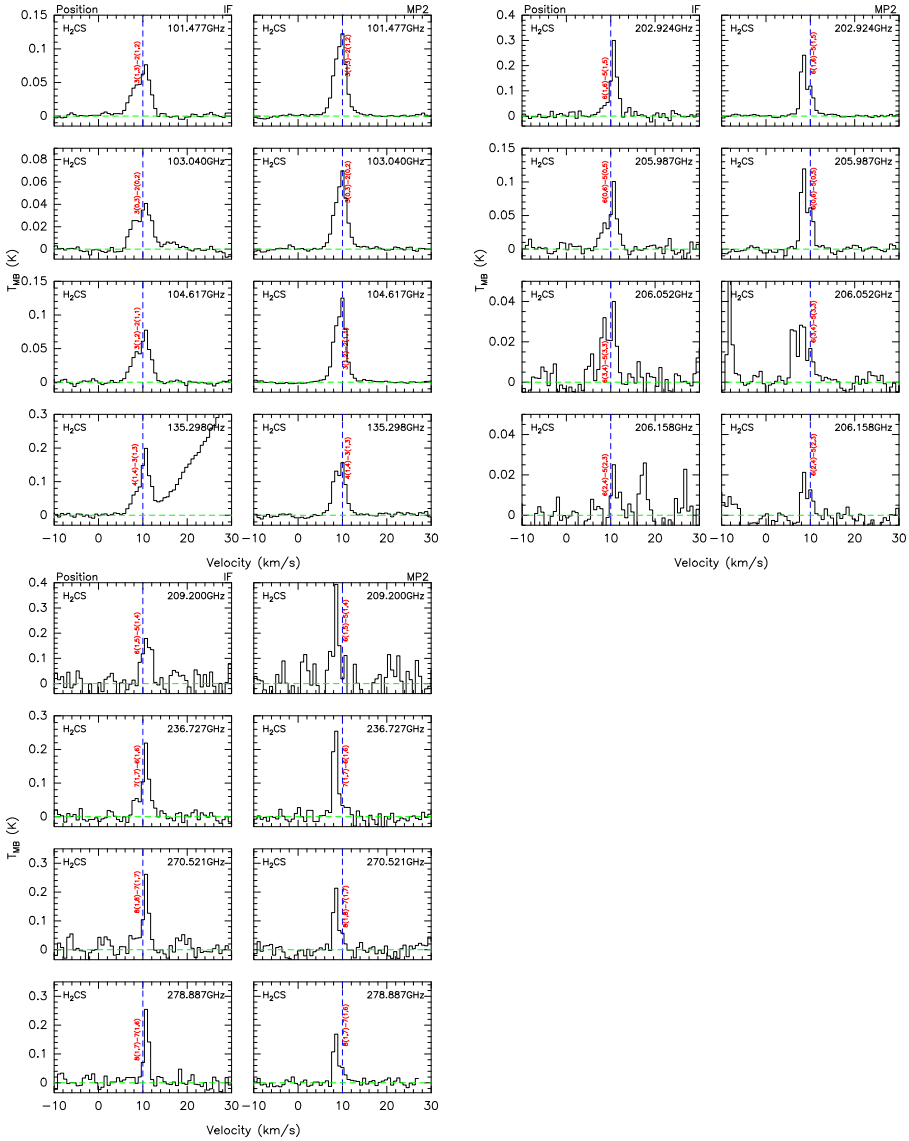
Figure B.35: Observed spectra of the H$_2$CS molecules at the IF (column 1 and 3) and MP2 position (column 2 and 4).
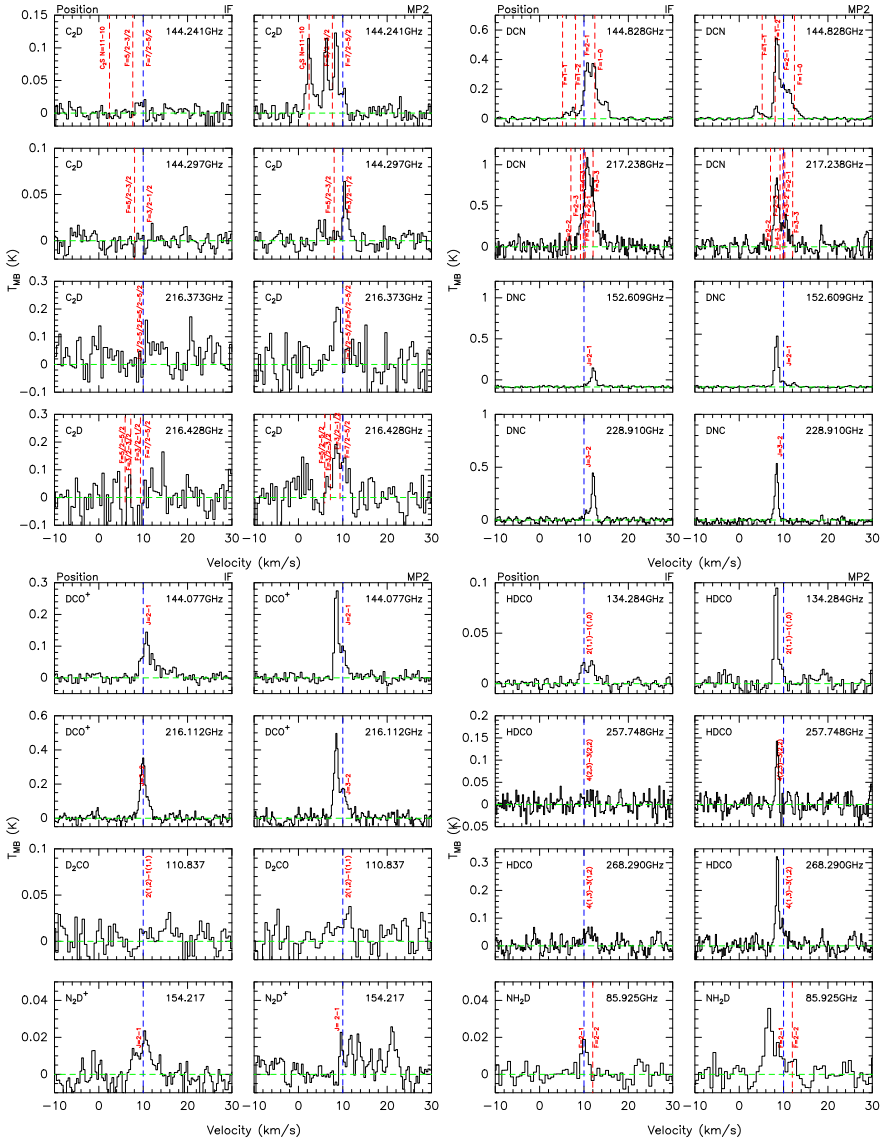
Figure B.36: Observed spectra of the deuterated molecule at the IF (column 1 and 3) and MP2 position (column 2 and 4).
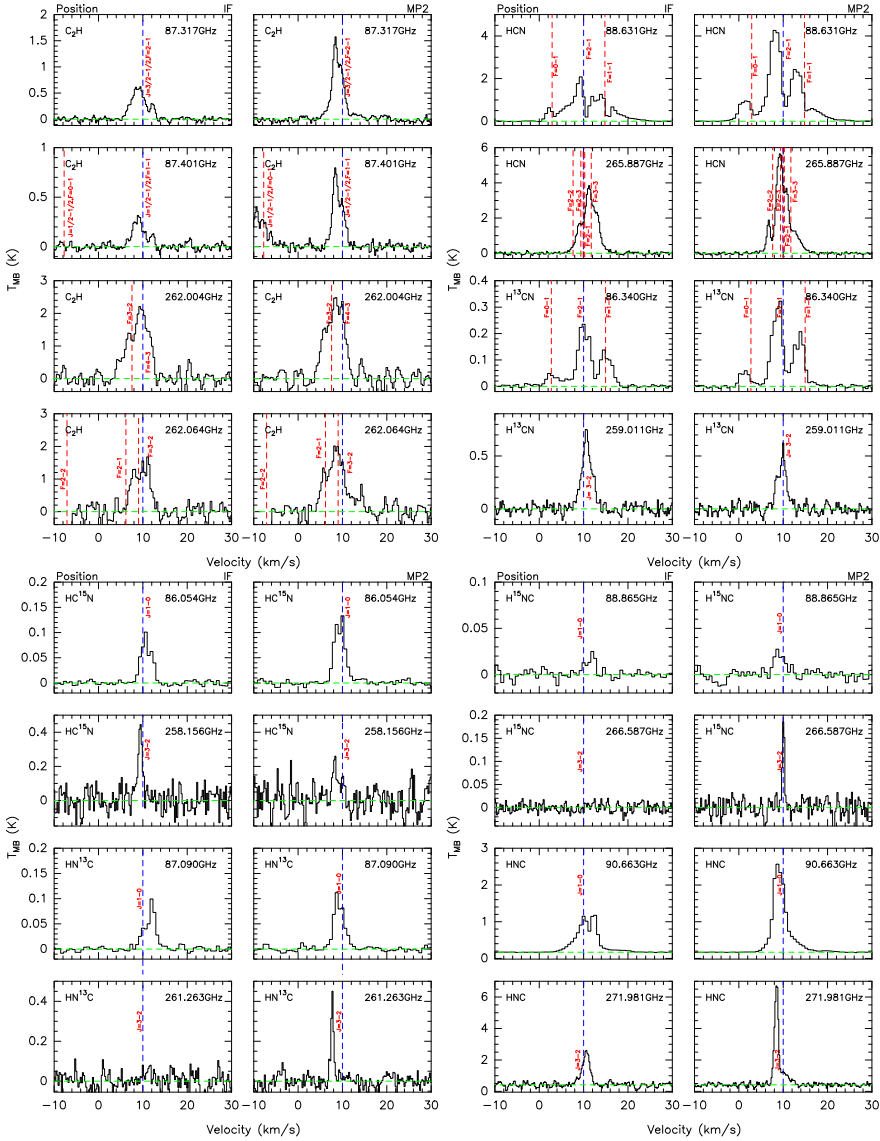
Figure B.37: Observed spectra of the hydrogenated molecule, corresponding to the deuterated molecules, at the IF (column 1 and 3) and MP2 position (column 2 and 4).
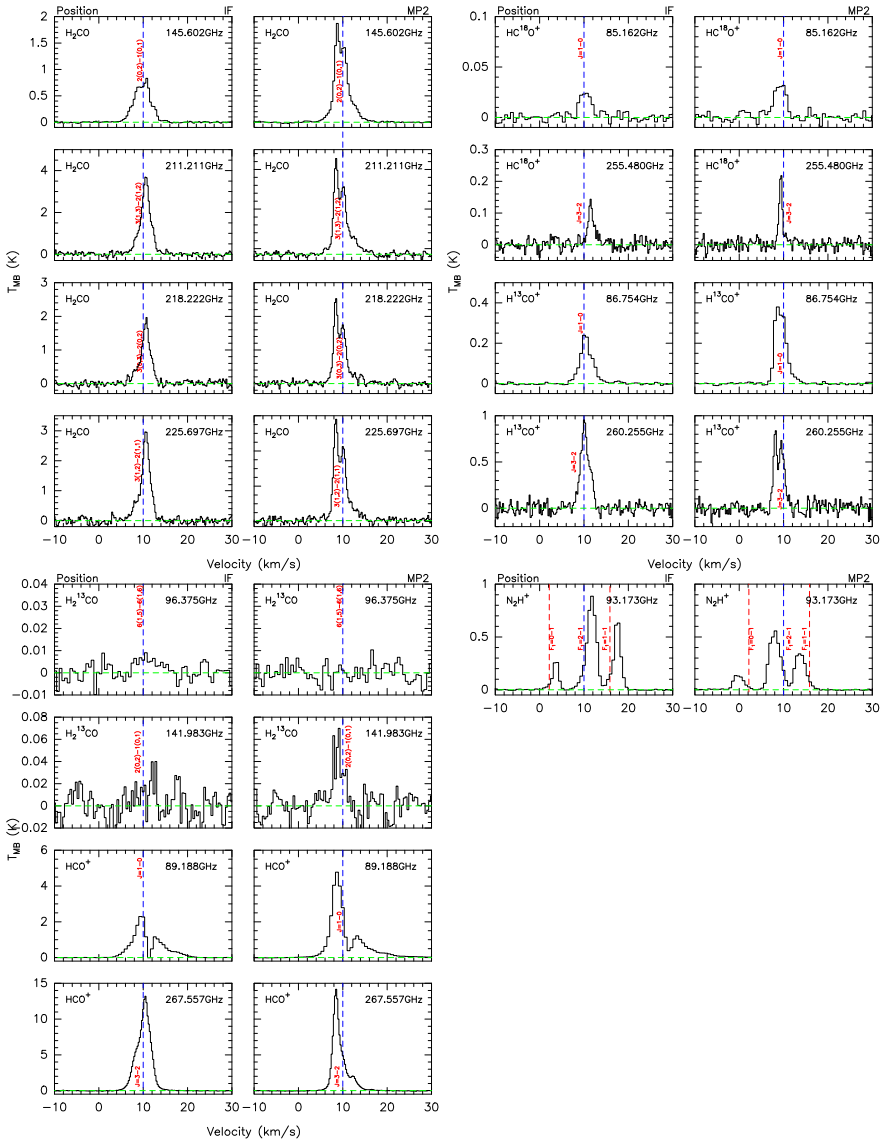
Figure B.38: Observed spectra of the hydrogenated molecule, corresponding to the deuterated molecules, at the IF (column 1 and 3) and MP2 position (column 2 and 4).

B.3　Gaussian fits

This section contains the Gaussian fits in the IF and MP2 position (from Table B.1 to B.6) for the detected species. The the tables list the following parameters for both position: specie, transition, frequency, beam size (HPBW), area (in K km s^{-1}), line velocity (in km s^{-1}), line width (in km s^{-1}), main beam temperature (in K) and rms (in mK). In the tables, the blank mark indicate that this line was not observed, the "−" mark indicate that it was not detected. The tables for the MP2 position also indicate if the line was mapped (with a ✓mark).

Table B.1: Gaussian fits of the 3mm lines at IF position.

Specie	Trans	Freq	HPBW	IF				
				Area	V	Width	T_{MB}	rms
		[GHz]	["]	[K km s^{-1}]	[km s^{-1}]	[km s^{-1}]	[K]	[mK]
$^{13}C_2H$	N=1–0	84.1241	29.2	–	–	–	–	4.07
DC_3N	J=10–9	84.4298	29.2	0.09±0.01	11.57±0.54	7.78±1.54	0.010	3.40
CH_3OH	5(-1,5)–4(0,4)	84.5212	29.1	0.06±0.03	-0.29±2.42	7.93±0.73	0.006	4.02
		84.5212	29.1	0.29±0.01	10.15±0.09	4.03±0.22	0.068	4.02
c-C_3H_2	J=3–2	84.7277	29.0	0.07±0.01	10.76±0.50	6.93±1.22	0.010	3.13
H60γ		84.9139	29.0	2.66±0.02	11.67±0.12	30.36±0.26	0.082	2.99
He60γ		84.9506	29.0	0.47±0.02	7.93±1.02	42.25±2.08	0.010	2.79
C60γ		84.9506	29.0	–	–	–	–	2.79
OCS	J=7–6	85.1391	28.9	0.04±0.01	10.26±0.22	2.72±0.61	0.013	2.76
		85.1391	28.9	0.01±0.01	16.58±0.25	1.57±0.51	0.008	2.76
$HC^{18}O^+$	J=1–0	85.1622	28.9	0.08±0.01	10.31±0.15	2.92 ± 0.30	0.026	2.92
HC_5N	J=32–31	85.2019	28.9	0.01±0.01	12.40±0.11	0.77±0.50	0.009	3.19
		85.2019	28.9	0.01±0.01	14.33±0.19	1.12±0.33	0.012	3.19
$C^{13}CH$	N=1–0	85.2293	28.9	0.03^c	–	–	–	3.12
$C^{13}CH$	N=1–0	85.2300	28.9	0.02^c	–	–	–	3.14
$C^{13}CH$	N=1–0	85.2320	28.9	–	–	–	–	2.99
c-C_3H_2	2(1,2)–1(0,1)	85.3388	28.8	0.36±0.02	8.96±0.05	2.16±0.11	0.157	8.79
		85.3388	28.8	0.14±0.03	13.91±0.17	2.23±0.28	0.057	8.79
		85.3388	28.8	0.37±0.04	18.03±0.29	5.65±0.57	0.061	8.79
HCS^+	J=2–1	85.3478	28.8	0.21±0.01	9.71±0.15	5.13±0.40	0.038	4.09
CH_3CCH	5(3)–4(3)	85.4426	28.8	0.05±0.02	12.42±1.08	6.79±2.73	0.008	3.22
		85.4426	28.8	0.02±0.01	11.20±0.29	1.75±0.81	0.009	3.22
CH_3CCH	5(2)–4(2)	85.4507	28.8	0.10±0.01	10.21±0.29	5.90±0.85	0.016	3.26
CH_3CCH	5(1)–4(1)	85.4556	28.8	0.15±0.02	11.07±0.14	3.50±0.30	0.041	4.08
CH_3CCH	5(0)–4(0)	85.4573	28.8	0.27±0.02	10.96±0.15	5.91±0.41	0.043	3.44
C_4H	9(10,9)–8(9,8)	85.6340	28.7	0.16±0.02	12.21±0.69	13.30±2.27	0.012	3.00
		85.6340	28.7	0.07±0.01	9.84±0.16	2.88±0.51	0.021	3.00
c-C_3H_2	4(3,2)–4(2,3)	85.6564	28.7	0.11±0.01	10.71±0.15	4.33±0.32	0.023	2.82
C_4H	9(9,8)–8(8,7)	85.6725	28.7	0.11±0.01	9.71±0.18	4.18±0.44	0.025	3.37
		85.6725	28.7	0.03±0.01	16.41±0.80	3.91±1.66	0.006	3.37

Continued on next page

Table B.1 – *Continued from previous page*

Specie	Trans	Freq	HPBW	IF				
				Area	V	Width	T_{MB}	rms
		[GHz]	["]	[K km s^{-1}]	[km s^{-1}]	[km s^{-1}]	[K]	[mK]
H42α		85.6885	28.7	19.38±0.02	13.34±0.02	30.42±0.03	0.599	2.72
He42α		85.7219	28.7	0.29±0.02	10.71±0.59	18.68±1.21	0.014	3.43
C42α		85.7309	28.7	0.26±0.01	9.60±0.11	5.47±0.25	0.045	3.60
NH$_2$D	1(1,1)0s–1(0,1)0a	85.9262	28.6	0.05±0.01	11.69±0.81	7.07±1.78	0.006	3.26
		85.9262	28.6	0.02±0.01	11.96±0.14	1.13±0.30	0.017	3.26
HC^{15}N	J=1–0	86.0549	28.6	0.15±0.01	10.11±0.03	1.67±0.07	0.082	3.90
		86.0549	28.6	0.12±0.01	11.78±0.05	1.75±0.13	0.061	3.90
SO	2(2)–1(1)	86.0939	28.6	0.18±0.02	9.12±0.37	6.71±0.69	0.025	4.09
		86.0939	28.6	0.18±0.02	10.39±0.05	2.14±0.15	0.080	4.09
C$_2$S	N=7–6, J=6–5	86.1813	28.5	0.04±0.01	10.64±0.43	3.77±0.70	0.010	3.30
H^{13}CN	J=1–0, F=1–1	86.3387	28.5	0.30±0.02	10.47±0.06	2.21±0.13	0.128	3.92
		86.3387	28.5	0.11±0.01	12.33±0.07	1.58±0.14	0.068	3.92
	J=1–0, F=2–1	86.3401	28.5	0.64±0.03	10.70±0.06	2.49±0.17	0.241	3.92
		86.3401	28.5	0.11±0.01	12.45±0.07	0.75±0.36	0.128	3.92
	J=1–0, F=0–1	86.3422	28.5	0.13±0.03	10.80±0.31	2.61±0.67	0.046	3.92
		86.3422	28.5	0.07±0.03	14.08±0.63	2.59±0.14	0.027	3.92
H70ε		86.4879	28.4	0.82±0.02	11.28±0.41	30.18±0.88	0.025	3.19
t-HCOOH	4(1,4)–3(1,3)	86.5461	28.4	0.02^c	–	–	–	3.42
HCO	1(0,1)–0(0,0)	86.6707	28.4	0.08±0.01	9.04±0.10	1.73±0.19	0.042	5.03
		86.6707	28.4	0.04±0.01	14.04±0.220	1.62±0.35	0.023	5.03
		86.6707	28.4	0.05±0.01	18.07±0.586	5.27±0.89	0.010	5.03
H74ζ		86.6883	28.4	0.78±0.02	7.41±0.46	34.48±1.02	0.021	2.84
HCO	1(0,1)–0(0,0)	86.7083	28.4	0.06±0.01	9.07±0.15	1.89±0.25	0.028	4.87
		86.7083	28.4	0.03±0.01	14.15±0.25	1.65±0.44	0.017	4.87
H^{13}CO$^+$	J=1–0	86.7543	28.3	0.77±0.01	10.45±0.03	3.23±0.07	0.224	3.69
		86.7543	28.3	0.08±0.01	12.53±0.05	1.26±0.11	0.058	3.69
HCO	1(0,1)–0(0,0), J=1/2–1/2, F=1–1	86.7775	28.3	0.04±0.01	9.10±0.16	1.49±0.28	0.024	4.68
		86.7775	28.3	0.04±0.01	18.77±1.00	5.61±1.32	0.007	4.68
HCO	1(0,1)–0(0,0), J=1/2–1/2, F=0–1	86.8058	28.3	0.03^c	–	–	–	3.86
SiO	J=2–1	86.8469	28.3	0.11±0.01	9.32±0.06	1.95±0.12	0.055	3.61
		86.8469	28.3	0.04±0.01	17.13±0.75	5.95±1.09	0.067	3.61
HN^{13}C	J=1–0	87.0908	28.2	0.08±0.01	10.04 ± 0.12	1.67±0.27	0.042	2.97

Table B.1 – *Continued from previous page*

Specie	Trans	Freq	HPBW	IF				
				Area	V	Width	T_{MB}	rms
		[GHz]	["]	[K km s^{-1}]	[km s^{-1}]	[km s^{-1}]	[K]	[mK]
		87.0908	28.2	0.17±0.01	12.14 ± 0.05	1.60±0.13	0.097	2.97
$C_3^{13}CC_2H$	31(1323131)–30(13)	87.2725	28.2	–	–	–	–	3.35
C_2H	N=1–0, J=3/2–1/2, F=1–1	87.2841	28.2	0.26±0.01	8.79±0.05	3.20±0.12	0.076	3.51
		87.2841	28.2	0.12±0.01	12.10±0.19	3.60±0.55	0.030	3.51
		87.2841	28.2	0.07±0.01	17.63±0.36	4.21±0.97	0.016	3.51
Phenol		87.2924	28.2	–	–	–	–	3.51
C_2H	1(2,2)–0(1,1)	87.3169	28.2	1.35±0.02	8.71±0.01	2.59±0.02	0.489	3.52
		87.3169	28.2	2.31±0.01	10.88±0.05	7.07±0.07	0.307	3.52
		87.3169	28.2	0.71±0.02	18.72±0.07	5.23±0.14	0.128	3.52
C_2H	1(2,1)–0(1,0)	87.3286	28.2	1.33±0.01	9.01±0.01	3.37±0.03	0.372	3.25
		87.3286	28.2	0.23±0.01	12.46±0.02	1.71±0.08	0.125	3.25
		87.3286	28.2	0.67±0.02	16.91±0.13	7.73±0.28	0.081	3.25
C_2H	1(1,1)–0(1,1)	87.4020	28.1	1.16±0.10	8.85±0.70	3.58±0.70	0.304	5.56
		87.4020	28.1	0.78±0.10	12.56±0.70	6.58±0.70	0.111	5.56
		87.4020	28.1	0.32±0.10	19.08±0.70	5.05±0.70	0.060	5.56
C_2H	1(1,0)–0(1,1)	87.4071	28.1	0.37±0.02	8.59±0.02	2.76±0.06	0.125	2.93
		87.4071	28.1	0.37±0.01	11.09±0.18	5.31±0.15	0.066	2.93
		87.4071	28.1	0.24±0.02	18.51±0.49	8.93±0.47	0.025	2.93
C_2H	1(1,1)–0(1,0)	87.4465	28.1	0.27±0.02	15.05±0.59	16.08±0.76	0.016	2.71
		87.4465	28.1	0.26±0.01	9.026±0.04	3.18±0.11	0.077	2.71
		87.4465	28.1	0.06±0.01	12.23±0.08	1.74±0.15	0.032	2.71
		87.4465	28.1	0.02±0.01	18.55±0.07	1.43±0.29	0.014	2.71
H65γ		87.6146	28.1	1.44±0.02	11.66±0.20	28.59±0.43	0.047	3.03
HC_5N	J=33–32	87.8636	28.0	0.04±0.01	12.07±0.19	2.39±0.40	0.017	3.51
HNCO	4(0,4)–3(0,3)	87.9252	28.0	0.07±0.01	10.15±0.38	4.53±0.60	0.014	3.90
H52β		88.4056	27.8	5.59±0.03	12.80±0.09	30.25±0.19	0.174	4.69
He52β		88.4417	27.8	0.01^c	–	–	–	4.49
C52β		88.4498	27.8	0.04^c	–	–	–	4.17
$C_2H_5^{13}CN$	12(2,11)- 12(1,12)	88.5713	27.8	–	–	–	–	3.63
$C^{13}CCN$	N=9–8	88.5773	27.8	0.71±0.02	12.48±0.41	28.12±0.90	0.024	3.18
HCN	J=1–0	88.6316	27.7	0.88±0.44	2.32±0.70	1.77±0.70	0.467	14.60
		88.6316	27.7	7.83±0.44	9.10±0.70	9.39±0.70	0.783	14.60

Continued on next page

Table B.1 – *Continued from previous page*

Specie	Trans	Freq	HPBW	IF				
				Area	V	Width	T_{MB}	rms
		[GHz]	["]	[K km s^{-1}]	[km s^{-1}]	[km s^{-1}]	[K]	[mK]
		88.6316	27.7	1.88±0.44	9.08±0.70	1.21±0.70	1.455	14.60
		88.6316	27.7	3.59±0.44	15.04±0.70	7.11±0.70	0.475	14.60
H^{15}NC	J=1–0	88.8657	27.7	0.10±0.01	11.19±0.25	4.91±0.68	0.019	3.67
C$_2$H$_3$CN	17(1,16)–17(0,17)	89.1130	27.6	0.03±0.03	-3.93±0.65	9.63±2.05	0.003	3.54
		89.1130	27.6	0.22±0.04	10.80±0.99	14.01±2.05	0.014	3.54
		89.1130	27.6	7.95±0.02	27.87±0.91	8.77±2.05	0.010	3.49
HCO$^+$	J=1–0	89.1885	27.6	14.10±0.01	8.72±0.01	2.82±0.02	4.698	4.61
		89.1885	27.6	4.32 ± 0.08	13.90±0.04	3.77±0.10	1.078	4.61
H59γ		89.1982	27.6	2.58±0.03	12.70±0.18	31.99±0.45	0.076	3.83
HCCNC	J=9–8, F=10–9	89.4193	27.6	0.05±0.01	11.98±0.57	5.66±1.11	0.009	3.72
HOC$^+$	1(0,0)–0(0,0)	89.4874	27.5	0.04±0.01	9.10±0.15	1.76±0.34	0.019	3.79
t-HCOOH	4(0,4)–3(0,3)	89.5791	27.5	0.03$^{\mathrm{c}}$	–	–	–	3.18
U		89.8591	27.5	0.06$^{\mathrm{c}}$	–	–	–	3.46
t-HCOOH	4(2,3)–3(2,2)	89.8614	27.5	0.03$^{\mathrm{c}}$	–	–	–	3.59
C$_3$H	4 0 1 4 3 – 3 0 1 4 4	89.8688	27.5	–	–	–	–	3.43
gG'a-1,2-P	29(10,20)–29(9,21)	89.8899	27.5	0.15$^{\mathrm{c}}$	–	–	–	3.67
HOONO$_2$	N=11–10 J=6–6 F$_1$=6–5 F=1–1	89.9157	27.5	–	–	–	–	3.81
t-HCOOH	4(3,1)–3(3,0)	89.9503	27.5	–	–	–	–	3.49
C$_3$H$^+$	J=4–3	89.9576	27.5	0.08$^{\mathrm{c}}$	–	–	–	3.40
H73ζ		90.1697	27.3	1.62±0.04	11.10±0.63	54.52±1.3	0.028	3.40
^{15}NNH$^+$	J=1–0	90.2638	27.3	–	–	–	–	3.33
U		90.2730	27.3	0.07$^{\mathrm{c}}$	–	–	–	2.72
HC$_5$N	J=34–33	90.5258	27.1	0.02±0.01	12.20±0.16	1.44±0.32	0.015	3.33
HC^{13}CCN	J=10–9	90.5930	27.1	0.03$^{\mathrm{c}}$	–	–	–	4.23
HC^{13}CCN		90.6017	27.1	0.03±0.01	12.30±0.41	2.70±0.76	0.010	4.01
HNC	J=1–0	90.6635	27.1	4.43±0.04	10.33±0.02	4.26±0.04	0.977	6.79
		90.6635	27.1	0.75±0.03	12.55±0.01	1.21±0.03	0.584	6.79
		90.6635	27.1	0.51±0.03	17.39±0.03	6.87±0.41	0.069	6.79
CCS	N=7–6, J=7–6	90.6863	27.1	0.07$^{\mathrm{c}}$	–	–	–	8.25
HC$_3$N	J=10–9	90.9790	27.0	0.77±0.03	10.69±0.07	3.52±0.09	0.205	4.68
		90.9790	27.0	0.50±0.03	12.16±0.01	1.43±0.04	0.327	4.68
^{15}NNH$^+$	J=1–0	91.2056	26.9	0.06$^{\mathrm{c}}$	–	–	–	3.62

Table B.1 – *Continued from previous page*

Specie	Trans	Freq	HPBW	IF				
				Area	V	Width	T_{MB}	rms
		[GHz]	["]	[K km s^{-1}]	[km s^{-1}]	[km s^{-1}]	[K]	[mK]
Phenol		91.2564	26.9	0.01^{c}	–	–	–	3.71
Glyceraldehyde		91.4545	26.9	0.03±0.01	7.41±0.48	2.81±1.12	0.010	3.51
		91.4545	26.9	0.02±0.01	10.01±0.22	1.43±0.41	0.015	3.51
H2CCCHCN	4(2,2)–3(1,3)	91.4945	26.9	0.05±0.01	9.49±0.16	1.85±0.26	0.023	4.27
		91.4945	26.9	0.02±0.01	17.01±0.66	3.01±0.82	0.005	4.27
c-HCCCD	8(3,5)–7(6,2)	91.4971	26.9	0.03±0.01	7.64±0.21	1.91±0.47	0.016	3.97
		91.4971	26.9	0.04±0.01	12.75±0.24	2.23±0.52	0.015	3.97
H64δ		91.6629	26.9	1.72±0.03	11.80±0.28	31.33±0.64	0.052	4.41
c-C$_3$H	2 1 2 2 1–1 1 1 1 0	91.6927	26.8	–	–	–	–	3.72
c-C$_3$H	2 1 2 2 2–1 1 1 1 1	91.6994	26.8	0.03±0.01	8.61±0.20	1.74±0.41	0.015	3.75
		91.6994	26.8	0.07±0.01	16.26±0.48	5.79±0.84	0.011	3.75
CH$_3$CN	5(3)–4(3)	91.9711	26.7	0.18^{c}	–	–	–	11.10
CH$_3$CN	5(2)–4(2)	91.9799	26.7	–	–	–	–	10.80
CH$_3$CN	5(1)–4(1)	91.9853	26.7	0.11^{c}	–	–	–	10.40
CH$_3$CN	5(0)–4(0)	91.9870	26.7	0.17±0.03	12.18±0.23	3.04±0.63	0.056	10.40
		91.9870	26.7	0.05±0.02	17.55±0.19	1.07±0.47	0.040	10.40
H41α		92.0335	26.7	16.87±0.03	10.36±0.01	29.87±0.05	0.531	3.95
He41α		92.0686	26.7	0.25±0.02	8.01±0.73	17.49±1.81	0.013	3.81
C41α		92.0801	26.7	0.26±0.02	9.98±0.17	4.89±0.45	0.050	6.68
Glyceraldehyde	18(2,16)–17(2,15)	92.1804	26.7	0.12^{c}	–	–	–	3.93
^{13}CH$_2$CHCN	10(3,8)–9(3,7)	92.4323	26.7	0.22±0.02	8.48±0.63	16.57±2.07	0.012	3.23
C$_3$S	J=16–15	92.4884	26.7	–	–	–	–	3.87
^{13}CS	2(0)–1(0)	92.4943	26.6	0.28±0.01	10.50±0.06	3.46±0.17	0.074	4.05
U		92.8586	26.6	0.01^{c}	–	–	–	4.05
DC$_3$N	J=11–10	92.8723	26.5	0.06±0.01	11.80±0.17	2.55±0.59	0.023	4.05
t-HCOOH	4(1,3)–3(1,2)	93.0983	26.5	0.02^{c}	–	–	–	19.65
N$_2$H$^+$	J=1–0, F=1–1	93.1718	26.4	1.28±0.01	11.66±0.01	1.84±0.01	0.652	4.21
	J=1–0, F=2–1	93.1733	26.4	2.27±0.01	11.74±0.01	2.46±0.01	0.868	4.21
	J=1–0, F=0–1	93.1761	26.4	0.45±0.01	11.47±0.02	1.50±0.04	0.283	4.21
HC$_5$N	J=35–34	93.1881	26.4	0.05±0.01	11.89±0.17	2.60±0.38	0.018	3.36
A-CH$_3$CHO	5(1,5)–4(1,4)A	93.5809	26.3	0.14±0.02	11.60±0.41	8.64±1.15	0.015	3.55
		93.5809	26.3	0.12±0.02	28.01±0.95	12.65±1.83	0.009	3.19

Continued on next page

Table B.1 – *Continued from previous page*

Specie	Trans	Freq	HPBW	IF				
				Area	V	Width	T_{MB}	rms
		[GHz]	["]	[K km s^{-1}]	[km s^{-1}]	[km s^{-1}]	[K]	[mK]
E-CH$_3$CHO	5(1,5)-4(1.4)	93.5952	26.3	0.13±0.03	9.21±0.67	8.37±2.38	0.015	4.06
H51β		93.6065	26.3	5.53±0.03	10.88±0.07	30.04±0.15	0.173	3.58
H58γ		93.7751	26.2	2.87±0.02	11.04±0.07	31.08±0.27	0.087	3.56
He58γ		93.8097	26.2	0.12±0.02	9.63±0.58	8.10±2.48	0.014	3.95
C58γ		93.8252	26.2	0.97±0.01	11.36±0.70	28.39±0.70	0.032	3.39
		93.8252	26.2	0.14±0.01	34.43±0.70	16.20±0.70	0.008	3.39
CCS	N=7–6, J=8–7	93.8701	26.2	0.22±0.03	6.04±1.17	20.66±2.38	0.010	3.97
		93.8701	26.2	0.06±0.01	10.95±0.26	3.42±0.63	0.018	3.97
C$_2$H$_5$CN		93.9493	26.2	0.05±0.02	4.23±0.71	3.71±1.33	0.012	3.91
		93.9493	26.2	0.04±0.02	0.98±0.23	2.02±0.57	0.020	3.91
CH$_3$OOH		93.9608	26.2	0.05±0.02	7.72±0.40	2.51±1.29	0.020	7.41
		93.9608	26.2	0.06±0.02	11.97±0.55	3.31±2.02	0.016	7.41
HC$_5$N	N=35–34, J=4–4	93.9706	26.2	0.08±0.02	4.62±0.90	6.79±2.59	0.011	5.39
		93.9706	26.2	0.06±0.01	11.81±0.12	1.59±0.30	0.036	5.39
		93.9706	26.2	0.09±0.01	14.84±0.14	2.39±0.42	0.036	5.39
H68ε		94.0720	26.2	1.17±0.03	13.80±0.44	34.70±1.04	0.032	4.19
U		94.2693	26.1	0.17±0.02	7.87±0.96	13.83±1.55	0.012	3.62
		94.2693	26.1	0.02±0.01	8.36±0.07	0.80±0.11	0.024	3.62
		94.2693	26.1	0.05±0.02	11.49±0.22	2.87±0.74	0.017	3.62
CH$_3$CHO		94.2897	26.1	0.04±0.02	7.72±0.33	2.74±1.26	0.015	3.64
		94.2897	26.1	0.05±0.01	11.22±0.29	2.59±0.52	0.018	3.64
^{13}CCCH		94.2974	26.1	0.01^c	–	–	–	3.67
U		94.3164	26.1	0.07±0.01	8.18±0.18	2.74±0.51	0.024	3.97
		94.3164	26.1	0.07±0.01	12.14±0.19	2.73±0.44	0.023	3.97
CH$_3$OH		94.5417	26.1	0.08^c	–	–	–	3.42
C$_4$H	10(11,10)–9(10,9)	95.1503	25.9	0.20±0.01	9.70±0.14	5.48±0.41	0.034	3.72
	10(11,11)–9(10,10)	95.1503	25.9	0.05±0.01	18.42±0.41	3.97±1.28	0.013	3.72
CH$_3$OH		95.1694	25.8	0.03±0.01	3.33±0.44	3.25±1.10	0.009	3.77
		95.1694	25.8	0.20±0.01	10.65±0.08	3.43±0.18	0.054	3.77
C$_4$H		95.1794	25.8	0.01^c	–	–	–	3.83
C$_4$H		95.1851	25.8	0.11±0.02	5.61±1.07	10.06±2.14	0.012	3.95
		95.1851	25.8	0.14±0.02	-2.86±0.22	4.69±0.51	0.027	3.95

Continued on next page

Table B.1 – *Continued from previous page*

Specie	Trans	Freq	HPBW	IF				
				Area	V	Width	T_{MB}	rms
		[GHz]	["]	[K km s^{-1}]	[km s^{-1}]	[km s^{-1}]	[K]	[mK]
C$_4$H		95.1889	25.8	0.13±0.02	9.20±0.25	4.50±0.55	0.026	4.24
		95.1889	25.8	0.10±0.02	17.60±1.21	9.62±2.37	0.001	4.24
C$_2$H$_3$CHO		95.4726	25.7	0.14±0.02	7.57±0.85	14.84±1.86	0.009	3.32
g'Ga-(CH$_2$OH)$_2$		95.5375	25.7	0.15±0.03	1.00±1.25	12.76±2.53	0.011	3.63
		95.5375	25.7	0.19±0.03	16.21±0.92	12.08±1.85	0.015	3.63
HC$_5$N		95.8506	25.7	0.03±0.01	13.24±0.18	1.47±0.45	0.020	5.21
U		95.8636	25.7	−	−	−	−	5.25
CH$_3$OH		95.9143	25.6	0.09±0.02	11.03±0.45	4.24±0.61	0.020	4.24
		95.9143	25.6	0.02±0.01	10.20±0.25	1.23±0.64	0.018	4.24
E-CH$_3$CHO		95.9474	25.6	0.06±0.01	11.20±0.38	4.27±1.03	0.013	4.02
		95.9474	25.6	0.03±0.01	17.72±0.56	3.36±1.30	0.009	4.02
A-CH$_3$CHO		95.9634	25.6	−	−	−	−	4.02
H63δ		95.9637	25.6	1.41±0.02	10.63±0.21	25.26±0.45	0.052	3.77
A-CH$_3$CHO		96.2742	25.5	0.11±0.02	11.22±0.36	7.70±1.48	0.013	2.96
		96.2742	25.5	0.02±0.01	18.64±0.41	2.38±0.97	0.009	2.96
		96.2742	25.5	0.06±0.01	25.13±0.61	6.82±1.99	0.008	2.96
C^{34}S		96.4129	25.5	0.01±0.01	10.26±0.02	3.57±0.05	0.217	3.69
E-CH$_3$CHO		96.4256	25.5	0.01^c	−	−	−	3.21
A-CH$_3$CHO		96.6326	25.5	0.03^c	−	−	−	3.82
CH$_3$OH		96.7393	25.4	0.25±0.03	8.09±0.09	2.85±0.34	0.081	3.16
		96.7393	25.4	0.23±0.02	11.28±0.11	2.71±0.19	0.080	3.16
CH$_3$OH		96.7413	25.4	0.36±0.07	8.18±0.22	3.41±0.31	0.098	3.42
		96.7413	25.4	0.49±0.07	11.51±0.21	3.85±0.36	0.119	3.42
CH$_3$OH		96.7445	25.4	0.18±0.02	10.00±0.29	6.21±0.60	0.028	3.18
		96.7445	25.4	0.06±0.02	11.22±0.15	2.35±0.41	0.022	3.18
CH$_3$OH		96.7555	25.4	0.06±0.02	7.70±1.97	8.17±2.12	0.007	3.40
		96.755	25.4	0.05±0.02	10.95±0.19	2.37±0.84	0.020	3.40
C$_2$H$_3$CN		96.9824	25.4	0.09^c	−	−	−	3.60
C^{33}S		97.1720	25.3	0.09±0.01	10.76±0.13	3.16±0.35	0.028	3.42
c-C$_3$H		97.1736	25.3	0.07±0.01	5.40±0.58	6.94±1.10	0.010	3.46
OCS	j=8–7	97.3012	25.3	0.03±0.01	10.32±0.14	1.66±0.36	0.015	2.81
CH$_3$OH		97.5828	25.2	0.06±0.02	3.48±0.78	8.42±3.11	0.007	2.59

Continued on next page

Table B.1 – *Continued from previous page*

Specie	Trans	Freq	HPBW	IF				
				Area	V	Width	T_{MB}	rms
		[GHz]	["]	[K km s^{-1}]	[km s^{-1}]	[km s^{-1}]	[K]	[mK]
		97.5828	25.2	0.08±0.01	10.61±0.15	3.28±0.37	0.022	2.59
CH$_3$OH		97.6777	25.2	0.09±0.01	8.84±0.14	2.37±0.29	0.035	2.65
		97.6777	25.2	0.04±0.01	11.73±0.40	2.62±0.78	0.013	2.65
H71ζ		97.6906	25.2	0.55±0.02	12.97±0.38	28.39±0.83	0.018	2.26
SO$_2$		97.7023	25.2	0.08^c	–	–	–	2.41
^{34}SO		97.7153	25.2	0.04±0.01	9.42±0.33	2.58±0.60	0.013	2.45
		97.7153	25.2	0.03±0.01	13.26±0.76	3.42±1.48	0.001	2.45
CS		97.9809	25.1	0.29±0.57	18.93±0.70	3.67±0.70	0.073	4.67
		97.9809	25.1	5.95±0.57	9.23±0.70	7.05±0.70	0.793	4.67
		97.9809	25.1	6.26±0.57	10.31±0.70	3.03±0.70	1.943	4.67
C$_3$H		97.9951	25.1	0.03±0.01	6.39±0.780	6.07±0.64	0.005	2.24
		97.9951	25.1	0.01±0.01	9.93±0.28	1.65±0.62	0.006	2.24
		97.9951	25.1	0.06±0.01	12.06±0.87	9.29±2.02	0.006	2.24
C$_3$H		98.0125	25.1	0.05^c	–	–	–	4.77
H67ε		98.1994	25.1	1.56±0.02	14.02±0.17	35.41±0.39	0.041	1.90
^{33}SO		98.2867	25.0	0.03±0.01	8.45±0.14	1.67±0.35	0.015	2.58
		98.2867	25.0	0.02±0.01	12.04±0.50	2.66±1.17	0.005	2.58
HC$_5$N		98.5125	24.9	0.04±0.01	12.43±0.19	2.78±0.49	0.015	2.77
H57γ		98.6500	24.9	0.13±0.01	7.20±0.78	18.59±1.77	0.007	2.25
He57γ		98.6708	24.9	2.61±0.02	9.65±0.10	29.60±0.23	0.083	2.63
E-CH$_3$CHO		98.8633	24.9	0.04±0.01	10.04±0.30	3.19±0.82	0.011	2.65
		98.8633	24.9	0.01±0.01	12.56±0.29	0.90±1.07	0.007	2.65
A-CH$_3$CHO	5(1,4)–4(1,3)A	98.9009	24.9	0.081±0.008	10.50±0.30	5.280±0.634	0.015	2.92
C$_3$N	N=10–9, J=21/2–19/2, F=19/2–17/2	98.9400	24.9	–	–	–	–	2.47
H40α		99.0219	24.9	18.75±0.02	10.35±0.01	30.59±0.03	0.576	2.16
He40α		99.0619	24.8	0.60±0.02	6.34±0.35	25.54±0.86	0.022	2.45
C40α		99.0722	24.8	0.31±0.01	10.32±0.10	6.61±0.26	0.045	2.75
H$_2^{13}$CS	3(2,1)–2(2,0)	99.0989	24.8	0.02±0.01	5.01±0.14	1.33±0.40	0.014	2.57
		99.0989	24.8	0.04±0.01	9.86±0.52	4.76±0.95	0.010	2.57
H50β		99.2252	24.8	5.66±0.02	13.58±0.06	30.12±0.12	0.176	3.08
C50β		99.2741	24.8	0.07±0.01	9.32±0.31	5.06±0.92	0.013	3.14
SO	3(2)–2(1)	99.2999	24.8	1.01±0.02	9.51±0.04	4.23±0.06	0.224	4.09

Table B.1 – *Continued from previous page*

Specie	Trans	Freq	HPBW	IF				
				Area	V	Width	T_{MB}	rms
		[GHz]	["]	[K km s^{-1}]	[km s^{-1}]	[km s^{-1}]	[K]	[mK]
				0.20±0.01	10.93±0.02	1.07±0.06	0.175	4.09
				0.31±0.03	18.74±0.01	18.53±1.90	0.016	4.09
HCCNC	J=10–9	99.3543	24.8	0.01^c	–	–	–	3.01
CH$_3$C^{13}CH	6(1)–5(1)	99.4779	24.7	0.01±0.01	10.33±0.77	14.01±2.01	0.007	3.01
HC^{13}CCN	J=11–10	99.6524	24.7	0.05^c	–	–	–	2.74
HCC^{13}CN	J=11–10	99.6615	24.7	0.02±0.01	12.02±0.17	1.37±0.43	0.011	2.84
CCS	N= 8–7, J= 7–6	99.8665	24.7	0.08±0.01	11.33±0.32	5.16±0.86	0.014	3.13
				0.01±0.01	15.62±0.34	1.37±0.50	0.007	3.13
SO	4(5)–4(4)	100.0296	24.7	0.04±0.01	10.42±0.11	1.51±0.27	0.023	3.31
				0.02±0.01	13.67±0.51	3.04±1.57	0.010	3.31
HC$_3$N	J=11–10	100.0764	24.7	0.68±0.02	10.81±0.04	3.10±0.05	0.206	3.10
				0.52±0.02	12.07±0.02	1.35±0.02	0.361	3.10
H$_2$CCO	5(1,5)– 4(1,4)	100.0945	24.7	0.08±0.01	9.85±0.26	4.94±0.60	0.015	2.93
H62δ		100.5403	24.7	1.15±0.02	14.73±0.19	27.85±0.42	0.039	2.93
CH$_3$CHO	13(2,11)–12(3,9)	100.6388	24.6	0.01^c	–	–	–	2.65
H$_2$CCO	5(3,3)–4(3,2)	101.0026	24.6	0.04^c	–	–	–	2.91
H$_2$CCO	5(0,5)–4(0,4)	101.0363	24.6	0.08±0.01	11.46±0.83	11.35±1.89	0.063	2.53
HC$_5$N	J=38–37	101.1747	24.6	0.02±0.01	12.12±0.16	1.57±0.30	0.013	2.70
DC$_3$N	J=12–11, F=11–10	101.3141	24.6	0.04±0.01	11.89±0.16	2.14±0.52	0.017	3.25
H$_2$CO	6(1,5)–6(1,6)	101.3329	24.6	0.02±0.01	10.86±0.19	1.80±0.34	0.012	2.90
H$_2$CS	3(1,3)–2(1,2)	101.4778	24.6	0.14±0.02	8.15±0.23	3.14±0.44	0.041	2.78
			24.6	0.17±0.02	10.81±0.10	2.35±0.16	0.067	2.89
H70ψ		101.7687	24.5	0.50±0.02	10.01±0.46	25.70±1.01	0.019	2.89
^{13}CCCO		101.9186	24.5	–	–	–	–	2.56
H$_2$CCO	5(1,4)–4(1,3)	101.9814	24.5	0.01±0.01	6.15±0.47	2.10±1.02	0.005	2.56
				0.07±0.01	10.15±0.16	3.39±0.35	0.019	2.56
CH$_3$NH$_2$	17(6)A2–18(5)A1	102.2064	24.5	0.11^c	–	–	–	1.91
C$_2$H$_5$CN	17(3,14)–17(2,15)	102.2274	24.5	0.04±0.01	7.86±0.31	4.98±0.74	0.007	1.52
			24.5	0.09±0.01	6.54±1.21	18.79±3.27	0.004	1.52
			24.5	0.12±0.01	3.17±0.15	11.33±0.50	0.011	1.52
CH$_3$CCH	6(3)–5(3)	102.5310	24.5	0.07±0.01	12.54±0.11	3.25±0.23	0.020	2.16
CH$_3$CCH	6(2)–5(2)	102.5401	23.5	0.11±0.01	10.77±0.13	3.57±0.34	0.028	3.39

Continued on next page

Table B.1 – *Continued from previous page*

Specie	Trans	Freq	HPBW	IF				
				Area	V	Width	T_{MB}	rms
		[GHz]	["]	[K km s^{-1}]	[km s^{-1}]	[km s^{-1}]	[K]	[mK]
CH$_3$CCH	6(1)–5(1)	102.5460	23.5	0.20±0.01	10.64±0.06	3.55±0.14	0.053	2.74
CH$_3$CCH	6(0)–5(0)	102.5479	24.5	0.29±0.01	10.86±0.07	4.64±0.18	0.059	2.78
H66ε		102.5690	23.5	0.85±0.02	8.03±0.34	29.35±0.72	0.027	2.92
CF$^+$	J=1–0	102.5875	23.5	0.15±0.01	9.08±0.09	3.81±0.22	0.036	2.78
^{13}CH$_3$OH	10(2,9)–9(3,7)	102.7900	23.5	–	–	–	–	3.13
H$_2$C^{34}S	3(1,2)–2(1,1)	102.8074	23.5	–	–	–	–	3.00
l-C$_3$H$_2$	5(1,5)–4(1,4)	102.9924	23.4	0.05±0.01	9.10±0.75	6.77±1.77	0.006	2.32
			23.4	0.02±0.01	9.52±0.86	3.55±1.09	0.007	2.32
H$_2$CS	3(0,3)–2(0,2)	103.0405	23.4	0.05±0.01	7.68±0.19	2.06±0.34	0.021	2.95
			23.5	0.13±0.01	10.70±0.14	3.31±0.36	0.038	2.95
H$_2$CS	3(2,1)–2(2,0)	103.0518	23.4	0.03±0.01	9.96±0.29	2.85±0.57	0.091	2.68
C$_2$H$_3$CN	15(4,12)–14(4,11)	103.2513	23.4	0.33±0.02	10.45±0.54	23.80±1.16	0.013	2.46
l-C$_3$H	J=9/2–7/2, Ω=3/2, F=5–4	103.3193	23.4	0.07±0.01	11.93±0.65	8.83±2.08	0.007	2.66
l-C$_3$H	J=9/2–7/2, Ω=3/2, F=4–3	103.3731	23.4	0.03^c	–	–	–	2.52
CH$_3$OH	12(-2,11)–12(1,11)	103.3811	23.4	0.01^c	–	–	–	2.63
CCS	N=8–7, J=8–7	103.6407	23.4	0.02±0.01	11.84±0.16	1.68±0.39	0.012	2.46
U		103.7103	23.4	0.02±0.01	7.62±0.22	2.10±0.43	0.010	2.38
			23.4	0.03±0.01	11.02±0.12	1.72±0.27	0.016	2.38
HC$_5$N	J=39–38	103.8368	23.4	0.03±0.01	11.93±0.20	2.38±0.52	0.011	2.46
CCH	17-11818–17 11818	103.9009	23.4	0.03^c	–	–	–	1.79
H$_2$CCCHCN	20(14,6-)-19(14,5)	103.9094	23.4					
CH$_2$CH^{13}CN	J=12(3,9)–13(2,12), F=12–12	103.9122	23.4					
H56γ		103.9137	23.4	2.67±0.02	10.74±0.12	29.93±0.31	0.084	2.73
l-C$_3$H$_2$	5(0,5)–4(0,4)	103.9529	23.4	0.05±0.009	8.32±0.81	8.23±1.49	0.006	2.55
CH$_2$CHCN	49(7,42)–50(6,45)	104.0100	23.4	0.01^c	–	–	–	2.35
SO$_2$	3(1,3)–2(0,2)	104.0294	23.2	0.08±0.01	10.51±0.08	2.77±0.21	0.027	2.25
C$_3$S	J=18–17	104.0489	23.2	0.04^c	–	–	–	2.50
CH$_3$OH		104.0570	23.2	–	–	–	–	2.54
CH$_2$DCN	6(0,6)–5(0,5)	104.1981	23.2	0.03^c	–	–	–	2.29
CH$_3$C$_5$N	67(8)–66(8), F=68–67	104.2093	23.2	–	–	–	–	2.34
U		104.2306	23.2	–	–	–	–	2.53
SO$_2$	10(1,9)–10(0,10)	104.2392	23.2	0.09±0.01	10.52±0.06	2.23±0.14	0.041	2.57

Continued on next page

Table B.1 – *Continued from previous page*

Specie	Trans	Freq	HPBW	IF				
				Area	V	Width	T_{MB}	rms
		[GHz]	["]	[K km s^{-1}]	[km s^{-1}]	[km s^{-1}]	[K]	[mK]
U		104.2560	23.2	0.01^c	–	–	–	2.23
^{33}SO$_2$	10(1,9)–10(0,10), F=21/2–23/2	104.3006	23.2	0.04^c	–	–	–	2.00
ONCN	10(3,7)–9(3,6)	104.3090	23.2	–	–	–	–	2.03
CH$_3$OH	13(-2,12)–13(1,12)	104.3364	23.2	0.03^c	–	–	–	1.98
CH$_3$OH	10(4,7)–11(3,8)	104.3548	23.2	0.01^c	–	–	–	2.47
t-H^{13}COOH	14(4,11)–15(3,12)	104.3765	23.2	–	–	–	–	2.22
C$_2$H$_3$CN	11(4,8)–10(4,7)	104.4114	23.2	0.01±0.01	12.31±0.22	1.28±0.75	0.007	2.01
C$_2$H$_3$CN	11(3,9)–10(3,8)	104.4327	23.2	–	–	–	–	2.63
H$_2$CS	3(1,2)–2(1,1)	104.6170	23.2	0.10±0.02	8.05±0.18	2.55±0.32	0.035	2.44
			23.2	0.19±0.02	10.73±0.09	2.52±0.16	0.069	2.44
C$_4$H	N=11–10, J=23/2–21/2, F=11–10	104.6665	23.2	0.14±0.01	9.42±0.12	4.84±0.33	0.027	2.39
			23.2	0.05±0.01	17.02±0.30	4.54±0.63	0.011	2.39
C$_4$H	N=11–10, J=21/2–19/2, F=10–9	104.7051	23.2	0.11±0.01	9.33±0.14	4.17±0.34	0.025	2.36
			23.2	0.07±0.01	18.12±0.75	8.94±1.53	0.007	2.36
C$_4$H		104.7059	23.2					
^{13}C^{18}O	J=1–0, F=1/2–1/2	104.7114	23.2	0.07±0.01	10.37±0.12	2.94±0.30	0.021	2.35
l-C$_3$H$_2$	5(1,4)–4(1,3)	104.9156	23.2	0.04^c	–	–	–	2.80
CH$_3$OH	1(13,0)–12(2,1)	105.0646	23.1	0.02^c	–	–	–	2.85
^{13}C^{15}N	1 1 1 2 – 0 1 0 1	105.1723	23.1	0.17±0.02	8.70±1.70	25.63±3.39	0.006	2.78
			23.1	0.02±0.01	11.71±0.33	1.93±0.75	0.007	2.78
H49β		105.3019	23.1	5.58±0.02	13.71±0.05	30.87±0.12	0.170	2.67
He49β		105.3405	23.1	0.07±0.02	10.63±1.12	12.00±2.92	0.006	3.04
C49β		105.3555	23.1	0.07±0.02	4.80±1.57	11.23±2.87	0.006	3.39
			23.1	0.09±0.02	13.75±0.32	5.02±0.87	0.016	3.39
H61δ		105.4083	23.1	1.45±0.03	8.84±0.30	28.09±0.70	0.048	4.80
CH$_3$OCHO	3(3,0)–2(2,0)E	106.0327	23.0	0.19±0.02	9.67±0.87	14.93±1.79	0.012	4.21
H69ψ		106.0785	23.0	0.35±0.02	11.11±0.78	22.23±1.71	0.015	4.07
CCS	N=8–7, J=9–8	106.3477	23.0	–				4.97
HC$_5$N	J=40–39	106.4989	23.0	0.03^c	–	–	–	4.38
H39α		106.7374	23.0	18.52±0.03	13.56±0.02	30.83±0.05	0.564	4.07
^{34}SO	2(3)–1(2)	106.7432	23.0					4.07
He39α		106.7791	23.0	0.55±0.024	10.36±0.55	25.20±1.20	0.021	3.81

Continued on next page

Table B.1 – *Continued from previous page*

Specie	Trans	Freq	HPBW	IF				
				Area	V	Width	T_{MB}	rms
		[GHz]	["]	[K km s^{-1}]	[km s^{-1}]	[km s^{-1}]	[K]	[mK]
C39α		106.7910	23.0	0.19±0.037	9.90±1.21	16.21±2.58	0.011	3.95
			23.0	0.19±0.032	11.90±0.15	4.78±0.58	0.036	3.95
CH$_3$OH	3(1,3)–4(0,4)+ +	107.0138	23.0	0.06±0.007	10.56±0.09	1.55±0.19	0.035	4.69
H65ε		107.2074	23.0	1.30±0.030	13.49±0.33	27.34±0.72	0.045	4.67
U		107.2526	23.0	0.84±0.036	13.29±0.48	21.75±0.98	0.036	6.34
t-HCOOH	5(1,5)–4(1,4)	108.1267	22.7	0.16±0.029	14.21±1.76	16.78±3.65	0.010	5.35
^{13}CN	N=1–0, J=1/2–1/2, F1=0–1, F=1–2	108.4269	22.7	0.29±0.048	9.03±1.29	14.48±3.00	0.019	9.66
^{13}CN	N=1–0, J=1/2–1/2, F1=1–0, F=2–1	108.6513	22.7	0.01^c	–	–	–	9.96
^{13}CN	N=1–0, J=3/2–1/2, F1=2–1, F=3–2	108.7802	22.7	0.01^c	–	–	–	9.03
^{13}CN	N=1–0, J=3/2–1/2, F1=2–1, F=2–1	108.7824	22.7	–	–	–	–	8.64
^{13}CN	N=1–0, J=3/2–1/2, F1=2–1, F=1–0	108.7869	22.7	–	–	–	–	8.71
CH$_3$OH	0(0,0)–1(-1,1)	108.8939	22.6	0.14±0.070	8.66±1.28	5.28±2.11	0.024	8.32
			23.6	0.08±0.062	11.59±0.45	2.93±0.84	0.024	8.32
HC$_3$N	J=12–11	109.1736	22.5	1.27±0.019	11.54±0.02	2.47±0.05	0.481	9.29
SO	2(3)-1(2)	109.2522	22.5	0.47±0.020	10.30±0.06	2.96±0.16	0.150	8.64
OCS	J=9–8	109.4631	22.5	0.07^c	–	–	–	8.77
H55γ		109.5360	22.4	2.47±0.058	14.59±0.33	27.82±0.73	0.083	8.91
C^{18}O	J=1–0	109.7822	22.4	4.99± 0.031	10.24±0.01	3.18±0.03	1.474	13.1
HNCO	5(4,1)–4(4,0)	109.7984	22.4	–	–	–	–	7.90
HNCO	5(0,5)–4(0,4), F=6–5	109.9057	22.4	0.09±0.021	9.93±0.40	3.59±0.95	0.024	8.57
C^{15}N	N=1–0, J=3/2–1/2, F=2–1	110.0246	22.4	0.03±0.011	9.88±0.23	1.06±0.43	0.028	9.07
NH$_2$D	1(1,1)0a–1(0,1)0s	110.1535	22.4	–	–	–	–	10.26
^{13}CO	J=1–0, F=1/2–1/2	110.2014	22.3	58.91±0.142	9.80±0.01	4.48±0.01	12.352	5.41
CH$_3$CN	6(3)–5(3)	110.3644	22.3	0.09pm0.020	11.01±0.32	2.37±0.67	0.034	9.80
CH$_3$CN	6(2)–5(2)	110.3749	22.3	0.09±0.041	10.60±1.41	3.64±3.01	0.023	9.19
CH$_3$CN	6(1)–5(1)	110.3814	22.3	0.16±0.020	11.420±0.20	2.78±0.41	0.054	9.70
CH$_3$CN	6(0)–5(0)	110.3835	22.3	0.20±0.023	11.81±0.10	2.04±0.35	0.093	10.60
H60δ		110.6009	22.3	1.83±0.062	15.35±0.54	31.27±1.15	0.055	9.04
H68ψ		110.6346	22.3	1.00±0.064	10.85±1.04	32.20±2.28	0.029	9.21
U		111.5184	22.2	0.15^c	–	–	–	10.41
t-HCOOH	5(0,5)–4(0,4)	111.7468	22.2	0.25^c	–	–	–	9.58
HC$_5$N	J=42-41	111.8230	22.1	0.09±0.03	7.86±0.54	3.65±1.25	0.023	9.58

Table B.1 – *Continued from previous page*

Specie	Trans	Freq	HPBW	IF				
				Area	V	Width	T_{MB}	rms
		[GHz]	["]	[K km s^{-1}]	[km s^{-1}]	[km s^{-1}]	[K]	[mK]
H48β		111.8851	22.0	4.71±0.08	13.59±0.26	29.65±0.57	0.149	9.58
A-CH$_3$CHO	6(1,6)–5(1,5)A	112.2487	22.0	–	–	–	–	16.76
E-CH$_3$CHO	6(-1,6)–5(-1,5) E	112.2545	22.0	0.18^c	–	–	–	15.32
C^{17}O	J=1–0, F=3/2–5/2	112.3588	22.0	1.08±0.10	7.61±0.21	4.68±0.45	0.216	17.80
				0.45±0.08	10.41±0.07	1.90±0.19	0.221	17.80
CN	N=1–0, J=1/2–1/2, F=1/2–1/2	113.1234	21.9	0.44±0.05	10.59±0.18	3.26±0.41	0.126	21.30
CN	N=1–0, J=1/2–1/2, F=1/2–3/2	113.1442	21.7	2.56±0.06	10.89±0.05	4.05±0.10	0.594	20.00
				0.47±0.08	20.11±0.57	7.12±1.65	0.067	20.00
CN	N=1–0, J=1/2–1/2, F=3/2–1/2	113.1705	21.7	2.64±0.05	10.84±0.04	3.87±0.08	0.641	19.50
				0.40±0.05	18.57±0.29	4.52±0.60	0.083	19.50
CN	N=1–0, J=1/2–1/2, F=3/2–3/2	113.1913	21.7	2.89±0.06	10.81±0.04	4.09±0.09	0.664	19.90
				0.52±0.05	18.23±0.30	4.76±0.54	0.102	19.90
CCS	N=9–8, J= 8–7	113.4102	21.7	0.01^c	–	–	–	21.20
CN	N=1–0, J=3/2–1/2, F=3/2–1/2	113.4881	21.7	1.99±0.14	9.52±0.70	5.70±0.70	0.328	26.20
				1.86±0.14	11.40±0.70	3.31±0.70	0.527	26.20
CN	N=1–0, J=3/2–1/2, F=5/2–3/2	113.4910	21.7	5.50±0.07	10.45±0.01	4.39±0.07	1.176	27.80
				0.71±0.03	12.40±0.01	0.71±0.01	0.946	27.80
CN	N=1–0, J=3/2–1/2, F=1/2–1/2	113.4996	21.7	1.84±0.10	10.61±0.11	3.81±0.23	0.454	28.20
				0.25±0.05	12.42±0.03	0.70±0.87	0.333	28.20
CN	N=1–0, J=3/2–1/2, F=3/2–3/2	113.5089	21.7	2.19±1.02	10.75±0.97	4.19±1.13	0.492	30.00
				0.18±0.44	12.27±0.79	0.74±1.33	0.223	30.00
CN	N=1–0, J=3/2–1/2, F=1/2–3/2	113.5204	21.7	0.33±0.050	11.33±0.25	3.48±0.61	0.088	20.00
C$_4$H	N=12–11, J=25/2–23/2, F=12–11	114.1825	21.7	–	–	–	–	22.51
C$_4$H	N=12–11, J=23/2–21/2, F=11–10	114.2210	21.7	0.28^c	–	–	–	23.46
E-CH$_3$CHO	6(0,6)–5(0,5) E	114.9402	21.7	0.30^c	–	–	–	28.82
A-CH$_3$CHO	6(0,6)–5(0,5) A	114.9599	21.7	0.09^c	–	–	–	31.38
NS	J=5/2–3/2, Ω=1/2, F=7/2–5/2	115.1539	21.7	0.02^c	–	–	–	27.38
NS	J=5/2–3/2, Ω=1/2, F=5/2–3/2	115.1568	21.7	–	–	–	–	29.11
CO	J=1–0	115.2712	21.3	158.09±0.67	8.23±0.01	5.66±0.03	26.239	140.00
				64.74±0.24	13.23±0.02	3.77±0.02	16.123	140.00
				45.35±0.50	18.56±0.01	5.37±0.07	7.929	140.00
NS	J=5/2–3/2, Ω=1/2, F=7/2–5/2	115.5563	21.3	–	–	–	–	39.32

Continued on next page

Table B.1 – *Continued from previous page*

Specie	Trans	Freq	HPBW	IF				
				Area	V	Width	T_{MB}	rms
		[GHz]	["]	[K km s^{-1}]	[km s^{-1}]	[km s^{-1}]	[K]	[mK]
NS	J=5/2–3/2, Ω=1/2, F=5/2–3/2	115.5708	21.3	0.12^c	–	–	–	39.13
NS	J=5/2–3/2, Ω=1/2, F=3/2–1/2	115.5720	21.3	0.60^c	–	–	–	36.83
E-CH$_3$CHO	6(2,5)–5(2,4)E	115.6950	21.3	–	–	–	–	43.44
SO$^+$	J=5/2–3/2, Ω=1/2,	115.8044	21.3	0.16^c	–	–	–	44.90
U		116.4262	21.3	0.92^c	–	–	–	96.47
U		116.4279	21.3	0.97^c	–	–	–	95.11

Table B.2: Gaussian fits of the 3mm lines at MP2 positions.

Specie	Trans	Freq	HPBW	MP2					OTF
				Area	V	Width	T_{MB}	rms	
		[GHz]	["]	[K km s^{-1}]	[km s^{-1}]	[km s^{-1}]	[K]	[mK]	
$^{13}C_2H$	N=1–0	84.1241	29.2	0.14±0.02	8.98±0.55	9.16±1.25	0.014	4.43	–
DC_3N	J=10–9	84.4298	29.2	0.06^c	–	–	–	3.88	✓
CH_3OH	5(-1,5)–4(0,4)	84.5212	29.1	0.46±0.01	9.48±0.03	2.82±0.07	0.152	4.20	✓
c-C_3H_2	J=3–2	84.7277	29.0	0.07±0.01	8.33±0.12	2.01±0.30	0.031	3.11	✓
		84.7277	29.0	0.04±0.01	11.35±0.40	2.86±0.91	0.012	3.11	✓
H60γ		84.9139	29.0	0.20^c	–	–	–	2.58	✓
He60γ		84.9506	29.0	–	–	–	–	2.65	–
C60γ		84.9506	29.0	–	–	–	–	2.65	✓
OCS	J=7–6	85.1391	28.9	0.05±0.01	9.68±0.13	1.99±0.36	0.024	3.42	✓
		85.1391	28.9	0.07±0.02	13.13±1.18	8.11±1.79	0.008	3.42	✓
$HC^{18}O^+$	J=1–0	85.1622	28.9	0.11±0.01	9.21±0.10	3.05±0.24	0.034	3.86	✓
HC_5N	J=32–31	85.2019	28.9	0.04±0.01	10.34±0.09	1.51±0.21	0.026	3.17	✓
$C^{13}CH$	N=1–0	85.2293	28.9	0.13±0.01	8.37±1.84	22.19±3.79	0.005	3.52	✓
$C^{13}CH$	N=1–0	85.2300	28.9	0.05±0.01	11.35±0.70	3.21±0.70	0.014	3.42	✓
$C^{13}CH$	N=1–0	85.2320	28.9	0.04±0.01	9.32±0.34	2.83±0.78	0.013	4.06	✓
c-C_3H_2	2(1,2)–1(0,1)	85.3388	28.8	1.24±0.08	8.55±0.70	3.21±0.70	0.363	4.79	✓
		85.3388	28.8	0.52±0.08	13.18±0.70	4.95±0.70	0.098	4.79	✓
		85.3388	28.8	0.26±0.08	18.42±0.70	9.41±0.70	0.026	4.79	✓
HCS^+	J=2–1	85.3478	28.8	0.19±0.01	9.73±0.07	3.74±0.18	0.042	3.19	✓
CH_3CCH	5(3)–4(3)	85.4426	28.8	0.08±0.04	9.29±0.64	2.84±1.27	0.026	17.00	✓
CH_3CCH	5(2)–4(2)	85.4507	28.8	0.08±0.03	9.14±0.46	2.33±0.85	0.033	16.60	✓
CH_3CCH	5(1)–4(1)	85.4556	28.8	0.26±0.01	9.10±0.04	3.28±0.10	0.073	8.03	✓
CH_3CCH	5(0)–4(0)	85.4573	28.8	0.28±0.01	9.15±0.04	2.95±0.10	0.089	6.09	✓
C_4H	9(10,9)–8(9,8)	85.6340	28.7	0.08±0.01	8.34±0.04	1.28±0.09	0.060	3.23	✓
		85.6340	28.7	0.19±0.01	9.69±0.21	5.71±0.40	0.032	3.23	✓
c-C_3H_2	4(3,2)–4(2,3)	85.6564	28.7	0.08±0.01	8.34±0.04	1.08±0.13	0.066	2.66	✓
		85.6564	28.7	0.12±0.02	9.50±0.33	5.35±0.68	0.021	2.66	✓
C_4H	9(9,8)–8(8,7)	85.6725	28.7	0.08±0.02	8.39±0.07	1.55±0.22	0.047	2.56	✓
		85.6725	28.7	0.20±0.02	9.49±0.26	6.88±0.91	0.028	2.56	✓
H42α		85.6885	28.7	1.30±0.02	11.25±0.22	33.23±0.53	0.039	3.67	✓

Continued on next page

Table B.2 – *Continued from previous page*

Specie	Trans	Freq	HPBW	MP2					OTF
				Area	V	Width	T_{MB}	rms	
		[GHz]	["]	[K km s^{-1}]	[km s^{-1}]	[km s^{-1}]	[K]	[mK]	
He42α		85.7219	28.7	–	–	–	–	3.54	–
C42α		85.7309	28.7	0.09±0.01	8.98±0.21	4.25±0.46	0.020	3.50	✓
NH$_2$D	1(1,1)0s–1(0,1)0a	85.9262	28.6	0.13±0.01	9.20±0.01	4.65±0.47	0.027	3.67	✓
HC^{15}N	J=1–0	86.0549	28.6	0.25±0.01	8.81±0.04	1.99±0.11	0.119	3.98	✓
		86.0549	28.6	0.11±0.01	10.24±0.02	0.97±0.12	0.101	3.98	
SO	2(2)–1(1)	86.0939	28.6	0.53±0.01	9.74±0.02	2.26±0.05	0.219	4.42	✓
C$_2$S	N=7–6, J=6–5	86.1813	28.5	0.09±0.01	8.38±0.09	2.49±0.27	0.035	3.45	✓
H^{13}CN	J=1–0, F=1–1	86.3387	28.5	0.17±0.01	8.14±0.06	1.47±0.13	0.106	3.78	✓
		86.3387	28.5	0.45±0.02	9.92±0.06	1.98±0.13	0.211	3.78	✓
	J=1–0, F=2–1	86.3401	28.5	0.27±0.01	8.29±0.03	1.50±0.08	0.166	3.78	✓
		86.3401	28.5	0.68±0.02	9.98±0.02	1.87±0.07	0.341	3.78	✓
	J=1–0, F=0–1	86.3422	28.5	0.13±0.05	9.22±0.26	2.43±0.27	0.050	3.78	✓
		86.3422	28.5	0.07±0.04	10.56±0.90	3.37±0.80	0.020	3.78	✓
H70ε		86.4879	28.4	0.06±0.01	1.55±0.86	8.52±1.48	0.007	3.12	–
t-HCOOH	4(1,4)–3(1,3)	86.5461	28.4	–	–	–	–	3.60	✓
HCO	1(0,1)–0(0,0)	86.6707	28.4	0.56±0.01	9.93±0.05	5.25±0.13	0.010	3.67	✓
H74ζ		86.6883	28.4	0.24±0.02	-3.91±1.26	26.22±2.80	0.008	3.55	–
HCO	1(0,1)–0(0,0)	86.7083	28.4	0.41±0.01	10.64±0.07	6.01±0.17	0.064	3.27	✓
H^{13}CO$^+$	J=1–0	86.7543	28.3	1.20±0.01	9.22±0.01	2.87±0.03	0.393	4.40	✓
		86.7543	28.3	0.31±0.01	10.58±0.02	1.73±0.05	0.167	4.40	✓
HCO	1(0,1)–0(0,0), J=1/2–1/2, F=1–1	86.7775	28.3	0.33±0.01	10.42±0.08	5.33±0.19	0.058	3.48	✓
HCO	1(0,1)–0(0,0), J=1/2–1/2, F=0–1	86.8058	28.3	0.07±0.01	10.89±0.29	4.58±0.57	0.014	2.93	✓
SiO	J=2–1	86.8469	28.3	0.28±0.01	9.54±0.06	3.93±0.16	0.066	3.25	✓
HN^{13}C	J=1–0	87.0908	28.2	0.20±0.01	8.59±0.08	1.84±0.11	0.101	3.25	✓
		87.0908	28.2	0.10±0.01	10.40±0.09	1.75±0.32	0.056	3.25	✓
C$_3^{13}$CC$_2$H	31(1323131)–30(13)	87.2725	28.2	0.05±0.01	10.26±0.46	3.65±0.88	0.012	4.49	–
C$_2$H	N=1–0, J=3/2–1/2, F=1–1	87.2841	28.2	0.43±0.01	8.93±0.04	2.91±0.05	0.138	3.44	✓
		87.2841	28.2	0.29±0.01	11.58±0.15	7.61±0.62	0.036	3.44	✓
Phenol		87.2924	28.2	0.01±0.01	8.42±0.44	1.50±0.71	0.007	4.17	–
		87.2924	28.2	0.09±0.02	13.89±0.93	9.17±2.27	0.009	4.17	–
C$_2$H	1(2,2)–0(1,1)	87.3169	28.2	5.21±0.11	9.02±0.03	3.57±0.09	1.370	4.15	✓
		87.3169	28.2	2.20±0.09	12.22±0.13	7.53±0.25	0.275	4.15	✓

Continued on next page

Table B.2 – *Continued from previous page*

Specie	Trans	Freq	HPBW	MP2					OTF
				Area	V	Width	T_{MB}	rms	
		[GHz]	["]	[K km s^{-1}]	[km s^{-1}]	[km s^{-1}]	[K]	[mK]	
		87.3169	28.2	0.43±0.02	20.11±0.07	4.01±0.16	0.100	4.15	✓
C$_2$H	1(2,1)–0(1,0)	87.3286	28.2	1.64±0.14	8.63±0.09	2.46±0.15	0.626	5.58	✓
		87.3286	28.2	1.04±0.03	10.46±0.29	3.89±0.80	0.252	5.58	✓
		87.3286	28.2	0.67±0.15	15.91±1.08	9.24±0.93	0.069	5.58	✓
C$_2$H	1(1,1)–0(1,1)	87.4020	28.1	1.97±0.01	8.82±0.01	2.86±0.02	0.648	4.58	✓
		87.4020	28.1	1.29±0.01	11.51±0.06	7.52±0.10	0.161	4.58	✓
		87.4020	28.1	0.24±0.02	19.78±0.15	4.81±0.35	0.047	4.58	✓
C$_2$H	1(1,0)–0(1,1)	87.4071	28.1	1.04±0.01	8.85±0.01	3.18±0.04	0.309	3.29	✓
		87.4071	28.1	0.37±0.01	13.66±0.20	7.65±0.33	0.046	3.29	✓
C$_2$H	1(1,1)–0(1,0)	87.4465	28.1	0.58±0.04	9.13±0.70	3.45±0.70	0.158	6.82	✓
		87.4465	28.1	0.11±0.04	13.75±0.70	4.75±0.70	0.021	6.82	✓
		87.4465	28.1	0.06±0.04	19.96±0.70	6.61±0.70	0.009	6.82	✓
H65γ		87.6146	28.1	0.33±0.02	27.23±0.89	25.05±1.95	0.013	3.79	
HC$_5$N	J=33–32	87.8636	28.0	0.07±0.01	8.49±0.10	1.91±0.27	0.032	3.67	✓
HNCO	4(0,4)–3(0,3)	87.9252	28.0	0.09±0.01	10.03±0.22	3.95±0.40	0.022	4.12	✓
H52β		88.4056	27.8	0.22±0.02	7.57±0.70	18.63±1.72	0.011	3.02	✓
He52β		88.4417	27.8	–	–	–	–	3.82	–
C52β		88.4498	27.8	0.05^c	–	–	–	3.78	–
C$_2$H$_5^{13}$CN	12(2,11)- 12(1,12)	88.5713	27.8	0.04±0.01	7.81±0.26	2.56± 0.60	0.014	3.66	–
C^{13}CCN	N=9–8	88.5773	27.8	0.03±0.01	10.15±1.00	5.52±1.96	0.005	3.54	–
HCN	J=1–0	88.6316	27.7	4.09±0.55	1.62±0.70	4.29±0.70	0.894	4.95	✓
		88.6316	27.7	13.96±0.55	8.20±0.70	2.89±0.70	4.537	4.95	✓
		88.6316	27.7	7.33±0.55	12.94±0.70	2.79±0.70	2.465	4.95	✓
		88.6316	27.7	2.99±0.55	16.96±0.70	5.74±0.70	0.489	4.95	✓
H^{15}NC	J=1–0	88.8657	27.7	0.09±0.01	9.28±0.16	3.30±0.35	0.027		✓
C$_2$H$_3$CN	17(1,16)–17(0,17)	89.1130	27.6	0.01	–	–	–	3.54	–
HCO$^+$	J=1–0	89.1885	27.6	14.10±0.011	8.72±0.01	2.82±0.02	4.698	6.41	✓
		89.1885	27.6	4.32±0.08	13.90±0.04	3.77±0.10	1.078	6.41	✓
H59γ		89.1982	27.6	–	–	–	–	3.59	–
HCCNC	J=9–8, F=10–9	89.4193	27.6	0.04^c	–	–	–	4.29	✓
HOC$^+$	1(0,0)–0(0,0)	89.4874	27.5	0.09±0.01	10.62±0.33	4.73±0.65	0.018	4.56	✓
t-HCOOH	4(0,4)–3(0,3)	89.5791	27.5	0.03±0.01	10.36±0.39	2.63±0.70	0.010	3.90	✓

Continued on next page

Table B.2 – *Continued from previous page*

Specie	Trans	Freq	HPBW	MP2					OTF
				Area	V	Width	T_{MB}	rms	
		[GHz]	["]	[K km s^{-1}]	[km s^{-1}]	[km s^{-1}]	[K]	[mK]	
U		89.8591	27.5	0.02±0.01	10.06±0.16	1.71±0.40	0.011	2.14	–
t-HCOOH	4(2,3)–3(2,2)	89.8614	27.5	0.02±0.01	10.98±0.28	2.25±0.57	0.010	2.16	–
C_3H	4 0 1 4 3 – 3 0 1 4 4	89.8688	27.5	0.02±0.01	5.70±0.41	2.81±0.92	0.007	1.77	–
		89.8688	27.5	0.08±0.01	9.89±0.19	3.52±0.23	0.022	1.77	–
		89.8688	27.5	0.04±0.01	12.10±0.09	1.73±0.18	0.021	1.77	–
gG'a-1,2-P	29(10,20)–29(9,21)	89.8899	27.5	0.20±0.01	11.75±0.11	5.72±0.32	0.033	2.59	–
$HOONO_2$	N=11–10 J=6–6 F_1=6–5 F=1–1	89.9157	27.5	0.03±0.01	6.07±0.41	2.82±0.96	0.010	2.50	–
		89.9157	27.5	0.12±0.01	10.43±0.12	3.37±0.28	0.033	2.50	–
t-HCOOH	4(3,1)–3(3,0)	89.9503	27.5	0.02±0.01	9.46±0.19	2.22±0.54	0.010	1.85	–
		89.9503	27.5	0.04±0.01	14.99±0.57	6.10±1.66	0.006	1.85	–
C_3H^+	J=4–3	89.9576	27.5	0.07±0.01	10.24±0.26	4.98±0.62	0.014	2.37	✓
		89.9576	27.5	0.01±0.01	14.91±0.39	1.96±0.77	0.005	2.37	
H73ζ		90.1697	27.3	–	–	–	–	5.67	–
$^{15}NNH^+$	J=1–0	90.2638	27.3	0.02±0.01	9.37±0.23	2.42±0.45	0.009		✓
U		90.2730	27.3	0.07±0.01	9.54±0.34	10.35±1.05	0.007	1.14	–
HC_5N	J=34–33	90.5258	27.1	0.05±0.01	8.54±0.07	1.62±0.15	0.026	2.27	✓
$HC^{13}CCN$	J=10–9	90.5930	27.1	0.03±0.01	8.84±0.23	2.15±0.44	0.011	3.00	✓
$HC^{13}CCN$		90.6017	27.1	0.02±0.01	27.84±0.39	2.25±0.66	0.007	2.95	✓
HNC	J=1–0	90.6635	27.1	8.39±0.14	19.06±0.02	3.13±0.06	2.518	3.00	✓
		90.6635	27.1	1.18±0.04	13.0±0.05	3.63±0.14	0.306	3.00	✓
CCS	N=7–6, J=7–6	90.6863	27.1	0.09±0.01	8.51±0.07	2.17±0.19	0.039	3.05	✓
HC_3N	J=10–9	90.9790	27.0	1.34±0.01	8.94±0.01	2.58±0.01	0.488	2.69	✓
$^{15}NNH^+$	J=1–0	91.2056	26.9	0.09^c	–	–	–	2.44	✓
Phenol		91.2564	26.9	–	–	–	–	2.43	✓
Glyceraldehyde		91.4545	26.9	–	–	–	–	3.09	–
H2CCCHCN	4(2,2)–3(1,3)	91.4945	26.9	0.16±0.01	10.02±0.14	5.65±0.34	0.026	2.48	✓
c-HCCCD	8(3,5)–7(6,2)	91.4971	26.9	0.07±0.01	8.44±0.30	4.66±0.76	0.014	2.80	✓
H64δ		91.6629	26.9	0.18±0.02	6.49±1.47	28.44±2.87	0.059	2.80	✓
c-C_3H	2 1 2 2 1–1 1 1 1 0	91.6927	26.8	0.08±0.01	11.05±0.65	8.87±1.49	0.009	3.13	✓
c-C_3H	2 1 2 2 2–1 1 1 1 1	91.6994	26.8	0.08±0.01	10.24±0.34	5.13±0.68	0.014	3.20	✓
CH_3CN	5(3)–4(3)	91.9711	26.7	0.09±0.02	9.61±0.25	4.37±0.72	0.019	3.85	✓
		91.9711	26.7	0.08±0.02	10.70±1.59	12.67±3.02	0.006	3.85	✓

Table B.2 – *Continued from previous page*

Specie	Trans	Freq	HPBW	MP2					OTF
				Area	V	Width	T_{MB}	rms	
		[GHz]	["]	[K km s^{-1}]	[km s^{-1}]	[km s^{-1}]	[K]	[mK]	
CH_3CN	5(2)–4(2)	91.9799	26.7	0.04±0.02	7.99±0.30	1.84±0.52	0.020	3.68	✓
		91.9799	26.7	6.06±0.02	10.61±0.49	3.03±1.18	0.019	3.68	✓
CH_3CN	5(1)–4(1)	91.9853	26.7	0.21±0.02	8.94±0.15	4.92±0.45	0.040	3.58	✓
CH_3CN	5(0)–4(0)	91.9870	26.7	0.19±0.02	9.24±0.11	3.58±0.23	0.051	3.52	✓
H41α		92.0335	26.7	0.63±0.02	7.41±0.33	25.87±0.69	0.023	2.50	✓
He41α		92.0686	26.7	–	–	–	–	1.92	–
C41α		92.0801	26.7	0.14±0.01	7.85±0.23	8.25±0.62	0.016	2.00	✓
		92.0801	26.7	0.17±0.02	28.40±1.02	22.78±2.31	0.069	2.00	✓
Glyceraldehyde	18(2,16)–17(2,15)	92.1804	26.7	0.02±0.01	7.15±0.19	1.56±0.40	0.011	2.22	–
		92.1804	26.7	0.01±0.01	10.21±0.61	2.51±1.06	0.005	2.22	–
$^{13}CH_2CHCN$	10(3,8)–9(3,7)	92.4323	26.7	0.03±0.01	–	–	–	2.16	–
C_3S	J=16–15	92.4884	26.7	0.05±0.01	6.26±1.15	8.05±2.03	0.006	2.67	–
		92.4884	26.7	0.02±0.01	8.32±0.18	1.46±0.51	0.012	2.67	–
^{13}CS	2(0)–1(0)	92.4943	26.6	0.41±0.01	9.62±0.02	2.89±0.05	0.135	2.89	✓
U		92.8586	26.6	0.56±0.01	9.70±0.04	5.57±0.10	0.096	3.00	–
DC_3N	J=11–10	92.8723	26.5	0.05[c]	–	–	–	3.05	–
t-HCOOH	4(1,3)–3(1,2)	93.0983	26.5	0.05[c]	–	–	–	2.53	✓
N_2H^+	J=1–0, F=1–1	93.1718	26.4	1.08±0.01	7.90±0.01	2.85±0.03	0.357	3.62	✓
	J=1–0, F=2–1	93.1733	26.4	1.75±0.01	8.05±0.01	2.95±0.02	0.556	3.62	✓
	J=1–0, F=0–1	93.1761	26.4	0.40±0.01	7.67±0.03	2.68±0.07	0.140	3.62	✓
HC_5N	J=35–34	93.1881	26.4	0.05±0.01	8.27±0.08	1.88±0.24	0.025	2.60	–
A-CH_3CHO	5(1,5)–4(1,4)A	93.5809	26.3	0.04±0.01	8.79±0.32	2.76±1.06	0.013	4.50	✓
E-CH_3CHO	5(1,5)-4(1.4)	93.5952	26.3	0.05±0.01	9.93±0.39	4.17±0.82	0.012	4.00	✓
H51β		93.6065	26.3	0.03±0.01	0.57±0.61	3.18±1.46	0.009	3.59	✓
		93.6065	26.3	0.16±0.02	9.90±1.57	18.88±2.67	0.009	3.59	–
H58γ		93.7751	26.2	0.05±0.01	6.48±0.34	5.36±0.84	0.010	2.20	–
He58γ		93.8097	26.2	0.01[c]	–	–	–	2.96	–
C58γ		93.8252	26.2	0.02±0.01	15.01±0.33	2.80±0.69	0.009	2.45	–
CCS	N=7–6, J=8–7	93.8701	26.2	0.15±0.01	8.50±0.06	2.32±0.17	0.062	4.25	✓
C_2H_5CN		93.9493	26.2	0.06±0.01	1.96±0.24	4.67±0.59	0.012	2.28	–
CH_3OOH		93.9608	26.2	0.07±0.01	9.43±0.19	4.63±0.44	0.015	2.22	–
HC_5N	N=35–34, J=4–4	93.9706	26.2	0.12±0.01	3.66±0.70	4.38±0.70	0.026	2.49	–

Continued on next page

Table B.2 – *Continued from previous page*

Specie	Trans	Freq	HPBW	MP2					OTF
				Area	V	Width	T_{MB}	rms	
		[GHz]	["]	[K km s^{-1}]	[km s^{-1}]	[km s^{-1}]	[K]	[mK]	
		93.9706	26.2	0.08±0.01	9.45±0.70	5.26±0.70	0.015	2.49	–
		93.9706	26.2	0.20±0.01	13.56±0.70	3.50±0.70	0.052	2.49	–
H68ε		94.0720	26.2	–	–	–	–	2.90	–
U		94.2693	26.1	0.05±0.02	6.87±0.83	5.40±1.10	0.009	2.32	–
		94.2693	26.1	0.07±0.02	10.18±0.15	2.84±0.31	0.022	2.32	–
CH$_3$CHO		94.2897	26.1	0.11±0.01	8.59±0.13	4.71±0.36	0.022	2.27	–
		94.2897	26.1	0.02±0.01	2.45±0.26	2.29±0.55	0.008	2.27	–
^{13}CCCH		94.2974	26.1	0.02±0.01	12.43±0.38	1.99±0.99	0.007	2.23	–
		94.2974	26.1	0.03±0.01	17.60±1.09	6.70±1.92	0.005	2.23	–
U		94.3164	26.1	0.07±0.01	8.47±0.40	5.34±0.87	0.012	2.20	–
		94.3164	26.1	0.03±0.01	10.63±0.10	1.44±0.24	0.017	2.20	–
CH$_3$OH		94.5417	26.1	0.09±0.01	8.63±0.35	7.03±1.19	0.011	2.56	–
C$_4$H	10(11,10)–9(10,9)	95.1503	25.9	0.12±0.01	8.37±0.02	1.53±0.07	0.076	2.40	✓
	10(11,11)–9(10,10)	95.1503	25.9	0.23±0.01	11.20±0.27	9.64±0.57	0.023	2.40	
CH$_3$OH		95.1694	25.8	0.27±0.01	9.38±0.04	3.25±0.07	0.077	2.69	✓
C$_4$H		95.1794	25.8	–	–	–	–	2.63	✓
C$_4$H		95.1851	25.8	0.08^c	–	–	–	2.63	✓
C$_4$H		95.1889	25.8	0.09±0.01	8.40±0.03	1.30±0.07	0.066	2.48	✓
		95.1889	25.8	0.13	–	–	–	2.48	–
C$_2$H$_3$CHO		95.4726	25.7	0.02^c	–	–	–	2.33	✓
g'Ga-(CH$_2$OH)$_2$		95.5375	25.7	0.01^c	–	–	–	2.65	✓
HC$_5$N		95.8506	25.7	0.06±0.01	9.68±0.10	2.23±0.26	0.026	2.42	✓
		95.8506	25.7	0.03±0.01	14.13±0.82	4.21±1.52	0.006	2.42	–
U		95.8636	25.7	0.03±0.01	10.01±0.24	3.04±0.47	0.009	2.42	–
CH$_3$OH		95.9143	25.6	0.17±0.01	9.42±0.05	3.12±0.14	0.050	2.42	✓
		95.9143	25.6	0.02±0.01	14.85±0.27	2.07±0.47	0.008	2.42	–
E-CH$_3$CHO		95.9474	25.6	0.09±0.01	8.98±0.24	4.50±0.46	0.019	2.28	–
		95.9474	25.6	0.05±0.01	15.43±0.82	6.97±2.11	0.007	2.28	–
A-CH$_3$CHO		95.9634	25.6	0.12±0.01	9.68±0.13	5.10±0.29	0.023	2.20	✓
H63δ		95.9637	25.6	–	–	–	–	2.20	✓
A-CH$_3$CHO		96.2742	25.5	0.05^c	–	–	–	2.79	–
C^{34}S		96.4129	25.5	1.26±0.01	9.44±0.01	3.05±0.02	0.388	3.11	✓

Continued on next page

Table B.2 – *Continued from previous page*

Specie	Trans	Freq	HPBW	MP2					OTF
				Area	V	Width	T_{MB}	rms	
		[GHz]	["]	[K km s^{-1}]	[km s^{-1}]	[km s^{-1}]	[K]	[mK]	
E-CH$_3$CHO		96.4256	25.5	–	–	–	–	2.63	–
A-CH$_3$CHO		96.6326	25.5	0.03±0.01	8.84±0.19	2.14±0.45	0.012	2.68	–
CH$_3$OH		96.7393	25.4	0.59±0.01	9.37±0.02	3.66±0.06	0.150	2.77	✓
CH$_3$OH		96.7413	25.4	0.91±0.01	9.45±0.01	3.60±0.04	0.238	2.82	✓
CH$_3$OH		96.7445	25.4	0.28±0.01	9.57±0.03	2.94±0.08	0.090	2.73	✓
CH$_3$OH		96.7555	25.4	0.19±0.01	9.58±0.06	3.49±0.19	0.050	2.76	✓
C$_2$H$_3$CN		96.9824	25.4	0.05^c	–	–	–	2.96	✓
C^{33}S		97.1720	25.3	0.21±0.01	10.08±0.06	3.28±0.14	0.061	3.07	✓
		97.1720	25.3	0.05±0.01	16.79±0.31	4.23±0.71	0.012	3.07	–
c-C$_3$H		97.1736	25.3	0.03±0.02	5.17±1.15	3.56±2.21	0.009	9.21	✓
OCS	j=8–7	97.3012	25.3	0.07pm0.01	9.89±0.08	2.07±0.20	0.032	2.25	✓
		97.3012	25.3	0.02±0.01	7.03±0.35	2.25±0.75	0.008	2.25	–
CH$_3$OH		97.5828	25.2	0.18±0.02	9.14±0.39	9.17±1.55	0.018	2.61	✓
		97.5828	25.2	0.09±0.02	9.74±0.07	2.32±0.32	0.036	2.61	–
		97.5828	25.2	0.02±0.01	16.54±0.25	2.12±0.53	0.009	2.61	–
CH$_3$OH		97.6777	25.2	0.01±0.01	3.76±0.18	1.14±0.31	0.008	1.95	–
		97.6777	25.2	0.07±0.01	6.92±0.12	3.68±0.32	0.018	1.95	–
H71ζ		97.6906	25.2	0.01^c	–	–	–	1.89	–
SO$_2$		97.7023	25.2	0.03±0.01	9.73±0.25	2.75±0.77	0.009	2.10	–
^{34}SO		97.7153	25.2	0.07±0.01	9.60±0.09	2.37±0.21	0.026	2.51	✓
CS		97.9809	25.1	3.67±0.04	9.42±0.05	6.57±0.10	0.525	12.4	✓
		97.9809	25.1	9.96±0.01	9.36±0.01	2.94±0.01	3.184	12.4	–
C$_3$H		97.9951	25.1	0.02±0.02	5.93±0.29	1.32±0.75	0.015	5.81	✓
		97.9951	25.1	0.04±0.02	8.20±0.24	1.64±0.69	0.020	5.81	–
		97.9951	25.1	0.10±0.05	10.28±1.91	7.50±2.85	0.013	5.81	–
C$_3$H		98.0125	25.1	0.02±0.01	8.12±0.04	1.18±0.21	0.016	2.00	✓
		98.0125	25.1	0.04±0.01	10.83±0.08	1.79±0.15	0.020	2.00	–
		98.0125	25.1	0.04±0.01	12.98±0.44	5.00±0.78	0.007	2.00	–
H67ε		98.1994	25.1	–	–	–	–	1.75	–
^{33}SO		98.2867	25.0	–	–	–	–	1.85	–
HC$_5$N		98.5125	24.9	0.03±0.01	10.28±1.04	6.88±2.24	0.004	1.89	✓
		98.5125	24.9	0.04±0.01	8.45±0.06	1.42±0.17	0.023	1.89	–

Continued on next page

Table B.2 – *Continued from previous page*

Specie	Trans	Freq [GHz]	HPBW ["]	Area [K km s^{-1}]	V [km s^{-1}]	Width [km s^{-1}]	T$_{MB}$ [K]	rms [mK]	OTF
H57γ		98.6500	24.9	0.03±0.01	-7.10±0.12	1.95±0.31	0.012	1.76	✓
		98.6500	24.9	0.07±0.01	11.76±0.55	10.23±1.05	0.006	1.76	–
He57γ		98.6708	24.9	0.02^c	–	–	–	1.58	✓
E-CH$_3$CHO		98.8633	24.9	0.11±0.01	12.16±0.90	19.29±2.41	0.005	1.63	–
		98.8633	24.9	0.06±0.01	9.12±0.11	3.39±0.29	0.016	1.63	–
A-CH$_3$CHO	5(1,4)–4(1,3)A	98.9009	24.9	0.07±0.01	9.43±0.13	3.84±0.30	0.0164	1.80	–
C$_3$N	N=10–9, J=21/2–19/2, F=19/2–17/2	98.9400	24.9	0.04^c	10.00	4.50	0.008	1.74	✓
H40α		99.0219	24.9	0.43±0.01	6.99±0.39	25.49±0.92	0.016	2.08	✓
He40α		99.0619	24.8	–	–	–	–	1.41	–
C40α		99.0722	24.8	0.06±0.01	8.63±0.12	4.29±0.30	0.013	1.33	✓
H$_2^{13}$CS	3(2,1)–2(2,0)	99.0989	24.8	–	–	–	–	1.31	–
H50β		99.2252	24.8	10.57±1.40	27.31±3.24	–	0.040	1.83	✓
C50β		99.2741	24.8	0.017^c	–	–	–	1.64	–
SO	3(2)–2(1)	99.2999	24.8	0.69±0.09	9.32±0.08	5.16±0.44	0.126	4.80	
				1.30±0.10	9.77±0.02	2.46±0.07	0.495	4.80	
HCCNC	J=10–9	99.3543	24.8	0.01^c	–	–	–	1.38	✓
CH$_3$C^{13}CH	6(1)–5(1)	99.4779	24.7	0.02^c	–	–	–	1.31	✓
HC^{13}CCN	J=11–10	99.6524	24.7	0.02±0.01	10.40±0.18	2.36±0.50	0.009	1.46	✓
HCC^{13}CN	J=11–10	99.6615	24.7	0.03±0.01	9.12±0.17	2.80±0.43	0.010	1.72	✓
				0.02±0.01	16.02±0.48	3.52±1.01	0.004	1.72	
CCS	N= 8–7, J= 7–6	99.8665	24.7	0.07±0.01	8.57±0.04	1.81±0.10	0.035	1.28	✓
				0.01±0.01	12.46±1.17	4.80±1.69	0.003	1.28	
SO	4(5)–4(4)	100.0296	24.7	0.08±0.01	10.03±0.04	2.19±0.11	0.035	1.77	✓
HC$_3$N	J=11–10	100.0764	24.7	1.24±0.01	8.72±0.01	2.39±0.02	0.487	4.45	✓
H$_2$CCO	5(1,5)– 4(1,4)	100.0945	24.7	0.10±0.01	9.61±0.07	4.85±0.17	0.019	1.10	✓
H62δ		100.5403	24.7	0.02^c	–	–	–	1.66	–
CH$_3$CHO	13(2,11)–12(3,9)	100.6388	24.6	0.05±0.01	8.30±0.22	5.91±0.54	0.009	1.29	–
H$_2$CCO	5(3,3)–4(3,2)	101.0026	24.6	0.03±0.01	8.43±0.24	4.06±0.54	0.007	1.54	✓
H$_2$CCO	5(0,5)–4(0,4)	101.0363	24.6	0.05±0.01	9.51±0.21	4.62±0.56	0.010	1.61	✓
HC$_5$N	J=38–37	101.1747	24.6	0.04±0.01	8.28±0.04	1.58±0.10	0.022	1.13	✓
DC$_3$N	J=12–11, F=11–10	101.3141	24.6	0.02±0.01	8.57±0.14	1.14±0.23	0.013	2.68	–
H$_2$CO	6(1,5)–6(1,6)	101.3329	24.6	0.05±0.01	-8.60±0.79	10.54±2.32	0.005	1.73	–

Table B.2 – *Continued from previous page*

Specie	Trans	Freq [GHz]	HPBW ["]	Area [K km s^{-1}]	V [km s^{-1}]	Width [km s^{-1}]	T$_{MB}$ [K]	rms [mK]	OTF
			24.6	0.04±0.01	8.85±0.16	3.39±0.46	0.012	1.73	–
			24.6	0.02±0.01	16.15±0.60	4.93±1.05	0.004	1.73	–
H$_2$CS	3(1,3)–2(1,2)	101.4778	24.6	0.38±0.01	9.51±0.01	3.11±0.04	0.115	1.58	✓
H70ψ		101.7687	24.5	0.01^c	–	–	–	1.51	–
^{13}CCCO		101.9186	24.5	0.01^c	–	–	–	1.42	–
H$_2$CCO	5(1,4)–4(1,3)	101.9814	24.5	0.10±0.01	9.57±0.09	4.52±0.21	0.022	1.52	✓
CH$_3$NH$_2$	17(6)A2–18(5)A1	102.2064	24.5	–	–	–	–	1.19	–
C$_2$H$_5$CN	17(3,14)–17(2,15)	102.2274	24.5	0.02±0.01	1.45±0.13	2.10±0.29	0.008	1.23	–
			24.5	0.01±0.01	6.60±0.17	3.69±0.41	0.008	1.23	
			24.5	0.09±0.01	15.43±0.39	2.51±0.60	0.003	1.23	
CH$_3$CCH	6(3)–5(3)	102.5310	24.5	0.01±0.01	10.83±0.06	2.77±0.14	0.031	1.73	✓
CH$_3$CCH	6(2)–5(2)	102.5401	23.5	0.12±0.01	8.77±0.03	2.33±0.07	0.050	1.61	✓
CH$_3$CCH	6(1)–5(1)	102.5460	23.5	0.27±0.01	8.89±0.016	2.73±0.04	0.092	1.54	✓
CH$_3$CCH	6(0)–5(0)	102.5479	24.5	0.34±0.01	8.94±0.014	2.80±0.03	0.112	1.52	✓
H66ε		102.5690	23.5	–	–	–	–	1.39	–
CF$^+$	J=1–0	102.5875	23.5	0.21±0.01	9.85±0.078	5.64±0.16	0.035	1.21	✓
			23.5	0.02±0.01	15.87±2.080	9.40±1.97	0.003	1.21	
^{13}CH$_3$OH	10(2,9)–9(3,7)	102.7900	23.5	0.00^c	–	–	–	1.74	✓
H$_2$C^{34}S	3(1,2)–2(1,1)	102.8074	23.5	0.02±0.01	9.44±0.288	2.71±0.66	0.007	1.47	✓
			23.5	0.01±0.01	13.13±0.779	2.68±1.51	0.003	1.47	
l-C$_3$H$_2$	5(1,5)–4(1,4)	102.9924	23.4	0.04±0.01	8.28±0.261	2.22±0.57	0.017	1.69	✓
			23.4	0.03±0.01	10.79±0.507	2.47±0.79	0.011	1.69	
H$_2$CS	3(0,3)–2(0,2)	103.0405	23.4	0.21±0.01	9.66±0.030	3.12±0.08	0.063	1.92	✓
H$_2$CS	3(2,1)–2(2,0)	103.0518	23.4	0.03±0.01	9.25±0.204	2.99±0.48	0.008	1.54	–
C$_2$H$_3$CN	15(4,12)–14(4,11)	103.2513	23.4	0.01^c	–	–	–	1.29	–
l-C$_3$H	J=9/2–7/2, Ω=3/2, F=5–4	103.3193	23.4	0.04±0.01	8.07±0.09	2.82±0.23	0.014	1.26	–
l-C$_3$H	J=9/2–7/2, Ω=3/2, F=4–3	103.3731	23.4	0.08±0.01	9.00±0.13	4.60±0.30	0.016	1.83	✓
			23.4	0.02±0.01	13.23±0.19	1.99±0.51	0.007	1.83	
CH$_3$OH	12(-2,11)–12(1,11)	103.3811	23.4	0.02±0.01	9.30±0.34	3.36±1.14	0.006	1.88	–
CCS	N=8–7, J=8–7	103.6407	23.4	0.09±0.01	98.44±0.02	1.65±0.06	0.052	1.63	✓
U		103.7103	23.4	0.04^c	–	–	–	1.51	–
HC$_5$N	J=39–38	103.8368	23.4	0.03±0.01	98.40±0.03	1.11±0.08	0.027	1.25	✓

Continued on next page

Table B.2 – *Continued from previous page*

Specie	Trans	Freq [GHz]	HPBW ["]	MP2 Area [K km s^{-1}]	V [km s^{-1}]	Width [km s^{-1}]	T$_{MB}$ [K]	rms [mK]	OTF
CCH	17-11818–17 11818	103.9009	23.4	–	–	–	–	2.14	✓
H$_2$CCCHCN	20(14,6-)-19(14,5)	103.9094	23.4	0.03^c	–	–	–	2.03	✓
CH$_2$CH^{13}CN	J=12(3,9)–13(2,12), F=12–12	103.9122	23.4	0.02±0.01	92.68±0.19	2.57±0.57	0.008	1.53	✓
			23.4	0.06±0.01	7.73±1.23	14.57±2.30	0.004	1.53	
H56γ		103.9137	23.4	0.07±0.01	10.85±0.62	15.22±1.16	0.004	1.00	✓
			23.4	0.02±0.01	6.97±0.16	2.93±0.30	0.006	1.00	
l-C$_3$H$_2$	5(0,5)–4(0,4)	103.9529	23.4	0.08±0.01	10.29±0.21	6.32±0.53	0.011	1.61	–
CH$_2$CHCN	49(7,42)–50(6,45)	104.0100	23.4	–	–	–	–	1.33	✓
SO$_2$	3(1,3)–2(0,2)	104.0294	23.2	0.06±0.01	8.87±0.51	10.11±1.67	0.006	1.28	✓
			23.2	0.11±0.01	9.83±0.03	2.20±0.09	0.047	1.28	
C$_3$S	J=18–17	104.0489	23.2	0.02±0.01	9.90±0.07	1.29±0.16	0.013	1.31	–
CH$_3$OH		104.0570	23.2	0.04±0.01	-1.54±0.32	6.23±0.62	0.006	1.36	✓
CH$_2$DCN	6(0,6)–5(0,5)	104.1981	23.2	0.01^c	–	–	–	1.80	✓
CH$_3$C$_5$N	67(8)–66(8), F=68–67	104.2093	23.2	–	–	–	–	1.66	✓
U		104.2306	23.2	0.01^c	–	–	–	1.40	✓
SO$_2$	10(1,9)–10(0,10)	104.2392	23.2	0.12±0.01	9.72±0.03	2.63±0.08	0.044	1.36	✓
U		104.2560	23.2	–	–	–	–	1.14	✓
^{33}SO$_2$	10(1,9)–10(0,10), F=21/2–23/2	104.3006	23.2	0.09±0.01	9.78±0.16	7.03±0.41	0.012	1.19	–
ONCN	10(3,7)–9(3,6)	104.3090	23.2	0.03^c	–	–	–	1.28	✓
			23.2	0.02±0.01	8.63±0.34	3.70±1.02	0.005	1.31	
CH$_3$OH	13(-2,12)–13(1,12)	104.3364	23.2	0.01±0.01	8.41±0.30	1.78±0.72	0.003	1.22	–
			23.2	0.01±0.01	14.66±0.28	2.52±0.85	0.004	1.22	
CH$_3$OH	10(4,7)–11(3,8)	104.3548	23.2	0.04±0.01	8.66±0.33	7.07±0.76	0.006	1.19	✓
t-H^{13}COOH	14(4,11)–15(3,12)	104.3765	23.2	–	–	–	–	1.26	✓
C$_2$H$_3$CN	11(4,8)–10(4,7)	104.4114	23.2	0.02±0.01	8.99±0.40	3.20±0.77	0.007	1.24	–
			23.2	0.02±0.01	13.09±0.52	3.72±1.47	0.006	1.24	–
C$_2$H$_3$CN	11(3,9)–10(3,8)	104.4327	23.2	0.01^c	–	–	–	1.55	–
H$_2$CS	3(1,2)–2(1,1)	104.6170	23.2	0.37±0.01	9.54±0.01	3.02±0.03	0.115	1.37	✓
C$_4$H	N=11–10, J=23/2–21/2, F=11–10	104.6665	23.2	0.14±0.01	10.16±0.06	5.52±0.33	0.024	1.87	✓
			23.2	0.11±0.01	8.33±0.02	1.33±0.02	0.081	1.87	–
C$_4$H	N=11–10, J=21/2–19/2, F=10–9	104.7051	23.2	0.31^c	10.00±0.02	8.00±0.50	0.040	1.41	✓
C$_4$H		104.7059	23.2	0.19±0.01	10.82±0.04	2.17±0.16	0.084	3.50	–

Continued on next page

Table B.2 – *Continued from previous page*

Specie	Trans	Freq	HPBW	MP2					OTF
				Area	V	Width	T_{MB}	rms	
		[GHz]	["]	[K km s^{-1}]	[km s^{-1}]	[km s^{-1}]	[K]	[mK]	
$^{13}C^{18}O$	J=1–0, F=1/2–1/2	104.7114	23.2	0.05±0.01	9.53±0.10	3.41±0.23	0.014	1.38	✓
l-C$_3$H$_2$	5(1,4)–4(1,3)	104.9156	23.2	0.04±0.01	11.12±0.07	4.10±0.73	0.008	1.07	–
CH$_3$OH	1(13,0)–12(2,1)	105.0646	23.1	0.04±0.01	11.55±0.26	5.35±0.70	0.007	1.07	–
$^{13}C^{15}N$	1 1 1 2 – 0 1 0 1	105.1723	23.1	0.02^c	–	–	–	2.49	–
H49β		105.3019	23.1	0.18±0.01	8.35±0.95	30.09±2.33	0.006	1.65	–
He49β		105.3405	23.1	0.01^c	–	–	–	1.32	–
C49β		105.3555	23.1	–	–	–	–	1.81	–
H61δ		105.4083	23.1	0.02±0.01	8.75±0.20	2.33±0.48	0.009	2.03	–
CH$_3$OCHO	3(3,0)–2(2,0)E	106.0327	23.0	0.02^c	–	–	–	2.16	–
H69ψ		106.0785	23.0	0.01^c	–	–	–	2.12	–
CCS	N=8–7, J=9–8	106.3477	23.0	0.10±0.01	9.11±0.12	3.13±0.13	0.029	1.48	✓
			23.0	0.08±0.01	8.24±0.01	0.97±0.13	0.075	1.48	
HC$_5$N	J=40–39	106.4989	23.0	0.02±0.01	9.76±0.38	2.18±0.54	0.006	1.92	–
			23.0	0.03±0.01	8.28±0.02	0.70±0.53	0.034	1.92	
H39α		106.7374	23.0	0.39	10.00	40.00	0.020	1.73	✓
^{34}SO	2(3)–1(2)	106.7432	23.0	0.03±0.01	9.77±0.70	2.36±0.70	0.010	2.25	–
He39α		106.7791	23.0	0.01^c	–	–	–	1.78	–
C39α		106.7910	23.0	0.05±0.02	11.51±0.86	6.50±1.10	0.006	1.81	–
			23.0	0.03±0.02	10.25±0.28	3.07±0.67	0.010	1.81	–
CH$_3$OH	3(1,3)–4(0,4)+ +	107.0138	23.0	0.15±0.01	9.73±0.04	2.49±0.11	0.056	2.24	–
H65ε		107.2074	23.0	0.01^c	–	–	–	8.31	–
U		107.2526	23.0	0.01^c	–	–	–	6.87	–
t-HCOOH	5(1,5)–4(1,4)	108.1267	22.7	0.04^c	–	–	–	5.31	✓
^{13}CN	N=1–0, J=1/2–1/2, F1=0–1, F=1–2	108.4269	22.7	0.04^c	–	–	–	10.3	✓
^{13}CN	N=1–0, J=1/2–1/2, F1=1–0, F=2–1	108.6513	22.7	0.10±0.03	5.30±0.29	2.39±0.98	0.040	12.50	✓
			23.7	0.10±0.03	8.61±0.24	1.98±0.61	0.048	12.50	
^{13}CN	N=1–0, J=3/2–1/2, F1=2–1, F=3–2	108.7802	22.7	0.18±0.03	8.42±0.21	3.37±0.58	0.051	10.00	✓
^{13}CN	N=1–0, J=3/2–1/2, F1=2–1, F=2–1	108.7824	22.7	0.03±0.02	7.54±0.50	1.76±1.00	0.018	10.00	✓
^{13}CN	N=1–0, J=3/2–1/2, F1=2–1, F=1–0	108.7869	22.7	–	–	–	–	9.23	✓
CH$_3$OH	0(0,0)–1(-1,1)	108.8939	22.6	0.29±0.02	9.20±0.11	3.49±0.33	0.077	7.92	✓
			23.6	0.05±0.01	13.38±0.22	1.55±0.35	0.028	7.92	
HC$_3$N	J=12–11	109.1736	22.5	1.55±0.02	8.57±0.01	2.03±0.04	0.721	10.6	✓

Continued on next page

Table B.2 – *Continued from previous page*

Specie	Trans	Freq	HPBW	MP2					OTF
				Area	V	Width	T_{MB}	rms	
		[GHz]	["]	[K km s^{-1}]	[km s^{-1}]	[km s^{-1}]	[K]	[mK]	
SO	2(3)-1(2)	109.2522	22.5	0.59±0.02	9.93±0.03	2.00±0.07	0.275	8.95	✓
OCS	J=9–8	109.4631	22.5	0.05±0.02	5.44±0.22	1.58±0.58	0.030	9.10	✓
			23.4	0.13±0.02	9.93±0.18	2.58±0.48	0.047	9.10	
H55γ		109.5360	22.4	0.08^c	–	–	–	9.03	✓
C^{18}O	J=1–0	109.7822	22.4	4.97±0.03	9.62±0.01	3.61±0.03	1.293	13.4	✓
HNCO	5(4,1)–4(4,0)	109.7984	22.4	0.13±0.02	11.61±0.29	3.36±0.61	0.037	9.29	✓
HNCO	5(0,5)–4(0,4), F=6–5	109.9057	22.4	0.13±0.03	10.06±0.42	3.48±1.22	0.034	11.7	✓
C^{15}N	N=1–0, J=3/2–1/2, F=2–1	110.0246	22.4	0.16±0.03	10.60±0.41	4.44±0.76	0.034	10.9	✓
NH$_2$D	1(1,1)0a–1(0,1)0s	110.1535	22.4	0.05^c	–	–	–	11.0	✓
^{13}CO	J=1–0, F=1/2–1/2	110.2014	22.3	56.37±0.02	9.68±0.01	4.67±0.01	11.339	14.80	✓
CH$_3$CN	6(3)–5(3)	110.3644	22.3	0.09^c	–	–	–	11.13	✓
CH$_3$CN	6(2)–5(2)	110.3749	22.3	0.08^c	–	–	–	11.2	✓
CH$_3$CN	6(1)–5(1)	110.3814	22.3	0.21±0.03	9.17±0.25	3.62±0.66	0.054	11.4	✓
CH$_3$CN	6(0)–5(0)	110.3835	22.3	0.26±0.03	9.20±0.17	3.50±0.36	0.070	10.4	✓
H60δ		110.6009	22.3	0.07^c	–	–	–	11.84	–
H68ψ		110.6346	22.3	0.07^c	–	–	–	10.3	–
U		111.5184	22.2						✓
t-HCOOH	5(0,5)–4(0,4)	111.7468	22.2	0.06±0.04	10.59±0.28	1.38±0.76	0.041	10.3	–
			22.2	0.06±0.04	13.05±1.15	2.33±1.87	0.023	10.3	–
HC$_5$N	J=42-41	111.8230	22.1	0.01^c	–	–	–	11.26	–
H48β		111.8851	22.0	–	–	–	–	11.78	✓
A-CH$_3$CHO	6(1,6)–5(1,5)A	112.2487	22.0	0.03^c	–	–	–	22.81	✓
E-CH$_3$CHO	6(-1,6)–5(-1,5) E	112.2545	22.0	0.06^c	–	–	–	24.75	✓
C^{17}O	J=1–0, F=3/2–5/2	112.3588	22.0	1.44±0.06	8.20±0.13	5.76±0.27	0.239	21.10	✓
CN	N=1–0, J=1/2–1/2, F=1/2–1/2	113.1234	21.9	0.67±0.07	9.30±0.16	3.40±0.43	0.185	26.90	✓
CN	N=1–0, J=1/2–1/2, F=1/2–3/2	113.1442	21.7	2.36±0.27	10.56±0.36	6.33±0.48	0.351	31.3	✓
				1.82±0.27	8.63±0.06	2.27±0.22	0.753	31.3	
CN	N=1–0, J=1/2–1/2, F=3/2–1/2	113.1705	21.7	2.13±1.03	10.47±1.29	4.50±0.88	0.445	33.0	✓
				1.68±1.04	8.35±0.23	2.07±0.68	0.762	33.0	
CN	N=1–0, J=1/2–1/2, F=3/2–3/2	113.1913	21.7	2.41±0.28	11.08±0.32	5.59±0.38	0.405	31.2	✓
				2.31±0.28	8.60±0.05	2.46±0.17	0.885	31.2	
CCS	N=9–8, J= 8–7	113.4102	21.7	0.12^c	–	–	–	33.13	✓

Continued on next page

Table B.2 – *Continued from previous page*

Specie	Trans	Freq	HPBW	MP2					OTF
				Area	V	Width	T_{MB}	rms	
		[GHz]	["]	[K km s^{-1}]	[km s^{-1}]	[km s^{-1}]	[K]	[mK]	
CN	N=1–0, J=3/2–1/2, F=3/2–1/2	113.4881	21.7	7.94±0.20	6.09±0.02	10.61±0.20	0.703	31.9	✓
				1.63±0.08	8.72±0.03	2.11±0.10	0.724	31.9	
CN	N=1–0, J=3/2–1/2, F=5/2–3/2	113.4910	21.7	6.50±0.74	8.67±0.07	2.46±0.23	2.487	31.9	✓
CN	N=1–0, J=3/2–1/2, F=1/2–1/2	113.4996	21.7	1.85±0.29	10.83±0.48	6.38±0.60	0.272	31.9	✓
				1.56±0.25	8.64±0.07	2.22±0.24	0.658	31.9	
CN	N=1–0, J=3/2–1/2, F=3/2–3/2	113.5089	21.7	1.67±5.46	11.38±0.63	5.84±0.40	0.269	31.6	✓
				1.96±4.82	8.65±0.82	2.46±0.62	0.748	31.6	
CN	N=1–0, J=3/2–1/2, F=1/2–3/2	113.5204	21.7	0.41±0.08	8.83±0.34	3.34±0.87	0.114	31.6	✓
C_4H	N=12–11, J=25/2–23/2, F=12–11	114.1825	21.7	0.29^c	–	–	–	33.8	✓
C_4H	N=12–11, J=23/2–21/2, F=11–10	114.2210	21.7	0.21±0.06	8.03±0.32	2.02±0.65	0.098	31.7	✓
E-CH_3CHO	6(0,6)–5(0,5) E	114.9402	21.7	0.08^c	–	–	–	35.70	✓
A-CH_3CHO	6(0,6)–5(0,5) A	114.9599	21.7	0.07^c	–	–	–	33.98	✓
NS	J=5/2–3/2, Ω=1/2, F=7/2–5/2	115.1539	21.7	–	–	–	–	41.98	✓
NS	J=5/2–3/2, Ω=1/2, F=5/2–3/2	115.1568	21.7	0.01^c	–	–	–	43.71	✓
CO	J=1–0	115.2712	21.3	202.00±0.16	8.54±0.01	4.48±0.01	42.335	52.10	✓
				63.30±0.13	13.17±0.01	2.26±0.01	26.355	52.10	
				22.27±0.19	16.64±0.01	5.80±0.06	3.609	52.10	
NS	J=5/2–3/2, Ω=1/2, F=7/2–5/2	115.5563	21.3	–	–	–	–	41.15	✓
NS	J=5/2–3/2, Ω=1/2, F=5/2–3/2	115.5708	21.3	–	–	–	–	44.04	✓
NS	J=5/2–3/2, Ω=1/2, F=3/2–1/2	115.5720	21.3	–	–	–	–	43.32	✓
E-CH_3CHO	6(2,5)–5(2,4)E	115.6950	21.3	–					✓
SO^+	J=5/2–3/2, Ω=1/2,	115.8044	21.3	0.80^c	–	–	–	54.28	✓
U		116.4262	21.3	0.70^c	–	–	–	75.19	✓
U		116.4279	21.3	0.15 ^{c}	–	–	–	75.13	✓

Table B.3: Gaussian fits of the 2mm lines at IF position.

Specie	Trans	Freq	HPBW	IF				
				Area	V	Width	T_{MB}	rms
		[GHz]	["]	[K km s^{-1}]	[km s^{-1}]	[km s^{-1}]	[K]	[mK]
CH$_3$OH	6(-1,6)–5(0,5)	132.8907	18.5	0.29±0.03	10.49±0.12	2.66±0.26	0.101	12.20
C$_3$S	J=23–22	132.9466	18.5	−	−	−	−	9.40
C$_4$H	N=14–13, J=29/2–27/2, F=14–13	133.2136	18.5	0.14±0.03	9.28±0.63	7.47±1.51	0.018	6.07
				0.08±0.02	20.10±0.87	6.15±1.93	0.013	6.07
C$_4$H	N=14–13, J=27/2–25/2, F=13–12	133.2521	18.5	0.20±0.07	9.90±1.07	11.34±3.72	0.017	7.42
				0.09±0.07	9.66±0.47	3.73±1.72	0.023	7.42
CH$_3$OCH$_3$	11(3,8)–11(2,9)AE	133.2654	18.5	0.14±0.02	11.73±0.36	5.53±0.72	0.024	5.95
t-HCOOH	6(0,6)–5(0,5)	133.7672	18.5	0.15±0.02	7.65±0.52	9.87±0.94	0.014	4.01
CH$_3^{13}$CH$_2$CN	15(5,11)–14(5,10)	133.7769	18.5	0.13±0.02	9.99±0.50	5.95±1.05	0.020	6.95
OCS	J=11-10	133.7859	18.4	0.12±0.04	9.34±1.40	8.65±3.02	0.013	8.33
				0.04±0.02	10.57±0.22	1.37±0.60	0.028	8.33
E-CH$_3$CHO	7(0,7)–6(0,6)E	133.8305	18.4	0.11±0.02	10.39±0.24	3.92±0.68	0.026	5.32
				0.02±0.01	14.78±0.52	1.89±0.94	0.009	5.32
CH$_3$CHO	7(0,7)–6(0,6)A	133.8530	18.4	0.05±0.01	8.53±0.30	2.89±0.93	0.017	5.40
A-CH$_3$CHO	7(0,7)–6(0,6)A	133.8541	18.4	0.05±0.01	10.83±0.31	2.79±0.90	0.017	5.11
SO$_2$	8(2,6)–8(1,7)	134.0049	18.4	0.12±0.01	10.55±0.09	2.27±0.24	0.051	4.85
HDCO	2(1,1)–1(1,0)	134.2848	18.3	0.05±0.01	11.02±0.35	3.07±0.59	0.014	4.65
^{33}SO	5(6)–5(5), F=11/2-11/2	134.4558	18.3	0.04±0.02	11.33±0.48	3.46±1.06	0.010	4.21
				0.07±0.02	18.76±2.51	12.39±3.64	0.052	4.21
A-CH$_3$CHO	7(2,6)–6(2,5) A	134.6944	18.3	0.07^c	−	−	−	4.75
E-CH$_3$CHO	7(2,6)–6(2,5) E	134.8956	18.3	0.03^c	−	−	−	6.10
C$_3$H$^+$	J=6–5	134.9327	18.2	0.16±0.03	11.80±1.33	14.16±2.44	0.011	6.05
CH$_3$CHO	12(1,11)–11(2,10) A	134.9619	18.2	0.06±0.02	7.98±0.47	2.98±1.71	0.017	6.33
CH$_3$CHO	7(3,5)–6(3,4) A	134.9632	18.2	0.05±0.02	10.75±0.45	2.88±1.41	0.017	6.35
CH$_3$CHO	7(3,4)–6(3,3) E	134.9739	18.2	0.10±0.02	12.80±0.43	4.35±0.90	0.021	7.19
CH$_3$CHO	7(3,4)–6(3,3) A	134.9872	18.2	−	−	−	−	12.62
DC$_3$N	J=16–15	135.0821	18.2	0.11±0.02	9.88±0.28	3.55±0.85	0.029	5.78
				0.07±0.02	15.23±0.47	3.35±1.17	0.020	5.78
H60ε		135.1053	18.2	0.78±0.03	3.65±0.63	31.91±1.55	0.023	4.34
H56δ		135.1353	18.2	1.62±0.04	8.05±0.39	30.20±0.93	0.050	6.23

Continued on next page

Table B.3 – *Continued from previous page*

Specie	Trans	Freq	HPBW	IF				
				Area	V	Width	T_{MB}	rms
		[GHz]	["]	[K km s^{-1}]	[km s^{-1}]	[km s^{-1}]	[K]	[mK]
H45β		135.2476	18.2	4.76±0.02	9.70±0.07	30.52±0.17	0.147	3.37
H36α		135.2837	18.2	16.84±0.04	9.09±0.03	30.75±0.08	0.515	5.32
H$_2$CS	4(1,4)–3(1,3)	135.2983	18.2	0.62±0.01	10.51±0.03	3.66±0.08	0.158	3.64
CH$_3$CHO	7(3,5)–6(3,4)A	135.3173	18.2	0.28±0.02	8.39±0.42	12.50±0.87	0.021	4.34
He36α		135.3363	18.2	0.37±0.03	7.01±1.26	26.56±2.64	0.013	5.44
C36α		135.3515	18.2	0.06±0.02	-3.72±0.78	6.04±1.30	0.010	4.69
				0.28±0.02	7.04±0.27	8.40±0.71	0.031	4.69
E-CH3CHO	9(4,5)–10(3,8)A	135.4767	18.2	–	–	–	–	4.10
CH$_3$CHO	7(2,5)–6(2,4)A++	135.6855	18.1	0.09^c	–	–	–	4.48
SO$_2$	5(1,5)–4(0,4)	135.6960	18.1	0.15±0.01	10.58±0.07	2.20±0.19	0.065	4.95
^{34}SO	4(3)–3(2)	135.7757	18.1	0.07±0.01	10.39±0.21	2.87±0.45	0.024	4.70
CH$_2$C^{13}HCN	J=17(0,17)–16(1,16), F=16–16	136.0777	18.1	0.02±0.01	10.65±0.13	1.01±0.23	0.022	4.77
				0.08±0.02	12.15±0.59	5.02±1.06	0.015	4.77
CH$_3$CHO	9(4,5)-10(3,8) A	136.1192	18.1	0.04±0.01	9.05±0.28	2.34±0.61	0.014	4.77
				0.01±0.01	11.85±0.33	0.71±8.84	0.006	4.35
HC$_3$N	J=15–14	136.4644	18.0	1.15±0.01	11.54±0.01	2.62±0.03	0.414	5.02
H51γ		136.5565	18.0	3.43±0.05	8.54±0.24	34.08±0.53	0.095	6.76
SO	5(6)–5(5)	136.6348	18.0	0.06±0.01	11.03±0.25	2.24±0.65	0.027	7.21
CH$_3$CCH	8(3)–7(3)	136.7045	18.0	0.09±0.04	10.48±0.44	2.06±1.35	0.040	19.60
CH$_3$CCH	8(2)–7(2)	136.7176	18.0	0.18±0.04	10.70±0.36	3.08±0.86	0.054	19.00
CH$_3$CCH	8(1)–7(1)	136.7254	18.0	0.27±0.03	10.56±0.21	3.79±0.48	0.066	11.50
CH$_3$CCH	8(0)–7(0)	136.7280	18.0	0.35±0.03	10.88±0.14	3.73±0.38	0.086	10.40
^{33}SO	4(3)–3(2), F=7/2–9/2	136.8528	18.0	0.26±0.02	9.78±0.16	4.42±0.41	0.054	6.84
H$_2$^{13}CO	2(0,2)–1(0,1)	141.9837	17.3	0.14^c	–	–	–	14.56
H55δ		142.3883	17.3	0.68±0.10	4.64±0.53	9.09±0.95	0.071	13.0
			17.3	1.28±0.14	20.02±0.57	15.41±2.01	0.078	13.0
			17.3	0.85±0.07	38.83±0.42	10.74±0.92	0.075	13.0
CCS	N=11–10, J=11–10	142.5017	17.3	–	–	–	–	10.79
C$_4$H	N=15–14, J=31/2–29/2, F=15–14	142.7288	17.2	0.21^c	–	–	–	9.57
H$_2$CCO	7(1,6)–6(1,5)	142.7689	17.2	0.12±0.02	10.92±0.25	3.22±0.58	0.036	8.72
CH$_3$OH	3(1,3)–2(1,2)+ +	143.8658	17.2	0.08±0.02	10.79±0.21	1.68±0.64	0.046	12.90

Continued on next page

Table B.3 – *Continued from previous page*

Specie	Trans	Freq	HPBW	IF				
				Area	V	Width	T_{MB}	rms
		[GHz]	["]	[K km s^{-1}]	[km s^{-1}]	[km s^{-1}]	[K]	[mK]
DCO$^+$	J=2–1	144.0773	17.1	0.15±0.02	10.62±0.07	1.53±0.23	0.092	12.40
			17.1	0.27±0.03	12.34±0.76	5.83±0.86	0.044	12.40
C$_2$D	N=2–1, J=5/2–3/2, F=7/2–5/2	144.2419	17.1	0.18^c	–	–	–	8.50
C$_2$D	N=2–1, J=5/2–3/2, F=3/2–1/2	144.2431	17.1	0.15^c	–	–	–	8.16
C$_2$S	N=11–10, J=12–11	144.2448	17.1	0.16^c	–	–	–	8.88
C$_2$D	N=2–1, J=3/2–1/2, F=5/2–3/2	144.2967	17.0	–	–	–	–	7.61
C$_2$D	N=2–1, J=3/2–1/2, F=3/2–1/2	144.2977	17.0	–	–	–	–	7.34
H44β		144.4717	17.0	5.041±0.05	7.51±0.14	29.65±0.32	0.160	7.12
C^{34}S	J=3–2	144.6171	17.0	0.58±0.04	9.19±0.16	5.28±0.27	0.104	7.69
			17.0	0.39±0.03	10.63±0.03	1.49±0.08	0.245	7.69
H50γ		144.6789	17.0	1.92±0.05	12.51±0.38	27.59±0.82	0.065	8.13
DCN	J=2–1, F=2–2	144.8268	17.0	0.07±0.01	11.26±0.05	0.78±0.09	0.087	6.67
			17.0	0.18±0.01	12.47±0.04	1.34±0.11	0.125	6.69
DCN	J=2–1, F=2–1	144.8279	17.0	0.69±0.02	10.82±0.02	1.76±0.06	0.367	6.69
			17.0	0.44±0.01	12.43±0.02	1.34±0.04	0.304	6.69
DCN	J=2–1, F=1–2	144.8303	17.0	0.05±0.02	10.81±0.20	1.13±0.53	0.045	6.69
			17.0	0.08±0.03	12.39±0.11	0.99±0.36	0.074	6.69
c-C$_3$H$_2$	3(1,2)–2(2,1)	145.0896	16.9	0.43±0.09	10.74±0.97	11.81±2.45	0.034	6.83
			16.9	0.18±0.04	9.25±0.15	2.77±0.43	0.061	6.83
CH$_3$OH	3(0,3)–2(0,2)	145.0938	16.9	0.08±0.09	7.85±1.16	2.86±1.74	0.026	9.62
			16.9	0.20±0.10	10.81±0.64	3.35±1.56	0.056	9.62
CH$_3$OH	3(-1,3)–2(-1,2)	145.0974	16.9	0.48±0.07	8.18±0.16	2.70±0.42	0.167	17.10
			16.9	0.25±0.06	10.93±0.20	2.03±0.44	0.117	17.10
CH$_3$OH	3(,)–2(,)	145.1022	16.9	0.29±0.12	6.16±0.10	1.31±0.45	0.211	24.30
			16.9	0.58±0.12	8.46±0.29	2.96±0.68	0.182	24.30
CH$_3$OH	3(2,1)–2(2,0)	145.1262	16.9	0.05±0.02	7.48±0.36	1.78±0.52	0.024	8.35
			16.9	0.14±0.03	10.59±0.25	3.07±0.97	0.042	8.35
CH$_3$OH	3(1,2)–2(1,1)	145.1319	16.9	0.08±0.05	7.73±0.71	3.06±1.61	0.026	8.31
			16.9	0.12±0.04	10.82±0.33	2.48±0.68	0.047	8.31
HC$_3$N	J=16–15	145.5609	16.9	0.67±0.02	11.47±0.05	2.98±0.11	0.212	10.20
H$_2$CO	2(0,2)–1(0,1)	145.6029	16.9	3.61±0.03	9.52±0.02	4.43±0.04	0.766	11.00
C^{33}S	9(4,6)–9(2,7)A	145.7557	16.9	0.28±0.03	10.32±0.26	4.68±0.59	0.056	11.50

Table B.3 – *Continued from previous page*

Specie	Trans	Freq	HPBW	IF				
				Area	V	Width	T_{MB}	rms
		[GHz]	["]	[K km s^{-1}]	[km s^{-1}]	[km s^{-1}]	[K]	[mK]
c-C$_3$H$_2$	4(0,4)–3(1,3)	150.8207	16.3	0.26±0.04	9.73±0.41	5.20±0.89	0.048	13.70
c-C$_3$H$_2$	4(1,4)-3(0,3)	150.8519	16.3	0.70±0.04	9.44±0.10	3.86±0.24	0.172	13.50
c-C$_3$H$_2$		151.1056	16.3	0.09±0.02	9.09±0.41	4.42±0.84	0.020	6.64
c-C$_3$H$_2$	5(1,4)–5(0,5)	151.3439	16.2	0.05^c	–	–	–	15.09
C$_4$H	N=16–15, J=33/2–31/2, F=16–15	152.2436	16.1	0.09±0.02	8.07±2.99	11.384±6.207	0.008	5.26
				0.04±0.02	9.25±0.18	1.638±0.532	0.022	5.26
C$_4$H	N=16–15, J=31/2–29/2, F=15–14	152.2821	16.1	0.08±0.02	9.48±0.34	3.929±0.748	0.020	5.70
DNC	J=2–1	152.6097	16.1	0.03±0.01	10.60±0.15	1.145±0.241	0.024	6.13
				0.21±0.01	12.14±0.02	1.122±0.056	0.173	6.13
A-CH$_3$CHO	(0,8)–7(0,7)A	152.6352	16.1	0.075±0.012	9.54±0.35	4.01±0.67	0.017	
CCS	N=12–11, J=11–10	153.4498	16.0					
H49γ		153.4553	16.0	2.67±0.04	12.16±0.23	31.78±0.52	0.079	
CH$_3$CCH	9(3)–8(3)	153.7904	16.0	0.08±0.01	9.21±0.34	4.30±0.69	0.018	5.19
CH$_3$CN		153.8040	16.0	0.12±0.02	7.65±0.28	4.70±0.75	0.024	5.23
CH$_3$CCH	9(1)–8(1)	153.8143	16.0	0.19±0.02	9.72±0.20	5.76±0.71	0.031	5.02
CH$_3$CCH	9(0)–8(1)	153.8172	16.0	0.28±0.04	10.43±0.38	5.31±0.68	0.049	5.02
HNCO	7(0,7)–6(0,6)	153.8651	16.0	0.09±0.02	8.44±0.29	2.76±0.82	0.029	8.45
A-CH$_3$CHO	8(2,7)–7(2,6)A	153.8727	16.0	–	–	–	–	8.13
A-CH$_3$CHO	8(3,6)–7(3,5)A	154.2747	16.0	0.03^c	–	–	–	8.49
A-CH$_3$CHO	8(3,5)–7(3,4)A	154.3225	16.0	–	–	–	–	6.60
H43β		154.5572	15.9	4.45±0.04	12.16±0.14	29.03±0.31	0.144	5.40
HC$_3$N	J=17–16	154.6573	15.9	0.43±0.01	11.35±0.04	2.76±0.08	0.147	5.50
CH$_3$OCH$_3$	12(3,10)–12(2,11)AA	155.1315	15.8	0.10^c	–	–	–	23.94
U		155.2309	15.8	0.19^c	–	–	–	24.39
CCS	N=12–11, J=12–11	155.4545	15.8	0.10^c	–	–	–	21.93
^{34}SO	3(4)–2(3)	155.5065	15.8	–	–	–	–	24.32
c-C$_3$H$_2$	3(2,2)–2(1,1)	155.5183	15.8	0.60^c	–	–	–	26.28
t-HCOOH	7(0,7)–6(0,6)	155.6178	15.7	–	–	–	–	26.10
t-HCOOH	7(0,7)–6(0,6)	155.6179	15.7	–	–	–	–	26.94
CH$_3$OH	9(0,9)–9(-1,9)	155.9975	15.7	–	–	–	–	24.46
CH$_3$OH	8(0,8)–8(-1,8)	156.4889	15.5	0.02^c	–	–	–	24.62
HNO$_3$		156.5976	15.5	0.40^c	–	–	–	26.64

Continued on next page

Table B.3 – *Continued from previous page*

Specie	Trans	Freq	HPBW	IF				
				Area	V	Width	T_{MB}	rms
		[GHz]	["]	[K km s^{-1}]	[km s^{-1}]	[km s^{-1}]	[K]	[mK]
CH$_3$OH	2(1,2)–3(0,3)	156.6024	15.5	0.34^c	–	–	–	27.23
C$_2$H$_5$C^{15}N		156.6122	15.5	–	–	–	–	26.96
CH$_3$OH	7(0,7)–7(-1,7)	156.8285	15.5	0.04^c	–	–	–	25.12
CCS	N=12–11, J=13–12	156.9817	15.5	0.16^c	–	–	–	27.32
t-HCOOH	7(2,6)–6(2,5)	157.0539	15.2	–	–	–	–	23.53
CH$_3$OH	6(0,6)–6(-1,6)	157.0486	15.2	0.20^c	–	–	–	24.62
CH$_3$OH	5(0,5)–5(-1,5)	157.1790	15.2	0.08^c	–	–	–	22.51
CH$_3$OH	4(0,4)–4(-1,4)	157.2461	15.2	0.28±0.06	10.68±0.24	2.60±0.85	0.102	24.90
CH$_3$OH	1(0,1)–1(-1,1)	157.2709	15.2	0.76±0.07	8.71±0.27	5.83±0.64	0.123	23.70
CH$_3$OH	2(0,2)–2(-1,2)	157.2761	15.2	0.38±0.07	10.46±0.26	3.20±0.83	0.113	23.50
C$_3$H$^+$	J=7-6	157.4187	15.2	0.20^c	–	–	–	26.39
CH$_3$CHO	8(1,7)–7(1,6)E	157.9377	15.2	0.23^c	–	–	–	25.79
CH$_3$CHO	8(1,7)–7(1,6)A	157.9746	15.2	0.10^c	–	–	–	26.46
OCS	J=13–12	158.1074	15.1	0.26±0.07	10.61±0.61	3.59±1.25	0.068	27.90
SO$_2$	3(2,2)–3(1,3)	158.1997	15.1	0.11^c	–	–	–	26.61
H60ψ		158.5149	15.1	2.10±0.16	3.56±1.16	31.21±2.69	0.063	22.30
SO	3(4)–2(3)	158.9718	15.1	0.72±0.05	10.35±0.08	2.10±0.19	0.321	28.50
H$_2$CCO	8(1,8)–7(1,7)	160.1421	14.8	–	–	–	–	31.81
H34α		160.2107	14.8	19.86±0.20	11.94±0.16	31.89±0.36	0.585	28.30
SO$_2$	10(0,10)–9(1,9)	160.8279	14.8	0.18^c	–	–	–	27.00
NS	J=7/2–5/2, F=9/2–7/2	161.2972	14.6	0.10^c	–	–	–	25.24
NS	J=7/2–5/2, F=5/2–3/2	161.3017	14.6	0.31^c	–	–	–	25.31
NS	J=7/2–5/2, F=9/2–7/2	161.6973	14.6	0.02^c	–	–	–	26.42
NS	J=7/2–5/2, F=7/2–5/2	161.7034	14.6	–	–	–	–	25.67
NS	J=7/2–5/2, F=7/2–5/2	161.7039	14.6	–	–	–	–	25.31
C$_4$H	N=17–16, J=15/2–13/2	161.7581	14.6	0.12^c	–	–	–	22.13
C$_4$H	N=17–16, J=13/2–11/2	161.7966	14.6	0.14^c	–	–	–	27.82
SO$^+$	J=7/2–5/2	162.1986	14.4	0.05^c	–	–	–	26.38
SO$^+$	J=7/2–5/2	162.5741	14.4	0.30^c	–	–	–	22.27
t-HCOOH	7(1,6)–6(1,5)	162.5984	14.4	–	–	–	–	24.68

Table B.4: Gaussian fits of the 2mm lines at MP2 position.

Specie	Trans	Freq	HPBW	MP2				
		[GHz]	["]	Area [K km s^{-1}]	V [km s^{-1}]	Width [km s^{-1}]	T$_{MB}$ [K]	rms [mK]
CH$_3$OH	6(-1,6)–5(0,5)	132.8907	18.5	0.34±0.02	9.13±0.08	2.94±0.18	0.110	8.70
C$_3$S	J=23–22	132.9466	18.5	0.09±0.02	13.07±0.26	2.63±0.91	0.031	8.35
C$_4$H	N=14–13, J=29/2–27/2, F=14–13	133.2136	18.5	0.28±0.03	12.13±0.60	10.11±1.09	0.026	7.15
				0.10±0.01	8.42±0.06	1.16±0.15	0.080	7.15
C$_4$H	N=14–13, J=27/2–25/2, F=13–12	133.2521	18.5	0.12±0.03	10.02±0.77	6.84±1.34	0.017	7.55
				0.09±0.02	8.28±0.04	0.70±0.70	0.126	7.55
CH$_3$OCH$_3$	11(3,8)–11(2,9)AE	133.2653	18.5					7.55
t-HCOOH	6(0,6)–5(0,5)	133.7672	18.5	0.04^c	–	–	–	6.37
CH$_3^{13}$CH$_2$CN	15(5,11)–14(5,10)	133.7770	18.5					7.55
OCS	J=11-10	133.7859	18.4	0.07± 0.02	3.63±0.58	4.42±1.40	0.014	6.70
				0.11±0.02	10.11±0.22	3.10±0.51	0.032	6.70
E-CH$_3$CHO	7(0,7)–6(0,6)E	133.8305	18.4	0.07±0.01	9.46±0.70	2.54±0.70	0.025	6.93
				0.04±0.01	12.80±0.70	2.96±0.70	0.012	6.93
CH$_3$CHO	7(0,7)–6(0,6)A	133.8530	18.4	0.09^c	–	–	–	7.24
A-CH$_3$CHO	7(0,7)–6(0,6)A	133.8541	18.4	0.02^c	–	–	–	6.74
SO$_2$	8(2,6)–8(1,7)	134.0049	18.4	0.12±0.01	9.93±0.12	2.81±0.31	0.041	5.29
HDCO	2(1,1)–1(1,0)	134.2848	18.3	0.10±0.01	8.35±0.06	1.29±0.16	0.076	5.29
^{33}SO	5(6)–5(5), F=11/2-11/2	134.4558	18.3	–	–	–	–	4.28
A-CH$_3$CHO	7(2,6)–6(2,5) A	134.6944	18.3	0.05^c	–	–	–	6.93
E-CH$_3$CHO	7(2,6)–6(2,5) E	134.8956	18.3	0.01^c	–	–	–	5.83
C$_3$H$^+$	J=6–5	134.9327	18.2	0.10^c	–	–	–	6.64
CH$_3$CHO	12(1,11)–11(2,10) A	134.9619	18.2	0.06±0.02	2.52±1.46	6.71±2.20	0.008	6.40
				0.04±0.02	7.12±0.35	2.03±0.79	0.016	6.40
CH$_3$CHO	7(3,5)–6(3,4) A	134.9632	18.2	0.07±0.02	5.12±1.35	7.17±2.04	0.009	6.24
				0.04±0.02	9.89±0.31	2.12±0.79	0.016	6.24
CH$_3$CHO	7(3,4)–6(3,3) E	134.9739	18.2	–	–	–	–	6.71
CH$_3$CHO	7(3,4)–6(3,3) A	134.9872	18.2	–	–	–	–	6.93
DC$_3$N	J=16–15	135.0821	18.2	0.05^c	–	–	–	7.01
H60ε		135.1053	18.2	–	–	–	–	8.03
H56δ		135.1356	18.2	0.05^c	–	–	–	7.62

Continued on next page

Table B.4 – *Continued from previous page*

Specie	Trans	Freq	HPBW	MP2				
				Area	V	Width	T_{MB}	rms
		[GHz]	["]	[K km s^{-1}]	[km s^{-1}]	[km s^{-1}]	[K]	[mK]
H45β		135.2476	18.2	0.03±0.02	5.07±0.51	2.36±1.22	0.011	5.32
				0.09±0.03	7.82±1.96	10.27±2.81	0.010	5.32
H36α		135.2837	18.2	–	–	–	–	5.38
H$_2$CS	4(1,4)–3(1,3)	135.2983	18.2	0.50±0.01	9.34±0.03	3.21±0.08	0.148	4.84
CH$_3$CHO	7(3,5)–6(3,4)A	135.3173	18.2	0.12^c	–	–	–	5.13
He36α		135.3363	18.2	0.21±0.04	-3.14±2.49	26.23±5.42	0.007	5.68
C36α		135.3515	18.2	0.09±0.02	4.29±0.40	5.31±1.13	0.016	4.65
E-CH3CHO	9(4,5)–10(3,8)A	135.4768	18.2	0.03±0.01	8.55±0.46	1.71±0.86	0.016	4.31
				0.04±0.01	12.12±0.97	4.80±1.17	0.008	4.31
CH$_3$CHO	7(2,5)–6(2,4)A++	135.6855	18.1	0.04±0.02	9.14±0.66	2.10±1.13	0.016	11.60
				0.02±0.02	12.81±1.23	1.92±2.45	0.009	11.60
SO$_2$	5(1,5)–4(0,4)	135.6960	18.1	0.09±0.02	9.34±0.61	6.15±1.87	0.014	4.37
				0.09±0.02	9.91±0.11	1.99±0.30	0.044	4.37
^{34}SO	4(3)–3(2)	135.7757	18.1	0.10±0.01	9.99±0.09	2.24±0.26	0.042	4.04
CH$_2$C^{13}HCN	J=17(0,17)–16(1,16), F=16–16	136.0777	18.1	0.06±0.05	5.63±2.63	6.36±5.53	0.008	4.77
				0.14±0.04	10.44±0.21	3.35±0.51	0.040	4.77
CH$_3$CHO	9(4,5)–10(3,8) A	136.1192	18.1	0.03±0.01	9.87±0.12	1.16±0.28	0.024	4.17
HC$_3$N	J=15–14	136.4644	18.0	1.12±0.02	8.46±0.01	1.39±0.04	0.757	12.50
H51γ		136.5565	18.0	0.03^c	–	–	–	7.67
SO	5(6)–5(5)	136.6348	18.0	0.05±0.01	10.24±0.12	1.44±0.34	0.030	4.82
CH$_3$CCH	8(3)–7(3)	136.7045	18.0	0.14±0.01	8.78±0.121	2.75±0.34	0.047	5.69
CH$_3$CCH	8(2)–7(2)	136.7176	18.0	0.15±0.01	8.57±0.05	1.60±0.20	0.088	5.67
CH$_3$CCH	8(1)–7(1)	136.7254	18.0	0.32±0.01	8.74±0.04	2.06±0.11	0.146	5.55
CH$_3$CCH	8(0)–7(0)	136.7280	18.0	0.32±0.02	8.56±0.03	1.57±0.12	0.189	6.54
^{33}SO	4(3)–3(2), F=7/2–9/2	136.8528	18.0	0.07±0.02	8.32±0.37	3.07±1.27	0.020	5.06
				0.07±0.02	11.18±0.15	1.63±0.28	0.037	5.06
H$_2$^{13}CO	2(0,2)–1(0,1)	141.9837	17.3	0.14±0.03	9.11±0.21	2.69±0.61	0.050	11.10
H55δ		142.3883	17.3	–	–	–	–	8.06
CCS	N=11–10, J=11–10	142.5017	17.3	0.15±0.02	8.52±0.10	1.82±0.33	0.075	9.03
C$_4$H	N=15–14, J=31/2–29/2, F=15–14	142.7288	17.2	0.12±0.01	8.42±0.07	1.41±0.17	0.083	8.35
H$_2$CCO	7(1,6)–6(1,5)	142.7689	17.2	0.08±0.02	8.54±0.31	2.92±1.23	0.026	7.56
				0.14±0.01	11.91±0.06	1.37±0.14	0.093	7.56

Table B.4 – *Continued from previous page*

Specie	Trans	Freq	HPBW	MP2				
				Area	V	Width	T_{MB}	rms
		[GHz]	["]	[K km s^{-1}]	[km s^{-1}]	[km s^{-1}]	[K]	[mK]
CH$_3$OH	3(1,3)–2(1,2)+ +	143.8658	17.2	0.22±0.02	9.64±0.11	3.07±0.35	0.066	7.26
DCO$^+$	J=2–1	144.0773	17.1	0.33±0.02	8.60±0.03	1.36±0.10	0.228	9.70
C$_2$D	N=2–1, J=5/2–3/2, F=7/2–5/2	144.2419	17.1	0.12±0.01	2.35±0.05	1.19±0.12	0.098	7.63
				0.12±0.01	6.08±0.04	1.11±0.21	0.100	7.63
				0.17±0.02	8.38±0.07	1.75±0.29	0.092	7.63
C$_2$D	N=2–1, J=5/2–3/2, F=3/2–1/2	144.2431	17.1	0.13±0.02	8.50±0.09	1.32±0.19	0.093	11.70
				0.14±0.02	10.71±0.07	1.16±0.16	0.112	11.70
C$_2$S	N=11–10, J=12–11	144.2448	17.1	0.13±0.01	8.36±0.07	1.52±0.18	0.081	7.65
C$_2$D	N=2–1, J=3/2–1/2, F=5/2–3/2	144.2967	17.0	0.06±0.02	3.76±0.74	3.73±1.83	0.016	6.89
				0.08±0.01	8.56±0.09	1.39±0.25	0.055	6.89
C$_2$D	N=2–1, J=3/2–1/2, F=3/2–1/2	144.2977	17.0	0.05±0.01	5.16±0.34	2.14±0.72	0.021	7.17
				0.09±0.01	10.46±0.10	1.58±0.30	0.051	7.17
H44β		144.4717	17.0	0.10±0.02	13.09±0.91	7.35±1.78	0.013	7.01
C^{34}S	J=3–2	144.6171	17.0	1.56±0.02	9.34±0.02	2.91±0.04	0.506	8.29
H50γ		144.6789	17.0	0.06^c	–	–	–	7.62
DCN	J=2–1, F=2–2	144.8268	17.0	0.26±0.02	8.59±0.41	1.47±0.06	0.183	7.10
			17.0	0.19±0.03	10.07±0.19	2.71±0.20	0.065	7.10
DCN	J=2–1, F=2–1	144.8279	17.0	0.74±0.01	8.54±0.01	1.24±0.02	0.564	7.10
			17.0	0.18±0.01	9.97±0.01	0.90±0.03	0.182	7.10
DCN	J=2–1, F=1–2	144.8303	17.0	0.09±0.01	8.67±0.05	0.99±0.08	0.087	7.10
			17.0	0.04±0.01	1.10±0.14	1.27±0.24	0.033	7.10
c-C$_3$H$_2$	3(1,2)–2(2,1)	145.0896	16.9	0.55±0.03	10.78±0.21	6.85±0.45	0.075	7.64
			16.9	0.42±0.02	8.34±0.02	1.25±0.05	0.319	7.64
CH$_3$OH	3(0,3)–2(0,2)	145.0938	16.9	0.42±0.11	9.33±0.44	3.47±1.19	0.114	10.0
CH$_3$OH	3(-1,3)–2(-1,2)	145.0974	16.9	0.87±0.12	9.43±0.21	3.26±0.52	0.252	10.0
CH$_3$OH	3(,)–2(,)	145.1022	16.9	1.12±0.15	7.51±0.20	3.13±0.48	0.337	66.1
CH$_3$OH	3(2,1)–2(2,0)	145.1262	16.9	0.29±0.14	9.39±0.80	3.41±1.93	0.079	56.9
CH$_3$OH	3(1,2)–2(1,1)	145.1319	16.9	0.30±0.04	9.26±0.24	3.83±0.63	0.074	15.3
HC$_3$N	J=16–15	145.5609	16.9	1.02±0.02	8.45±0.01	1.36±0.04	0.704	13.20
H$_2$CO	2(0,2)–1(0,1)	145.6029	16.9	5.96±0.02	9.18±0.01	3.45±0.01	1.624	12.50
C^{33}S	9(4,6)–9(2,7)A	145.7557	16.9	0.36±0.02	9.10±0.10	3.81±0.24	0.089	8.15
c-C$_3$H$_2$	4(0,4)–3(1,3)	150.8207	16.3	0.43±0.15	8.39±0.21	1.27±0.56	0.316	14.38

Continued on next page

Table B.4 – *Continued from previous page*

Specie	Trans	Freq	HPBW	MP2					
				Area	V	Width	T_{MB}	rms	
		[GHz]	["]	[K km s^{-1}]	[km s^{-1}]	[km s^{-1}]	[K]	[mK]	
c-C$_3$H$_2$	4(1,4)-3(0,3)	150.8519	16.3	0.93±0.03	8.40±0.01	1.12±0.04	0.779	14.38	
				1.10±0.06	10.52±0.20	6.73±0.39	0.154	14.38	
c-C$_3$H$_2$		151.1057	16.3	0.14±0.03	12.20±0.36	3.79±0.75	0.034	10.80	
c-C$_3$H$_2$	5(1,4)–5(0,5)	151.3439	16.2	0.14±0.01	8.26±0.04	0.94±0.26	0.142	10.50	
C$_4$H	N=16–15, J=33/2–31/2, F=16–15	152.2436	16.1	0.12±0.01	8.37±0.04	0.96±0.14	0.118	5.82	
				0.12±0.02	10.89±0.33	4.03±0.61	0.029	5.82	
C$_4$H	N=16–15, J=31/2–29/2, F=15–14	152.2821	16.1	0.10±0.01	8.31±0.04	0.91±0.24	0.104	6.04	
				0.11±0.02	10.08±0.67	6.68±1.32	0.016	6.04	
DNC	J=2–1	152.6097	16.1	0.48±0.01	8.44±0.01	0.94±0.03	0.486	7.39	
				0.10±0.01	10.02±0.13	1.72±0.37	0.055	7.39	
A-CH$_3$CHO	(0,8)–7(0,7)A	152.6352	16.1	0.13±0.02	9.65±0.37	4.23±0.91	0.028	8.53	
CCS	N=12–11, J=11–10	153.4498	16.0	0.11±0.01	8.41±0.05	1.22±0.12	0.087	6.22	
H49γ		153.4553	16.0	0.10^c	–	–	–	5.34	
CH$_3$CCH	9(3)–8(3)	153.7904	16.0	0.13±0.07	7.72±0.32	1.45±1.21	0.083	10.0	
CH$_3$CN		153.8040	16.0	0.11±0.02	5.54±0.04	0.70±1.94	0.153	11.0	
				0.17±0.04	6.89±0.39	3.54±0.88	0.045	11.0	
CH$_3$CCH	9(1)–8(1)	153.8143	16.0	0.31±0.02	9.45±0.09	3.49±0.19	0.084	5.39	
				0.18±0.01	8.34±0.01	0.70±0.31	0.247	5.39	
CH$_3$CCH	9(0)–8(1)	153.8172	16.0	0.37±0.02	8.42±0.03	1.10±0.09	0.314	6.23	
				0.13±0.03	10.14±0.10	1.39±0.33	0.090	6.23	
HNCO	7(0,7)–6(0,6)	153.8651	16.0	0.14±0.02	8.98±0.18	3.44±0.55	0.037	5.85	
A-CH$_3$CHO	8(2,7)–7(2,6)A	153.8727	16.0	0.01^c	–	–	–	7.91	
A-CH$_3$CHO	8(3,6)–7(3,5)A	154.2747	16.0	0.04^c	–	–	–	10.26	
A-CH$_3$CHO	8(3,5)–7(3,4)A	154.3225	16.0	0.14±0.03	17.19±0.68	5.53±1.78	0.024	10.00	
H43β		154.5572	15.9	0.12±0.03	15.37±0.36	3.27±0.71	0.034	11.70	
HC$_3$N	J=17–16	154.6573	15.9	0.98±0.02	8.37±0.01	1.18±0.03	0.782	10.60	
CH$_3$OCH$_3$	12(3,10)–12(2,11)AA	155.1315	15.8	0.15±0.02	20.51±0.75	9.87±1.49	0.015	4.20	✓
				0.096±0.01	24.17±0.08	1.92±0.20	0.047	4.20	–
U		155.2308	15.8	0.02^c	–	–	–	4.25	
CCS	N=12–11, J=12–11	155.4545	15.8	0.14±0.01	8.40±0.03	1.32±0.07	0.100	4.34	✓
^{34}SO	3(4)–2(3)	155.5065	15.8	0.07±0.05	9.40±0.93	2.33±2.21	0.026	10.0	✓
c-C$_3$H$_2$	3(2,2)–2(1,1)	155.5183	15.8	0.25±0.02	10.39±0.25	6.10±0.44	0.039	5.08	✓

Continued on next page

Table B.4 – *Continued from previous page*

Specie	Trans	Freq	HPBW	MP2					
				Area	V	Width	T_{MB}	rms	
		[GHz]	["]	[K km s^{-1}]	[km s^{-1}]	[km s^{-1}]	[K]	[mK]	
				0.31±0.01	8.32±0.011	1.08±0.05	0.268	5.08	✓
t-HCOOH	7(0,7)–6(0,6)	155.6178	15.7	0.01^c	–	–	–	4.85	✓
t-HCOOH	7(0,7)–6(0,6)	155.6179	15.7	0.01^c	–	–	–	4.93	✓
CH$_3$OH	9(0,9)–9(-1,9)	155.9975	15.7	0.10±0.01	8.70±0.24	4.54±0.65	0.021	4.00	✓
CH$_3$OH	8(0,8)–8(-1,8)	156.4889	15.5	0.12±0.01	8.85±0.24	5.12±0.54	0.022	3.83	✓
HNO$_3$		156.5976	15.5	–	–	–	–	4.04	✓
CH$_3$OH	2(1,2)–3(0,3)++	156.6024	15.5	0.19± 0.01	9.23±0.10	3.59±0.24	0.051	4.15	✓
C$_2$H$_5$C^{15}N		156.6122	15.5	0.01^c	–	–	–	8.84	✓
CH$_3$OH	7(0,7)–7(-1,7)	156.8285	15.5	0.15±0.01	9.140±0.18	4.78±0.44	0.030	4.09	✓
CCS	N=12–11, J=13–12	156.9817	15.5	0.20±0.01	8.36±0.02	1.22±0.04	0.152	4.30	✓
t-HCOOH	7(2,6)–6(2,5)	157.0539	15.2	0.18^c	–	–	–	4.35	✓
CH$_3$OH	6(0,6)–6(-1,6)	157.0486	15.2	0.21±0.01	9.01±0.08	3.52±0.20	0.056	4.16	✓
CH$_3$OH	5(0,5)–5(-1,5)	157.1790	15.2	0.28±0.01	9.14±0.06	3.38±0.15	0.077	4.64	✓
CH$_3$OH	4(0,4)–4(-1,4)	157.2466	15.2	0.37±0.01	9.07±0.04	3.40±0.10	0.103	3.91	✓
CH$_3$OH	1(0,1)–1(-1,1)	157.2708	15.2	0.88±0.02	7.55±0.05	5.71±0.12	0.134	4.87	✓
CH$_3$OH	2(0,2)–2(-1,2)	157.2761	15.2	0.43±0.01	9.16±0.03	3.38±0.08	0.119	3.74	✓
C$_3$H$^+$	J=7-6	157.4187	15.2	0.09±0.01	9.78±0.48	5.55±1.06	0.015	3.67	–
CH$_3$CHO	8(1,7)–7(1,6)E	157.9377	15.2	0.08±0.01	8.88±0.14	2.35±0.34	0.030	4.19	✓
CH$_3$CHO	8(1,7)–7(1,6)A	157.9746	15.2	0.06±0.01	9.02±0.20	2.59±0.40	0.020	4.10	✓
OCS	J=13–12	158.1074	15.1	0.09±0.01	9.65±0.14	2.95±0.33	0.029	3.81	✓
SO$_2$	3(2,2)–3(1,3)	158.1997	15.1	0.06±0.01	10.03±0.08	1.66±0.20	0.036	3.75	✓
H60ψ		158.5149	15.1	0.03^c	–	–	–	4.32	–
SO	3(4)–2(3)	158.9718	15.1	0.91±0.01	9.77±0.01	2.58±0.03	0.333	4.49	✓
H$_2$CCO	8(1,8)–7(1,7)	160.1421	14.8	0.11± 0.01	8.71±0.15	3.30±0.38	0.030	4.11	✓
H34α		160.2107	14.8	0.01^c	–	–	–	3.77	✓
SO$_2$	10(0,10)–9(1,9)	160.8279	14.8	0.18±0.01	9.77±0.07	2.85±0.17	0.061	4.28	✓
NS	J=7/2–5/2, F=9/2–7/2	161.2972	14.6	0.13±0.01	8.97±0.18	4.48±0.47	0.028	4.02	✓
NS	J=7/2–5/2, F=5/2–3/2	161.3017	14.6						✓
NS	J=7/2–5/2, F=9/2–7/2	161.6973	14.6	0.06±0.01	9.47±0.33	2.94±0.60	0.019	5.50	✓
NS	J=7/2–5/2, F=7/2–5/2	161.7034	14.6	0.08±0.03	8.67±0.56	3.09±0.88	0.024	3.89	✓
			0.02±0.03	11.38±0.95	2.18±1.33	0.010	3.89		
NS	J=7/2–5/2, F=7/2–5/2	161.7039	14.6	0.08±0.02	9.67±0.43	2.97±0.73	0.024	3.73	✓

Table B.4 – *Continued from previous page*

Specie	Trans	Freq [GHz]	HPBW ["]	MP2 Area [K km s^{-1}]	V [km s^{-1}]	Width [km s^{-1}]	T$_{MB}$ [K]	rms [mK]	
				0.03±0.02	12.07±0.37	1.78±1.08	0.013	3.73	
C$_4$H	N=17–16, J=15/2–13/2	161.7581	14.6	0.09±0.02	10.34±0.56	6.10±0.92	0.014	3.87	−
				0.14±0.01	8.39±0.02	1.10±0.07	0.122	3.87	
C$_4$H	N=17–16, J=13/2–11/2	161.7966	14.6	0.09±0.02	10.71±0.56	6.60±1.16	0.013	3.52	−
				0.13±0.01	8.32±0.02	0.98±0.07	0.124	3.52	
SO$^+$	J=7/2–5/2	162.1986	14.4	0.05±0.01	12.05±0.70	2.86±0.70	0.016	3.61	✓
				0.13±0.01	9.22±0.70	2.86±0.70	0.043	3.61	
SO$^+$	J=7/2–5/2	162.5741	14.4	0.18±0.01	9.67±0.14	3.82±0.33	0.044	3.68	✓
				0.02±0.011	12.92±0.45	1.78±0.72	0.008	3.68	−
t-HCOOH	7(1,6)–6(1,5)	162.5984	14.4	0.06^c	−	−	−	3.86	−

Table B.5: Gaussian fits of the 1mm lines at IF position.

Specie	Trans	Freq [GHz]	HPBW ["]	Area [K km s^{-1}]	V [km s^{-1}]	Width [km s^{-1}]	T$_{MB}$ [K]	rms [mK]
C$_4$H		199.8124	13.3					
C$_4$H		199.8508	13.3					
HC$_3$N		200.1354	13.3					
			13.3					
H$_2$CCO		200.1676	13.3					
			13.3					
c-C$_3$HD		200.2946	12.3					
H$_2$CCN		201.1444	12.3					
			12.3					
H$_2$CCN		201.1569	12.3					
SO		201.1628	12.3					
HDCO		201.3414	12.3					9.17
t-H$_2$CCO		201.6744	12.3	0.10130^c	–	–	–	9.46
^{34}SO		201.8465	12.3		–	–	–	8.65
H$_2$CCO		202.0143	12.3	7.3336×10$^{-2\,c}$	–	–	–	8.65
S^{17}O		202.2621	12.0	0.49150±0.052	10.608±1.153	21.709±2.480	2.12690×10^{-2}	9.03
CH$_3$CN		202.2932	12.0	0.10424^c	–	–	–	9.00
CH$_3$CN		202.3204	12.0	3.51385×10^{-2}±0.042	9.283±0.546	1.092±1.443	3.02284×10^{-2}	12.3
			12.0	6.32019×10^{-2}±0.038	10.949±0.294	1.038±1.485	5.71744×10^{-2}	12.3
CH$_3$CN		202.3390	11.9	9.99722×10^{-2}±0.028	9.955±0.436	2.924±0.843	3.21167×10^{-2}	13.9
CH$_3$CN		202.3512	11.9	0.13820±0.029	10.404±0.342	3.110±0.665	4.17468×10^{-2}	14.0
CH$_3$CN		202.3528	11.9	0.14929±0.029	12.742±0.325	3.328±0.651	4.21421×10^{-2}	12.9
CH$_3$CN		202.3555	11.9	8.21597×10^{-2}±0.016	10.621±0.111	1.089±0.216	7.08648×10^{-2}	11.7
C$_3$H$^+$		202.3874	11.9	7.69079×10^{-2}±0.024	10.119±0.654	3.837±1.027	1.88300×10^{-2}	10.5
H$_2$CS		202.9241	11.9	9.25075×10^{-2}±0.028	8.511±0.273	2.082±0.742	4.17402×10^{-2}	9.73
			11.9	0.45832±0.028	10.767±0.033	1.506±0.089	0.28593	9.73
H55ζ		203.3077	11.9	0.19641^c	–	–	–	10.2
SO$_2$		203.3916	11.9	1.57480×10^{-2}±0.011	16.157±0.506	1.071±0.948	1.38166×10^{-2}	8.79
			11.9	0.17358±0.014	10.741±0.061	1.566±0.152	0.10413	8.79
H$_2$CCO		203.9400	11.9	0.12186^c	–	–	–	12.0

Table B.5 – *Continued from previous page*

Specie	Trans	Freq	HPBW	IF				
				Area	V	Width	T_{MB}	rms
		[GHz]	["]	[K km s^{-1}]	[km s^{-1}]	[km s^{-1}]	[K]	[mK]
CH_2CO		203.9404	11.9	0.10970^c	–	–	–	12.0
^{33}SO		203.9415	11.9	4.65642×10^{-2c}	–	–	–	12.3
H52ε		203.9730	11.9	0.91954 ± 0.056	8.995 ± 0.935	30.742 ± 2.041	2.81001×10^{-2}	
c-C_3H_2		204.7889	11.9	4.60373×10^{-2c}	–	–	–	9.22
CH_3CCH		205.0454	11.9	3.40556×10^{-2c}	–	–	–	6.18
CH_3CCH		205.0650	11.9	0.12414 ± 0.032	10.311 ± 0.338	2.831 ± 0.947	4.11971×10^{-2}	14.20
			11.9	$1.06472\times10^{-2}\pm0.017$	13.270 ± 0.519	0.700 ± 0.947	1.42883×10^{-2}	14.20
CH_3CCH		205.0765	11.9	0.15478 ± 0.018	10.155 ± 0.162	3.246 ± 0.446	4.47915×10^{-2}	6.43
			11.9	$3.30666\times10^{-2}\pm0.013$	10.247 ± 0.070	0.700 ± 1.725	4.43771×10^{-2}	6.43
CH_3CCH		205.0803	11.9	0.14819 ± 0.018	9.925 ± 0.085	1.656 ± 0.230	8.40629×10^{-2}	6.21
			11.9	$4.14226\times10^{-2}\pm0.017$	11.850 ± 0.258	1.449 ± 0.567	2.68496×10^{-2}	6.21
t-H_2CCO		205.1277	11.9		–	–	–	6.28
CF^+		205.1705	11.8	0.18483 ± 0.016	9.513 ± 0.141	3.393 ± 0.327	5.11793×10^{-2}	6.76
SO_2		205.3006	11.8	$7.43264\times10^{-2}\pm0.017$	9.952 ± 0.477	3.871 ± 0.751	1.80365×10^{-2}	6.57
			11.8	$1.56919\times10^{-2}\pm0.007$	10.645 ± 0.280	0.700 ± 1.893	2.10593×10^{-2}	6.57
U		205.3053	11.8					
H39β		205.7556	11.8	4.6161 ± 0.083	6.918 ± 0.279	31.112 ± 0.625	0.13939	12.0
U		205.7748	11.8					
CH_3OH		205.7913	11.8	0.13522 ± 0.011	10.542 ± 0.088	2.170 ± 0.216	5.85480×10^{-2}	6.03
$H_2^{13}O$		205.9615	11.8					
H_2CS		205.9879	11.8	0.16757 ± 0.021	9.670 ± 0.264	4.038 ± 0.382	3.89890×10^{-2}	6.02
			11.8	$7.23444\times10^{-2}\pm0.015$	10.766 ± 0.066	0.988 ± 0.138	6.87773×10^{-2}	6.02
H_2CS		206.0526	11.8	$6.04949\times10^{-2}\pm0.013$	8.550 ± 0.164	1.779 ± 0.463	3.19522×10^{-2}	5.79
			11.8	$5.35919\times10^{-2}\pm0.011$	10.734 ± 0.126	1.287 ± 0.271	3.91306×10^{-2}	5.79
C_2S		206.0645	11.8					5.83
$H_2^{13}CO$		206.1316	11.8	$4.25784\times10^{-2}\pm0.057$	9.055 ± 1.034	1.835 ± 1.702	2.17975×10^{-2}	6.84
			11.8	$6.51093\times10^{-2}\pm0.059$	10.769 ± 0.610	1.778 ± 0.941	3.44075×10^{-2}	6.84
H_2CS		206.1586	11.8	$3.31747\times10^{-2}\pm0.010$	10.725 ± 0.188	1.303 ± 0.554	2.39163×10^{-2}	5.74
			11.8	$4.49137\times10^{-2}\pm0.010$	17.420 ± 0.159	1.584 ± 0.359	2.66344×10^{-2}	5.74
SO		206.1760	11.8	0.83905 ± 0.010	10.551 ± 0.011	1.977 ± 0.030	0.39862	5.54
U		206.4589	11.8	7.23607×10^{-3c}	–	–	–	6.55
U		206.5269	11.8	1.47119×10^{-2c}	–	–	–	5.97

Continued on next page

Table B.5 – *Continued from previous page*

Specie	Trans	Freq	HPBW	IF				
				Area	V	Width	T_{MB}	rms
		[GHz]	["]	[K km s^{-1}]	[km s^{-1}]	[km s^{-1}]	[K]	[mK]
U		206.5407	11.8	0.20501 ± 0.012	7.720 ± 0.068	2.319 ± 0.167	8.30564×10^{-2}	6.27
U		206.5508	11.8	$3.64560\times10^{-3\,c}$	–	–	–	5.89
U		207.1613	11.8	–	–	–	–	5.38
CCS		207.2620	11.8	$9.23237\times10^{-3\,c}$	–	–	–	6.91
l-C3H		207.2809	11.8	$4.51618\times10^{-2\,c}$	–	–	–	7.10
NS		207.4366	11.8	$4.22932\times10^{-2}\pm0.013$	8.371 ± 0.242	1.521 ± 0.547	2.61139×10^{-2}	6.98
			11.8	$8.95805\times10^{-2}\pm0.015$	11.338 ± 0.213	2.410 ± 0.462	3.49253×10^{-2}	6.98
l-C$_3$H		207.4598	11.8	$7.47616\times10^{-2}\pm0.024$	11.984 ± 1.338	8.074 ± 2.671	8.69918×10^{-3}	7.00
C$_2$H$_3$CN		207.6037	11.8	–	–	–	–	6.92
U		207.8011	11.8					
NS		207.8347	11.8	$5.09982\times10^{-2}\pm0.018$	5.388 ± 0.226	1.421 ± 0.566	3.37180×10^{-2}	10.8
			11.8	$8.05560\times10^{-2}\pm0.032$	10.462 ± 0.844	4.912 ± 2.500	1.54074×10^{-2}	10.8
NS		207.8384	11.8	$4.92862\times10^{-2}\pm0.014$	10.469 ± 0.227	1.580 ± 0.502	2.93026×10^{-2}	8.80
			11.8	$6.00987\times10^{-2}\pm0.023$	15.550 ± 0.676	3.872 ± 1.947	1.45823×10^{-2}	8.80
U		207.8791	11.8	$7.10035\times10^{-2\,c}$	–	–	–	10.8
c-C$_3$H		208.2163	11.8	$6.29759\times10^{-2}\pm0.017$	11.725 ± 0.235	1.674 ± 0.502	3.53515×10^{-2}	10.9
E-CH$_3$CHO		208.2286	11.8	–	–	–	–	10.6
C$_2$H$_5$CN		208.2513	11.8	$2.22750\times10^{-2\,c}$	–	–	–	11.2
CH$_3$COCH$_3$		208.2627	11.8	0.10601^c	–	–	–	10.2
CH$_3$OCH$_3$		208.2783	11.8	$4.26875\times10^{-2\,c}$	–	–	–	9.39
CH3$_C$HO		208.4454	11.8	–	–	–	–	10.8
U		208.5406	11.8	$2.15223\times10^{-2\,c}$	–	–	–	11.70
SO$^+$		208.5906	11.8	0.13085 ± 0.027	10.909 ± 0.277	2.596 ± 0.568	4.73549×10^{-2}	13.6
U		208.6773	11.8	0.85047 ± 0.060	5.224 ± 0.478	13.505 ± 1.067	5.91609×10^{-2}	13.1
SO$_2$		208.6998	11.8	$9.00154\times10^{-2}\pm0.023$	9.904 ± 0.245	1.966 ± 0.568	4.30185×10^{-2}	12.9
U		208.8017	11.8	0.11002^c	–	–	–	10.5
U		208.8631	11.8	$9.39608\times10^{-2}\pm0.021$	7.454 ± 0.268	2.176 ± 0.433	4.05569×10^{-2}	12.2
SO$^+$		208.9660	11.8	0.18432 ± 0.027	11.126 ± 0.205	2.777 ± 0.473	6.23449×10^{-2}	12.6
H$_2$CS		209.2006	11.7	0.48320 ± 0.064	10.895 ± 0.170	2.541 ± 0.358	0.17864	33.2
HC$_3$N		209.2302	11.7	0.24069^c	–	–	–	28.7
c-C$_3$H		209.2507	11.7	–	–	–	–	32.7
c-C$_3$H		209.2687	11.7	0.29192 ± 0.053	22.493 ± 0.204	2.220 ± 0.449	0.12351	28.9

Continued on next page

Table B.5 – *Continued from previous page*

Specie	Trans	Freq	HPBW	Area	V	Width	T_{MB}	rms
						IF		
		[GHz]	["]	[K km s^{-1}]	[km s^{-1}]	[km s^{-1}]	[K]	[mK]
CH_3COCH_3		209.3045	11.7	–	–	–	–	30.3
$^{13}C^{18}O$		209.4191	11.7	–	–	–	–	35.9
U		209.7382	11.7	1.42638×10^{-2c}	–	–	–	39.4
U		209.7795	11.7	0.14596^c	–	–	–	34.2
H31α		210.5001	11.7	19.169±0.144	11.883±0.117	31.391±0.267	0.57369	20.7
H48δ		211.1066	11.6	2.1854±0.134	10.607±1.047	33.642±2.226	6.10281×10^{-2}	19.0
H_2CO		211.2115	11.6	6.6874±0.092	10.146±0.021	3.835±0.046	1.6381	21.5
			11.6	2.8336±0.084	10.761±0.003	1.233±0.021	2.1593	21.5
E-CH_3CHO		212.3847	11.6	–	–	–	–	19.4
$H_2^{13}CO$		213.2936	11.5	2.43658×10^{-2c}	–	–	–	21.2
HCS^+		213.3606	11.5	7.40484×10^{-2}±0.028	8.487±0.260	1.029±0.358	6.75941×10^{-2}	20.2
			11.5	0.34394±0.034	10.649±0.061	1.595±0.176	0.20260	20.2
U		213.9868	11.5					
SO		215.2207	11.4	0.17977±0.041	9.814±0.381	2.932±0.129	5.76075×10^{-2}	17.6
			11.4	1.0745±0.026	10.665±0.024	1.584±0.036	0.63714	17.6
HCOOH		215.4078	11.4	0.25447^c	–	–	–	15.9
^{34}SO		215.8399	11.4	8.53881×10^{-2c}	–	–	–	16.4
DCO^+		216.1126	11.4	0.40022±0.212	11.081±0.326	2.106±0.480	0.17850	17.4
			11.4	0.20544±0.207	10.500±0.250	0.966±0.744	0.19987	17.4
c-C_3H_2		216.2788	11.4	0.22146±0.035	8.908±0.156	2.015±0.378	0.10323	16.6
			11.4	0.11393±0.035	11.653±0.230	1.624±0.518	6.59157×10^{-2}	16.6
C_2D		216.3733	11.4	0.24255^c	–	–	–	17.3
C_2D		216.4303	11.4	0.12825^c	–	–	–	14.5
E-CH_3CHO		216.5819	11.4	–	–	–	–	14.0
^{13}CN		216.7101	11.3	0.42948±0.027	10.408±1.112	1.487±0.106	0.27132×10^{-2}	
			11.3	0.26346±0.055	18.445±0.039	8.354±1.960	2.96282	
^{13}CN		216.8838	11.3	1.21209×10^{-2c}	–	–	–	30.5
SiO		217.1049	11.3	0.16567±0.033	10.230±0.229	2.322±0.500	6.70382×10^{-2}	17.5
DCN		217.2385	11.3	1.730 ± 0.134	10.876 ± 0.048	1.677 ± 0.170	0.969	17.7
			11.3	0.382 ± 0.062	12.215 ± 0.069	0.874 ± 0.197	0.411	17.7
^{13}CN		217.4691	11.3	3.33496×10^{-2}±0.026	8.737±0.912	2.064±1.507	1.51801×10^{-2}	15.7
			11.3	0.18927±0.037	13.753±0.385	3.729±0.748	4.76783×10^{-2}	15.7

Table B.5 – *Continued from previous page*

Specie	Trans	Freq	HPBW	IF				
				Area	V	Width	T_{MB}	rms
		[GHz]	["]	[K km s^{-1}]	[km s^{-1}]	[km s^{-1}]	[K]	[mK]
c-C$_3$H$_2$		217.8221	11.3	1.0751±0.034	10.234±0.065	3.982±0.132	0.25366	14.2
U			11.3					
c-C$_3$H$_2$		217.9400	11.3	0.16519±0.040	8.494±0.134	1.415±0.219	0.10966	14.5
U			11.3	0.39553±0.052	10.982±0.192	3.044±0.442	0.12206	14.5
H$_2$CO		218.2222	11.3	5.8893±0.070	10.605±0.014	2.456±0.035	2.2523	35.0
HC$_3$N		218.3244	11.3	0.53697±0.081	10.428±0.231	2.943±0.454	0.17142	39.9
CH$_3$OH		218.4401	11.2	0.31857±0.060	10.552±0.128	1.460±0.361	0.20496	36.6
H$_2$CO		218.4756	11.2	1.4720±0.083	10.639±0.061	2.297±0.158	0.60202	41.9
H$_2$CO		218.7601	11.2	1.5209±0.076	10.579±0.056	2.407±0.151	0.59356	36.9
OCS		218.9034	11.2	0.18915^c	–	–	–	38.4
C^{18}O		219.5604	11.2	12.893±0.095	10.384±0.008	2.309±0.022	5.2453	47.2
H$_2$^{13}CO		219.9085	11.2	3.59329×10^{-2}^{c}	–	–	–	40.1
SO		219.9494	11.2	3.0597±0.063	10.462±0.022	2.195±0.053	1.3094	34.2
^{13}CO		220.3987	11.2	78.347±0.189	9.785±0.005	4.488±0.013	16.400	68.7
			11.2	4.6757±0.204	18.233±0.132	5.639±0.260	0.77890	68.7
U		221.8260	11.2	0.42447^c	–	–	–	36.4
SO$_2$		221.9652	11.2	0.47915±0.124	0.752±1.145	8.063±2.376	5.58295×10^{-2}	34.7
			11.2	0.47677±0.073	10.737±0.181	2.504±0.442	0.17890	34.7
H38β		222.0118	11.2	0.26254^c	–	–	–	35.6
C^{17}O		224.7153	11.2	3.7425±0.114	8.536±0.059	3.839±0.130	0.91570	16.7
H$_2$CO		225.6978	11.2					
CN		226.2874	11.2	0.23429±0.031	10.848±0.162	2.269±0.310	9.70022×10^{-2}	17.2
CN		226.2989	11.2	0.24960±0.040	9.745±0.272	3.295±0.569	7.11683×10^{-2}	17.6
CN		226.3030	11.2	0.12221±0.033	10.546±0.202	1.655±0.607	6.93725×10^{-2}	18.7
CN		226.3145	11.2	8.16645×10^{-2}±0.038	8.271±0.348	1.508±0.539	5.08707×10^{-2}	18.3
			11.2	0.35257±0.048	10.730±0.139	2.261±0.375	0.14652	18.3
CN		226.3325	11.2	0.15943±0.030	10.915±0.181	1.878±0.368	7.97386×10^{-2}	18.2
CN		226.3419	11.2	0.12107±0.025	10.706±0.119	1.130±0.243	0.10069	17.7
CN		226.3599	11.2	0.92011±0.048	10.643±0.078	3.049±0.180	0.28354	21.9
A-CH$_3$CHO		226.5927	11.2	4.95772×10^{-2}^{c}	–	–	–	19.9
CN		226.6166	11.2	0.16131^c	–	–	–	20.8
CN		226.6322	11.2	1.3423±0.047	10.684±0.048	2.842±0.119	0.44363	21.6

Table B.5 – *Continued from previous page*

Specie	Trans	Freq	HPBW	IF				
				Area	V	Width	T_{MB}	rms
		[GHz]	["]	[K km s^{-1}]	[km s^{-1}]	[km s^{-1}]	[K]	[mK]
CN		226.6596	11.2	3.7386±0.037	10.579±0.013	2.817±0.035	1.2467	16.8
CN		226.6637	11.2	1.4167±0.048	10.715±0.052	3.385±0.160	0.39320	17.7
CN		226.6793	11.2	1.5978±0.048	10.640±0.034	2.624±0.100	0.57197	20.3
CN		226.8742	11.2	7.5315±0.057	9.799±0.015	4.040±0.037	1.7512	22.2
CN		226.8874	11.2	0.97143±0.049	10.740±0.073	2.957±0.178	0.30865	22.2
CN		226.8921	11.2	1.0744±0.051	10.627±0.066	2.936±0.174	0.34379	25.2
U		226.9271	11.2	0.15543±0.025	9.817±0.104	1.265±0.254	0.11545	17.6
U		226.9415	11.2	0.14968±0.033	10.208±0.322	2.778±0.617	5.06173×10^{-2}	16.7
c-C$_3$H$_2$		227.1691	11.2	0.30870±0.040	9.814±0.189	2.912±0.423	9.95756	18.9
HC$_3$N		227.4189	11.2	0.25230±0.034	11.047±0.161	2.238±0.317	0.10590×10^{-2}	18.7
U		228.8861	10.8	0.36978±0.091	10.462±0.393	3.476±1.148	9.99318×10^{-2}	35.7
DNC		228.9105	10.7	0.086 ± 0.013	10.634 ± 0.073	0.963 ± 0.169	0.085	25.7
			10.7	0.413 ± 0.016	12.106 ± 0.016	0.889 ± 0.044	0.437	25.7
CH$_3$OH		229.7588	10.7	0.73175^c	–	–	–	46.2
CO		230.5380	10.6	85.763±0.154	5.863±0.002	4.618±0.008	17.448	33.3
			10.6	47.843±0.269	8.848±0.003	2.904±0.012	15.478	33.3
			10.6	76.580±0.575	12.979±0.005	4.081±0.018	17.630	33.3
			10.6	28.205±0.502	17.226±0.069	7.865±0.073	3.3691	33.3
OCS		231.0610	10.6	$2.07297\times10^{-2\,c}$	–	–	–	21.0
^{13}CS		231.2207	10.6	0.39738±0.083	9.594±0.573	4.573±0.708	8.16441×10^{-2}	23.4
			10.6	0.26622±0.055	10.731±0.016	0.992±0.136	0.25208	23.4
A-CH$_3$CHO		231.4675	10.6	–	–	–	–	21.4
U		231.5218	10.6	0.11104^c	–	–	–	22.8
H30α		231.8958	10.6	17.598±0.170	7.459±0.153	31.035±0.320	0.53271	20.3
U		232.1936	10.6	0.30902^c	–	–	–	22.1
C^{13}CC-H		232.7886	10.5	0.29431±0.048	7.781±0.187	2.399±0.482	0.11524	19.1
HCCN		233.1118	10.5	–	–	–	–	22.0
U		233.4785	10.5	0.10334^c	–	–	–	22.5
H$_2$C^{33}S		234.6790	10.5	0.12262^c	–	–	–	23.5
SO$_2$		235.1517	10.4	0.26501±0.049	11.302±0.330	3.501±0.756	7.11188×10^{-2}	21.0
CO$^+$		236.0626	10.4	0.37699±0.041	10.361±0.244	4.333±0.493	8.17421×10^{-2}	16.5
t-HOCO		236.0812	10.4	0.25460^c	–	–	–	15.1

Table B.5 – *Continued from previous page*

Specie	Trans	Freq	HPBW	IF				
				Area	V	Width	T_{MB}	rms
		[GHz]	["]	[K km s^{-1}]	[km s^{-1}]	[km s^{-1}]	[K]	[mK]
SO$_2$		236.2167	10.4	$2.53933\times10^{-2\,c}$	–	–	–	14.0
U		236.4131	10.4	7.23427 ± 0.016	11.083 ± 0.059	0.700 ± 0.269	9.70878×10^{-2}	15.5
HC$_3$N		236.5144	10.4	0.19226^{c}	–	–	–	15.0
H$_2$CS		236.7270	10.3	$9.21783\times10^{-2}\pm0.022$	8.385 ± 0.185	1.427 ± 0.354	6.06692×10^{-2}	13.4
			10.3	0.34513 ± 0.026	10.744 ± 0.049	1.555 ± 0.160	0.20849	13.5
SO$_2$		237.0689	10.3	$2.42890\times10^{-2\,c}$	–	–	–	15.7
CH$_3$CCH		239.2110	10.2					
CH$_3$CCH		239.2340	10.2					
CH$_3$CCH		239.2477	10.2					
CH$_3$CCH		239.2523	10.2					
CH$_3$OH		239.7463	10.2					
H$_2$CS		240.2669	10.2					
H$_2$CS		240.5482	10.2					
C^{34}S		241.0169	10.2					
SO$_2$		241.6150	10.2					
CH$_3$OH		241.7002	10.2					
CH$_3$OH		241.7672	10.2					
CH$_3$OH		241.7914	10.2					
CH$_3$OH		241.8423	10.2					
CH$_3$OH		241.8791	10.2					
CH$_3$OH		241.9042	10.2					
U		242.2751	10.2					
C^{33}S		242.9136	10.1	0.35682^{c}	–	–	–	48.1
CH$_3$OH		243.9158	10.1	0.44689 ± 0.086	10.910 ± 0.167	1.784 ± 0.470	0.23530	46.9
H$_2$CS		244.0485	10.1	0.63311 ± 0.068	6.352 ± 0.062	1.056 ± 0.135	0.56312	50.5
			10.1	0.52442 ± 0.103	10.553 ± 0.184	2.121 ± 0.554	0.23229	50.5
c-C$_3$H$_2$		244.2221	10.0	$6.00926\times10^{-2\,c}$	–	–	–	49.5
SO$_2$		244.2542	10.0					48.7
U		244.6181	10.0					53.5
CS		244.9356	10.0	5.5622 ± 0.187	10.175 ± 0.047	3.755 ± 0.098	1.3917	56.7
			10.0	7.5030 ± 0.152	10.643 ± 0.001	1.610 ± 0.008	4.3779	56.7
U		245.2533	10.0	0.13970^{c}	–	–	–	71.4

Table B.5 – *Continued from previous page*

Specie	Trans	Freq	HPBW	IF				
				Area	V	Width	T_{MB}	rms
		[GHz]	["]	[K km s^{-1}]	[km s^{-1}]	[km s^{-1}]	[K]	[mK]
HC$_5$N		245.2749	10.0					70.7
SO$_2$		245.5634	10.0					51.8
HC$_3$N		245.6063	10.0	0.27769^c	–	–	–	54.0
HDCO		246.9246	9.9	0.16229^c	–	–	–	50.4
c-C$_3$H$_2$		249.0544	9.9	0.22514^c	–	–	–	57.3
A-CH$_3$CHO		250.7956	9.8	6.34859×10^{-2c}	–	–	–	13.8
A-CH$_3$CHO		250.8147	9.8	5.22814×10^{-2}±0.020	7.378±0.315	1.535±0.493	3.20066×10^{-2}	12.5
			9.8	7.14505×10^{-2}±0.020	9.733±0.163	1.313±0.623	5.11326×10^{-2}	12.5
SO$_2$		251.1997	9.8	0.27019±0.042	10.929±0.248	3.812±0.824	6.65892×10^{-2}	14.7
SO$_2$		251.2106	9.8	0.10527±0.028	10.496±0.285	1.904±0.531	5.19331×10^{-2}	16.8
c-C$_3$H$_2$		251.3144	9.8	0.82963±0.033	10.054±0.077	3.768±0.173	0.20682	13.8
c-C$_3$H$_2$		251.5087	9.8	0.10732±0.040	9.741±0.481	2.788±1.274	3.61598×10^{-2}	18.0
CH$_3$OH		251.5173	9.8	5.86264×10^{-2}±0.020	10.942±0.103	0.700±0.274	7.86797×10^{-2}	18.3
c-C$_3$H$_2$		251.5273	9.8	0.17663±0.042	8.570±0.226	2.429±0.763	6.83102×10^{-2}	13.7
			9.8	0.16015±0.032	11.313±0.166	1.689±0.292	8.90792×10^{-2}	13.7
CH$_3$OH		251.6411	9.7	0.12937±0.016	10.030±0.084	1.309±0.152	9.28241×10^{-2}	11.5
CH$_3$OH		251.7385	9.7	9.72414×10^{-2}±0.014	10.996±0.059	0.874±0.341	0.10448	11.4
CH$_3$OH		251.8120	9.7	8.90894×10^{-2}±0.075	10.512±0.680	1.132±0.341	7.39584×10^{-2}	57.0
			9.8	7.49010×10^{-2}±0.084	11.954±2.469	2.845±0.141	2.47332×10^{-2}	57.0
SO		251.8258	9.7	0.99376±0.032	10.653±0.028	1.859±0.077	0.50210	17.8
CH$_3$OH		251.8666	9.7	0.13664±0.038	10.939±0.164	1.284±0.479	9.99694×10^{-2}	24.6
CH$_3$OH		251.8909	9.7	0.15838±0.036	10.810±0.158	1.444±0.402	0.10306	23.5
CH$_3$OH		251.8957	9.7	0.15706±0.045	10.676±0.234	1.798±0.703	8.20398×10^{-2}	24.4
CH$_3$OH		251.9005	9.7	0.22994±0.063	10.875±0.222	2.288±1.042	9.44120×10^{-2}	23.2
CH$_3$OH		251.9058	9.7	9.65266×10^{-2}±0.035	10.668±0.251	1.342±0.537	6.75934×10^{-2}	24.7
CH$_3$OH		251.9170	9.7	6.43568×10^{-2}±0.030	10.896±0.303	1.200±0.598	5.03976×10^{-2}	22.9
CH$_3$OH		251.9236	9.7	0.11315±0.029	10.710±0.163	1.205±0.313	8.82355×10^{-2}	21.3
CH$_3$OH		251.9847	9.7	9.24515×10^{-2}±0.026	10.618±0.190	1.391±0.464	6.24280×10^{-2}	17.0
CH$_3$OH		252.0904	9.7	6.27870×10^{-2}±0.016	10.895±0.161	0.905±0.425	6.51612×10^{-2}	12.2
^{13}CCH		252.4241	9.7	9.03882×10^{-3c}	–	–	–	14.1
^{13}CCH		252.4493	9.7	5.60766×10^{-2c}	–	–	–	18.0
^{13}CCH		252.4579	9.7					11.8

Continued on next page

Table B.5 – *Continued from previous page*

Specie	Trans	Freq	HPBW	IF				
				Area	V	Width	T_{MB}	rms
		[GHz]	["]	[K km s^{-1}]	[km s^{-1}]	[km s^{-1}]	[K]	[mK]
SO^{17}O		252.4981	9.7					13.0
U		252.5599	9.7					13.4
			9.7	0.24248±0.026	10.559±0.127	2.410±0.302	9.45155×10^{-2}	13.0
c-C$_3$H		252.8816	9.7	1.38154×10$^{-2\,c}$	–	–	–	13.0
NS		253.5705	9.7	0.11303±0.028	10.551±0.175	1.522±0.507	6.97556×10^{-2}	16.2
CH$_3$OH		254.0153	9.7	0.15600±0.054	11.567±1.082	6.586±1.762	2.22523×10^{-2}	
			9.7	7.23787×10^{-2}±0.029	10.497±0.151	1.147±0.408	5.92714×10^{-2}	
C$_2$H$_5$^{13}CN		254.1551	9.7	3.29765×10$^{-2\,c}$	–	–	–	16.7
H$_2$CCCHCN		254.1628	9.7	6.53045×10$^{-2\,c}$	–	–	–	16.9
CH$_2$NH		254.6848	9.6	7.54547×10$^{-2\,c}$	–	–	–	17.3
HC$_3$N		254.6995	9.6	0.16484±0.049	11.954±0.629	4.644±0.320	3.33444×10^{-2}	15.7
			9.6	5.19571×10^{-2}±0.022	11.004±0.089	0.700±0.587	6.9729×10^{-2}	15.7
SO$^+$		254.9764	9.6	0.15259±0.031	8.692±0.200	2.037±0.615	7.03653×10^{-2}	14.2
SO$^+$		254.9790	9.6	0.12892±0.024	11.864±0.147	1.559±0.415	7.77018×10^{-2}	13.6
c-C$_3$H$_2$		254.9877	9.6	8.26943×10$^{-2\,c}$	–	–	–	15.3
SO$^+$		255.3515	9.6	0.10907±0.019	8.741±0.106	1.251±0.272	8.19303×10^{-2}	13.2
SO$^+$		255.3762	9.6	8.10256×10$^{-2\,c}$	–	–	–	14.1
A-CH$_3$CHO		255.3848	9.6					14.4
HC^{18}O$^+$		255.4794	9.6	0.20788±0.019	10.609±0.070	1.546±0.173	0.12635	11.6
C^{13}CH		255.7473	9.6	6.47559×10$^{-2\,c}$	–	–	–	10.6
C^{13}CH		255.7588	9.6		–	–	–	11.6
C^{13}CH		255.8220	9.6					11.8
C^{13}CH		255.8283	9.6					12.0
HCS$^+$		256.0271	9.6	9.47984×10^{-2}±0.043	8.954±0.299	1.604±0.780	5.55314×10^{-2}	12.3
			9.6	0.27504±0.041	10.791±0.075	1.295±0.177	0.19958	12.3
U		256.2941	9.6					
H29α		256.3020	9.6	16.932±0.116	13.723±0.106	31.813±0.245	0.50002	16.7
CH$_3$CCH		256.3184	9.6					
CH$_3$CCH		256.3317	9.6	0.14578±0.682	10.497±3.328	2.336±1.001	5.86208×10^{-2}	20.0
CH$_3$CCH		256.3338	9.6					
CH$_3$CCH		256.3366	9.6	0.10660±0.252	10.517±1.491	1.162±9.645	8.61584×10^{-2}	20.0
HDCO		256.5854	9.6					11.9

Continued on next page

Table B.5 – *Continued from previous page*

Specie	Trans	Freq	HPBW	IF					
					Area	V	Width	T_{MB}	rms
		[GHz]	["]		[K km s^{-1}]	[km s^{-1}]	[km s^{-1}]	[K]	[mK]
^{34}SO		256.8778	9.6		$9.69075\times10^{-2}\pm0.035$	5.896 ± 0.901	4.660 ± 0.719	1.95361×10^{-2}	13.4
			9.6		$8.42035\times10^{-2}\pm0.020$	10.577 ± 0.154	1.332 ± 0.320	5.93956×10^{-2}	13.4
SO$_2$		257.0981	9.6		$9.60657\times10^{-3\,c}$	–	–	–	13.7
H41γ		257.6355	9.5		2.9962 ± 0.083	14.124 ± 0.488	35.269 ± 1.109	7.98094×10^{-2}	11.2
HDCO		257.7501	9.5		$2.34692\times10^{-2\,c}$	–	–	–	11.0
U		257.9014	9.5		$6.86229\times10^{-2}\pm0.015$	10.094 ± 0.132	1.125 ± 0.236	5.72877×10^{-2}	11.4
HC^{15}N		258.1570	9.5		0.66106 ± 0.021	10.665 ± 0.022	1.427 ± 0.052	0.43508	13.5
C2H3CHO		258.2457	9.5		0.20512^c	–	–	–	11.1
SO		258.2558	9.5		0.19108 ± 0.031	10.792 ± 0.081	0.904 ± 0.137	0.19847	11.9
			9.5		0.84158 ± 0.040	10.609 ± 0.039	2.167 ± 0.056	0.36485	11.9
SO$_2$		258.9422	9.5		0.14575^c	–	–	–	19.32
H^{13}CN		259.0118	9.5		0.47222 ± 0.048	10.807 ± 0.287	4.943 ± 0.806	8.97438×10^{-2}	17.0
			9.5		0.81403 ± 0.027	10.767 ± 0.029	1.634 ± 0.066	0.46802	17.0
H36β		260.0328	9.5		4.9144 ± 0.185	14.883 ± 0.594	31.982 ± 1.375	0.14436	26.2
H^{13}CO$^+$		260.2553	9.4		0.26650 ± 0.068	10.476 ± 0.046	0.700 ± 0.042	0.35766	25.7
			9.4		0.98239 ± 0.072	10.556 ± 0.060	2.690 ± 0.277	0.34307	25.7
HN^{13}C		261.2635	9.4		0.28637 ± 0.056	11.999 ± 0.321	2.969 ± 0.590	9.06113×10^{-2}	27.2
CH$_3$CHO		261.8381	9.4		0.11199^c	–	–	–	38.40
SO		261.8437	9.4		1.0190 ± 0.082	10.570 ± 0.090	2.488 ± 0.273	0.38474	37.5
C$_2$H		261.9792	9.4		–	–	–	–	47.0
C$_2$H		262.0043	9.4		1.6764 ± 0.156	8.180 ± 0.056	1.708 ± 0.166	0.92192	38.1
			9.4		4.7596 ± 0.146	9.668 ± 0.013	4.690 ± 0.171	0.95342	38.1
C$_2$H		262.0065	9.4		2.3323 ± 0.131	8.802 ± 0.061	2.235 ± 0.148	0.98017	41.0
C$_2$H		262.0650	9.4		2.1614 ± 0.349	10.441 ± 0.089	3.481 ± 0.165	0.58325	33.6
			9.4		2.1097 ± 0.135	8.244 ± 0.053	1.975 ± 0.138	1.0035	33.6
C$_2$H		262.0675	9.4		2.1176 ± 0.220	9.371 ± 0.186	3.516 ± 0.390	0.56575	34.0
C$_2$H		262.0789	9.4		0.60314^c	–	–	–	34.00
C$_2$H		262.2086	9.4		0.36113 ± 0.059	9.730 ± 0.234	2.922 ± 0.534	0.11612	27.50
C$_2$H		262.2370	9.4		–	–	–	–	27.70
C$_2$H		262.2509	9.4		0.20484^c	–	–	–	27.00
HCOCH$_2$OH		265.5691	9.3		0.10585^c	–	–	–	37.00
c-C$_3$H$_2$		265.7595	9.3		0.15638 ± 0.056	9.060 ± 0.281	1.468 ± 0.573	0.10010	26.10

Table B.5 – *Continued from previous page*

Specie	Trans	Freq	HPBW	IF				
				Area	V	Width	T_{MB}	rms
		[GHz]	["]	[K km s^{-1}]	[km s^{-1}]	[km s^{-1}]	[K]	[mK]
			9.3	0.12277±0.060	11.370±0.475	1.784±0.977	6.46593×10^{-2}	26.10
HCN		265.8864	9.2	5.8089±0.772	9.169±0.700	3.826±0.700	1.4265	33.00
U			9.2	9.0080±0.772	11.255±0.700	3.214±0.700	2.6333	33.00
H^{15}NC		266.5878	9.2	2.08410×10^{-2} c	–	–	–	12.1
^{33}SO		266.5892	9.2	6.05656×10^{-2} c	–	–	–	12.1
CH$_3$OH		266.8381	9.2	0.44504±0.022	10.802±0.041	1.788±0.113	0.23383	12.5
HCO$^+$		267.5576	9.2	34.987±0.309	10.051±0.012	4.276±0.021	7.6862	41.8
			9.2	9.1927±0.295	10.725±0.012	1.662±0.030	5.1971	41.8
HDCO		268.2920	9.1	0.10642 c	–	–	–	21.6
H$_2$CS		270.5219	9.1	0.11919±0.043	8.224±0.475	2.410±0.138	4.64604×10^{-2}	18.1
			9.1	0.35645±0.038	10.766±0.058	1.303±0.138	0.25706	8.1

Table B.6: Gaussian fits of the 1mm lines at MP2 position.

Specie	Trans	Freq	HPBW	MP2					OTF
				Area	V	Width	T_{MB}	rms	
		[GHz]	["]	[K km s^{-1}]	[km s^{-1}]	[km s^{-1}]	[K]	[mK]	
C_4H		199.8124	13.3	$7.59152\times10^{-2}\pm0.010$	8.471 ± 0.074	1.229 ± 0.189	5.80285×10^{-2}	6.50	
C_4H		199.8508	13.3	$9.02931\times10^{-2}\pm0.010$	8.246 ± 0.093	1.535 ± 0.218	5.52698×10^{-2}	6.50	
HC_3N		200.1354	13.3	0.19456 ± 0.009	8.838 ± 0.072	2.924 ± 0.128	6.25168×10^{-2}	3.30	
			13.3	0.35270 ± 0.007	8.292 ± 0.003	0.700 ± 0.174	0.47334	3.30	
H_2CCO		200.1676	13.3	$1.53874\times10^{-2}\pm0.013$	8.704 ± 0.356	0.742 ± 1.945	1.94733×10^{-2}	4.30	
			13.3	$6.56527\times10^{-2}\pm0.015$	9.598 ± 0.458	3.495 ± 1.190	1.76492×10^{-2}	4.30	
c-C_3HD		200.2946	12.3	$3.86868\times10^{-2}\pm0.011$	9.067 ± 0.529	3.599 ± 1.377	1.00979×10^{-2}	4.30	
H_2CCN		201.1444	12.3	$2.70349\times10^{-2}\pm0.016$	5.482 ± 1.560	4.636 ± 3.061	5.47849×10^{-3}	4.50	
			12.3	$1.36604\times10^{-2}\pm0.013$	7.769 ± 0.263	1.252 ± 0.981	1.02503×10^{-2}	4.50	
H_2CCN		201.1569	12.3	$4.97611\times10^{-2}\pm0.008$	9.269 ± 0.245	3.008 ± 0.511	1.55400×10^{-2}	3.50	
SO		201.1628	12.3	$2.22127\times10^{-2}\pm0.008$	10.598 ± 0.328	1.986 ± 0.893	1.05080×10^{-2}	4.23	
HDCO		201.3414	12.3	0.25270 ± 0.006	8.403 ± 0.013	1.200 ± 0.034	0.19784	3.93	
t-H_2CCO		201.6744	12.3	$1.93424\times10^{-2}\pm0.006$	10.991 ± 0.247	1.613 ± 0.757	1.12654×10^{-2}	3.00	
^{34}SO		201.8465	12.3	$7.75427\times10^{-2}\pm0.007$	9.792 ± 0.126	2.904 ± 0.362	2.50811×10^{-2}	3.20	
H_2CCO		202.0143	12.3	$3.18435\times10^{-2}\pm0.006$	8.757 ± 0.286	2.435 ± 0.506	1.22864×10^{-2}	3.40	
$S^{17}O$		202.2621	12.0	$1.34413\times10^{-2\,c}$	–	–	–	3.13	
CH_3CN		202.2932	12.0	$3.65326\times10^{-2}\pm0.007$	7.799 ± 0.317	3.240 ± 0.723	1.05922×10^{-2}	3.06	
CH_3CN		202.3204	12.0	$1.44166\times10^{-2}\pm0.010$	8.318 ± 0.233	0.700 ± 0.723	1.93421×10^{-2}	6.73	–
			12.0	$6.72692\times10^{-2}\pm0.022$	9.633 ± 0.978	5.835 ± 2.539	1.08298×10^{-2}	6.73	–
CH_3CN		202.3390	11.9	$3.69161\times10^{-2}\pm0.018$	6.957 ± 0.320	1.550 ± 1.069	2.23735×10^{-2}	9.02	–
			11.9	$1.76779\times10^{-2}\pm0.018$	9.648 ± 1.060	2.261 ± 2.756	7.34589×10^{-3}	9.02	–
CH_3CN		202.3512	11.9	$5.05314\times10^{-2}\pm\,0.005$	9.752 ± 0.700	3.658 ± 0.700	1.29767×10^{-2}	2.82	–
CH_3CN		202.3528	11.9	$9.55399\times10^{-2}\pm0.008$	10.332 ± 0.090	2.494 ± 0.355	3.59887×10^{-2}	2.82	–
CH_3CN		202.3555	11.9	$4.85171\times10^{-2}\pm0.004$	8.285 ± 0.028	0.775 ± 0.162	5.88327×10^{-2}	2.96	–
			11.9	$8.29204\times10^{-2}\pm0.010$	8.970 ± 0.212	4.688 ± 0.925	1.66179×10^{-2}	2.96	–
C_3H^+		202.3874	11.9	$3.85527\times10^{-2}\pm0.007$	9.955 ± 0.276	3.094 ± 0.770	1.17048×10^{-2}	3.18	–
H_2CS		202.9241	11.9	0.19988 ± 0.008	8.276 ± 0.006	0.700 ± 0.073	0.26824	3.73	✓
			11.9	0.36630 ± 0.013	9.444 ± 0.052	2.949 ± 0.096	0.11670	3.73	✓
$H55\zeta$		203.3077	11.9	$5.67024\times10^{-2\,c}$	–	–	–	3.86	–
SO_2		203.3916	11.9	$8.48641\times10^{-2}\pm0.029$	8.791 ± 0.315	1.955 ± 0.512	4.07889×10^{-2}	4.53	✓

Continued on next page

Table B.6 – *Continued from previous page*

Specie	Trans	Freq	HPBW	MP2					OTF
				Area	V	Width	T_{MB}	rms	
		[GHz]	["]	[K km s^{-1}]	[km s^{-1}]	[km s^{-1}]	[K]	[mK]	
			11.9	$8.15514\times10^{-2}\pm0.029$	10.348 ± 0.129	1.301 ± 0.244	5.88918×10^{-2}	4.53	–
H_2CCO		203.9400	11.9	0.15237 ± 0.020	11.093 ± 0.189	3.466 ± 0.551	4.12951×10^{-2}	6.19	✓
			11.9	$4.42494\times10^{-2}\pm0.012$	7.947 ± 0.117	1.033 ± 0.209	4.02317×10^{-2}	6.19	–
CH_2CO		203.9404	11.9						–
^{33}SO		203.9415	11.9	0.15652 ± 0.021	13.406 ± 0.222	3.468 ± 0.540	4.24002×10^{-2}	6.33	–
			11.9	$4.85787\times10^{-2}\pm0.016$	10.240 ± 0.116	1.140 ± 0.410	4.00313×10^{-2}	6.33	–
$H52\varepsilon$		203.9730	11.9	$6.44194\times10^{-2\,c}$	–	–	–	7.26	–
c-C_3H_2		204.7889	11.9	0.14502 ± 0.005	8.292 ± 0.018	1.117 ± 0.061	0.12199	3.63	–
CH_3CCH		205.0454	11.9	0.12674 ± 0.060	8.142 ± 0.241	1.186 ± 0.800	0.10035	10.0	✓
CH_3CCH		205.0650	11.9	0.13552 ± 0.008	8.249 ± 0.010	0.755 ± 0.072	0.16871	4.10	✓
			11.9	$8.19753\times10^{-2}\pm0.012$	9.062 ± 0.194	2.796 ± 0.319	2.75424×10^{-2}	4.10	–
CH_3CCH		205.0765	11.9	0.31153 ± 0.007	7.907 ± 0.011	1.065 ± 0.018	0.27484	3.97	✓
			11.9	$7.59896\times10^{-2}\pm0.009$	9.495 ± 0.013	1.931 ± 0.269	3.69691×10^{-2}	3.97	–
CH_3CCH		205.0803	11.9	0.33582 ± 0.028	7.768 ± 0.025	0.983 ± 0.060	0.32082	4.05	✓
			11.9	0.12191 ± 0.032	9.412 ± 0.251	2.161 ± 0.512	5.29968×10^{-2}	4.05	–
t-H_2CCO		205.1277	11.9	$3.71688\times10^{-2\,c}$	–	–	–	5.11	–
CF^+		205.1705	11.8	0.13179 ± 0.029	8.281 ± 0.108	2.448 ± 0.326	5.05801×10^{-2}	4.25	✓
			11.8	0.25459 ± 0.034	11.399 ± 0.436	6.189 ± 0.564	3.86421×10^{-2}	4.25	–
SO_2		205.3006	11.8	$5.26199\times10^{-2}\pm0.008$	9.967 ± 0.139	1.959 ± 0.341	2.52350×10^{-2}	4.30	–
			11.8	$1.59636\times10^{-2}\pm0.006$	13.950 ± 0.350	1.629 ± 0.623	9.20888×10^{-2}	4.30	–
U		205.3053	11.8	$2.01608\times10^{-2}\pm0.008$	7.786 ± 0.429	1.719 ± 0.768	1.10206×10^{-2}	4.81	–
			11.8	$2.51063\times10^{-2}\pm0.008$	9.776 ± 0.174	1.118 ± 0.339	2.10945×10^{-2}	4.81	–
$H39\beta$		205.7556	11.8	$3.64378\times10^{-2\,c}$	–	–	–	3.52	–
U		205.7748	11.8	$2.67696\times10^{-2}\pm0.016$	6.507 ± 0.544	1.888 ± 0.151	1.33219×10^{-2}	7.56	–
			11.8	$3.45942\times10^{-2}\pm0.017$	9.546 ± 0.648	2.532 ± 0.404	1.28376×10^{-2}	7.56	–
			11.8	$1.55407\times10^{-2}\pm0.012$	14.984 ± 0.830	2.008 ± 0.647	7.27022×10^{-3}	7.56	–
CH_3OH		205.7913	11.8	$3.86311\times10^{-2}\pm0.012$	8.263 ± 0.032	0.701 ± 0.429	5.17724×10^{-2}	3.99	✓
			11.8	0.11165 ± 0.015	9.920 ± 0.133	2.499 ± 0.429	4.19646×10^{-2}	3.99	–
$H_2^{13}O$		205.9615	11.8	$1.45925\times10^{-2}\pm0.010$	12.188 ± 0.526	1.660 ± 1.240	8.25645×10^{-2}	3.43	–
			11.8	$3.49573\times10^{-2}\pm0.010$	10.247 ± 0.160	1.410 ± 0.376	2.32940×10^{-2}	3.43	–
H_2CS		205.9879	11.8	0.17756 ± 0.015	8.405 ± 0.051	1.328 ± 0.129	0.12557	4.28	✓

Continued on next page

Table B.6 – *Continued from previous page*

Specie	Trans	Freq	HPBW	MP2					OTF
				Area	V	Width	T_{MB}	rms	
		[GHz]	["]	[K km s^{-1}]	[km s^{-1}]	[km s^{-1}]	[K]	[mK]	
			11.8	$8.77229\times10^{-2}\pm0.015$	10.179 ± 0.104	1.324 ± 0.250	6.22378×10^{-2}	4.28	–
H_2CS		206.0526	11.8	$3.88242\times10^{-2}\pm0.011$	6.135 ± 0.117	1.084 ± 0.441	3.36508×10^{-2}	5.85	–
			11.8	$5.16646\times10^{-2}\pm0.016$	8.194 ± 0.177	1.513 ± 0.584	3.20721×10^{-2}	5.85	–
			11.8	$2.30363\times10^{-2}\pm0.015$	10.205 ± 0.267	1.329 ± 1.219	1.62892×10^{-2}	5.85	–
C_2S		206.0645	11.8	$6.49339\times10^{-2}\pm 0.007$	9.207 ± 0.067	1.050 ± 0.122	5.81214×10^{-2}	5.71	–
$H_2^{13}CO$		206.1316	11.8	$6.17678\times10^{-2}\pm0.017$	8.261 ± 0.038	0.703 ± 0.679	8.25335×10^{-2}	9.20	–
			11.8	0.14236 ± 0.028	9.431 ± 0.297	2.935 ± 0.597	4.55700×10^{-2}	9.20	–
H_2CS		206.1586	11.8	$2.41754\times10^{-2}\pm0.004$	8.309 ± 0.040	0.700 ± 0.534	3.24446×10^{-2}	3.11	–
			11.8	$2.65608\times10^{-2}\pm0.007$	9.949 ± 0.199	1.776 ± 0.534	1.40491×10^{-2}	3.11	–
SO		206.1760	11.8	1.0174 ± 0.010	9.733 ± 0.012	2.463 ± 0.030	0.38802	5.15	✓
U		206.4589	11.8	$3.11297\times10^{-2\,c}$	–	–	–	3.11	–
U		206.5269	11.8	$1.28127\times10^{-2}\pm0.007$	6.446 ± 0.506	1.811 ± 0.891	6.64683×10^{-3}	4.00	–
			11.8	$3.45971\times10^{-2}\pm0.009$	10.521 ± 0.365	3.002 ± 1.013	1.08273×10^{-2}	4.00	–
U		206.5407	11.8	$2.19322\times10^{-2}\pm0.011$	8.225 ± 0.864	2.769 ± 1.152	7.44001×10^{-3}	3.65	–
			11.8	$1.52934\times10^{-2}\pm0.009$	10.177 ± 0.260	1.047 ± 0.457	1.37280×10^{-2}	3.65	–
U		206.5508	11.8	$2.35650\times10^{-2}\pm0.014$	9.851 ± 0.348	1.771 ± 0.797	1.24986×10^{-2}	3.71	✓
			11.8	$1.94954\times10^{-2}\pm0.014$	12.501 ± 1.217	3.040 ± 1.993	6.02466×10^{-3}	3.71	–
CCS		207.2620	11.8	$6.83228\times10^{-2}\pm0.009$	10.859 ± 0.073	1.092 ± 0.173	5.88019×10^{-2}	6.65	–
l-C3H		207.2809	11.8	$8.94074\times10^{-2}\pm0.009$	10.180 ± 0.196	1.534 ± 0.196	5.47413×10^{-2}	6.02	–
NS		207.4366	11.8	0.19675 ± 0.009	9.200 ± 0.152	6.033 ± 0.356	3.06353×10^{-2}	3.25	✓
l-C_3H		207.4598	11.8	$8.94404\times10^{-2}\pm0.012$	8.743 ± 0.113	1.666 ± 0.237	5.04435×10^{-2}	7.63	✓
C_2H_3CN		207.6037	11.8	–	–	–	–	3.42	✓
NS		207.8347	11.8	$8.15090\times10^{-2}\pm0.041$	9.236 ± 0.481	3.523 ± 1.213	2.17330×10^{-2}	5.77	✓
			11.8	$4.01818\times10^{-2}\pm0.037$	14.465 ± 3.984	6.804 ± 5.198	5.54783×10^{-3}	5.77	✓
NS		207.8384	11.8	$7.37173\times10^{-2}\pm0.014$	9.386 ± 0.333	2.995 ± 0.737	2.31247×10^{-2}	6.25	✓
U		207.8791	11.8	$9.50160\times10^{-2}\pm0.013$	9.832 ± 0.203	2.738 ± 0.436	3.26042×10^{-2}	6.44	–
c-C_3H		208.2163	11.8	$9.65629\times10^{-2}\pm0.008$	8.954 ± 0.023	0.789 ± 0.620	0.11504	6.73	–
			11.8	$3.24627\times10^{-2}\pm0.008$	12.489 ± 0.312	1.656 ± 0.496	1.84212×10^{-2}	6.73	–
E-CH_3CHO		208.2286	11.8	$1.06323\times10^{-3\,c}$	–	–	–	6.70	✓
C_2H_5CN		208.2513	11.8		–	–	–	–	6.70	✓
CH_3COCH_3		208.2627	11.8	$2.70456\times10^{-2\,c}$	–	–	–	27.0	✓

Continued on next page

Table B.6 – *Continued from previous page*

Specie	Trans	Freq	HPBW	MP2					OTF
				Area	V	Width	T_{MB}	rms	
		[GHz]	["]	[K km s^{-1}]	[km s^{-1}]	[km s^{-1}]	[K]	[mK]	
CH_3OCH_3		208.2783	11.8	5.32652±0.010	9.045±0.092	0.998±0.308	5.01563×10^{-2}	7.36	✓
CH3$_C$HO		208.4454	11.8	1.91502×10^{-3}[c]	–	–	–	6.98	✓
U		208.5406	11.8	8.78974×10^{-3}[c]				7.95	✓
SO^+		208.5906	11.8	0.16411±0.007	9.869±0.142	2.556±0.216	6.03140×10^{-2}	7.58	✓
			11.8	$7.42591 \times 10^{-2} \pm 0.021$	12.527±0.583	3.788±1.120	1.84155×10^{-2}	7.58	–
U		208.6773	11.8	–	–	–	–	8.72	–
SO_2		208.6998	11.8	0.11648±0.017	8.895±0.179	2.372±0.450	4.61308×10^{-2}	7.93	✓
U		208.8017	11.8		6.46917×10^{-2}[c]			7.20	✓
U		208.8631	11.8	4.18922×10^{-2}[c]				7.70	–
SO^+		208.9660	11.8	0.20314±0.019	10.353±0.184	4.114±0.464	4.63927×10^{-2}	6.96	✓
H_2CS		209.2006	11.7	0.28309±0.119	8.748±0.111	0.880±0.183	0.30209	60.00	✓
			11.7	0.39633±0.492	7.737±2.271	3.715±3.313	0.10021	60.00	✓
HC_3N		209.2302	11.7	0.41822±0.091	8.441±0.112	1.051±0.302	0.37397	60.00	✓
c-C_3H		209.2507	11.7	0.85152±0.889	6.517±0.843	2.531±1.584	0.31607	66.00	✓
			11.7	0.23093±0.112	8.878±0.128	0.700±1.584	0.30988	66.00	✓
c-C_3H		209.2687	11.7					74.0	✓
CH_3COCH_3		209.3045	11.7					69.0	✓
$^{13}C^{18}O$		209.4191	11.7					68.3	✓
U		209.7382	11.7					65.8	✓
U		209.7795	11.7					66.5	✓
H31α		210.5001	11.7	–	–	–	–	27.4	✓
H48δ		211.1066	11.6	–	–	–	–	27.4	✓
H_2CO		211.2115	11.6	9.2889±0.146	9.686±0.032	3.792±0.050	2.3015	37.5	✓
			11.6	3.4288±0.113	8.445±0.002	1.146±0.025	2.8103	37.5	
E-CH_3CHO		212.3847	11.6	–	–	–	–	25.4	–
$H_2^{13}CO$		213.2936	11.5	0.29414[c]	–	–	–	39.8	–
HCS^+		213.3606	11.5	0.24257±0.078	4.606±0.569	3.177±0.997	7.17215×10^{-2}	34.0	✓
			11.5	0.44433±0.085	8.917±0.251	2.844±0.631	0.14680	34.0	
U		213.9868	11.5	1.4159±0.050	9.946±0.034	1.993±0.090	0.66735	26.5	✓
SO		215.2207	11.4	–	–	–	–	25.8	✓
HCOOH		215.4078	11.4						✓
^{34}SO		215.8399	11.4	0.24854±0.044	9.801±0.213	2.500±0.535	9.33859×10^{-2}	21.7	✓

Table B.6 – *Continued from previous page*

Specie	Trans	Freq	HPBW	Area	V	Width	T_{MB}	rms	OTF
		[GHz]	["]	[K km s^{-1}]	[km s^{-1}]	[km s^{-1}]	[K]	[mK]	
DCO$^+$		216.1126	11.4	0.44333±0.027	8.320±0.017	0.720±0.082	0.57809	20.3	✓
			11.4	0.35612±0.039	9.927±0.083	1.658±0.224	0.20181	20.3	
c-C$_3$H$_2$		216.2788	11.4	0.79564±0.035	8.374±0.028	1.318±0.071	0.56692	23.8	✓
C$_2$D		216.3733	11.4	0.46186±0.034	8.706±0.052	1.402±0.118	0.30952	23.3	✓
C$_2$D		216.4303	11.4	0.31452±0.040	11.117±0.082	1.432±0.241	0.20635	24.4	✓
E-CH$_3$CHO		216.5819	11.4	–	–	–	–	23.2	–
^{13}CN		216.7101	11.3	0.96567±0.136	12.113±1.251	17.753±2.927	5.10988×10^{-2}	25.1	–
^{13}CN		216.8838	11.3	–	–	–	–	–	–
SiO		217.1049	11.3	0.42057±0.088	10.684±0.944	8.864±1.993	4.45721×10^{-2}	24.5	✓
DCN		217.2385	11.3	0.974 ± 0.064	8.466 ± 0.037	1.151 ± 0.089	0.794	21.8	✓
			11.3	0.401 ± 0.069	10.390 ± 0.117	1.418 ± 0.293	0.266	21.8	
^{13}CN		217.4691	11.3	0.18411±0.037	11.061±0.142	1.479±0.386	0.11698	23.1	✓
			11.3	7.95744×10^{-2}±0.033	13.534±0.272	1.240±0.529	6.03099×10^{-2}	23.1	
c-C$_3$H$_2$		217.8221	11.3	0.86921±0.060	8.952±0.100	3.071±0.307	0.26586	23.8	✓
U			11.3	0.95578±0.007	8.294±0.010	0.787±0.047	1.1406	23.8	
c-C$_3$H$_2$		217.9400	11.3	0.82014±0.037	8.357±0.025	1.194±0.071	0.64514	25.7	✓
H$_2$CO		218.2222	11.3						✓
HC$_3$N		218.3244	11.3						✓
CH$_3$OH		218.4401	11.2						✓
H$_2$CO		218.4756	11.2						✓
H$_2$CO		218.7601	11.2						✓
OCS		218.9034	11.2						✓
C^{18}O		219.5604	11.2						✓
H$_2$^{13}CO		219.9085	11.2						✓
SO		219.9494	11.2						✓
^{13}CO		220.3987	11.2						✓
U		221.8260	11.2						–
SO$_2$		221.9652	11.2						–
H38β		222.0118	11.2						–
C^{17}O		224.7153	11.2						✓
H$_2$CO		225.6978	11.2						✓
CN		226.2874	11.2	0.23484±0.111	8.378±0.499	2.609±1.709	8.45524×10^{-2}	47.2	✓

Table B.6 – *Continued from previous page*

Specie	Trans	Freq	HPBW	MP2					OTF
				Area	V	Width	T_{MB}	rms	
		[GHz]	["]	[K km s^{-1}]	[km s^{-1}]	[km s^{-1}]	[K]	[mK]	
CN		226.2989	11.2	0.23371±0.053	8.737±0.274	2.452±0.625	8.95392×10^{-2}	27.3	✓
CN		226.3030	11.2	0.33441±0.058	9.358±0.326	3.601±0.652	8.72507×10^{-2}	25.5	✓
CN		226.3145	11.2	0.16938±0.051	8.322±0.139	0.701±0.139	0.22689	29.9	✓
			11.2	0.52972±0.087	9.276±0.284	3.377±0.639	0.14736	29.9	−
CN		226.3325	11.2	0.30367±0.055	8.872±0.267	2.597±0.526	0.10984	28.7	✓
			11.2	5.04560×10^{-2}±0.031	12.541±0.194	0.700±3.088	6.77145×10^{-2}	28.7	−
CN		226.3419	11.2	0.16052±0.088	8.182±0.122	1.081±0.580	0.13951	28.1	✓
			11.2	0.27302±0.119	10.206±0.825	3.916±1.811	6.54945×10^{-2}	28.1	−
CN		226.3599	11.2	0.94955±0.058	8.315±0.035	1.394±0.101	0.64010	29.2	✓
			11.2	0.55592±0.043	10.289±0.154	2.239±0.305	0.23325	29.2	−
A-CH$_3$CHO		226.5927	11.2	−	−	−	−	26.5	−
CN		226.6166	11.2	0.19381^c	−	−	−	26.5	✓
CN		226.6322	11.2	1.2841±2.133	8.319±0.486	1.401±1.315	0.86081	27.0	✓
			11.2	0.99219±2.133	10.160±2.174	2.518±1.315	0.37018	27.0	✓
CN		226.6596	11.2	4.8985±0.011	8.656±0.000	2.225±0.024	2.0678	27.0	✓
			11.2	2.8560±0.069	11.273±0.011	5.529±0.183	0.48525	27.0	✓
CN		226.6637	11.2	0.66199±0.085	8.306±0.055	0.817±0.394	0.76125	28.0	−
			11.2	1.4293±0.134	9.459±0.174	3.408±0.237	0.39403	28.0	✓
CN		226.6793	11.2	0.80345±0.811	8.284±0.438	0.771±0.237	0.97943	30.0	−
			11.2	2.0836±0.521	9.534±1.411	3.302±0.237	0.59282	30.0	✓
CN		226.8742	11.2	13.216±0.070	7.865±0.001	3.096±0.024	4.0107	29.3	✓
			11.2	4.8780±0.080	12.128±0.020	4.299±0.075	1.0661	29.3	−
CN		226.8874	11.2	0.58795±0.070	8.349±0.041	0.971±0.139	0.56867	27.1	✓
			11.2	1.6829±0.108	9.554±0.161	5.074±0.404	0.31157	27.1	−
CN		226.8921	11.2	0.75958±0.122	8.327±0.032	1.003±0.182	0.71171	28.2	✓
			11.2	1.3615±0.139	9.525±0.177	3.384±0.216	0.37792	28.2	−
U		226.9271	11.2	1.36901×10^{-2c}	−	−	−	26.5	−
U		226.9415	11.2	1.75582×10^{-2c}	−	−	−	25.5	−
c-C$_3$H$_2$		227.1691	11.2	0.73114±0.044	8.357±0.037	1.209±0.096	0.56813	31.2	✓
HC$_3$N		227.4189	11.2	6.96946×10^{-2c}	−	−	−	30.3	✓
U		228.8861	10.8	0.38074^c	−	−	−	56.9	−
DNC		228.9105	10.7	0.50189±0.039	8.339±0.024	0.700±0.217	0.67350	36.2	✓

Table B.6 – *Continued from previous page*

Specie	Trans	Freq [GHz]	HPBW ["]	Area [K km s^{-1}]	V [km s^{-1}]	Width [km s^{-1}]	T$_{MB}$ [K]	rms [mK]	OTF
			10.7	0.12748±0.051	10.396±0.284	1.384±0.603	8.65004×10^{-2}	36.2	–
CH$_3$OH		229.7588	10.7	0.99771$^{\mathrm{c}}$	–	–	–	59.4	✓
CO		230.5380	10.6	138.24±0.668	7.351±0.001	5.055±0.011	25.689	160	✓
			10.6	37.373±0.503	8.929±0.004	2.200±0.022	15.957	160	–
			10.6	115.39±0.340	13.542±0.005	2.955±0.007	36.685	160	–
			10.6	21.665±0.498	18.510±0.020	5.482±0.120	3.7127	160	–
OCS		231.0610	10.6	–	–	–	–	34.2	–
^{13}CS		231.2207	10.6	0.40210$^{\mathrm{c}}$	–	–	–	38.1	✓
A-CH$_3$CHO		231.4675	10.6	0.23661$^{\mathrm{c}}$	–	–	–	32.8	–
U		231.5218	10.6	2.72696×10$^{-2\,\mathrm{c}}$	–	–	–	33.0	✓
H30α		231.8958	10.6	–	–	–	–	32.0	–
U		232.1936	10.6	–	–	–	–	33.0	–
C^{13}CC-H		232.7886	10.5	0.34227±0.049	9.440±0.146	1.929±0.334	0.16665	27.0	✓
HCCN		233.1118	10.5	–	–	–	–	27.0	–
U		233.4785	10.5	0.29410$^{\mathrm{c}}$	–	–	–	30.0	–
H$_2$C^{33}S		234.6790	10.5	–	–	–	–	20.6	–
SO$_2$		235.1517	10.4	1.68140×10$^{-2\,\mathrm{c}}$	–	–	–	17.7	✓
CO$^+$		236.0626	10.4	0.21295±0.051	10.086±0.594	5.421±1.558	3.69072×10^{-2}	16.2	✓
t-HOCO		236.0812	10.4	7.37824×10^{-2}±0.030	10.100±0.273	1.489±0.928	4.65371×10^{-2}	16.2	✓
SO$_2$		236.2167	10.4	0.11202$^{\mathrm{c}}$	–	–	–	14.2	✓
U		236.4131	10.4	6.67165×10$^{-2\,\mathrm{c}}$	–	–	–	14.4	✓
HC$_3$N		236.5144	10.4	9.51179×10^{-2}±0.019	10.078±0.114	1.029±0.205	8.68188×10^{-2}	14.7	✓
H$_2$CS		236.7270	10.3	0.29871±0.084	8.320±0.046	1.035±0.279	0.27111	14.4	✓
			10.3	0.14059±0.086	9.505±1.106	3.199±0.987	4.12889×10^{-2}	14.4	–
SO$_2$		237.0689	10.3	7.76769×10$^{-3\,\mathrm{c}}$	–	–	–	18.7	✓
CH$_3$CCH		239.2110	10.2						✓
CH$_3$CCH		239.2340	10.2						✓
CH$_3$CCH		239.2477	10.2						✓
CH$_3$CCH		239.2523	10.2						✓
CH$_3$OH		239.7463	10.2						✓
H$_2$CS		240.2669	10.2						✓
H$_2$CS		240.5482	10.2						✓

Table B.6 – *Continued from previous page*

Specie	Trans	Freq	HPBW	MP2					OTF
				Area	V	Width	T_{MB}	rms	
		[GHz]	["]	[K km s^{-1}]	[km s^{-1}]	[km s^{-1}]	[K]	[mK]	
C^{34}S		241.0169	10.2						✓
SO$_2$		241.6150	10.2						✓
CH$_3$OH		241.7002	10.2						✓
CH$_3$OH		241.7672	10.2						✓
CH$_3$OH		241.7914	10.2						✓
CH$_3$OH		241.8423	10.2						✓
CH$_3$OH		241.8791	10.2						✓
CH$_3$OH		241.9042	10.2						✓
U		242.2751	10.2						✓
C^{33}S		242.9136	10.1						✓
CH$_3$OH		243.9158	10.1						✓
H$_2$CS		244.0485	10.1						✓
c-C$_3$H$_2$		244.2221	10.0						−
SO$_2$		244.2542	10.0						−
U		244.6181	10.0						✓
CS		244.9356	10.0						✓
U		245.2533	10.0						✓
HC$_5$N		245.2749	10.0						✓
SO$_2$		245.5634	10.0						−
HC$_3$N		245.6063	10.0						−
HDCO		246.9246	9.9						−
c-C$_3$H$_2$		249.0544	9.9						✓
A-CH$_3$CHO		250.7956	9.8	0.11155±0.028	7.968±0.218	1.807±0.596	5.80060×10^{-2}	15.1	✓
A-CH$_3$CHO		250.8147	9.8	0.17304±0.031	8.945±0.263	3.046±0.685	5.33705×10^{-2}	13.7	✓
SO$_2$		251.1997	9.8	5.17824×10$^{-2\,c}$	−	−	−	13.7	✓
SO$_2$		251.2106	9.8	6.64155×10$^{-2\,c}$	−	−	−	13.3	✓
c-C$_3$H$_2$		251.3144	9.8	1.1683±0.019	8.403±0.009	1.058±0.024	1.0374	14.6	✓
c-C$_3$H$_2$		251.5087	9.8	0.34903±0.019	8.359±0.131	1.204±0.329	0.27236	54.4	✓
CH$_3$OH		251.5173	9.8	0.33155^{c}	−	−	−	10.7	−
c-C$_3$H$_2$		251.5273	9.8	0.70316±0.037	8.356±0.027	1.063±0.095	0.62167	27.0	✓
CH$_3$OH		251.6411	9.7	9.52580×10$^{-2\,c}$	−	−	−	13.3	...
CH$_3$OH		251.7385	9.7	5.17898×10$^{-2\,c}$	−	−	−	10.8	−

Continued on next page

Table B.6 – *Continued from previous page*

Specie	Trans	Freq [GHz]	HPBW ["]	Area [K km s^{-1}]	V [km s^{-1}]	Width [km s^{-1}]	T$_{MB}$ [K]	rms [mK]	OTF
CH$_3$OH		251.8120	9.7	1.72391×10^{-2c}	–	–	–	11.0	–
SO		251.8258	9.7	0.66899±0.023	9.334±0.049	2.777±0.107	0.22630	11.3	✓
CH$_3$OH		251.8666	9.7	–	–	–	–	11.0	–
CH$_3$OH		251.8909	9.7	6.18628×10^{-3c}	–	–	–	11.8	–
CH$_3$OH		251.8957	9.7	0.11536^c	–	–	–	11.5	–
CH$_3$OH		251.9005	9.7	0.17242^c	–	–	–	11.3	–
CH$_3$OH		251.9058	9.7	–	–	–	–	11.7	–
CH$_3$OH		251.9170	9.7	8.12325×10^{-3c}	–	–	–	11.6	–
CH$_3$OH		251.9236	9.7	0.10464^c	–	–	–	11.6	–
CH$_3$OH		251.9847	9.7	–	–	–	–	11.6	–
CH$_3$OH		252.0904	9.7	0.12340^c	–	–	–	12.6	–
^{13}CCH		252.4241	9.7	0.14103±0.034	9.552±0.426	3.378±0.940	3.92169×10^{-2}	14.9	–
^{13}CCH		252.4493	9.7	0.12029±0.034	8.820±0.291	2.106±0.709	5.36514×10^{-2}	15.2	–
^{13}CCH		252.4579	9.7	0.11752^c	–	–	–	12.4	–
SO^{17}O		252.4981	9.7	0.11309±0.027	10.670±0.335	2.777±0.728	3.82653×10^{-2}	13.3	–
U		252.5599	9.7	4.39828×10^{-2}±0.015	10.307±0.092	0.700±0.728	5.90217×10^{-2}	14.0	–
			9.7	0.23184±0.017	12.672±0.048	1.104±0.089	0.19730	14.0	–
c-C$_3$H		252.8816	9.7	7.42352×10^{-2}±0.021	8.393±0.322	1.913±0.572	3.64522×10^{-2}	12.7	–
NS		253.5705	9.7	8.21142×10^{-2c}	–	–	–	18.0	–
CH$_3$OH		254.0153	9.7	8.21142×10^{-2c}	–	–	–	15.0	✓
C$_2$H$_5$^{13}CN		254.1551	9.7	5.83932×10^{-2}±0.029	3.057±0.284	1.360±0.901	4.03275×10^{-2}	14.8	✓
H$_2$CCCHCN		254.1628	9.7	–	–	–	–	14.9	✓
CH$_2$NH		254.6848	9.6	0.29253^c	–	–	–	12.3	–
HC$_3$N		254.6995	9.6	0.27794^c	–	–	–	13.0	–
SO$^+$		254.9764	9.6	7.71010×10^{-2}±0.037	9.801±0.406	1.704±1.004	4.25162×10^{-2}	21.6	–
SO$^+$		254.9790	9.6	6.05351×10^{-2}±0.027	9.971±0.258	1.040±0.459	5.47030×10^{-2}	22.2	–
c-C$_3$H$_2$		254.9877	9.6	5.00706×10^{-2}±0.018	6.067±0.248	1.340±0.551	3.51114×10^{-2}	11.9	–
			9.6	0.25397±0.018	8.416±0.041	1.215±0.102	0.19640	11.9	–
SO$^+$		255.3515	9.6	7.91351×10^{-2}±0.019	6.374±0.143	1.249±0.348	5.95364×10^{-2}	12.7	–
			9.6	6.66539×10^{-2}±0.024	9.762±0.505	2.490±0.839	2.51505×10^{-2}	12.7	–
SO$^+$		255.3762	9.6	2.63210×10^{-2c}	–	–	–	12.8	–
A-CH$_3$CHO		255.3848	9.6	2.79522×10^{-2c}	–	–	–	11.4	–

Continued on next page

Table B.6 – *Continued from previous page*

Specie	Trans	Freq	HPBW	MP2					OTF
				Area	V	Width	T_{MB}	rms	
		[GHz]	["]	[K km s^{-1}]	[km s^{-1}]	[km s^{-1}]	[K]	[mK]	
HC^{18}O$^+$		255.4794	9.6	$4.67074\times10^{-2}\pm0.028$	10.856 ± 1.050	3.294 ± 1.160	1.33193×10^{-2}	11.2	–
			9.6	0.23933 ± 0.025	8.401 ± 0.034	1.040 ± 0.136	0.21618	11.2	–
C^{13}CH		255.7473	9.6	0.13507 ± 0.023	8.903 ± 0.162	1.806 ± 0.292	7.02771×10^{-2}	14.6	✓
C^{13}CH		255.7588	9.6	$8.21600\times10^{-2}\pm0.018$	8.410 ± 0.120	1.043 ± 0.337	7.39878×10^{-2}	13.3	✓
			9.6	$8.58997\times10^{-2}\pm0.021$	11.458 ± 0.161	1.374 ± 0.419	5.87510×10^{-2}	13.3	
C^{13}CH		255.8220	9.6	–	–	–	–	11.6	✓
C^{13}CH		255.8283	9.6	$3.26766\times10^{-2\,c}$	–	–	–	12.2	✓
HCS$^+$		256.0271	9.6	0.12505 ± 0.026	8.263 ± 0.030	0.700 ± 0.660	0.16783	11.3	✓
			9.6	0.15163 ± 0.040	9.340 ± 0.341	2.658 ± 0.660	5.35872×10^{-2}	11.3	–
U		256.2941	9.6	$9.93371\times10^{-2}\pm0.043$	10.209 ± 0.265	0.903 ± 0.777	0.10338	35.0	–
H29α		256.3020	9.6	$1.86011\times10^{-2\,c}$	–	–	–	12.4	–
CH$_3$CCH		256.3184	9.6	0.10389 ± 0.044	9.943 ± 0.287	0.846 ± 0.403	0.11541	33.5	–
CH$_3$CCH		256.3317	9.6	0.25916 ± 0.031	8.379 ± 0.078	0.858 ± 0.225	0.28388	26.9	✓
CH$_3$CCH		256.3338	9.6	0.26071 ± 0.037	10.749 ± 0.086	1.006 ± 0.139	0.24338	26.9	✓
CH$_3$CCH		256.3366	9.6	0.27944 ± 0.035	8.473 ± 0.079	0.865 ± 0.147	0.30341	26.9	✓
HDCO		256.5854	9.6	0.40830 ± 0.014	8.369 ± 0.018	0.952 ± 0.060	0.40278	10.6	✓
^{34}SO		256.8778	9.6	$8.67501\times10^{-2\,c}$	–	–	–	11.0	–
SO$_2$		257.0981	9.6	0.11819^c	–	–	–	10.5	–
H41γ		257.6355	9.5	$6.42560\times10^{-2\,c}$	–	–	–	10.8	–
HDCO		257.7501	9.5	$9.58296\times10^{-2}\pm0.014$	10.162 ± 0.116	0.818 ± 0.223	0.11001	11.6	–
U		257.9014	9.5	$8.34867\times10^{-3\,c}$	–	–	–	10.8	–
HC^{15}N		258.1570	9.5	0.19476 ± 0.017	8.408 ± 0.049	1.013 ± 0.118	0.18054	11.8	✓
			9.5	$6.86216\times10^{-2}\pm0.025$	11.242 ± 0.587	2.702 ± 1.074	2.38597×10^{-2}	11.8	–
C2H3CHO		258.2457	9.5	0.14377^c	–	–	–	12.6	–
SO		258.2558	9.5	0.70687 ± 0.029	9.302 ± 0.058	2.924 ± 0.145	0.22709	13.3	✓
SO$_2$		258.9422	9.5	0.16491 ± 0.027	9.181 ± 0.130	1.539 ± 0.249	0.10069	18.10	✓
H^{13}CN		259.0118	9.5	0.45460 ± 0.052	8.308 ± 0.025	0.700 ± 0.257	0.61009	23.40	✓
			9.5	0.58020 ± 0.088	9.347 ± 0.227	3.026 ± 0.432	0.18015	23.40	–
H36β		260.0328	9.5	0.15253^c	–	–	–	30.83	–
H^{13}CO$^+$		260.2553	9.4	0.65736 ± 0.143	9.647 ± 0.143	2.688 ± 0.342	0.22974	26.50	✓
			9.4	1.7310 ± 0.121	8.373 ± 0.121	0.894 ± 0.082	1.8184	26.50	–
HN^{13}C		261.2635	9.4	0.35796 ± 0.031	8.378 ± 0.031	0.914 ± 0.180	0.36782	25.20	✓

Continued on next page

Table B.6 – *Continued from previous page*

Specie	Trans	Freq	HPBW	MP2					OTF
				Area	V	Width	T_{MB}	rms	
		[GHz]	["]	[K km s^{-1}]	[km s^{-1}]	[km s^{-1}]	[K]	[mK]	
CH$_3$CHO		261.8381	9.4	0.19412±0.074	10.558±0.469	2.446±1.147	7.45692×10^{-2}	22.0	–
SO		261.8437	9.4	0.42819±0.040	8.340±0.043	1.016±0.076	0.39599	19.70	✓
			9.4	0.92423±0.062	9.911±0.057	1.986±0.199	0.43723	19.70	–
C$_2$H		261.9792	9.4	0.43365±0.867	9.446±1.355	1.227±0.070	0.33193	30.0	–
C$_2$H		262.0043	9.4	3.5733±0.932	9.575±0.700	3.889±0.700	0.86310	30.0	✓
			9.4	6.6595±0.932	8.242±0.700	1.246±0.700	5.0221	30.0	–
C$_2$H		262.0065	9.4	4.6929±0.093	8.296±0.006	1.044±0.013	4.2246	30.0	✓
C$_2$H		262.0650	9.4	4.7891±0.132	8.374±0.058	5.213±0.191	0.86300	27.90	✓
			9.4	4.1435±0.086	8.337±0.005	0.963±0.026	4.0433	27.90	–
C$_2$H		262.0675	9.4	4.3378±0.052	8.364±0.007	1.261±0.019	3.2328	36.50	✓
C$_2$H		262.0789	9.4	0.82190±0.037	8.316±0.024	1.208±0.076	0.63941	25.10	✓
C$_2$H		262.2086	9.4	0.81400±0.049	8.341±0.034	1.186±0.096	0.64495	34.10	✓
C$_2$H		262.2370	9.4	5.10088×10$^{-2\,c}$	–	–	–	35.10	–
C$_2$H		262.2509	9.4	0.32642±0.038	8.394±0.060	1.175±0.197	0.26104	24.70	–
HCOCH$_2$OH		265.5691	9.3	–	–	–	–	44.15	✓
c-C$_3$H$_2$		265.7595	9.3	0.44166±0.120	10.724±1.106	8.516±2.720	4.87236×10^{-2}	27.10	
			9.3	0.61504±0.057	8.280±0.039	0.775±0.818	0.74518	27.10	
HCN		265.8864	9.2	11.036±0.996	9.658±0.700	7.340±0.700	1.4126	34.50	
U			9.2	10.486±0.996	8.788±0.700	2.375±0.700	4.1474	34.50	
H^{15}NC		266.5878	9.2	0.13028±0.019	8.404±0.084	0.851±0.224	0.14373	12.7	
			9.2	0.18190±0.079	13.305±2.700	10.478±0.473	1.63096×10^{-2}	12.7	
^{33}SO		266.5892	9.2	0.14983±0.017	9.983±0.065	0.935±0.094	0.15053	13.2	
CH$_3$OH		266.8381	9.2	0.25320±0.027	8.608±0.098	1.767±0.302	0.13461	12.3	
HCO$^+$		267.5576	9.2	19.165±1.207	8.563±0.700	1.633±0.700	11.027	18.5	
			9.2	16.910±1.207	10.228±0.700	4.579±0.700	3.4691	18.5	
HDCO		268.2920	9.1	0.21994±0.052	8.544±0.080	0.852±0.135	0.24256	14.3	
			9.1	0.11335±0.054	9.773±0.556	2.125±0.777	5.01194×10^{-2}	14.3	
H$_2$CS		270.5219	9.1	0.23106±0.039	8.301±0.040	0.700±8.882	0.31006	17.1	
			9.1	0.12230±0.046	9.568±0.302	1.637±0.753	7.01799×10^{-2}	17.1	

Table B.7: Gaussian fits of the 0.8mm lines at IF position.

Specie	Trans	Freq	HPBW	IF				
				Area	V	Width	T_{MB}	rms
		[GHz]	["]	[K km s^{-1}]	[km s^{-1}]	[km s^{-1}]	[K]	[mK]
SO$_2$		271.5290	9.1	0.21±0.03	10.65±0.23	2.73±0.44	0.073	17.6
HNC		271.9811	9.0	5.29±0.18	10.66±0.02	2.85±0.07	1.744	21.6
			9.0	1.89±0.18	10.64±0.01	1.20±0.04	1.489	21.6
U		273.2242	9.0					15.7
CH$_3$CCH		273.3744	8.9	0.09^c	–	–	–	19.0
CH$_3$CCH		273.4007	8.9					17.0
CH$_3$CCH		273.4147	8.9	0.14±0.03	10.74±0.144	1.47±0.37	0.090	18.3
CH$_3$CCH		273.4161	8.9					18.3
CH$_3$CCH		273.4199	8.9	0.19±0.04	10.52±0.277	2.79±0.91	0.063	18.1
^{13}CS		277.4554	8.8	0.22±0.03	10.63±0.081	1.24±0.17	0.165	20.0
CH$_3$OH		278.3045	8.8	0.22±0.03	10.88±0.073	1.27±0.19	0.161	18.1
H$_2$CS		278.8877	8.8	0.34±0.03	10.83±0.045	1.21±0.10	0.262	17.8
N$_2$H$^+$		279.5117	8.8	2.89±0.08	11.01±0.046	3.41±0.07	0.795	18.7
U			8.8	0.39±0.06	12.06±0.046	1.08±0.10	0.340	18.7
H$_2$CO		281.5269	8.7	5.13±0.12	10.23±0.032	3.91±0.07	1.232	20.0
U			8.7	2.96±0.12	10.79±0.008	1.40±0.03	1.981	20.0
SO$_2$		281.7626	8.7	0.10±0.02	10.66±0.157	1.45±0.30	0.066	14.70
c-C$_3$H$_2$		282.0366	8.7	0.08^c	–	–	–	20.4
HCS		282.0602	8.7	0.06^c	–	–	–	16.9
H35β		282.3282	8.7	6.36±0.15	9.04±0.43	37.53±0.99	0.159	19.30
c-C$_3$H$_2$		282.3813	8.7	0.18±0.06	9.88±0.58	3.32±1.11	0.052	28.10
SO$_2$		283.4646	8.7	0.13±0.03	10.15±0.15	1.58±0.36	0.077	16.10
H28α		284.2444	8.7	14.99±0.10	6.71±0.11	33.44±0.26	0.421	14.10
H$_2$CN		293.7815	8.7	0.24±0.04	10.60±0.25	2.75±0.52	0.083	21.00
H$_2$CN		293.7965	8.7	–	–	–	–	21.00
CS		293.9121	8.3	10.57±0.05	10.63±0.01	1.89±0.01	5.261	29.70
SO		296.5501	8.3	0.97±0.03	10.61±0.03	1.72±0.07	0.530	18.70
HCS$^+$		298.6905	8.2	0.31±0.03	10.77±0.07	1.33±0.14	0.217	21.50
C^{18}O		329.3306	7.4	17.17±1.91	10.47±0.10	2.04±0.32	7.917	930.0
^{13}CO		330.5880	7.2	34.56±3.48	9.71±0.31	10.03±0.65	3.236	460.0

Table B.7 – *Continued from previous page*

Specie	Trans	Freq	HPBW	IF				
				Area	V	Width	T_{MB}	rms
		[GHz]	["]	[K km s^{-1}]	[km s^{-1}]	[km s^{-1}]	[K]	[mK]
			7.2	63.12±2.56	9.64±0.05	3.98±0.11	14.91	460.0
CS		342.8829	7.1	10.95±0.20	10.62±0.02	1.71±0.04	6.031	120.0
SO		344.3106	7.1	1.056±0.19	10.66±0.12	1.34±0.26	0.742	130.0
H^{13}CN		345.3398	7.1	1.63±0.31	10.65±0.15	1.74±0.42	0.882	170.0
CO		345.7960	7.1	69.34±0.45	6.20±0.09	5.70±0.09	11.434	280.0
			7.1	85.74±0.28	8.72±0.01	5.94±0.15	13.571	280.0
			7.1	93.68±0.84	14.04±0.02	5.01±0.08	17.559	280.0
SO		346.528	7.1	2.83±0.31	10.50±0.11	2.04±0.28	1.302	160.0
H^{13}CO$^+$		346.998	7.1	4.45±0.34	10.59±0.09	2.38±0.23	1.755	170.0
c-C$_3$H$_2$		349.264	7.0	–	–	–	–	169.0
C$_2$H		349.340	7.0	8.10±0.38	12.17±0.09	3.63±0.19	2.096	160.0
C$_2$H		349.401	7.0	6.30±0.39	11.08±0.11	3.56±0.26	1.662	160.0

Table B.8: Gaussian fits of the 0.8mm lines at MP2 position.

Specie	Trans	Freq	HPBW	MP2				
				Area	V	Width	T_{MB}	rms
		[GHz]	["]	[K km s^{-1}]	[km s^{-1}]	[km s^{-1}]	[K]	[mK]
SO$_2$		271.5290	9.1	0.09±0.03	10.96±0.50	2.67±0.93	0.031	16.20
HNC		271.9811	9.0	6.01±0.06	8.46±0.01	1.04±0.01	1.018	15.80
			9.0	3.55±0.07	9.68±0.03	3.27±0.05	5.453	15.80
U		273.2242	9.0	0.18±0.02	9.82±0.09	1.52±0.20	0.114	14.00
CH$_3$CCH		273.3744	8.9	0.07^c	–	–	–	14.30
CH$_3$CCH		273.4007	8.9	0.11±0.04	10.02±0.20	1.04±0.32	0.102	28.90
CH$_3$CCH		273.4147	8.9	0.23±0.03	8.54±0.07	1.00±0.12	0.219	22.40
CH$_3$CCH		273.4161	8.9	0.22±0.03	10.09±0.10	0.91±0.14	0.227	25.30
CH$_3$CCH		273.4199	8.9	0.23±0.03	8.60±0.10	0.92±0.12	0.231	25.00
^{13}CS		277.4554	8.8	0.19±0.02	8.48±0.06	1.33±0.14	0.132	10.40
CH$_3$OH		278.3045	8.8	0.13±0.02	8.36±0.28	3.52±0.75	0.035	8.86
H$_2$CS		278.8877	8.8	0.13±0.03	9.64±0.20	2.07±0.46	0.059	9.90
U			8.8	0.18±0.02	8.29±0.02	0.70±1.36	0.237	9.90
N$_2$H$^+$		279.5117	8.8	3.70±0.05	9.45±0.02	3.81±0.04	0.913	12.00
U			8.8	2.20±0.03	8.37±0.01	0.92±0.02	2.256	12.00
H$_2$CO		281.5269	8.7	4.95±0.07	9.65±0.03	3.56±0.04	1.306	16.20
U			8.7	3.89±0.06	8.38±0.01	1.08±0.01	3.392	16.20
SO$_2$		281.7626	8.7	0.09±0.02	9.70±0.46	3.69±0.97	0.023	8.78
c-C$_3$H$_2$		282.0366	8.7	0.13±0.02	9.12±0.19	2.50±0.40	0.047	9.55
HCS		282.0602	8.7	0.03c	–	–	–	10.74
H35β		282.3282	8.7	0.02c	–	–	–	10.85
c-C$_3$H$_2$		282.3813	8.7	0.25±0.02	8.50±0.04	0.94±0.06	0.253	11.90
SO$_2$		283.4646	8.7	0.11c	–	–	–	23.00
H28α		284.2444	8.7	0.18c	–	–	–	14.86
H$_2$CN		293.7815	8.7					
H$_2$CN		293.7965	8.7					
CS		293.9121	8.3					
SO		296.5501	8.3	0.84±0.05	9.54±0.08	2.71±0.18	0.291	22.90
HCS$^+$		298.6905	8.2	0.32c	–	–	–	27.43
C^{18}O		329.3306	7.4	14.25±0.53	10.39±0.09	4.65±0.15	2.880	120.00

Table B.8 – *Continued from previous page*

Specie	Trans	Freq	HPBW	MP2				
				Area	V	Width	T_{MB}	rms
		[GHz]	["]	[K km s^{-1}]	[km s^{-1}]	[km s^{-1}]	[K]	[mK]
			7.4	9.049±0.35	8.41±0.01	1.17±0.04	7.266	120.00
^{13}CO		330.5880	7.2	92.13±0.25	8.67±0.01	2.53±0.01	34.190	100.00
			7.2	49.57±0.24	12.35±0.01	2.74±0.02	16.991	100.00
CS		342.8829	7.1	3.96±0.06	9.33±0.03	2.72±0.05	1.366	26.10
			7.1	3.123±0.04	8.32±0.01	0.84±0.01	3.476	26.10
SO		344.3106	7.1	0.43±0.09	9.36±0.33	3.04±0.70	0.132	41.30
H^{13}CN		345.3398	7.1	0.59±0.10	8.76±0.23	2.54±0.57	0.218	43.90
CO		345.7960	7.1	199.71±6.68	8.08±0.70	5.07±0.70	36.990	160.00
			7.1	112.51±6.68	13.67±0.70	2.71±0.70	38.966	160.00
			7.1	37.05±6.68	19.39±0.70	6.63±0.70	5.250	160.00
SO		346.5280	7.1	0.69±0.07	9.27±0.14	2.66±0.26	0.243	34.70
H^{13}CO$^+$		346.9980	7.1	1.73±0.05	8.51±0.02	1.00±0.03	1.635	40.30
c-C$_3$H$_2$		349.2640	7.0	0.72±0.40	8.40±0.12	2.05±0.38	0.326	180.00
C$_2$H		349.3400	7.0	12.03±0.94	10.37±0.09	2.18±0.20	5.185	200.00
C$_2$H		349.4010	7.0	9.12±0.10	9.21±0.01	2.23±0.03	3.843	180.00

B.4   Integrated and channel maps

In this section we present some integrated and channels maps towards Mon R2. Figures B.39 to B.45 show the integrated line intensity maps of some representative molecules at 3 mm (Figures B.39 –B.42) and at 1 mm (Figures B.43–B.45). The maps have an angular resolution between $9''$ and $29''$. The integrated intensity maps were done considering velocity ranges where we have identified emission for the different species. These velocity ranges have been chosen where line intensity falls below 5σ. For example, the emission for radio recombination lines is wide and spans a velocity range over 30 km s^{-1} around the velocity source (10 km s^{-1}). For the most abundant species the emission spans a velocity range of around 15–20 km s^{-1}. For species less abundant, we integrate a velocity range between 5 and 8 km s^{-1}(depending of the molecule). Figures B.46 to B.55 show the channel maps for H$_2$CS (at 202.924 GHz), SO (at 206.176 GHz), C^{17}O (at 224.714 GHz), H$_2$CO (at 225.697 GHz), CN (at 226.659 GHz), C^{34}S (at 241.016 GHz), CH$_3$OH (at 241.791 GHz), CS (at 244.935 GHz), H^{13}CN (at 259.011 GHz) and C$_2$H (at 262.004 GHz) molecules.
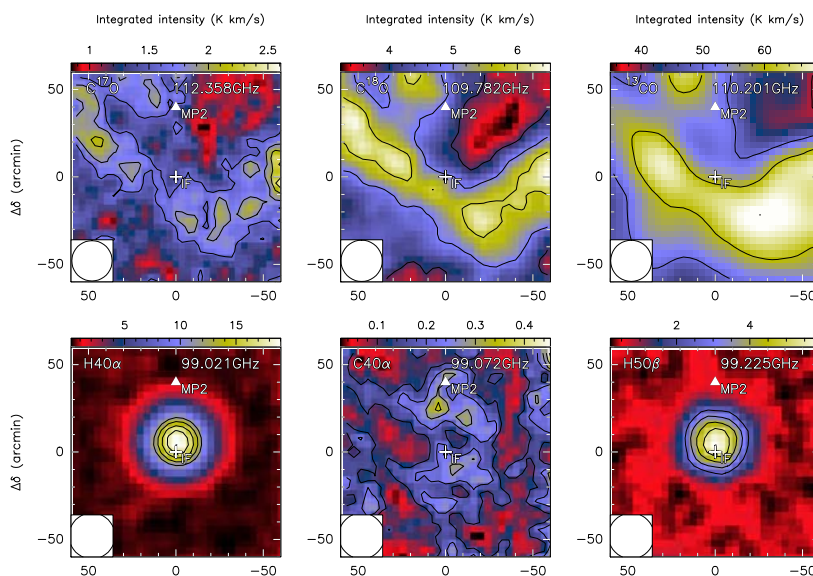
Figure B.39: $2'\times2'$ OTF maps of CO species and RRL at 3 mm. The cross marks the IF position, the triangle indicates the MP2 position. The contour levels are 40% to 100%, in steps of 15% of the peak intensity.
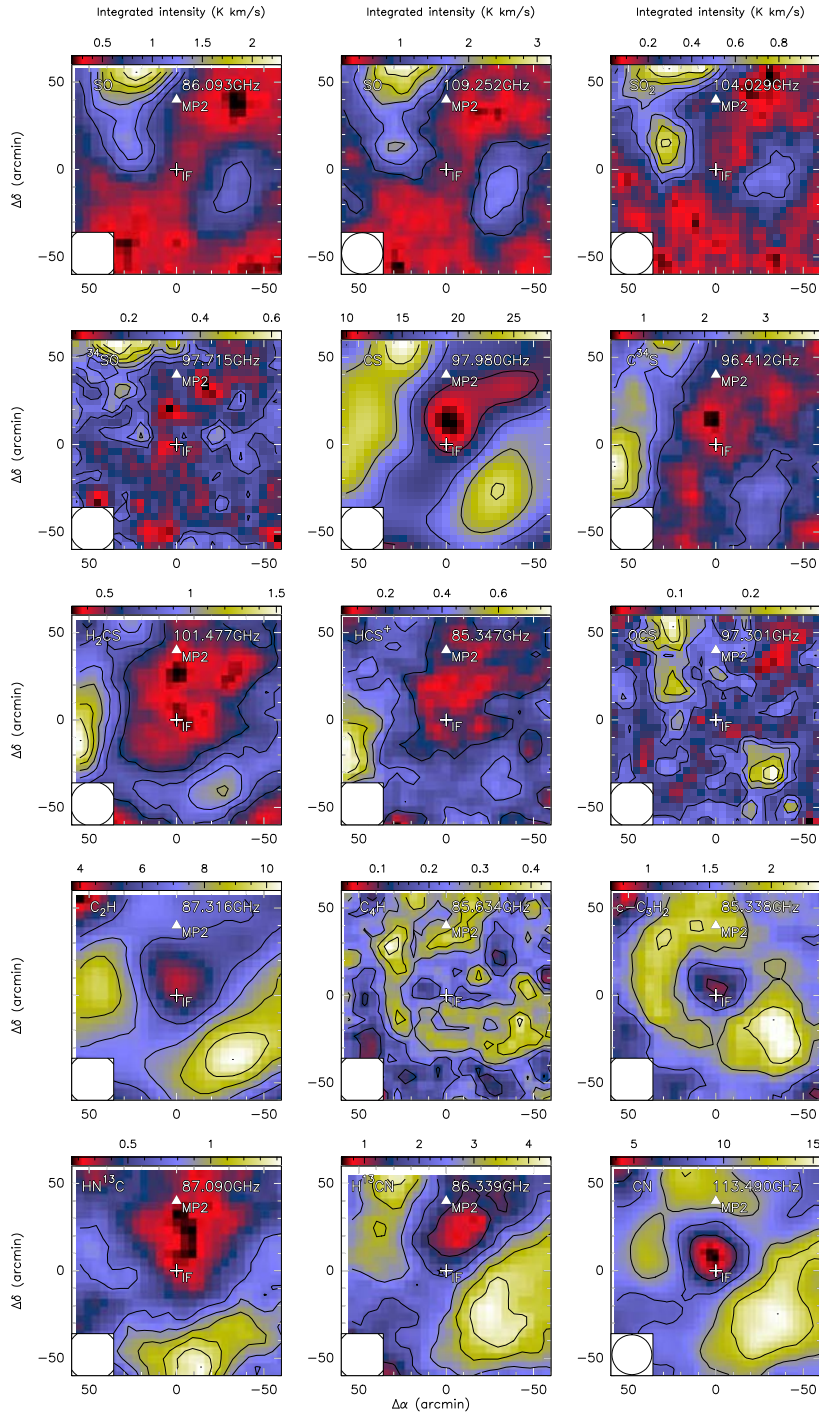
Figure B.40: $2' \times 2'$ OTF maps of several species at 3 mm. The cross marks the IF position, the triangle indicates the MP2 position. The contour levels are 40% to 100%, in steps of 15% of the peak intensity. *Continued in next page.*
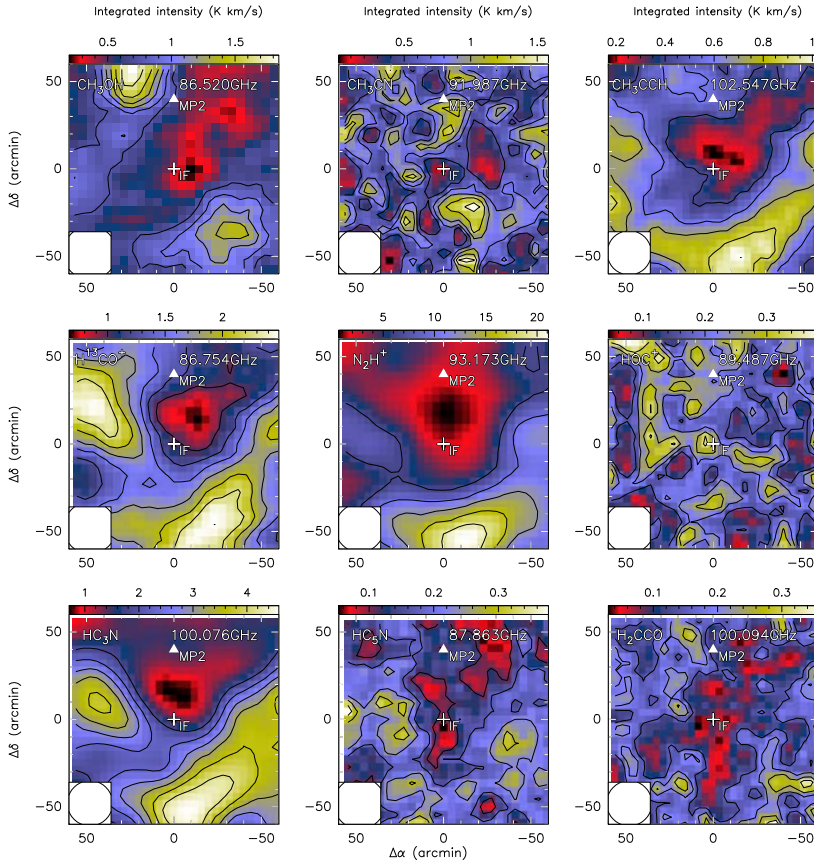
Figure B.41: *Continued from previous page.*
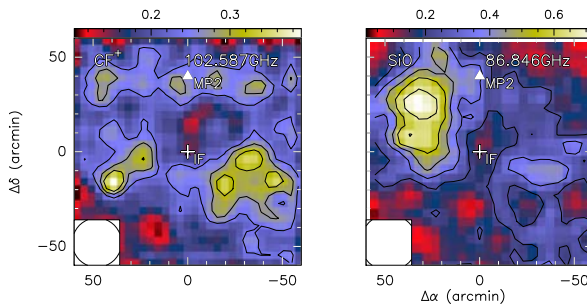
Figure B.42: $2' \times 2'$ OTF maps of the CF$^+$ and SiO molecules. The cross marks the IF position, the triangle indicates the MP2 position. The contour levels are 40% to 100%, in steps of 15% of the peak intensity.
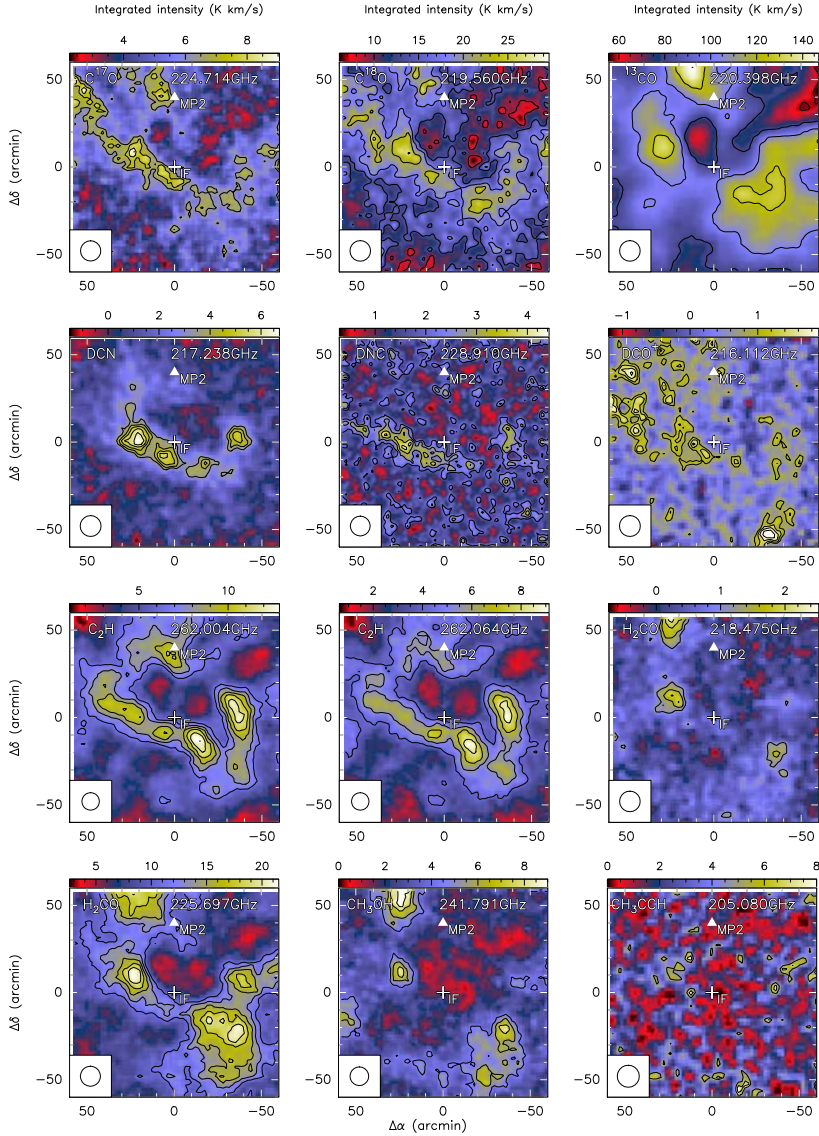
Figure B.43: $2' \times 2'$ OTF maps of several species at 1 mm. The cross marks the IF position, the triangle indicates the MP2 position. The contour levels are 40% to 100%, in steps of 15% of the peak intensity. *Continued in next page.*
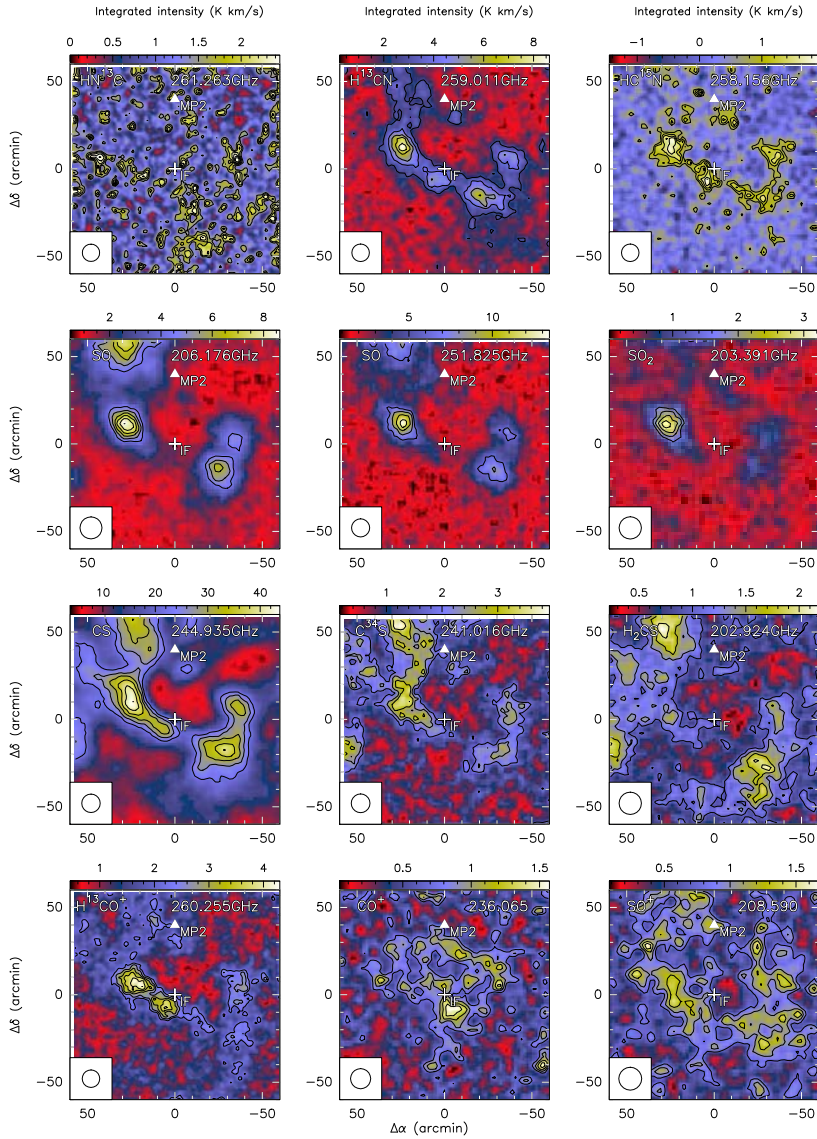
Figure B.44: *Continued from previous page.*
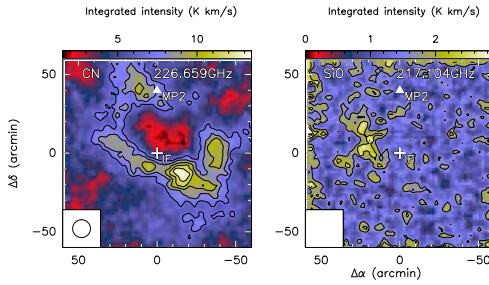
Figure B.45: *Continued from previous page.*
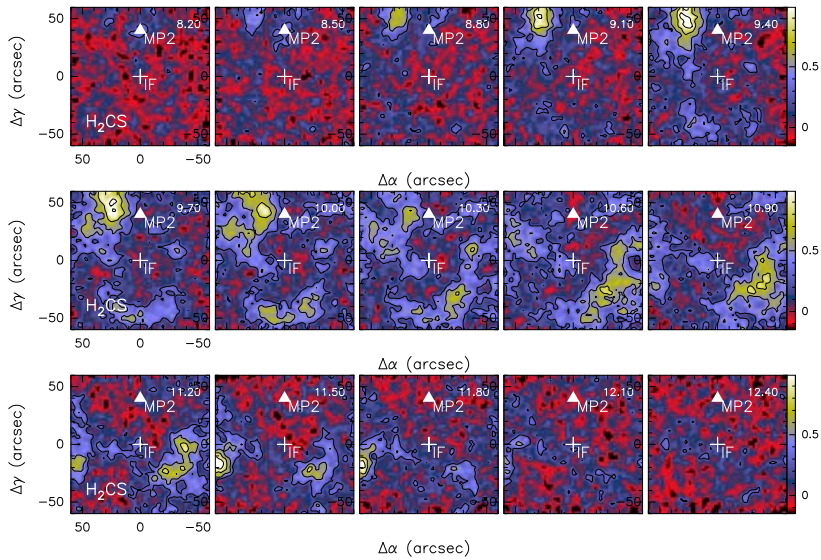
Figure B.46: Channel maps of the H_2CS molecule at 202.924 GHz. The velocities range for the map are from 8.20 to 12.40 km s^{-1} by steps of 0.30 km s^{-1}.
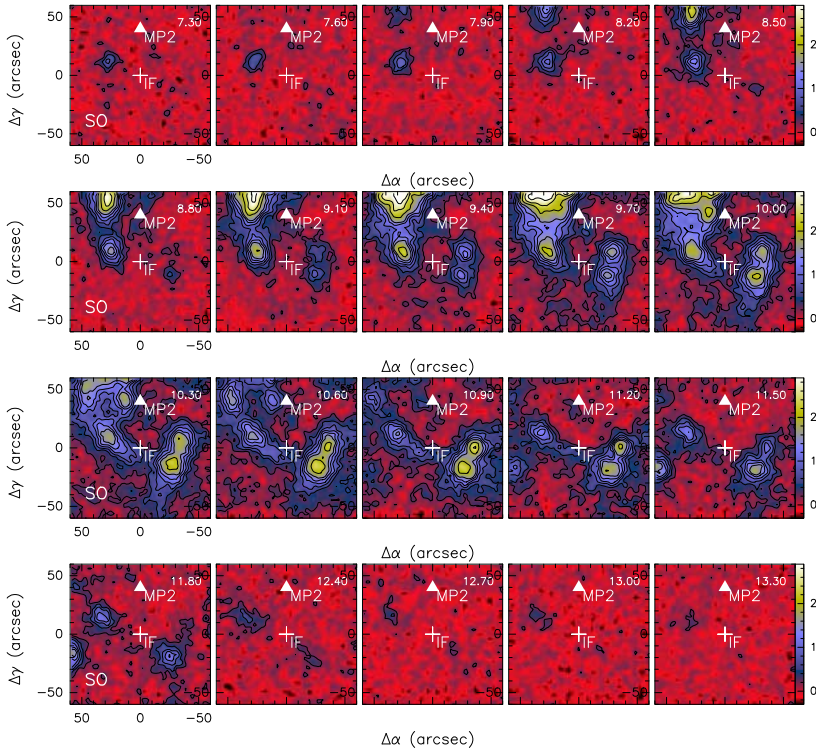
Figure B.47: Channel maps of the SO molecule at 206.176 GHz. The velocities range for the map are from 7.30 to 13.30 km s^{-1} by steps of 0.30 km s^{-1}.
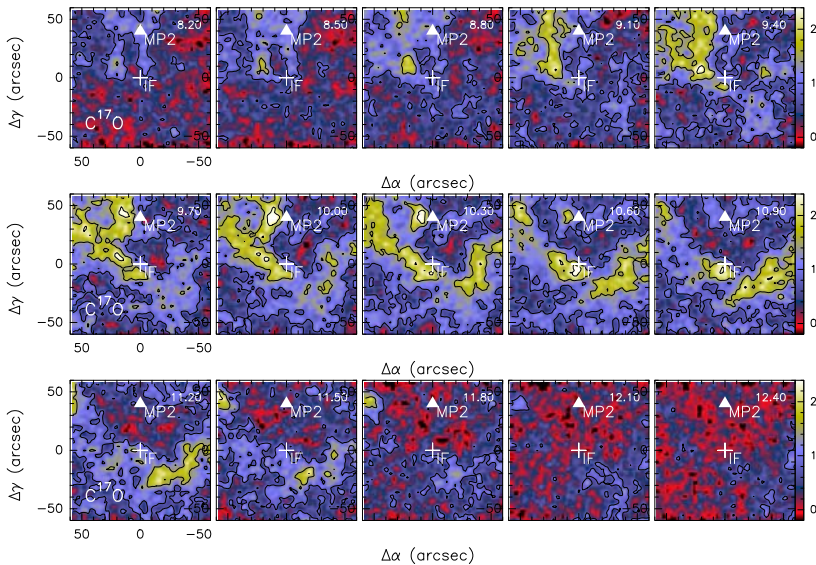
Figure B.48: Channel maps of C^{17}O at 224.714 GHz. The velocities range for the map are from 8.20 to 12.40 km s^{-1} by steps of 0.30 km s^{-1}.
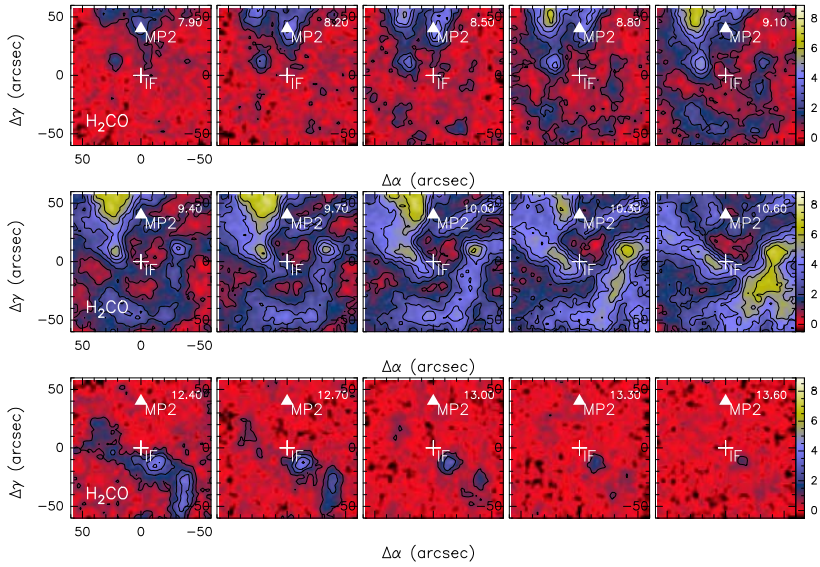
Figure B.49: Channel maps of H_2CO at 225.697 GHz. The velocities range for the map are from 7.90 to 13.60 km s^{-1} by steps of 0.30 km s^{-1}.
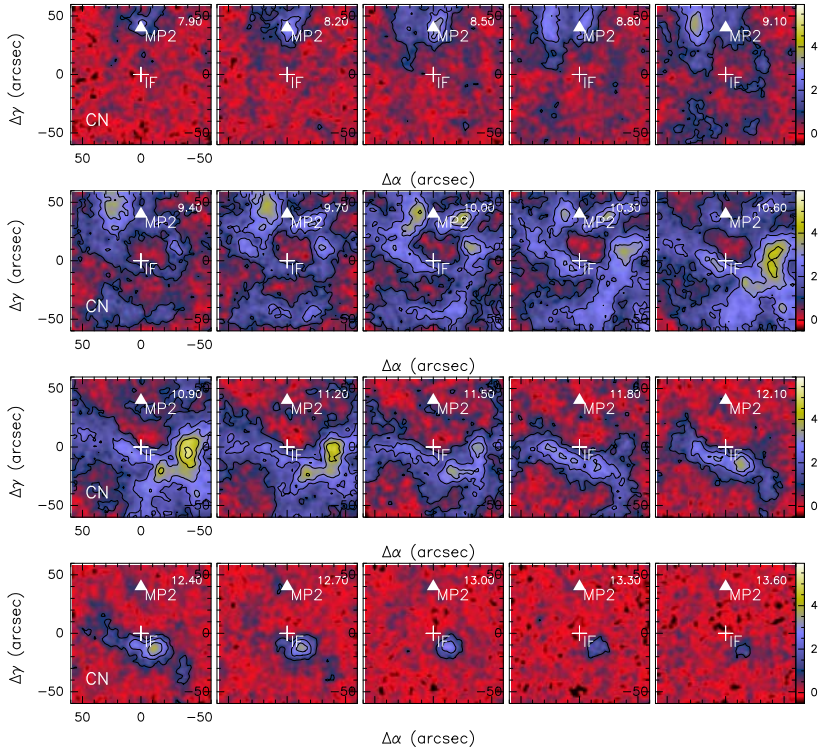
Figure B.50: Channel maps of CN at 226.659 GHz. The velocities range for the map are from 7.90 to 13.60 km s^{-1} by steps of 0.30 km s^{-1}.
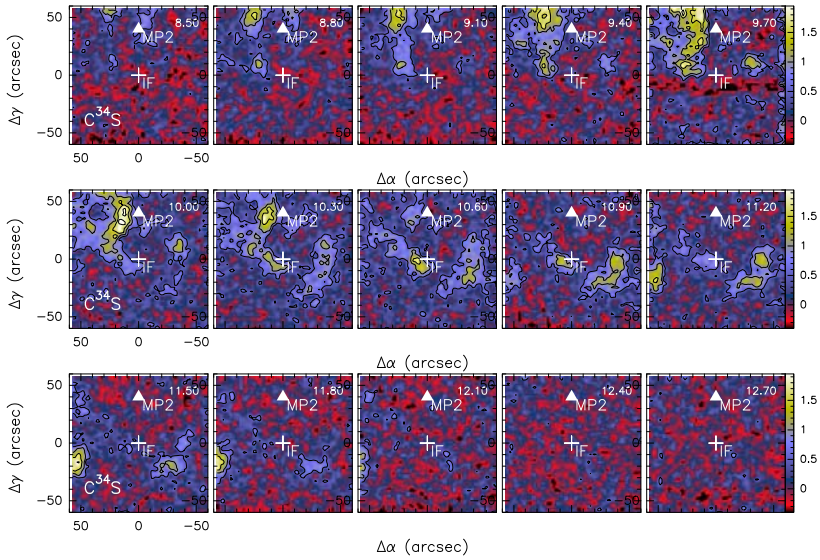
Figure B.51: Channel maps of $C^{34}S$ at 241.016 GHz. The velocities range for the map are from 8.50 to 12.70 km s^{-1} by steps of 0.30 km s^{-1}.
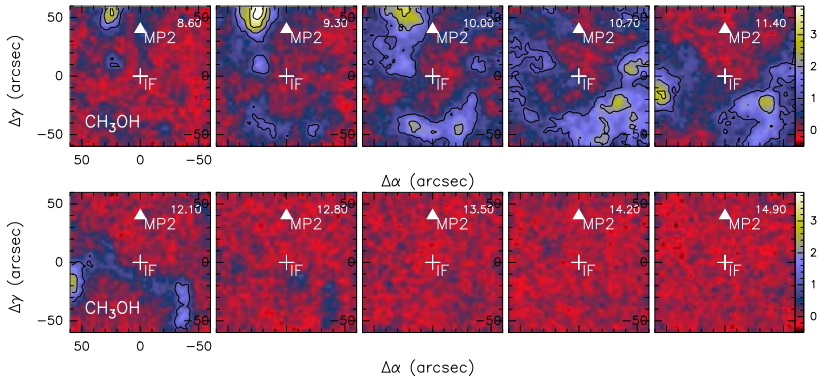
Figure B.52: Channel maps of CH_3OH at 241.791 GHz. The velocities range for the map are from 8.60 to 14.90 km s^{-1} by steps of 0.70 km s^{-1}.
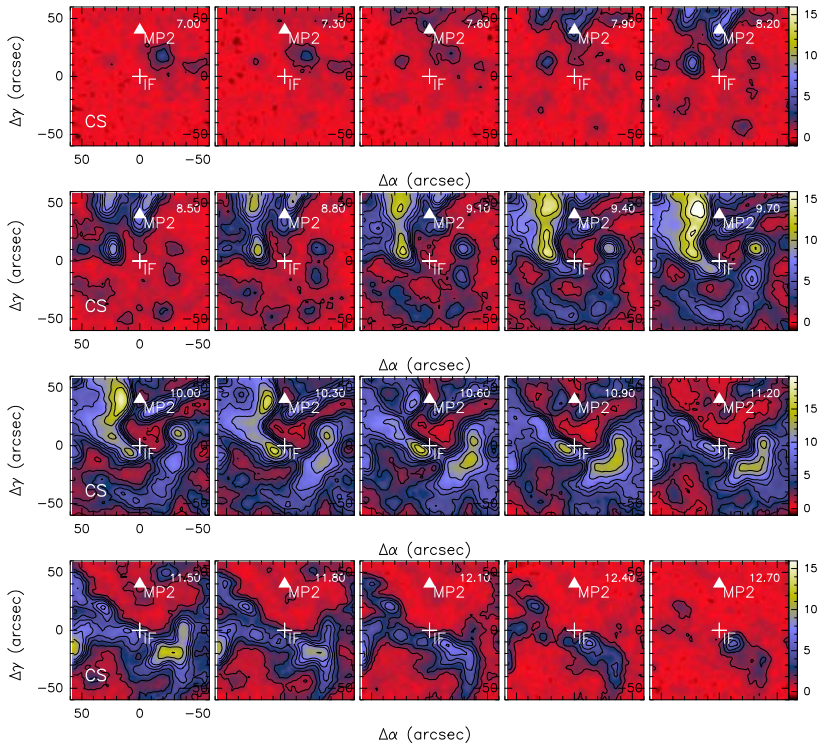
Figure B.53: Channel maps of CS at 244.935 GHz. The velocities range for the map are from 12.70 km s^{-1} by steps of 0.70 km s^{-1}.
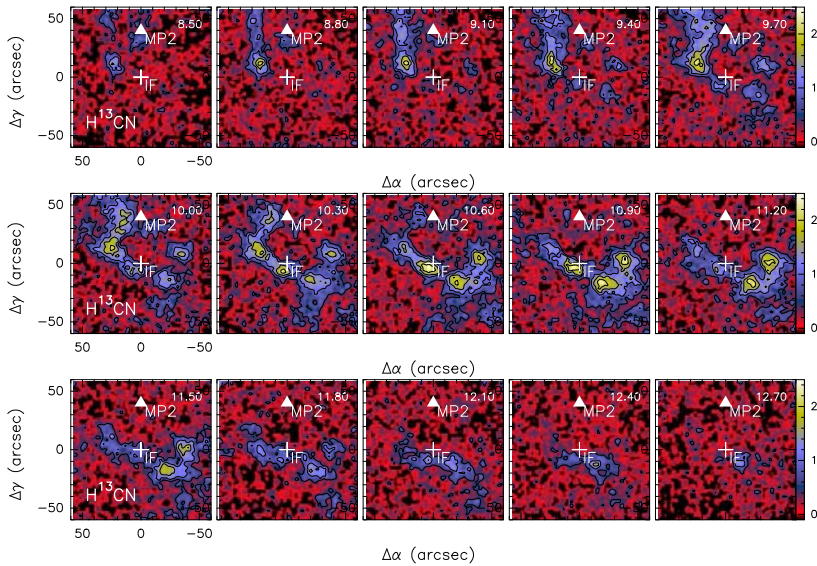
Figure B.54: Channel maps of H^{13}CN at 259.011 GHz. The velocities range for the map are from 8.50 to 12.70 km s^{-1} by steps of 0.30 km s^{-1}.
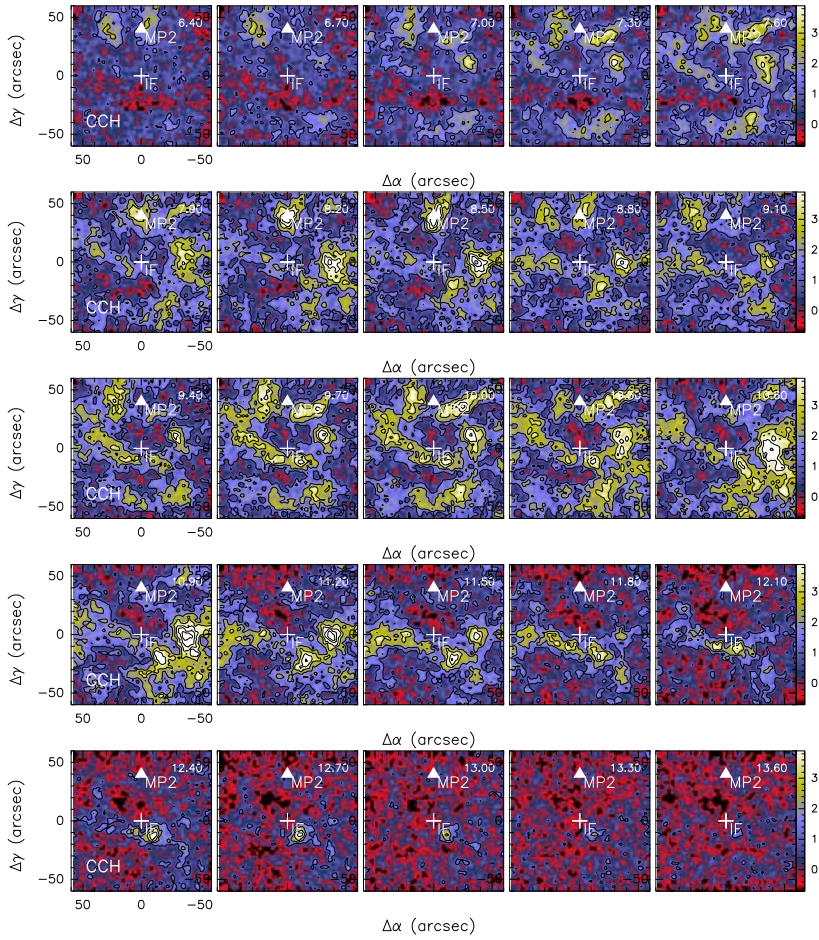
Figure B.55: Channel maps of the C_2H molecules at 262.004 GHz. The velocities range for the map are from 6.40 to 13.60 km s^{-1} by steps of 0.30 km s^{-1}.

B.5   Statistical analysis

Figures B.56 to B.59 show the plots comparing D_v and T_{mb} for the IF (Figures B.56 to B.57) and the MP2 (Figures B.58 to B.59) position. The different panels indicate different species and velocity ranges or components discussed in Chapter 6. Regarding the intensity, we have considered three ranges depending on the signal-to-noise ratio: *(i)* lines moderately detected with $4 <$S/N< 7 (gray circles), *(ii)* lines well detected with $7 <$S/N< 15 (black circles), and *(iii)* lines clearly detected with S/N> 15 (red circles).
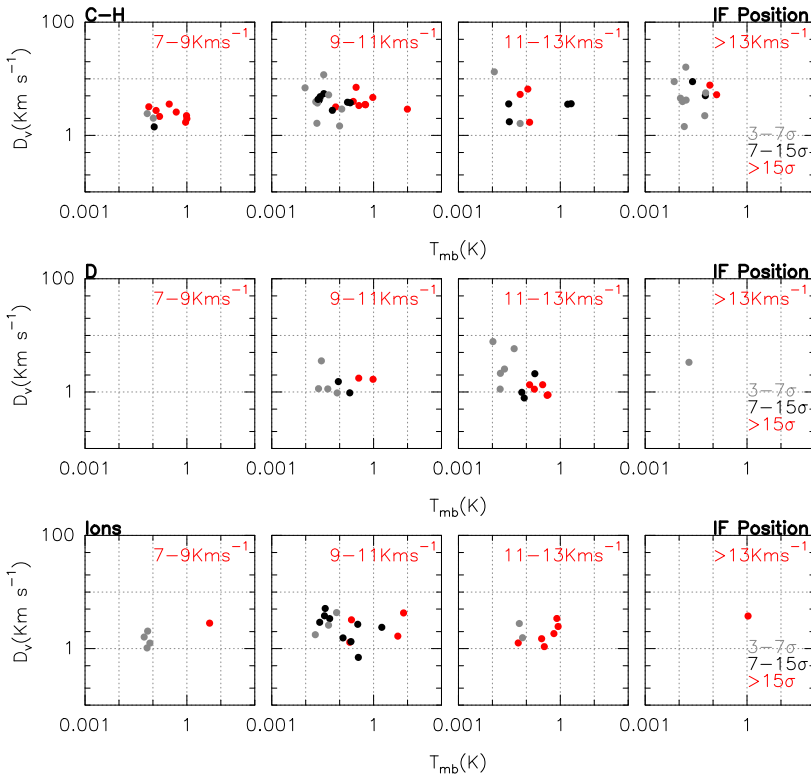
Figure B.56: This figure shows the a comparison between the line width (D_v) and the mail beam temperature (in K) of the detected lines in the IF position. The comparison is done for C–H lines, deuterated molecules and ionic species, form top to bottom. The panels are separated in 4 velocity ranges; 7–9 km s^{-1}, 9–11 km s^{-1}, 11–13 km s^{-1} and > 13 km s^{-1}, from left to right. The gray circle mark the lines with σ between 3 and 7, the black circle with σ between 7 and 15, and the red ones the lines with $\sigma > 15$.
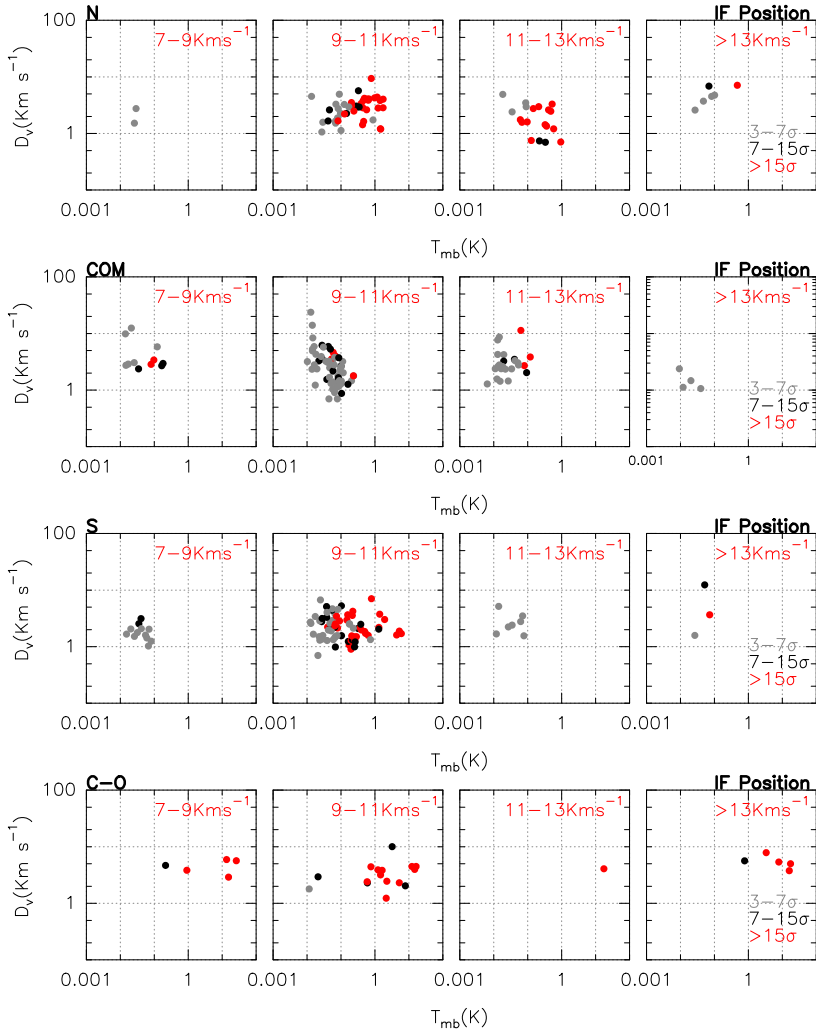
Figure B.57: This figure shows the a comparison between the line width (D_v) and the mail beam temperature (in K) of the detected lines in the IF position. The comparison is done for nitrogenated molecules, complex molecules, sulphurated molecules and C–O lines, form top to bottom. The panels are separated in 4 velocity ranges; 7–9 km s^{-1}, 9–11 km s^{-1}, 11–13 km s^{-1} and > 13 km s^{-1}, from left to right. The gray circle mark the lines with σ between 3 and 7, the black circle with σ between 7 and 15, and the red ones the lines with $\sigma > 15$.
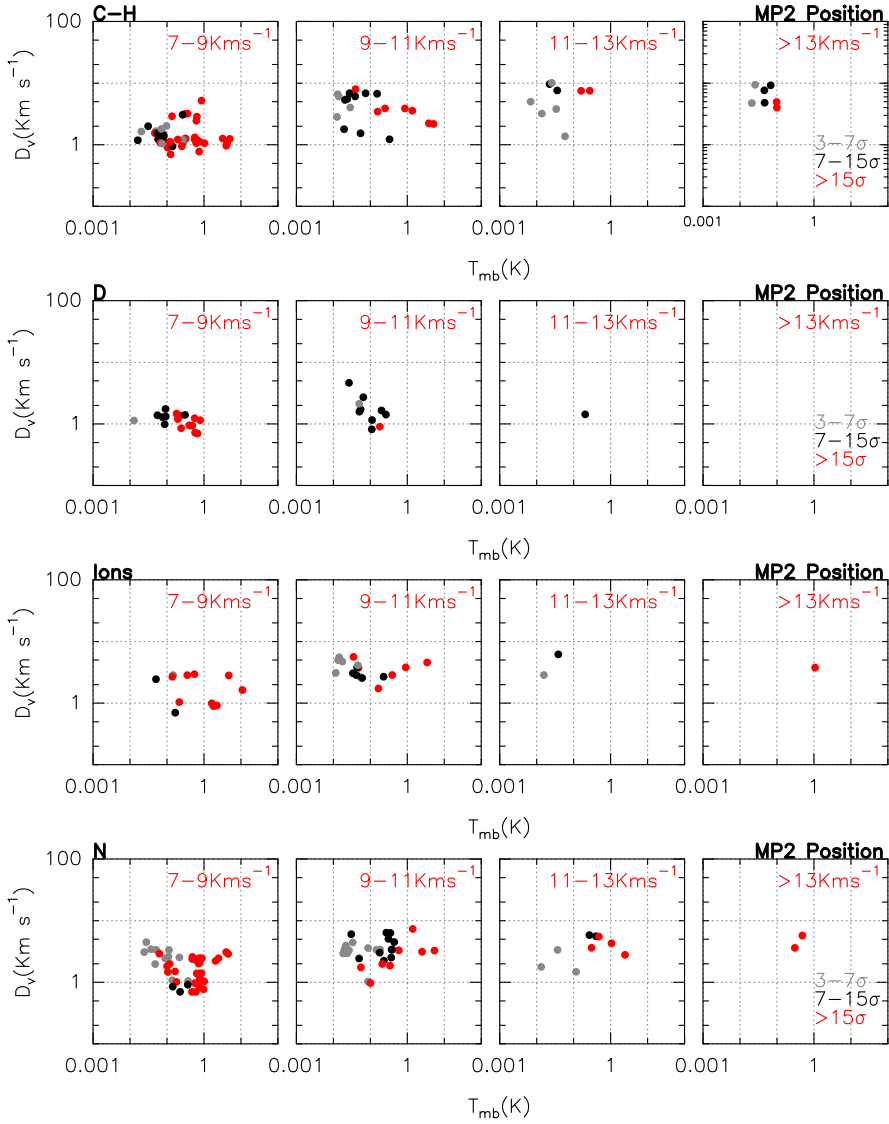
Figure B.58: This figure shows the a comparison between the line width (D_v) and the mail beam temperature (in K) of the detected lines in the MP2 position. The comparison is done for C–H lines, deuterated molecules, ionic species and nitrogenated molecules, form top to bottom. The panels are separated in 4 velocity ranges; 7–9 km s^{-1}, 9–11 km s^{-1}, 11–13 km s^{-1} and > 13 km s^{-1}, from left to right. The gray circle mark the lines with σ between 3 and 7, the black circle with σ between 7 and 15, and the red ones the lines with $\sigma > 15$.
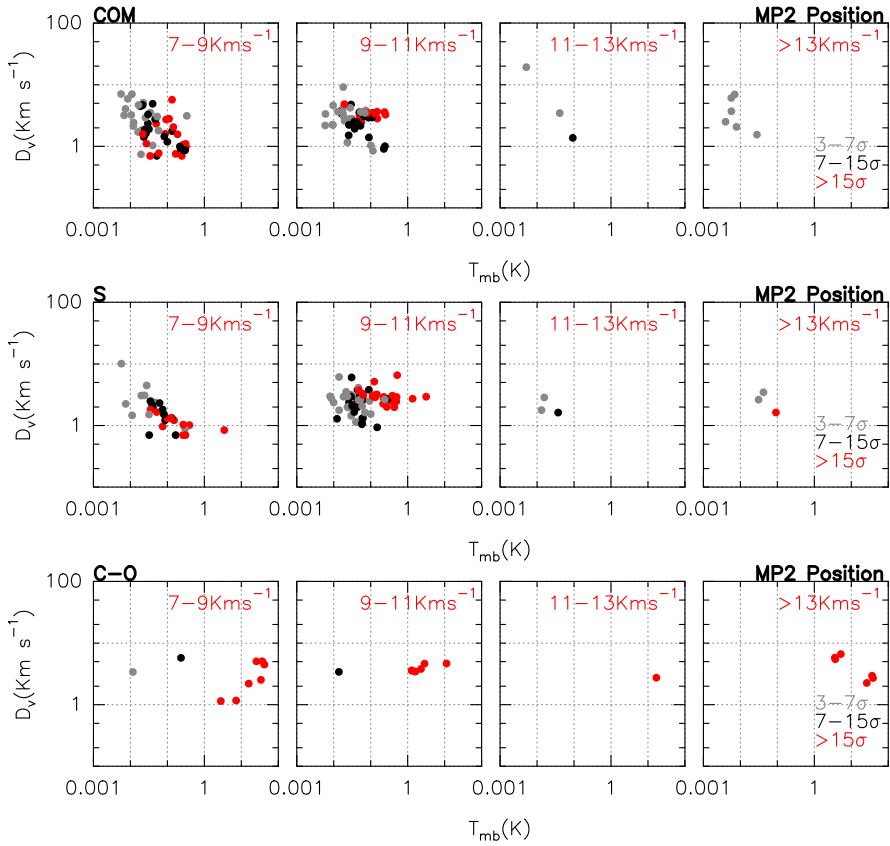
Figure B.59: This figure shows the a comparison between the line width (D_v) and the mail beam temperature (in K) of the detected lines in the MP2 position. The comparison is done for complex molecules, sulphurated molecules and C–O lines, form top to bottom. The panels are separated in 4 velocity ranges; 7–9 km s^{-1}, 9–11 km s^{-1}, 11–13 km s^{-1} and > 13 km s^{-1}, from left to right. The gray circle mark the lines with σ between 3 and 7, the black circle with σ between 7 and 15, and the red ones the lines with $\sigma > 15$.

B.6 Rotational diagrams

Figures B.60 to B.65 show the rotational diagram for the IF (Figures B.60 to B.62) and the MP2 (Figures B.63 to B.65) position. Rotational diagrams for most of the observed lines were performed using a FORTRAN program (called ColDens.f) developed by Sanchez-Monge (2011). For the ^{13}C and ^{18}O isotopologues we assumed $[^{12}C]/[^{13}C]=50$ (Savage et al. 2002; Ginard et al. 2012) and $[^{16}O]/[^{18}O]=500^{i}$ (Wilson & Rood 1994; Ginard et al. 2012).
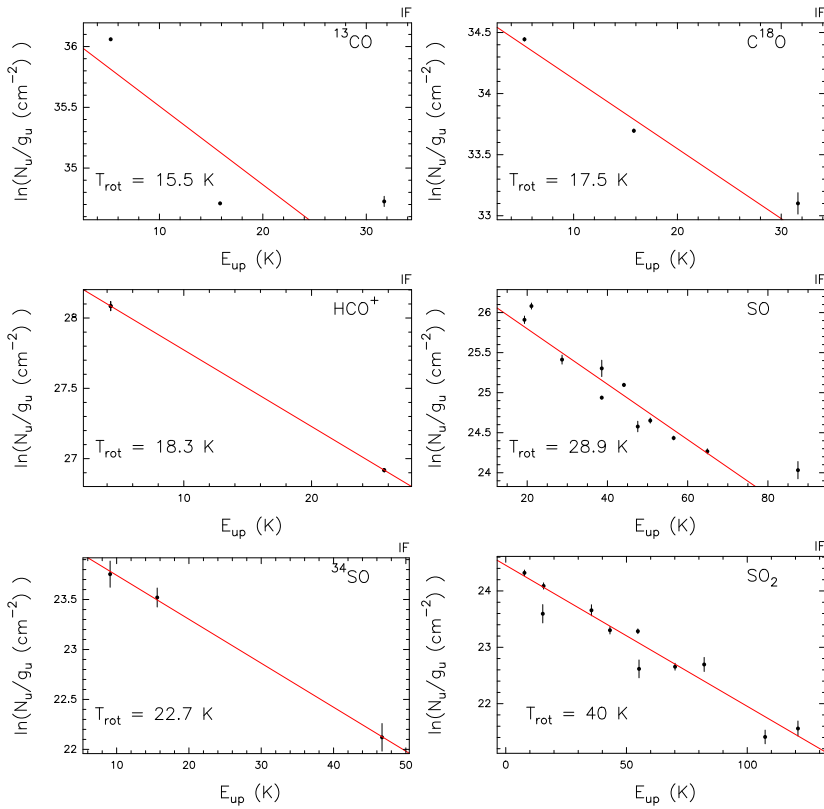
Figure B.60: Rotational Diagrams for several species in the IF position. *Continued in next page.*

---

[i]The values of the $[^{12}C]/[^{13}C]$ and $[^{16}O]/[^{18}O]$ ratios correspond to the galactocentric distance of Mon R2, i. e., $\sim$9 Kpc.
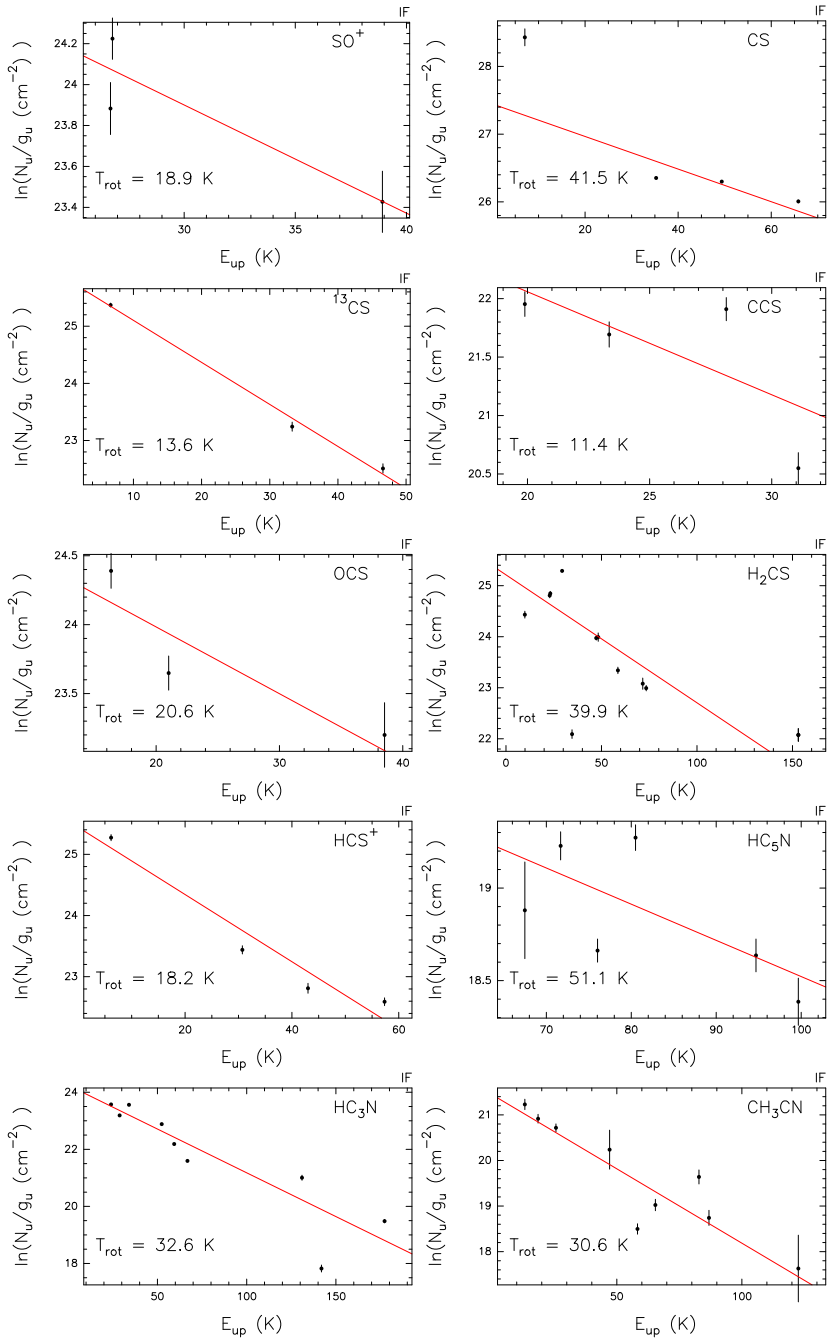
Figure B.61: *Continued from previous page.*
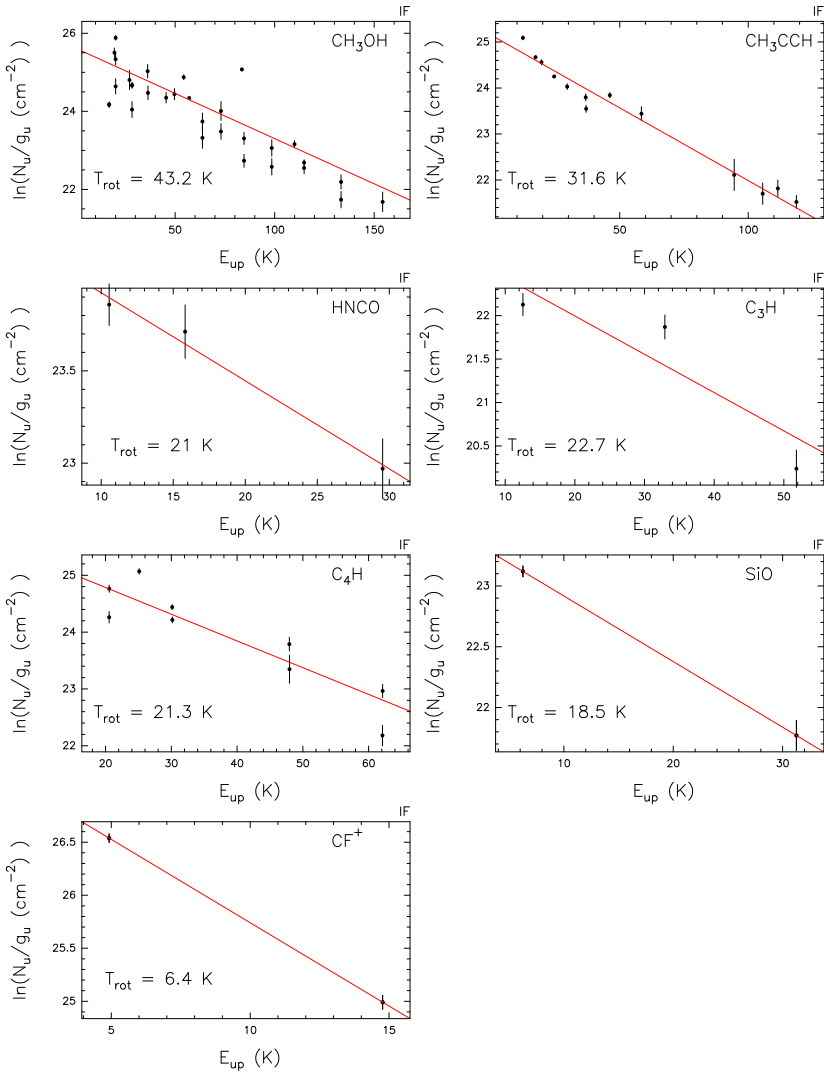
Figure B.62: *Continued from previous page.*
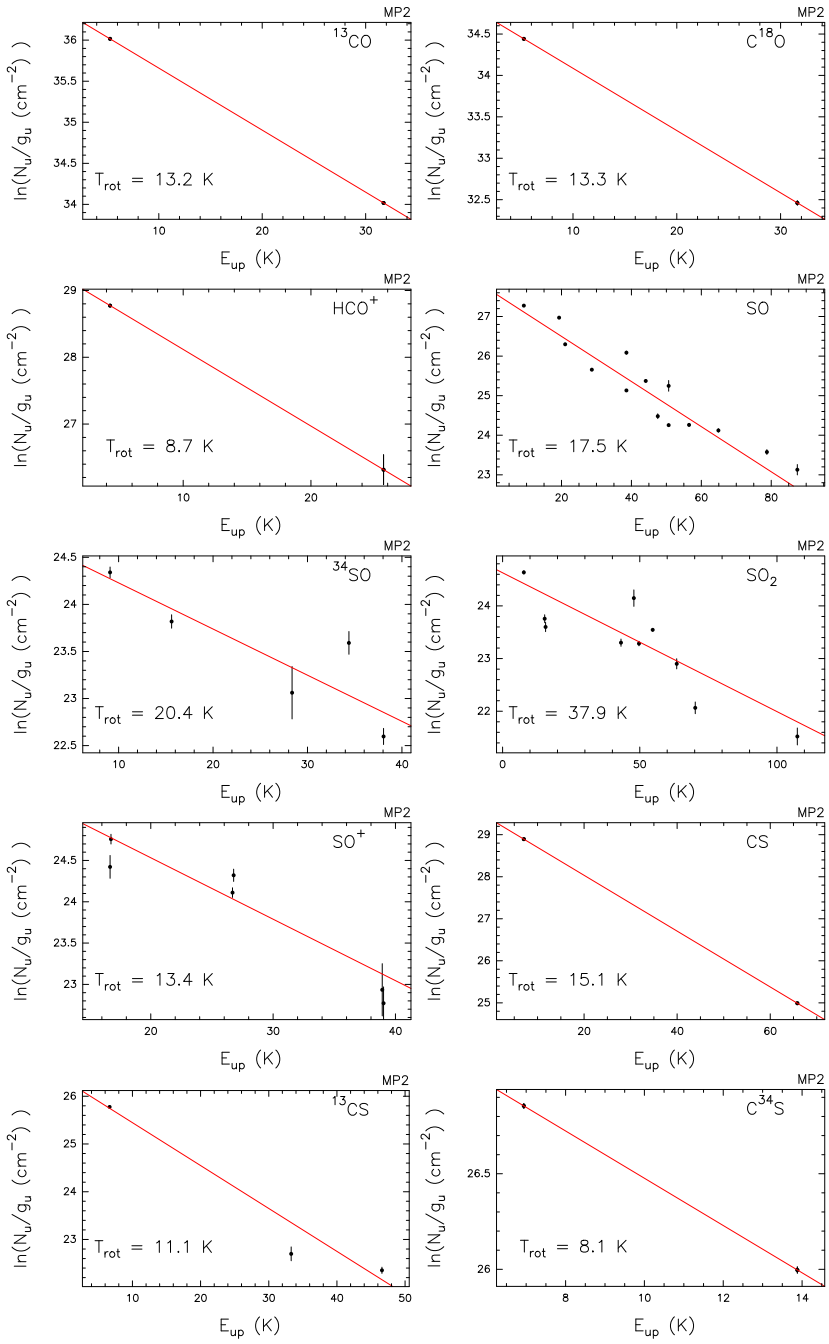
Figure B.63: Rotational Diagrams for several species in the MP2 position. *Continued in next page.*
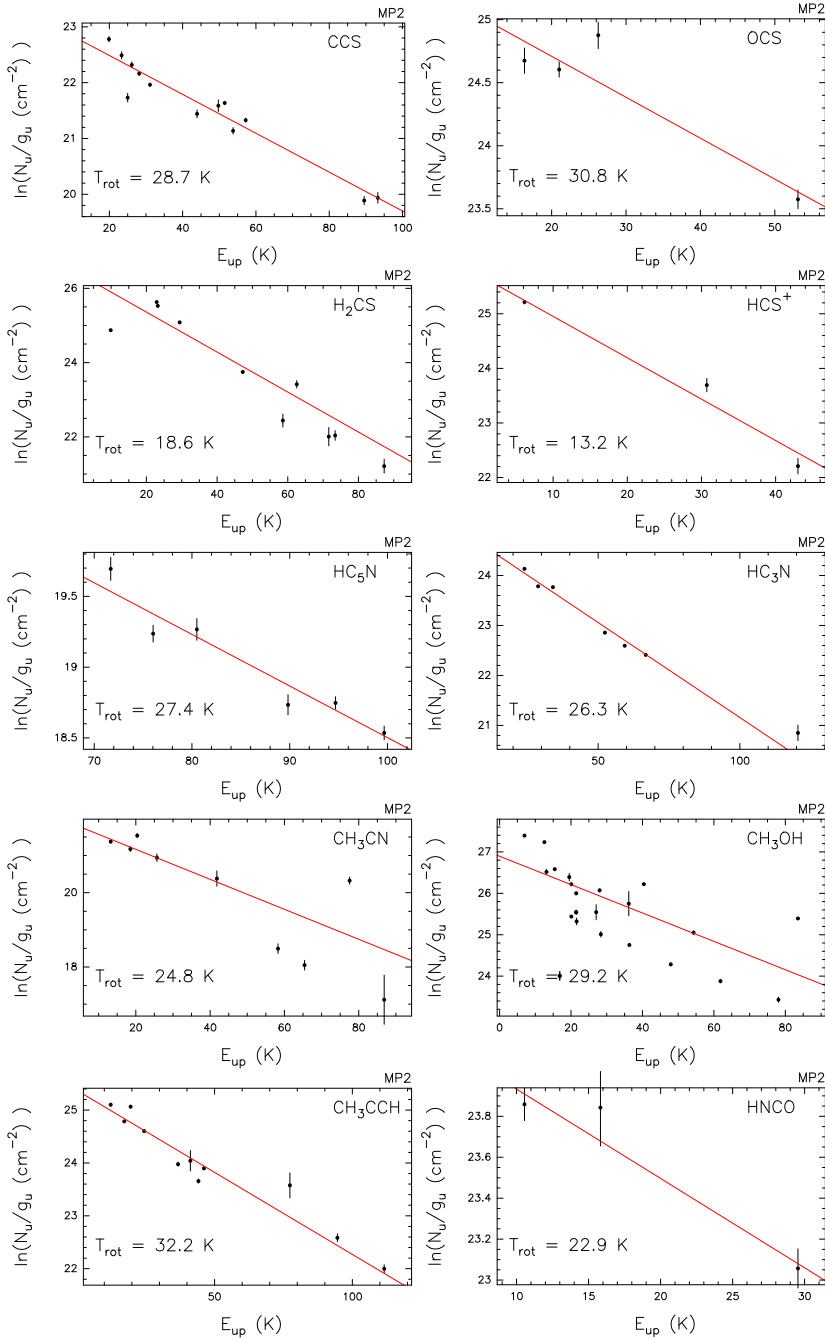
Figure B.64: *Continued from previous page.*
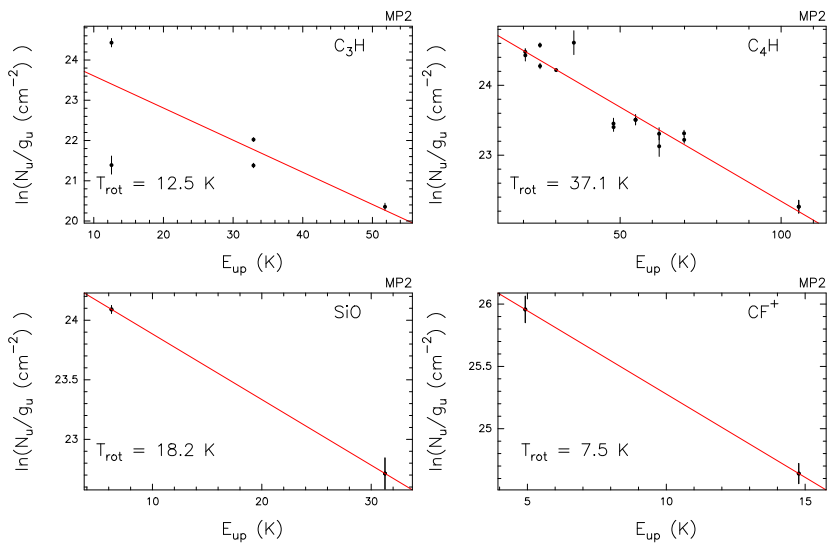
Figure B.65: *Continued from previous page.*

C

DEUTERATION: TABLES & FIGURES

This appendix includes the observational parameters, Gaussian fits and the observed spectral in wich is based the Chapter 7.

Contents

C.1   Deuterium chemistry: Gaussian fits

This section present the Tables corresponding to Chapter 7. The Table C.1 lists the summarize the observational parameters for the deuterated molecules and their corresponding hydrogenated species. The Table indicates the lines frequencies, the beam size (HPBW), the beam efficiency corresponding to the line frequency (B_{eff}), the rms, and the original and fixed resolution. Tables C.2–C.5 lists the Gaussian fits in the IF and MP2 position for the deuterated and hydrogenated molecules. The the tables list the following parameters for both position: specie, transition, frequency, beam size (HPBW), area (in K km s^{-1}), line velocity (in km s^{-1}), line width (in km s^{-1}) and main beam temperature (in K).

C.2   Deuterium chemistry: Observed spectra

This section present the Figures corresponding to Chapter 7. Figures from C.1 to C.12 present all the spectra of the hydrogenated (Figures. C.1–C.8) and deuterated (Figures. C.9–C.12) species toward the IF and MP2 positions. In the Figures, the blue dashed lines show the velocity source, 10km s^{-1}. While the red dashed lines mark different transitions present in the Figures.

Table C.1: Observational parameters. [a]Observing Modes: on the fly (OTF), single pointing (SP); [b]Original resolution; [c] rms of the spectra for the smoothed resolution of 0.65 km s^{-1}.

Species	Freq (MHz)	HPBW ($''$)	B_{eff}	Position	OM[a]	Res[b] (km s^{-1})	rms (mK)	rms[c] (mK)
C_2D	144.24193	16	0.74	IF & MP2	SP	0.40	6	4
	144.24305	16	0.74	IF & MP2	SP	0.40	6	4
	144.29672	16	0.74	IF & MP2	SP	0.40	8	6
	144.29766	16	0.74	IF & MP2	SP	0.40	8	6
	216.37332	11	0.63	MAP	OTF	0.50	56	47
	216.42876	11	0.63	MAP	OTF	0.50	56	44
	216.43034	11	0.63	MAP	OTF	0.50	56	45
	216.43126	11	0.63	MAP	OTF	0.50	56	45
DCN	144.82682	16	0.74	IF & MP2	SP	0.40	8	7
	144.82800	16	0.74	IF & MP2	SP	0.40	8	7
	144.83033	16	0.74	IF & MP2	SP	0.40	8	7
	217.23830	11	0.63	MAP	OTF	0.25	64	39
DNC	152.60974	16	0.74	IF & MP2	SP	0.38	7	5
	228.91048	11	0.60	MAP	OTF	0.25	18	14
DCO^+	144.07728	16	0.74	IF & MP2	SP	0.40	10	7
	216.11258	11	0.63	MAP	OTF	0.25	65	43
D_2CO	110.83780	29	0.78	IF & MP2	SP	0.54	14	12
HDCO	134.28483	16	0.78	IF & MP2	SP	0.43	4	3
	256.58553	9	0.53	MAP	OTF	0.25	16	10

Table C.1 – *Continued from previous page*

Species	Freq (MHz)	HPBW ($''$)	B_{eff}	Position	OM[a]	Res[b] (km s^{-1})	*rms* (mK)	*rms*[c] (mK)
	257.74870	9	0.53	MAP	OTF	0.25	17	8
	268.29056	9	0.53	IF & MP2	SP	0.25	23	18
NH_2D	85.92627	29	0.81	IF & MP2	SP	0.65	4	4
N_2D^+	154.21700	16	0.74	IF & MP2	SP	0.38	6	5
	231.32182	9	0.58	IF & MP2	SP	0.25	30	20
C_2H	87.31692	29	0.81	IF & MP2	SP	0.25	37	28
	87.32862	29	0.81	IF & MP2	SP	0.25	26	16
	87.40198	29	0.81	IF & MP2	SP	0.25	33	26
	87.40735	29	0.81	IF & MP2	SP	0.25	25	15
	262.00426	9	0.53	MAP	OTF	0.25	99	65
	262.00640	9	0.53	MAP	OTF	0.25	99	65
	262.06484	9	0.53	MAP	OTF	0.25	123	95
	262.06733	9	0.53	MAP	OTF	0.25	123	95
	262.20843	9	0.53	MAP	OTF	0.25	130	58
$H^{13}CN$	86.33876	29	0.81	IF & MP2	SP	0.65	5	5
	86.34018	29	0.81	IF & MP2	SP	0.65	5	5
	86.34227	29	0.81	IF & MP2	SP	0.65	5	5
	259.01182	9	0.53	MAP	OTF	0.25	42	25
$HC^{15}N$	86.05496	29	0.81	IF & MP2	SP	0.65	6	6
	258.15699	9	0.53	MAP	OTF	0.25	67	39
HCN	88.63160	29	0.81	IF & MP2	SP	0.65	9	9

Table C.1 – *Continued from previous page*

Species	Freq (MHz)	HPBW ($''$)	B_{eff}	Position	OM[a]	Res[b] (km s^{-1})	*rms* (mK)	*rms*[c] (mK)
	265.88704	9	0.53	IF & MP2	SP	0.25	62	35
HNC	90.66356	29	0.81	IF & MP2	SP	0.65	5	5
	271.98114	9	0.53	IF & MP2	SP	0.21	148	105
HN^{13}C	87.09082	29	0.81	IF & MP2	SP	0.65	5	5
	261.26348	9	0.53	MAP	OTF	0.25	40	26
H^{15}NC	88.86571	29	0.81	IF & MP2	SP	0.65	5	5
	266.58780	9	0.53	IF & MP2	SP	0.25	10	6
HCO^{+}	89.18852	29	0.81	IF & MP2	SP	0.65	6	6
	267.55752	9	0.53	IF & MP2	SP	0.25	34	29
H^{13}CO^{+}	86.75428	9	0.81	IF & MP2	SP	0.65	5	5
	260.25533	9	0.53	MAP	OTF	0.25	55	33
HC^{18}O^{+}	85.16223	29	0.81	IF & MP2	SP	0.65	4	4
	255.48021	9	0.63	MAP	OTF	0.25	14	8
H$_2$CO	145.60294	16	0.74	IF & MP2	SP	0.40	10	7
	211.21146	11	0.63	MAP	OTF	0.25	77	46
	218.22219	11	0.63	MAP	OTF	0.25	73	46
	218.47563	11	0.63	MAP	OTF	0.25	68	45
	218.76006	11	0.63	MAP	OTF	0.25	76	47
	225.69777	11	0.63	MAP	OTF	0.25	95	63
H$_2{}^{13}$CO	96.37575	29	0.81	IF & MP2	SP	0.60	4	4
	141.98374	16	0.63	IF & MP2	SP	0.40	14	10

Continued on next page

Table C.1 – *Continued from previous page*

Species	Freq (MHz)	HPBW ($''$)	B_{eff}	Position	OM[a]	Res[b] (km s^{-1})	*rms* (mK)	*rms*[c] (mK)
	212.81118	11	0.63	MAP	OTF	0.25	107	65
	213.29356	11	0.63	MAP	OTF	0.25	121	74
	219.90852	11	0.63	MAP	OTF	0.25	108	66
N_2H^+	93.17188	29	0.81	IF & MP2	SP	0.60	4	4
	93.17370	29	0.81	IF & MP2	SP	0.60	4	4
	93.17613	29	0.81	IF & MP2	SP	0.60	4	4

Table C.2: Gaussian fit parameters of the deuterated molecules at the IF position. [a] Area calculated between two velocities. [b] Upper limit of the area, assuming a Gaussian profile. [*] Spectrum obtained by convolving the map with a Gaussian to obtain the same spatial resolution of the lower-frequency transition.

IF Species	Trans	Freq (MHz)	HPBW (″)	Area (K km s^{-1})	V (km s^{-1})	Width (km s^{-1})	T_{MB} (K)
C$_2$D	N= 2–1, J= 5/2–3/2, F= 5/2–3/2	144.24305	16	0.05 ± 0.01^a	9.52 ± 0.05	7.3–11	
	N= 2–1, J= 3/2–1/2, F= 5/2–3/2	144.29672	16	$< 0.024^b$	$rms =8$ mK	$W =1$	N_c=2.5
	N= 3–2, J= 7/2–5/2, F= 7/2–5/2	216.37332	16*	$< 0.147^b$	$rms =56$ mK	$W =1$	N_c=4.0
	N= 3–2, J= 5/2–3/2, F= 3/2–3/2	216.43034	16*	$< 0.225^b$	$rms =56$ mK	$W =1$	N_c=4.0
DCN	J= 2–1, F= 1–0	144.82682	16	0.07 ± 0.01	11.26 ± 0.05	0.78 ± 0.09	0.09
	J= 2–1, F= 1–0			0.18 ± 0.01	12.47 ± 0.04	1.34 ± 0.11	0.13
	J= 2–1, F= 2–1	144.82800	16	0.70 ± 0.02	10.82 ± 0.02	1.76 ± 0.06	0.37
	J= 2–1, F= 2–1			0.44 ± 0.01	12.43 ± 0.02	1.34 ± 0.04	0.30
	J= 2–1, F= 1–1	144.83033	16	0.05 ± 0.02	10.81 ± 0.20	1.13 ± 0.53	0.05
	J= 2–1, F= 1–1			0.08 ± 0.02	12.39 ± 0.11	0.99 ± 0.36	0.07
	J= 3–2, F= 2–1	217.23830	16*	1.73 ± 0.13	10.88 ± 0.05	1.68 ± 0.17	0.97
	J= 3–2, F= 2–1			0.38 ± 0.06	12.22 ± 0.07	0.87 ± 0.20	0.41
DNC	J= 2–1	152.60974	16	0.03 ± 0.01	10.60 ± 0.15	1.15 ± 0.24	0.02
	J= 2–1			0.21 ± 0.01	12.14 ± 0.02	1.12 ± 0.06	0.17
	J= 3–2	228.91048	16*	0.09 ± 0.01	10.63 ± 0.07	0.96 ± 0.17	0.09
	J= 3–2			0.41 ± 0.02	12.11 ± 0.02	0.89 ± 0.04	0.44
DCO$^+$	J= 2–1	144.07728	16	0.15 ± 0.02	10.62 ± 0.07	1.53 ± 0.23	0.09
	J= 2–1			0.27 ± 0.03	12.34 ± 0.8	5.83 ± 0.86	0.05

IF Species	Trans	Freq (MHz)	HPBW (″)	Area (K km s^{-1})	V (km s^{-1})	Width (km s^{-1})	$T_{\rm MB}$ (K)
	J= 3–2	216.11258	16*	0.40 ± 0.05	10.75 ± 0.07	1.16 ± 0.17	0.32
D$_2$CO	2(1,2)–1(1,1)	110.83783	29	$< 0.530^b$	rms =143 mK	W =1.5	N_c=4.6
	2(1,2)–1(1,1)			$< 0.335^b$	rms =143 mK	W =1.5	N_c=1.9
HDCO	2(1,1)–1(1,0)	134.28483	16	0.03 ± 0.01	9.86 ± 0.09	1.12 ± 0.21	0.02
	2(1,1)–1(1,0)			0.04 ± 0.01	11.85 ± 0.08	1.50 ± 0.19	0.02
	4(0,4)–3(0,3)	256.58553	9	$< 0.148^b$	rms =16 mK	W =1	N_c=4.0
	4(0,4)–3(0,3)			$< 0.375^b$	rms =16 mK	W =1	N_c=4.0
	4(1,3)–3(1,2)	268.29256	9	0.15 ± 0.03	11.08 ± 0.25	$2.68 \pm .53$	0.05
NH$_2$D	1(1,1)0s-1(0,1)0a, F=2-1	85.92627	29	0.03 ± 0.01	10.08 ± 0.19	1.49 ± 0.29	0.02
N$_2$D$^+$	J= 2–1	154.21700	16	0.02 ± 0.01	7.88 ± 0.30	1.31 ± 0.52	0.01
	J= 2–1			0.05 ± 0.01	10.57 ± 0.22	2.67 ± 0.90	0.02
	J= 3–2	231.32182	9	$< 0.059^b$	rms =29 mK	W =1	N_c=6.0

Table C.2 – *Continued from previous page*

Table C.3: Gaussian fit parameters of the deuterated molecules at the MP2 position. [a] Area calculated between two velocities. [b] Upper limit of the area, assuming a Gaussian profile. * Spectrum obtained by convolving the map with a Gaussian to obtain the same spatial resolution of the lower-frequency transition.

MP2 Species	Trans	Freq (MHz)	HPBW (")	Area (K km s^{-1})	V (km s^{-1})	Width (km s^{-1})	T_{MB} (K)
C$_2$D	N= 2–1, J= 5/2–3/2, F= 5/2–3/2	144.24305	16	0.13 ± 0.02	8.56 ± 0.044	1.12 ± 0.12	0.11
	N= 2–1, J= 5/2–3/2, F= 5/2–3/2	144.24193	16	0.15 ± 0.01	8.49 ± 0.042	1.20 ± 0.14	0.12
	N= 2–1, J= 5/2–3/2, F= 5/2–3/2			0.04 ± 0.01	10.20 ± 0.118	1.05 ± 0.24	0.04
	N= 2–1, J= 3/2–1/2, F= 5/2–3/2	144.29766	16	0.05 ± 0.01	8.52 ± 0.038	1.03 ± 0.18	0.06
	N= 3–2, J= 7/2–5/2, F= 7/2–5/2	216.37332	16*	0.39 ± 0.07	8.84 ± 0.147	1.70 ± 0.40	0.22
	N= 3–2, J= 5/2–3/2, F= 3/2–1/2	216.42876	16*	0.58 ± 0.09	9.11 ± 0.260	3.29 ± 0.49	0.16
DCN	J= 2–1, F= 1–0	144.82682	16	0.26 ± 0.02	8.59 ± 0.404	1.47 ± 0.06	0.18
	J= 2–1, F= 1–0			0.19 ± 0.03	10.07 ± 0.189	2.71 ± 0.20	0.07
	J= 2–1, F= 2–1	144.82800	16	0.74 ± 0.01	8.54 ± 0.005	1.24 ± 0.02	0.56
	J= 2–1, F= 2–1			0.18 ± 0.01	9.97 ± 0.014	0.91 ± 0.03	0.18
	J= 2–1, F= 1–1	144.83033	16	0.09 ± 0.01	8.66 ± 0.049	0.99 ± 0.08	0.09
	J= 2–1, F= 1–1			0.04 ± 0.01	1.10 ± 0.140	1.27 ± 0.24	0.03
	J= 3–2, F= 2–1	217.23830	16*	0.97 ± 0.06	8.47 ± 0.037	1.15 ± 0.09	0.79
	J= 3–2, F= 2–1			0.40 ± 0.07	10.39 ± 0.117	1.42 ± 0.29	0.27
DNC	J= 2–1	152.60974	16	0.48 ± 0.01	8.44 ± 0.008	0.94 ± 0.03	0.49
	J= 2–1			0.10 ± 0.01	10.02 ± 0.127	1.72 ± 0.37	0.06
	J= 2–1			0.04 ± 0.01	12.35 ± 0.071	0.99 ± 0.20	0.04
	J= 3–2	228.91048	16*	0.45 ± 0.02	8.44 ± 0.015	0.80 ± 0.04	0.53

Table C.3 – *Continued from previous page*

MP2 Species	Trans	Freq (MHz)	HPBW (")	Area (K km s^{-1})	V (km s^{-1})	Width (km s^{-1})	T_{MB} (K)
DCO$^+$	J= 2–1	144.07728	16	0.29 ± 0.02	8.58 ± 0.023	0.90 ± 0.06	0.30
	J= 2–1			0.14 ± 0.01	10.10 ± 0.056	1.30 ± 0.14	0.10
	J= 3–2	216.11258	16*	0.47 ± 0.05	8.36 ± 0.053	0.98 ± 0.12	0.45
	J= 3–2			0.14 ± 0.05	10.05 ± 0.125	0.76 ± 0.28	0.17
D$_2$CO	2(1,2)–1(1,1)	110.83783	29	0.06 ± 0.04	9.29 ± 0.950	3.19 ± 2.28	0.02
				0.04 ± 0.04	11.43 ± 0.334	1.25 ± 0.68	0.03
HDCO	2(1,1)–1(1,0)	134.28483	16	0.10 ± 0.01	8.30 ± 0.020	0.92 ± 0.05	0.11
	2(1,1)–1(1,0)			0.02 ± 0.01	9.62 ± 0.097	0.76 ± 0.18	0.19
	4(0,4)–3(0,3)	256.58553	9	0.40 ± 0.01	8.36 ± 0.077	0.74 ± 0.03	0.51
	4(2,3)–3(2,2)	257.74870	9	0.11 ± 0.01	8.56 ± 0.034	0.68 ± 0.07	0.15
	4(1,3)–3(1,2)	268.29056	9	0.45 ± 0.05	7.86 ± 0.049	0.87 ± 0.05	0.48
NH$_2$D	1(1,1)0s-1(0,1)0a, F=2-1	85.92627	29	0.07 ± 0.01	8.70 ± 0.083	1.81 ± 0.18	0.04
	1(1,1)0s-1(0,1)0a, F=2-1			0.03 ± 0.01	11.11 ± 0.145	1.20 ± 0.56	0.02
N$_2$D$^+$	J= 2–1	154.21700	16	$< 0.011^b$	$rms = 50$ mK	$W = 1$	N_c=2.6
	J= 2–1			$< 0.011^b$	$rms = 50$ mK	$W = 1$	N_c=2.6
	J= 3–2	231.32182	9	$< 0.977^b$	$rms = 50$ mK	$W = 1$	N_c=6.0

Table C.4: Gaussian fit parameters of the hydrogenated molecules at the IF position[a] Area calculated between two velocities. [b] Upper limit of the area, assuming a Gaussian profile. * Spectrum obtained by convolving the map with a Gaussian to obtain the same spatial resolution of the lower-frequency transition.

IF Species	Trans	Freq (MHz)	HPBW (")	Area (K km s^{-1})	V (km s^{-1})	Width (km s^{-1})	T_{MB} (K)
H^{13}CN	J=1–0, F=1–1	86.33876	29	0.30 ± 0.02	10.47 ± 0.06	2.21 ± 0.13	0.13
	J=1–0, F=1–1			0.11 ± 0.02	12.33 ± 0.07	1.58 ± 0.14	0.07
	J=1–0, F=2–1	86.34018	29	0.64 ± 0.03	10.70 ± 0.06	2.49 ± 0.17	0.24
	J=1–0, F=2–1			0.11 ± 0.01	12.45 ± 0.07	0.75 ± 0.36	0.13
	J=1–0, F=0–1	86.34227	29	0.13 ± 0.03	10.80 ± 0.31	2.61 ± 0.67	0.05
	J=1–0, F=0–1			0.07 ± 0.03	14.08 ± 0.63	2.59 ± 0.14	0.03
	J=3–2	259.01182	29*	1.75 ± 0.08	10.64 ± 0.04	2.43 ± 0.14	0.68
	J=3–2			0.11 ± 0.05	12.46 ± 0.07	0.58 ± 0.22	0.17
HC^{15}N	J=1–0	86.05496	29	0.15 ± 0.01	10.11 ± 0.03	1.67 ± 0.07	0.08
	J=1–0			0.12 ± 0.01	11.78 ± 0.05	1.75 ± 0.13	0.06
	J=3–2	258.15699	29*	0.52 ± 0.05	9.41 ± 0.04	1.14 ± 0.15	0.43
HNC	J=1–0	90.66356	29	3.14 ± 0.20	9.93 ± 0.05^a	7.79 ± 0.05	
	J=1–0			2.39 ± 0.04	12.35 ± 0.01^a	2.01 ± 0.06	
	J=3–2	271.98114	9	0.31 ± 0.49	8.45 ± 0.60	0.62 ± 0.89	0.47
	J=3–2			4.50 ± 0.14	10.64 ± 0.03	1.88 ± 0.07	2.25
HN^{13}C	J=1–0	87.09082	29	0.07 ± 0.01	10.04 ± 0.12	1.67 ± 0.27	0.04
	J=1–0			0.17 ± 0.01	12.14 ± 0.05	1.60 ± 0.13	0.10
	J=3–2	261.26348	9	$< 0.09^b$	$rms = 46$ mK	$W = 2$	N_c=6.4

Continued on next page

Table C.4 – *Continued from previous page*

IF Species	Trans	Freq (MHz)	HPBW (")	Area (K km s^{-1})	V (km s^{-1})	Width (km s^{-1})	T_{MB} (K)
	J=3–2		9	$< 0.10^{b}$	$rms =$ 46 mK	$W = 2$	N_c=7.5
H^{15}NC	J=1–0	88.86571	29	0.019 ± 0.01	10.90 ± 0.21	1.23 ± 0.22	0.02
	J=1–0			0.06 ± 0.01	11.90 ± 0.16	2.06 ± 0.39	0.03
	J=3–2	266.58780	9	$< 0.02^{b}$	$rms = 94$ mK	$W = 1$	N_c=5.5
	J=3–2			$< 0.02^{b}$	$rms = 94$ mK	$W = 1$	N_c=5.0
HCO^{+}	J=1–0	89.18852	29	7.46 ± 0.04	9.24 ± 0.05^{a}	3–11	
	J=1–0			4.46 ± 0.01	12.90 ± 0.05^{a}	11–23	
	J=3–2	267.55752	9	6.64 ± 0.04	7.87 ± 0.01	1.82 ± 0.01	3.43
	J=3–2			36.61 ± 0.04	10.47 ± 0.01	2.78 ± 0.01	12.35
H^{13}CO^{+}	J=1–0	86.75428	29	0.77 ± 0.01	10.45 ± 0.03	3.23 ± 0.07	0.22
	J=1–0			0.08 ± 0.01	12.53 ± 0.05	1.26 ± 0.11	0.06
	J=3–2	260.25533	29*	1.79 ± 0.08	10.06 ± 0.04	1.91 ± 0.11	0.88
	J=3–2			0.30 ± 0.07	11.78 ± 0.08	0.99 ± 0.16	0.29
HC^{18}O^{+}	J=1–0	85.16215	29	0.08 ± 0.01	10.31 ± 0.15	2.92 ± 0.30	0.03
	J=3–2	255.48021	9	0.20 ± 0.02	11.56 ± 0.05	1.55 ± 0.16	0.12
H$_2$CO	$2_{0,2}$–$1_{0,1}$	145.60294	16	0.79 ± 0.02	8.00 ± 0.02	2.49 ± 0.05	0.30
	$2_{0,2}$–$1_{0,1}$			2.62 ± 0.06	10.39 ± 0.04	3.29 ± 0.07	0.76
	$3_{1,3}$–$2_{1,2}$	211.21146	16*	9.26 ± 0.11	10.57 ± 0.01	2.63 ± 0.04	3.31
	$3_{0,3}$–$2_{0,2}$	218.22219	16*	0.66 ± 0.11	8.05 ± 0.13	1.91 ± 0.35	0.32
	$3_{0,3}$–$2_{0,2}$			4.14 ± 0.11	10.67 ± 0.03	2.25 ± 0.07	1.73

Continued on next page

Table C.4 – *Continued from previous page*

IF Species	Trans	Freq (MHz)	HPBW (")	Area (K km s^{-1})	V (km s^{-1})	Width (km s^{-1})	T_{MB} (K)
	$3_{2,2}$–$2_{2,1}$	218.47563	16*	1.17 ± 0.08	10.62 ± 0.08	2.51 ± 0.22	0.44
	$3_{2,1}$–$2_{2,0}$	218.76006	16*	0.24 ± 0.38	10.04 ± 0.14	0.96 ± 0.67	0.24
	$3_{2,1}$–$2_{2,0}$			0.66 ± 0.43	11.19 ± 0.70	2.12 ± 1.02	0.29
	$3_{1,2}$–$2_{1,1}$	225.69777	16*	0.97 ± 0.11	8.14 ± 0.08	1.64 ± 0.21	0.56
	$3_{1,2}$–$2_{1,1}$			6.24 ± 0.13	10.66 ± 0.02	2.08 ± 0.05	2.82
H$_2^{13}$CO	$6_{1,5}$–$6_{1,6}$	96.37575	29	$< 0.01^b$	$rms = 3.4$ mK	$W = 2$	N$_c$=3.0
	$6_{1,5}$–$6_{1,6}$			$< 0.01^b$	$rms = 3.4$ mK	$W = 2$	N$_c$=2.7
	$2_{0,2}$–$1_{0,1}$	141.98374	16	$< 0.01^b$	$rms = 10$ mK	$W = 2$	N$_c$=3.0
	$2_{0,2}$–$1_{0,1}$			$< 0.01^b$	$rms = 10$ mK	$W = 2$	N$_c$=2.7
	$3_{0,3}$–$2_{0,2}$	212.81118	16*	$< 0.28^b$	$rms = 107$ mK	$W = 2$	N$_c$=10.5
	$3_{2,1}$–$2_{2,0}$	213.29356	16*	$< 0.31^b$	$rms = 118$ mK	$W = 2$	N$_c$=10.5
	$3_{1,2}$–$2_{1,1}$	219.90852	16*	$< 0.21^b$	$rms = 97$ mK	$W = 2$	N$_c$=7.7
	$3_{1,2}$–$2_{1,1}$			$< 0.23^b$	$rms = 9$ mK	$W = 2$	N$_c$=9.0
N$_2$H$^+$	J=1–0, F=1–1	93.17188	29	1.280 ± 0.01	11.66 ± 0.01	1.84 ± 0.01	0.652
	J=1–0, F=2–1	93.17370	29	2.273 ± 0.01	11.74 ± 0.01	2.46 ± 0.01	0.868
	J=1–0, F=0–1	93.17613	29	0.452 ± 0.01	11.47 ± 0.02	1.50 ± 0.04	0.283

Table C.5: Gaussian fit parameters of the hydrogenated molecules at the MP2 position[a] Area calculated between two velocities. [b] Upper limit of the area, assuming a Gaussian profile. [*] Spectrum obtained by convolving the map with a Gaussian to obtain the same spatial resolution of the lower-frequency transition.

MP2 Species	Trans	Freq (MHz)	HPBW (")	Area (K km s^{-1})	V (km s^{-1})	Width (km s^{-1})	T_{MB} (K)
H^{13}CN	J=1–0, F=1–1	86.33876	29	0.17 ± 0.01	8.14 ± 0.06	1.47 ± 0.13	0.11
	J=1–0, F=1–1			0.45 ± 0.02	9.92 ± 0.06	1.98 ± 0.13	0.21
	J=1–0, F=2–1	86.34018	29	0.27 ± 0.01	8.29 ± 0.03	1.50 ± 0.08	0.17
	J=1–0, F=2–1			0.68 ± 0.02	9.98 ± 0.02	1.87 ± 0.07	0.34
	J=1–0, F=0–1	86.34227	29	0.13 ± 0.05	9.22 ± 0.26	2.43 ± 0.27	0.05
	J=1–0, F=0–1			0.07 ± 0.03	10.56 ± 0.90	3.37 ± 0.80	0.02
	J=3–2	259.01182	29*	0.24 ± 0.03	8.46 ± 0.05	0.85 ± 0.11	0.27
	J=3–2			0.95 ± 0.06	10.01 ± 0.04	1.68 ± 0.14	0.53
HC^{15}N	J=1–0	86.05496	29	0.25 ± 0.01	8.81 ± 0.04	1.99 ± 0.11	0.12
	J=1–0			0.11 ± 0.01	10.24 ± 0.02	0.97 ± 0.12	0.10
	J=3–2	258.15699	29*	0.22 ± 0.05	8.35 ± 0.10	0.89 ± 0.25	0.23
	J=3–2			0.16 ± 0.05	10.14 ± 0.28	1.69 ± 0.67	0.09
HNC	J=1–0	90.66356	29	8.39 ± 0.14	9.06 ± 0.02	3.13 ± 0.06	2.52
	J=1–0			1.18 ± 0.04	13.00 ± 0.05	3.63 ± 0.14	0.30
	J=3–2	271.98114	9	7.59 ± 0.08	8.54 ± 0.01	1.05 ± 0.01	6.77
	J=3–2			1.59 ± 0.12	10.62 ± 0.07	1.87 ± 0.18	0.80
HN^{13}C	J=1–0	87.09082	29	0.20 ± 0.01	8.59 ± 0.08	1.84 ± 0.11	0.10
	J=1–0			0.10 ± 0.01	10.40 ± 0.09	1.75 ± 0.32	0.06

Continued on next page

Table C.5 – *Continued from previous page*

MP2 Species	Trans	Freq (MHz)	HPBW (")	Area (K km s^{-1})	V (km s^{-1})	Width (km s^{-1})	T_{MB} (K)
	J=3–2	261.26348	9	0.32 ± 0.02	8.35 ± 0.02	0.70 ± 0.06	0.43
	J=3–2			0.03 ± 0.01	9.99 ± 0.06	0.36 ± 0.06	0.07
H^{15}NC	J=1–0	88.86571	29	0.07 ± 0.01	9.06 ± 0.15	2.64 ± 0.34	0.03
	J=3–2	266.58780	9	0.13 ± 0.01	8.41 ± 0.03	0.59 ± 0.06	0.20
HCO$^+$	J=1–0	89.18852	29	14.10 ± 0.01	8.72 ± 0.01	2.82 ± 0.02	4.70
	J=1–0			4.32 ± 0.08	13.90 ± 0.04	3.77 ± 0.10	1.08
	J=3–2	267.55752	9	28.89 ± 0.05	8.62 ± 0.01	2.17 ± 0.01	12.50
	J=3–2			7.34 ± 0.07	11.67 ± 0.01	3.24 ± 0.04	2.13
H^{13}CO$^+$	J=1–0	86.75428	29	1.20 ± 0.01	9.22 ± 0.01	2.87 ± 0.03	0.39
	J=1–0			0.31 ± 0.01	10.58 ± 0.02	1.73 ± 0.05	0.17
	J=3–2	260.25533	29*	1.98 ± 0.03	8.45 ± 0.03	0.93 ± 0.02	2.01
	J=3–2			0.30 ± 0.04^a	10.10 ± 0.08	9.5–12	
HC^{18}O$^+$	J=1–0	85.16223	29	0.11 ± 0.01	9.21 ± 0.11	3.06 ± 0.24	0.04
	J=3–2	255.48021	9	0.20 ± 0.01	9.35 ± 0.02	0.86 ± 0.06	0.22
H$_2$CO	$2_{0,2}$–$0_{,1}$	145.60294	16	3.21 ± 0.10	8.82 ± 0.02	1.69 ± 0.06	1.79
	$2_{0,2}$–$0_{,1}$			2.27 ± 0.10	10.67 ± 0.04	1.84 ± 0.11	1.16
	$3_{1,3}$–$2_{1,2}$	211.21146	16*	6.37 ± 0.12	8.51 ± 0.01	1.33 ± 0.03	4.50
	$3_{1,3}$–$2_{1,2}$			8.63 ± 0.23	10.28 ± 0.03	8.30 ± 0.00	2.95
	$3_{0,3}$–$2_{0,2}$	218.22219	16*	3.57 ± 0.06	8.50 ± 0.01	1.37 ± 0.03	2.44
	$3_{0,3}$–$2_{0,2}$			2.49 ± 0.08	10.23 ± 0.02	1.40 ± 0.05	1.67

Continued on next page

Table C.5 – *Continued from previous page*

MP2 Species	Trans	Freq (MHz)	HPBW (")	Area (K km s^{-1})	V (km s^{-1})	Width (km s^{-1})	T_{MB} (K)
	$3_{2,2}$–$2_{2,1}$	218.47563	16*	0.97 ± 0.10	8.59 ± 0.08	1.76 ± 0.23	0.51
	$3_{2,2}$–$2_{2,1}$			0.54 ± 0.06	10.33 ± 0.08	1.21 ± 0.14	0.41
	$3_{2,1}$–$2_{2,0}$	218.76006	16*	0.68 ± 0.08	8.39 ± 0.07	1.33 ± 0.20	0.48
	$3_{2,1}$–$2_{2,0}$			0.51 ± 0.06	10.10 ± 0.06	1.17 ± 0.15	0.41
	$3_{1,2}$–$2_{1,1}$	225.69777	16*	5.17 ± 0.09	8.51 ± 0.01	1.46 ± 0.03	3.33
	$3_{1,2}$–$2_{1,1}$			3.50 ± 0.11	10.29 ± 0.02	1.44 ± 0.06	2.29
H$_2^{13}$CO	$6_{1,5}$–$6_{1,6}$	96.3755	29	$< 0.01^b$	$rms = 5.5$ mK	$W = 5$	N_c=5.30
	$6_{1,5}$–$6_{1,6}$			$< 0.01^b$	$rms = 5.5$ mK	$W = 5$	N_c=3.80
	$2_{0,2}$–$1_{0,1}$	141.98374	16	0.15 ± 0.08^a	9.15	7–12	
	$3_{0,3}$–$2_{0,2}$	212.811184	16*	$< 0.24^b$	$rms = 128$ mK	$W = 5$	N_c=5.40
	$3_{0,3}$–$2_{0,2}$			$< 0.59^b$	$rms = 128$ mK	$W = 5$	N_c=33.20
	$3_{2,1}$–$2_{2,0}$	213.293560	16*	$< 0.23^b$	$rms = 127$ mK	$W = 5$	N_c=5.47
	$3_{2,1}$–$2_{2,0}$			$< 0.58^b$	$rms = 127$ mK	$W = 5$	N_c=33.20
	$3_{1,2}$–$2_{1,1}$	219.908	16*	$< 0.19^b$	$rms = 101$ mK	$W = 5$	N_c=5.50
	$3_{1,2}$–$2_{1,1}$			$< 190.00^b$	$rms = 101$ mK	$W = 5$	N_c=5.60
N$_2$H$^+$	J=1–0, F=1–1	93.17188	29	1.08 ± 0.01	7.90 ± 0.01	2.85 ± 0.03	0.36
	J=1–0, F=2–1	93.17370		1.75 ± 0.01	8.05 ± 0.01	2.95 ± 0.02	0.56
	J=1–0, F=0–1	93.17613		0.40 ± 0.01	7.67 ± 0.03	2.68 ± 0.07	0.14
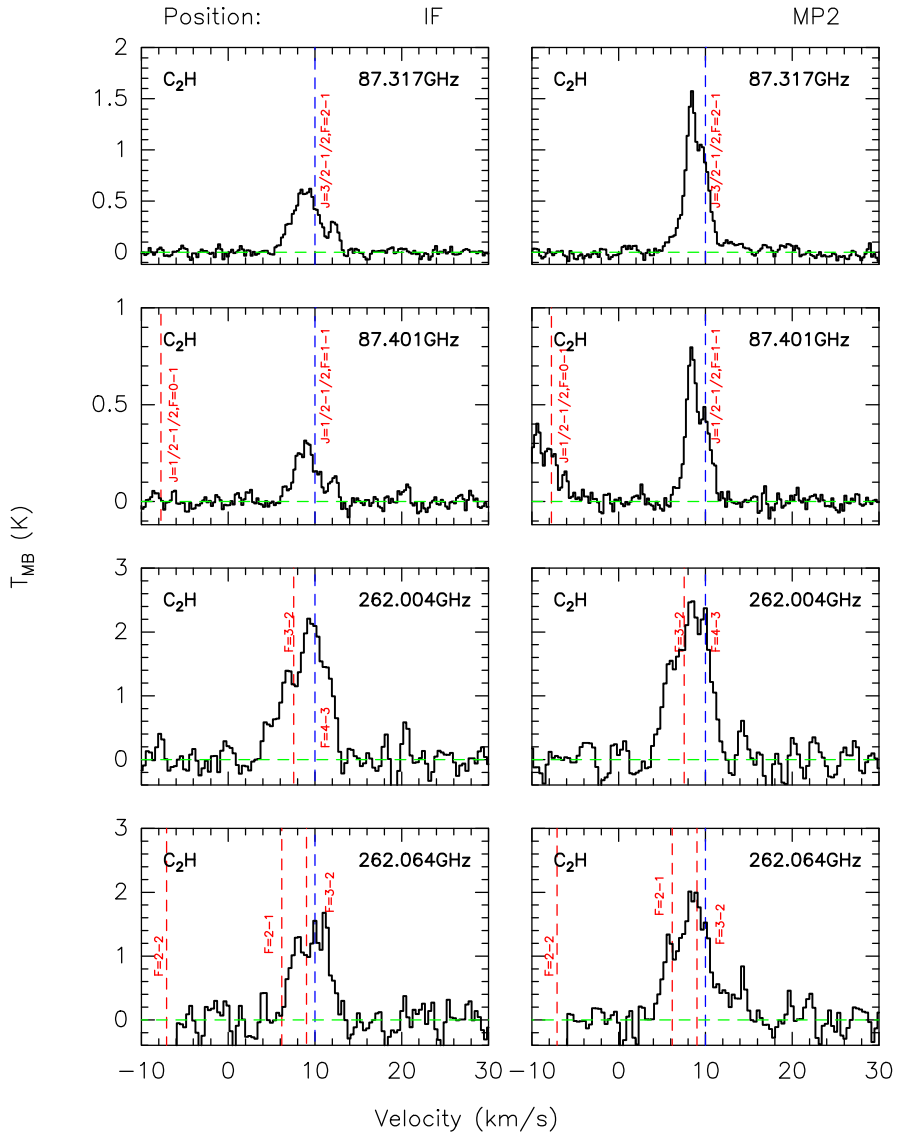
Figure C.1: C_2H spectra at the IF and MP2 positions. The red dashed lines mark different C_2H transitions. The blue dashed line shows the velocity of $10\,\mathrm{km\ s^{-1}}$, relative to the frequencies 87.317, 87.401, 262.004, and 262.064 GHz, from top to bottom.
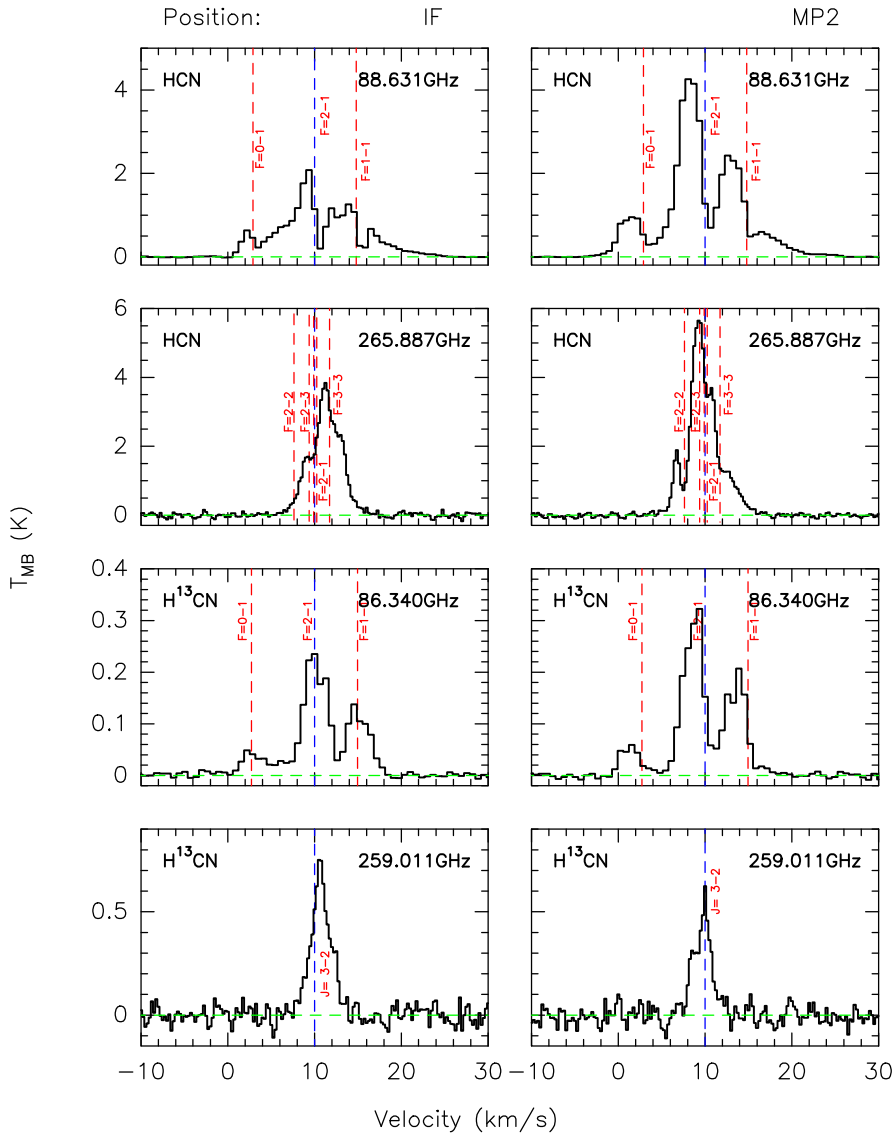
Figure C.2: Panels 1 and 2: HCN spectra at the IF and MP2 positions. The red dashed lines mark different HCN transitions. The blue dashed line shows the velocity of 10km s^{-1}, relative to the rest frequency of the transitions, 88.631 and 265.88 GHz. Panels 3 and 4: H^{13}CN spectra at the IF and MP2 positions, the red dashed lines mark different H^{13}CN transitions. The blue dashed line shows the velocity of 10km s^{-1}, relative to the frequencies 86.340 (panel 3) and 259.054 GHz (panel 4).
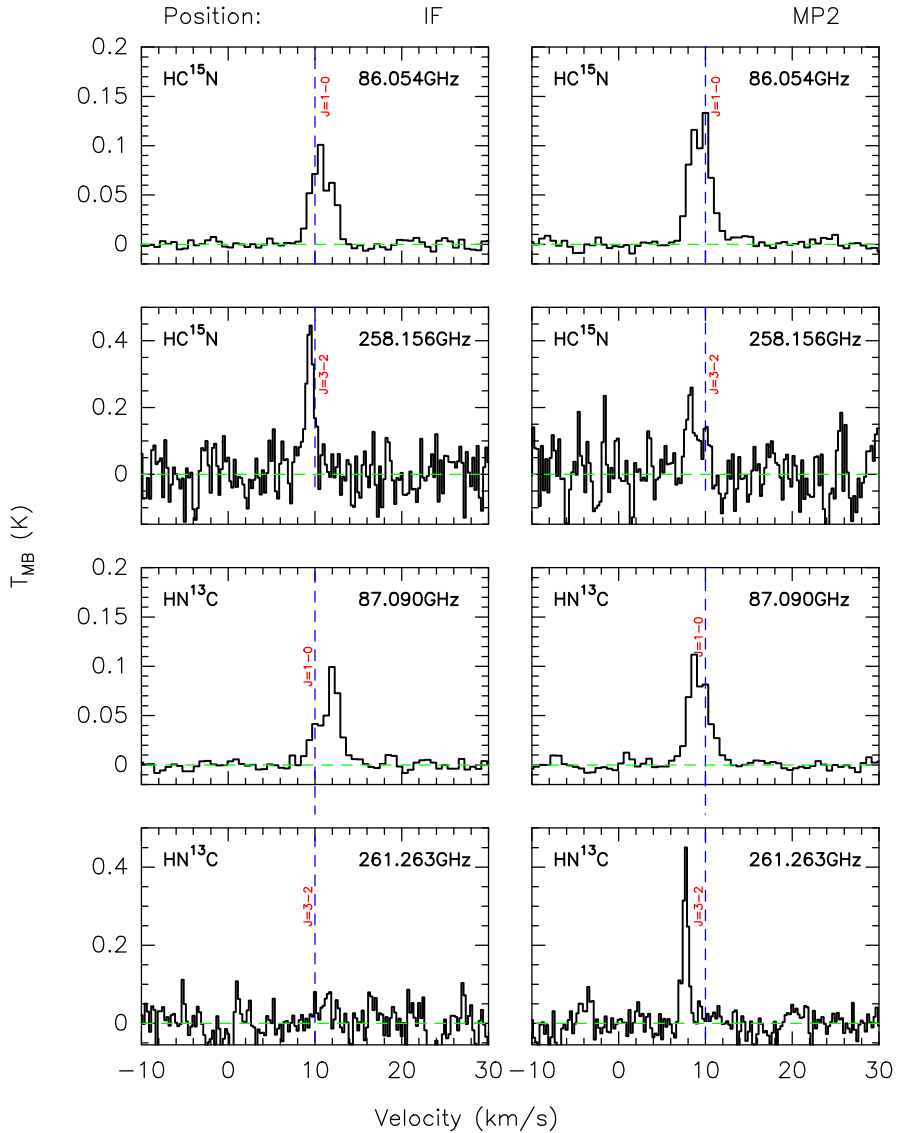
Figure C.3: Panels 1 and 2: HC^{15}N spectra at the IF and MP2 positions. The blue dashed line shows the velocity of 10km s^{-1} relative to 86.054, and 258.156 GHz, for the panel 1 and 2, respectively. Panels 3 and 4: HN^{13}C spectra at the IF and MP2 positions at 87.090, and 261.263 GHz.
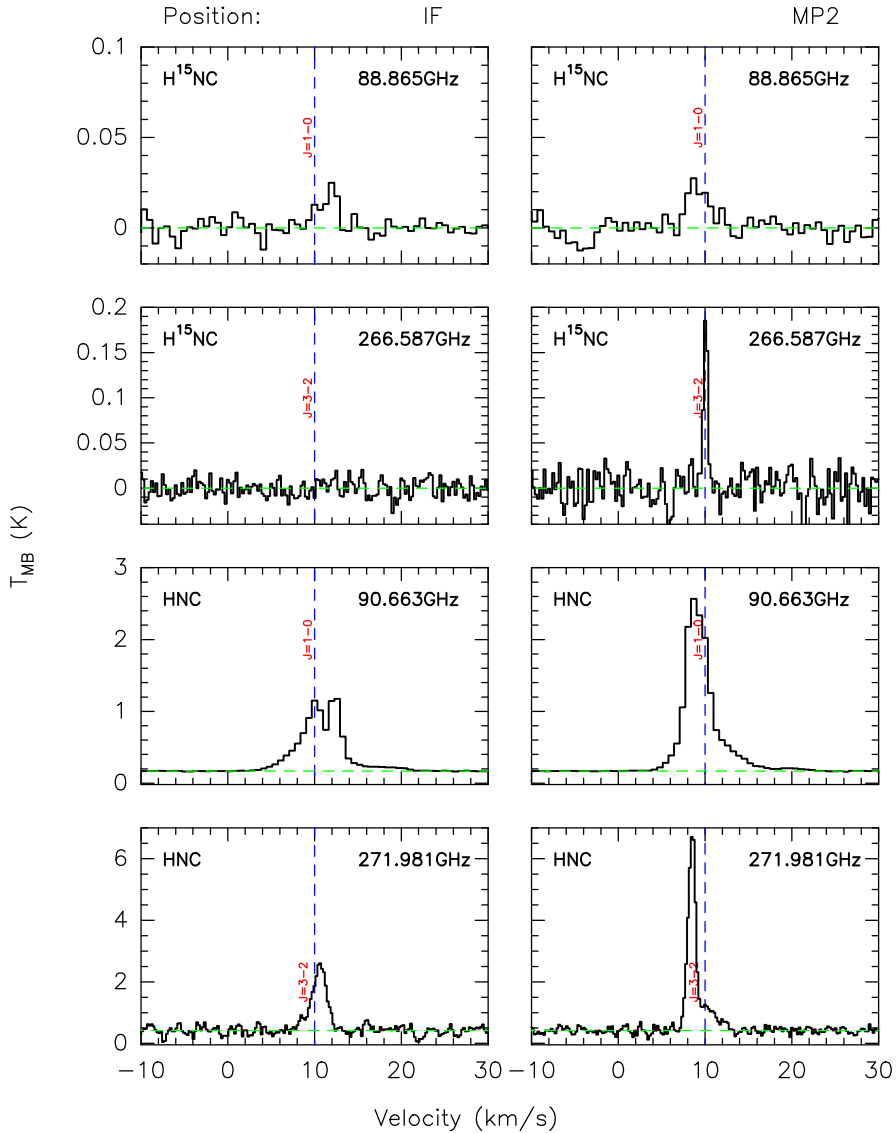
Figure C.4: Panels 1 and 2: $H^{15}NC$ spectra at the IF and MP2 positions. Panels 3 and 4: HNC spectra **at** the IF and MP2 positions. The blue dashed line shows the velocity of 10km s^{-1} relative to 88.865, 266.587, 90.663, and 271.981 GHz, respectively.
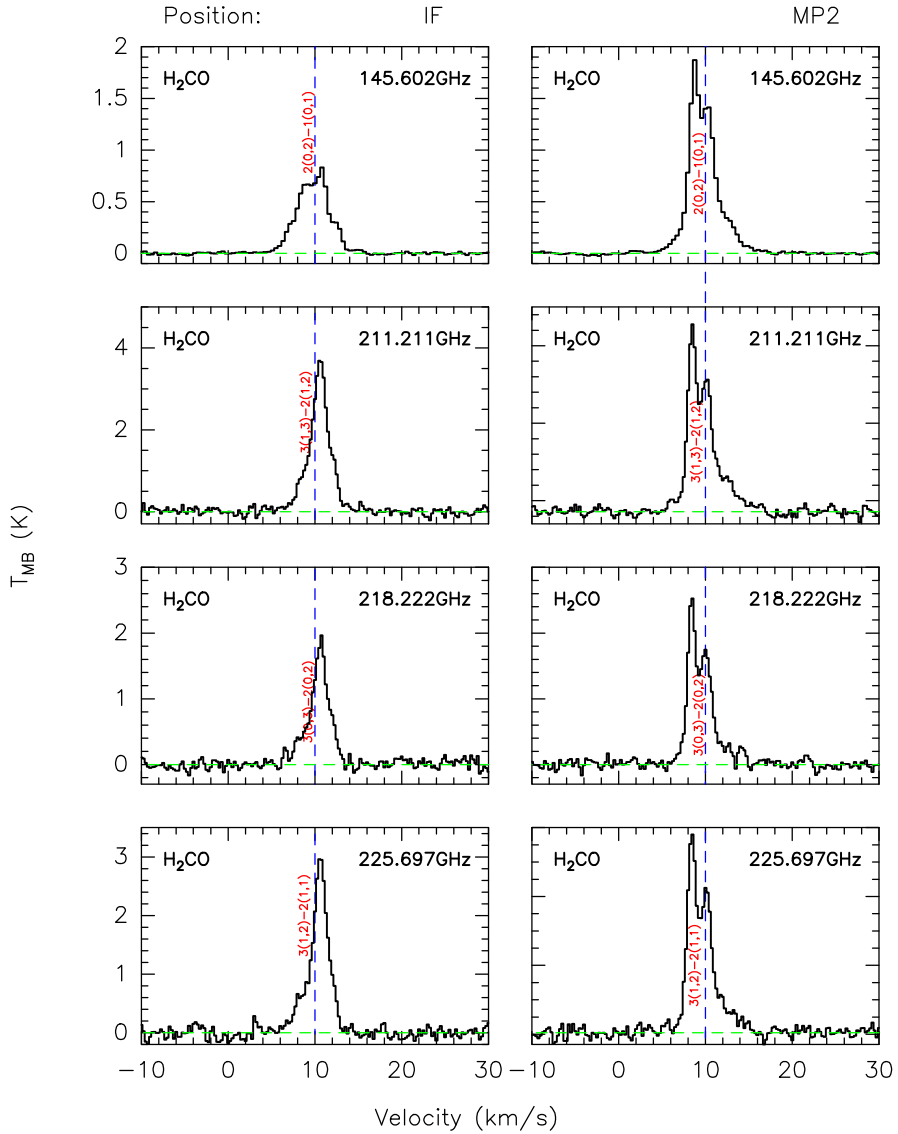
Figure C.5: H₂CO spectra at the two positions IF and MP2. The blue dashed line shows the velocity of 10km s^{-1}, relative to the frequencies 145.602, 211.211, 218.222, and 218.697 GHz, from top to bottom.
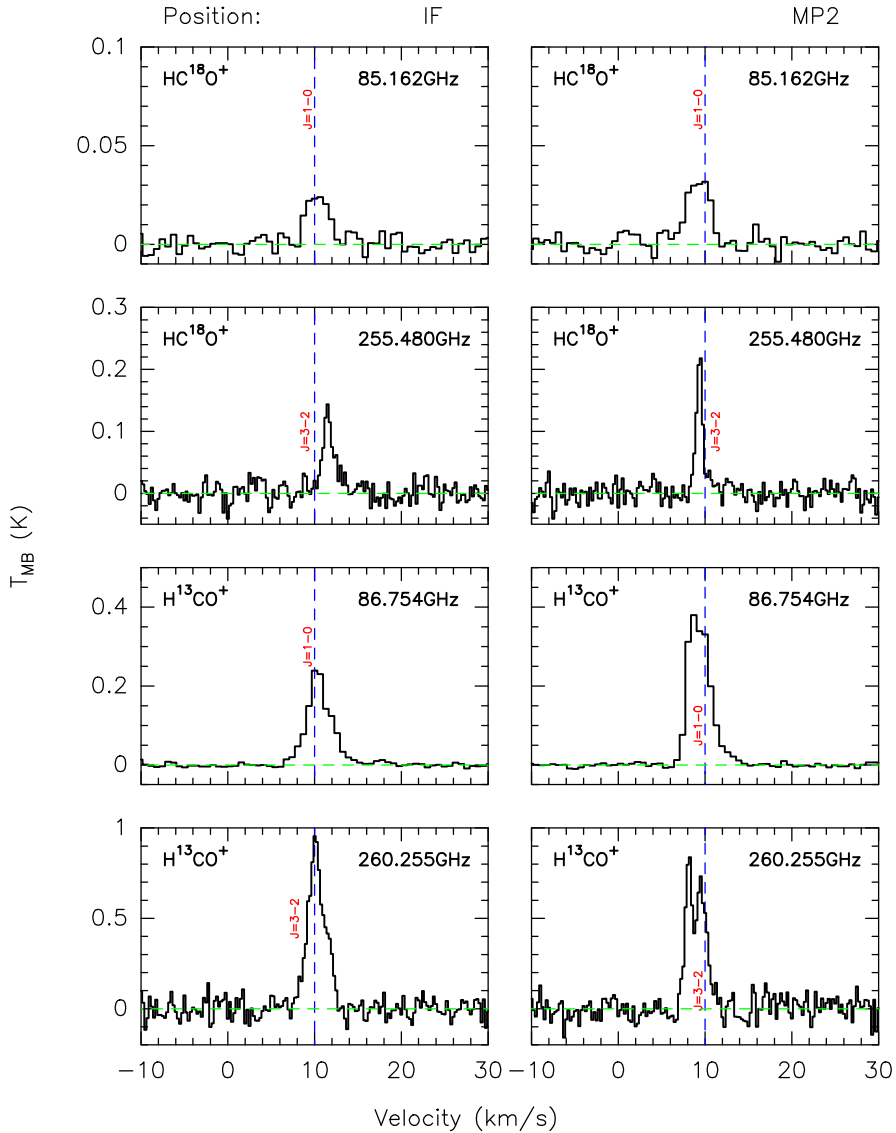
Figure C.6: Panels 1 and 2: $HC^{18}O^+$ spectra at the two positions IF and MP2. Panels 3 and 4: $H^{13}CO^+$ spectra at the two positions IF and MP2. The blue dashed line shows the velocity of $10km\,s^{-1}$, relative to the frequencies 85.162, 255.480, 86.745, and 260.255 GHz, from top to bottom.
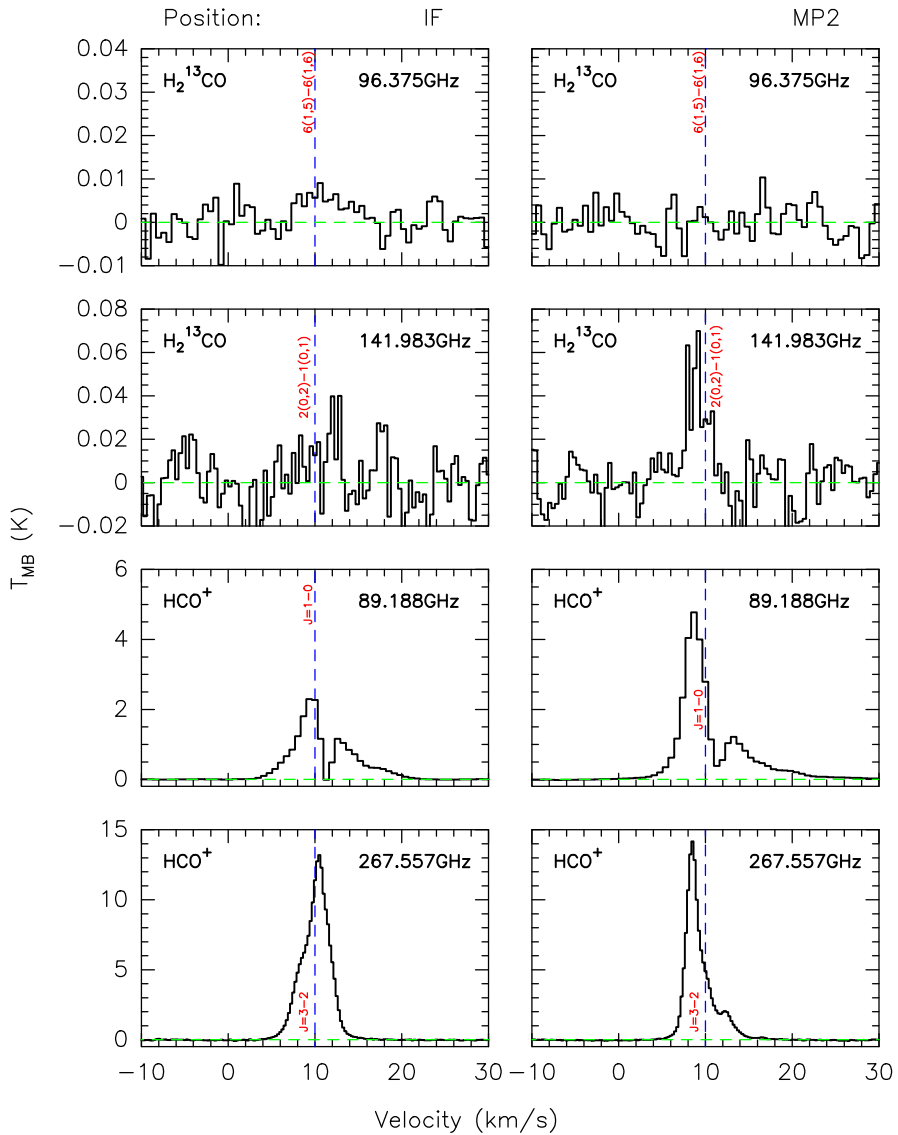
Figure C.7: In the panel 1 and 2 are the $H_2^{13}CO$ spectra at the two positions IF and MP2. The blue dashed line shows the velocity of 10km s^{-1}, relative to the frequency 96.375 GHz, in the panel 1, and 141.983 GHz, in panel 2. Panel 3 and 4 show the HCO$^+$ spectra toward the two positions IF and MP2. The blue dashed line shows the velocity of 10km s^{-1}, relative to the frequency 89.188 GHz, in panel 3, and 267.557 GHz, in panel 4.
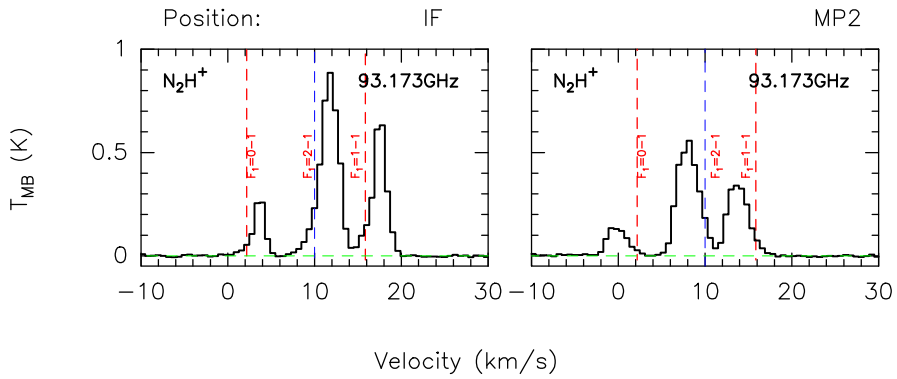
Figure C.8: N_2H^+ spectra at 93.173 GHz at the two positions IF and MP2. The red dashed lines mark different transitions of this molecule. The blue dashed line shows the velocity of 10km s^{-1} relative to the frequency of 93.137 GHz.
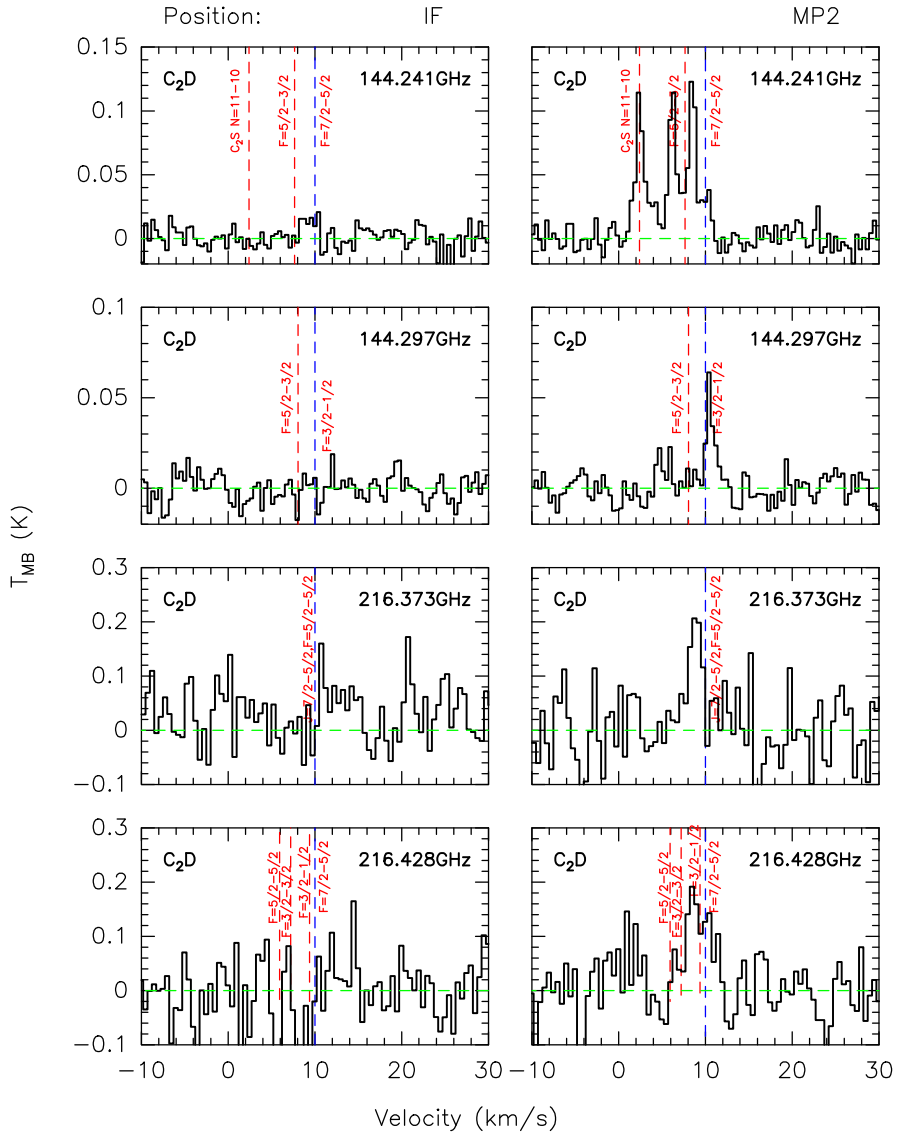
Figure C.9: C$_2$D spectra at the two positions IF and MP2. The red dashed lines mark different C$_2$D transitions. The blue dashed line shows the velocity of 10km s^{-1}, relative to the frequencies 144.241, 144.297, 216.373, and 216.428 GHz, from top to bottom.
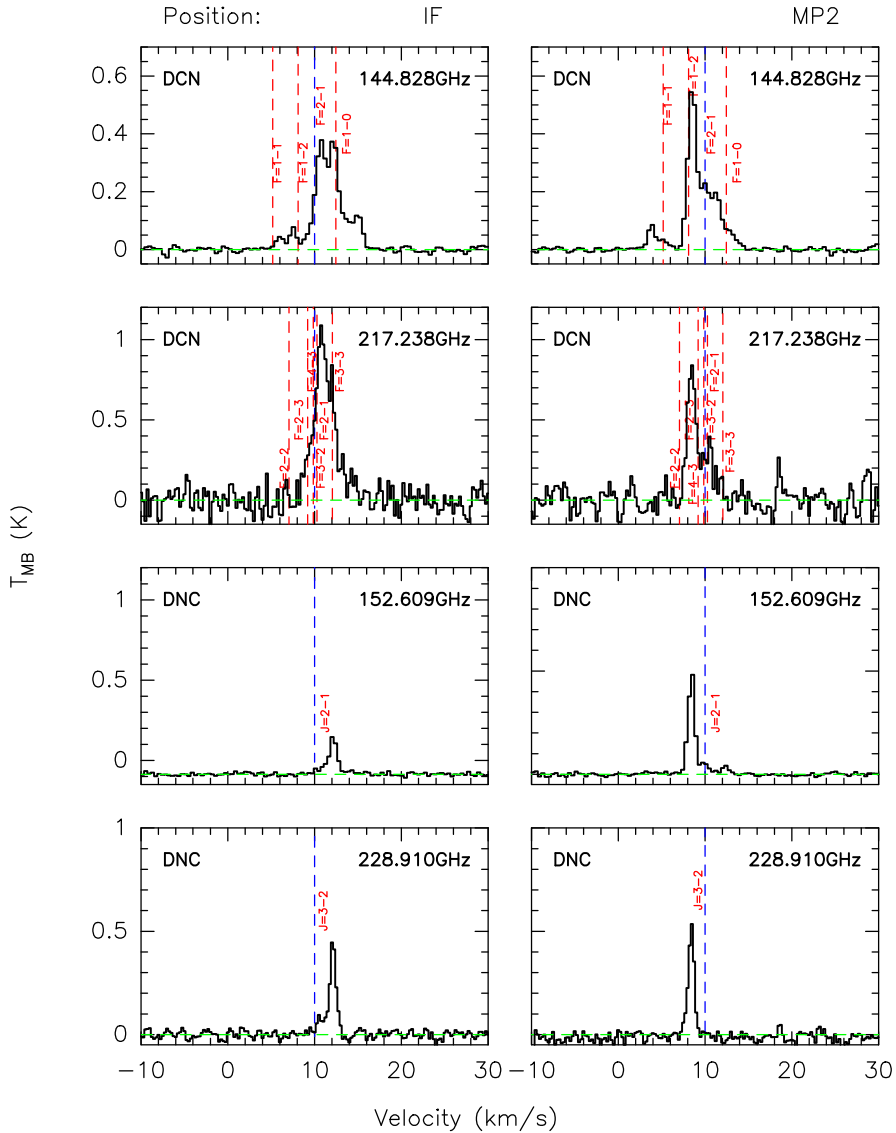
Figure C.10: DCN and DNC spectra at the two positions IF and MP2. The red dashed lines mark different transitions. The blue dashed line shows the velocity of 10km s^{-1}, relative to the frequencies 144.828, 217.238 (for DCN), 152.609, and 228.91 GHz (for DNC), from top to bottom.
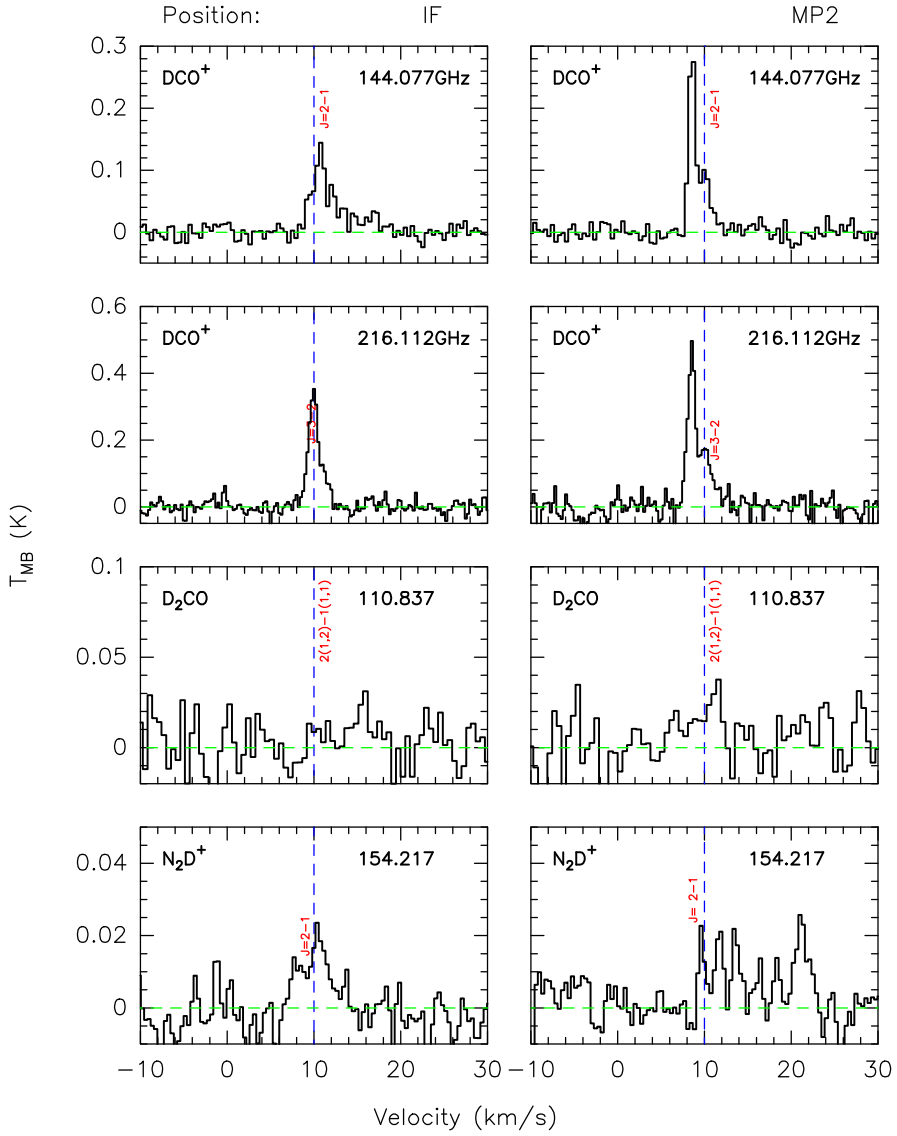
Figure C.11: Panels 1 and 2: DCO$^+$ spectra at the two positions IF and MP2. The blue dashed line shows the velocity of 10km s^{-1}, relative to the frequencies 144.077 (in the top panel) and 216.112 GHz (in the bottom panel). Panel 3: D$_2$CO spectra at the two positions IF and MP2. The blue dashed line shows the velocity of 10km s^{-1}, relative to the frequency 110.837 GHz. Panel 4: N$_2$D$^+$ spectra at the two positions IF and MP2. The blue dashed line shows the velocity of 10km s^{-1}, relative to the frequency 154.217 GHz.
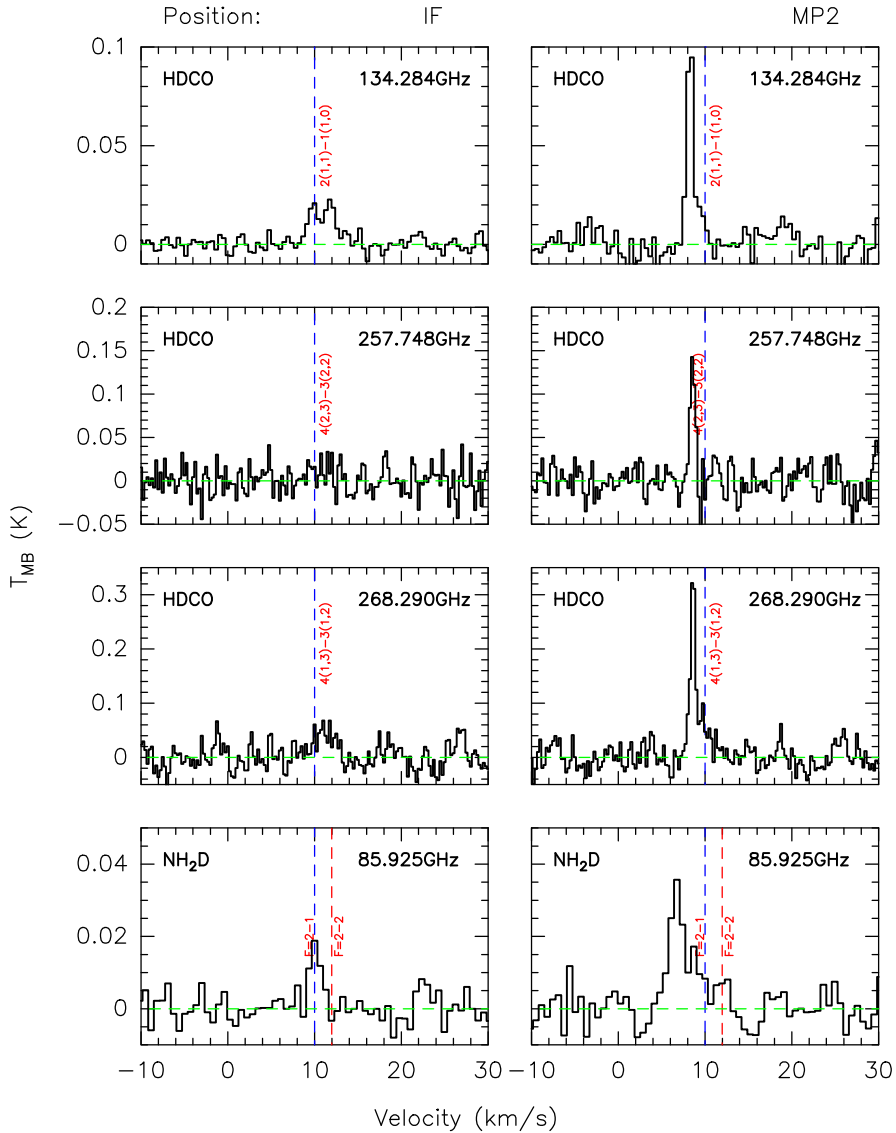
Figure C.12: Panels 1 to 3: HDCO spectra at the two positions IF and MP2. The blue dashed line shows the velocity of 10km s^{-1}, relative to the frequencies 134.284, 257.748, and 268.290 GHz. Panel 4: NH2D spectra at IF and MP2 positions, the blue dashed line shows the velocity of 10km s^{-1}, relative to 85.925 GHz.

Astrophysical constants and conversion factors

Constant	Symbol	Number[*]
Mathematical constants		
Number pi	π	3.1415926536
Euler's constant	e	2.7182818285
Physical constants		
Speed of light	c	$2.99792458 \times 10^{10}$ cm s^{-1}
Planck constant	h	$6.62607550 \times 10^{-27}$ erg s
		$6.62607550 \times 10^{-34}$ J s
		$4.13567150 \times 10^{-15}$ eV s
Boltzmann constant	k	$1.38065800 \times 10^{-16}$ erg Ks^{-1}
		$1.38065800 \times 10^{-23}$ J Ks^{-1}
		$8.61738500 \times 10^{-5}$ eV Ks^{-1}
Gravitation constant	G	$6.67259000 \times 10^{-8}$ dyn cm^2 gs^{-2}
		$6.67259000 \times 10^{-11}$ m^3 kg^{-1} s^{-2}
Units of distance		
Astronomical unit	AU	$1.4959787066 \times 10^{13}$ cm
Parsec	pc	3.0856776×10^{18} cm
		3.2615638 light (Julian) year
		206264.806 AU
Light (Julian) year	-	$9.460730472 \times 10^{17}$ cm
Solar radius	$R_\odot$	6.95508×10^{10} cm
Units of mass		
Solar mass	$M_\odot$	1.9891×10^{33} g
Mass of electron	m_e	$5.48579903 \times 10^{-28}$ g
Mass of proton	m_p	$1.6726231 \times 10^{-24}$ g
Mass of neutron	m_n	$1.6749286 \times 10^{-24}$ g
Mass of H atom	m_H	$1.6735344 \times 10^{-24}$ g
Units of time		
Julian year	-	3.15576 SI seconds
		525960 minutes
		8766 hours
		365.25 days
Units of energy,		
electric charge and flux density		
Solar luminosity	$L_\odot$	3.845×10^{33} erg s^{-1}
Elementary charge	e	$4.8032068 \times 10^{-19}$ C
		$1.60217733 \times 10^{20}$ esu
Joule	J	10^7 erg
Electron Volt	ev	$1.60217646 \times 10^{-19}$ J
		$1.60217646 \times 10^{-12}$ erg
Jansky	Jy	10^{-23} erg s^{-1}cm^{-2} Hz^{-1}
		10^{-26} W m^{-2} Hz^{-1}
Debye	D	10^{-18} statC cm

[*]Values from Cox (1999).

LIST OF FIGURES

LIST OF TABLES

Bibliography

Abel, N. P., Ferland, G. J., Shaw, G., & van Hoof, P. A. M. 2005, ApJs, 161, 65

André, P., Men'shchikov, A., Bontemps, S., et al. 2010, A&A, 518, L102

Andre, P., Ward-Thompson, D., & Barsony, M. 1993, ApJ, 406, 122

Aikawa, Y., Kamuro, D., Sakon, I., et al. 2012, A&A, 538, A57

Alvarez, C., Feldt, M., Henning, T., et al. 2004, ApJs, 155, 123

Aspin, C., & Walther, D. M. 1990, A&A, 235, 387

Asvany, O., Schlemmer, S., & Gerlich, D. 2004, ApJ, 617, 685

Agúndez, M., & Wakelam, 2015, A&A, in prep.

Agúndez, M., Cernicharo, J., Pardo, J. R., et al. 2008, APSS, 313, 229

Aalto, S., Wilner, D., Spaans, M., et al. 2009, A&A, 493, 481

Baan, W. A., Henkel, C., & Loenen, E. 2008, EAS Publications Series, 31, 111

Baan, W. A., Loenen, E., & Spaans, M. 2010, Highlights of Astronomy, 15, 411

Bachiller, R., & Pérez Gutiérrez, M. 1997, ApJL, 487, L93

Beckwith, S., & Evans, N. J., II 1975, Bulletin of the American Astronomical Society, 7, 417

Beckwith, S., Evans, N. J., II, Becklin, E. E., & Neugebauer, G. 1976, ApJ, 208, 390

Beckwith, S., Becklin, E. E., Neugebauer, G., & Persson, S. E. 1976, Bulletin of the American Astronomical Society, 8, 564

Bacmann, A., Taquet, V., Faure, A., Kahane, C., & Ceccarelli, C. 2012, A&A, 541, L12

Bally, J., & Langer, W. D. 1982, ApJ, 255, 143

Bally, J., & Lane, A. P. 1982, ApJ, 257, 612

Bally, J., & Lada, C. J. 1983, ApJ, 265, 824 Bally & Langer 1982

Bally, J., Langer, W. D., & Liu, W. 1991, ApJ, 383, 645

Bakes, E., Hudgins, D., Allamandola, L., & Tielens, X. 1998, Bulletin of the American Astronomical Society, 30, # 118.01

Bakes, E. L. O., & Tielens, A. G. G. M. 1994, ApJ, 427, 822

Bakes, E. L. O., & Tielens, A. G. G. M. 1998, ApJ, 499, 258

Beltrán, M. T., Brand, J., Cesaroni, R., et al. 2006, A&A, 447, 221

Bensch, F., Pak, I., Wouterloot, J. G. A., Klapper, G., & Winnewisser, G. 2003, SFChem 2002: Chemistry as a Diagnostic of Star Formation, 254

Beichman, C. A., Myers, P. C., Emerson, J. P., et al. 1986, ApJ, 307, 337

Bell, J. M., Bougher, S. W., de Lahaye, V., & Waite, J. H. 2005, AGU Fall Meeting Abstracts, 258

Berné, O., Fuente, A., Goicoechea, J. R., et al. 2009, ApJ, 706, L160

Breen, S., Caswell, J., Green, J., et al. 2014, ATNF Proposal, 6257

Beuther, H., & Shepherd, D. 2005, Cores to Clusters: Star Formation with Next Generation Telescopes, 105

Boger, G. I., & Sternberg, A. 2005, ApJ, 632, 302

Busquet, G., Zhang, Q., Palau, A., et al. 2013, ApJL, 764, L26

Bonnell, I. A., Bate, M. R., Clarke, C. J., & Pringle, J. E. 2001, MNRAS, 323, 785

Bonnell, I. A., & Bate, M. R. 2006, MNRAS, 370, 488

Bonnell, I. A., Smith, R. J., Clark, P. C., & Bate, M. R. 2011, MNRAS, 410, 2339

Bonnell, I. A., & Smith, R. J. 2011, Computational Star Formation, 270, 57

Brooks, K. J., Cox, P., Schneider, N., et al. 2003, A&A, 412, 751

Burton, M. G., Hollenbach, D. J., & Tielens, A. G. G. M. 1990, ApJ, 365, 620

Burke, J. R., & Hollenbach, D. J. 1983, ApJ, 265, 223

Black, J. H. 1998, The Molecular Astrophysics of Stars and Galaxies, edited by Thomas W. Hartquist and David A. Williams. Clarendon Press, Oxford, 1998., p.469, 4, 469

Brünken, S., Kluge, L., Stoffels, A., Asvany, O., & Schlemmer, S. 2014, ApJL, 783, L4

Buckle, J. V., & Fuller, G. A. 2003, A&A, 399, 567

Black, J. H., & van Dishoeck, E. F. 1987, ApJ, 322, 412

Carter, M., Lazareff, B., Maier, D., et al. 2012, A&A, 538, A89

Caselli, P., van der Tak, F. F. S., Ceccarelli, C., & Bacmann, A. 2003, A&A, 403, L37

Caselli, P., Vastel, C., Ceccarelli, C., et al. 2008, A&A, 492, 703

Casoli, F., Combes, F., Dupraz, C., Gerin, M., & Boulanger, F. 1986, A&A, 169, 281

Carpenter, J. M., Meyer, M. R., Dougados, C., Strom, S. E., & Hillenbrand, L. A. 1997, AJ, 114, 1275

Carpenter, J. M. 2000, AJ, 120, 3139

Carpenter, J. M., & Hodapp, K. W. 2008, Handbook of Star Forming Regions, Volume I, 899

Cernicharo, J. 2012, EAS Pub. Ser., 58, 251

Cernicharo, J., Bailleux, S., Alekseev, E., et al. 2014, ApJ, 795, 40

Choi, M., Evans, N. J., II, Tafalla, M., & Bachiller, R. 2000, ApJ, 538, 738

Crapsi, A., Caselli, P., Walmsley, C. M., et al. 2005, ApJ, 619, 379

Csengeri, T., Bontemps, S., Schneider, N., & Motte, F. 2011, Computational Star Formation, 270, 53

Codella, C., Podio, L., Fontani, F., et al. 2015, Advancing Astrophysics with the Square Kilometre Array (AASKA14), 123

Cox, A. N. (1999). Allen's astrophysical quantities.

Cuadrado, S., Goicoechea, J. R., Pilleri, P., et al. 2015, A&A, 579, C1

Cutri, R. M., Skrutskie, M. F., van Dyk, S., et al. 2003, VizieR Online Data Catalog, 2246, 0

Caux, E., Kahane, C., Castets, A., et al. 2011, A&A, 532, A23

Churchwell, E., Nash, A. G., & Walmsley, C. M. 1984, ApJ, 287, 681 Cernicharo 2002

Daniel, F., Gerin, M., Roueff, E., et al. 2013, arXiv:1309.5782

Dallier, R., Boisson, C., & Joly, M. 1996, VizieR Online Data Catalog, 411, 60239

Daranlot, J., Jorfi, M., Xie, C., et al. 2011, Science, 334, 1538

Daranlot, J., Hu, X., Xie, C., et al. 2013, Physical Chemistry Chemical Physics (Incorporating Faraday Transactions), 15, 13888

D'Hendecourt, L. B., & Leger, A. 1987, A&A, 180, L9

Didelon, P., Motte, F., Tremblin, P., et al. 2015, arXiv:1510.09175

Dierickx, M., Jiménez-Serra, I., Rivilla, V. M., & Zhang, Q. 2015, ApJ, 803, 89

Dislaire, V., Hily-Blant, P., Faure, A., et al. 2012, A&A, 537, A20

Draine, B. T., & Bertoldi, F. 1996, ApJ, 468, 269

Draine, B. T. 1978, ApJs, 36, 595

Dorschner, J., Gürtler, J. 1963, Astronomische Nachrichten, 287, 257

Dorschner, J., Gürtler, J. 1966, Astronomische Nachrichten, 289, 57

Downes, D., Winnberg, A., Goss, W. M., & Johansson, L. E. B. 1975, A&A, 44, 243

Dyck, H. M., & Howell, R. R. 1982, AJ, 87, 400

Eidelsberg, M., Benayoun, J. J., Viala, Y., et al. 1992, A&A, 265, 839

Ehrenfreund, P., Cox, N., Cami, J., et al. 2005, Highlights of Astronomy, 13, 864

Emprechtinger, M., Caselli, P., Volgenau, N. H., Stutzki, J., & Wiedner, M. C. 2009, A&A, 493, 89

Esplugues, G. B., Cernicharo, J., Viti, S., et al. 2011, IAU Symposium, 280, 88P

Esplugues, G. B., Tercero, B., Cernicharo, J., et al. 2013, A&A, 556, A143

Esplugues, G. B., Viti, S., Goicoechea, J. R., & Cernicharo, J. 2014, A&A, 567, A95

Estalella, R. and Anglada, G. (1999). Introducción a la física del medio interestelar.

Falgarone, E., Pineau des Forets, G., & Roueff, E. 1995, A&A, 300, 870

Federrath, C., Roman-Duval, J., Klessen, R. S., Schmidt, W., & Mac Low, M.-M. 2010, A&A, 512, A81

Feng, S., Beuther, H., Henning, T., et al. 2015, A&A, 581, A71

Ferland, G. J., Korista, K. T., Verner, D. A., et al. 1998, PASP, 110, 761

Field, G. B., Somerville, W. B., & Dressler, K. 1966, Annu. Rev. Astron. Astrophys., 4, 207

Fleming, B., France, K., Lupu, R. E., & McCandliss, S. R. 2010, ApJ, 725, 159

Fortenberry, R. C., Huang, X., Crawford, T. D., & Lee, T. J. 2013, ApJ, 772, 39

Fontani, F., Palau, A., Caselli, P., et al. 2011, IAU Symposium, 280, 161P

Fuente, A., Martin-Pintado, J., Cernicharo, J., & Bachiller, R. 1993, A&A, 276, 473

Fuente, A., Martin-Pintado, J., & Gaume, R. 1995, ApJL, 442, L33

Fuente, A., Rodriguez-Franco, A., & Martin-Pintado, J. 1996, A&A, 312, 599

Fuente, A., Rodrıguez-Franco, A., Garcıa-Burillo, S., Martın-Pintado, J., & Black, J. H. 2003, A&A, 406, 899

Fuente, A., Neri, R., & Caselli, P. 2005, A&A, 444, 481

Fuente, A., Rizzo, J. R., Neri, R., Caselli, P., & Bachiller, R. 2005, ESA Special Publication, 577, 87

Fuente, A., García-Burillo, S., Usero, A., et al. 2008, A&A, 492, 675

Fuente, A., Berné, O., Cernicharo, J., et al. 2010, A&A, 521, L23

Geen et al. 2016, in prep.

Gerin, M., Roueff, E., Le Bourlot, J., et al. 2005, Astrochemistry: Recent Successes and Current Challenges, 231, 153

Gerin, M., Pety, J., & Goicoechea, J. R. 2009, Submillimeter Astrophysics and Technology: a Symposium Honoring Thomas G. Phillips, 417, 165

Gerin, M., Kaźmierczak, M., Jastrzebska, M., et al. 2011, A&A, 525, A116 Gerlich et al. 2002

Gerin, M., de Luca, M., Lis, D. C., et al. 2013, Journal of Physical Chemistry A, 117, 10018

Giannakopoulou, J., Mitchell, G. F., Hasegawa, T. I., Matthews, H. E., & Maillard, J.-P. 1997, ApJ, 487, 346

Giannakopoulou, J., Fich, M., & Wilson, C. D. 1996, Bulletin of the American Astronomical Society, 28, 894

Gerin, M., Pearson, J. C., Roueff, E., Falgarone, E., & Phillips, T. G. 2001, ApJ, 551, L193

Gerin, M., Lis, D. C., Philipp, S., et al. 2006, A&A, 454, L63

Gerlich, D., Herbst, E., & Roueff, E. 2002, Planet. Space Sci., 50, 1275

Ginard, D., González-García, M., Fuente, A., et al. 2012, A&A, 543, A27

Glassgold, A. E., Huggins, P. J., & Langer, W. D. 1985, ApJ, 290, 615

Godard, B., Falgarone, E., Gerin, M., Hily-Blant, P., & de Luca, M. 2010, A&A, 520, A20

Goicoechea, J. R., Pety, J., Gerin, M., et al. 2006, A&A, 456, 565

Goicoechea, J. R., Berné, O., Gerin, M., Joblin, C., & Teyssier, D. 2008, ApJ, 680, 466

Goicoechea, J. R., Pety, J., Gerin, M., et al. 2009, Bioastronomy 2007: Molecules, Microbes and Extraterrestrial Life, 420, 43

Goicoechea, J. R., Swinyard, B., & Spica/Safari Science Team 2009, The Next-Generation Infrared Space Mission: SPICA, 2002

Gómez, Y., Lebrón, M., Rodríguez, L. F., et al. 1998, ApJ, 503, 297

Gómez, Y., Garay, G., Rodríguez-Rico, C. A., et al. 2010, AJ, 140, 913

Goldsmith, P. F., & Langer, W. D. 1999, ApJ, 517, 209

Goldsmith, P. F., Heyer, M., Narayanan, G., et al. 2008, ApJ, 680, 428

Gratier, P., Pety, J., Guzmán, V., et al. 2013, A&A, 557, A101 Gregorio-Hetem et al. 1998

Gregorio-Hetem, J., Montmerle, T., Casanova, S., & Feigelson, E. D. 1998, A&A, 331, 193

Guelin, M., Langer, W. D., & Wilson, R. W. 1982, A&A, 107, 107

Guilloteau, S., Piétu, V., Dutrey, A., & Guélin, M. 2006, A&A, 448, L5

Guzmán, V., Pety, J., Goicoechea, J. R., Gerin, M., & Roueff, E. 2011, A&A, 534, A49

Guzmán, V., Roueff, E., Gauss, J., et al. 2012, A&A, 548, A94

Guzmán, V., Pety, J., Gratier, P., et al. 2012, A&A, 543, L1

Guzmán, V. V., Goicoechea, J. R., Pety, J., et al. 2013, A&A, 560, A73

Guzmán, V. V., Pety, J., Gratier, P., et al. 2014, Faraday Discussions, 168, 103

Guzmán, V. V., Pety, J., Goicoechea, J. R., et al. 2015, ApJL, 800, L33

Gyulbudaghian, A. L., Glushkov, Y. I., & Denisyuk, E. K. 1978, ApJL, 224, L137

Habart, E., Natta, A., & Krügel, E. 2004, A&A, 427, 179

Habing, H. J. 1968, Bull. Astron. Inst. Netherlands, 20, 120

Habing, H. J. 1968, Leiden, Sterrewacht, 1968.,

Habing, H. J. 1968, BAIN, 19, 421

Hacar, A., Tafalla, M., Kauffmann, J., & Kovács, A. 2013, A&A, 554, A55

Harvey, P. M., Wilking, B. A., Joy, M., & Lester, D. F. 1985, ApJ, 288, 725

Hatchell, J., Thompson, M. A., Millar, T. J., & MacDonald, G. H. 1998, A&As, 133, 29

Hennemann, M., Motte, F., Schneider, N., et al. 2012, A&A, 543, L3

Henning, T., Chini, R., & Pfau, W. 1992, A&A, 263, 285

Henshaw, J. D., Caselli, P., Fontani, F., Jiménez-Serra, I., & Tan, J. C. 2014, MNRAS, 440, 2860

Herbst, W., & Racine, R. 1976, Bulletin of the American Astronomical Society, 8, 336

Herbst, W., & Racine, R. 1976, AJ, 81, 840

Herbst, E., Adams, N. G., Smith, D., & Defrees, D. J. 1987, ApJ, 312, 351

Herbst, E., & Leung, C. M. 1989, ApJs, 69, 271

Herbst, E., & van Dishoeck, E. F. 2009, ARAA, 47, 427

Herrmann, F., Madden, S. C., Nikola, T., et al. 1997, ApJ, 481, 343

Hily-Blant, P., Maret, S., Bacmann, A., et al. 2010, A&A, 521, L52

Hirota, T., Yamamoto, S., Mikami, H., & Ohishi, M. 1998, ApJ, 503, 717

Hoare, M., Urquhart, J., Lumsden, S., & Purcell, C. 2007, ATNF Proposal, 1186

Hodapp, K.-W. 1994, Infrared Physics and Technology, 35, 167

Hodapp, K.-W. 1994, ApJs, 94, 615

Hodapp, K. W. 2007, AJ, 134, 2020

Hollenbach, D., & McKee, C. F. 1979, ApJs, 41, 555

Hollenbach, D. J. 1990, The Evolution of the Interstellar Medium, 12, 167

Hollenbach, D. J., Takahashi, T., & Tielens, A. G. G. M. 1991, ApJ, 377, 192

Hollenbach, D., & Natta, A. 1995, ApJ, 455, 133

Hollenbach, D. J., & Tielens, A. G. G. M. 1995, The Physics and Chemistry of Interstellar Molecular Clouds, 459, 164

Hollenbach, D. J., & Tielens, A. G. G. M. 1997, ARAA, 35, 179

Hollenbach, D. J., & Tielens, A. G. G. M. 1999, Reviews of Modern Physics, 71, 173

Howard, E. M., Pipher, J. L., & Forrest, W. J. 1994, ApJ, 425, 707

Howell, R. R., McCarthy, D. W., & Low, F. J. 1981, ApJL, 251, L21

Huang, R. Q., & Yu, K. N. 1998, Stellar astrophysics / R.Q. Huang AMP K.N. Yu. New York : Springer Verlag, 1998. QB801 .H73 1998,

Hubble, E. P. 1922, ApJ, 56, 162

Hughes, V. A., & Baines, J. G. N. 1985, ApJ, 289, 238

Inutsuka, S.-i., & Miyama, S. M. 1997, ApJ, 480, 681

Iffrig, O., & Hennebelle, P. 2015, A&A, 576, A95

Jacoby, G. H., Hunter, D. A., & Christian, C. A. 1984, ApJs, 56, 257

Jansen, D. J., Spaans, M., Hogerheijde, M. R., & van Dishoeck, E. F. 1995, A&A, 303, 541

Jaffe, D. T., Zhu, Q., Lacy, J. H., & Richter, M. 2003, ApJ, 596, 1053

Jeans, J. H. 1929, New York, The Macmillan company; Cambridge, Eng., The University press [c1929]

Jiménez-Serra, I., Báez-Rubio, A., Rivilla, V. M., et al. 2013, ApJL, 764, L4

Jørgensen, J. K., Schöier, F. L., & van Dishoeck, E. F. 2004, A&A, 416, 603

Jørgensen, J. K. 2004, Ph.D. Thesis,

Jura, M. 1976, AJ, 81, 178

Jura, M. 1976, ApJ, 204, 12

Kahn, F. D. 1974, A&A, 37, 149

Kamp, I., & Bertoldi, F. 2000, A&A, 353, 276

Kamp, I., & van Zadelhoff, G.-J. 2001, A&A, 373, 641

Kaufman, M. J., Wolfire, M. G., Hollenbach, D. J., & Luhman, M. L. 1999, ApJ, 527, 795

Kaufman, M. J., Wolfire, M. G., & Hollenbach, D. J. 2006, ApJ, 644, 283

Keene, J., Blake, G. A., Phillips, T. G., Huggins, P. J., & Beichman, C. A. 1985, ApJ, 299, 967

Keto, E., & Wood, K. 2006, ApJ, 637, 850

Keto, E., Zhang, Q., & Kurtz, S. 2008, ApJ, 672, 423

Kirk, H., Myers, P. C., Bourke, T. L., et al. 2013, ApJ, 766, 115

Kirk, H., Klassen, M., Pudritz, R., & Pillsworth, S. 2015, ApJ, 802, 75

Klein, C., Hoffmann, P., & Priesack, E. 2012, EGU General Assembly Conference Abstracts, 14, 8825

Klein, B., Hochgürtel, S., Krämer, I., et al. 2012, A&A, 542, L3

Knapp, G. R., & Brown, R. L. 1976, ApJ, 204, 21

Kohno, M., Koyama, K., & Hamaguchi, K. 2002, ApJ, 580, 626

Koresko, C. D., Beckwith, S., Ghez, A. M., et al. 1993, AJ, 105, 1481

Krumholz, M. R., & Bonnell, I. A. 2007, arXiv:0712.0828

Krumholz, M. R. 2014, Physics Reports, 539, 49

Krumholz, M. R. 2014, American Astronomical Society Meeting Abstracts #223, 223, #318.01

Krumholz, M. R., Bate, M. R., Arce, H. G., et al. 2014, Protostars and Planets VI, 243

Kuiper, R., Klahr, H., Dullemond, C., Kley, W., & Henning, T. 2010, A&A, 511, A81

Kurtz, S., Churchwell, E., Wood, D. O. S., & Myers, P. 1994, Bulletin of the American Astronomical Society, 26, 907

Kurtz, M. J., Henneken, E., Accomazzi, A., et al. 2005, Bulletin of the American Astronomical Society, 37, 1218

Kurtz, S. 2005, Astrochemistry: Recent Successes and Current Challenges, 231, 47

Kutner, M. L., & Tucker, K. D. 1975, ApJ, 199, 79

Larson, R. B. 1969, MNRAS, 145, 271

Larson, R. B. 1984, MNRAS, 206, 197

Larson, R. B. 1985, MNRAS, 214, 379

Larson, R. B. 2003, Galactic Star Formation Across the Stellar Mass Spectrum, 287, 65

Larson, R. B. 2003, Reports on Progress in Physics, 66, 1651

Larson, R. B. 2005, MNRAS, 359, 211

Larson, R. B. 2005, The Initial Mass Function 50 Years Later, 327, 329

Latter, W. B., & Walker, C. K. 1994, Bulletin of the American Astronomical Society, 26, 1458

Le Bourlot, J., Pineau des Forets, G., & Roueff, E. 1993, New Aspects of Magellanic Cloud Research, 416, 173

Lebrón, M. E., Rodríguez, L. F., & Lizano, S. 2003, Commmunications of the Konkoly Observatory Hungary, 103, 53

Lee, H.-H., Herbst, E., Pineau des Forets, G., Roueff, E., & Le Bourlot, J. 1996, A&A, 311, 690

Leger, A., & Puget, J. L. 1984, A&A, 137, L5

Le Petit, F., Nehmé, C., Le Bourlot, J., & Roueff, E. 2006, ApJs, 164, 506

Lepp, S., & Dalgarno, A. 1988, ApJ, 335, 769

Lepp, S., & Dalgarno, A. 1988, ApJ, 324, 553

Lepp, S., & Dalgarno, A. 1988, BAAS, 20, 643

Leurini, S., Rolffs, R., Thorwirth, S., et al. 2006, A&A, 454, L47

Li, J., Junzhi, W., Qingfeng, Z., Jiangshui Z., Di Li, 2015, arXiv:1501.06018v1

Linsky, J. L., Draine, B. T., Moos, H. W., et al. 2006, ApJ, 647, 1106

Lis, D. C., Keene, J., Phillips, T. G., et al. 2001, ApJ, 561, 823

Lis, D. C., & Schilke, P. 2003, ApJL, 597, L145

Liszt, H., & Lucas, R. 2001, A&A, 370, 576

Little, L. T., Heaton, B. D., & Dent, W. R. F. 1990, A&A, 232, 173

Baobab Liu, H., Ho, P. T. P., Zhang, Q., et al. 2010, ApJ, 722, 262

Liu, H. B., Jiménez-Serra, I., Ho, P. T. P., et al. 2012, ApJ, 756, 10

Loison, J.-C., Wakelam, V., & Hickson, K. M. 2014, MNRAS, 443, 398

Loren, R. B. 1977, ApJ, 215, 129

Loren, R. B. 1981, ApJ, 249, 550

Loren, R. B. 1989, ApJ, 338, 902

Loren, R. B. 1989, ApJ, 338, 925

Louvet, F., Motte, F., Hennebelle, P., et al. 2014, A&A, 570, A15

Loren, R. B., Peters, W. L., & Vanden Bout, P. A. 1974, ApJL, 194, L103

Loinard, L., Castets, A., Ceccarelli, C., et al. 2000, A&A, 359, 1169

Loinard, L., Castets, A., Ceccarelli, C., Caux, E., & Tielens, A. G. G. M. 2001, ApJ, 552, L163

Loinard, L., Castets, A., Ceccarelli, C., et al. 2003, SFChem 2002: Chemistry as a Diagnostic of Star Formation, 351

Lynds, B. T. 1962, ApJs, 7, 1

Maciá, E. Chem. Soc. Rev., 2005, 34, 691-701

Maddalena, R. J., Morris, M., Moscowitz, J., & Thaddeus, P. 1986, ApJ, 303, 375

Maddalena, R. J. 1986, Ph.D. Thesis

Marcelino, N., Cernicharo, J., Roueff, E., Gerin, M., & Mauersberger, R. 2005, ApJ, 620, 308

Martí, J., Rodriguez, L. F., & Reipurth, B. 1993, ApJ, 416, 208

Martí, J., Paredes, J. M., & Estalella, R. 1993, Stellar Jets and Bipolar Outflows, 186, 363

Martí, J., Rodriguez, L. F., Mirabel, I. F., & Paredes, J. M. 1996, A&A, 306, 449

Martí, J., Luque-Escamilla, P. L., Muñoz-Arjonilla, A. J., et al. 2013, A&A, 556, A131

Martin, P. G., & Mandy, M. E. 1995, ApJL, 455, L89

Massi, M., Felli, M., & Simon, M. 1985, A&A, 152, 387

McCall, B. J. 2001, Ph.D. Thesis

McCarthy, D. W. 1982, ApJ, 257, L93

McKee, C. F., Storey, J. W. V., Watson, D. M., & Green, S. 1982, ApJ, 259, 647

McKee, C. F., & Ostriker, E. C. 2007, ARAA, 45, 565

Meijerink, R., Spaans, M., & Israel, F. P. 2007, A&A, 461, 793

Meijerink, R., & Spaans, M. 2005, A&A, 436, 397

Mendoza, E., Lefloch, B., López-Sepulcre, A., et al. 2014, MNRAS, 445, 151

Melnick, G., Gull, G. E., & Harwit, M. 1979, ApJL, 227, L29

Melnick, G., Gull,G. E., & Harwit, M. 1979, ApJL, 227, L35

Miesch, M. S., Scalo, J., & Bally, J. 1999, ApJ, 524, 895

Miettinen, O., Hennemann, M., & Linz, H. 2011, A&A, 534, A134

Millar, T. J., Bennett, A., & Herbst, E. 1989, ApJ, 340, 906

Miyama, S. M., Narita, S., & Hayashi, C. 1987, Progress of Theoretical Physics, 78, 1051

Miyama, S. M., Narita, S., & Hayashi, C. 1987, Progress of Theoretical Physics, 78, 1273

Montalban, J., Bachiller, R., Martin-Pintado, J., Tafalla, M., & Gomez-Gonzalez, J. 1990, A&A, 233, 527

Molinari, S., Swinyard, B., Bally, J., et al. 2010, A&A, 518, L100

Müller, H. S. P., Thorwirth, S., Roth, D. A., & Winnewisser, G. 2001, A&A, 370, L49

Müller, H. S. P., Schlöder, F., Stutzki, J., & Winnewisser, G. 2005, Journal of Molecular Structure, 742, 215

Nagai, T., Inutsuka, S.-i., & Miyama, S. M. 1998, ApJ, 506, 306

Nagasawa, M. 1987, Progress of Theoretical Physics, 77, 635

Nagaoka, A., Watanabe, N., & Kouchi, A. 2005, ApJ, 624, L29

Nagy, Z., Van der Tak, F. F. S., Ossenkopf, V., et al. 2013, A&A, 550, A96

Nagy, Z. 2013, Ph.D. Thesis

Nagy, Z., van der Tak, F. F. S., Fuller, G. A., & Plume, R. 2015, A&A, 577, A127

Nakajima, H., Imanishi, K., Takagi, S.-I., Koyama, K., & Tsujimoto, M. 2003, PASJ, 55, 635

Natta, A., Walmsley, C. M., & Tielens, A. G. G. M. 1994, ApJ, 428, 209

Neufeld, D. A., Schilke, P., Menten, K. M., et al. 2006, A&A, 454, L37

Pagani, L., Salez, M., & Wannier, P. G. 1992, A&A, 258, 479

Pagani, L., Vastel, C., Hugo, E., et al. 2009, A&A, 494, 623

Pagani, L., Roueff, E., & Lesaffre, P. 2011, ApJ, 739, L35

Pagani, L., Lesaffre, P., Roueff, E., et al. 2012, Royal Society of London Philosophical Transactions Series A, 370, 5200

Pagani, L., Lesaffre, P., Jorfi, M., et al. 2013, A&A, 551, A38

Palau, A., Ho, P. T. P., Zhang, Q., et al. 2006, ApJL, 636, L137

Palla, F., & Stahler, S. W. 1993, ApJ, 418, 414

Palmeirim, P., Andre, P., Kirk, J., et al. 2013, A&A, 550, A38

Papadopoulos, P. P., Thi, W.-F., & Viti, S. 2002, ApJ, 579, 270

Peretto, N., Fuller, G. A., Duarte-Cabral, A., et al. 2013, A&A, 555, A112

Peretto, N., Fuller, G. A., André, P., et al. 2014, A&A, 561, A83

Parise, B., Ceccarelli, C., Tielens, A. G. G. M., et al. 2002, A&A, 393, L49

Parise, B., Castets, A., Herbst, E., et al. 2004, A&A, 416, 159

Parise, B., Ceccarelli, C., Tielens, A. G. G. M., et al. 2006, A&A, 453, 949

Parise, B., Leurini, S., Schilke, P., Roueff, E., & Thorwirth, S. 2007, Molecules in Space and Laboratory

Parise, B., Leurini, S., Schilke, P., et al. 2009, A&A, 508, 737

Parker, N. D. 1991, MNRAS, 251, 63

Phillips, T. G., & Huggins, P. J. 1981, ApJ, 251, 533

Pickett, H. M., Poynter, R. L., Cohen, E. A., et al. 1998, Journal of Quantitative Spectroscopy and Radiative Transfer, 60, 883

Pilleri, P., Fuente, A., Cernicharo, J., et al. 2012, A&A, 544, A110

Pilleri, P., Treviño-Morales, S., Fuente, A., et al. 2013, A&A, 554, A87

Pilleri, P., Fuente, A., Gerin, M., Cernicharo, J., Goicoechea, J. R., Ossenkopf, V., Joblin, C., González-García, M., Treviño-Morales, S. P., Sánchez-Monge, Á., Pety, J.; Berné, O.; Kramer, C., 2013, A&A, 561, A69s.

Pilleri, P., Fuente, A., Gerin, M., et al. 2014, A&A, 561, A69

Pineau des Forets, G., Roueff, E., & Flower, D. R. 1990, MNRAS, 244, 668

Pety, J., Teyssier, D., Fossé, D., et al. 2005, A&A, 435, 885

Pety, J., Goicoechea, J. R., Hily-Blant, P., Gerin, M., & Teyssier, D. 2007, A&A, 464, L41

Pety, J., Gratier, P., Guzmán, V., et al. 2012, A&A, 548, A68

Podio, L., Lefloch, B., Ceccarelli, C., Codella, C., & Bachiller, R. 2014, A&A, 565, A64

Preibisch, T., Balega, Y. Y., Schertl, D., & Weigelt, G. 2002, A&A, 392, 945

Racine, R. 1968, AJ, 73, 233

Ridge, N. A., Wilson, T. L., Megeath, S. T., Allen, L. E., & Myers, P. C. 2003, AJ, 126, 286

Rizzo, J. R., Fuente, A., Rodríguez-Franco, A., & García-Burillo, S. 2003, ApJ, 597, L153

Rizzo, J. R., Fuente, A., & García-Burillo, S. 2005, The Cool Universe: Observing Cosmic Dawn, 344, 184

Roberts, H., & Millar, T. J. 2000, A&A, 364, 780

Rodríguez, L. F., Gómez, Y., López, J. A., García-Díaz, M. T., & Clark, D. M. 2010, Revista Mexicana de Astronomía y Astrofísica, 46, 29

Röllig, M., Ossenkopf, V., Jeyakumar, S., Stutzki, J., & Sternberg, A. 2006, A&A, 451, 917

Röllig, M., Abel, N. P., Bell, T., et al. 2007, A&A, 467, 187

Roshi, D. A., Goss, W. M., Anantharamaiah, K. R., & Jeyakumar, S. 2005, ApJ, 626, 253

Roshi, D. A., Balser, D. S., Bania, T. M., Goss, W. M., & De Pree, C. G. 2005, ApJ, 625, 181

Rosolowsky, E. W., Pineda, J. E., Kauffmann, J., & Goodman, A. A. 2008, ApJ, 679, 1338

Roueff, E., Lis, D. C., van der Tak, F. F. S., Gerin, M., & Goldsmith, P. F. 2005, A&A, 438, 585

Roueff, E., Herbst, E., Lis, D. C., & Phillips, T. G. 2007, ApJ, 661, L159

Roueff, E., Gerin, M., Lis, D. C., et al. 2013, arXiv:1306.6795

Roueff, E. M., & Petit, F. L. 2005, Astrochemistry: Recent Successes and Current Challenges, 231, 197

Roueff, E., Loison, J. C., & Hickson, K. M. 2015, A&A, 576, A99

Russell, R. W., Melnick, G., Gull, G. E., & Harwit, M. 1980, ApJL, 240, L99

Russell, R. W., Melnick, G., Smyers, S. D., et al. 1981, ApJL, 250, L35

Sánchez-Monge, Á., 2011, PhD Thesis, Universitat de Barcelona, Spain

Sánchez-Monge, Á., Pandian, J. D., & Kurtz, S. 2011, ApJL, 739, L9

Sánchez-Monge, Á., López-Sepulcre, A., Cesaroni, R., et al. 2013, A&A, 557, A94

Sánchez-Monge, Á., Palau, A., Fontani, F., et al. 2013, MNRAS, 432, 3288

Sánchez-Monge, Á., Lopez-Sepulcre, A., Cesaroni, R., et al. 2013, VizieR Online Data Catalog, 355, 70094

Sánchez-Monge, Á., Beltrán, M. T., Cesaroni, R., et al. 2014, A&A, 569, A11

Savage, C., Apponi, A. J., Highberger, J. L., & Ziurys, L. M. 2000, Bulletin of the American Astronomical Society, 32, 712

Savage, C., Apponi, A. J., Ziurys, L. M., & Wyckoff, S. 2002, ApJ, 578, 211

Shaw, G., Ferland, G. J., Abel, N. P., Stancil, P. C., & van Hoof, P. A. M. 2005, ApJ, 624, 794

Shaw, G., Ferland, G. J., Srianand, R., & Abel, N. P. 2006, ApJ, 639, 941

Schilke, P. 1992, Ph.D. Thesis

Schilke, P., Walmsley, C. M., Pineau Des Forets, G., et al. 1992, A&A, 256, 595

Schilke, P., Groesbeck, T. D., Blake, G. A., Phillips, & T. G. 1997, ApJs, 108, 301

Schilke, P., Pineau des Forêts, G., Walmsley, C. M., & Martín-Pintado, J. 2001, A&A, 372, 291

Schneider, S., & Elmegreen, B. G. 1979, ApJs, 41, 87

Schneider, N., Csengeri, T., Bontemps, S., et al. 2010, A&A, 520, A49

Schneider, N., Csengeri, T., Hennemann, M., et al. 2012, A&A, 540, L11

Shu, F. H., Lizano, S., & Adams, F. C. 1987, Star Forming Regions, 115, 417

Shu, F., Najita, J., Galli, D., Ostriker, E., & Lizano, S. 1993, Protostars and Planets III, 3

Seares, F. H., & Hubble, E. P. 1920, ApJ, 52, 8

Seifried, D., & Walch, S. 2015, arXiv:1510.06544

Seifried, D., & Walch, S. 2015, arXiv:1511.01033

Seifried, D., & Walch, S. 2015, MNRAS, 452, 2410

Smith, M. A., Schlemmer, S., von Richthofen, J., & Gerlich, D. 2002, ApJL, 578, L87

Smith, M. A., Schlemmer, S., v. Richthofen, J., & Gerlich, D. 2002, Bulletin of the American Astronomical Society, 34, 1179

Smith, R. J., Glover, S. C. O., & Klessen, R. S. 2014, MNRAS, 445, 2900

Smits, D. P., Cohen, R. J., & Hutawarakorn, B. 1998, MNRAS, 296, L11

Spaans, M., Tielens, A. G. G. M., van Dishoeck, E. F., & Bakes, E. L. O. 1994, ApJ, 437, 270

Spaans, M. 1995, Ph.D. Thesis

Spaans, M., & van Dishoeck, E. F. 1997, A&A, 323, 953

Stahler, S. W., Shu, F. H., & Taam, R. E. 1980, ApJ, 242, 226

Stahler, S. W., Shu, F. H., & Taam, R. E. 1980, ApJ, 241, 637

Stahler, S. W., Shu, F. H., & Taam, R. E. 1981, ApJ, 248, 727

Stahler, S. W., Palla, F., & Ho, P. T. P. 2000, Protostars and Planets IV, 327

Stantcheva, T., & Herbst, E. 2003, MNRAS, 340, 983

Sternberg, A., & Dalgarno, A. 1995, ApJs, 99, 565

Stoerzer, H., Stutzki, J., & Sternberg, A. 1996, A&A, 310, 592

Storey, J. W. V., Watson, D. M., & Townes, C. H. 1979, ApJ, 233, 109

Skrutskie, M. F., Cutri, R. M., Stiening, R., et al. 2006, AJ, 131, 1163

Tackenberg, J., Beuther, H., Henning, T., et al. 2014, A&A, 565, A101

Tafalla, M., Bachiller, R., Wright, M. C. H., & Welch, W. J. 1997, ApJ, 474, 329

Tafalla, M., & Hacar, A. 2015, A&A, 574, A104

Tan, J. C., & McKee, C. F. 2002, Hot Star Workshop III: The Earliest Phases of Massive Star Birth, 267, 267

Tan, J. C., Krumholz, M. R., & McKee, C. F. 2006, ApJL, 641, L121

Tan, Q., Daddi, E., Sargent, M. T., et al. 2013, arXiv:1309.5448

Tan, J. C., Beltrán, M. T., Caselli, P., et al. 2014, Protostars and Planets VI, 149

Tatematsu, K., Umemoto, T., Kameya, O., et al. 1993, ApJ, 404, 643

Taylor, C. L., Brinks, E., & Skillman, E. D. 1993, Evolution of Galaxies and their Environment, 227

Taylor, C., Brinks, E., & Skillman, E. D. 1993, AJ, 105, 128

Tercero, B., Cernicharo, J., Pardo, J. R., & Goicoechea, J. R. 2010, A&A, 517, A96

Teyssier, D., Fossé, D., Gerin, M., et al. 2004, A&A, 417, 135

Teyssier, D., Hily-Blant, P., Gerin, M., et al. 2005, ESA Special Publication, 577, 423

Tielens, A. G. G. M. 1983, A&A, 119, 177

Tielens, A. G. G. M., & Hollenbach, D. 1985, ApJ, 291, 747

Tielens, A. G. G. M., & Hollenbach, D. 1985, ApJ, 291, 722

Tielens, A. G. G. M. 1995, JRASC, 89, 163

Tielens, A. G. G. M. 1995, From Gas to Stars to Dust, 73, 3

Tielens, A. G. C. M. 1997, Diffuse Infrared Radiation and the IRTS, 124, 255

Tielens, A. G. G. M. 2005, The Physics and Chemistry of the Interstellar Medium, by A. G. G. M. Tielens, pp. . ISBN 0521826349. Cambridge, UK: Cambridge University Press, 2005

Tiné, S., Roueff, E., Falgarone, E., Gerin, M., & Pineau des Forêts, G. 2000, A&A, 356, 1039

Thronson, H. A., Jr., Harper, D. A., Keene, J., et al. 1978, AJ, 83, 492

Thronson, H. A., Jr., Gatley, I., Harvey, P. M., Sellgren, K., & Werner, M. W. 1980, ApJ, 237, 66

Treviño-Morales, S. P., Gómez, Y., Rodríguez-Rico, C. A., Garay, G., Rodríguez, L. F., Sánchez-Monge, Á. 2011, Revista Mexicana de Astronomía y Astrofísica Conference Series, 40, 297.

Turner, B. E. 1990, ApJ, 362, L29

Turner, B. E. 1992, ApJ 396, L107

Turner, B. E. 1994, ApJ 420, 661

Turner, B. E. 1994, ApJ 430, 727

Turner, B. E. 1996, ApJ, 468, 694

Turner, B. E. 1996, ApJ, 461, 246

Turner, B. E., et al. 2000, ApJS, 126, 427

Turner, B. E. 2001, ApJS, 136, 579

van den Bergh, S. 1966, AJ, 71, 990

van Dishoeck, E. F. and Black, J. H., 1988, ApJ, 334, 771

van Dishoeck, E. F. and Black, J. H., 1986, ApJs, 62, 109

van Dishoeck, E. F. and Blake, G. A., 1998, A&A, 36, 317

van Dishoeck, E. F., Thi, W.-F., & van Zadelhoff, G.-J. 2003, Ap&SS, 285, 691

van der Tak, F. F. S., Boonman, A. M. S., Braakman, R., & van Dishoeck, E. F. 2003, A&A, 412, 133

van der Tak, F. F. S., Boonman, A. M. S., Braakman, R., & van Dishoeck, E. F. 2003, SFChem 2002: Chemistry as a Diagnostic of Star Formation, 437

Verstraete, L., Leger, A., D'Hendecourt, L., Defourneau, D. and Dutuit, O., 1990, A&A, 237, 436

Viala, Y. P., Letzelter, C., Eidelsberg, M., & Rostas, F. 1988, A&A, 193, 265

Viti, S. 2013, Astrophysics Source Code Library, 1303.004

Viti, S. 2013, Astrophysics Source Code Library, 1303.006

Wakelam, V., Caselli, P., Ceccarelli, C., Herbst, E., & Castets, A. 2004, A&A, 422, 159

Wakelam, V., Castets, A., Ceccarelli, C., et al. 2004, A&A, 413, 609

Wakelam, V., et al. 2010, VizieR Online Data Catalog, 351, 79021.

Wakelam, V., Hersant, F., & Herpin, F. 2011, A&A, 529, A112

Wakelam, V., Smith, I. W. M., Loison, J.-C., et al. 2013, arXiv:1310.4350

Wang, K., Zhang, Q., Testi, L., et al. 2014, MNRAS, 439, 3275

Watson, W. D. 1972, ApJ, 176, 271

Watson, W. D. 1972, ApJ, 176, 103

Ward-Thompson, D. and Whitworth, A. P., 2015, Cambridge, UK: Cambridge University Press

Werner, M. W., Roellig, T. L., Low, F. J., et al. 2004, ApJs, 154, 1

Wilson, T. L., & Rood, R. 1994, ARA&A, 32, 191

Wilson, B. A., Dame, T. M., Masheder, M. R. W., & Thaddeus, P. 2005, A&A, 430, 523

Wright, E. L., Eisenhardt, P. R. M., Mainzer, A. K., et al. 2010, AJ, 140, 1868

Wolf, G. A., Lada, C. J. and Bally, J., 1990, ApJ, 100, 1982

Wolfire, M. G. and Cassinelli, J. P., 1987, ApJ, 319, 850

Wolfire, M. G., McKee, C. F., Hollenbach, D. and Tielens, A. G. G. M., 2003, ApJ, 587, 278

Wolfire, M. G., 2010, Highlights of Astronomy, 15, 409

Wood, D. O. S. and Churchwell, E., 1989, ApJs, 69, 831

Wu et al., 2012, ApJ 746, 175

Xie, T., 1992, PhD Thesis, Massachusetts Univ., Boston.

Xie, T. and Goldsmith, P. F., 1994, ApJ, 430, 252

Yorke, H. W. and Sonnhalter, C., 2002, ApJ, 569, 846

Zinnecker, H. and Yorke, H. W., 2007, A&A, 45, 481

Zhu, Q.-F., Lacy, J. H., Jaffe, D. T., Richter, M. J., & Greathouse, T. K. 2005, ApJ, 631, 381

Zhu, Q.-F., Lacy, J. H., Jaffe, D. T., Richter, M. J., & Greathouse, T. K. 2008, ApJs, 177, 584